



Universidad
Carlos III de Madrid

TESIS DOCTORAL

Behavioral Modeling and Identification of Power Electronics Converters and Subsystems Based on Transient Response

Autor:

Virgilio Valdivia Guerrero

Director/es:

Andrés Barrado Bautista

Antonio Lázaro Blanco

DEPARTAMENTO DE TECNOLOGÍA ELECTRÓNICA

Leganés, Enero 2013

TESIS DOCTORAL

BEHAVIORAL MODELING AND IDENTIFICATION OF POWER ELECTRONICS CONVERTERS AND SUBSYSTEMS BASED ON TRANSIENT RESPONSE

Autor: Virgilio Valdivia Guerrero

Director/es: Andrés Barrado Bautista
Antonio Lázaro Blanco

Firma del Tribunal Calificador:

Firma

Presidente:

Vocal:

Secretario:

Calificación:

Leganés, de de

*A mis padres Adela y Virgilio,
y a Yeny.*

Agradecimientos

A mis directores de tesis, Andrés Barrado y Antonio Lázaro, por la oportunidad que me ofrecieron para poder desarrollar este trabajo, su confianza, consejos y ayuda.

A todos mis compañeros del Grupo de Sistemas Electrónicos de Potencia, por la ayuda que me han ofrecido siempre que lo he necesitado y por todos los buenos ratos que hemos pasado juntos. Una mención especial a Pablo Zumel, por su alegría y por todos los “fast coffees”, de los que siempre he salido con una sonrisa.

A Pablo Rueda y Andrew Forsyth, por la oportunidad ofrecida de realizar estancias en sus respectivos centros de trabajo, en los cuales he desarrollado parte de esta tesis.

A mis padres, Adela y Virgilio, y a mi hermano Alejandro, por su cariño y ánimos todos estos años. Una mención muy especial a mi padre, por su ejemplo y por los valores y principios que me ha transmitido y sin los cuales no habría desarrollado este trabajo.

A Yeny, por estar siempre a mi lado, por su paciencia y su incondicional apoyo, especialmente en los momentos más duros, y sin el cual no habría llegado hasta aquí.

A mis abuelos y tíos, por todo el cariño que me dan cada vez que vuelvo a Almería, y a Carmen y Ramón, por haberme hecho sentir como en casa.

A todos mis amigos, por sus ánimos y por las inolvidables experiencias que hemos vivido juntos estos años

Resumen de la tesis

En la actualidad, los ingenieros eléctricos están haciendo frente a cambios significativos en la manera en que la energía eléctrica se genera y distribuye a los consumidores. Por una parte, el número de cargas eléctricas y electrónicas en los sistemas de distribución de potencia está creciendo significativamente. Los desarrollos en electrónica de potencia durante las últimas décadas permiten la utilización de subsistemas basados en electrónica de potencia como una alternativa a subsistemas mecánicos, hidráulicos y neumáticos. Ello permite obtener sistemas más robustos y ligeros así como menores costes de mantenimiento e impacto medioambiental. Por otra parte, debido al crecimiento de las fuentes de energía alternativas, las cargas en los sistemas de distribución de potencia son suministradas con energía proveniente de múltiples fuentes de energía, tales como baterías, paneles solares, generadores electromecánicos, pilas de combustible, etc.

En consecuencia, los sistemas de distribución de potencia están incorporando más y más convertidores electrónicos de potencia, pasando de las tradicionales estructuras centralizadas a estructuras distribuidas. En estas últimas, una variedad de convertidores interconectados suministran potencia a varias cargas eléctricas y electrónicas, con distintos niveles de tensión y requerimientos dinámicos, desde varias fuentes de energía. Las tendencias actuales en sistemas para aviones, barcos, vehículos híbridos y eléctricos, telecomunicaciones, centros de datos, así como las microrredes ilustran este concepto.

Tal incremento en el número de convertidores de potencia significa un incremento en la complejidad del comportamiento de los sistemas. Interacciones dinámicas entre convertidores regulados, activación de protecciones, conexión y desconexión de cargas y fuentes son algunos problemas a los que los ingenieros deben hacer frente. El modelado y la simulación son herramientas potentes para asegurar buenas prestaciones de los sistemas bajo todas las condiciones de funcionamiento.

Sin embargo, el modelado en electrónica de potencia se ha enfocado tradicionalmente al diseño de los convertidores en sí mismo, en vez de a la integración de sistemas compuestos por múltiples convertidores. La mayoría de las técnicas de modelado dan una descripción detallada de las señales internas de los convertidores, y requieren un profundo conocimiento de la estructura interna de los mismos. Sin embargo, los nuevos sistemas de distribución de potencia están compuestos por convertidores y subsistemas suministrados por una variedad fabricantes. Las compañías necesitan proteger su “know-how”, y debido a ello dan información limitada de sus productos a los usuarios, la cual habitualmente es insuficiente para poder construir un modelo convencional (por ejemplo, un modelo promediado o un modelo conmutado). Por otra parte, utilizar modelos excesivamente detallados suele llevar a tiempos de simulación inaceptables cuando se simulan sistemas de potencia grandes.

Con el fin de hacer frente a esta carencia de modelos, se han propuesto las primeras propuestas de modelado a nivel de sistema de convertidores de potencia en los últimos años. Estos modelos se denominan “modelos comportamentales” debido a que sólo reproducen el comportamiento de las señales de entrada/salida de los convertidores y además no representan en detalle su estructura

interna. Esto permite que puedan ser suministrados por los fabricantes sin revelar información confidencial.

Por otra parte, los modelos comportamentales pueden ser identificados a partir de ensayos eléctricos y medidas de la respuesta de entrada-salida, con lo cual los usuarios pueden obtener modelos de los equipos si el fabricante no los suministra. Sin embargo, por el momento las técnicas existentes se centran en convertidores CC-CC, bien no regulados o con tensión de salida regulada.

El objetivo de esta tesis es proponer nuevas técnicas de modelado e identificación a nivel de sistema para convertidores electrónicos de potencia y otros subsistemas basados en convertidores, que típicamente se integran en arquitecturas de distribución. Las principales características de los métodos propuestos son las siguientes.

- Los modelos no representan detalles sobre la estructura interna del convertidor/subsistema modelado. Los modelos son sencillos y se componen básicamente de funciones de transferencia dinámicas combinadas con funciones estáticas no lineales. Estos modelos reproducen el funcionamiento de gran señal del convertidor/subsistema modelado en términos de las señales requeridas para análisis a nivel de sistema, típicamente tensiones y corrientes de entrada/salida.
- Los parámetros de los modelos se identifican completamente a partir de ensayos experimentales. El método de identificación propuesto está basado en la respuesta transitoria de las señales de entrada/salida de los convertidores/subsistemas ante una serie de ensayos sencillos de tipo escalón. Los tests son sencillos y se pueden llevar a cabo utilizando equipos de bajo coste, tales como interruptores, cargas pasivas y un sistema de adquisición de datos (por ejemplo, un osciloscopio). A partir de la respuesta transitoria, se aplican algoritmos de identificación paramétrica para identificar modelos de función de transferencia.

La tesis está organizada como se indica a continuación.

- **Capítulo 1:** Primero, se realiza una revisión de tendencias actuales en sistemas de distribución de potencia. Después, los principales problemas y preocupaciones a los que se debe hacer frente durante la integración de un sistema se discuten. Finalmente, se describen unos requerimientos generales sobre modelado e identificación.
- **Capítulo 2:** Se lleva a cabo una revisión estado del arte en modelado e identificación a nivel de sistema de convertidores electrónicos de potencia. Tras esto, se discuten las limitaciones de las técnicas existentes.
- **Capítulo 3:** Los puntos clave y los conceptos básicos manejados a lo largo de esta tesis son presentados, y las bases de los métodos de modelado e identificación son establecidas.

En los siguientes capítulos, los métodos de modelado e identificación propuestos se aplican sistemáticamente sobre distintos convertidores electrónicos de potencia y subsistemas basados en los mismos.

- **Capítulos 4 y 5:** En estos capítulos se describen métodos de modelado e identificación para convertidores CC-CC e inversores trifásicos, provistos con cualquier tipo de estrategia de control de la tensión de salida. Estos capítulos abordan una detallada descripción de los métodos de modelado e identificación propuestos en esta tesis. Se presenta además una detallada

validación de los modelos, operando tanto de manera aislada como integrados en sistemas multi-convertidor con otros modelos.

- **Capítulos 6 y 7:** Se trata el modelado e identificación de otros subsistemas basados en electrónica de potencia: pilas de combustible combinadas con convertidores CC-CC con control de corriente de entrada, y simuladores de paneles solares. En el capítulo 7, se discuten además problemas de estabilidad relacionados con el uso de simuladores de panel solar en el diseño de sistemas de potencia para satélites, y dichos problemas se analizan mediante el modelo propuesto.
- **Capítulo 8:** Se plantea un método de modelado e identificación de un arrancador/generador bidireccional de reluctancias conmutadas.

Todos los métodos propuestos son validados experimentalmente. Para ello, se identifican modelos de convertidores/subsistemas experimentales, y su respuesta se compara con la de los modelos ante una variedad de ensayos de validación de gran señal.

Tras esto, se cubren aspectos adicionales sobre la identificación de los modelos. En el **capítulo 9** se presenta un método de identificación de modelos alternativo a los métodos convencionales, basados en algoritmos de optimización. El método consiste en la división de la respuesta transitoria como suma de respuestas básicas de primer y segundo orden, y la identificación de las mismas a partir de ecuaciones sencillas.

A continuación, en el **capítulo 10**, los modelos propuestos y los métodos de identificación se resumen y se plantean de una manera general y sistemática. Ello permite que las técnicas planteadas en esta tesis se puedan adaptar fácilmente para hacer frente a otros convertidores o subsistemas basados en electrónica de potencia.

Finalmente, las contribuciones y conclusiones de la tesis, así como algunos trabajos futuros, son resumidas en el **capítulo 11**. El **capítulo 12** incluye una revisión de los proyectos de I+D relacionados con esta tesis, colaboraciones con otras instituciones y artículos publicados en conferencias y revistas científicas.

Thesis outline

Nowadays, electrical engineers face significant changes in the way the electrical energy is generated and distributed to the consumers. On the one hand, the number of electronic and electrical loads in power distribution systems is continuously growing. Developments in power electronics technology during last decades have enabled the use of power-electronics-based subsystems as an alternative to mechanical, hydraulic and pneumatic subsystems, looking for more reliable and light systems, and a reduction in maintenance costs and environmental impact. On the other hand, due to the growth of alternative energy sources, power distribution systems supply the load not only from a single source but from a variety of energy sources such as batteries, fuel cells, solar panels and electromechanical generators.

Consequently, power distribution systems are incorporating more and more power electronics converters, thus moving from traditional centralized architectures to distributed ones, where a variety of interconnected power converters supply a number of electrical and electronic loads with different voltage levels and dynamic requirements from a variety of energy sources. Current trends in power distribution systems for aircrafts, naval ships, hybrid/electric vehicles, telecommunications, datacenters, satellites as well as initiatives in micro-grids illustrate this concept.

Such increase of power converters means increasing complexity of the power distribution architecture, at system-level rather than at converter-level. Dynamic interactions between regulated converters, activation of protections, connections and disconnections of load and sources are some problems to be faced by system engineers. Hence, modeling and simulation becomes a powerful system integration tool to ensure proper performance of the whole system at all operating conditions.

However, modeling in power electronics have been traditionally focused on the design of the converters itself, rather than the integration of systems comprised of multiple converters. Most modeling approaches provide a detailed description of the internal signals of the power converter as well as requires detailed knowledge of its internal structure. However, new power distribution systems are comprised of a number of power converters provided by a variety of manufacturers. Companies need to protect their know-how, so they provide limited information about their products, which is rarely sufficient to build a conventional average model or switching model. Also, excessively detailed models lead to unacceptable simulation time when large power distribution systems are analyzed.

In order to cope with this lack of models, first proposals on system-level modeling of power converters have been recently proposed. The models are referred to as “behavioral models” since they only reproduces the behavior of the input-output voltages and currents and do not represent in detail the internal structure of the converter. Hence, they can be provided by the manufacturer while keeping confidential information. Moreover, behavioral models can be fully parameterized from a set of experimental measurements by the end user. However, the reported references so far are focused on DC-DC converters, either un-regulated or output voltage-regulated.

The aim of this thesis is to propose novel system-level behavioral modeling and identification methods for several types of power electronics converters and other power-electronics-based subsystems typically integrated in power distribution architectures. The main characteristics of the proposed methods are the following ones:

- The models are fully parameterized from a set of experimental tests and do not represent details about the internal structure of the modeled converter/subsystem. The models are simple, are built using dynamic transfer functions combined with nonlinear static functions, and reproduce the large-signal behavior of the converter/subsystem in terms of the signals required for system-level analysis, typically input-output voltage and currents.
- The proposed identification method is based on the transient response of the input-output signals under a set of step tests. The tests are simple and can be carried out using low-cost equipment: switches, passive loads and a data acquisition system (e.g. an oscilloscope). From the transient response, a parametric identification algorithm is applied to identify transfer function models.

The thesis is organized as follows:

- **Chapter 1.** Current trends in power distribution systems are reviewed. Second, the main problems and concerns to be faced during system integration are discussed. Finally, general system-level modeling and identification requirements are stated.
- **Chapter 2.** The state of the art in system-level modeling and identification of power electronics converters is covered. The limitations of the existing proposals are discussed.
- **Chapter 3.** The key points and concepts managed along this thesis are introduced, regarding modeling and identification. The bases of the proposed methods are established.

The proposed modeling and identification procedures are systematically applied in subsequent chapters on different power converters and power-electronics-based subsystems.

- **Chapters 4 and 5.** Black-box modeling and identification methods for DC-DC converters and three phase voltage source inverters, provided with any output voltage regulation scheme, are covered in this chapter. A detailed description of the techniques is presented, and a comprehensive validation of the models is carried out both, for stand alone operation and when integrated in multi-converter systems with other black-box models. Main features and limitations of the modeling and identification techniques are demonstrated and discussed.
- **Chapters 6 and 7.** Black-box modeling and identification techniques of other power-electronics-based subsystems are described: fuel cells cascaded with input current controlled DC-DC converters, and solar array simulators. In chapter 7, stability issues related to solar array simulators applied to spacecraft power systems are discussed and analyzed by means of the proposed modeling technique.
- **Chapter 8.** A modeling and identification method of a bidirectional switched reluctance starter-generator is developed.

Every proposed model and identification method is experimentally validated. To do so, behavioral model of experimental converters/subsystems are identified by following the proposed method, and

the response of the real converter/subsystem and the identified model are compared under a set of large-signal tests.

Following that, additional aspects on the identification method are covered. An alternative identification method to the usual ones (based on optimization algorithms) is presented in **chapter 9**. It consists in splitting the response as the sum of first and second order basic response, and identifying them by means of simple equations.

After that, in **chapter 10**, a summary of the proposed models and identification experiments is presented. Guidelines toward the generalization of the method are presented, so that the methods can be easily adapted to tackle other power electronics converters and subsystems.

Finally, contributions and conclusions of the thesis, as well as some future works, are summarized in **chapter 11**. **Chapter 12** includes an outline of related R&D projects, collaborations with other institutions and papers published in journals and conferences.

Contents

1	INTRODUCTION.....	1
1.1	Introduction.....	3
1.2	Trends in power distribution systems	3
1.2.1	Telecommunications, computers and datacenters	3
1.2.2	Transportation	5
1.2.3	Distributed generation: microgrids and nanogrids	8
1.3	Integration of multi-converter power distribution systems: main issues	10
1.3.1	Dynamic interactions between power converters.....	11
1.3.2	Integration of protections	13
1.3.3	Power quality: static and dynamic performance	15
1.3.4	Other issues	15
1.4	System-level modeling of multi-converter power architectures	16
1.4.1	General requirements	16
1.4.2	Modeling features.....	17
1.4.3	Identification features.....	18
1.5	Conclusions.....	18
2	MODELING AND IDENTIFICATION IN POWER ELECTRONICS: STATE OF THE ART.....	19
2.1	Introduction.....	21
2.2	Modeling and identification techniques. Classification and concepts.....	21
2.2.1	Modeling techniques	21
2.2.2	Identification techniques	22
2.3	Modeling oriented to converter-level design	23
2.3.1	Switching modeling.....	24
2.3.2	Continuous-time average modeling.....	24
2.3.3	Discrete-time modeling	25
2.3.4	Black-box models.....	25
2.4	Modeling oriented to system-level design	27
2.4.1	G-parameters black-box model	27
2.4.2	Hybrid Wiener Hammerstein grey-box model.....	33
2.4.3	Others	34
2.5	Current lacks in the state of the art	35

2.6	Proposed solution.....	36
3	PROPOSED APPROACH: OVERVIEW AND BASIC CONCEPTS.....	39
3.1	Introduction.....	41
3.2	Modeling concepts.....	41
3.2.1	Selection of the basic model structure: linear approach.....	41
3.2.2	Extending to nonlinear large-signal modeling	43
3.2.3	Simulation based example.....	45
3.3	System identification concepts.....	50
3.3.1	Experimental tests	51
3.3.2	Transfer function models identification: basic approach	52
3.3.3	Cross-coupling effect	53
3.3.4	Simulation based example.....	54
3.4	Summary and overview.....	58
3.4.1	Summary of concepts	58
3.4.2	Overview of the thesis.....	59
4	BLACK-BOX MODELING OF DC-DC CONVERTERS WITH OUTPUT VOLTAGE CONTROL.....	63
4.1	Introduction.....	65
4.2	Model description	66
4.2.1	Description of the modeled converter	66
4.2.2	Model structure	67
4.2.3	Modeling dynamic networks.....	68
4.2.4	Model simplification: merging static and dynamic networks	71
4.2.5	Soft-start and enabling networks modeling.....	73
4.3	Model identification.....	75
4.3.1	Identification step tests.....	75
4.3.2	Parametric identification of transfer function models.....	78
4.3.3	Cross-coupling effects.....	82
4.3.4	Parameterization of the large-signal black-box model.....	86
4.3.5	Overview of the identification procedure.....	87
4.4	Experimental results: modeling of a commercial buck converter.....	89
4.4.1	Introduction	89
4.4.2	Preliminary tests.....	89
4.4.3	Dynamic networks modeling	94
4.4.4	Identification of terminated transfer functions.....	95
4.4.5	Analysis and removal of cross-coupling effects	100
4.4.6	Parameterization of the large-signal model.....	104

4.4.7	Validation	104
4.4.8	Summary	115
4.5	Experimental results: modeling of other commercial converters	116
4.5.1	Forward converter	117
4.5.2	Multi-stage AC-DC converter (output port modeling).....	128
4.5.3	Discussion of results and introduction to model improvements	133
4.6	Experimental results: modeling of a DC distributed power system.....	136
4.6.1	System-level test 1: Step decrease in point-of-load power	137
4.6.2	System-level test 2: Step increase in intermediate-bus power	138
4.6.3	System-level test 3: Dynamic interaction of subsystems	140
4.6.4	System-level test 4: Hot-swap of a point-of-load converter.....	143
4.7	Conclusions.....	145
5	BLACK-BOX MODELING OF THREE-PHASE VOLTAGE SOURCE INVERTERS WITH OUTPUT VOLTAGE CONTROL.....	147
5.1	Introduction.....	149
5.2	Model description: balanced conditions	149
5.2.1	Converter description	149
5.2.2	Model basis: definition of interface signals	150
5.2.3	The synchronous ‘d-q’ reference frame	151
5.2.4	Model structure	153
5.3	Model identification.....	158
5.3.1	Experimental tests	158
5.3.2	Park’s transformation (AC signals only).....	162
5.3.3	Cross-coupling effects.....	163
5.3.4	Parameterization of large-signal black-box model.....	167
5.3.5	Overview of the identification procedure.....	167
5.4	Simplifying the modeling and identification of the output impedance	169
5.4.1	Linear properties	169
5.4.2	Orthogonal properties.....	170
5.4.3	Limitations	172
5.5	Simulation results.....	173
5.5.1	Introduction and system description.....	173
5.5.2	Modeling	175
5.5.3	Identification	178
5.5.4	Validation	184
5.5.5	Summary	188
5.6	Experimental results.....	189

5.6.1	Introduction and system description	189
5.6.2	Modeling	190
5.6.3	Identification	193
5.6.4	Validation.....	202
5.6.5	Summary	207
5.7	Modeling unbalanced conditions: first approach	207
5.7.1	Basic concepts: symmetrical components and d-q-0 transformation.....	207
5.7.2	Extensions of the black-box model	210
5.7.3	Identification of zero-sequence impedance.....	213
5.7.4	Simulation results.....	213
5.8	Conclusions.....	218
6	BLACK-BOX MODELING OF A FUEL CELL POWER SUPPLY BASED ON DC-DC CONVERTER WITH INPUT CURRENT CONTROL.....	221
6.1	Introduction.....	223
6.2	Model description	224
6.2.1	Description of the modeled subsystem.....	224
6.2.2	Model structure	224
6.3	Model identification.....	228
6.3.1	Identification step tests.....	228
6.3.2	Cross-coupling effects.....	232
6.3.3	Transfer functions post-processing	233
6.3.4	Overview of the identification procedure.....	233
6.4	Experimental results.....	235
6.4.1	Subsystem description.....	235
6.4.2	Preliminary tests: linearity analysis	236
6.4.3	Dynamic networks modeling	238
6.4.4	Identification of transfer functions.....	238
6.4.5	Analysis and removal of crosscoupling effects.....	241
6.4.6	Parameterization of the large-signal model.....	242
6.4.7	Model validation	243
6.5	Conclusions.....	247
7	BLACK-BOX MODELING OF SOLAR ARRAY SIMULATORS FOR SPACECRAFT	249
7.1	Introduction.....	251
7.2	Electrical behavior of solar arrays and comparison with solar array simulators	253
7.2.1	Static behavior.....	253
7.2.2	Dynamic behavior	253

7.2.3	Frequency response comparison	254
7.3	Model description.....	256
7.3.1	Small-signal approach	256
7.3.2	Extension to large signal	256
7.4	Model identification.....	257
7.4.1	Identification step tests.....	258
7.4.2	Large-signal model parameterization	259
7.5	Experimental results.....	260
7.5.1	Modeling	260
7.5.2	Identification	261
7.5.3	Validation	263
7.5.4	Summary	266
7.6	Analysis of dynamic interactions between a solar array simulator and a power conditioning and distribution unit for spacecraft.....	266
7.6.1	Operating models and dynamic behavior of the solar array regulator	266
7.6.2	Experimental system description	267
7.6.3	Experimental analysis	268
7.6.4	Prediction of dynamic interactions using black-box models.....	270
7.7	Conclusions.....	272
8	GREY-BOX MODELING OF A SWITCHED RELUCTANCE STARTER GENERATOR.....	273
8.1	Introduction.....	275
8.2	The switched reluctance starter/generator: basic concepts	276
8.2.1	Principle of operation	276
8.2.2	Control strategy	277
8.3	Proposed modeling and identification method.....	279
8.3.1	Basic approach	279
8.3.2	Modeling and identification for the generator operation.....	280
8.3.3	Modeling and identification for the starter operation.....	283
8.3.4	Identification	285
8.4	Experimental results.....	287
8.4.1	System description	287
8.4.2	Generator operation.....	288
8.4.3	Starter operation	297
8.5	Conclusions.....	305

9 SIMPLE IDENTIFICATION METHOD BASED ON SEQUENTIAL CHARACTERIZATION OF LOW-ORDER SUBMODELS.....	307
9.1 Introduction.....	309
9.2 Proposed reduced order transfer function models	309
9.2.1 Modelling of systems with overdamped response	310
9.2.2 Modelling of systems with underdamped response	312
9.2.3 Summary of reduced order transfer function models.....	313
9.3 Sequential identification of submodels	314
9.3.1 Identification of first-order submodel	315
9.3.2 Identification of second-order critically damped submodel.....	315
9.3.3 Identification of second-order under-damped submodel	316
9.3.4 Discussion	316
9.4 Experimental validation.....	316
9.4.1 Output impedance of a DC-DC buck converter	317
9.4.2 Output impedance of a line commutated rectifier	319
9.5 Conclusions.....	321
10 SYSTEMATIZATION OF THE MODELING AND IDENTIFICATION METHODS	323
10.1 Introduction.....	325
10.2 Modeling of unidirectional subsystems.....	325
10.2.1 Systematization of the procedure and review of models.....	325
10.2.2 Deriving models of other subsystems	328
10.3 Identification of unidirectional subsystems	329
10.3.1 Systematization of the procedure and review of proposed methods.....	329
10.3.2 Deriving identification methods of other subsystems.....	333
10.4 Modeling and identification of bidirectional subsystems	334
10.4.1 Revision of proposed model.....	334
10.4.2 Conceptual approach for power converters.....	335
10.5 Conclusions.....	335
11 CONCLUSIONS, CONTRIBUTIONS AND FUTURE WORK	337
11.1 Conclusions and contributions	339
11.1.1 Modeling	340
11.1.2 Identification	342
11.2 Future work.....	343
11.2.1 Modeling	343

11.2.2	Identification	344
12	DIFUSSION OF RESULTS AND RELATED PROJECTS AND COLLABORATIONS..	345
12.1	Publications	347
12.1.1	International Journal Papers	347
12.1.2	International Conference Papers	347
12.1.3	National Conference Papers	348
12.1.4	Other publications on behavioral modeling (not included in this thesis).....	348
12.2	Related Research and Development Projects.....	349
12.2.1	Private Projects.....	349
12.2.2	Public Projects.....	350
12.3	Collaboration with Research Centres and Universities.....	350
A.	APPENDIX	351
A.1.	Mathematical derivation of behavioral models from switching models	353
A.1.1.	Buck converter (chapter 3).....	353
A.1.2.	Three-phase voltage source inverter (chapter 5).....	359
A.2.	Black-box model of buck-boost converter	367
A.2.1.	Converter description	367
A.2.2.	Analysis of linearity	367
A.2.3.	Black-box model parameters.....	368
A.3.	Small-signal stability analysis of power distribution systems	371
A.3.1.	Basics	371
A.3.2.	Stability of intermediate bus architecture (chapter 4)	371
A.3.3.	Stability of spacecraft system involving a solar array simulator (chapter 7)	374
A.4.	Some mathematical aspects about parametric identification	377
A.4.1.	Model structures	377
A.4.2.	Optimization problem	379
B.	REFERENCES.....	385
B.1.	Power distribution systems	387
B.1.1.	Telecommunications, datacenters and computers	387
B.1.2.	The more electric aircraft	387
B.1.3.	Electric vehicles	388
B.1.4.	All Electric Ships	388
B.1.5.	Microgrids and Nanogrids.....	388
B.1.6.	Spacecraft	389
B.2.	Constant Power Loads and system-level stability	389

B.3. System Identification	390
B.4. Modeling and identification of Power Electronics Converters.....	391
B.4.1. Converter-level modeling and identification.....	391
B.4.2. System-level modeling and identification.....	394
B.5. Three Phase Voltage Source Converters	396
B.6. Fuel Cells	398
B.7. Switched Reluctance Starter Generators	398
B.8. Solar arrays and solar array simulators.....	400
B.9. Various.....	400
B.10. Technical notes, datasheets and software tools.....	400

List of acronyms

3JGaAs	Triple Junction Gallium Arsenide
AES	All Electric Ship
ARMAX	Autoregressive Moving Average with Exogenous Input
ARX	Autoregressive with Exogenous Input
APU	Auxiliary Power Unit
ATRU	Autotransformer Rectifier Unit
BJ	Bob Jenkins
BW	Bandwidth
CERTS	Consortium for Electric Reliability Technology Solutions
CF	Clamping Function
CHP	Combined Heat Power
CMC	Current Mode Control
CPL	Constant Power Load
COF	Cost Function
COTS	Commercial off the Shelf
CHP	Combined Heat Power
CMC	Current Mode Control
CPL	Constant Power Load
CSVPWM	Continuous Space Vector Pulse Width Modulation
DCM	Discontinuous Conduction Mode
DFT	Discrete Fourier Transform
DG	Distributed Generator
EADS	European Aeronautic Defence and Space Company
EMF	Electromotive Force
EMI	Electromagnetic Interference
ESR	Equivalent Series Resistor
FC	Fuel Cell
FCS	Flight Control System

FPGA	Field Programmable Gate Array
GS	Gain Scheduled
HVDC	High Voltage Direct Current
IBA	Intermediate Bus Architecture
IGBT	Insulated Gate Bipolar Transistor
LUT	Look up Table
LLMN	Local Linear Models Network
LTI	Linear Time Invariant
LTV	Linear Time Variant
MEA	More Electric Aircraft
MIMO	Multiple Input Multiple Output
MPP	Maximum Power Point
MPPT	Maximum Power Point Tracker
MOSFET	Metal Oxide Semiconductor Field Effect Transistor
PEM	Polymer Electrolyte Membrane
PCU	Power Conditioning Unit
PCDU	Power Conditioning and Distribution Unit
PFC	Power Factor Corrector
PLMU	Power Load Management Unit
PI	Proportional Integral
POL	Point of Load
PSD	Power Spectral Density
PR	Proportional Resonant
PV	Photovoltaic
PWM	Pulse Width Modulation
PRBS	Pseudo-Random Binary Signal
RMS	Root Mean Square
SA	Solar Array
SAR	Solar Array Regulator
SAS	Solar Array Simulator
SISO	Single Input Single Output

SNR	Signal to Noise Ratio
SOGI	Second Order Generalized Integrator
SRM	Switched Reluctance Machine
SRSG	Switched Reluctance Starter Generator
SSPC	Solid State Power Controller
TRU	Transformer Rectifier Unit
VF	Variable Frequency
VMC	Voltage Mode Control
VR	Voltage Regulation
VSI	Voltage Source Inverter
WF	Weighting Function
ZOH	Zero Order Hold

List of symbols

$1\emptyset$	Single Phase
$3\emptyset$	Three Phase
*	Convolution operator
η	Efficiency
η'	Efficiency without considering no-load losses.
φ	Regression vector
θ	Parameters vector
d	Duty cycle
e	White noise
ε	Prediction error
G	Generic transfer function model
G_o	Audiosusceptibility
G_{ref}	Reference to output transfer function or dynamic network
H_i	Back current gain
i_i	Input current
i_L	Inductor current
i_o	Output current
f	Frequency
f_c	Cross-over frequency of loop gain
f_o	Fundamental frequency (only AC signals)
f_{sw}	Switching frequency
J	Moment of Inertia
s	Laplace domain operator
q	Discrete forward shift operator
P_i	Input power
P_{i0}	Input power at no load conditions
P_o	Output power
T_s	Sampling time

T_{load}	Load Torque
$[T]$	Decoupling matrix
$[T_s]$	Simplified decoupling matrix
T_{rm}	'Transimpedance' transfer function
T_{gm}	'Transconductance' transfer function
t_0	Reference time
u	Generic input signal of a dynamic system
v_i	Input voltage
v_o	Output voltage
v_{streg}	Static line and load regulation effects
y	Generic output signal of a dynamic system
Y_i	Input admittance
Y_o	Output admittance
Y_l	Load admittance
Z_s	Source Impedance
Z_o	Output impedance
z	Discrete Z domain operator
ZC_o	Output capacitor impedance
Z_i	Input impedance
ω	Angular frequency (also speed in chapter 8)
ω_o	Fundamental angular frequency
ω_{ref}	Reference speed (chapter 8)

Notation rules for transfer functions and dynamic networks

<i>Subscript 'm'</i>	Terminated transfer function
<i>Subscript 'n'</i>	Normalized transfer function (unity gain)
<i>Subscript 'r'</i>	Reduced order transfer function
<i>Subscript '0'</i>	Transfer function with null response at steady-state
<i>Subscript 'OL'</i>	Open loop transfer function
Brackets	Matrix composed of transfer functions

In addition, subscript includes operating point when required.

Some examples

- $G_o(s)$: Un-terminated audiosusceptibility (de-coupled from the load/source subsystems).
- $G_{om}(s)$: Terminated audiosusceptibility (coupled with load impedance).
- $G_{o0}(s)$: Un-terminated audiosusceptibility with null response at steady state.
- $[G_o(s)]_{dq}$: d - q frame audiosusceptibility matrix comprised of transfer functions $G_{od}(s)$ and $G_{oq}(s)$.

Notation rules for signals

<i>Uppercase signal</i>	Steady-state operating point.
<i>Lowercase signal</i>	Time-varying signal.
<i>Subscript 'p'</i>	Pre-processed signal.
<i>Subscript 'Y', 'G', 'Z' or 'H'</i>	Output of a single dynamic network.
<i>Subscripts 'a', 'b' or 'c'</i>	Coordinate a , b or c for signal mapped into stationary ' abc ' frame.
<i>Subscripts 'α' or 'β'</i>	Coordinate α or β for signal mapped into stationary ' $\alpha\beta$ ' frame.
<i>Subscripts 'd' or 'q'</i>	Coordinate d or q for signal mapped into synchronous ' dq ' frame.
<i>Tilde '~' over a signal</i>	Signal subjected to small-signal perturbation (time domain)*.
<i>Hat '^' over a signal</i>	Predicted output of an identified transfer function model
<i>Arrow '→' over a signal</i>	Vector of signals.

* Tilde symbol is not used when a linearized circuit or dynamic input-output relationship is expressed into Laplace domain.

Some examples

- v_{op} : Output voltage after pre-processing (typically offset subtraction and sometimes pre-filtering).
- V_o : Output voltage operating point.
- \tilde{v}_o : Output voltage subjected to small-signal perturbations (time-domain).
- v_{od} : 'd' coordinate of three-phase voltage mapped into d - q frame (time varying signal).
- i_{iy} : Input current due only to input admittance.

List of figures

Fig. 1-1: Centralized power system with battery back-up [3].	3
Fig. 1-2: Traditional distributed power architecture [3], [4].	4
Fig. 1-3: DC Intermediate bus architecture [3], [5].	4
Fig. 1-4: More electric aircraft power distribution system based on 270 V _{DC} bus [15]-[17].	5
Fig. 1-5: More electric aircraft power distribution system based on variable frequency AC bus [19].	6
Fig. 1-6: Hybrid Electric Vehicle architecture based on high voltage DC bus [24].	7
Fig. 1-7: A Fuel Cell Vehicle Power Distribution System [25].	7
Fig. 1-8: Shipboard integrated power system with zonal architecture [32].	8
Fig. 1-9: CERTS microgrid experimental test bed [35]-[36].	9
Fig. 1-10: DC nanogrid for future homes proposed by the CPES-REN Miniconsortium [39]-[40].	10
Fig. 1-11: Low-frequency constant-power-load behavior of regulated DC-DC converters.	11
Fig. 1-12: Instability of DC power system due to CPL behavior of DC-DC converter.	12
Fig. 1-13: Instability of AC power system due to CPL behavior of AC/DC converter reported in [62].	13
Fig. 1-14: Solid State Power Controller cascaded with a downstream DC-DC converter.	14
Fig. 1-15: Experimental measurements of transient response of commercial SSPCs during connection and disconnection of RC passive load, reported in [15], [174].	14
Fig. 1-16: Dynamic interactions between SSPC current loop and downstream converter reported in [63].	15
Fig. 1-17: Transient specifications for 270 V _{DC} and 115 V _{AC} bus for aircraft given in MIL-STD-704F [263].	15
Fig. 2-1: Identification and modeling options for single-input single-output linear-time-invariant systems.	23
Fig. 2-2: Classical average modeling of the buck converter in continuous conduction mode (CCM).	24
Fig. 2-3: Identification of a nonparametric frequency-response model of a buck converter by applying cross-correlation followed by DFT. PRBS is used as excitation signal. Method proposed in [120], 2005.	26
Fig. 2-4: Typical block-oriented nonlinear models for dynamic systems.	27
Fig. 2-5: Two-port cascaded subsystems represented as input-output networks for implementation in system-level simulators [137]-[139], 1985.	28
Fig. 2-6: Small-signal model of a DC-DC converter using a two-port g-parameters network, [137]-[138], 1985.	28
Fig. 2-7: Modifications on the linear g-parameters model for large-signal nonlinear modeling of DC-DC converters proposed in [144]-[146], 2007-2008.	29
Fig. 2-8: Experimental tests for identification of g-parameters DC-DC converter model reported in [134], [144], 2007.	30
Fig. 2-9: Non-linear hybrid g-parameters model of DC-DC converter, load and source proposed in [149], 2011.	30
Fig. 2-10: Small-signal g-parameters behavioral model of a generic AC-AC converter into synchronous d-q frame reported in [153], 2007.	31
Fig. 2-11: Practical experimental tests for AC impedance measurements through AC sweep into d-q frame, reported in [156], 2009.	32
Fig. 2-12: Practical implementation of an AC impedance measurement equipment into d-q frame, reported in [157], 2011.	32
Fig. 2-13: Hybrid Wiener-Hammerstein Grey-Box model for DC-DC converters reported in [159]-[160], 2006.	33

Fig. 2-14: Behavioral model of a commercial un-regulated isolated DC-DC converter by Vicor Corporation ($V_i = 48$ V, $V_o = 1.5$ V, $I_o = 100$ A) given in the datasheet [173].	35
Fig. 2-15: Main contributions to system-level behavioral modeling of power electronics converters. Inspiring ideas for this thesis are highlighted using green color.	37
Fig. 3-1: Commercial DC-DC power converter [264] analyzed as a two-port input-output network.	41
Fig. 3-2: Linear two-port g-parameters model of a DC-DC converter.	42
Fig. 3-3: General large-signal black-box model of a DC-DC converter with output voltage regulation loop.	43
Fig. 3-4: Dynamic networks modeling.	44
Fig. 3-5: Simplified large-signal model of a DC-DC converter with tightly regulated output voltage.	45
Fig. 3-6: Switching model of an average CMC buck converter.	45
Fig. 3-7: Average model and small-signal model of the average CMC buck converter.	46
Fig. 3-8: Frequency response of $Z_o(j\omega)$ and $G_o(j\omega)$ as a function of V_i .	47
Fig. 3-9: Frequency response of $H_i(j\omega)$ and $Y_i(j\omega)$ as a function of V_i and I_o .	48
Fig. 3-10: Behavioral model of a CMC buck converter.	49
Fig. 3-11: Validation test 1.	49
Fig. 3-12: Validation test 2.	50
Fig. 3-13: Identification experiments of black-box models for DC-DC converters with regulated output voltage: conceptual approach.	52
Fig. 3-14: Parametric identification of a transfer function model from step response: Basic approach.	53
Fig. 3-15: The cross-coupling problem: perturbations of v_i under an output current step.	54
Fig. 3-16: Transient response of the CMC buck converter under an i_o step from 1 A to 2 A with $V_i = 10$ V. Black traces: Simulated response. Grey traces: Filtered response (moving-average-filter).	54
Fig. 3-17: Transient response of the CMC buck converter to a v_i step from 9 V to 9.5 V with $I_o = 1$ A. Black traces: Simulated response. Grey traces: Filtered response (moving-average-filter).	55
Fig. 3-18: Fitting results of $Y_i(q)$, $G_o(q)$, $Z_o(q)$ and $H_i(q)$.	55
Fig. 3-19: Identified models (grey dashed traces) vs theoretical models (black solid traces).	56
a. Schematic and simulated waveforms.	57
b. $H_i(j\omega)$ (black trace) vs $H_{im}(j\omega)$ (grey trace).	57
Fig. 3-20: Cross-coupling effects on $H_i(s)$.	57
Fig. 3-21: Flowchart of the black-box modeling procedure.	58
Fig. 3-22: Overview of the thesis.	60
Fig. 3-23: Power distribution systems comprising the modeled converters and subsystems along this thesis.	61
Fig. 4-1: Generic DC-DC converter with output voltage control.	66
Fig. 4-2: Small-signal black-box model of a DC-DC converter.	67
Fig. 4-3: General black-box model of a DC-DC converter with output voltage control.	67
Fig. 4-4: Output impedance of a DC-DC converter modeled by a transfer function.	69
Fig. 4-5: Audio-susceptibility of a DC-DC converter made up by a local linear models network.	69
Fig. 4-6: Back-current gain of a DC-DC converter modeled by a gain-scheduled transfer function.	70
Fig. 4-7: Simplifying the black-box model of the DC-DC converter in case of nearly constant V_o .	72
Fig. 4-8: Simplifying the black-box model of the DC-DC converter in case of nearly constant V_o , including no-load losses.	73
Fig. 4-9: Modeling soft-start profile of DC-DC converters.	74
Fig. 4-10: Incorporating the soft-start and enabling functionalities into the behavioral black-box model.	74
Fig. 4-11: Flowchart of the proposed identification procedure based on time domain measurements.	75
Fig. 4-12: Identification experiments of black-box models for DC-DC converter with regulated output voltage.	76

Fig. 4-13: Practical implementations of an output current step.....	76
Fig. 4-14: Practical implementations of an input voltage step.	77
Fig. 4-15: Identification procedure of transfer function models from step transient response.....	78
Fig. 4-16: Small-signal equivalent circuits having real DC source and load.	82
Fig. 4-17: Analyzing cross-coupling on $Z_o(q)$. t_{st} : stepping time. t_{ss} : setting time. T_s : sampling time.....	84
Fig. 4-18: Overview of the proposed identification process for large-signal black-box behavioral models of DC-DC converters with output voltage regulation.	88
Fig. 4-19: Black-box modeling of a DC-DC converter with regulated output voltage.	89
Fig. 4-20: Commercial DC-DC step down converter by Texas Instruments PTN78020W.	89
Fig. 4-21: Experimental setup.	90
Fig. 4-22: Transient response under an output current step from 3.85 A to 4.28 A for different input voltage levels.....	91
Fig. 4-23: Transient response under two output current steps with magnitude $\Delta i_o = 0.4$ A from different initial levels, both of them for $V_i = 12$ V.....	92
Fig. 4-24: Transient response under two input voltage steps with magnitude $\Delta v_i = 0.65$ V from different initial levels, both of them for $I_o = 3.92$ A.....	93
Fig. 4-25: Transient response under an input voltage step from 11.7 V to 12.3 V for different current levels.....	94
Fig. 4-26: Black-box model of the commercial converter PTN78020W by Texas Instruments for $V_i \in [8, 16]$ V and $I_o \in [2, 6]$ A.	95
Fig. 4-27: Transient response of the commercial converter PTN78020W to a load current step from 3.3 A to 4.3 A at $V_i = 8$ V.....	96
Fig. 4-28: Pre-filtering v_o with a moving average filter.	97
Fig. 4-29: Fitting results of $Z_{om}(q)$ and $H_{im}(q)$	98
Fig. 4-30: Fitting results $G_{o8m}(q)$ and $Y_{im}(q)$	99
Fig. 4-31: Transient response of the commercial converter PTN78020W to input voltage steps from 11.7 V to 12.3 V and 15.4 V to 16 V at $I_o = 2$ A (only input-output voltages are shown).....	99
Fig. 4-32: Fitting results $G_{o12m}(q)$ and $G_{o16m}(q)$	100
Fig. 4-33: Analysis of cross-coupling effects on identified transfer functions.....	101
Fig. 4-34: Fitting results of $T_{rm}(q)$ and $T_{gm}(q)$	102
Fig. 4-35: Cross-coupling removal results.	102
Fig. 4-36: Hankel singular values of the resulting $H_i(s)$ and $G_{os}(s)$ from the decoupling process.	103
Fig. 4-37: Transfer functions $H_{iL}(s)$ and $G_{os}(s)$ before and after model order reduction.....	104
Fig. 4-38: Efficiency of PTN78020W as a function of I_o and V_i	104
Fig. 4-39: AC sweep test: experimental setup.....	105
Fig. 4-40: Comparison of the AC sweep test results with the frequency response of the transfer functions $Z_{om}(s)$ and $H_{im}(s)$. Solid red line: Transfer functions. Dots: AC sweep test.	106
Fig. 4-41: Comparison of the AC sweep test results with the frequency response of $H_{im}(s)$ as a function of the model order.....	107
Fig. 4-42: Comparison of the AC sweep test results with the frequency response of the identified transfer functions $Y_{im}(j\omega)$ and $G_{o8m}(j\omega)$. Solid red line: Transfer functions. Dots: AC sweep test.....	107
Fig. 4-43: Experimental setup with cross-coupling prevention.....	108
Fig. 4-44: Response of the converter to i_o step from 3.3 A to 4.3 A for $V_i = 8$ V. Blue lines: with cross-coupling prevention (averaged signals in red). Green lines: without cross-coupling prevention (averaged signals in cyan).....	109
Fig. 4-45: Response of the converter to v_i step from 8.05 V to 8.65 V for $I_o = 4$ A. Blue lines: with cross-coupling prevention (averaged signals in red). Green lines: without cross-coupling prevention (averaged signals in cyan).....	109

Fig. 4-46: Fitting results of $H_{iprev}(q)$ and $G_{osprev}(q)$	109
Fig. 4-47: Evaluation of cross-coupling effects after prevention.	110
Fig. 4-48: Frequency response of transfer function models identified with cross-coupling effects (subscript 'm'), after cross-coupling removal (no subscript) and with cross-coupling prevention (subscript 'prev').....	110
Fig. 4-49: Test 1. Large resistive load step under constant input voltage.	111
Fig. 4-50: Validation test 1. Comparison of experimental waveforms (dark traces) and simulation results (grey traces).....	111
Fig. 4-51: Validation test 2. Large input voltage step.	112
Fig. 4-52: Validation test 2. Comparison of experimental waveforms (dark traces) and simulation results (grey traces).....	112
Fig. 4-53: Weighted response of the local linear models $G_{os}(s)$, $G_{o12}(s)$ and $G_{o16}(s)$	113
Fig. 4-54: Validation test 3. Large RC load step while fed from a weak DC bus.	113
Fig. 4-55: Validation test 3. Comparison of experimental waveforms (dark traces) and simulation results (grey traces).....	114
Fig. 4-56: Validation test 4. Experimental setup.	115
Fig. 4-57: Validation test 4. Comparison of experimental waveforms (dark traces) and simulation results (grey traces).....	115
Fig. 4-58: Commercial DC-DC isolated bus converter by Murata UCH-12/12.5-D48NB-C [257].....	117
Fig. 4-59: Experimental setup, with cross-coupling prevention, for linearity analysis and model identification.....	118
Fig. 4-60: Response of the forward converter under output current steps (averaged waveforms in red).	119
Fig. 4-61: Response of the forward converter under input voltage steps (averaged waveforms in red) for different current levels.....	120
Fig. 4-62: Black-box model of the commercial forward converter UCH-12/12.5-D48NB-C by Murata for $V_i = 12$ V and $I_o \in [0, 12.5]$ A.	121
Fig. 4-63: Fitting results of some local linear models for H_i and Z_o	122
Fig. 4-64: Frequency response of $Z_o(j2\pi f)$ and $H_i(j2\pi f)$ at load levels from 0% to 20% of rated power..	123
Fig. 4-65: Frequency response of $Z_o(j2\pi f)$ and $H_i(j2\pi f)$ at load levels from 20% to 100% of rated power.	123
Fig. 4-66: Identification of $Y_i(q)$ and its frequency response for different values of I_o	124
Fig. 4-67: Efficiency of the commercial forward converter, with (blue trace) and without considering no-load losses (green traces) as a function of I_o , for $V_i = 48$ V.....	124
Fig. 4-68: Validation test 1. Large load current step from 4 A to 9 A.....	126
Fig. 4-69: Validation test 1. Experimental results (dark lines, averaged in red) compared to simulation results (grey lines).	126
Fig. 4-70: Validation test 2. Load current step (using electronic load) from 0.5 A to 2.2 A.....	127
Fig. 4-71: Validation test 2. Comparison of experimental measurements (dark lines, averaged in red) and simulation results (grey lines).....	127
Fig. 4-72: Commercial PFC AC/DC converter LPS208-M by Emerson [259].....	128
Fig. 4-73: Testing the response of the AC/DC converter to load current steps.	129
Fig. 4-74: Static load regulation. Measured curve and approximation through a linear function.	129
Fig. 4-75: Model for the output port of the AC-DC converter LPS208-M by Emerson for $V_i = 220$ V _{AC} , 50 Hz and $I_o \in [0, 5]$ A.	130
a. Fitting results for $I_o = 0.25$ A.	131
Fig. 4-76: Fitting results and frequency of local linear models for $Z_o(j2\pi f)$	131
Fig. 4-77: Experimental setup for model validation.	131

Fig. 4-78: Validation test 1. Experimental results (dark lines) compared to simulation results (grey lines).	132
Fig. 4-79: Validation test 2. Experimental results (dark lines) compared to simulation results (grey lines).	132
Fig. 4-80: Validation test 3. Experimental results (dark lines) compared to simulation results (grey lines).	133
Fig. 4-81: Detail of waveforms shown in Fig. 4-82, where the influence of local linear models over the global response is shown.	133
Fig. 4-83: Possible implementation of nonlinear structures made up by weighted local linear models. .	134
Fig. 4-84: Validation test for AC-DC converter model: comparison of experimental measurements (dark traces) with model response using local feedback (grey), and global feedback (red).	135
Fig. 4-85: Validation test for AC-DC converter model, consisting in stepping a resistive load: comparison of experimental measurements (dark traces) with model response using local feedback (grey traces), and global feedback (red traces).	135
Fig. 4-86: DC distributed power system for system-level validation of black-box models.	137
Fig. 4-87: system-level test 1. Step decrease in point-of load converter power.	137
Fig. 4-88: System-level test 1. Comparison of experimental measurements (dark lines, averaged in red) and simulation results (grey lines).	138
Fig. 4-89: System-level test 2. Large step increase in intermediate bus power.	139
Fig. 4-90: System-level test 2. Comparison of experimental measurements (dark lines, averaged in red) and simulation results (grey lines).	139
Fig. 4-91: System-level test 3. Step increase and decrease in intermediate bus power, with a series RL cell interconnected between the front-end converter and the bus converter.	140
Fig. 4-92: System-level test 3.1. Comparison of experimental measurements (dark lines, averaged in red) and simulation results (grey lines).	141
Fig. 4-93: system-level test 3.2. Comparison of experimental measurements (dark lines, averaged in red) and simulation results (grey lines).	142
Fig. 4-94: System-level validation test 4: hot swap connection of the buck-boost converter.	143
Fig. 4-95: Measured soft-start of the buck-boost converter with resistive load at the output.	143
Fig. 4-96: System-level validation test 4. Comparison of experimental measurements (dark lines, averaged in red) and simulation results (grey lines).	144
Fig. 4-97: System-level validation test 4. Detail of the initial transient. Comparison of experimental measurements (dark lines, averaged in red) and simulation results (grey lines).	145
Fig. 5-1: Three phase Voltage Source inverter with LC output filter and voltage regulation.	150
Fig. 5-2: System-level model of the three phase VSI with regulated output voltage.	151
Fig. 5-3: Three phase balanced signals represented into $a-b-c$ frame, $\alpha-\beta$ frame and $d-q$ frame.	152
Fig. 5-4: Small-signal d-q black-box model of three phase VSIs with regulated output voltage (Laplace domain).	153
Fig. 5-5: Large-signal black-box model of three phase VSIs with regulated output voltage.	154
Fig. 5-6: Simplifying the black-box model of the three-phase VSI in case of nearly constant V_{od} , V_{oq} .	156
Fig. 5-7: Simplifying the black-box model of the three-phase VSI including no load losses.	157
Fig. 5-8: Soft-start and enabling networks.	157
a. Input network.	158
b. Output network.	158
Fig. 5-9: Modifications on the input-output networks to be driven by the soft-start networks.	158
Fig. 5-10: Identification procedure of the large-signal black-box model for a three-phase VSI.	158
Fig. 5-11: Identification experiments of black-box models for three phase VSI with regulated output voltage.	159

Fig. 5-12: stepping i_{od} by means of a resistive load switch-on (switch-off is also valid).....	160
Fig. 5-13: stepping i_{oq} by means of a capacitive load switch-off.	160
Fig. 5-14: practical implementations of the v_i step test.	161
Fig. 5-15: Some load configurations and corresponding d - q operating point.	162
Fig. 5-16: Small-signal d-q ‘terminated’ equivalent circuit for the identification tests of a three-phase VSI.	164
Fig. 5-17: Analyzing cross-coupling on $Z_{oddm}(q)$. t_{si} : stepping time. t_{ss} : setting time. T_s : sampling period.	166
Fig. 5-18: Overview of the proposed identification process for large-signal black-box behavioral models of three-phase (3 \emptyset) voltage source inverters (VSIs).	168
Fig. 5-19: Power stage of a three-leg, three-phase VSI with capacitive input filter (plant only).	169
Fig. 5-20: a-b-c frame large-signal average model of the VSI (plant only).	170
Fig. 5-21: d-q frame large-signal average model of the VSI (plant only).	170
Fig. 5-22: simplified equivalent circuit of a VSI with fast inner current controller and a much slower outer voltage controller (only one phase is shown).....	172
Control scheme.....	173
Is Z_o orthogonal?	173
Fig. 5-23: Validation procedure through simulation results.....	174
Fig. 5-24: Three-phase VSI simulated in PSIM (switching model).	175
Fig. 5-25: Frequency response of the output impedance.....	176
Fig. 5-26: Frequency response of the audiosusceptibility.	176
Fig. 5-27: Frequency response of the back-current gain.	177
Fig. 5-28: Frequency response of the input admittance.....	177
Fig. 5-29: Black-box model of the simulated VSI.....	178
Fig. 5-30: Transient response of the simulated VSI to resistive load step from 1.8 kW to no-load (averaged signals in red).....	179
Fig. 5-31: Fitting results of Z_{odd} , Z_{oqd} and H_{id0}	180
Fig. 5-32: Experimental tests and fitting results corresponding to the identification of $H_{id10}(q)$	180
Fig. 5-33: Comparison of identified transfer functions (dashed grey lines) and theoretical ones (solid black traces) from the resistive load steps.	181
Fig. 5-34: Transient response of the simulated VSI to capacitive load step from 1.8 kVAr to no-load (averaged signals in red).....	182
Fig. 5-35: Fitting results of Z_{oqq} , Z_{oqd} and H_{iq}	182
Fig. 5-36: Comparison of identified transfer functions (dashed grey lines) and theoretical ones (solid traces) from the capacitive load switch-off.	183
Fig. 5-37: Transient response of the simulated VSI to an input voltage step at no load conditions (averaged signals in red).....	183
Fig. 5-38: Fitting results of G_{od} , G_{oq} and Y_i	184
Fig. 5-39: Comparison of identified transfer functions (dashed grey lines) and theoretical ones (solid black traces) from the input voltage step.....	184
Fig. 5-40: Validation test 1. Large RL step load with series RL cell at the input.	185
Fig. 5-41: Validation test 1. comparison of switching model response (dark lines) and black-box model response (red lines).....	185
Fig. 5-42: Validation test 2. Step increase in nonlinear load power.....	186
Fig. 5-43: Validation test 2. Comparison of switching model response (dark lines) and black-box model response (red lines).....	186
Fig. 5-44: Validation test 3. Step increase in nonlinear load power.....	187

Fig. 5-45: Validation test 3. Comparison of switching model response (dark lines) and black-box model response (red lines).....	188
Fig. 5-46: Three phase 5 kVA Voltage Source Inverter by <i>Ingeniería Viesca S.L.</i>	189
Fig. 5-47: Schematic of experimental system (part of a MEA test bed).	189
Fig. 5-48: Transient response of the VSI to a resistive load step from 3.3 kW to 4.4 kW ($R_1 = 11\Omega$).	190
Fig. 5-49: Spectral analysis of the steady-state output voltage (d channel) and frequency response of suggested MAF filter for harmonic cancelation.	191
Fig. 5-50: Output voltage v_{od} pre-filtering through MAF with $M = 125$	192
Fig. 5-51: Comparison of transient response to load steps from 1.1 kW to 2.2 kW (black traces) and from 3.3 kW to 4.4 kW (grey traces). Signals pre-filtered through MAF with $M=125$ in red.	192
Fig. 5-52: Black-Box model of the experimental VSI.	193
Fig. 5-53: Transient response to resistive load step from $P_o=2.3$ to 4.5 kW, $Q_o = 0$ kVAr.	194
Fig. 5-54: Fitting results of H_{idm} , Z_{oddm} and Z_{odqm}	194
Fig. 5-55: Transient response to capacitive load step from $Q_o=1.5$ kVAr to 0 kVAr. $P_o = 4.5$ kW. Averaged signals in red.	195
Fig. 5-56: Fitting results of H_{iqm} , Z_{odqm} and Z_{oqqm}	195
Fig. 5-57: Piece of equipment used to carry out input voltage steps, consisting of an array of diodes in parallel with a solid state switch.	196
Fig. 5-58: Transient response to input voltage step (no-load condition).	196
Fig. 5-59: Fitting results of Y_i , G_{od} and G_{oq}	197
Fig. 5-60: Evaluating the cross-coupling effects on Z_{oddm}	197
Fig. 5-61: Evaluating the cross-coupling effects on H_{iqm}	197
Fig. 5-62: Removing cross-coupling effects from H_{iqm}	198
Fig. 5-63: Frequency response of $Y_i(j\omega)$, $H_{id}(j\omega)$ and $H_{iq}(j\omega)$	199
Fig. 5-64: Frequency response of $Z_{odd}(j\omega)$, $Z_{odq}(j\omega)$, $Z_{oqd}(j\omega)$, $Z_{oqq}(j\omega)$ $G_{od}(j\omega)$, $G_{oq}(j\omega)$	199
Fig. 5-65: Global efficiency η and efficiency without considering no-load losses η'	200
Fig. 5-66: Modeling the enabling functionality.	201
Fig. 5-67: Soft-start of the VSI.	201
Fig. 5-68: Modeling the soft-start functionality.	201
Fig. 5-69: Validation test 1.	202
Fig. 5-70: Validation test 1. Comparison of experimental response (dark lines) and black-box model response (red lines).	203
Fig. 5-71: Validation test 2.	203
Fig. 5-72: Black-box model for the output port of the line-commutated rectifier (power level ranging from 0 kW to 4 kW).	204
Fig. 5-73: Validation test 2a. Comparison of experimental response (dark lines) and black-box model response (red lines). Filtered experimental response (using MAF) corresponds to cyan traces.	204
Fig. 5-74: Validation test 2b. Comparison of experimental response (dark lines) and black-box model response (red lines). Filtered experimental response (using MAF) corresponds to cyan traces.	205
Fig. 5-75: Validation test 3.	206
Fig. 5-76: Validation test 3. Comparison of experimental response (dark lines) and black-box model response (red lines).	206
Fig. 5-77: Detail of the i_i under a hot swap to the DC bus: measured (black trace) and simulated (red trace).	207
Fig. 5-78: Symmetrical components decomposition of three-phase unbalanced signals.	208
Fig. 5-79: From balanced to un-balanced conditions in a three-phase three-wire system.	208
Fig. 5-80: From balanced to un-balanced conditions in a three-phase four-wire system.	209
Fig. 5-81: Four wire VSI configuration based on delta-triangle transformer.	210

Fig. 5-82: Equivalent zero-sequence circuit in case of neutral wire tied to a delta-star transformer.	211
Fig. 5-83: Black-box model of a three-phase four-wire VSI with neutral wire tied to the delta-star transformer.	211
Fig. 5-84: Four wire VSI configuration based on split DC link capacitor.....	212
Fig. 5-85: Four-wire VSI configuration based on four-leg power stage.	212
Fig. 5-86: Experimental tests for identification of zero-sequence network.....	213
Fig. 5-87: Validation test. Load step from balanced to un-balanced conditions in a three-wire VSI.....	214
Fig. 5-88: Validation test. Comparison of switching model response (dark traces) and black-box model response (red traces).....	214
Fig. 5-89: Frequency response of the output impedance within d - q , remarking the response at 100 Hz.	215
Fig. 5-90: Modifications done in the simulated VSI when adding a delta-triangle transformer.	216
Fig. 5-91: Transient response of the four-wire VSI under a load step from balanced to unbalanced conditions.	216
Fig. 5-92: Filtering the zero-sequence components through a Notch filter.	217
Fig. 5-93: Identifying the zero-sequence.....	217
Fig. 5-94: Validation test. Comparison of switching model response (dark traces) and black-box model response (red traces).....	218
Fig. 6-1: Fuel cell based power supply tied to a battery bus.	223
Fig. 6-2: Diagram of the modeled subsystem (dashed by red line).	224
Fig. 6-3: Proposed black-box model: basic approach.....	225
Fig. 6-4: Large-signal model of a FC power supply based on DC-DC converter with input current control.	225
Fig. 6-5: Static response of a PEM FC [269].	226
Fig. 6-6: Modeling G_{ref0n} as a gain-scheduled transfer function.....	226
Fig. 6-7: Equivalent model of the PCU for frequencies below the cross-over frequency of the control loop, f_c	227
Fig. 6-8: Modeling the output admittance through a single transfer function.	228
Fig. 6-9: Identification procedure of the black-box model for the fuel cell power conditioning unit.	228
Fig. 6-10: Proposed identification tests. Conceptual approach.	229
Fig. 6-11: Alternative test for identification of Y_o . Conceptual approach.	229
Fig. 6-12: i_{ref} step while v_o is kept constant. Identification of G_{ref}	229
Fig. 6-13: v_o step while i_{ref} is kept constant. Identification of Y_o	230
Fig. 6-14: i_o step while i_{ref} is kept constant. Identification of Z_o , from which Y_o is obtained.	230
Fig. 6-15: Examples of transient response of PEM FCs to current steps, under lack of air flow.....	231
Fig. 6-16: Small-signal terminated equivalent circuit of the FC+PCU subsystem under reference signal step.....	232
Fig. 6-17: Analyzing cross-coupling on $G_{ref}(q)$. t_{st} : stepping time. t_{ss} : setting time. T_s : sampling period.	233
Fig. 6-18: Overview of the identification process for behavioral modeling of subsystem comprised of a FC+PCU. Identification based on output voltage steps.....	234
Fig. 6-19: Overview of the identification process for behavioral modeling of subsystem comprised of a FC+PCU. Identification based on output current steps.	234
Fig. 6-20: Experimental subsystem under study.	235
Fig. 6-21: Black-box modeling procedure.....	236
Fig. 6-22: Step tests. Experimental setups.....	236
Fig. 6-23: Transient response of the FC + PCU to reference signal steps.....	237
Fig. 6-24: Transient response of the FC + PCU to output current steps.....	237
Fig. 6-25: Black-box model of the FC + PCU by Brandner GmbH for $I_{ref} \in [2-8]$ V.....	238
Fig. 6-26: Fitting results of $G_{ref0}(s)$ on two different operating points from i_{ref} steps.....	239

Fig. 6-27: Validation of identification results of $G_{refm}(s)$ at $I_{ref} = 2.75$ V and $I_{ref} = 7.5$ V.	239
Fig. 6-28: Fitting results of $Z_o(q)$ on different I_{ref} levels.	240
Fig. 6-29: Frequency response of $Y_o(s)$ as a function of I_{ref}	240
Fig. 6-30: Analysis of cross-coupling effects.	241
Fig. 6-31: Removing cross-coupling effects and checking results.	242
Fig. 6-32: Frequency response of $G_{refm}(s)$ (6 th order), $G_{ref}(s)$ (12 th order) and $G_{refr}(s)$ (6 th order).	242
Fig. 6-33: Fitting the steady-state response of the converter by a second-order polynomial.	243
Fig. 6-34: Validation test 1. Large reference step under constant output voltage.	244
Fig. 6-35: Validation test 1. Comparison between experimental measurements and simulation results.	244
Fig. 6-36: Validation test 2. Reference signal step followed by battery bus power step.	245
Fig. 6-37: Validation test 2. Comparison between experimental measurements and simulation results.	245
Fig. 6-38: Validation test 3. Resistive load step at constant reference signal.	246
Fig. 6-39: Validation test 3. Comparison between experimental measurements and simulation results.	246
Fig. 6-40: Validation test 4. Triangular reference waveform with resistive load.	246
Fig. 6-41: Validation test 4. Comparison between experimental measurements (dark lines) and simulation results (dark lines).	247
Fig. 7-1: Solar wing of spacecraft (Alphabus) made up by 3JGaAs cells. Photo reported in [241].	251
Fig. 7-2: Power distribution system for spacecraft based on regulated bus architecture.	251
Fig. 7-3: Illustration of dynamic interactions between the SASs and the PCDU as a potential source of system-level stability problems.	252
Fig. 7-4: Static behavior of a SA, well emulated by a SAS.	253
Fig. 7-5: Small-signal response of a SA, not well emulated by a SAS.	254
Fig. 7-6: Experimental setup for small-signal dynamic characterization of solar array simulators.	254
Fig. 7-7: Simplified diagram of the 3JGaAs cell model [241].	255
Fig. 7-8: Comparison between frequency responses of two commercial solar array simulators (a, b) and the simulation model of a 3JGaAs solar array (c).	255
Fig. 7-9: Small-signal black-box models for a SAS.	256
Fig. 7-10: Large-signal black-box models for a SAS.	257
Fig. 7-11: Black-box linear model of SAS (valid for local linear region of the I-V curve).	257
Fig. 7-12: Identification procedure of the black-box model for solar array simulators.	258
Fig. 7-13: Proposed identification tests: conceptual approach.	258
Fig. 7-14: Practical setups to make voltage steps within current region and current steps within voltage region.	259
Fig. 7-15: Black-box model of the experimental SAS referred to as ‘SAS1’.	260
Fig. 7-16: Transient response of SAS1 under step tests, carried out through the array of diodes based setup (Fig. 7-14b), for several operating points.	261
Fig. 7-17: Transient response of SAS1 under step tests, carried out through the array of diodes based setup (Fig. 7-14b), for several operating points (indicated in the subscript of each transfer function name).	262
Fig. 7-18: Comparison of frequency response measured through AC sweep test (dots) with frequency response of the identified transfer function models (solid lines) as a function of the operating point.	263
Fig. 7-19: Comparison between model response (red traces) and experimental measurements (black traces) under small magnitude steps within current region.	264
Fig. 7-20: Comparison between model response (red traces) and experimental measurements (black traces) under small magnitude steps within voltage region.	265
Fig. 7-21: Comparison between model response (red traces) and experimental measurements (black traces) under large magnitude steps.	266

Fig. 7-22: High-level control scheme of a solar array regulator for a spacecraft PCDU based on regulated bus.	267
Fig. 7-23: System under experimental study.	268
Fig. 7-24: Frequency response of SAS2 and SAS3 within voltage region.	268
Fig. 7-25: Transient response of the SAR under a resistive load step from 4.5 W to 12 W and back.	269
Fig. 7-26: Detail of the transient response of the SAR under a resistive load step from 4.5 W to 12 W.	269
Fig. 7-27: ‘Terminated’ output impedance magnitude of the SAR for load power equal to 4.5 W.	270
Fig. 7-28: Transient response of the SAR under a resistive load step from 4.5 W to 28 W and back.	270
Fig. 7-29: Simulation schematic for analysis of dynamic interactions.	271
Fig. 7-30: Transient response of the SAR under a resistive load step from 4.5 W to 28 W and back.	271
Fig. 8-1: A 6 stator poles and 4 rotor poles (6/4) SRM.	276
Fig. 8-2: Three-phase asymmetrical converter for a 6/4 SRM.	276
Fig. 8-3: Idealized phase inductance and phase current of a SRM.	277
Fig. 8-4: Starting process of a gas engine for aerospace.	278
Fig. 8-5: Control scheme of a SRM for aerospace during starting of a gas engine.	278
Fig. 8-6: Control scheme of a SRM for aerospace during generating process.	278
Fig. 8-7: Possible black-box model structures for the starter-generator.	279
Fig. 8-8: Proposed grey-box starter/generator model.	279
Fig. 8-9: Detail of the generator network.	280
Fig. 8-10: Detail of the generator network.	281
Fig. 8-11: Flowchart of the generator network identification.	281
Fig. 8-12: Starter network: basic schematic.	283
Fig. 8-13: Phase current of a SRM reported in [211].	284
Fig. 8-14: Small-signal model of the speed control loop.	284
Fig. 8-15: Detail of the starter network.	285
Fig. 8-16: Proposed estimation method of the total moment of inertia J	286
Fig. 8-17: Proposed identification tests of the speed dynamics network.	287
Fig. 8-18: Experimental system under study.	288
Fig. 8-19: SRSG response under a load step from 15 kW to 20 kW at constant speed $n_m = 7,000$ rpm.	288
Fig. 8-20: Fitting results of $Z_o(q)$	289
Fig. 8-21: Frequency response of the identified output impedance $Z_o(j\omega)$ (dark solid line) and the estimated output capacitor $ZC_{bus}(j\omega)$ (grey dashed line).	289
Fig. 8-22: Estimated machine current i_m	290
Fig. 8-23: Transport delay between the load switching and the beginning of the i_m transient response.	290
Fig. 8-24: Fitting results of $R_v(q)H_v(q)$	290
Fig. 8-25: Frequency response of $R_v(j\omega)H_v(j\omega)$	291
Fig. 8-26: Comparison between the output impedance of the SRSG model (grey dashed line) with the output impedance directly identified from the measured v_{bus} and i_{bus} (dark line).	291
Fig. 8-27: SRSG response under a load step from 15 kW to 20 kW at constant speed $n_m = 7,000$ rpm.	292
Fig. 8-28: Implementation of the generator network for the experimental SRSG.	293
Fig. 8-29: Identified output impedance as a function of the operating point.	294
Fig. 8-30: Validation of the model under generating operation with a passive stepped load.	294
Fig. 8-31 Measured response (dark traces) vs simulated response (red traces) under resistive load steps.	295
Fig. 8-32: Measured response (black traces) vs simulated response (red traces). Resistive load step up from 10 kW to 20 kW and back at $n_m = 15,000$ rpm.	295
Fig. 8-33: Measured response (black traces) vs simulated response (red traces). Resistive load step up from 10 kW to 20 kW and back at $n_m = 15,000$ rpm without the clamping functions CF.	296

Fig. 8-34: Validation of the model under generating operation with a constant power load.	296
Fig. 8-35: Measured response (black traces) vs simulated response (grey traces) under constant power load steps at $n_m = 7,000$ rpm.	297
Fig. 8-36: Constant acceleration test from 0 to 5000 rpm at constant $T_{load} = 15$ Nm.	297
Fig. 8-37: Power losses as a function of load torque T_{load} and speed n_m	298
Fig. 8-38: Speed transient responses at constant load torque.	298
Fig. 8-39: Fitting results of $G_{\omega}(q)$ for $T_{load} = 10$ Nm and $T_{load} = 40$ Nm.	299
Fig. 8-40: Frequency response of the closed-loop speed transfer function, at two operating points. Dark line: $G_{\omega 0}(j\omega)$. Grey line: $G_{\omega \neq 0}(j\omega)$	299
Fig. 8-41: Speed responses for a load torque step at constant reference speed.	300
Fig. 8-42: Fitting results of $G_T(q)$ for $\omega = 1000$ rpm and $\omega = 2000$ rpm.	300
Fig. 8-43: Frequency response of the load torque transfer function, as a function of the operating point given by speed. Dark line: $G_{T2000}(j\omega)$. Grey line: $G_{T1000}(j\omega)$	301
Fig. 8-44: Diagram of speed dynamics block.	301
Fig. 8-45: Validation of the model under motoring operation.	302
Fig. 8-46: Identifying the output impedance of the APU Z_{APU}	302
Fig. 8-47: Frequency response of the APU impedance.	302
Fig. 8-48: Measured response (black traces) vs simulated response (red traces) under a constant acceleration profile of 100 rpm/s at $T_{load} = 8$ Nm, the green trace corresponds to the reference speed.	303
Fig. 8-49: Measured response (black traces) vs simulated response (red traces) under a real starting profile, the green trace corresponds to the reference speed.	304
Fig. 9-1: Overdamped transient response of an average CMC buck converter under a load current step.	311
Fig. 9-2: Fitting the overdamped response of a CMC buck using first-order submodels.	311
Fig. 9-3: Underdamped transient response of a VMC buck converter under a load current step.	312
Fig. 9-4: Fitting the underdamped response of a VMC buck using first-order and second-order submodels.	313
Fig. 9-5: Iterative identification procedure applied on the response of a VMC buck shown in Fig. 9-3.	314
Fig. 9-6: Fitting the output impedance of a buck converter through sequential identification of submodels.	317
Fig. 9-7: Fitting response of a buck converter through a nonlinear optimization algorithm.	318
Fig. 9-8: Comparison of the frequency response of identified models using sequential estimation with the response of a model identified using a nonlinear optimization algorithm: buck converter.	318
Fig. 9-9: Transient response of a 40 kW line commutated rectifier under a load step.	319
Fig. 9-10: Fitting the response of a line commutated rectifier through sequential identification of submodels.	320
Fig. 9-11: Fitting the response of a line commutated rectifier through a nonlinear optimization algorithm.	320
Fig. 9-12: Comparison of the frequency response of identified models using sequential estimation with the response of a model identified using a nonlinear optimization algorithm: line commutated rectifier.	321
Fig. 10-1: Flowchart of the systematic modeling procedure.	325
Fig. 10-2: Deriving behavioral models for DC converters and subsystems.	326
a. Task 1. Determine interface signals (highlighted in blue).	327
b. Task 2. Sort signals as model input and model outputs. Build small-signal model.	327
c. Task 3. Extend to large signal: static networks, dynamic networks and d-q / a-b-c interface.	327
Fig. 10-3: Deriving a behavioral model for three-phase VSI with output voltage control (chapter 5).	327
a. Task 1. Determine interface signals (highlighted in blue).	328
b. Task 2. Sort signals as model input and model outputs. Build a small-signal model.	328

c. Task 3. Extend to large signal: static networks, dynamic networks and $d-q / a-b-c$ interface.....	328
Fig. 10-4: Deriving a behavioral black-box model for a three-phase active front end (AFE) rectifier. ...	328
Fig. 11-5: Flowchart of the systematic identification procedure.....	329
Fig. 10-6: Identification of behavioral model for a DC-DC converter with output voltage control (chapter 4).....	330
Fig. 10-7: Identification of behavioral model for a three-phase VSI with output voltage control (chapter 5).....	331
Fig. 10-8: Identification of DC-DC converter with output voltage regulation.....	332
Fig. 10-9: Identification of behavioral model for a solar array simulator within the whole I-V curve. ...	332
Fig. 10-10: Identification of behavioral model for a three-phase AFE with output voltage control (chapter 5).....	333
Fig. 10-11: Behavioral modeling of a DC starter-generator system.....	334
Fig. 10-12: Conceptual diagram of a behavioral model for a bidirectional DC-DC converter.	335
Fig. 11-1: Overview of main contributions of this thesis.	339
Fig. A-1: Current-Mode-Controlled (CMC) buck converter: switching model.	353
Fig. A-2: Terminal g-parameters black-box model for a DC-DC converter.	353
Fig. A-3: Small-signal model of an average current-mode-controlled DC-DC converter.	354
Fig. A-4: Small-signal model for the buck-converter under CCM.....	354
Fig. A-5: Small-signal model for the control stage of a buck-converter with averaged current mode control.....	356
Fig. A-6: Three-phase VSI simulated in PSIM (switching model).	359
a. Damped PR regulator. SOGI means ‘Second Order Generalized Integrator’.	359
b. PI regulator.	359
Fig. A-7: Discrete voltage and current regulators.	359
Fig. A-8: Terminal d-q g-parameters black-box model for a three-phase Voltage Source Inverter.....	360
Fig. A-9: d-q frame small-signal model of a three-phase VSI comprised of double loop control scheme.	360
Fig. A-10: Small-signal $d-q$ model of a three-phase Voltage Source Inverter (power stage only).	361
Fig. A-11: Small-signal model of the control stage into $\alpha-\beta$ coordinates.	362
Fig. A-12: Commercial DC-DC buck-boost converter by Texas Instruments PTN78020A [256].	367
Fig. A-13: Bode plot of $Y_i(j\omega)$ and $G_o(j\omega)$ for $I_o=0.5$ A, 2.25 A and 4 A.	368
Fig. A-14: Bode plot of $Z_o(j\omega)$ and $H_i(j\omega)$ for $I_o=0.75$ A, 2.25 A and 3.75 A.....	368
Fig. A-15: Black-box model of the buck-boost converter PTN78020A for $V_i = 12$ V and $I_o \in [0.5- 4]$ A.	369
Fig. A-16: Transient response of the commercial POL buck-boost converter as a function of I_o	369
Fig. A-17: Interconnected source subsystem and load subsystem.....	371
Fig. A-18: Diagram of the interconnected system.....	372
Fig. A-19: Response of the system to an step in load current from $I_{bus} = 3.5$ A to $I_{bus} = 9.3$ A.....	372
Fig. A-20: Equivalent circuit made up by black-box models, particularized for constant bus current I_{bus}	373
Fig. A-21: Analysis of system-level stability.	374
Fig. A-22: System under experimental study.	374
Fig. A-23: Transient response of the SAR under a resistive load step from 4.5 W to 28 W and back.....	375
Fig. A-24: Frequency response characterization of the subsystem impedances and obtained results.....	375
Fig. A-25: Nyquist diagram $L(j2\pi f)$ from experimental measurements for $f \in (10$ Hz, 10 kHz).....	376
Fig. A-26: Equation error family of models.	378
Fig. A-27: Output error family of models.	379

List of tables

Table 2.1: Classification of models as a function of physical meaning and available information.	22
Table 2.2: Summary of current contributions on system-level behavioral modeling of power electronics converters based on system identification, indicating main features and lacks.	36
Table 3-1. Comparison of simulation times as a function of the converter model using PSIM.....	57
Table. 5.1: Examples of control schemes for VSI and related orthogonal properties.....	173
Table 9.1 Reduced-order models for the output port of a DC-DC converter.....	313

1 Introduction

1.1	Introduction.....	3
1.2	Trends in power distribution systems	3
1.2.1	Telecommunications, computers and datacenters	3
1.2.2	Transportation	5
1.2.2.1	The More Electric Aircraft	5
1.2.2.2	Electric, Hybrid Electric, Plug-in Hybrid Electric and Fuel Cell Vehicles	6
1.2.2.3	All Electric Ships.....	7
1.2.3	Distributed generation: microgrids and nanogrids	8
1.3	Integration of multi-converter power distribution systems: main issues	10
1.3.1	Dynamic interactions between power converters.....	11
1.3.1.1	DC bus	11
1.3.1.2	AC bus	12
1.3.2	Integration of protections	13
1.3.3	Power quality: static and dynamic performance	15
1.3.4	Other issues	15
1.4	System-level modeling of multi-converter power architectures	16
1.4.1	General requirements	16
1.4.2	Modeling features.....	17
1.4.3	Identification features.....	18
1.5	Conclusions.....	18

1.1 Introduction

The aim of this chapter is to present an overview of current trends and challenges in distributed power systems, as well as to discuss the need for new system-level modeling and identification techniques for power electronics converters and other subsystems.

This chapter is organized as follows.

- Section 1.1 presents an overview of current trends in power distribution systems, focusing on telecommunications, computers, transportation and utility grid applications, where the architectures are evolving from centralized to distributed ones.
- Section 1.2 discusses the main issues and challenges related to the integration of distributed power systems, such as system-level stability assessment.
- Section 1.3 introduces the modeling requirements for integration of new power distribution systems. The characteristics of a system-level model are drawn, and the need for identification methods is justified as well.

1.2 Trends in power distribution systems

1.2.1 Telecommunications, computers and datacenters

In the past, most power distribution systems were based on a centralized architecture. Centralized architectures are those comprised of a single power converter that delivers power to the loads through multiple outputs and buses [1]-[3]. Telecommunications is a segment where centralized architectures have been typically used. Fig. 1-1 shows a traditional system with battery back-up that was dominant until mid 80s. A -48 V bus is supplied by a rectifier/charger unit and back-up batteries, and then a DC-DC converter provides +5 V and ± 12 V buses to supply electronic loads [3].

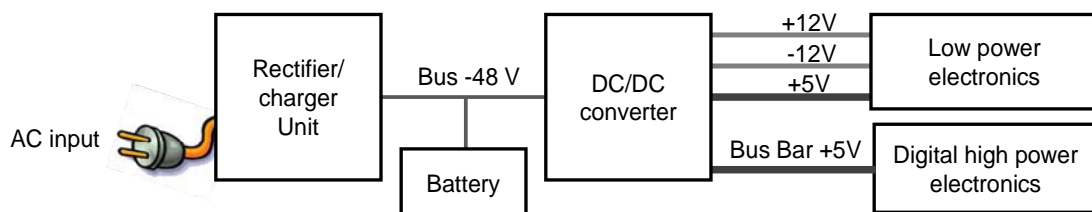


Fig. 1-1: Centralized power system with battery back-up [3].

Centralized architectures integrate power processing technology, thermal management, control, protection, etc. into a single unit that can be purchased or manufactured as a stand-alone system. However, centralized power architectures have the following drawbacks, among others:

- Centralized power supplies typically require customized design, meaning long time-to-market and lack of flexibility.
- Failure of the converter means failure of the whole system.
- Static and dynamic regulation of DC voltage is poor.

In early 90s, distributed power architectures emerged as an alternative to centralized ones [1]-[8]. Distributed architectures comprise a multi-converter network, where the loads are supplied by a

number of small power converters which are distributed throughout the system, typically trying to perform the power processing close to the load. Distributed power systems were primarily developed for telecommunications and computer applications. A traditional distributed power architecture for telecommunication is shown in Fig. 1-2, where isolated DC-DC converters supply each load from the -48 V bus.

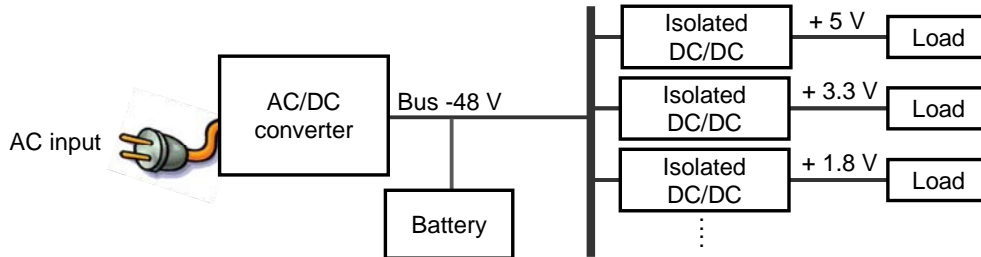


Fig. 1-2: Traditional distributed power architecture [3], [4].

Compared to centralized architectures, distributed ones offer the following advantages, among others:

- The modularity of the system permits easy reconfiguration and flexibility. Optimized commercial off-the-shelf (COTS) converters can be combined to make up a system, thus reducing dramatically the time-to-market as well as the development cost.
- Parallel configurations allow for on-line replacement (hot-swapping) of damaged converters, so the system can be maintained in a non-interrupting way.
- Redundancy can be easily added by using more modules than is required to deliver the load power.
- Cascaded power converters allow de-coupling between load and source dynamics, so modern microprocessor can be supplied with a very low voltage and extremely high dynamic response.

Other remarkable architecture is the intermediate bus architecture (IBA), which has been adopted by the market since early 2000s [3], [5], [6]. An example of IBA for telecommunication is shown in Fig. 1-3, where an isolated bus converter creates an intermediate regulated or unregulated 12 V bus from the 48 V bus.

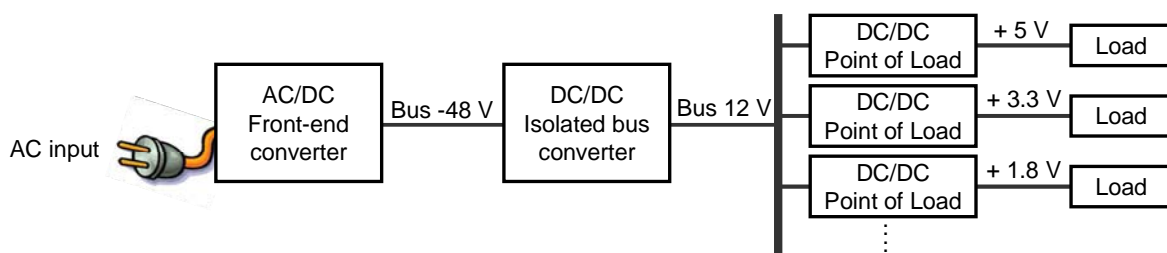


Fig. 1-3: DC Intermediate bus architecture [3], [5].

In Fig. 1-3, point-of-load (POL) converters are tied to the intermediate bus and supply each load with the corresponding voltage level and demanded dynamic performance. As the isolation is provided by the bus converter, non-isolated POL can be used to supply low-voltage electronics with reasonable duty cycle.

1.2.2 Transportation

Recently, distributed power systems are being adapted in emerging technologies for transportation such as the More Electric Aircraft, All-Electric-Ships and Electric/Hybrid-Electric Vehicles [6]. These systems include multiple energy sources, energy storage units and numerous passive and active loads that can be not only DC but also AC. Then, multiple power electronics converters are required to distributed power throughout the system with the required performance.

1.2.2.1 The More Electric Aircraft

Aircraft power systems are facing major changes. Since early 90's, intensive research has been carried out toward the 'More Electric Aircraft' (MEA). Onboard electrical equipment is being introduced to drive loads that have conventionally been supplied by pneumatic, hydraulic or mechanical means. Some loads are the flight control system, anti-icing system, environmental system, air conditioning system, fuel pumps, weapon systems and landing gear. MEA leads to improvements in efficiency and reliability while weight, size, maintenance cost and environmental impact are reduced [9]-[15].

The increase in onboard electrical power leads to the introduction of new voltage levels. Besides the traditional 28 V_{DC} and 115 V_{AC} levels, 270 V_{DC} , $\pm 270\text{ V}_{\text{DC}}$ and 230 V_{AC} buses are being introduced. Fig. 1-4 depicts a simplified schematic of the power distribution system developed in the High-Voltage-Direct-Current (HVDC) technological project by EADS [15]-[17]. This architecture comprises a primary 270 V_{DC} bus, a 28 V_{DC} bus and a 115 V_{AC} bus. The primary bus can be supplied by 270 V_{DC} generators and the auxiliary power unit (APU), which is based on a fuel cell. High voltage and low voltage batteries are used as energy storage units.

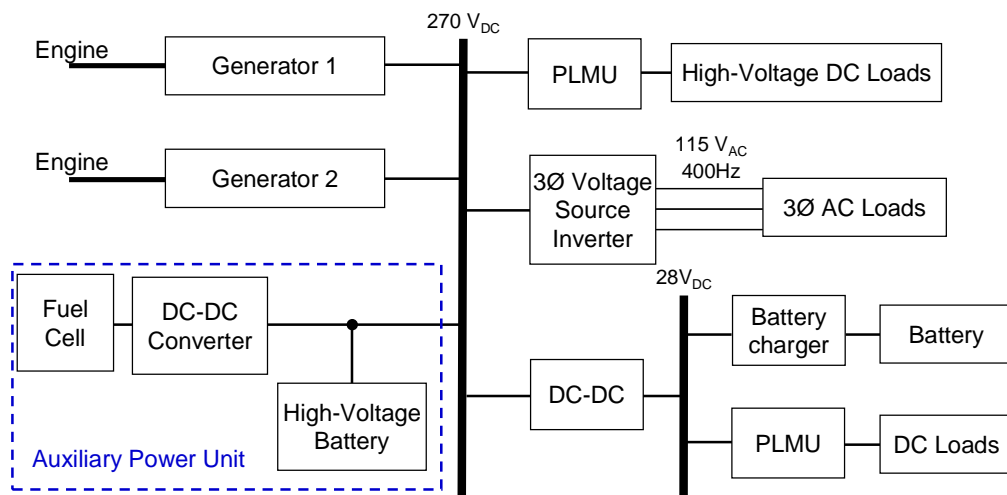


Fig. 1-4: More electric aircraft power distribution system based on 270 V_{DC} bus [15]-[17].

In Fig. 1-4, the power is distributed throughout the system through DC-DC converters and a three-phase ($3\emptyset$) Voltage Source Inverters (VSIs), and the DC loads are managed through power load management units (PLMUs), which are comprised of new Solid State Power Controllers (SSPCs) [15], [18]. New power systems for military aircrafts are based on a 270 V_{DC} distribution. For instance, the new F-22 system is based on 270 V_{DC} buses besides 28 V_{DC} and 115 V_{AC} buses [15].

Besides 270 V_{DC} distribution, power systems based on variable-frequency (VF) 230 V_{AC} bus are also being developed. VF generators are being introduced to replace the conventional constant-

frequency generator in order to remove the integrated driver-generator, which is costly to maintain [19]. A conceptual diagram of a power system based on a variable frequency AC bus, reported in [19], is shown in Fig. 1-5. Updated power quality standards require the use of autotransformer rectifier units (ATRUs), or PWM rectifiers with active power factor correction cascaded with inverters to feed the motors. Single phase ($1\emptyset$) AC loads, that represent in flight entertainment systems among others, are also tied to the bus through $1\emptyset$ Power Factor Correctors (PFCs). Transformer Rectifier Units (TRUs) and DC-DC converters are used to interface the VF AC and the 28 V_{DC} buses, where additional DC-DC converters deliver powers to DC loads such as avionics, communications, etc.

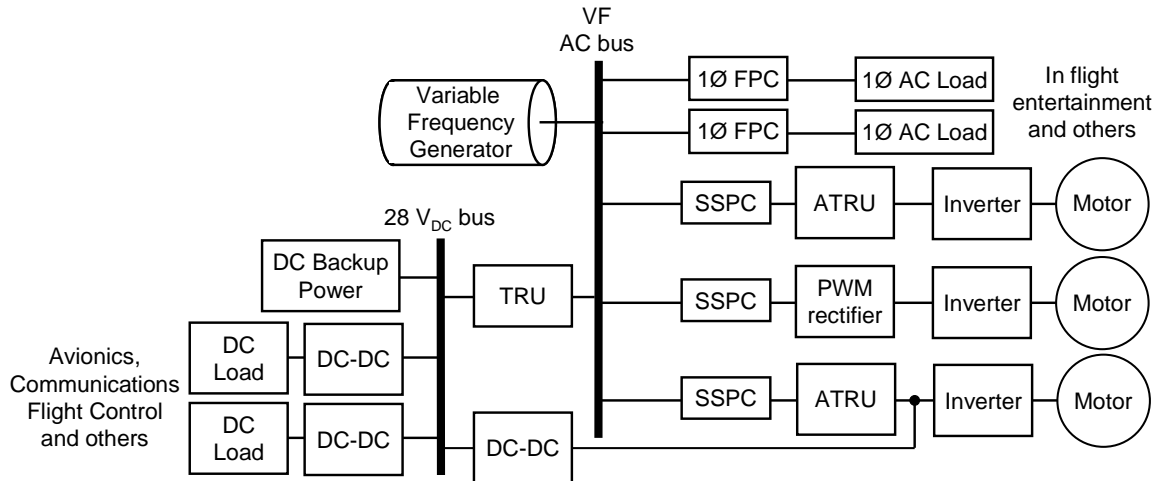


Fig. 1-5: More electric aircraft power distribution system based on variable frequency AC bus [19].

New power distribution systems for some passenger airplanes are based on 230 V_{AC} distribution. For instance, Boeing B-787 is based on a hybrid DC/AC architecture comprised of a 230 V_{AC} , 270 V_{DC} , 28 V_{DC} and 115 V_{AC} buses [15], [20].

1.2.2.2 Electric, Hybrid Electric, Plug-in Hybrid Electric and Fuel Cell Vehicles

Automotive industry is also facing important changes in the power distribution architectures. Environmental concerns and fuel economy are motivating companies to develop Electric Vehicles, Hybrid Electric Vehicles and Plug-In Hybrid Electric Vehicles [9], [21]-[27]. Similarly to the MEA, mechanical and pneumatic systems are being replaced by more electrical systems and new advanced electrical loads are being introduced as well. These include pumps, fans, electric motors, air conditioner/compressors, electromechanical valve control, anti-lock braking, throttle actuation, etc. [24].

A modern hybrid vehicle can handle up to ten times more electrical power than a conventional one. Consequently, higher bus voltage levels are required. Power distribution architecture for a hybrid electric vehicle, reported in [24], is depicted in Fig. 1-6. This structure comprises a high-voltage regulated bus, that could be about 300 V , and a low-voltage regulated bus. High voltage and low-voltage batteries are interfaced through bidirectional converters. On the other hand, a starter/generator system, cascaded with a bidirectional converter, allows starting the engine and subsequently delivering power to the system. As can be seen, this type of systems comprises a network of parallel and series interconnected unidirectional and bidirectional converters.

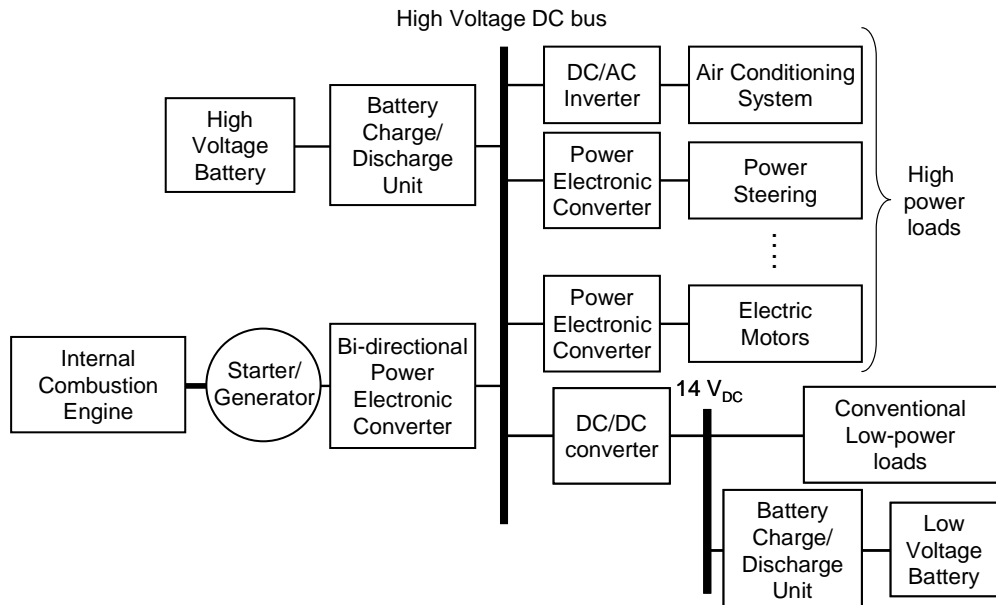


Fig. 1-6: Hybrid Electric Vehicle architecture based on high voltage DC bus [24].

Research is also being carried out in fuel cell (FC) electric vehicles, as they produce much less pollution than vehicle based on internal combustion engines, has no moving parts and are more quiet, among other advantages [25]-[27]. Fig. 1-7 depicts the power distribution architecture for a FC vehicle reported in [25]. A DC-DC converter performs the FC power control, as a function of the power system requirements, and delivers power to an un-regulated battery bus. A DC-AC inverter performs the voltage conversion into variable frequency AC to power the propulsion motor. Proton Exchange Membrane (PEM) is the most popular FC technology for vehicular applications.

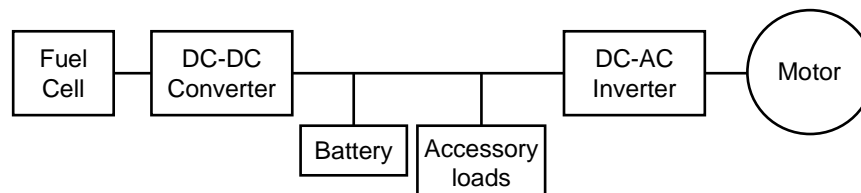


Fig. 1-7: A Fuel Cell Vehicle Power Distribution System [25].

1.2.2.3 All Electric Ships

Conventional military vessels have two set of engines. One set is used for vessel propulsion through a mechanical drive system and the other set is connected to electrical generators that supply electrical loads [28]. The on-board electrical power is about few megawatts, which is used to power ships services and other loads with relatively low electric consumption [29].

Today, research is being carried out toward the replacement of conventional mechanical drive propulsion systems with electrical drive ones. A single set of engines will provide propulsion power and simultaneously will supply the on-board electrical loads, such as service loads and advanced weaponry loads. This will constitute the so-called integrated power system for naval ships.

The introduction of electrical drive propulsion system, together with the conversion of auxiliary systems that are currently powered mechanically, hydraulically or pneumatically into electrical power, lead to the All Electric Ship (AES) concept [9], [28]-[32]. This means an increase in on-board

electrical power to tens of megawatts [29]. It is expected that electric drive technology in AESs will reduce life-cycle cost, increase energy efficiency and enhance survivability and reliability.

Zonal architectures have been introduced in the AES as an alternative to conventional radial distribution systems. Two main buses are used to provide redundant power flow to vital loads, whereas non-vital loads are powered from one bus. A shipboard integrated power system with zonal architecture based on two primary DC buses, reported in [32], is depicted in Fig. 1-8. As can be seen, it is a large hybrid AC/DC electrical network comprised of many power conversion, power generation, electric propulsion and energy storage modules, which deliver power to vital and non vital loads. Power generation modules could be constituted by gas turbines, diesel engines or FCs.

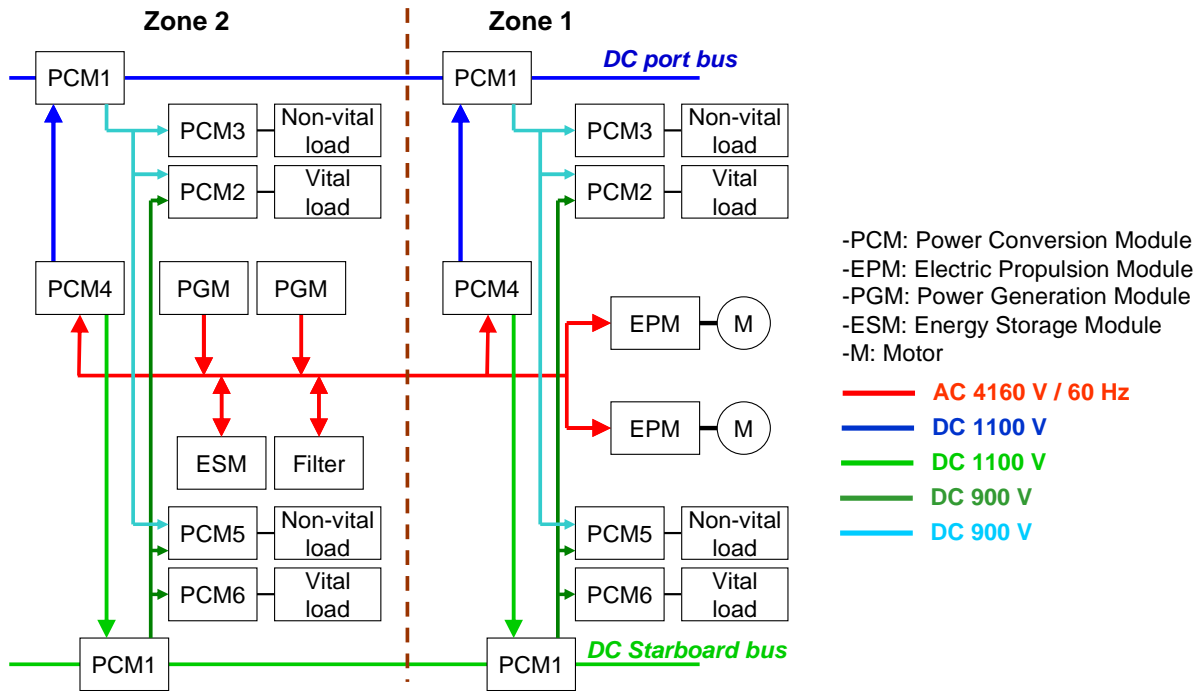


Fig. 1-8: Shipboard integrated power system with zonal architecture [32].

Power Electronics Building Blocks, which are general purpose converters that can perform different conversion function through software reconfiguration, play an important role in AESs [6]. Those allow for dynamic reconfiguration of the system by redirecting the power flow in real time scenarios [32].

1.2.3 Distributed generation: microgrids and nanogrids

The conception of power distribution into the electrical grid is also evolving. During the last years, distributed generators (DGs), such as wind turbines, photovoltaic (PV) panels or combined heat power (CHP) equipment, have been penetrating in the electricity distribution grid. Those allow a substantial reduction of carbon emissions and fossil fuel dependence. However, DGs mean that the electrical grid is powered by many small power generators together with the conventional large generators (nuclear, fossil fuel, gas, etc.). From the point of view of the grid operator, this opens new challenges in terms of control and operation of the system, which can be addressed by means of microgrids [33]-[38].

Essentially, a microgrid is an autonomous energy distribution network comprised of small local energy generators, storage units and loads. A microgrid typically would not exceed the megawatt range and can operate either tied to grid or in islanded mode. Microgrid offer important recognized benefits such as the following ones:

- Enhanced local reliability thanks to its islanding capabilities. The microgrids can be isolated seamlessly to the main grid in case of external fault, providing uninterrupted power supply to the local consumers.
- Distribution efficiency and power quality are improved thanks to the use of CHP generation, the proximity of local generators and consumers, and the use of power electronics converters to interface the DGs and storage units with the rest of the microgrid.
- Environmental benefits thanks to the use of low or zero emission generators.
- From the point of view of the grid operator, the whole microgrid is a single element: either a generator (more power is delivered by the DGs than requested by the loads) or a load (on the contrary case).

Several technological projects have been and are being undergone on microgrids [34], [35]. Fig. 1-9 illustrates a microgrid developed under the Consortium for Electric Reliability Technology Solutions (CERTS) [34], [36].

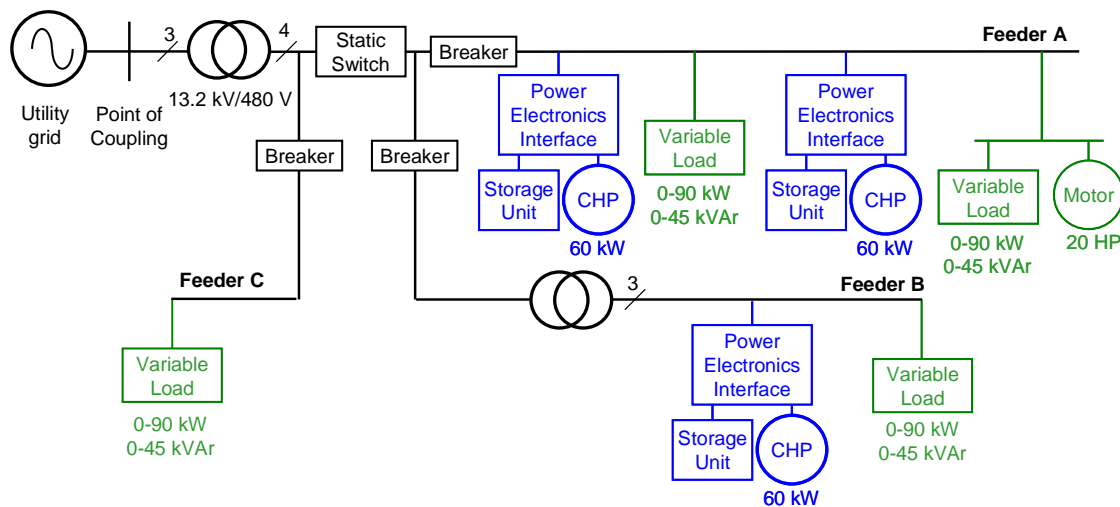


Fig. 1-9: CERTS microgrid experimental test bed [35]-[36].

The microgrid in Fig. 1-9 comprises three feeders named ‘A’, ‘B’ and ‘C’. The feeders A and B include DGs as well as critical loads, whereas the feeder C includes noncritical loads. Under a grid problem, the feeders A and B are islanded from the utility grid by means of a static switch, while the non-critical loads on the feeder C ride through the event. Each DG consists of a CHP generator and a storage unit that are interfaced using power electronics converters.

The CERTS microgrid architecture features a plug-and-play decentralized approach. Each DG has a localized controller so that there is no need of a master control for the dynamic operation of the microgrid. This allows expanding the microgrid without extensive re-engineering. Moreover, adding one additional source, complete functionality can be assured in case of losing any DG.

Looking at a smaller scale, the microgrid concept can be applied at building level. Then, it may be called a nanogrid (less than 100 kW) [39]-[40], where loads are powered by a mix of small-scale DGs and storage units. Going further, in the future distribution at the home-level could be done in DC, avoiding frequency stability concerns and AC losses, and simplifying the power electronics.

Fig. 1-10 shows the conceptual DC nanogrid for future homes, proposed under the Center for Power Electronics Miniconsortium for Renewable Energy and Nanogrids [39]-[40]. DC distribution allows reducing the number of power stages used to interface the generation and storage units with the main bus. Moreover, many home loads are more conveniently powered by DC. Then, a 380 V_{DC} can be chosen to match the standard intermediate DC voltage in typical appliances with PFC stage, so they can be powered just by bypassing the PFC. Following a similar concept, secondary 48 V_{DC} bus could be generated to supply consumer electronics such as TV and computers.

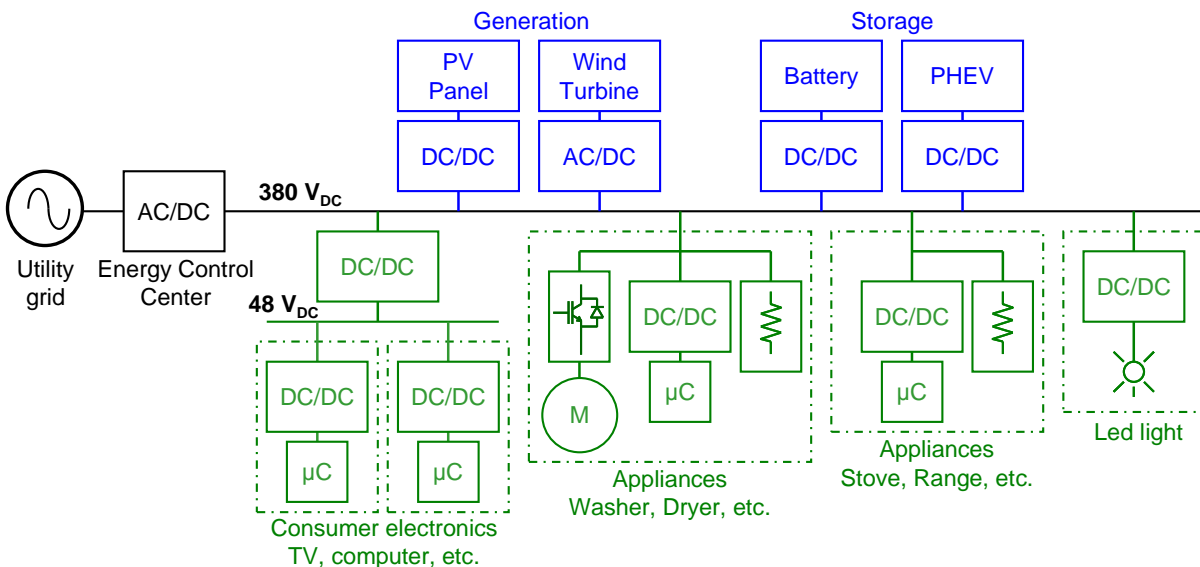


Fig. 1-10: DC nanogrid for future homes proposed by the CPES-REN Miniconsortium [39]-[40].

In Fig. 1-10, an AC/DC converter serves as energy-control-center and interfaces the utility grid with the nanogrid. It communicates with the grid operator for trading purposes and de-couples dynamically the nanogrid from the rest of the grid, among other features.

Nanogrids could be combined to form a microgrid, which at the same time can be combined to form a higher-level grid and so on, yielding the concept of ‘intergrid’ described in [41]-[42].

1.3 Integration of multi-converter power distribution systems: main issues

As described above, there is a clear trend in power distribution systems toward complex architectures where multiple electrical loads, power sources and storage units are interconnected throughout a number of DC and AC distribution buses. Hence, a network of power electronics converters is required to distribute power with appropriate performance. These include DC-DC, DC-AC, AC-DC and AC-AC converters, which can be unidirectional or bidirectional and can be interconnected in series or parallel.

However, the integration of a multi-converter distribution network presents several challenges that the system designer must address. In this section some of them are described, focusing on dynamic aspects.

1.3.1 Dynamic interactions between power converters

1.3.1.1 DC bus

Power converters are not only ‘electronic transformers’, but also active subsystems that can regulate voltage, current or power at the input or the output port. Thereby, power converters allow for **dynamic decoupling between loads and sources** [39]. For instance, POL converters supplies microprocessors with demanding dynamic performance from slower DC bus.

However, the active nature of power electronic converters results in complex dynamic behavior when they are interconnected to each other. To understand this concept, let consider the IBA previously shown in Fig. 1-3, which is particularized in Fig. 1-11. The POL converter is provided with a control loop which regulates the duty cycle so that, under steps in load power or disturbances in the intermediate bus, the output voltage is rapidly restored to 5 V. As a consequence, the POL output and the intermediate bus are dynamically decoupled.

Suppose that the intermediate bus is disturbed. For frequencies well below the cross-over frequency of the POL control loop ($f \ll f_c$), the duty cycle will be readjusted so that the output voltage is kept constant. Thereby, the power delivered to the microcontroller is constant and, due to the power balance, the input power is constant as well. Consequently, the POL behaves as a **constant power load (CPL)**.

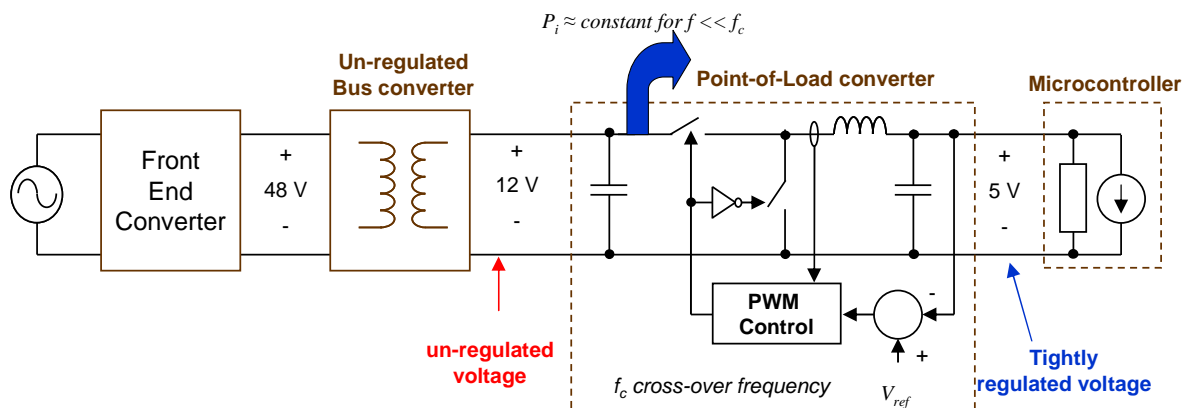


Fig. 1-11: Low-frequency constant-power-load behavior of regulated DC-DC converters.

Dynamically, a CPL has critical consequences. By applying small-signal perturbations, it is easy to find out that a CPL behaves as an incremental negative resistor. A negative resistor is a destabilizing element, since it tends to amplify oscillations instead of damping them. As a consequence, if the interface between the bus converter and the POL converter is not properly damped, the interconnected system can be unstable [52]. Summarizing, **two converters that are stable in stand alone conditions can become unstable when interconnected to each other.**

In order to illustrate this problem, a simplified equivalent circuit of the system shown in Fig. 1-11 has been simulated. The POL converter have been controlled using Current-Mode-Control (CMC)^{1.1}, the bus converter has been simply modeled using an ideal transformer in series with an LC filter, and the front-end converter has been modeled as an ideal DC source. The input filter of the POL converter has not been properly damped in order to intensify the dynamic interactions between converters.

The response of the system under several steps in load current has been simulated. As can be seen in Fig. 1-12, the system remains stable after the first step, although a significant oscillation is evidenced in the intermediate bus. However, after the second step the dynamic interactions are intensified, leading to instability. It is interesting to note the dynamic decoupling between v_i and v_o , which is due to the POL control loop.

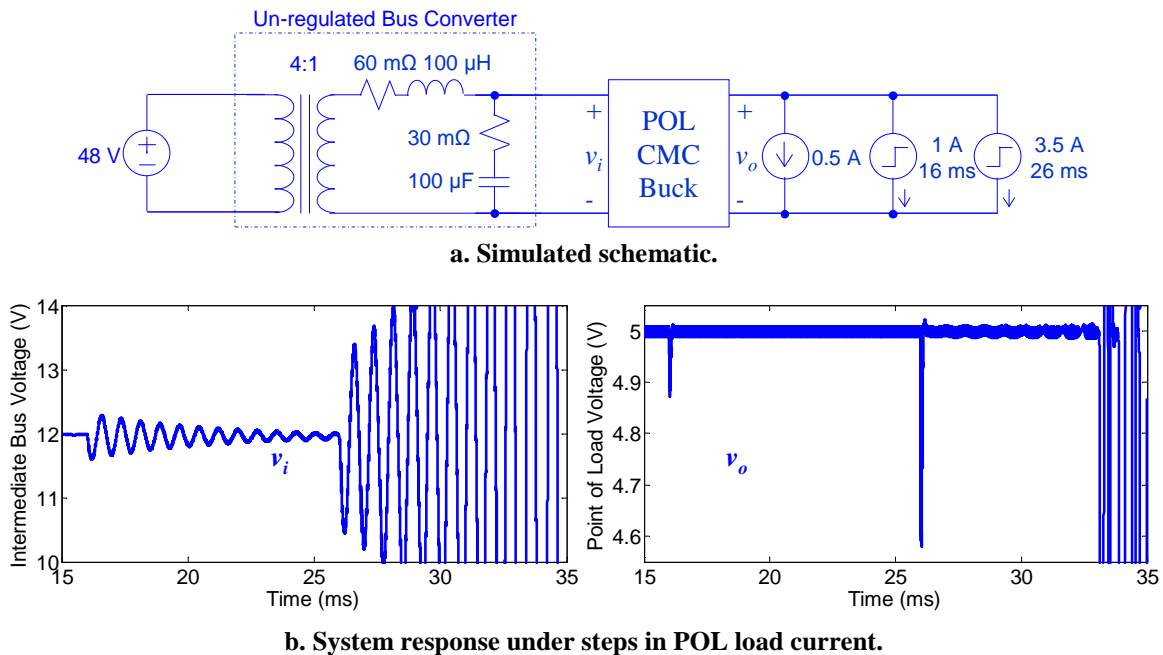


Fig. 1-12: Instability of DC power system due to CPL behavior of DC-DC converter.

The CPL behavior of regulated converters and related instability problems were firstly addressed for input filter design in the 70's [53]. Later on, it became a matter of concern for integration of DC power systems [54], [55]. Today, this problem is also tackled during power system integration for aircrafts [56], naval ships [57] and electric vehicles [58], where DC buses comprised of CPL are employed. An analytical technique to tackle this problem, based on small-signal modeling, is reviewed in appendix 0.

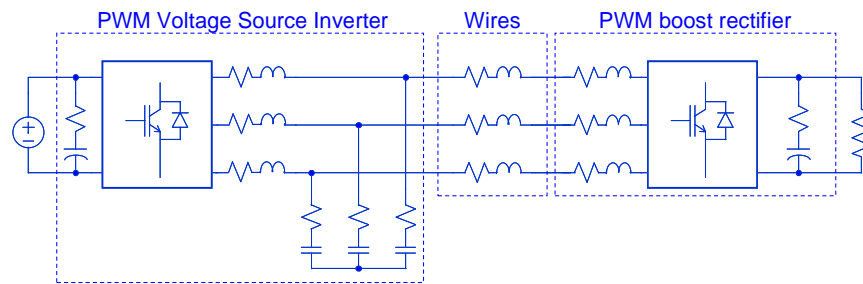
1.3.1.2 AC bus

Similarly to DC systems, AC distributed power systems relies on regulated converters to distribute power throughout the system with the required performance and efficiency. MEA, AES and microgrids employ AC distribution. An illustrate example has been depicted in Fig. 1-5, where an active PWM rectifier draws power from the AC VF bus with high power factor and delivers it to an inverter-motor subsystem.

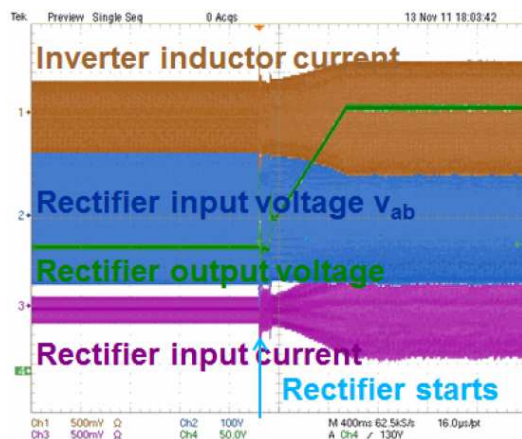
^{1.1} Details about the simulated POL converter are given in section 3.2.3.

At steady-state, instantaneous power flow is constant in three-phase balanced systems. Therefore, load converters can exhibit CPL characteristics that can lead to unstable situations. This phenomenon was firstly addressed in the mid 90's [59]. However, AC distributed power systems is a relatively new development, so this problem has only received wide attention since a few years ago [60]-[62].

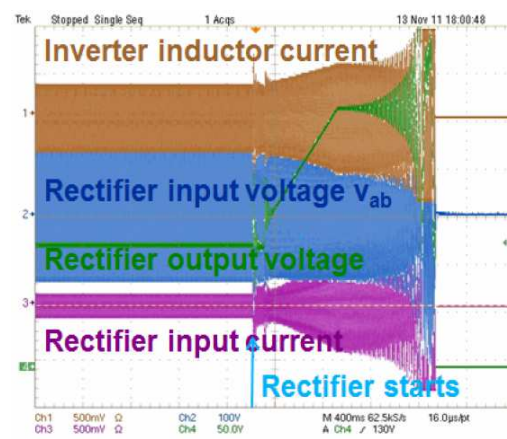
Fig. 1-13 depicts experimental results recently reported in [62] on dynamic interactions between a VSI and a boost rectifier. Rectifier starting was tested with two VSI voltage control loops. In the first case (fast loop, Fig. 1-13b) the system remained stable. In the second case (slow loop, Fig. 1-13c), the system became unstable. This shows that un-proper dynamic response of the source subsystem can lead to instability when the load subsystem is a CPL.



a. Experimental system under study (the power converters are provided with regulation loops).



b. Stable case: fast VSI AC voltage control loop.



c. Unstable case: slow VSI AC voltage control loop.

Fig. 1-13: Instability of AC power system due to CPL behavior of AC/DC converter reported in [62].

1.3.2 Integration of protections

Protections play a key role concerning safety and reliability of distributed power systems, and research is being carried out on this topic. For instance, SSPCs are being developed to replace conventional relays and magneto-thermal devices for MEA [18]. Basically, SSPCs protect wiring harness and loads from short-circuit, over-current and over-temperature, as well as perform controlled load connection/disconnection to the bus. Thus, power converters can be safety connected to the bus while the inrush current, related to the input filter capacitor energizing, is controlled.

Fig. 1-14 depicts a simplified schematic of a MOSFET-based SSPC cascaded with a downstream DC-DC converter. As can be seen, the SSPC comprises a current control loop for current limiting and a trip controller that features device protections.

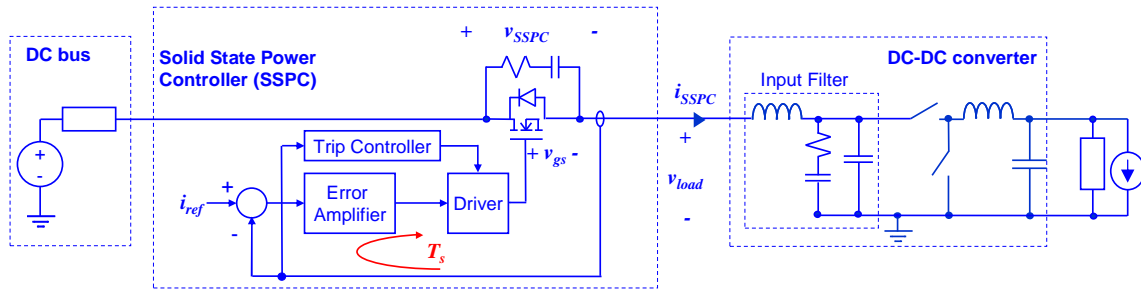
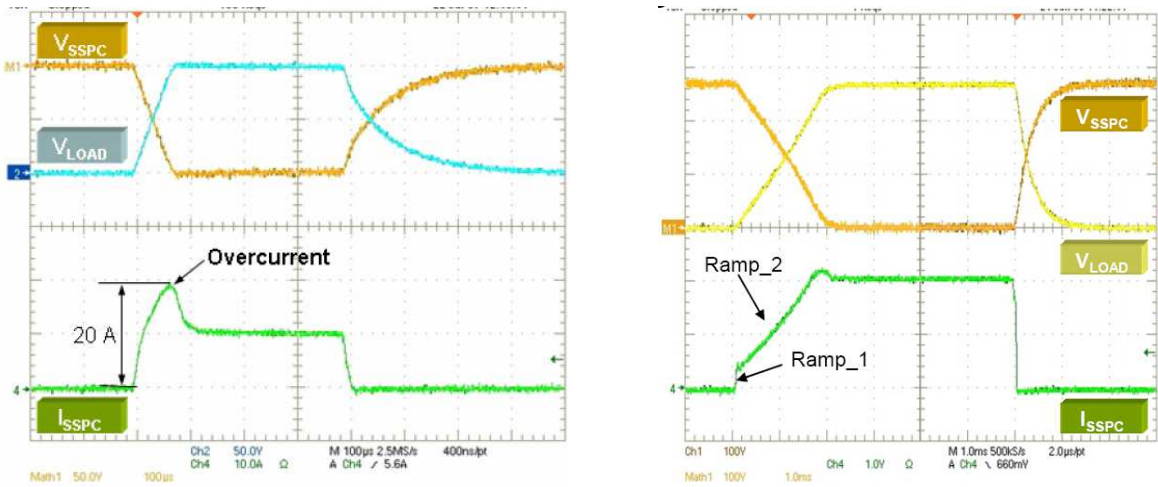


Fig. 1-14: Solid State Power Controller cascaded with a downstream DC-DC converter.

Experimental measurements of commercial SSPCs response under connection and disconnection of parallel RC load, reported in [15], [174], are plotted in Fig. 1-15. As can be seen, SSPCs regulate the load current flow by active control of the gate-source voltage of the MOSFET (or gate-emitter voltage in case of IGBT).



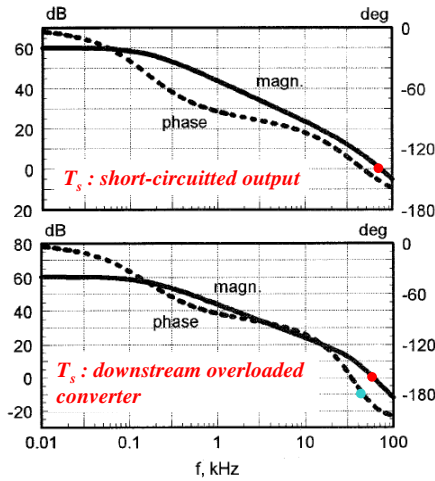
a. SSPC by DDC. $R_{load} = 10 \Omega$ $C_{load} = 10 \mu\text{F}$. $V_{bus} = 100 \text{ V}_{DC}$.

b. SSPC by Sensitron. $R_{load} = 27 \Omega$ $C_{load} = 12 \mu\text{F}$. $V_{bus} = 270 \text{ V}_{DC}$.

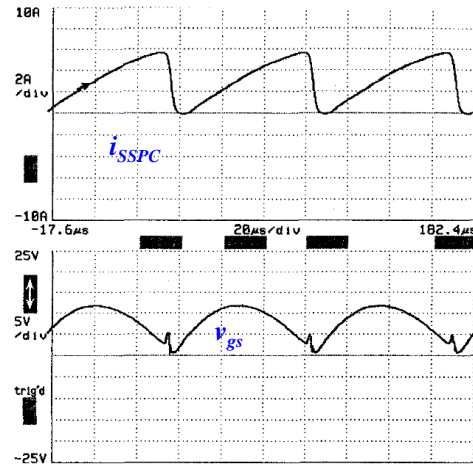
Fig. 1-15: Experimental measurements of transient response of commercial SSPCs during connection and disconnection of RC passive load, reported in [15], [174].

From the point of view of the system designer, the protections must be adequately set in term of current rating and inrush current limitation. However, when protections with active current limiting are employed, dynamic interactions between the control loop of the protections and the downstream converters have to be also considered.

Dynamic interactions between the control loop of SSPCs and downstream regulated converters have been analyzed in [63], in the frame of the International Space Station electrical system design. A system similar to that shown in Fig. 1-14 was considered, where T_s denotes the loop gain of the SSPC. Fig. 1-16a shows the simulated frequency response of T_s for two loading situations: short-circuited output and downstream converter overloaded. As can be seen, the converter introduces phase delay that makes the system unstable. Fig. 1-16b depicts experimental measurements corresponding to the latter situation, evidencing sustained oscillations that were attributed to the dynamic interactions between the converter and the SSPC. As explained in [63], the SSPC control loop and the converter impedance are coupled through the gate-source capacitance of the MOSFET.



a. Simulated open-loop SSPC transfer function for different loading conditions.

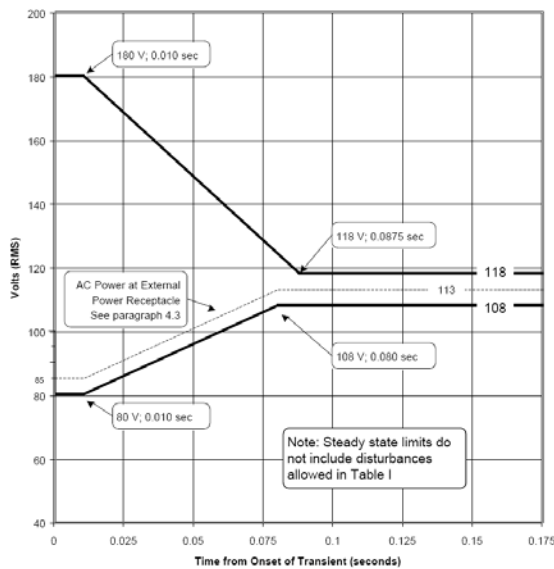


b. Experimental instability measured with downstream overloaded converter.

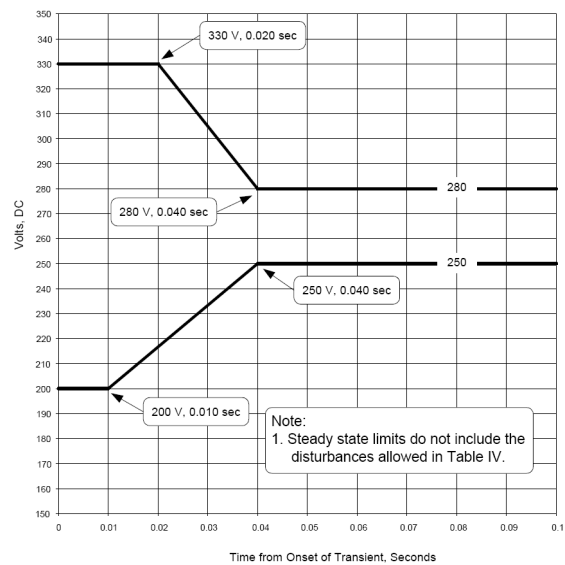
Fig. 1-16: Dynamic interactions between SSPC current loop and downstream converter reported in [63].

1.3.3 Power quality: static and dynamic performance

Besides stability, distributed power systems must comply with power quality specifications. Those include (but are not limited to) bus impedance mask, transient response envelope and harmonic distortion spectrum. For instance, Fig. 1-17 shows DC and AC voltage envelope for aircraft power systems specified in MIL-STD-704F for aircraft [263].



a. Voltage transient envelope for 115 V_{AC} bus.



b. Voltage transient envelope for 270 V_{DC} bus.

Fig. 1-17: Transient specifications for 270 V_{DC} and 115 V_{AC} bus for aircraft given in MIL-STD-704F [263].

1.3.4 Other issues

Design and integration of distributed power systems involves other issues such as the following ones:

- **Architecture design:** Selection of proper distribution architecture, including subsystems voltage and current rating, is a major task. Considerations to take into account are cost, volume,

size, safety, battery back-up requirements, isolation, regulation requirements (e.g. regulated or un-regulated intermediate bus when using IBA), system hold-up time, energy efficiency and thermal management [1], [39].

- **Power flow control:** Different strategies can be used to regulate the power flow throughout the system and ensure uninterruptible power supply to critical loads with appropriate power quality. For example, in case of microgrids, different power control strategies are being considered [35], [37]. These include (but are not limited to) distributed control, where each unit is controlled by measuring local variables (e.g. CERTS microgrid, Fig. 1-9) and central ‘virtual prime mover’ control, where a central controllers samples microgrid state variables and dispatch signals to dominant subsystems using fast telecommunications.
- **Conducted-electromagnetic-interference (EMI) filters design and integration:** Power electronics converters produce high level of EMI noise that has to be filtered [1]. Particular care has to be taken during filter design and integration in order to avoid unacceptable dynamic performance deterioration, which may even lead to instability due to reasons discussed in section 1.3.1.

1.4 System-level modeling of multi-converter power architectures

System-level modeling and simulation are regarded as powerful design tools for system-level integration of distributed power architectures [134]-[136]. These can be employed in order to evaluate multiple architecture designs working under multiple operating conditions. Thereby, the optimum architecture design can be found out, and those situations where the system may exhibit unacceptable dynamic response, or even be unstable, can be detected. Modeling and simulation can expedite design decisions and reduce experimental work, which decrease cost and accelerates time-to-market.

However, not every model is well suited to carry out a system-level analysis. Following points must be considered on system-level modeling.

1.4.1 General requirements

The main requirements to be fulfilled by system-level models are described below.

- **Modeling and simulation of large systems.** Modern power distribution systems comprise many electrical subsystems including energy sources and storage units, passive and active loads, and power electronics converters. In order to enable system-level simulation within reasonable time intervals, models of subsystems must be **simple** and should only represent the **input-output interface signals with the rest of the system**, capturing the main phenomena concerning system-level analysis.
- **Modeling of subsystems provided by external manufacturers.** Distributed architectures are typically built following a modular approach and using subsystems typically provided by external manufacturers. However, since manufacturers protect the ‘know-how’ of their products, the system designer may have no access to internal details of each piece of equipment. This fact has the following implications.

- The models should be **identifiable through input-output experiments**. Then, the system designer could obtain a model of the subsystem without knowing internal details about it. Moreover, empirical models are in general more accurate than theoretical ones (as long as identification is accurate), since uncertainties due to parasitics or tolerances are avoided.
- The models **should not include the internal structure of the modeled subsystem**. Thus, the manufacturers could provide models of their products, together with conventional datasheets and specifications, while confidential information is kept.

Taking into account the system integration issues discussed in section 1.3, as well as the general requirements described above, the main features of system-level models can be stated, as well as the characteristics of the identification method.

1.4.2 Modeling features

System-level models should feature the following characteristics.

- **Large-signal average input-output terminal behavior under normal operation.** The models should capture the averaged static and dynamic relationship between input and output terminal signals, taking into account dynamics dependence on operating point (if significant). Switching phenomena can be neglected if the focus is on static and dynamic analysis below switching frequency range (not EMI concerns). For instance, system-level models for power converters with output voltage control (that will be covered in chapter 4 and chapter 5) should address the phenomena listed below.
 - **Input impedance and output impedance characteristics** are critical aspects that system-level models should represent accurately, including **low-frequency constant-power-load** behavior at the input terminal. Thereby, subsystems interactions can be evaluated, as well as dynamic response under load transients. Moreover, if the input and output impedance is known, stability assessment can be done through analytical methods.
 - The models should address the **input-output power balance**. At steady-state, it is given by the energy **efficiency**, which in general is a function of the operating point. However, under **transient conditions** (e.g. load current steps), variations of energy storage into inductors and capacitors means **additional dynamics** that have been addressed as well.
 - **Line input-output susceptibility**. In case of regulated converters, the output voltage is determined by the control stage. However, the regulation is not ideal, so perturbations in the input voltage are reflected at the output port, both statically and dynamically. This effect is so-called **audiosusceptibility** and should be addressed. Nevertheless, it may be neglected for the sake of simplicity, in those cases where it is very small (e.g. in case of CMC converters).
- **Transient behavior during off/on transition.** When a power converter is connected to the distribution bus by closing a breaker, the following phenomena occurs.
 - First, significant amount of current is drawn due to energization of the input capacitors [135]. This is so-called **inrush current** or input surge current and should be represented by the models (for instance, to set protections with active current limiting during load on/off).

- After that, the output voltage gradually increases from zero to the nominal level. This is so-called **soft-start** and should be also addressed by the model.
- Other features, **such as over-current or under/over-voltage protections, temperature**, etc. should be easy to incorporate in the model. As demonstrated in [135], during soft-start of power converters, the input voltage drop upon the line impedance could trip the under-voltage protection, leading to sustained oscillations at the input port of the converter.

1.4.3 Identification features

The identification methods of system-level models should feature the following properties.

- The identification experiments should be **as simple as possible** and should require **low-cost equipment** typically found in power electronics laboratories.
- The parameters of the models should be obtained from measurements **using well established techniques** and, if possible, **ready-to-use tools**, thus avoiding long learning process.
- **Un-terminated dynamics** should be identified, that is, the obtained parameters should be independent of the load and source used during the experimental identification process.

1.5 Conclusions

In the first part of this chapter, current trends in power distribution systems for a variety of applications have been reviewed, including telecommunications, datacenters, transportation (aerospace, automotive and naval), and microgrids. It has been shown that power distribution systems for such applications are moving from centralized architectures to distributed ones, incorporating more and more power electronics converters and electrical loads.

In the second part, challenges during integration of new distributed power systems have been presented. Interactions between regulated converters, loads switching, activation of protections, etc., make the behavior of the whole system be highly complex. In fact, power converters can be stable when operating in stand alone conditions, but unstable when integrated in a whole system.

Modeling and simulation are powerful design tools to carry out the system-level analysis, and to ensure proper performance under all operating conditions. In the third part, requirements for system level modeling have been presented. Essentially, the models should represent the large-signal average behavior of the power converters/subsystems, but only at their input-output terminals. Moreover, the models should not have direct physical interpretation due to reasons of confidentiality, and should be identifiable from measurements of the input/output response of the converters/subsystems under a set of experimental tests. Both the models and the identification experiments should be as simple as possible, in order to allow for the simulation of large systems within reasonable times, and to facilitate the identification process as much as possible.

Development of new system-level modeling and identification techniques, which fulfill the above-described specifications, has opened new challenges for research on power electronics. The state of the art on this topic is reviewed along the next chapter and novel solutions are proposed in the subsequent ones.

2 Modeling and Identification in Power Electronics: State of the art

2.1	Introduction.....	21
2.2	Modeling and identification techniques. Classification and concepts.....	21
2.2.1	Modeling techniques	21
2.2.2	Identification techniques	22
2.3	Modeling oriented to converter-level design	23
2.3.1	Switching modeling.....	24
2.3.2	Continuous-time average modeling.....	24
2.3.2.1	DC-DC converters.....	24
2.3.2.2	AC-DC, DC-AC and AC-AC converters	25
2.3.3	Discrete-time modeling.....	25
2.3.4	Black-box models.....	25
2.3.4.1	Linear approaches.....	25
2.3.4.2	Nonlinear approaches	27
2.4	Modeling oriented to system-level design	27
2.4.1	G-parameters black-box model	27
2.4.1.1	DC-DC converters.....	27
2.4.1.2	Three-phase DC-AC, AC-DC and AC-AC converters.....	31
2.4.2	Hybrid Wiener Hammerstein grey-box model.....	33
2.4.3	Others	34
2.5	Current lacks in the state of the art	35
2.6	Proposed solution.....	36

2.1 Introduction

The aim of this chapter is to review the state of the art on modeling and identification of power electronics converters. It is structured as follows:

- **Section 2.2.** Some basic concepts on modeling and identification are introduced, and a classification of existing techniques is presented.
- **Section 2.3.** Modeling techniques oriented to converter-level design are reviewed, paying special attention to modeling based on system identification for control design.
- **Section 2.4.** Modeling techniques oriented to system-level design are reviewed, focusing mainly on those contributions based on model parameterization from experimental measurements.
- **Section 2.5.** Finally, the current lacks in the state of the art on system-level modeling are discussed and the key aspects of the solutions proposed in this thesis are presented.

2.2 Modeling and identification techniques. Classification and concepts

2.2.1 Modeling techniques

Depending on the considered criteria, models can be classified in different ways. In this thesis, prior knowledge, physical meaning, model complexity and model identifiability are key aspects to be taken into account. Modeling methods can be classified accordingly as follows [65]-[71]:

- **Structural models (or white box models).** These models are derived by applying first principles of physics (e.g. the Ampere's law). They reflect the internal structure of the modeled equipment in detail and have a clear physical interpretation. Switching models of power electronics converters fall within this category.
- **Behavioral models.** In contrast with structural models, behavioral models do not reflect the internal structure of the modeled equipment. Black-box models and grey-box models can be differentiated within this category.
 - **Black-box models.** The parameters of black-box models are just a vehicle to match input-output relationships, so they do not have physical interpretation. Therefore, these models can be completely derived from input-output experiments. System-level models, such as two-port g-parameter models, fall within this category.
 - **Grey-box modeling.** Grey-box models are an intermediate case between white-box and black-box modeling. Grey-box modeling is the term usually applied when part of the internal structure of the subsystem is known and part is not. Thus, part of the model reflects the structure of the equipment while other part is numerically modeled as a 'black-box'. Reduced-order average models may be considered a grey-box models.

A comparison between structural and behavioral modeling approaches is presented below^{2.1}.

	Structural modeling.	Behavioral modeling.	
	White-box.	Grey-box.	Black-box.
Physical meaning.	Complete.	Partial.	No.
Prior knowledge about internal structure.	Required.	Partially required.	Not required.
Identifiable from Measurements.	Difficult or not possible.	Yes.	
Simulation time (related to model complexity).	Typically time consuming.	Expedited simulation time.	

Table 2.1: Classification of models as a function of physical meaning and available information.

On the other hand, models of power converters can be sorted, as a function of the design level, as follows.

- **Converter-level design.** ‘Structural’ and ‘behavioral’ modeling with different abstraction levels can be found onto this group: switching models with a high level of detail, reduced-order average models, duty-cycle-to-output-voltage frequency response models, etc.
- **System-level design.** Models that focus on the input-output interface signals with the rest of the system fall within this category. Therefore, this only includes ‘behavioral’ approaches, being either a grey-box or a black-box.

In subsequent sections, modeling techniques for power converters are classified into ‘converter-level design’ and ‘system-level design’.

2.2.2 Identification techniques

In this thesis, behavioral models are identified from measurements. Identification of dynamic systems is a mature field of research and a wide variety of methods has been reported, oriented to both linear and nonlinear systems. Identification techniques can be classified into parametric and non-parametric techniques. In this thesis, identification of linear systems is applied. Typical methods for linear systems include the following ones:

- **Nonparametric methods.** Nonparametric methods return models that are described by a table or a graph, such as the impulse response or the frequency response.
 - *Impulse response estimation methods:* These methods aim to estimate the impulse response of the system from the transient response under a certain excitation. The correlation method is a typical estimation technique of impulse response. Other ones are the impulse analysis and the step analysis.

^{2.1} The classification herein presented varies slightly depending on authors. Some authors classify models as a function of prior knowledge only, meaning that white-box models require the system parameters to be completely known [70]. However, others authors define white-box models as those that represent the system physics, but some parameters could be unknown and would require white-box identification techniques [69].

- *Frequency response estimation methods:* These methods aim to estimate the frequency response from a certain experiment, for example an AC sweep. Typical methods include frequency response analysis, Fourier analysis and spectral analysis.
- **Parametric methods.** Parametric methods return models that can completely describe the system behavior using a finite number of parameters (typically relative small), such as transfer function models and state-space models. Parametric models are estimated from either time domain data or frequency domain data, typically by optimizing a cost function (e.g. mean squared prediction error) using a numerical optimization technique such as least squares and nonlinear optimization.

Sometimes, nonparametric models are used as input data for parametric identification techniques. A typical example consists in identifying a transfer function model from frequency response data. Fig. 2-1 illustrates the identification process of a single-input single-output (SISO) linear-time-invariant (LTI) model from experimental data for the physical system ‘G’.

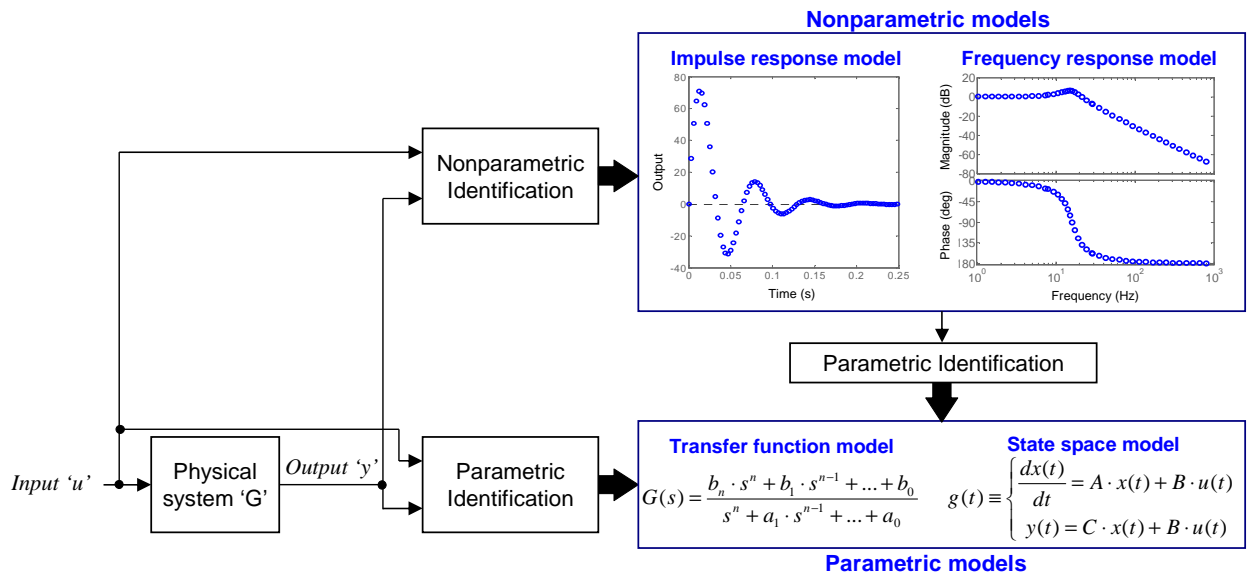


Fig. 2-1: Identification and modeling options for single-input single-output linear-time-invariant systems.

Nonparametric methods are well suited for control design, where the frequency response of the plant is enough to synthesize a compensator. On the other hand, parametric methods are appropriated for system-level simulation, where a model defined by a few number of parameters facilitate the model implementation. The application of identification techniques in power electronics will be reviewed in subsequent sections.

2.3 Modeling oriented to converter-level design

Traditionally, modeling of power electronics has been oriented from a converter-level point of view. The literature on this topic is vast and only major contributions are reviewed in this section. More attention is paid to black-box approaches oriented to control design, where system identification is applied.

2.3.1 Switching modeling

Switching modeling is applied to analyze the behavior of the converter under the different switching stages. They allow estimating voltage and current ripple and peak levels for every component into the power converter [75]. They are also important for designing soft-switching techniques [76] or control strategies based on switching ripple, such as current-mode-control, hysteresis or V^2 control, among others. Looking into a lower-level, detailed models of the semiconductors are used to study the on/off switching process [77]. Simulation of electrical power systems based on switching models has been reported since the 60's [78], [79].

2.3.2 Continuous-time average modeling

2.3.2.1 DC-DC converters

Average modeling was firstly described in 1972 by G. W. Wester and R. D. Middlebrook [80]-[82]. This contribution represents probably the most important advance on the modeling of power electronics converters up to now. Thanks to average modeling, power electronics converters, whose equivalent circuit topology is different during the 'on' and 'off' states (i.e. are time-variant circuits), can be represented with a **time-invariant continuous equivalent circuit** that is valid up to near half the switching frequency. Then, control design and stability analysis of power electronics converters can be readily addressed using well known small-signal linear techniques. Moreover, using average modeling, the behavior of power converters is greatly simplified and simulations can be drastically expedited. Other significant contributions during the mid and late 70's were the state-space averaging technique [83], [84] and the first continuous-time model for peak current-mode-control (CMC) [85].

During the 80's the first modeling approach of resonant converters was reported [86], [87]. During the 90's, a canonical three-port model of the PWM switch cell (comprised of the diode and the switch) was presented in [88], [89] and extended in [90]. The theoretical justification of average modeling was described in [91], and a generalized averaging approach, also valid for resonant converters, was presented in [92]. Fig. 2-2 depicts the average model of a buck-converter operating in continuous conduction mode (CCM), which results from any of the aforementioned techniques.

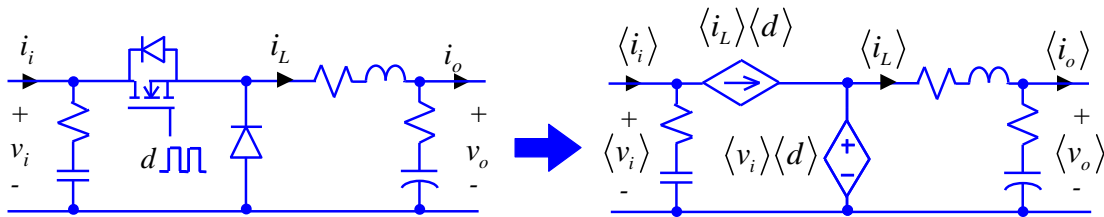


Fig. 2-2: Classical average modeling of the buck converter in continuous conduction mode (CCM).

Also during the 90's, frequency-dependant averaging techniques were proposed (e.g. [93]) to cope with high ripple conditions, where conventional techniques fail. The continuous time modeling of peak CMC at high frequency, looking for prediction of sub-harmonic oscillations, was addressed in [94].

Remarkable contributions during the early 00's include the extension of average modeling to multiple output converters [95] and the review of averaging into discontinuous conduction mode

(DCM) presented in [96]. Today, research is still being carried out toward better understanding of high frequency small-signal dynamics, where conventional averaging techniques fail [97]-[99].

2.3.2.2 AC-DC, DC-AC and AC-AC converters

The averaging techniques described above can be readily applied to AC-DC, DC-AC and AC-AC PWM converters. For example, average models for three-phase voltage source inverter (VSI), current source inverter (CSI), buck rectifier and boost rectifier are derived in [100]. The resulting average models of three-phase converters are usually mapped into d-q frame, in order to define a constant operating point at steady-state, so that conventional small-signal modeling techniques can be directly applied [100], [101]. Today, research is still done on this topic. An extension to average modeling of PWM VSI, including dead-time effects, have been recently reported [102], showing that dead-time can make influence mainly on the low-frequency dynamics.

Average modeling of three-phase line-commutated and diode rectifiers has been also a matter of research since more than twenty years ago. Averaging is performed over a line cycle divided by the number of pulses (6, 12, 18), [103], [104]. Recently, MEA developments have pushed researchers to extend and improve the existing approaches [105]-[108].

Concerning single phase AC-DC converters, it is worth appointing the classical reduced-order modeling of the boost power factor corrector by R. Ridley [109].

2.3.3 Discrete-time modeling

Simultaneously to continuous-time modeling, discrete modeling techniques have been proposed since the 70's to obtain invariant circuits from the switching ones. Some remarkable references on this topic are [110]-[113]. More discussion on this topic can be found in [134] and [135].

2.3.4 Black-box models

Black-box modeling of power electronics converters was firstly applied for control design purposes. Therefore, the aim was to identify input-output models for the control-to-output dynamics (for example, the duty-cycle to output-voltage frequency response). Remarkable contributions on this topic are reviewed below.

2.3.4.1 Linear approaches

Frequency response measurement, through AC sweep test, is the classical and most applied system identification method in power electronics. For example, R. D. Middlebrook reported in 1975 a method to measure the loop-gain frequency response experimentally through an AC sweep test [114]. According to the definitions given in section 2.2, the result is a non-parametric black-box model identified through a frequency response technique that uses sequential sinusoidal tones as excitation signal.

During the 90's, several publications were reported on characterization of the control-to-output dynamics of switching models by means of simulation, following either parametric approaches [115]-[117] or nonparametric ones [118], [119]. A remarkable example of parametric approach is [116], which identified the coefficients of a discrete difference equation using a pseudo-random binary signal (PRBS) as excitation input. This is a well suited signal for system identification

because it has maximum crest factor and flat spectrum (like white noise). In fact, this signal has been widely applied for on-line nonparametric identification of power converters later on. Other interesting contribution is [119], which used the impulse response in order to identify the frequency response of a power converter in a short period of time (nonparametric approach).

Due to the grown of digital control, auto-tuning of compensators for power electronics converters are gained popularity since the mid 00's. Hence, new on-line identification techniques have been reported for on-line characterization of control-to-output dynamics of power converters. Most of them follow a nonparametric approach, because a frequency response or impulse response curve is enough to design a compensator. **A major contribution on this topic was reported by B. Miao et al. in 2005, [120].** In this paper, the **cross-correlation technique** is proposed for impulse response identification, using the **PRBS** as excitation input. Then, the small-signal frequency response is obtained by applying Fourier analysis on the impulse response. Using this method, the required time for characterization is drastically reduced in comparison with a conventional AC sweep. Moreover both the PRBS and the correlation are straightforward to implement in a digital platform. Fig. 2-3 depicts the basis of this method.

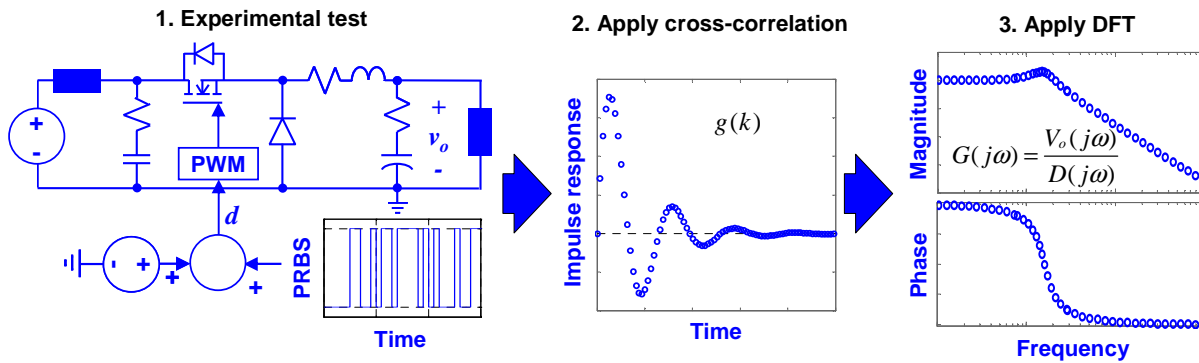


Fig. 2-3: Identification of a nonparametric frequency-response model of a buck converter by applying cross-correlation followed by DFT. PRBS is used as excitation signal. Method proposed in [120], 2005.

Practical implementations and improvements of the cross-correlation method based on PRBS were proposed [121] and [122], respectively. A method for analysis of identification uncertainty has been reported in [123]. In order to enhance accuracy, alternative binary signals different from PRBS, as well as spectrum-based identification approaches, have been proposed in [124] and [125].

In contrast to binary signals, C. Fernandez et al. proposed the multi-sine excitation in combination with Fourier analysis for fast characterization of the control-to-output frequency response [126]. Using multi-sine, the total measurement time corresponds to the period of the lowest harmonic, and the spectral shape of the excitation can be easily designed by adjusting the power of the individual tones.

Experimental identification of the control-to-output dynamics has been also tackled parametrically. [127] proposes using a parametric identification algorithm to fit a discrete duty-cycle to output-voltage transfer function from a step test.

All works described above focuses on DC-DC converters. However, on-line identification and auto-tuning of three-phase AC converters is also a matter of concern, especially in those cases where the grid impedance may vary significantly. Looking for an automatic identification, a parametric identification method of a state-space model for a grid connected VSI has been presented in [128].

Finally, it is worth appointing [129], where classical parametric and nonparametric identification techniques of LTI models are reviewed and applied on a forward converter by simulation.

2.3.4.2 Nonlinear approaches

Power converters are in general nonlinear systems, as the relationships between control and an output variable in general depends on the operating point. Therefore, previous approaches are in general valid around a local operating point.

In order to have models valid for a larger operating region, nonlinear black-box modeling and identification approaches for power converters have been reported in the literature since the 90's. A nonlinear autoregressive model with exogenous input (NARMAX), consisting of a nonlinear discrete differential equation, was identified in [130] to model the duty cycle to output voltage dynamics of both a buck and a boost converter. Later on, a large-signal nonparametric neural network model of a boost converter was identified in [131] and used for control design.

Other approach, quite common in system identification literature, is the **block-oriented modeling**, which essentially makes use of nonlinear static networks cascaded with linear dynamic networks (see Fig. 1-16). Applications of such structures in power electronics for control purposes have been reported during the 00's. The Hammerstein network is used in [132] to model the duty-cycle to output-voltage transfer function of a boost converter. A hybrid Hammerstein-Wiener network is applied in [133] to model a photovoltaic inverter.

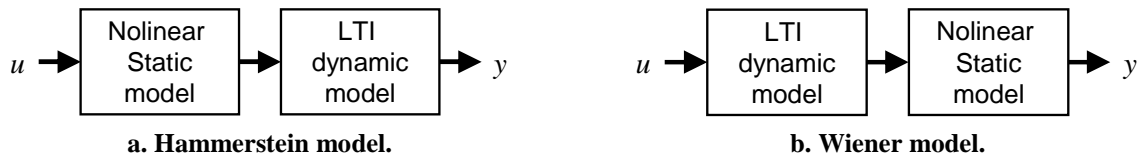


Fig. 2-4: Typical block-oriented nonlinear models for dynamic systems.

2.4 Modeling oriented to system-level design

Literature on system-level modeling is less extensive than literature on converter-level modeling. The reason is that, apart from some exceptions such as the International Space Station, systems made up by multiple converters have only been extensively used since the 90's. In this section, major contributions are reviewed. According to the focus of this thesis, special attention is paid to contributions where the model is identified from experimental measurements.

2.4.1 G-parameters black-box model

2.4.1.1 DC-DC converters

System-level behavioral modeling in power electronics emerged to simplify the analysis of large systems and expedite simulation times. The first, and a **major contribution on this topic, was reported by Bo Cho et al. in 1985** [137]-[139], in the frame of large spacecraft power systems (International Space Station). In this work, every component into the power system is modeled as an input-output network. For instance, DC-DC converters are modeled so that i_o , v_i are model inputs and v_o , i_i are model outputs (see Fig. 2-5).

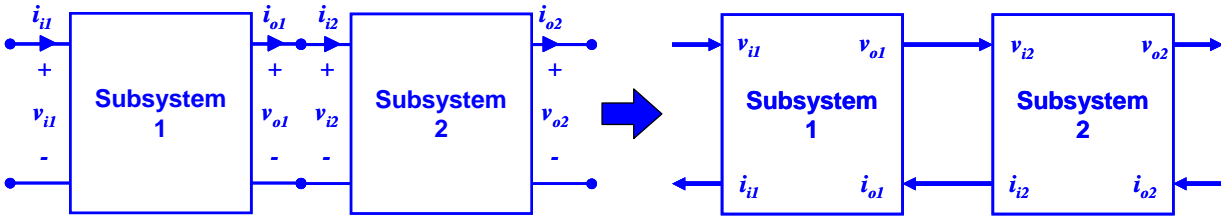


Fig. 2-5: Two-port cascaded subsystems represented as input-output networks for implementation in system-level simulators [137]-[139], 1985.

Subsystems are modeled in two ways:

- Large signal nonlinear switching approach: where each component is modeled using state-equations for each switching stage.
- Small-signal linear average approach: where the systems are modeled by means of a **two-port linear g-parameters network** made up by ‘un-terminated’ local transfer functions represented into Laplace domain: output-impedance $Z_o(s)$, back-current gain $H_i(s)$, audio-susceptibility $G_o(s)$ and input-admittance $Y_i(s)$ ^{2.2} (see Fig. 2-6). Un-terminated means that the transfer functions only contain the internal dynamics of the modeled subsystems (i.e. they are independent of the load-source dynamics). Those transfer functions are obtained in two ways.
 - By averaging state-space equations followed by small-signal perturbations.
 - By using input-output frequency response measurements and a parametric identification algorithm.

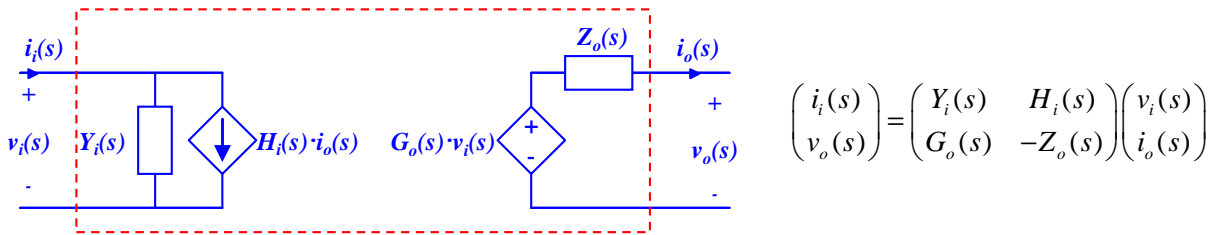


Fig. 2-6: Small-signal model of a DC-DC converter using a two-port g-parameters network, [137]-[138], 1985.

Major contributions on system-level modeling and analysis by B. Cho et al. [137]-[140] include the following ones.

- Un-terminated two-port network modeling of DC-DC converters based on g-parameters.
- Identification of g-parameters models of DC-DC converters using frequency response data and parametric identification techniques (curve fitting using magnitude and phase data).
- Reduced-order modeling through curve fitting with fewer poles and zeros than the real system actually includes. This allows the trade-off between accuracy and simplicity.
- Small-signal stability analysis of distributed power systems based on input-output impedances of the load-source subsystems and the Nyquist criteria. This is based on the analysis of interactions between input-filters and regulated converters presented by R.D. Middlebrook in 1976 [141].

^{2.2} Actually, B. Cho originally named the g-parameters as g_{11} , g_{12} , g_{21} , g_{22} . However, the nomenclature herein described has been typically used in subsequent works based on this modeling approach.

- Large-signal system-level stability analysis based on state-plane analysis.

Since 1985, small-signal g -parameters models have been widely used for analysis of small-signal subsystems interactions [142], [143].

Later on, due to the grown of distributed power systems made up by using many commercial converters (refer to chapter 1), research have been carried out toward developing new modeling techniques of power electronics converters oriented to system-level simulation and based on experimental identification. In 2007-2008, **L. Arnedo et al.** proposed in [134], [144]-[146] **modifications for the linear g -parameter model** in order to reproduce the **average large-signal behavior** of power converters by **simulation** (both un-regulated and output-voltage regulated). The following modifications were proposed:

- **Gain scheduled structures (Fig. 2-7a).** These structures are proposed to model nonlinearities mainly reflected at low-frequency. The **low-frequency constant-power-load behavior**, exhibited at the input port by every converter with regulated output voltage, can be well addressed using the structure Fig. 1-16b, so that the output of the convolution $H_i * i_o$ is scaled through a nonlinear static function, consisting of a look-up-table driven by v_i . This is called Wiener structure in [144], [146]. In addition, a DC source was added at the output port to represent the output voltage at steady-state, which in closed-loop converters is essentially determined by an internal reference signal.
- **Local linear model networks (LLMN, Fig. 2-7b).** These structures are proposed to model **dynamics dependence on operating point** in a more general way. They consist of a set of local LTI models, whose outputs are combined through weighting functions, as a function of the operating point. Fig. 2-7b depicts a one-dimensional structure comprised of three local models (G_i) and triangular weighting functions (W_i) driven by the input signal u . This is called Polytopic structure in [145].

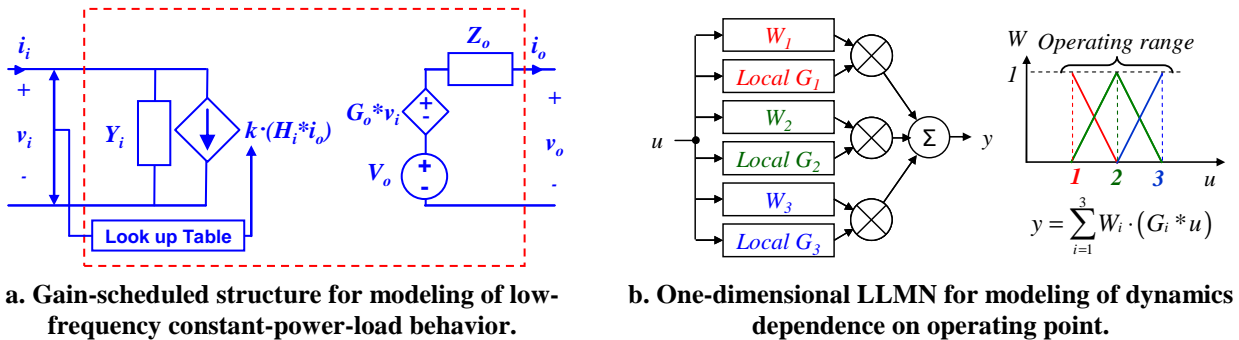


Fig. 2-7: Modifications on the linear g -parameters model for large-signal nonlinear modeling of DC-DC converters proposed in [144]-[146], 2007-2008.

The proposed solutions allow a trade-off between simplicity and performance. Good results were experimentally demonstrated for converters with nearly linear dynamics, or converters whose dynamics varies smoothly under transitions from one operating point to other. However, the proposed structures fail when such variations are non-smooth (e.g. transitions from DCM to CCM).

L. Arnedo et al. also described in [134], [144] practical tests for frequency response characterization based on AC sweep (which were not explicitly indicated by B. Cho et al.). The proposed setup consists of a network analyzer, a linear amplifier and a parallel current injection

circuit. The operating point is set by a DC source and an electronic load (see Fig. 2-8). From the measured frequency responses, transfer function models were obtained using parametric identification algorithms integrated in the System Identification Toolbox of Matlab [260]. Alternative experimental setups for frequency response characterization of DC-DC converters are discussed in [147] (focusing on input-output impedances).

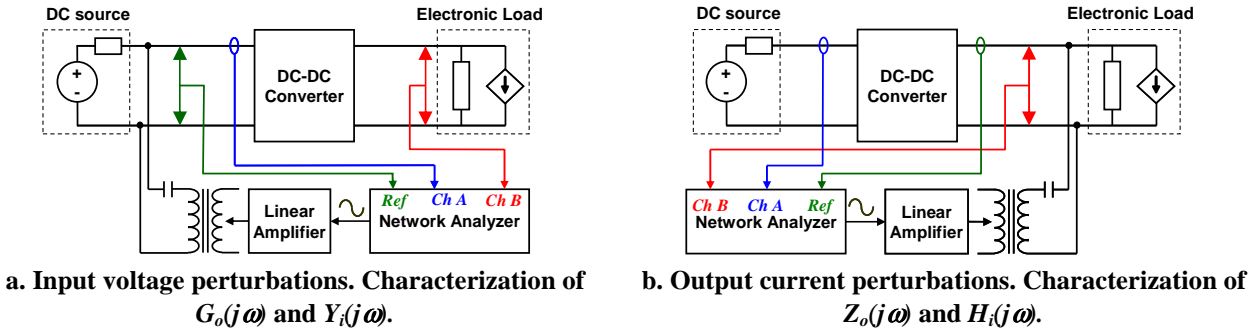


Fig. 2-8: Experimental tests for identification of g-parameters DC-DC converter model reported in [134], [144], 2007.

Last but not least, L. Arnedo et al. proposed in [148] the first method to de-couple the effect of the DC source/load dynamics on the measured frequency response. Model order reduction techniques of the resulting transfer functions were proposed as well, in order to expedite simulation times.

Later on, I. Cvetkovic et al. proposed in 2011 an alternative large-signal modeling method based on g-parameters models [149]. The idea consists in splitting the model into two networks: a static nonlinear network and a linear dynamic network. This way, the static model computes the operating point (uppercase signals) while the dynamic model reproduces the converter dynamics over the operating point (lowercase signals with tilde). This technique was used to model a nanogrid (see Fig. 2-9).

This elegant solution yields good results from the static point of view, but the dynamics is not well represented, under large perturbations, if significant dependence on operating point exists. Moreover, every subsystem must be modeled by means of this technique.

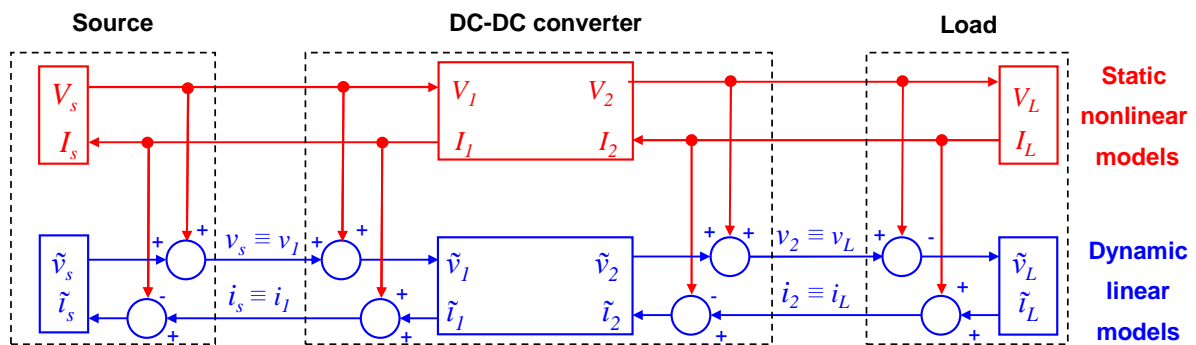


Fig. 2-9: Non-linear hybrid g-parameters model of DC-DC converter, load and source proposed in [149], 2011.

Also in 2011, I. Cvetkovic et al. proposed an alternative de-coupling method of load-source dynamics from measured frequency responses [150]. Compared to the first approach [148], the new method relies on simpler mathematics and avoids the need for additional experiments to characterize the load-source dynamics.

2.4.1.2 Three-phase DC-AC, AC-DC and AC-AC converters

New three-phase AC and hybrid DC-AC distribution systems for aircraft, naval ships and microgrids relies on power electronics converters, as discussed in chapter 1. Hence, behavioral modeling of three-phase AC converters has become a matter of interest during last years. However, few works have been reported on this topic at the moment. AC impedance/admittance modeling for input-filter design and system-level stability assessment was firstly reported during the 90's [151], [152]. **However, the first small-signal behavioral model of AC converters was reported in the late 2007 by D. Boroyevich et al. [153].** Fig. 2-10 shows the generic model for an AC-AC converter proposed in this paper. As can be seen, this is a g-parameters model represented into synchronous d - q frame. Synchronous frame is selected because three-phase AC signals are mapped into two DC signals at steady-state, and thus any three-phase AC port can be modeled using two DC ports. The model has four inputs (i_{od} , i_{oq} , v_{id} , v_{iq}) and four outputs (v_{od} , v_{oq} , i_{id} , i_{iq}), so 16 transfer function models are required to address every input-output dynamic relationship.

Models for three-phase DC-AC and AC-DC converters are obtained just by simplifying this structure. For example, the model of a three-phase DC-AC converter is obtained by setting to zero the 'q' channel at the input port (i.e. $v_{iq} = 0$, $i_{iq} = 0$).

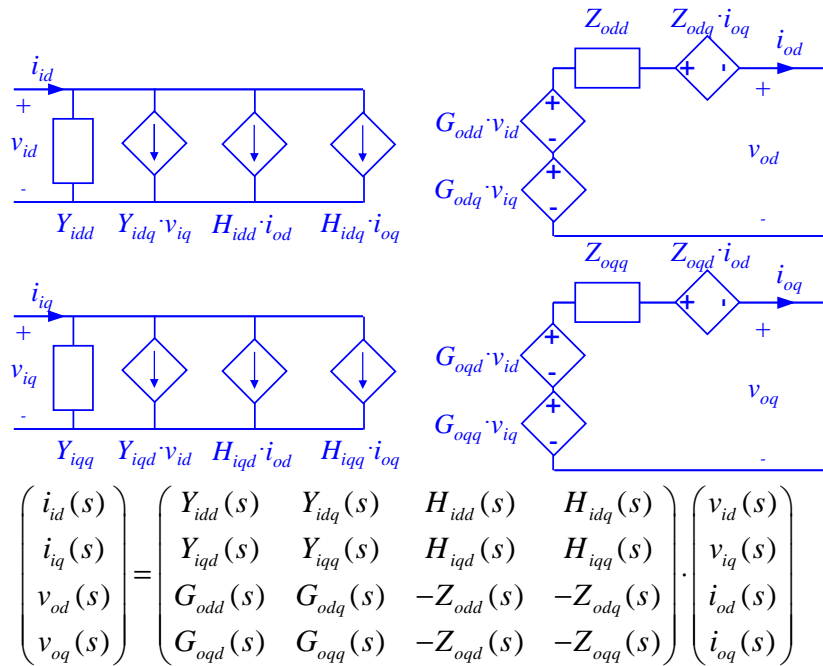


Fig. 2-10: Small-signal g-parameters behavioral model of a generic AC-AC converter into synchronous d - q frame reported in [153], 2007.

This model can be used to address small-signal dynamic interactions between subsystems under balanced conditions. However, neither nonlinear modeling for large-signal simulation nor modeling of un-balance conditions was discussed in [153]. Recently, I. Cvetkovic et al. proposed in 2011 an extension of this structure to large-signal modeling by following the approach depicted in Fig. 2-9 [154].

On the other hand, frequency response characterization of three-phase AC subsystems into d - q frame is more complex, and only a few papers have dealt with it at the moment. The first approach was reported by M. Belkhat et al in 2000 [155], where series injection of sinusoidal perturbations

within $d-q$ frame was proposed. In [156], Y. L. Familiant et al. described practical measurement techniques based on shunt current injection (Fig. 2-11a). Compared to series injection, shunt injection is more practical when large currents are present. In those references, AC sweep tests into $d-q$ frame are applied by using ‘suppressed-carrier-modulation’ so that sinusoidal perturbations can be drawn only on one $d-q$ channel at each time. Several implementations of the shunt current injection, such as that shown in Fig. 2-11b, were proposed.

An alternative method is presented in [158], which consider shunt-current injection but using only a single-phase injection circuit connected between two phases, thus simplifying the hardware.

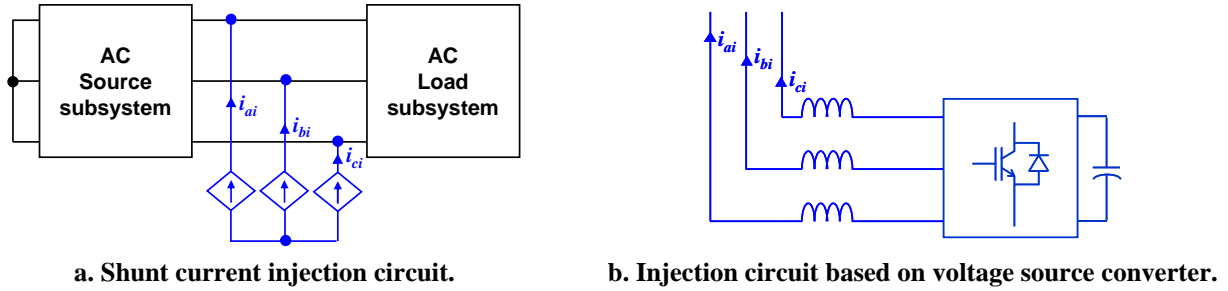


Fig. 2-11: Practical experimental tests for AC impedance measurements through AC sweep into $d-q$ frame, reported in [156], 2009.

In [157], a practical implementation and algorithm for $d-q$ impedance measurements is presented. In this case, the $d-q$ impedances are obtained from linearly independent tests, even if the perturbation in one of the $d-q$ channels is not identically zero under each test. Both the AC excitation and the $d-q$ impedance measurements are carried out using a Network analyzer and a shunt injection circuit. A diagram of the setup is shown in Fig. 2-12, where one can realize how complex the characterization is, in comparison with DC subsystems (Fig. 2-8). The $d-q$ transformation is synchronized with the three-phase system by using a variable bandwidth phase-locked-loop (PLL).

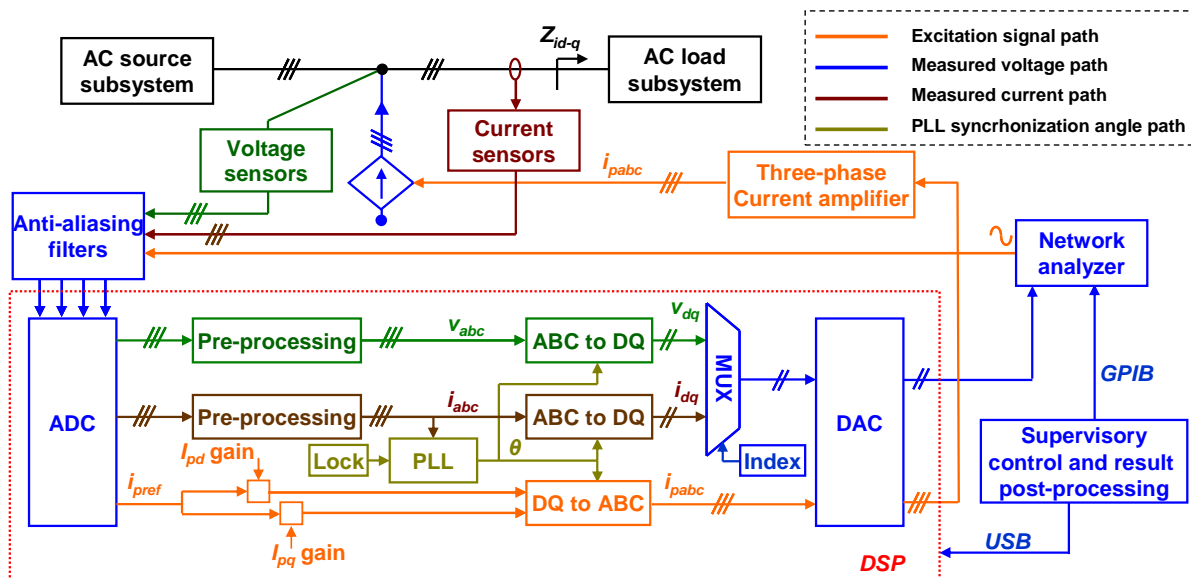


Fig. 2-12: Practical implementation of an AC impedance measurement equipment into $d-q$ frame, reported in [157], 2011.

Finally, it is worth pointing out that alternative three-phase AC impedance modeling techniques has been also reported, such as ‘harmonic balance’. By means of this technique, the impedance is

modeled in terms of sequences: positive sequence and negative sequence, without cross-coupling between them [61].

2.4.2 Hybrid Wiener Hammerstein grey-box model

A different (and the first) approach to large-signal behavioral modeling of closed-loop DC-DC converters, based on system identification, was proposed by J. A. Oliver et al., 2006 [159]-[160]. As a difference for the g-parameters model, J. A. Oliver et al. proposed a circuit-oriented approach that has partial physical meaning (i.e. a “grey-box” approach). The proposed model is shown in Fig. 2-13a. It relies on a hybrid Wiener-Hammerstein structure and comprises the following elements:

- An input dynamic linear network made up by the input filter of the converter.
- A static nonlinear network comprised of an electrical circuit and a thermal circuit.
 - The electrical circuit addresses the static input-output power transference. It accounts for the efficiency ‘ η ’, load regulation ‘ f_z ’ and line regulation ‘ f_v ’ as function of the operating point.
 - A thermal model that computes the case temperature ‘ T_c ’ as a function of the ambient temperature ‘ T_{amb} ’, power losses ‘ P_{loss} ’, thermal resistance ‘ R_{th} ’ and thermal capacitance ‘ C_{th} ’.
- An output linear dynamic network that is made up by the output capacitor of the converter and a parallel RL network that represents the dynamics of the outer voltage regulator^{2,3}.

The model is also provided with a logic control system (Fig. 2-13b) that includes protections and drives the soft-start profile. The protections are tripped depending on the case temperature, currents and voltages.

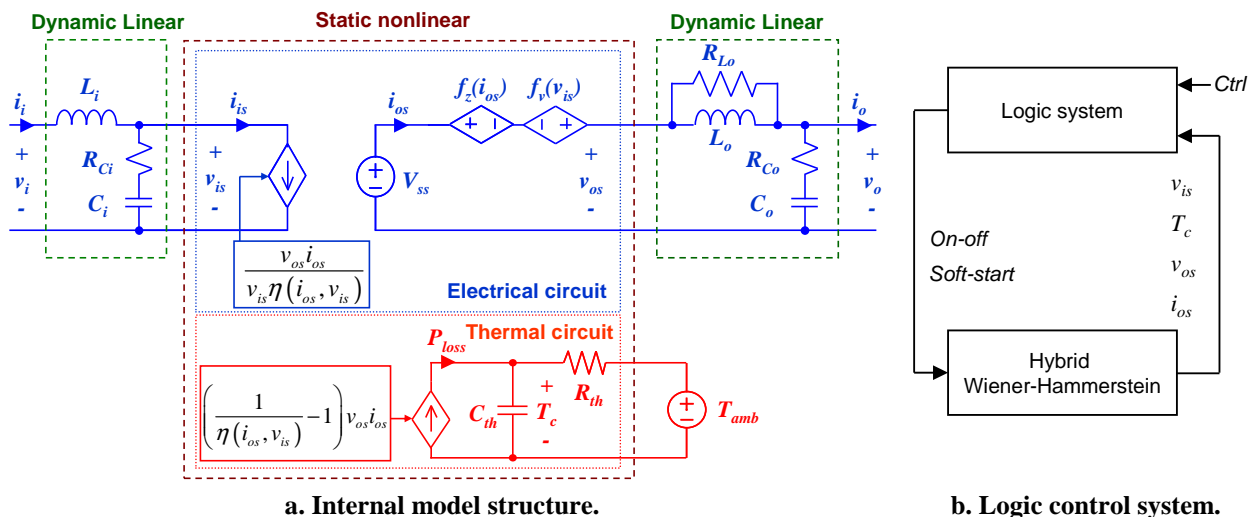


Fig. 2-13: Hybrid Wiener-Hammerstein Grey-Box model for DC-DC converters reported in [159]-[160], 2006.

^{2,3} To derive the model, the control stage is assumed to be comprised of an inner current loop (current injected to the output capacitor and the load) plus an outer voltage loop based on a proportional-integral (PI) compensator.

As can be seen, the audio-susceptibility is neglected in this model. Dynamic variation, during transients, of the energy stored in the inductor of the output filter is neglected over the input-output power balance. Such assumptions are acceptable in case of converters with CMC and relatively small inductors. Nevertheless, modifications to account for such effects as well as to represent outer voltage compensators different from a PI are reported in the thesis document [135].

This approach is quite effective for circuit simulators. It works properly in case of CMC converters (control of current injected to the output) and can also be used for voltage-mode-controlled (VMC) converters at the expense of higher error. Nevertheless, CMC buck-type converters are typically used in distributed power systems and can be well modeled by means of this approach.

The model can be identified from information provided in the datasheet and some additional tests (if required). The static network is identified from information about efficiency, static regulation and thermal characteristics. **The dynamic networks are identified from the transient response of the converter as follows.**

- The **input network** is identified from the **inrush current**. Simple analytical equations are used to fit the network parameters.
- The **output network** is identified from the transient response under a **load step**. A least-square algorithm is used to fit the network parameters (no details about the algorithm were indicated).

The identification method is a remarkable feature of this approach, as **step tests are in general much simpler than AC sweep tests.**

A power distribution system for an avionic application was modeled using this approach in [161]. Later on, extensions of this model to represent converters whose output impedance depends on the operating point, such as quasi-resonant converters, were proposed in [162].

On the other hand, a model for multi-output closed-loop DC-DC converters, based on the same type of structure, was reported by in [163].

2.4.3 Others

The works described above focuses on the averaged behavior of the converter for frequencies below half the switching frequency. However, behavioral modeling of EMI generated by power converters is important in order to facilitate EMI filter design and comply with regulation. Research on this direction has been reported since the 90's [164]-[166].

It is also worth pointing out the behavioral model for a single-phase grid-connected PV inverter recently reported in [167]. The model is quite simple and can be identified from datasheet and some additional tests. However, no identification method for some of the parameters is given.

Other remarkable works are [168]-[172], where the aim is to expedite simulation times and/or facilitate the system-level analysis, although knowledge about internal details of the converters is required. It is worth remarking the behavioral model provided by Vicor Corporation in the datasheet of some un-regulated converters [173]. This demonstrates that industry is currently interested on this modeling approach. This type of models can be readily applied in circuit simulators by customers while the manufacturer keeps confidential data. A behavioral model for an un-regulated converter by Vicor is depicted in Fig. 2-14.

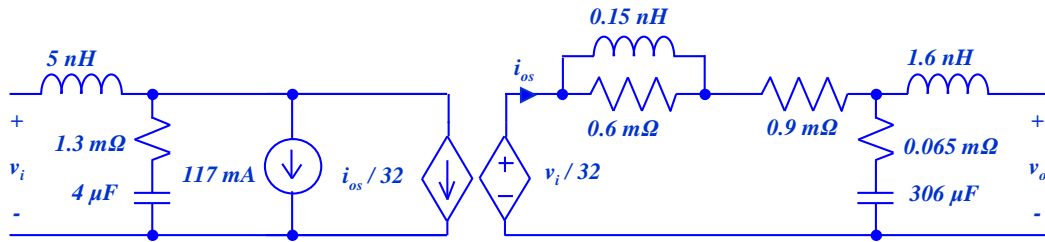


Fig. 2-14: Behavioral model of a commercial un-regulated isolated DC-DC converter by Vicor Corporation ($V_i = 48$ V, $V_o = 1.5$ V, $I_o = 100$ A) given in the datasheet [173].

However, power converters are not the only subsystems for which behavioral models are required. Protections such as SSPCs play also a critical role during system integration, as described along chapter 1. Behavioral modeling of SSPCs has been addressed in [174].

2.5 Current lacks in the state of the art

According to the state of the art, **only a few works have been reported on behavioral modeling of power electronics converters, oriented to large-signal averaged system-level simulation and based on system identification.** The reported contributions and current lacks are summarized below:

- **DC-DC converters.** Existing contributions include the Hybrid Wiener-Hammerstein model for DC-DC converter reported by J.A. Oliver et al. (2006) and the extended g-parameters models by L. Arnedo et al. (2007-2008) and I. Cvetkovic et al. (2011). **Those contributions cover converters either un-regulated or with regulated output voltage (either single voltage loop or multi-loop).** However, **power converters with other regulation schemes are also being applied in new power distribution systems.** For instance, converters that deliver power to a battery bus are regulated with current control (either input current or output current) because the bus voltage is fixed by the battery. The auxiliary power unit for the MEA, shown in Fig. 1.4, and the power-drive-train system for Fuel-Cell Vehicle, shown in Fig. 1.7, are some examples where this type of control is applied. On the other hand, input voltage control is applied used in power converters for renewable energy sources such as PV.
- **Three-phase AC converters.** At the moment, behavioral modeling has been **only reported from a small-signal point of view** by D. Boroyevich et al. (2007) [153]^{2,4}, and **neither experimental result nor a complete identification method has been yet reported.**

On the other hand, **only unidirectional power flow** has been considered at the moment. However, bidirectional converters are also being applied in new power systems. For example, starter/generator systems for electric vehicle and the MEA (Fig. 1.4, Fig. 1.6) require a bidirectional converter to deliver power from the bus to the engine during the starting process and, once the engine has been started, from the engine to the bus.

A summary of the current state of the art on this topic is given in Table 2.2, where main features and lacks of each approach are indicated (opinion of the author).

^{2,4} During the development of this thesis, a large-signal behavioral model for three-phase AC converters, based on the g-parameters d - q structure, has been presented in [154] (2011, see section 2.4). A first approach to the solution presented in this thesis has been initially reported in 2010 (refer to section 12.1.2).

Modeling approach	Main features and lacks
<p style="text-align: center;">Grey-box Wiener-Hammerstein model for DC-DC converter.</p>	<ul style="list-style-type: none"> • Very simple model. Well suited for circuit simulators. • Simple identification tests. Valid for a wide range of power levels. • Only CMC control using injected current to the output. Less accurate for other control schemes. • Only uni-directional power flow.
<p style="text-align: center;">Black-box g-parameters model for DC-DC converters.</p>	<ul style="list-style-type: none"> • Any power topology. • Voltage-mode-control and current-mode-control. • Dynamics dependence on operating point. • Only un-regulated and regulated converters with output voltage control. • Only uni-directional power flow. • Complex identification tests specially for medium and high power converters.
<p style="text-align: center;">Black-box g-parameters model for three-phase AC converters into d-q frame.</p>	<ul style="list-style-type: none"> • Any power topology and control strategy. • For the moment, only valid for small-signal analysis. • Complex identification tests. Only input-output impedance identification has been reported.

Table 2.2: Summary of current contributions on system-level behavioral modeling of power electronics converters based on system identification, indicating main features and lacks.

2.6 Proposed solution

In this thesis, novel system-level behavioral modeling and identification techniques for power electronics converters and subsystems are proposed.

- **The modeling techniques are based on the two-port terminal modeling method**, already reported for DC-DC and three-phase converters using g-parameters. This technique is selected because it is quite versatile, can be easily adapted to different type of power converters and can cover a wide variety of control strategies and power topologies. Moreover, no prior information about internal data of the modeled subsystem is required and the models do not have any physical interpretation, thus keeping manufacturer's confidentiality.
- **The models are identified from the transient response to step tests**, instead of frequency response under AC sweep tests. Transient response is selected because the **experimental tests are very simple and can be readily carried out using low-cost equipment**, such as passive load and switches.

Starting from the existing g-parameters model for **DC-DC converters**, a new identification method completely based on transient response analysis is presented. Some extensions for the existing model are proposed as well.

After that, both the modeling and identification technique is extended to **three-phase VSIs with output voltage control, and DC-DC converters with input current control**. Following this, other power electronics based subsystems are tackled, such as **solar array simulators and starter-generators based on switched reluctance machines**. Finally, **guidelines toward a generalization of the modeling and identification method to cover any power electronics converter**, or power electronics based subsystems, are indicated.

Fig. 2-15 shows an overview of the main contributions on system-level averaged behavioral modeling of power electronics converters, starting from the first average model by Wester et al. in 1972. Inspiring ideas for this thesis are also highlighted using green color.

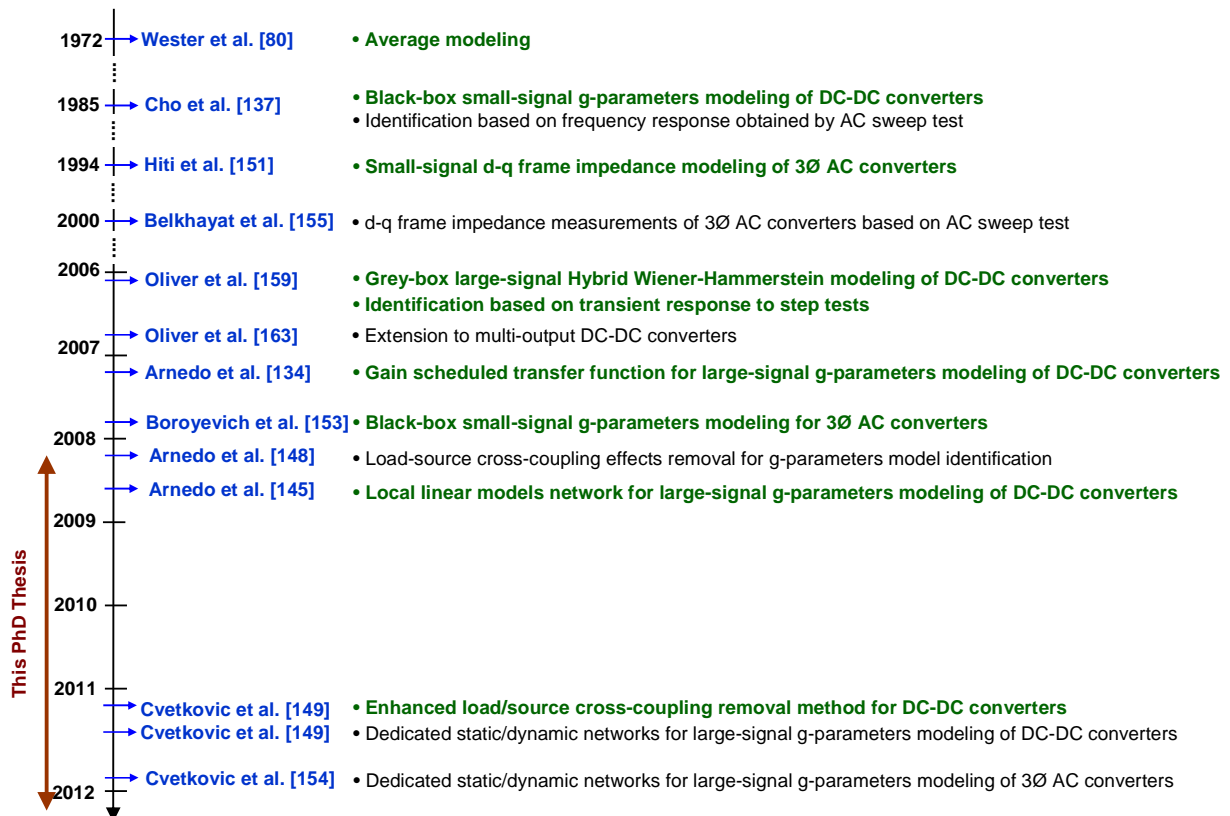


Fig. 2-15: Main contributions to system-level behavioral modeling of power electronics converters. Inspiring ideas for this thesis are highlighted using green color.

3 Proposed approach: overview and basic concepts

3.1	Introduction.....	41
3.2	Modeling concepts.....	41
3.2.1	Selection of the basic model structure: linear approach.....	41
3.2.2	Extending to nonlinear large-signal modeling	43
3.2.2.1	General approach.....	43
3.2.2.2	Simplified approach: merging static and dynamic networks.....	44
3.2.3	Simulation based example.....	45
3.3	System identification concepts.....	50
3.3.1	Experimental tests	51
3.3.2	Transfer function models identification: basic approach	52
3.3.3	Cross-coupling effect	53
3.3.4	Simulation based example.....	54
3.4	Summary and overview	58
3.4.1	Summary of concepts	58
3.4.2	Overview of the thesis.....	59

3.1 Introduction

Along this thesis, black-box models for a variety of converters are presented, together with their corresponding identification procedures. Despite each converter features particularities, every model and identification procedure is derived by applying systematically a common methodology, consisting of a set of sequential tasks.

This chapter introduces the main concepts managed along this thesis, regarding both modeling and identification. These concepts are illustrated on a simple simulation example. It is organized as follows:

- Section 3.2 describes the basis modeling concepts.
- Section 3.3 covers the identification procedure of the model parameters.
- Section 3.4 presents a summary of concepts, a brief description of the modeling procedure and an overview of the thesis.

It is important to note that the aim is just to introduce the reader to the key concepts and methods managed along this thesis. A comprehensive description of such methods is given in subsequent chapters.

3.2 Modeling concepts

3.2.1 Selection of the basic model structure: linear approach

The first step in modeling is to decide which signals are important to describe the converter under study. In order to design a particular power converter, internal signals such as the duty cycle are typically modeled since they are a matter of interest. However, if the goal is to design a system made up by multiple interconnected converters, only the input-output interface signals of each converter with the rest of the system should be important. Therefore, in this thesis **each converter/subsystem is analyzed as an n -port network, so that only the input-output signals of the converter are modeled.** For example, a single-input single-output DC-DC converter is modeled as a two-port network only in terms of the signals that interface it with the rest of the system (i.e. input voltage v_i , input current i_i , output voltage v_o and output current i_o), as shown in Fig. 3-1. Only **the averaged behavior of the input-output signals is modeled.** Switching phenomena is not addressed by the models because the focus is on large-signal behavior below half the switching frequency.

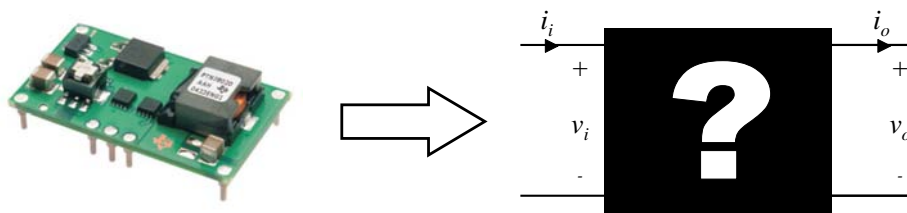


Fig. 3-1: Commercial DC-DC power converter [264] analyzed as a two-port input-output network.

The key idea of the modeling method, discussed along this thesis, is to model each converter as an input-output network, so that some interface signals are considered as model inputs and some others

as model outputs. Therefore, once the set of signals of interest have been defined, the next task consists in selecting which signals are model inputs and which ones are model outputs. Such a selection is done by looking at the basic functionalities of the power converter, from a system-level point of view.

For example, consider a DC-DC converter used as part of a distributed power system. This converter supplies a regulated output voltage to a certain load while its input port is connected to a DC bus. Regardless of the type of power stage and control scheme, the converter is a two-port network that exhibits the following system-level behavior:

- At the output port, the converter behaves as a regulated voltage source, so that the output current i_o is set by the load power demand.
- At the input port, the converter behaves as a current sink, so that the consumed input current i_i depends on the output current i_o demand and the input voltage v_i .

Taking into account the previous observations, the best option seems to be a Thevenin network for the output port and a Norton network for the input port. Therefore, the model inputs are v_i and i_o , while the model outputs are v_o and i_i . It corresponds to the so-called ‘*g parameters two-port network*’ in the literature [249], which has been presented in chapter 2. Some of the *g* parameter corresponds to concepts typically managed by power electronics engineers: g_{22} corresponds to the output impedance of the converter Z_o , g_{21} corresponds to the audio-susceptibility G_o , g_{11} represents the input-admittance Y_i and g_{12} refers to the back-current gain H_i .

Assuming linearity the model can be represented as shown in Fig. 3-2, where each parameter of the network represents a SISO LTI model.

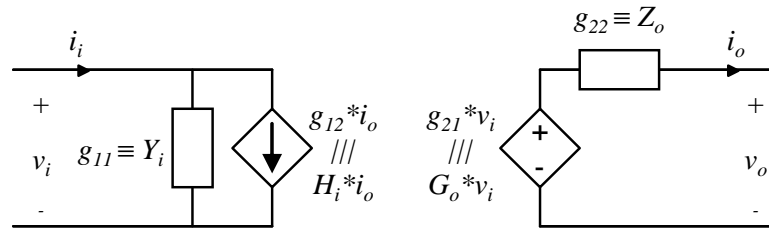


Fig. 3-2: Linear two-port *g*-parameters model of a DC-DC converter^{3.1}.

Hence, the input-output relationship can be expressed through a set of transfer functions as given by (3-1), in the Laplace domain. **Those transfer functions are said to be ‘un-terminated’** meaning that **they are independent of the load and source dynamics.**

$$\begin{pmatrix} i_i(s) \\ v_o(s) \end{pmatrix} = \begin{pmatrix} Y_i(s) & H_i(s) \\ G_o(s) & -Z_o(s) \end{pmatrix} \begin{pmatrix} v_i(s) \\ i_o(s) \end{pmatrix} \quad (3-1)$$

^{3.1} Symbol “*” refers hereinafter to the convolution operator, i.e. $G_o(t) * v_i(t) = \int_{-\infty}^{\infty} G_o(\tau) \cdot v_i(t-\tau) d\tau$

3.2.2 Extending to nonlinear large-signal modeling

3.2.2.1 General approach

However, power converters are in general nonlinear systems and the black-box models are intended to address not only the static behavior but also the average dynamic behavior in a large-signal sense. Hence, the model shown in Fig. 3-2 has to be complemented with additional elements.

- First, **static networks are incorporated into the model**, which determine the steady-state response of the output voltage ' v_{os} ' and the input current ' i_{is} ' as a function of the operating conditions given by the input signals (v_i, i_o). Such static networks allow accounting for **static line/load regulation** at the output port, as well as the **input-output power balance** taking into account **efficiency** dependence on operating point $\eta(V_i, I_o)$.
- Second, **the transfer functions into the linear model are replaced by dynamic networks that can be either linear or nonlinear**. The steady-state response of every dynamic network has to be null, as it is already addressed by the static networks.

The general large-signal black-box model for DC-DC converters with output voltage regulation is depicted in Fig. 3-3. Note that each dynamic network is expressed as a general function (either linear or nonlinear) of input signals. Moreover, each dynamic network is denoted by subscript '0', meaning that its static response is zero.

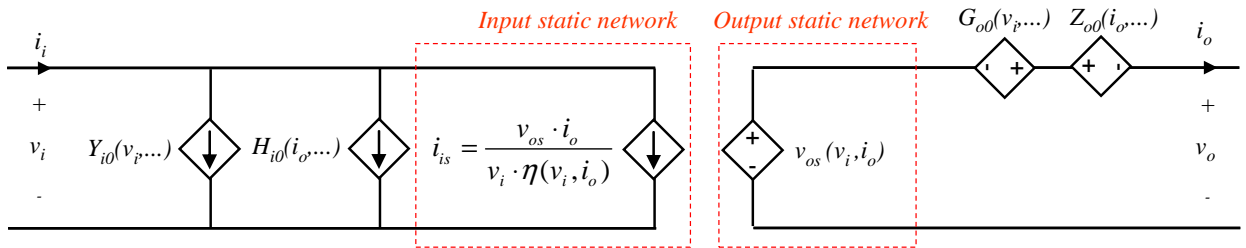


Fig. 3-3: General large-signal black-box model of a DC-DC converter with output voltage regulation loop.

Under small-signal perturbations, this approach is related to the linear one as indicated by the following expression (similar expressions can be derived for the other dynamic networks).

$$Y_i(s) = \left. \frac{i_i(s)}{v_i(s)} \right|_{i_o(s)=0} = Y_{i0}(s) + \frac{\partial i_{is}(V_i, I_o)}{\partial V_i} \quad (3-2)$$

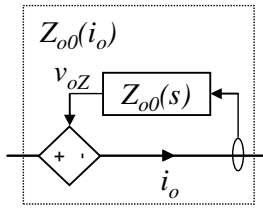
Such modeling approach, based on cascaded static and dynamic networks, is inspired in the proposal by J. Oliver et al. [160]. It also has some similarities to the method reported later on by I. Cvetkovic et al. in [149] (both works were described in chapter 2). Similarities and differences of the approach herein presented with them are discussed in chapter 4.

To make up the dynamic networks (Y_{i0} , H_{i0} , G_{o0} and Z_{o0}), the following structures are used along this thesis. Those are depicted in Fig. 3-4. Mathematical details about them are described in chapter 4.

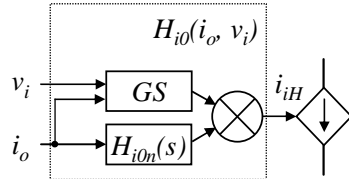
- **Transfer function model.** A simple transfer function model is applied when the relationship between input and output signals is linear, or nearly linear. Today, circuit and system-level simulators, such as PSIM, Pspice or Simulink, allows defining a LTI model by a 's' domain

transfer function, and return the time-domain convolution of its impulse response with the input signal. Fig. 3-4a. depicts the output impedance Z_{o0} made up by a transfer function model.

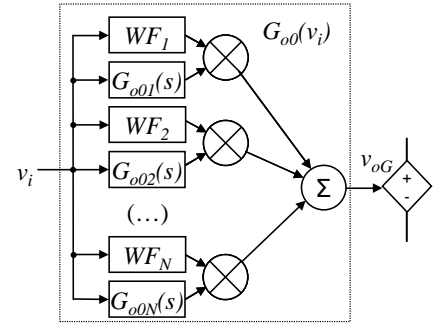
- **Gain scheduled transfer function model.** This is applied when the dynamics dependence on operating point is mostly reflected on the static gain. For instance, the back-current-gain of closed-loop converters exhibits dependence on V_i and $\eta(V_i, I_o)$. This is due to the fact that, under constant load power, the converter behaves as a constant-power-load (CPL) at low-frequency, so that I_i decreases if V_i increases. Such nonlinearity is directly reflected on the DC gain of the back-current gain. Fig. 3-4b. depicts the back-current gain made up by a ‘gain-normalized’ transfer function H_{i0n} , whose gain is driven by GS .
- **Local-linear models network:** Dynamics dependence on operating point is addressed in a more general manner by using a combination of local transfer function models, whose output is weighted as a function of the operating point. This way, the response of the whole model is dynamically adapted to the operating point of the converter. In this thesis, it is referred to as local-linear models network (LLMN). Fig. 3-4c. depicts the audio-susceptibility G_{o0} made up by ‘ N ’ transfer function models (G_{o0j}) combined by means of weighting functions (WF_j) driven by v_i . This technique was proposed in [134], [145].



$$v_{oZ}(s) = Z_{o0}(s) \cdot i_o(s)$$



$$i_{iH}(s) = GS(V_i, I_o) \cdot (H_{i0n}(s) \cdot i_o(s))$$



$$v_{oG}(s) = \sum_{j=1}^N G_{o0j}(s) \cdot v_i(s) \cdot WF_j(V_i)$$

a. Transfer function model.

b. Gain-scheduled transfer function.

c. Local-Linear model network.

Fig. 3-4: Dynamic networks modeling.

Despite more complex nonlinear approaches have been reported by the system identification community [68], the presented nonlinear structures allow a **good trade-off between accuracy and complexity**. Moreover, a key advantage of them over more complex approaches is that they can be parameterized using **linear system identification techniques**, instead of more complex nonlinear system identification approaches.

It is important to note that those approaches address smooth nonlinearities, meaning that the dynamics varies smoothly when changing from one operating point to other. Strong nonlinearities, such as transitions from continuous conduction mode to discontinuous conduction mode are not properly addressed by the presented techniques [134].

3.2.2.2 Simplified approach: merging static and dynamic networks

The approach above shown can be simplified if the output voltage is tightly regulated to a constant value into the whole working region. If the back current gain is modeled as a gain-scheduled model,

the output static network can be modeled as a DC source and the input static network can be merged with the back-current gain as depicted in Fig. 3-5^{3.2}.

This structure yields good results in many practical cases and allows a trade-off between simplicity and accuracy. A similar way of modeling the back-current-gain is described in [134], [144]. Mathematical aspects about it are described in chapter 4.

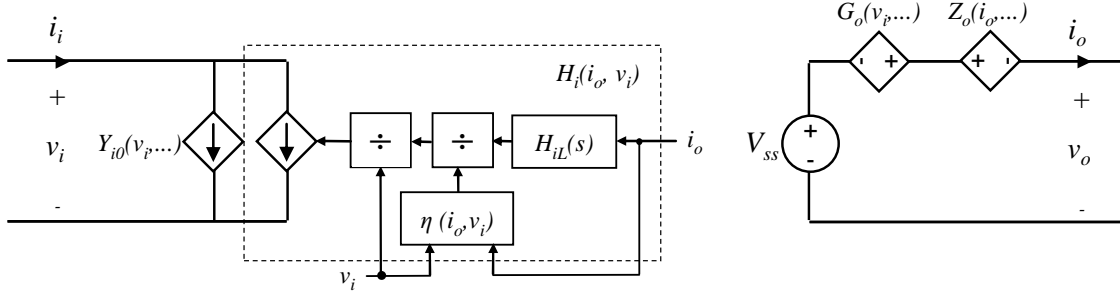
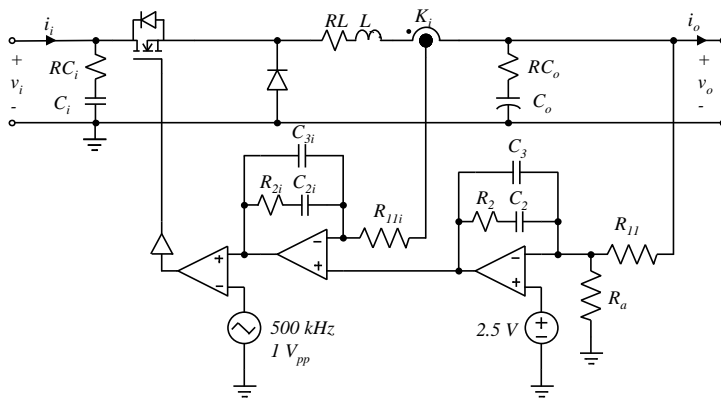


Fig. 3-5: Simplified large-signal model of a DC-DC converter with tightly regulated output voltage.

3.2.3 Simulation based example

In order to illustrate the presented concepts, a behavioral model of a Buck converter with average CMC is derived analytically. The schematic of the modeled converter and its parameters are depicted in Fig. 3-6. Both the inner and outer loop comprises a PI controller with high-frequency pole for switching ripple attenuation (so-called type 2 controller [250]), whose cross-over frequencies are $f_{crossi} = 100$ kHz and $f_{crossv} = 10$ kHz, respectively. The phase margin is 60° for both control loops. For the sake of simplicity, the converter only works within CCM and the switches are ideal.



a. Schematic.

Power stage	Control stage
$L = 6 \mu\text{H}$	$R_a = 10 \text{ k}\Omega$
$RL = 10 \text{ m}\Omega$	$R_{11i} = 10 \text{ k}\Omega$
$C_o = 100 \mu\text{F}$	$C_3 = 597 \text{ pF}$
$RC_o = 25 \text{ m}\Omega$	$C_2 = 2.72 \text{ nF}$
$C_i = 10 \mu\text{F}$	$R_2 = 13.8 \text{ k}\Omega$
$RC_i = 100 \text{ m}\Omega$	$C_{3i} = 27.5 \text{ pF}$
$V_i \in [9-15] \text{ V}$	$R_{11i} = 10 \text{ k}\Omega$
$I_o \in [0.5-5] \text{ A}$	$C_{2i} = 348 \text{ pF}$
$V_o = 5 \text{ V}$	$R_{2i} = 16.9 \text{ k}\Omega$
$f_{sw} = 500 \text{ kHz}$	$K_i = 0.2 \text{ V/A}$

b. Parameters.

Fig. 3-6: Switching model of an average CMC buck converter.

^{3.2} In this case, the transfer functions into G_o and Z_o corresponds to those of the local small-signal model (Fig. 3-2), as the V_o dependence on V_i and I_o is very small. This is the reason why subscript '0' is not used.

To derive the behavioral model analytically, the switching model is first averaged and second linearized by applying small-signal perturbations. This yields the circuits shown in Fig. 3-7^{3.3}.

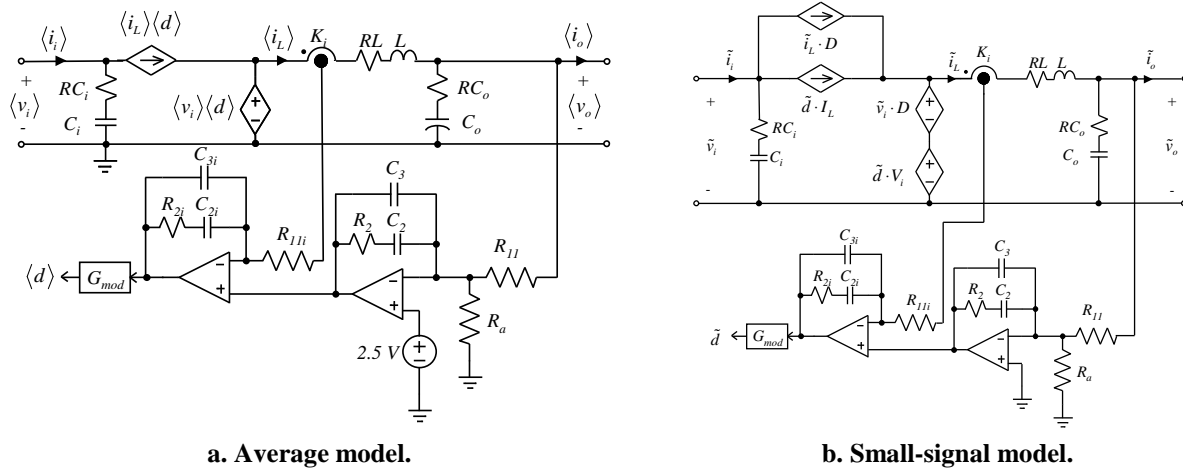


Fig. 3-7: Average model and small-signal model of the average CMC buck converter.

Before deriving the model, it is worth to remark the following aspects:

- In order to make easier the small-signal modeling, both the diode and the Mosfet have been assumed to be ideal (i.e. zero voltage drop and no parasitic resistance).
- The nonlinear dynamic nature of the converter is clearly seen in the average model, since each controlled source is defined by multiplication of two time-varying signals. Such nonlinearities result in dynamics dependence on operating point.
- After linearization, note that the reference voltage is clamped to zero, since the converter is regulated to a constant level.

The un-terminated transfer functions of the g-parameters model are analytically obtained by applying, sequentially, **perturbations on only one input signal while the other one is kept constant**. Moreover, **the operating point is expressed only as a function of input-output variables**). The transfer functions are analyzed up to $f_{sw}/2$, which is usually assumed to be the bandwidth of validity of average models (approximately).

The transfer functions corresponding to the output network are given by (3-3). Notice that **such expressions depend on neither the source nor the load dynamics, thus illustrating the un-terminated concept**. Details about derivation of transfer functions are given in appendix A.1.1.

$$\begin{cases} G_o(s) = \frac{D}{1 + Y_{C_o}(s) \cdot Z_L(s) + G_{mod} \cdot V_i \cdot (R_v(s) \cdot (1 + R_i(s)) + R_i(s) \cdot K_i \cdot Y_{C_o}(s))} \\ Z_o(s) = \frac{Z_L(s) + G_{mod} \cdot V_i \cdot K_i \cdot R_i(s)}{1 + Y_{C_o}(s) \cdot Z_L(s) + G_{mod} \cdot V_i \cdot (R_v(s) \cdot (1 + R_i(s)) + R_i(s) \cdot K_i \cdot Y_{C_o}(s))} \end{cases} \quad (3-3)$$

The duty cycle at steady-state can be expressed as a function of input-output variables as follows.

$$D = \frac{V_o}{V_i} + I_o \cdot R_L \quad (3-4)$$

^{3.3} Analytical derivation of the behavioral model is explained in detail in appendix A.1.

Since the expressions into (3-3) are relatively complex, the dynamics dependence on operating point is analyzed through Bode plots (Fig. 3-8). The main conclusions are listed below.

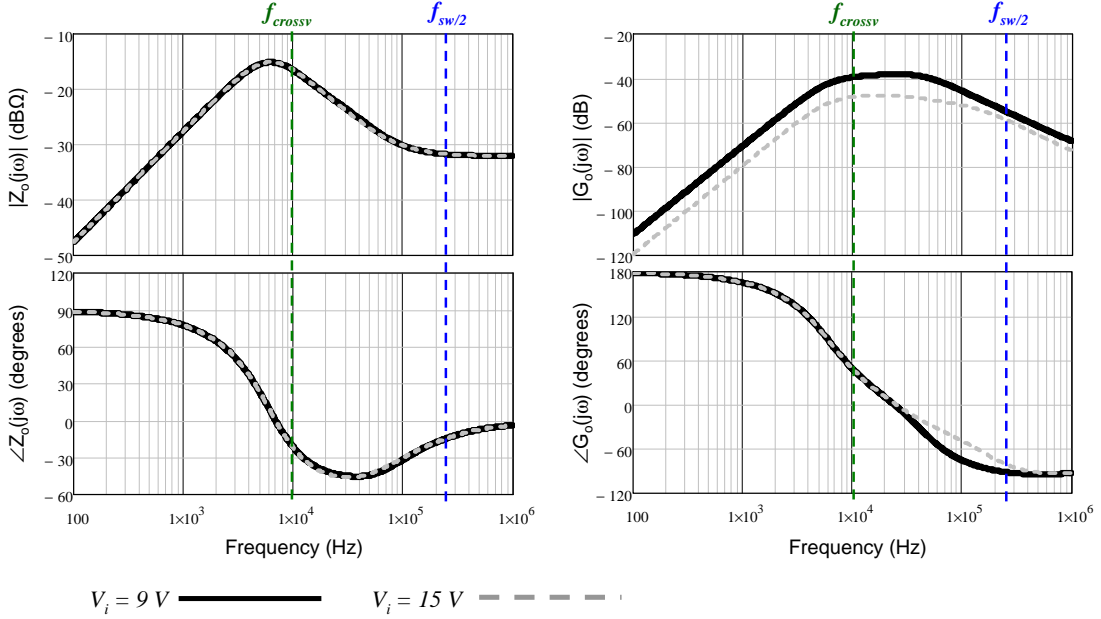


Fig. 3-8: Frequency response of $Z_o(j\omega)$ and $G_o(j\omega)$ as a function of V_i .

- $Z_o(j\omega)$ does not depend on V_i . This is due to the type of control strategy, since CMC makes the overall converter to behave as a programmed current source in parallel with the output capacitor. In fact, it can be seen that, at high frequency $Z_o(j\omega) \approx Z_{C_o}(j\omega)$ whereas at low frequency $Z_o(j\omega) \approx K_i \cdot R_v(j\omega)^{-1}$ [160]. Therefore, **the output impedance of this converter is properly modeled with a single transfer function.**
- $G_o(j\omega)$ strongly depends on V_i , so that the higher V_i the lower $|G_o(j\omega)|$. Moreover, it can be seen that, at low frequency $|G_o(j\omega)| \propto V_i^{-2}$ whereas at high frequency $|G_o(j\omega)| \propto V_i^{-1}$. Hence, **the audio-susceptibility is modeled with a LLMN.** In this example, it is made up by two local transfer functions evaluated at $V_i = 9 V$ and $V_i = 15 V$ combined through piece-wise linear weighting functions. On the other hand, dependence on I_o is negligible, as R_L is small.

The transfer functions corresponding to the input network are given by (3-5). As can be seen, $H_i(s)$ and $Y_i(s)$ depend on both V_i and I_o .

$$\begin{cases} Y_i(s) = Y_{C_i}(s) - \frac{G_{\text{mod}} \cdot I_o \cdot D \cdot (R_v(s) \cdot (1 + R_i(s)) + R_i(s) \cdot K_i \cdot Y_{C_o}(s)) - Y_{C_o}(s) \cdot D^2}{1 + Y_{C_o}(s) \cdot Z_L(s) + G_{\text{mod}} \cdot V_i \cdot (R_v(s) \cdot (1 + R_i(s)) + R_i(s) \cdot K_i \cdot Y_{C_o}(s))} \\ H_i(s) = \frac{D + G_{\text{mod}} \cdot (I_o \cdot (R_v(s) \cdot Z_L(s) + R_i(s) \cdot (-K_i + R_v(s) \cdot Z_L(s))) + V_i \cdot R_v(s) \cdot D \cdot (1 + R_i(s)))}{1 + Y_{C_o}(s) \cdot Z_L(s) + G_{\text{mod}} \cdot V_i \cdot (R_v(s) \cdot (1 + R_i(s)) + R_i(s) \cdot K_i \cdot Y_{C_o}(s))} \end{cases} \quad (3-5)$$

Again, dynamics dependence on operating point is graphically analyzed (see Fig. 3-9) and discussed below.

- $|H_i(j\omega)|$ is inversely proportional to V_i at low-medium frequencies. This is due to the regulation action on v_o . In fact, below f_{crossv} , $H_i(j\omega) \approx V_o \cdot (V_i \cdot \eta)^{-1}$, which corresponds to the input-output

power balance^{3.4}. Above f_{crossv} , the power stage dynamics is reflected, so dependences on I_o are found out. However, if the dependence on I_o is neglected, H_{i0} can be well modeled with a **gain-scheduled transfer function**. If such dynamic dependence on I_o should be considered, a LLMN could be used at the expense of a more complex model.

- $Y_i(j\omega)$ depends on both I_o and V_i at low frequency. Such an effect is due to the constant power load behavior of the regulated converter at low frequency, which is reflected as a negative resistor whose admittance is $-I_i/V_i \approx -I_o V_o/V_i^2$ [52] (efficiency is $\approx 100\%$ for this simplified example). As the frequency increases, $Y_{i0}(j\omega)$ is dominated by the input capacitor and thereby is not dependant on operating point. However, since the constant-power-load behavior of the converter is already modeled by the static network, Y_{i0} is **made up by a single transfer function corresponding essentially to $ZC_i(s)^{-1}$** .

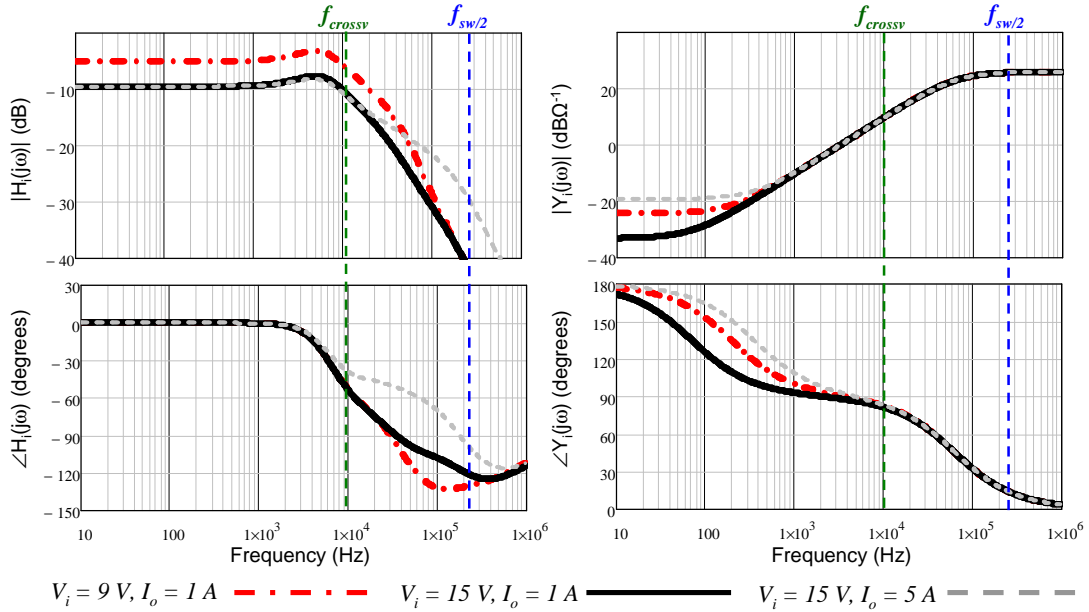


Fig. 3-9: Frequency response of $H_i(j\omega)$ and $Y_i(j\omega)$ as a function of V_i and I_o .

Hence, the behavioral model of the converter is that depicted in Fig. 3-10. Before using the model, some post-processing actions have to be done on some of the derived transfer functions. More specifically:

- The gain of $H_i(s)$ has to be readjusted, yielding $H_{iL}(s)$, in order to represent properly the input-output power balance.
- The static response of $Y_i(s)$ has to be subtracted. This yields $Y_{i0}(s)$ (note that the static relationship between i_i and v_i is already modeled by using the division block after $H_{iL}(s)$).

Such actions will be discussed more in detail in the next chapter. It is worth to point out that the efficiency is not modeled as a function of the operating point because it is very high over the whole operating range, as the switches are ideal. Note also that no post-processing actions have to be carried out on $Z_o(s)$ or $G_o(s)$, as they already has null response at steady-state due to the integral action of the outer compensator $R_v(s)$.

^{3.4} This statement is valid as long as the dynamic variations of the averaged energy stored in the inductor are negligible. As the frequency increases, such effect may be significant, even below the cross-over frequency of the outer loop.

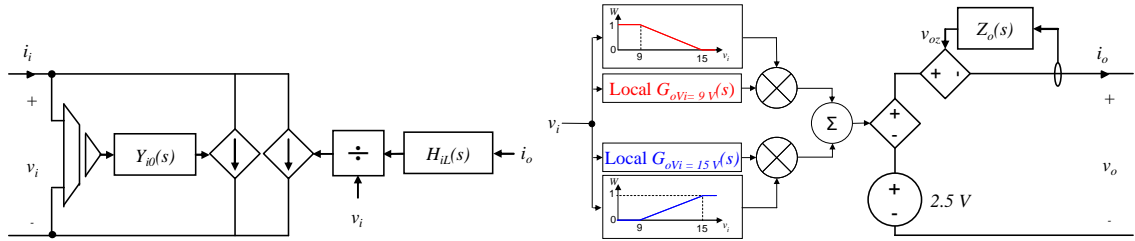
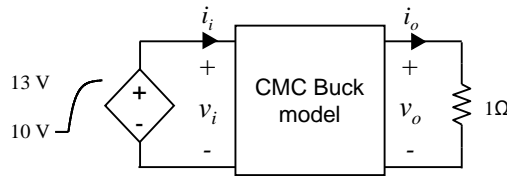


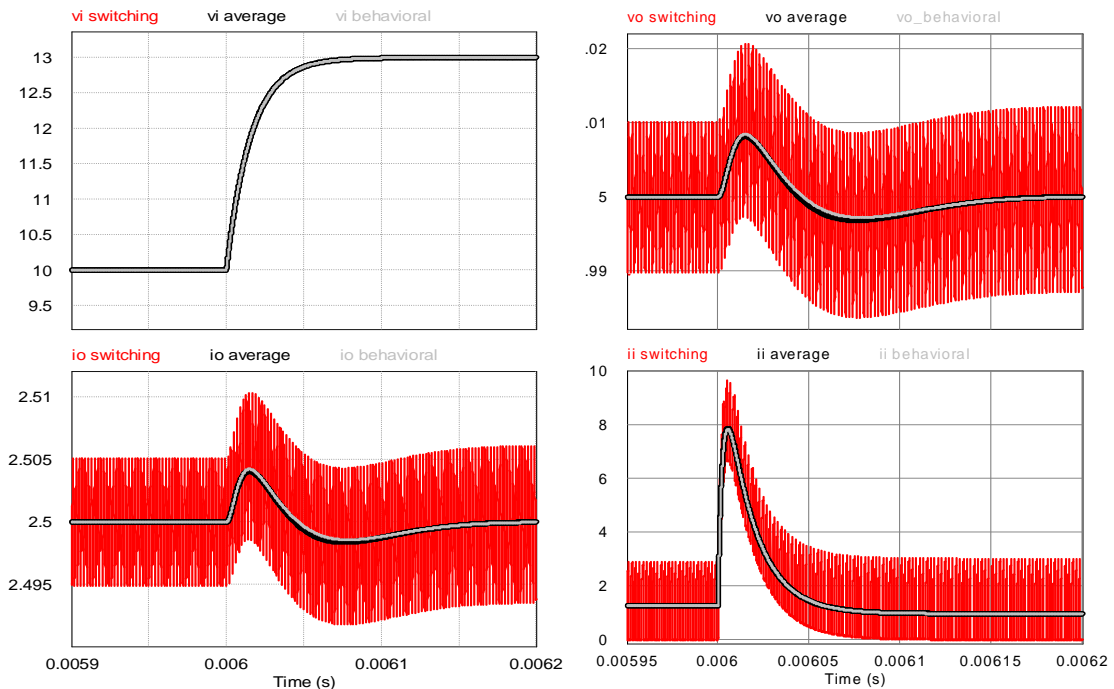
Fig. 3-10: Behavioral model of a CMC buck converter.

The response of the behavioral model has been compared to the response of the conventional switching model (Fig. 3-6) and average model (Fig. 3-7) under two electrical tests. All models have been simulated using PSIM.

Test 1: The simulated schematic is shown in Fig. 3-11a. The input voltage increases exponentially from 10 V to 13 V while a 1 Ω resistor is located at the output. This way, the model is subjected to large signal v_i disturbances. The response of the behavioral model, the average model and the switching model are compared in Fig. 3-11b. As can be seen, the behavioral model and average model responses are close to each other. This demonstrates the capability of the behavioral model to reproduce the large signal averaged response of the converter, as a conventional average model does. Note that the audio-susceptibility of the converter is well approximated by the LLMN, as well as the input-output power balance is accurately reproduced by the gain-scheduled transfer function.



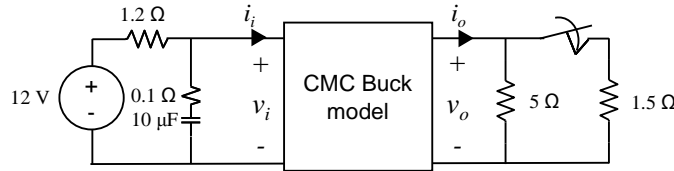
a. Schematic.



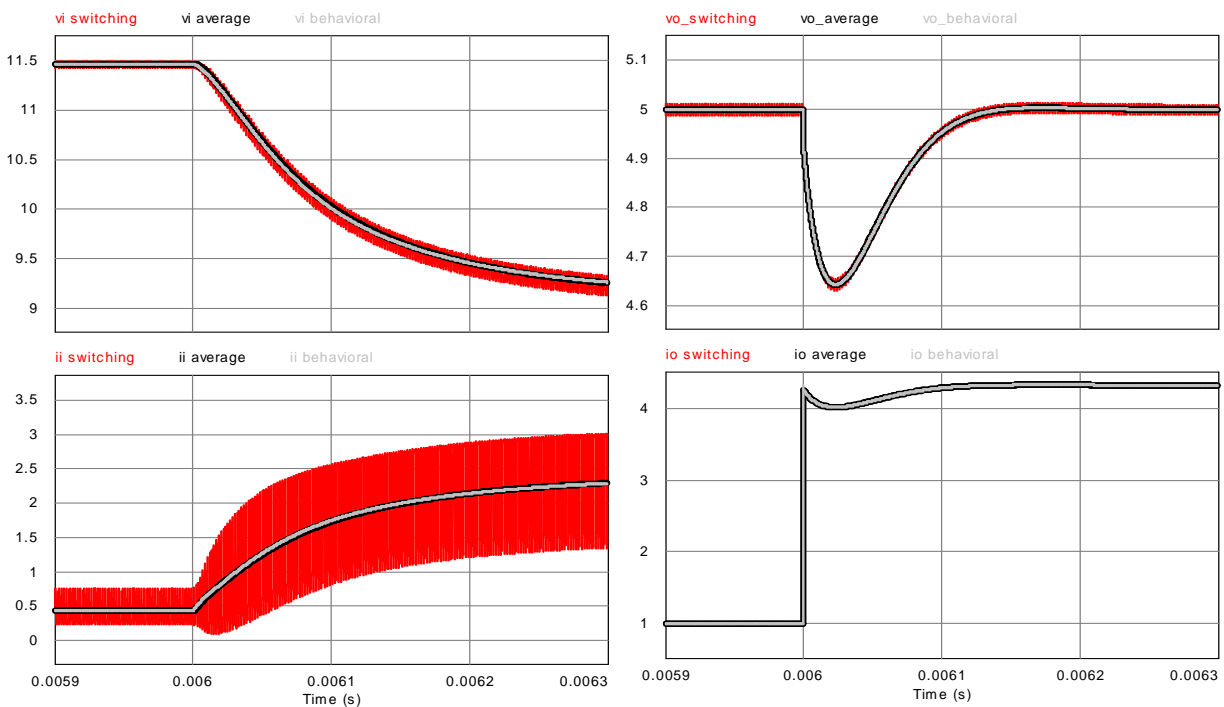
b. Simulation results: comparison of behavioral model, average model and switching model.

Fig. 3-11: Validation test 1.

Test 2: In this case the converter is subjected to a large load step while is supplied from a DC voltage source with a droop profile (emulated through a series resistor, see Fig. 3-12a). This way, both the input signals of the model (v_i and i_o) are simultaneously disturbed in a large-signal sense. As can be seen, the response of the behavioral model and the average model are very close to each other. Nevertheless, note that i_i is dominated by Y_{i0} at high frequency (current flowing through the input capacitor of the converter), and this is the reason why the H_i dependence on I_o at high frequency is not noticed.



a. Schematic.



b. Simulation results: comparison of behavioral model, average model and switching model.

Fig. 3-12: Validation test 2.

3.3 System identification concepts

At this point, the modeling of power converters has been tackled by assuming that detailed information about the modeled power converter is available. However, in this thesis, it is assumed that such information is not available, meaning that system identification techniques are required.

As presented in previous section, the behavioral black-box models are comprised of a variety of dynamic networks. Such networks are made up by single-input single-output (SISO) linear-time-invariant (LTI) model(s) sometimes combined with nonlinear static functions. Hence, **this thesis focuses on identification of SISO LTI models, represented by a transfer function.**

Basically, the system identification process of a behavioral model can be split into two tasks: experimental tests and model parameterization. These points are described in the next subsections.

3.3.1 Experimental tests

In this thesis, system identification focuses on SISO LTI models. However, in general black-box models of power converters are multiple-input multiple-output (MIMO) systems, where each output of the model depends on several input signals. Therefore, the experiments proposed in thesis are designed so that, under each test, only **one input signal is excited while the others are kept constant**. Moreover, those tests are applied so that **nearly local linear behavior is maintained**. This way, **the dynamic response of each output signal depends linearly on only input signal under each experimental test**, thus enabling the use to SISO system identification techniques. From this statement, it is easy to conclude that **the number of types of test is equal to the number of input signals**.

The next point is to select a proper excitation signal. This is a critical task since this is the way of gathering information about the dynamic system to be identified. From a general point of view, the excitation signal should fulfill the following requirements.

- The excitation signal have to be “informative enough”, meaning that the obtained data allow for accurate fitting of the model within the frequency range of interest.
- The experiments should be as simple as possible. Avoiding the need of complex experiments, as well as expensive equipment, may be desirable from a practical point of view.

Previous identification methods of black-box models for power converters, such as that shown in Fig. 3-2), are based on AC sweep tests. As a difference from previous works, **this thesis relies on the use of the step as excitation signal for model identification**, since this allows a good trade-off between simplicity and fitting performance. Main features of step tests are summarized below.

- **The experiments are very simple.** This is the key advantage of the step signal over other excitation signals. Step tests can be carried out in power electronics laboratories straightforwardly with low cost equipment, such as switches and passive loads. As a preliminary example, just two resistors and one mechanical contactor are sufficient to identify the output impedance of a black-box model for a 30 kW generator^{3.5}.
- **Good identification results are achieved.** The step signal has a continuous power spectrum which is inversely proportional to the frequency. This mean, all frequencies are simultaneously excited and low frequencies are emphasized over high frequencies. As will be shown along this thesis, good identification results are achieved using this method, thus capturing the most relevant dynamics of the converter **regarding system-level analysis**. Moreover, **accurate fitting results are achieved in many cases with low-order transfer functions**. This is an important point, since high order transfer function may lead to unacceptable simulation times in case of large systems. Nevertheless, the relatively low energy introduced by a step signal at high frequency sometimes yield to inaccurate identification results at high frequency.

^{3.5} This generator is analyzed in chapter 8.

Practical issues regarding transient data measurements (total time, time step) and limitations of the step signal will be discussed in subsequent chapters. Methods to evaluate the fitting performance both in time domain and frequency domain are presented as well.

For instance, consider the regulated DC-DC converter modeled in previous section. This is a two-input two-output model, where the inputs are v_i and i_o , and the outputs are v_o and i_i . If the model is linearized around a certain operating point, the dynamic relationship between input and output signals is given by (3-1). Therefore, two step tests have to be designed (see Fig. 3-13):

- *Test 1:* v_i has to be stepped while i_o is kept constant. This way, the transient responses of i_i and v_o depend only on $Y_i(s)$ and $G_o(s)$, respectively (Fig. 3-13a).
- *Test 2:* i_o has to be stepped while v_i is kept constant. This way, the transient response of i_i and v_o depends only on $H_i(s)$ and $Z_o(s)$, respectively (Fig. 3-13b).

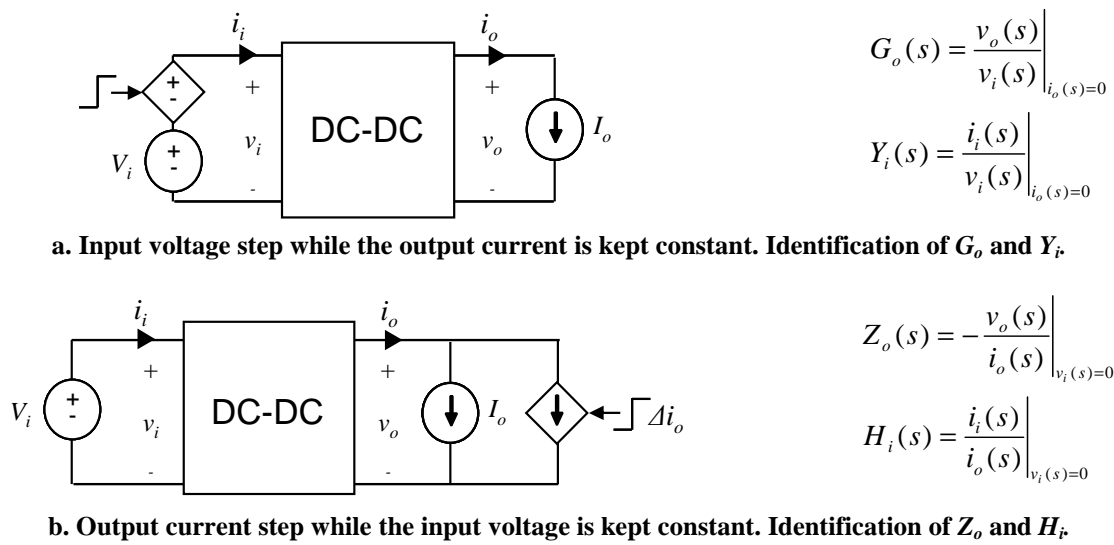


Fig. 3-13: Identification experiments of black-box models for DC-DC converters with regulated output voltage: conceptual approach.

In both cases, a voltage source and a current sink are used to set the operating point V_i and I_o , respectively. It is important to point out that, if the transfer function to be identified is not dependant on the stepped signal, any step magnitude would be valid. Otherwise, small magnitude steps should be applied around the considered operating point, so that local linear (or nearly linear) operation is ensured.

Practical implementations of these experiments are presented along this thesis.

3.3.2 Transfer function models identification: basic approach

Once the transient response of the converter has been recorded, the next task is to identify the parameters of each transfer function into the model. This is done using **parametric identification techniques of SISO LTI models**.

Basically, the parametric identification process consists in **selecting a certain candidate transfer function and applying an optimization algorithm**. The optimization algorithm searches for the coefficients of the transfer function so that **the error between the measured output and the predicted output is minimized**.

Fig. 3-14 illustrates this procedure on the output impedance of a regulated DC-DC converter. Once the step response has been measured, a candidate transfer function has to be selected. A good attempt can be done by looking at the type of step response. Clearly, it looks like a typical second-order overdamped response, so a second-order transfer function with two real poles should be a proper choice. After that, an optimization algorithm searches for the parameters of the transfer function in such a way that the difference between the predicted output $\hat{v}_o = -Z_o * i_o$ and the measured one v_o is minimized.

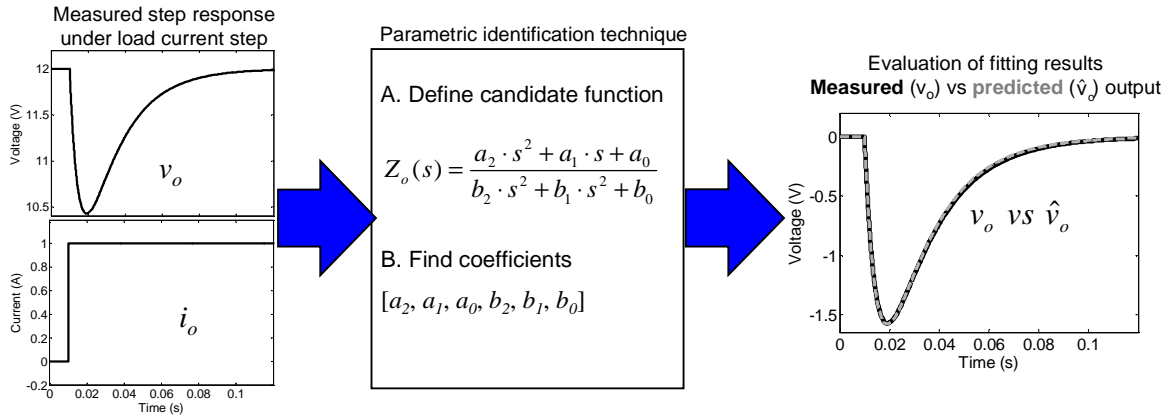


Fig. 3-14: Parametric identification of a transfer function model from step response: Basic approach.

Parametric identification of transfer function models is a well established and mature field of research [66], [68] and there are commercial tools available to apply them straightforwardly, such as the System Identification Toolbox of Matlab [260]. Along this thesis, those algorithms are applied to identify transfer function models from the step response. In addition, **an alternative method based on sequential identification of first and second order basic subsystems** is presented in the chapter 9. Such a method, although less general and more time-consuming, allows identifying the transfer function models by means of simple equations, thus avoiding the need of optimization algorithms. This is an important point, as those algorithms may be complex from the point of view of power electronics engineers, if a dedicated software tool is not available.

3.3.3 Cross-coupling effect

As discussed before, the proposed identification method assumes that only one input signal is disturbed while the other ones are kept absolutely constant. Rigorously speaking, in real conditions such requirement cannot be usually fulfilled. Therefore, the loads and sources used to set the operating point of the converter will be dynamically coupled with the identified subsystems.

For example, consider the output current step test introduced in section 3.3.1. Real voltage sources have nonzero output impedance, meaning that the input voltage will be disturbed under a load current step. As a consequence, the source exhibits a certain coupling effect with the identified subsystems (see Fig. 3-15). Such an effect is referred to hereinafter as **“cross-coupling effect”** as well as the undesired perturbations are referred to as **“cross-perturbations”**.

If the voltage source has low enough impedance, the cross-coupling problem can be prevented. Otherwise, such an effect has to be removed from the identified transfer function.

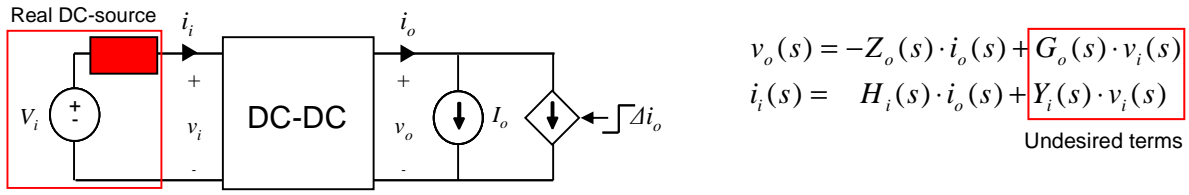


Fig. 3-15: The cross-coupling problem: perturbations of v_i under an output current step.

A general method to address the cross-coupling problem on DC-DC converters, based on frequency response measurements, has been presented in [150]. In this thesis, that method is adapted to time-domain measurements and extended to other converters. In addition, a simple method to analyze the significance of the cross-coupling effect is also proposed. Then, one can determine which cross-coupling effects are significant and remove only the important ones, thus simplifying the process. The method is applied using just the identification measurements, so no additional experimental test is required.

3.3.4 Simulation based example

The described identification concepts are next illustrated on the simulation example tackled in section 3.2.3. Fig. 3-16 shows the simulated response of the CMC buck converter (switching model) to an output current step while the input voltage is kept constant. This way, $Z_o(s)$ and $H_i(s)$ are identified. Since dynamic dependences on I_o were found to be quite slight, no limitations in the step magnitude are considered. The simulated waveforms have large switching ripple content, which should be filtered out before identifying, because the behavioral model accounts with the averaged response of the converter. As will be discussed in subsequent chapters, the moving-average-filter [247] is a well suited and simple option to pre-filter the signals. This filter has been herein tuned so that the switching signal is averaged over one period. As shown in Fig. 3-16, the average dynamic response is preserved while the switching ripple is removed.

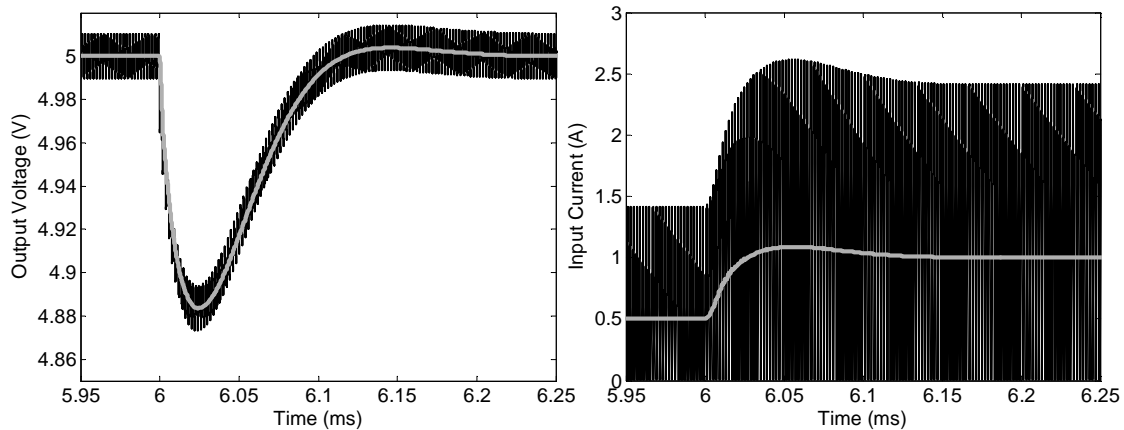


Fig. 3-16: Transient response of the CMC buck converter under an i_o step from 1 A to 2 A with $V_i = 10$ V. Black traces: Simulated response. Grey traces: Filtered response (moving-average-filter).

Fig. 3-17 shows the simulated response of the CMC buck converter (switching model) to an input voltage step while the output current is kept constant. As a difference from the previous case, the identified transfer functions ($G_o(s)$ and $Y_i(s)$) depends on V_i , so a small step has to be applied. A step has been carried out from 9 V to 9.5 V. Again, a moving-average-filter has been used to filter out the switching ripple.

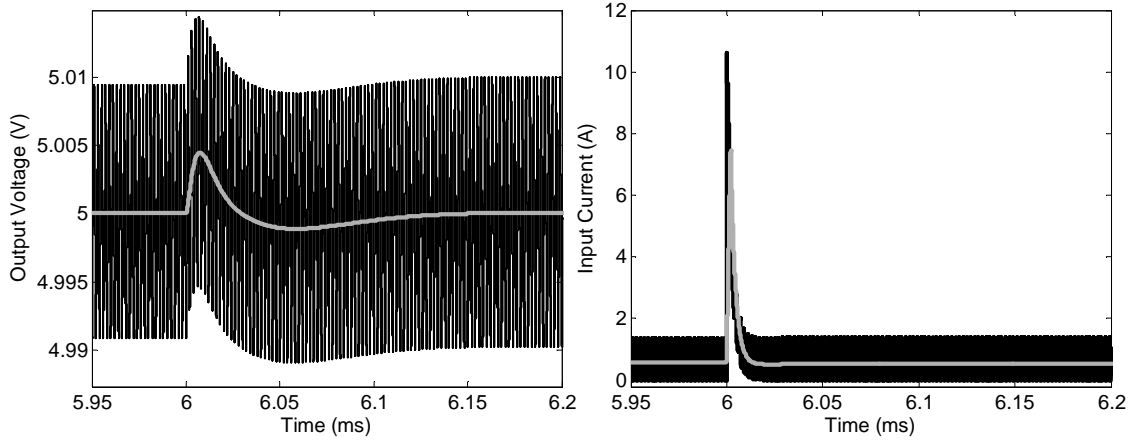


Fig. 3-17: Transient response of the CMC buck converter to a v_i step from 9 V to 9.5 V with $I_o = 1$ A. Black traces: Simulated response. Grey traces: Filtered response (moving-average-filter).

Following this, the steady-state value of the signals has been subtracted. After that, the corresponding transfer function models have been identified using the optimization function ‘*oe*’ of Matlab [254].

A comparison between the simulated, pre-processed signals and the output of the identified models is shown in Fig. 3-18. As can be seen, the identified model matches the pre-processed measurements in all cases. The identified models are defined as a function of the discrete forward-shift operator ‘*q*’ [66], [68] because the optimization algorithm deals with discrete data. These models can then be converted to continuous time domain before model implementation.

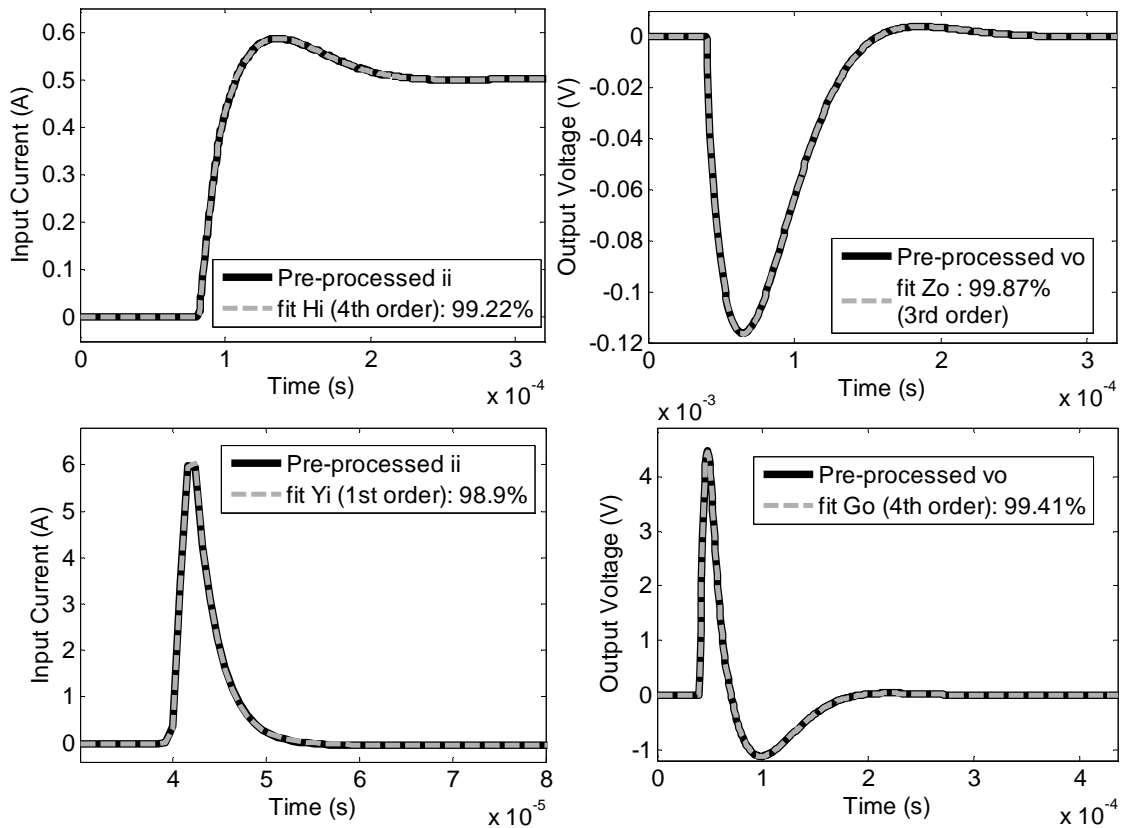


Fig. 3-18: Fitting results of $Y_i(q)$, $G_o(q)$, $Z_o(q)$ and $H_i(q)$.

The frequency response of the identified models is compared with the theoretical ones (3-3)-(3-5) in Fig. 3-19. The responses are close to each other up to one half the switching frequency, which is approximately the maximum frequency of validity of the models. This demonstrates the usefulness of the identification method based on the step response^{3,6}.

It is also important to point out that **the order of the identified transfer functions is significantly lower than that of the true model order**. Indeed, the highest order of the identified models is 4th whereas the true order is 6th to 7th. The model order is reduced because some poles and zeros of the system have a very low impact on the frequency response. For example, the inner loop dynamics is negligible in the output impedance bode plot. This model order reduction is an important point, since behavioral models should be as simple as possible in order to allow for fast simulation times.

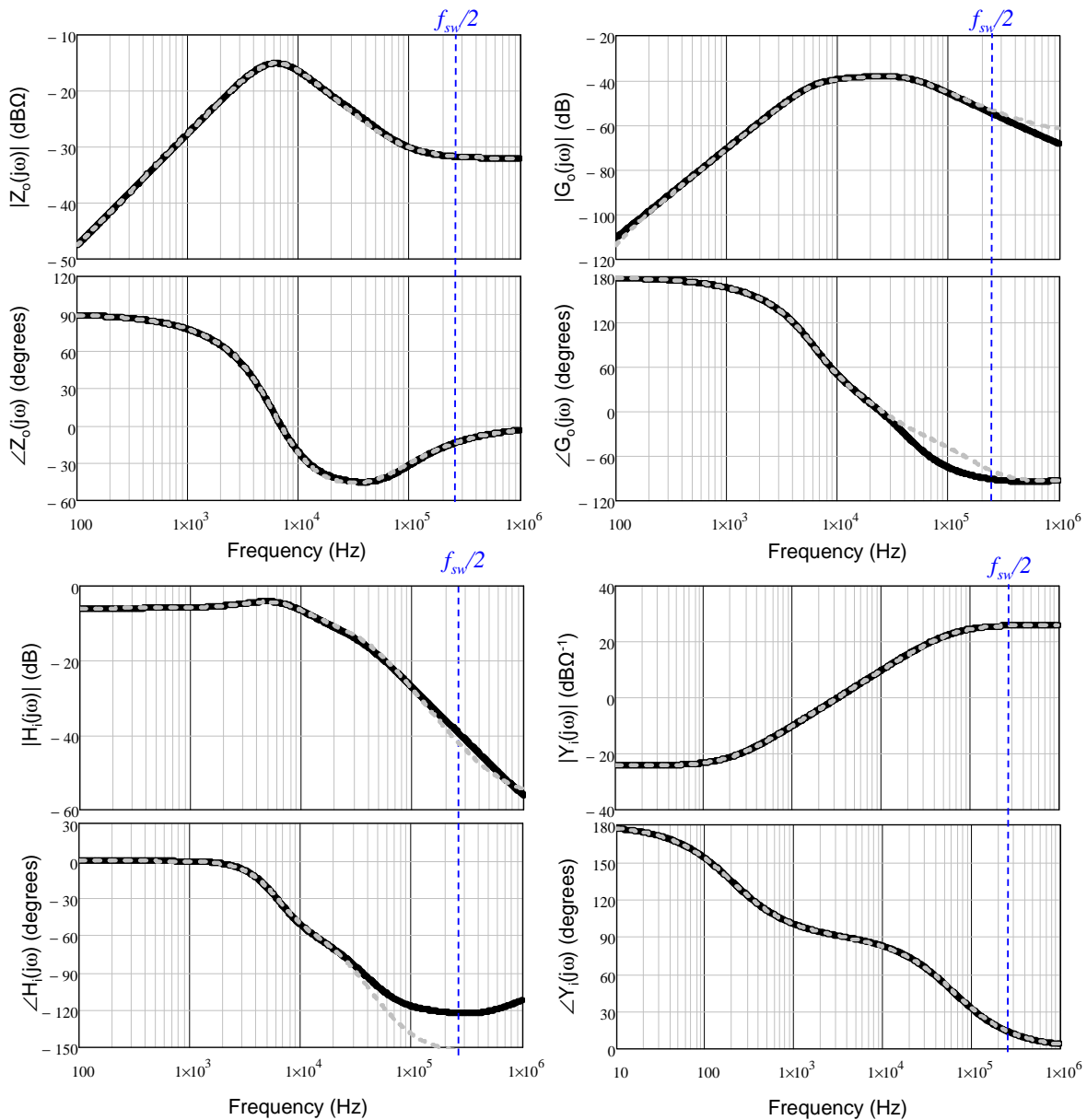


Fig. 3-19: Identified models (grey dashed traces) vs theoretical models (black solid traces).

^{3,6} The observed deviations at high frequency in some transfer functions are mostly due to linearity assumptions and the low energy content introduced by the step at high frequency. Nevertheless, such deviations may not have a high impact on the response of the converter due to the low-magnitude of the transfer functions in that frequency.

A comparison of the simulation time, required to simulate each model, is given in Table 3-1. In order to carry out the comparison in relative terms, the time step is 20 ns in all cases (average and behavioral models allow for higher time step). The computer is an Intel Core 2 Duo @2.33 GHz, 2GB RAM, and the operating system is Windows XP. As can be seen, the behavioral model requires less simulation time than both the average and the switching model. Moreover, the behavioral model based on true transfer functions require less time than the identified one.

Model	Simulation time
Switching model	20 s
Average model	14 s
Behavioral model (true transfer functions)	13 s
Behavioral model (identified transfer functions)	11 s

Table 3-1. Comparison of simulation times as a function of the converter model using PSIM.

Finally, the **cross-coupling problem is illustrated**. For this purpose, an inductor has been located between the ideal voltage source and the input port of the converter, thus emulating a voltage source with nonzero output impedance. The output current step has been repeated, returning the waveforms depicted in Fig. 3-20. Due to the inductor, v_i is disturbed, meaning that part of i_i is flowing through the input capacitor. In other words, the transient response of i_i is not only determined by $H_i(s)$ but also by $Y_i(s)$. This effect plays a significant role on the identification process, as demonstrated in Fig. 3-20b, where one may see that the identified transfer function with cross-coupling “ $H_{im}(s)$ ”^{3.7} is quite different from the identified transfer function without it above 10 kHz. This demonstrates that the **cross-coupling problem must be analyzed and removed if required**.

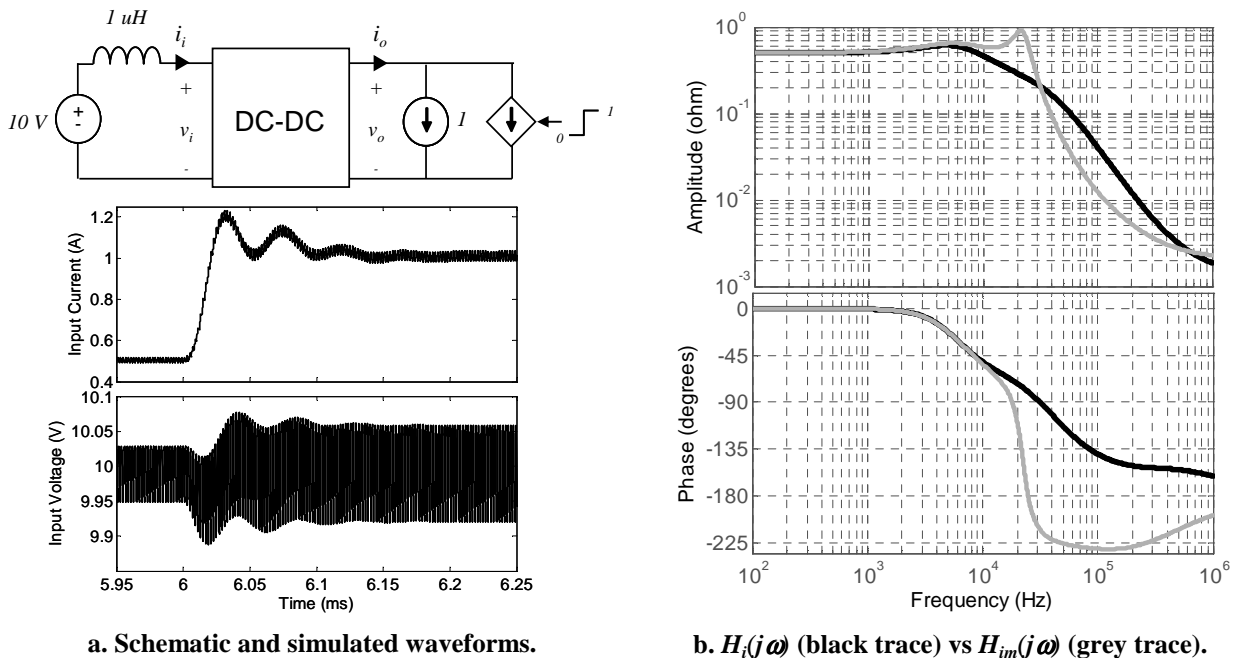


Fig. 3-20: Cross-coupling effects on $H_i(s)$.

^{3.7} Transfer functions identified with cross-coupling effects are denoted hereinafter with the subscript “m”.

3.4 Summary and overview

3.4.1 Summary of concepts

The main concepts tackled along this thesis, regarding modeling and identification, has been presented and illustrated in this chapter.

- Every power converter/subsystem is modeled as an n -port input-output network. The converters are modeled in terms of their input-output interface signals with the rest of the system, so that some signals are considered as model inputs and others as model outputs.
- The models are made up by a set of static and dynamic networks. These dynamic networks consist of transfer functions represented in the Laplace domain and nonlinear static functions. Such transfers functions are referred to as “un-terminated transfer functions”, since they only contains the internal dynamics of the converter and are independent of the load-source dynamics.
- The models are identified by applying a set of step tests. Under each type of test, only one input signal is stepped while the other ones are kept constant. The number of types of test is equal to the number of input signals.
- The transfer function models are identified from the measured transient responses by applying parametric identification algorithms.
- After that, possible cross-coupling effects with the load and the source have to be analyzed and removed if necessary.

The black-box modeling procedure consists of a set of sequential tasks. A **flowchart of the procedure** is depicted in Fig. 3-21 and described below.

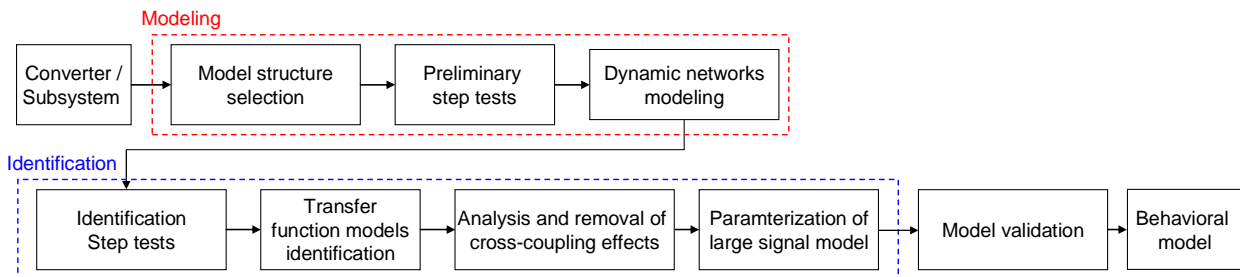


Fig. 3-21: Flowchart of the black-box modeling procedure.

- **Model structure selection:** The interface signals of the model are defined and then sorted in two groups: input signals and output signals. This leads to a certain model structure (i.e. g -parameters, y -parameters, etc).
- **Preliminary step tests:** A set of step tests is carried out in order to analyze the behavior of the converter from a qualitative point of view. Dynamics dependence on operating point is analyzed during this task.
- **Dynamic networks modeling:** Once the behavior of the converter has been analyzed, the types of dynamic networks which compose the black-box model are selected.
- **Identification step tests:** Next, the identification step tests are applied and the transient response of the converter is recorded.

- **Transfer function models identification:** After that, parametric identification techniques are applied on the recorded measurements to identify the parameters of the dynamic systems.
- **Analysis and removal of cross-coupling effects:** Once the transfer functions have been identified, the cross-coupling effects are analyzed and the significant ones are removed.
- **Parameterization of large-signal model:** Once un-terminated transfer functions have been obtained, some post-processing actions are carried out on them to build the large-signal model. Additional characterization of the static response, including efficiency and line/load regulation (if necessary) is done.
- **Model validation:** Finally, a set of validation tests is applied on both the real converter and the black-box model, in order to verify that the black-box model reproduces properly the average large-signal response of the real converter. The validation tests should be designed as follows:
 - The validation tests should be different from the identification tests.
 - Several input signals should be simultaneously perturbed in a large-signal sense.
 - Some validation tests should reproduce the real conditions that the actual converter is intended to be subjected to.

If satisfactory validation results are obtained, the black-box modeling procedure is finished. Otherwise, the parameters of the dynamic systems should be identified more accurately or different dynamic networks should be used to model the power converter / subsystem.

3.4.2 Overview of the thesis

This general black-box modeling procedure is particularized for several types of power converters and power electronics based subsystems along this thesis. It is organized as depicted in Fig. 3-22 and described below.

- Chapters 4 to 5 present black-box modeling techniques of power converters based on transient response measurements under step tests.
 - **Chapter 4:** Starting from the black-box model for DC-DC converters (reviewed in this chapter), a novel identification method based on step tests is proposed, and extensions to the existing proposal are presented.
 - **Chapter 5:** A large black-box modeling method of three-phase voltage source inverters with output voltage regulation is presented in this chapter, as well as a novel identification method.
- Chapters 6 to 8 extend the black-box modeling technique, based on step tests, to other power subsystems comprised of power electronics converters.
 - **Chapter 6:** A black-box modeling and identification method of a fuel-cell power supply, based on a DC-DC converter with input current control, is presented.
 - **Chapter 7:** Solar array simulators are modeled and identified in this chapter.
 - **Chapter 8:** A starter-generator for aircraft based on a switched reluctance machine is modeled and identified in this chapter.
- **Chapter 9** presents an alternative identification method of transfer function models from the step response.

- Finally, a synthesis of the presented modeling and identification procedures, and the main conclusions and future works, are described in chapter 10 and 11.
 - **Chapter 10:** A systematization of the methods is described, drawing guidelines to derive behavioral models of other power converters/subsystems in a systematic way.
 - **Chapter 11:** General conclusions of the thesis and future works are discussed.

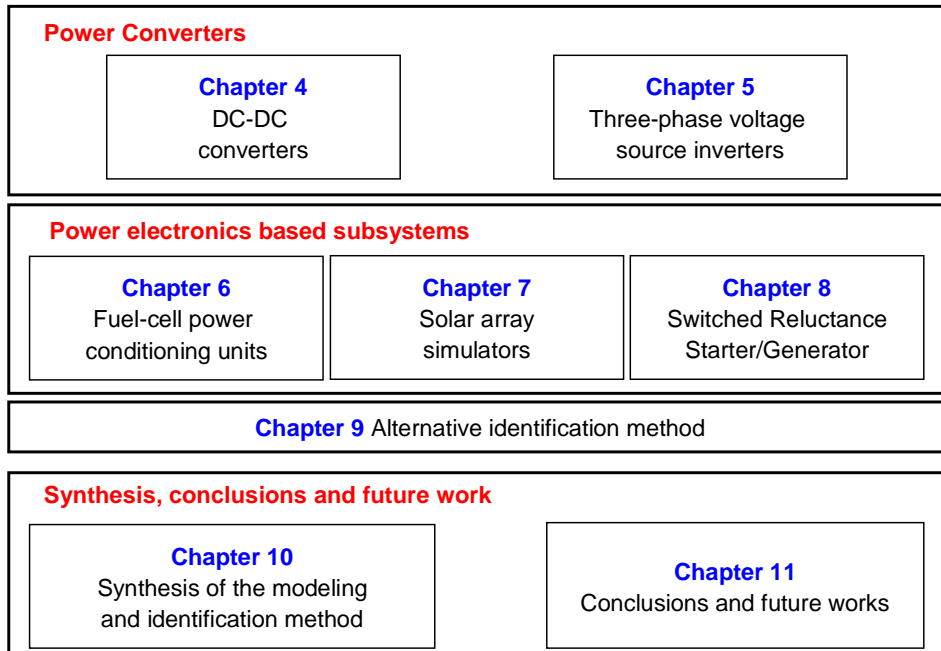
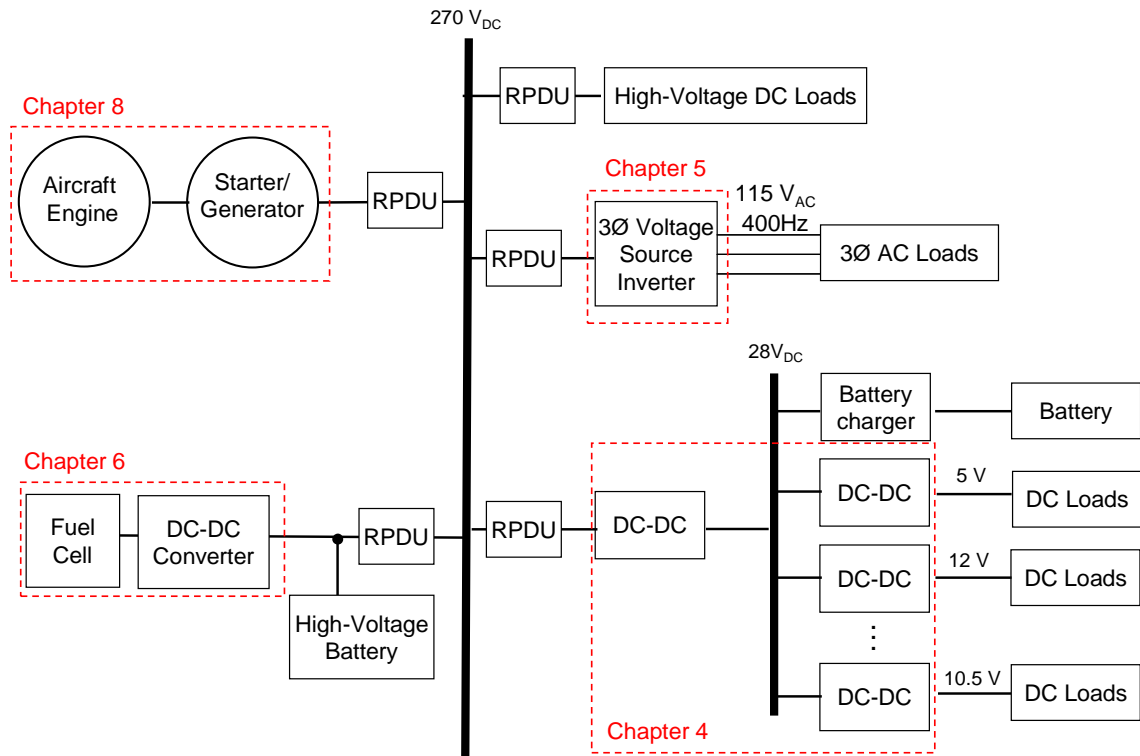
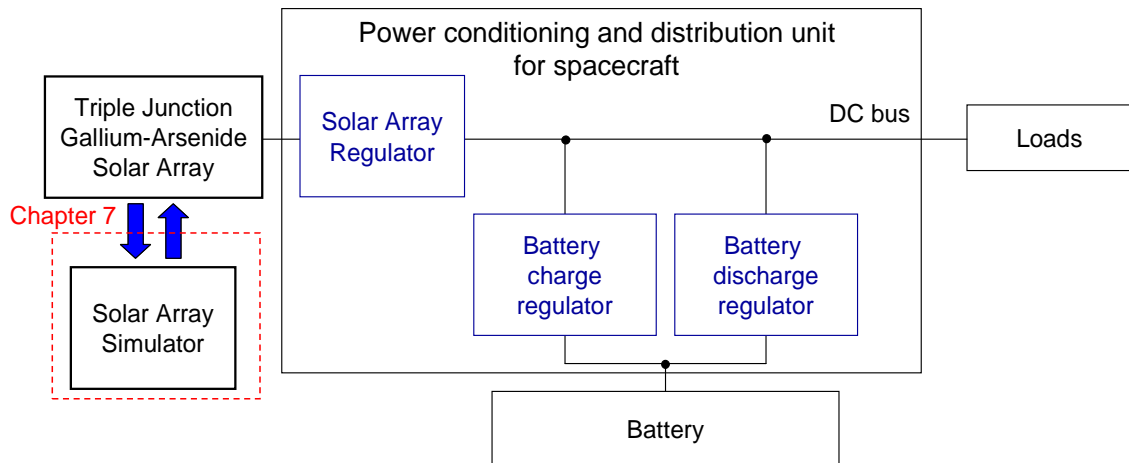


Fig. 3-22: Overview of the thesis.

The modeled power converters and subsystems tacked in this thesis are part of power distribution systems for the more electric aircraft, more electric ships, electric cars, microgrids, etc. For illustrative purposes, the practical application of the modeled subsystems in some of the aforementioned systems is illustrated in Fig. 3-23.



a. Power distribution systems of a more electric aircraft: partial diagram.



b. Power distribution system of a spacecraft based on a regulated bus.

Fig. 3-23: Power distribution systems comprising the modeled converters and subsystems along this thesis.

4 Black-box modeling of DC-DC converters with output voltage control

4.1	Introduction.....	65
4.2	Model description.....	66
4.2.1	Description of the modeled converter	66
4.2.2	Model structure	67
4.2.2.1	Small-signal approach	67
4.2.2.2	Large-signal approach	67
4.2.3	Modeling dynamic networks.....	68
4.2.3.1	Transfer function model	68
4.2.3.2	Local linear models network	69
4.2.3.3	Gain-scheduled transfer function	70
4.2.3.4	Comparison with previous proposals	71
4.2.4	Model simplification: merging static and dynamic networks	71
4.2.5	Soft-start and enabling networks modeling.....	73
4.3	Model identification.....	75
4.3.1	Identification step tests.....	75
4.3.1.1	Output current step	76
4.3.1.2	Input voltage step	77
4.3.1.3	Measuring the transient response	77
4.3.2	Parametric identification of transfer function models.....	78
4.3.2.1	Model structure selection	78
4.3.2.2	Signals pre-processing.....	79
4.3.2.3	Model order selection	80
4.3.2.4	Optimization algorithm	80
4.3.2.5	Validation	81
4.3.2.6	Transformation to continuous time domain.....	81
4.3.2.7	Parametric identification in practice.....	81
4.3.3	Cross-coupling effects.....	82
4.3.3.1	Removal.....	82
4.3.3.2	Analysis	84
4.3.3.3	Prevention.....	85
4.3.3.4	Model order reduction	85
4.3.4	Parameterization of the large-signal black-box model.....	86
4.3.4.1	Static networks characterization.....	86
4.3.4.2	Transfer functions post-processing.....	86
4.3.4.3	Soft-start and enabling networks	86
4.3.5	Overview of the identification procedure.....	87
4.4	Experimental results: modeling of a commercial buck converter.....	89
4.4.1	Introduction	89
4.4.2	Preliminary tests	89

4.4.2.1	Analysis of H_i and Z_o dependence on operating point.....	90
4.4.2.2	Analysis of G_o and Y_i dependence on operating point	92
4.4.2.3	Remarks on the analysis	94
4.4.3	Dynamic networks modeling	94
4.4.4	Identification of terminated transfer functions.....	95
4.4.4.1	Transfer functions $H_{im}(s)$ and $Z_{om}(s)$	95
4.4.4.2	Transfer functions $Y_{im}(s)$, $G_{o8m}(s)$, $G_{o12m}(s)$ and $G_{o16m}(s)$	98
4.4.5	Analysis and removal of cross-coupling effects	100
4.4.5.1	Analysis and simplification of the de-coupling matrix.....	100
4.4.5.2	Removal.....	102
4.4.5.3	Model order reduction	103
4.4.6	Parameterization of the large-signal model.....	104
4.4.7	Validation.....	104
4.4.7.1	Identification of transfer functions: comparison with AC sweep results.....	105
4.4.7.2	Validation of the cross-coupling removal method and prevention guidelines	108
4.4.7.3	Validation of the large-signal black-box model	110
4.4.8	Summary	115
4.5	Experimental results: modeling of other commercial converters	116
4.5.1	Forward converter	117
4.5.1.1	Preliminary tests: linearity analysis	117
4.5.1.2	Dynamic networks modeling.....	120
4.5.1.3	Model identification	122
4.5.1.4	Model validation.....	125
4.5.2	Multi-stage AC-DC converter (output port modeling)	128
4.5.2.1	Preliminary tests: linearity analysis	129
4.5.2.2	Dynamic networks modeling.....	130
4.5.2.3	Model Identification	130
4.5.2.4	Model validation.....	131
4.5.3	Discussion of results and introduction to model improvements	133
4.5.3.1	Limitations of local linear model networks based on local feedback.....	133
4.5.3.2	Local linear model networks based on global feedback.....	133
4.5.3.3	Weighted state-space model	136
4.6	Experimental results: modeling of a DC distributed power system.....	136
4.6.1	System-level test 1: Step decrease in point-of-load power	137
4.6.2	System-level test 2: Step increase in intermediate-bus power	138
4.6.3	System-level test 3: Dynamic interaction of subsystems.....	140
4.6.3.1	Step increase and decrease in bus power from 37.5 W to 85.5 W and back	140
4.6.3.2	Step increase and decrease in bus power from 37.5 W to 110 W and back	141
4.6.4	System-level test 4: Hot-swap of a point-of-load converter	143
4.7	Conclusions.....	145

4.1 Introduction

A black-box modeling method of DC-DC converters with regulated output voltage has been recently proposed. The model consists of a g-parameters two-port network (which has been introduced in chapters 2 and 3), and the existing identification method is based on frequency response measurements [134], [144]-[146]. Such a frequency response is obtained through AC sweep tests, and then a parametric identification algorithm is applied on the measured response.

This approach yields accurate identification results but, from a practical point of view, measuring the frequency response of a power converter usually requires complex experimental tests and expensive equipment: a network analyzer, a power amplifier and an adequate injection circuit of the perturbation signal. Such a complexity is especially significant in case of medium and high power systems [147].

In order to overcome that drawback, a novel identification method of black-box models for DC-DC converters, based on transient response measurements, is presented in this chapter as original contribution. The proposed method is based on the transient response of the converter to a set of step test and the use of parametric identification techniques. Compared to the previous approach, the main advantage is the ease of the experimental tests. The chapter is organized as follows:

- **Section 4.2.** The black-box modeling approach, already introduced in chapter 3, is described in detail and extended with additional features, such as sof-start modeling.
- **Section 4.3.** The proposed identification method, based on step tests, is described. The following aspects are discussed:
 - Practical implementation of the identification tests.
 - Parametric identification of transfer functions from transient response.
 - Removal, analysis and prevention of cross-coupling effects of the load/source dynamics with the identified transfer functions.
 - Parameterization of a large-signal model from the identified transfer functions.
- **Section 4.4.** A black-box model of a commercial converter is derived. A comprehensive validation of both the modeling and the identification method is presented.
- **Section 4.5.** The modeling and identification techniques are applied on other commercial converters. Limitations of the proposed technique are illustrated and discussed.
- **Section 4.6.** The modeling and identification techniques are applied to model other commercial converters. Limitations of the modeling technique are herein illustrated and discussed, and possible improvements are introduced.
- **Section 4.7.** A DC distributed power system, made up by four commercial converters, is modeled in this section. The usefulness of the black-box modeling method to carry out system-level simulations of a multi-converter architecture is demonstrated.
- **Section 4.8.** The main conclusions are drawn.

4.2 Model description

4.2.1 Description of the modeled converter

This chapter focuses on the modeling of DC-DC converters with regulated output voltage. A generic block-diagram of this type of converter is depicted in Fig. 4-1 and described below.

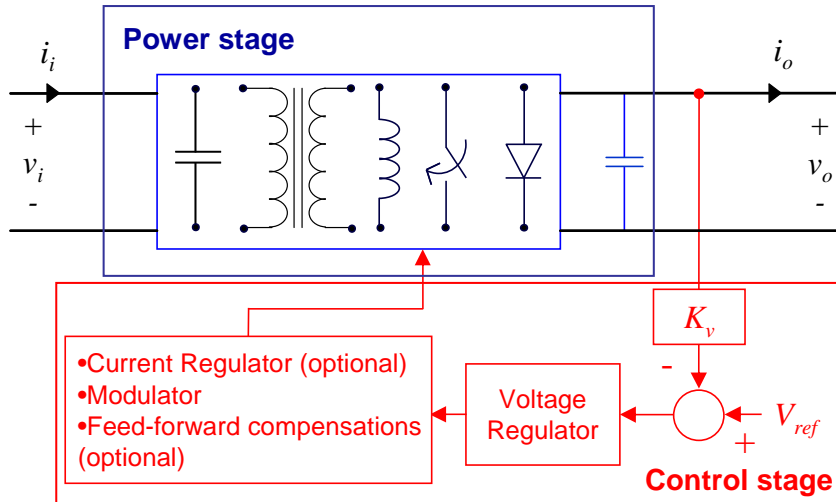


Fig. 4-1: Generic DC-DC converter with output voltage control.

In general, a regulated power converter consists of two blocks: the power stage and the control stage.

- The power stage manages the power transferred from the input port to the output port and consists of controlled and un-controlled active switches (diode, Mosfet, IGBT), passive reactive components (inductors and capacitors) and sometimes transformers or coupled inductors. What is common among those DC-DC converters is the capacitive output, i.e. they are provided with a capacitor at the output port.
- The control stage drives the switches of the power stage in order to maintain the v_o regulated to a reference signal, V_{ref} (scaled through the sensor gain K_v). Today, many types of control strategies are used in the industry, such as VMC, CMC based on average or peak current, etc. Every converter with regulated output voltage is provided with an outer voltage regulator and, sometimes, it is complemented with feed-forward paths of the input voltage or the output current.

The black-box models accounts for the average large-signal behavior of the converters, meaning that dynamics above half the switching frequency is neglected. Therefore, fast control schemes based on the switching ripple of the voltage (such as constant-on-time control, hysteresis control, etc) are not considered in this chapter. It is worth noting that the power converter may consist of several cascaded DC-DC converter stages, and the exposed modeling method would be also valid.

4.2.2 Model structure

4.2.2.1 Small-signal approach

The small-signal black-box model of DC-DC converters with regulated output voltage has been described along chapter 3 and is herein briefly reminded. The interface signals of the modeled converter are the input voltage v_i , input current i_i , output voltage v_o and output current i_o .

The converter behaves as a voltage source at the output port, and as a current sink at the output port, so a g-parameter two-port network is the selected modeling approach. The equivalent small-signal model is depicted in Fig. 4-2, where a set of four transfer function models, namely $Z_o(s)$, $Y_i(s)$, $G_o(s)$ and $H_i(s)$ define all the input-output relationships.

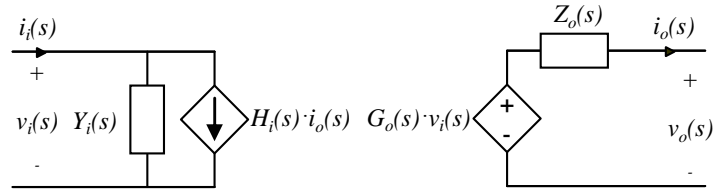


Fig. 4-2: Small-signal black-box model of a DC-DC converter.

4.2.2.2 Large-signal approach

To address large-signal operation, the modeling approach shown in Fig. 4-3 is proposed. Compared to the small-signal model, the following modifications have been carried out:

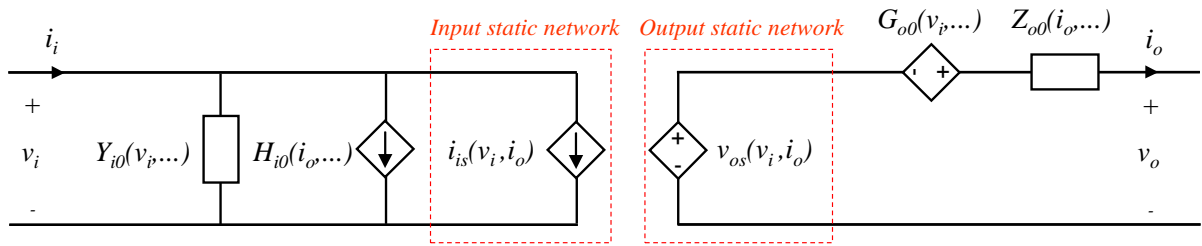


Fig. 4-3: General black-box model of a DC-DC converter with output voltage control.

- Static networks have been added to the input and the output port, which sets the steady-state output voltage, v_{os} , and input current, i_{is} , as a function of the model inputs. By means of this network, the following aspects are addressed:
 - Static line and load regulation, in a linear or a nonlinear manner.
 - Input-output power balance, including efficiency dependence on operating point.
- Each transfer function has been replaced by a dynamic network, which can be either linear or nonlinear. Moreover, every dynamic network has null response at steady-state (subscript '0'), because the static response is already addressed by the static network.

The output static network is defined by (4-1), where V_{ss} represents the nominal output voltage set by the control stage, and $v_{streg}(v_i, i_o)$ represents steady-state voltage dependence on operating point (i.e. related to load regulation and line regulation of the converter).

$$v_{os}(v_i, i_o) = V_{ss} + v_{streg}(v_i, i_o) \quad (4-1)$$

The input static network addresses the input-output power balance, according to the following expression, where η is the efficiency. This network also represents the constant-power-load behavior of regulated converter at the input port, meaning that v_i is inversely proportional to i_{is} under constant output power.

$$i_{is}(v_i, i_o) = \frac{v_{os}(v_i, i_o) \cdot i_o}{v_i \cdot \eta(v_i, i_o)} \quad (4-2)$$

Notice that input current consumptions at no-load conditions cannot be properly addressed by means of (4-2), as i_o is null under that circumstance. To overcome it, i_{is} can be alternatively calculated as follows, where P_{i0} represents the no-load losses and η' denotes the efficiency after subtraction of P_{i0} from the input power.

$$i_{is}(v_i, i_o) = \frac{1}{v_i} \cdot \left(\frac{v_{os}(v_i, i_o) \cdot i_o}{\eta'(v_i, i_o)} + P_{i0}(v_i) \right), \quad \eta'(v_i, i_o) = \frac{v_o \cdot i_o}{v_i \cdot i_i - P_{i0}(v_i)} \quad (4-3)$$

$v_{streg}(v_i, i_o)$, $\eta(v_i, i_o)$ and $\eta'(v_i, i_o)$ can be modeled by means of analytical expressions or look-up-tables (LUTs). It is worth pointing out that, as described in [135], the static load and line regulation can be well approximated by two single-variable functions instead of a two-variables function ($v_{streg}(v_i, i_o)$). This can lead to shorter simulation times.

The small-signal response of the model shown in Fig. 4-3 is given by the following expressions. As can be seen, it is determined by the small-signal response of the corresponding dynamic networks summed to the partial derivate of the static networks on the corresponding operating point.

$$\begin{cases} Y_i(s) = \left. \frac{i_i(s)}{v_i(s)} \right|_{i_o(s)=0} & = Y_{i0}(s) + \frac{\partial i_{is}(V_i, I_o)}{\partial V_i} \\ H_i(s) = \left. \frac{i_i(s)}{i_o(s)} \right|_{v_i(s)=0} & = H_{i0}(s) + \frac{\partial i_{is}(V_i, I_o)}{\partial I_o} \end{cases} \quad (4-4)$$

$$\begin{cases} G_o(s) = \left. \frac{v_o(s)}{v_i(s)} \right|_{i_o(s)=0} & = G_{o0}(s) + \frac{\partial v_{os}(V_i, I_o)}{\partial V_i} \\ Z_o(s) = \left. -\frac{v_o(s)}{i_o(s)} \right|_{v_i(s)=0} & = Z_{o0}(s) - \frac{\partial v_{os}(V_i, I_o)}{\partial I_o} \end{cases} \quad (4-5)$$

4.2.3 Modeling dynamic networks

4.2.3.1 Transfer function model

Transfer function models are used when the input-output relationship of the dynamic network is linear or nearly linear. Fig. 3-5 depicts the output impedance modeled with a transfer function. A transfer function is usually implemented in a circuit simulator into Laplace 's' domain or 'z' domain. However, in a time-domain simulation, the convolution of the input signal with the impulse response of the transfer function is performed by the simulator.

The input-output response of this model is given by (4-6) and (4-7) in time domain and Laplace domain, respectively. Since this is a LTI network, there is no difference between small-signal response and large-signal response.

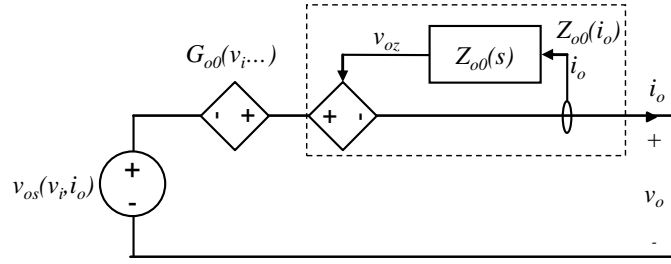


Fig. 4-4: Output impedance of a DC-DC converter modeled by a transfer function.

$$v_{oZ} = Z_{o0} * i_o \quad (4-6)$$

$$v_{oZ}(s) = Z_{o0}(s) \cdot i_o(s) \quad (4-7)$$

4.2.3.2 Local linear models network

A local linear models network (LLMN) is useful to reproduce dynamics dependence on operating point in a general way. It consists of a set of local transfer function models, each one obtained by linearization on a certain operating point, and weighting functions driven by any of the input signals of the model (v_i , i_o , or both of them). This structure has been briefly described in chapter 3 and is reminded in Fig. 4-5.

When a LLMN is used, the range partitioning has to be selected, i.e. number of local linear models and corresponding operating points, as well as the type of weighting functions. In this illustrative example, three small-signals local models evaluated on three different input voltages (V_{i1} , V_{i2} and V_{i3}) and piece-wise linear weighting functions are used.

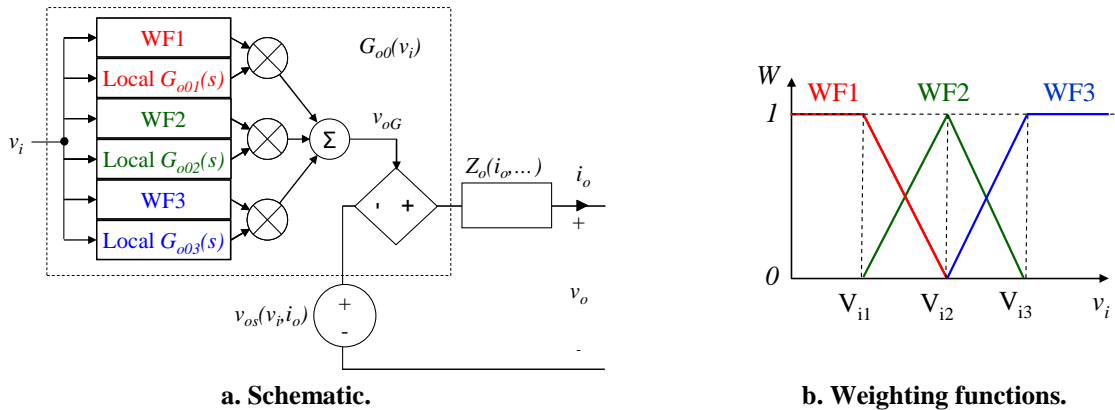


Fig. 4-5: Audio-susceptibility of a DC-DC converter made up by a local linear models network.

The time-domain response of this structure is given by the following equation, where N denotes the number of local linear models.

$$v_{oG} = \sum_{j=1}^N (G_{o0j} * v_i) \cdot WF_j(v_i) \quad (4-8)$$

On the other hand, the small-signal dynamic response is given by the following expression:

$$G_{o0}(s) = \frac{v_{oG}(s)}{v_i(s)} = \sum_{j=1}^N G_{o0j}(s) \cdot WF_j(V_i) \quad (4-9)$$

A variety of weighting functions can be used, such as piece-wise linear, sigmoid and trapezoidal functions [145]. Advantages of some functions over other ones are not explored in this thesis, and piece-wise linear functions are always applied. It is important to note that the sum of every weighting function has to be equal to one at every point within the working range.

$$\sum_{j=1}^N WF_j(v_i) = 1 \text{ for all } v_i \quad (4-10)$$

As explained in [134], this structure performs well if the transfer function parameters vary smoothly with the operating point. Therefore, sudden dynamic changes, such as jumps from DCM to CCM (or vice-versa) in VMC controlled converters, are not well modeled. A deeper discussion on it is given in section 4.5.

4.2.3.3 Gain-scheduled transfer function

A gain-scheduled transfer function can be used if the dynamic dependences on operating point are mostly reflected in the static gain. The utilization of this network to make up the back-current-gain is depicted in Fig. 4-6. It consists of a transfer function model, $H_{i0n}(s)$, multiplied by a gain-scheduling static function GS .

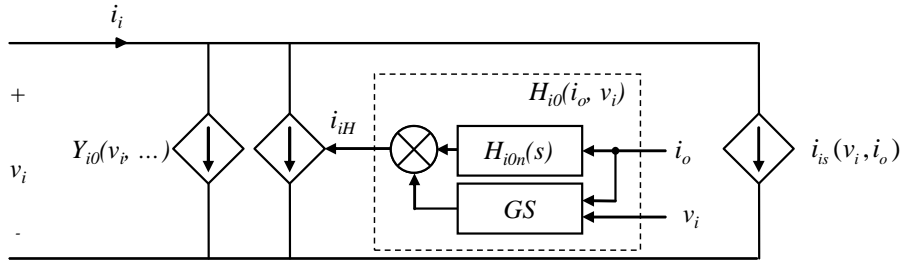


Fig. 4-6: Back-current gain of a DC-DC converter modeled by a gain-scheduled transfer function.

This scheduling function corresponds to the static gain of the whole model and is related to the static network as follows:

$$GS(i_o, v_i) = \frac{\partial i_{is}(v_i, i_o)}{\partial i_o} \quad (4-11)$$

The large-signal time-domain response of this model is given by the following expression:

$$i_{iH} = (H_{i0n} * i_o) \cdot GS(v_i, i_o) \quad (4-12)$$

By applying small-signal perturbations on i_o , the small-signal transfer function of this approach is obtained. As can be seen, this structure **behaves as a transfer function whose gain is equally scaled, at all frequencies, as a function of the operating point**^{4.1}.

^{4.1} Note that uppercase signals denote operating point and are used to define transfer function models, e.g. (4-13). In contrast, lowercase signals denote time-varying signals and are used to define other functions in the large-signal model, e.g. (4-11).

$$\left\{ \begin{array}{l} H_{i_0}(s) = \left. \frac{i_{iH}(s)}{i_o(s)} \right|_{v_i(s)=0} = H_{i_{0n}}(s) \cdot GS(V_i, I_o) \\ H_i(s) = \left. \frac{i_i(s)}{i_o(s)} \right|_{v_i(s)=0} = H_{i_0}(s) + \frac{\partial i_{is}(V_i, I_o)}{\partial I_o} = (H_{i_{0n}}(s) + 1) \cdot GS(V_i, I_o) \end{array} \right. \quad (4-13)$$

As demonstrated in chapter 3, the $H_i(s)$ dynamics dependence on operating point is mostly reflected into the static gain, so that it is inversely proportional to V_i and η . This phenomenon comes from the CPL behavior of the converter at the input port, and can be addressed by means of this structure in a simple manner.

On the other hand, it is worth pointing out that combinations of the previously described networks can be used. For instance, the transfer function model in Fig. 4-6 may be replaced by a LLMN to address additional dynamics dependence on I_o . It will be illustrated in section 4.5.1.

4.2.3.4 Comparison with previous proposals

This large-signal modeling approach is inspired in the behavioral model proposed by J. Oliver et al. in [135], where static networks, similar to those herein proposed, is cascaded with dynamic networks in a similar manner (see Fig. 2-13). However, using the technique presented in this thesis, every input-output dynamic relationship can be addressed in a more general manner, following either a linear or a nonlinear approach.

On the other hand, this approach has also some similarities with the model proposed by Cvetkovic et al. in [149] (see Fig. 2-9), where dedicated nonlinear static and linear dynamic networks are used. Major differences between them are discussed below.

- In [149], the instantaneous inputs (v_i and i_o) are split in DC and AC components, which are inputted into separated static and dynamic networks, respectively.
- In the model proposed in this thesis (Fig. 4-3), both the static and dynamic networks receive directly the instantaneous inputs (with superimposed ‘DC’ and ‘AC’ components), so no splitting action is required. The dynamic response is determined by the combined response of the dynamic networks (Z_{o0} , Y_{i0} , etc.) and the static networks.

The nonlinear dynamic networks used in this thesis are inspired in the work by L. Arnedo et al [134], which were reviewed in chapter 2.

Following this, some simplifications on the large-signal model are described, as well as methods to incorporate soft-start and enabling functionalities.

4.2.4 Model simplification: merging static and dynamic networks

The modeling approach shown in Fig. 4-3 can be rearranged into a simpler structure under some circumstances. If the converter is modeled only into nominal working conditions, so that the static line and load regulation are very narrow, i.e. $v_{streg}(v_i, i_o) \ll V_{ss}$ within the whole operating range. Then, the output static voltage can be approximated by a constant factor $v_{os} \approx V_{ss}$, as depicted at the top of Fig. 4-7.

Further simplifications can be done if a gain-scheduled transfer function is used to make up the back-current gain. In that case, the gain-scheduling function will be defined as follows.

$$GS(i_o, v_i) = \frac{\partial}{\partial i_o} \left(\frac{V_{ss} \cdot i_o}{v_i \cdot \eta(v_i, i_o)} \right) = \frac{V_{ss}}{v_i \cdot \eta(v_i, i_o)} \cdot \left[1 - \underbrace{\frac{i_o}{\eta(v_i, i_o)} \cdot \left(\frac{\partial \eta(v_i, i_o)}{\partial i_o} \right)}_{eff} \right] \quad (4-14)$$

If the second addend in (4-14), denoted as ‘*eff*’, can be neglected (i.e. *eff* << 1) then the whole small-signal back-current gain can be simply defined by the following expression^{4.2}.

$$H_i(s) = \left. \frac{i_i(s)}{i_o(s)} \right|_{v_i(s)=0} = \frac{V_{ss}}{V_i \cdot \eta(V_i, I_o)} \cdot (H_{i0n}(s) + 1) \quad (4-15)$$

Under such circumstances, the static network *i_{is}* and the back-current gain can be merged into the simple network depicted at the bottom of Fig. 4-7^{4.3}. Moreover, if the line and load regulation are not only very narrow but also nearly linear, the transfer function models into *Z_o* and *G_o* can directly incorporate them (this is the reason why subscript ‘*O*’ is not herein utilized).

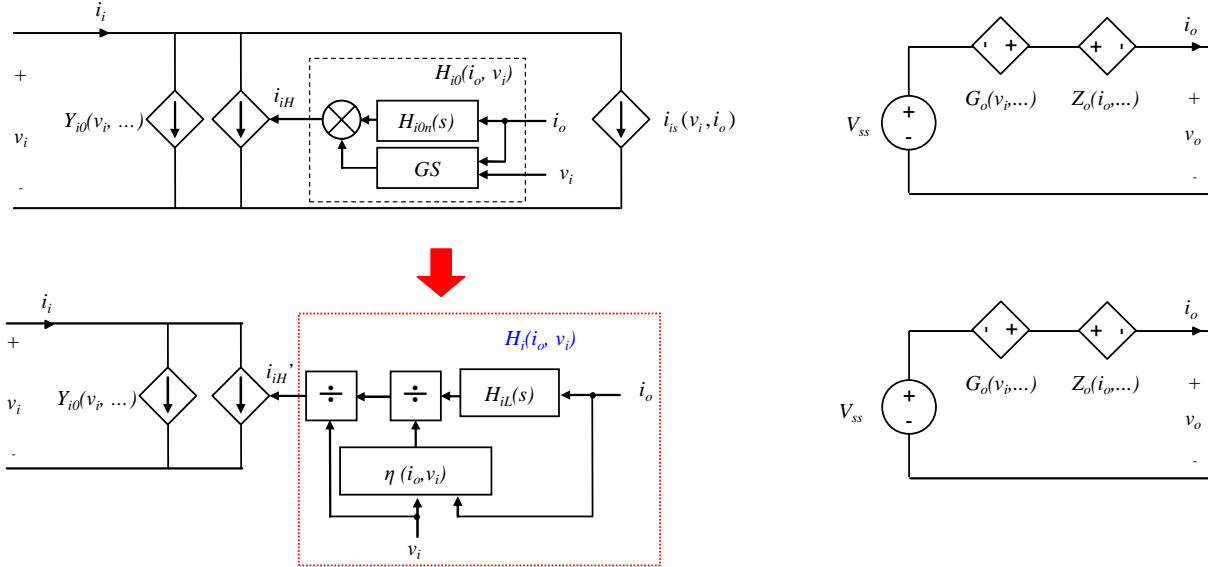


Fig. 4-7: Simplifying the black-box model of the DC-DC converter in case of nearly constant *V_o*.

This practical solution allows a trade-off between simplicity and accuracy. In fact, it is similar to that proposed by L. Arnedo et al. in [144], [153] to address the input-output power balance. The relationship between *H_{iL}*(*s*) and *H_{i0n}*(*s*) is given by the following expression.

$$H_{iL}(s) = V_{ss} \cdot (H_{i0n}(s) + 1) \quad (4-16)$$

On the other hand, similar simplification can be derived if the no-load losses are incorporated into the model as given by (4-3). The resulting simplified model is shown in Fig. 4-8. In this case, the relationship between *H_{iL}*(*s*) and *H_{i0n}*(*s*) is also given by (4-16).

^{4.2} For instance, in case of the DC-DC forward converter specified in [257] and modeled in section 4.5.1, *eff* < 0.1 from 25% to 100% of rated power.

^{4.3} $i_{iH}' = i_{iH} + i_{is}$

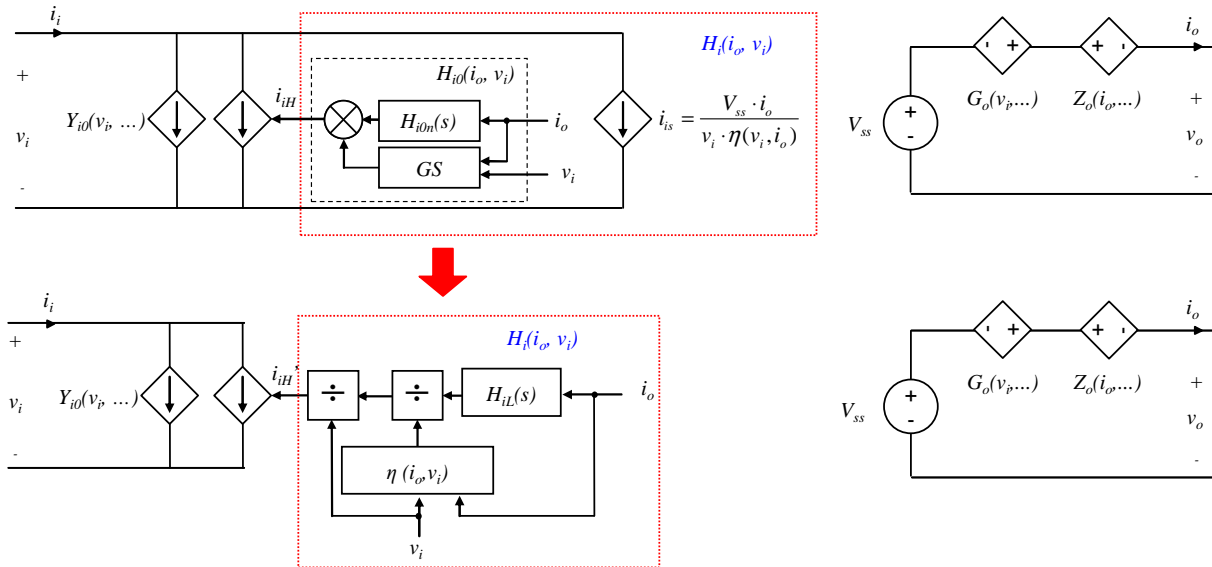


Fig. 4-8: Simplifying the black-box model of the DC-DC converter in case of nearly constant V_o , including no-load losses.

4.2.5 Soft-start and enabling networks modeling

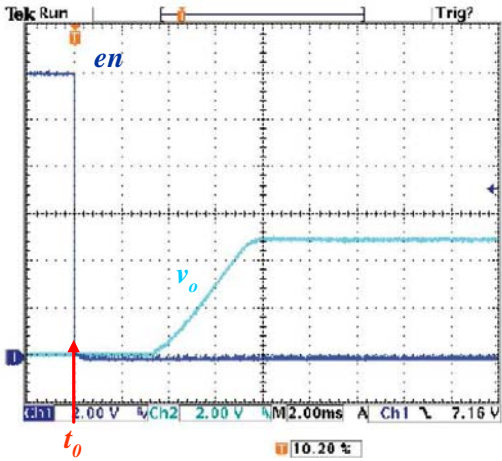
DC-DC converters are usually provided with ‘soft-start’ functionalities so that, once it is enabled, the output voltage gradually increases from zero to the nominal value following a preset profile. To enable the DC-DC converter, the input voltage must fulfill some conditions, typically determined in datasheet, and some external ‘enabling’ signal must be activated as well.

Fig. 4-9a shows the starting profile of a commercial DC-DC converter, provided in its datasheet [266]. Once the enable signal ‘en’ is grounded (time ‘ t_0 ’) and some additional time passes (≈ 4 ms), the output voltage rises gradually until the nominal voltage is reached (5 V).

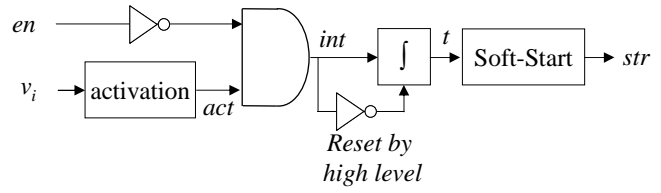
Modeling of enabling and soft-start of power converters is an important point when performing system-level simulations. The behavioral black-box model is a flexible structure that can be easily provided with this type of functionality. A simple approach is proposed in Fig. 4-9b.

The block ‘Activation’ is comprised of logic blocks and sets to ‘1’ a binary signal, namely ‘act’, if v_i fulfills the enabling conditions. In some cases, the converter is enabled when the input voltage falls within a certain range determined by threshold levels V_{imin} , V_{imax} , i.e. $v_i \in (V_{imin}, V_{imax})$. Then, this network may be just implemented using two comparators and one multiplication block, as depicted in Fig. 4-9c. These comparators could be also complemented by hysteresis bands if necessary. In addition, an additional signal ‘en’ could be required to activate the converter (see Fig. 4-9a).

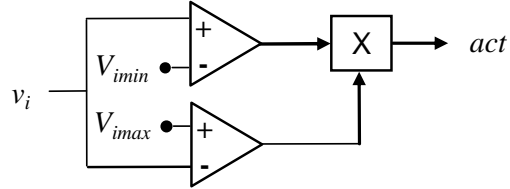
Once ‘act’ = 1 and ‘en’ = 0, the signal ‘int’ toggles from 0 to 1 and a counter (resettable integrator) is started. The integrator starts counting from the activation time ‘ t_0 ’ and drives the block ‘Soft-start’, which stores the soft-start profile and outputs the (non binary) signal ‘str’ as a function of time ‘ t ’. Note that such a soft-start profile is normalized, so that the signal ‘str’ = 1 when the converter has reached the nominal operation conditions.



a. Soft-start profile of a commercial DC-DC converter OKX2-T/16-D12-C [266].



b. Soft-start and enabling networks.



c. Possible implementation for the network ‘activation’.

Fig. 4-9: Modeling soft-start profile of DC-DC converters.

The signal ‘str’ is multiplied to both the input and the output of the static networks, thus addressing the input-output power balance. Fig. 4-10 shows the modifications to be done into the black-box model. If the simplified model is used (Fig. 4-7) then the signal *str* would be multiplied to the DC signal V_{ss} and the signal i_H .

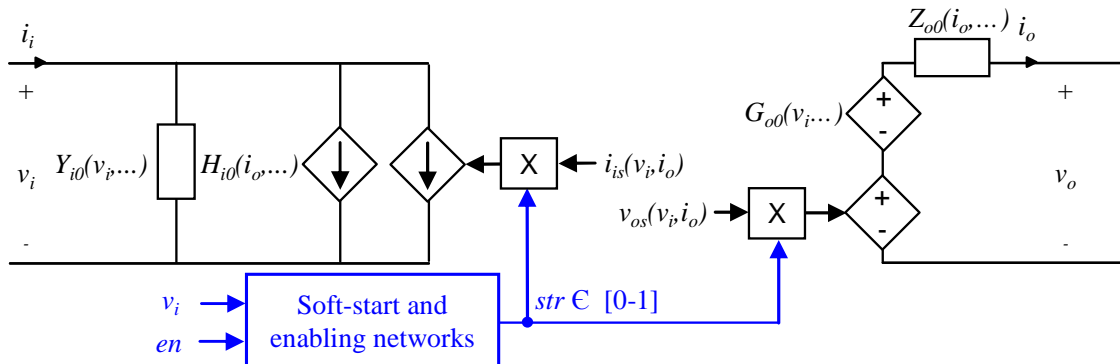


Fig. 4-10: Incorporating the soft-start and enabling functionalities into the behavioral black-box model.

The proposed approach is simple and easy to parameterize from either experimental measurements or datasheet. Nevertheless, the following considerations have to be taken into account.

- This is appropriated as long as the time constant of the soft-start is much slower than the closed-loop time constant under nominal operation. In other words, it is appropriated if the dynamics of the black-box model does not make significant influence during the soft-start process.
- The starting profile of some commercial converters may depend on input and output conditions [266]. In that case, the ‘Soft-Start’ profile may be also parameterized as a function of the operating conditions. However, doing so may add excessive complexity into the model. As appointed before, the trade-off between simplicity and accuracy is an important point in system-level modeling and has to be taken in mind during the modeling process.

4.3 Model identification

At the moment, the only identification method of black-box models for DC-DC converters is based on frequency response measurements, obtained from AC sweep tests. **In this section, a novel identification method based on transient response to step tests is proposed as original contribution.**

The process consists of a set of sequential tasks, which are depicted in Fig. 4-10 and briefly described below.

- **First** (section 4.3.1), **a set of identification test is applied** on different operating points, so that **local linear behavior is kept**, and the transient response of the converter is recorded.
- **Second** (section 4.3.2), **transfer function models are identified** from the recorded data by using a **parametric identification technique**.
- At this point, the identified transfer functions are ‘terminated’, meaning that they exhibit certain coupling with the load/source dynamics. Therefore, the **third** task (section 4.3.3) consists in **analyzing the cross-coupling effects and removing the significant ones**. This yields **‘un-terminated’ transfer functions**, which only contains the internal dynamics of the converter.
- The obtained ‘un-terminated’ transfer functions define linear black-box model(s), such as that shown in Fig. 4-2, each one only valid for a local operating point. Therefore, the final task (section 4.3.4) consists in **post-processing such transfer functions to build a large-signal black-box model**, such as those shown in Fig. 4-3 or Fig. 4-7, which comprise not only transfer function models, but also gain-scheduled transfer functions or LLMNs.

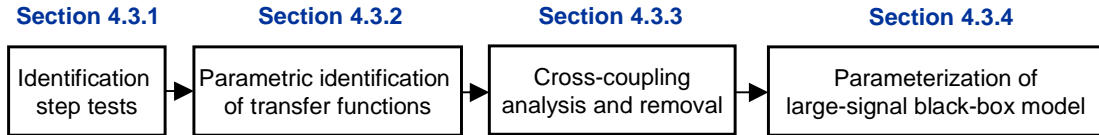


Fig. 4-11: Flowchart of the proposed identification procedure based on time domain measurements.

4.3.1 Identification step tests

If the converter is set on a stable operating point and “small” perturbations are applied so that linear behavior is kept, the dynamic relationship between the input-output signals can be written as given by (4-17). As can be seen, each output signal depends on two input signals and, consequently, two transfer functions.

$$\begin{pmatrix} i_i(s) \\ v_o(s) \end{pmatrix} = \begin{pmatrix} Y_i(s) & H_i(s) \\ G_o(s) & -Z_o(s) \end{pmatrix} \begin{pmatrix} v_i(s) \\ i_o(s) \end{pmatrix} \quad (4-17)$$

As explained in chapter 3, the key point of the identification method is to apply tests so that only one input signal is stepped under each test. This way, the transient response of each output signal will be determined only by one transfer function. Then, a SISO identification algorithm is applied to identify each one. Note that the magnitude of the step has to be chosen so that linear dynamic behavior is ensured.

Since the model has two input signals, two types of step tests have to be carried out:

- Output current steps while the input voltage is kept constant.
- Input voltage steps while the output current is kept constant.

This approach was introduced in chapter 3 and is illustrated in Fig. 3-13. Practical implementations of those step tests are described in the remainder of this section.

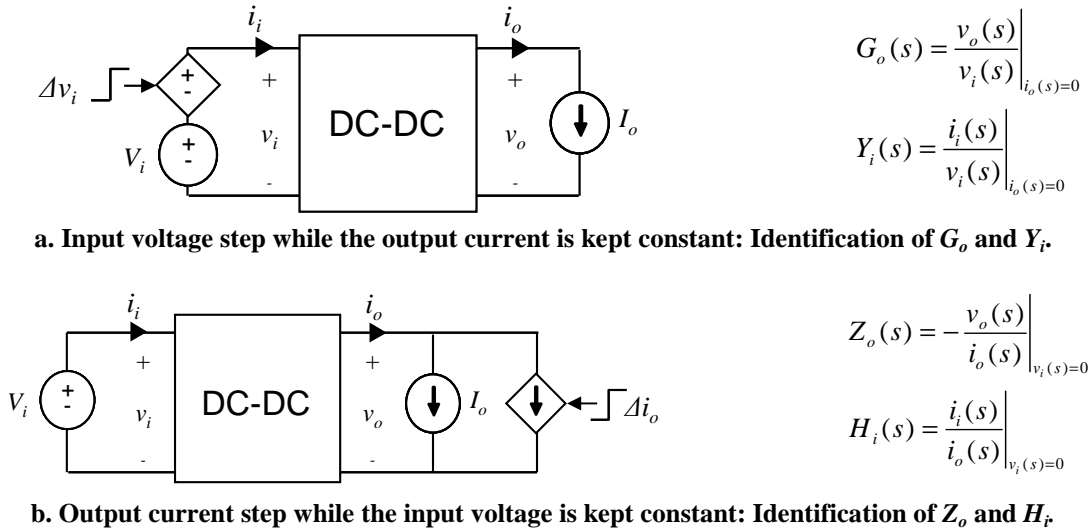


Fig. 4-12: Identification experiments of black-box models for DC-DC converter with regulated output voltage.

4.3.1.1 Output current step

Output current steps can be applied as shown in Fig. 4-13. A simple method consists in switching a resistive load while the converter is fed from a DC source. The operating point of the input voltage is set by the DC source as $V_i = V_s$, the operating point of the output current is set by R_1 as $I_o = V_o/R_1$, and the step magnitude is set by R_2 as $\Delta i_o = V_o/R_2$.

An alternative solution consists in using an electronic load in transient current mode. If this solution is considered, the slew rate for Δi_l may be severely limited by the electronic load, thus reducing the model identifiability at high frequency.

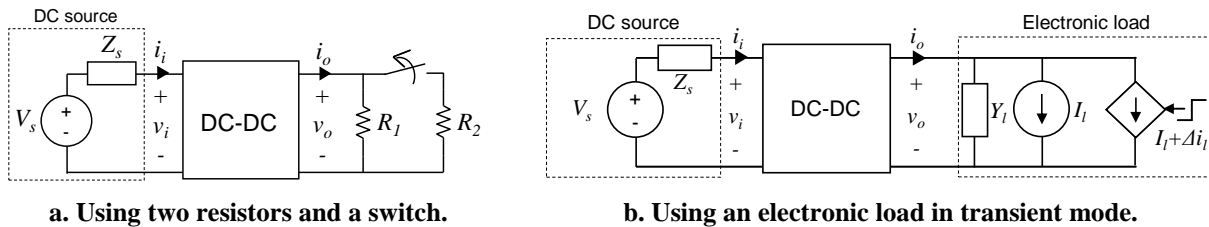


Fig. 4-13: Practical implementations of an output current step

Other solutions may be also considered e.g. using the electronic load to set I_o and then switching a resistor to make the step.

4.3.1.2 Input voltage step

Feasible solutions are depicted in Fig. 4-14. The circuit shown in Fig. 4-14a is based on an array of diodes in parallel with a switch. When the switch is off, there is a voltage drop in the diodes v_d . When the switch is turned on, such a voltage drop is suddenly transferred to the input port of the converter, so that v_i is stepped up ($\Delta v_i \approx v_d$). Other feasible solution consists in using a resistor instead of the diodes to make the step, as shown in Fig. 4-14b.

In order to keep the output current constant at the desired operating point, an electronic load working in constant current mode may be placed at the output port, so that $I_o = I_l$. A resistor could be used instead, but in that case larger cross-coupling effects could be caused.

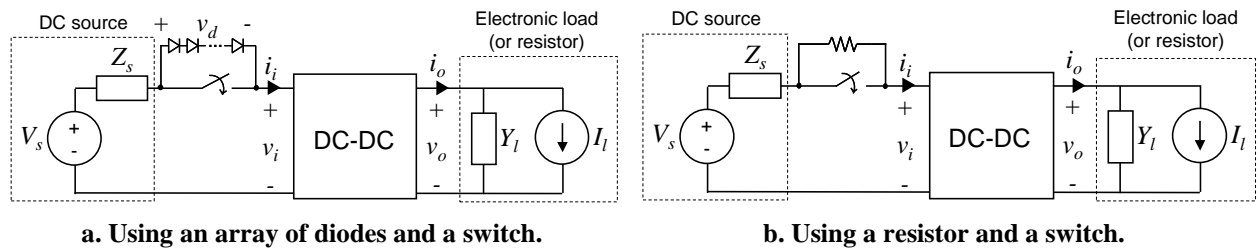


Fig. 4-14: Practical implementations of an input voltage step.

In both cases, a high slew rate can be achieved if the impedance path between the DC source and the converter (Z_s and the internal impedance of the switch) is minimized.

4.3.1.3 Measuring the transient response

The measurements of the input-output currents and voltages are the only source of information about the converter dynamics. Therefore, a proper selection and configuration of the probes and the data acquisition system is an important aspect.

The acquisition equipment feature high enough bandwidth and resolution. On the other hand, the sampling frequency and total measured time have to be adequately set. Guidelines are given below.

- **Total time:** In order to gather complete information about the system dynamics, the total time has to be set so that the transient response is measured from the stepping time to the setting time.
- **Sampling time:** At a first moment, one may think about sampling as fast as possible, in order to minimize the loss of information. However, an excessively low sampling time may lead to numerical problems [72]. From a practical point of view, mathematical optimization of the sampling time is a complex problem which is often not feasible to do in practical situations [72]. Rules of thumb are usually recommended in system identification literature to get a reasonable trade-off. Some of them are listed below [72].
 - Three times the smallest time constant of interest.
 - Sampling frequency ten times the frequency bandwidth of the identified system.

System-level black-box models are intended to reproduce the averaged dynamic behavior of the converter, as conventional average models do. Average models are typically assumed to be valid for frequencies below half the switching frequency ($f_{sw}/2$), so this is considered as the maximum

frequency of validity of the black-box models. Therefore, according to the latter rule of thumb, a suitable choice of the sampling frequency may be $f_s \approx 5 \cdot f_{sw}$. From a practical point of view, if no prior data about f_{sw} is available, it is recommended to use a high value of f_s and later re-sample the data [66].

Finally, it is important to point out some considerations about aliasing. According to the Nyquist-Shannon theorem, any frequency component ‘ f ’ above half the sampling frequency, i.e. $f \in [f_s/2, f_s]$, will be interpreted as contribution for a lower frequency ‘ f_a ’, so that $f_a = f_s - f$. This is known as the alias phenomenon and should be avoided. Therefore, if the switching ripple is very large and the data acquisition system is not equipped with anti-aliasing filter, then a larger sampling frequency should be selected, followed by low-pass filtering and decimation.

Once the transient response of the converter has been recorded, transfer function models are identified from the measured dataset.

4.3.2 Parametric identification of transfer function models

Parametric identification methods are proposed to identify the transfer function models from the measured step response. Parametric identification is a mature field of research [66], [68], [72], [73] and has been widely discussed in the literature. In fact, these techniques have been applied to identify black-box models of DC-DC converters from frequency response measurements in [134], [144].

In this section, the application of parametric identification techniques on transient response measurements from DC-DC converters is described. A flowchart of the identification procedure is illustrated in Fig. 4-15 and is described in the remainder of this section. A deeper discussion about mathematical aspects behind this procedure is given in appendix A.4.

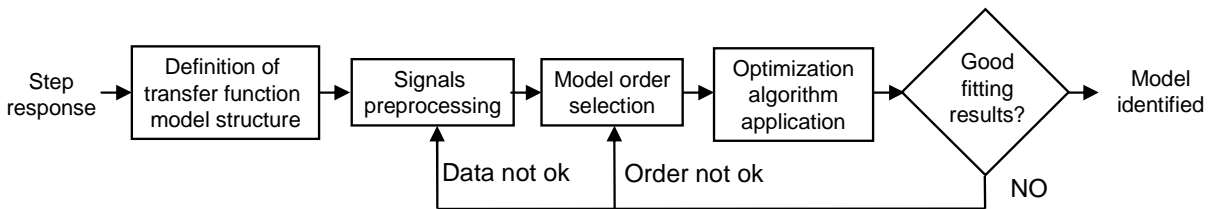


Fig. 4-15: Identification procedure of transfer function models from step transient response.

4.3.2.1 Model structure selection

In this thesis, identification of single-input single-output LTI models is done using discrete-domain time data. Mathematically, the output of a discrete LTI model can be expressed as a function of past outputs and past/current inputs as given by (4-18), where $u(k)$ is the model input, $y(k)$ is the model output, a_i and b_i are constant real coefficients and $m \leq n$.

$$y(k) = -\sum_{i=1}^n a_i y(k-i) + \sum_{i=0}^m b_i u(k-i) \quad (4-18)$$

Expression (4-18) can be rewritten in a compact form as given by (4-19), where the operator ‘ q ’ denotes the forward shift operator and means $q^{-n}u(k) = u(k-n)$ ^{4.4}. $G(q)$ represents the transfer function to identify.

^{4.4} The operator ‘ q ’ is the time-domain counterpart of the $z = e^{j\omega}$ operator in the frequency domain

$$\frac{y(k)}{u(k)} = G(q) = \frac{b_0 + b_1q^{-1} + \dots + b_mq^{-m}}{1 + a_1q^{-1} + \dots + a_nq^{-n}} \quad (4-19)$$

However, real measurements are always corrupted by noise. Therefore, if $y(k)$ and $u(k)$ of a certain system are experimental measurements, the input-output relationship cannot be expressed just by (4-19). In order to account for the noise, the model can be extended as given by (4-20), where $e(k)$ represents white noise and $H(q)$ is an additional transfer function, so-called noise transfer function.

$$y(k) = G(q) \cdot u(k) + H(q) \cdot e(k) \quad (4-20)$$

This way, $H(q)e(k)$ allows modeling any noise realization, with a frequency spectrum different from that of white noise, and reproduces the stochastic part of the measured $y(k)$. On the other hand, the term $G(q)u(k)$ represents the deterministic part of $y(k)$. Equation (4-20) represents the general LTI model identified by means of parametric identification methods.

Depending on the properties of $G(q)$ and $H(q)$, several transfer function models are defined. This is an important point, since the type of optimization algorithm, used for identification, will be strongly determined by those properties, as well as the fitting results. Along this and subsequent chapters, the Output-Error (OE) model is identified, which is featured by $H(q)= 1$. Although white noise characteristics are assumed for the noise model, the OE model is featured by several interesting properties and yield excellent identification results in practice, when applied on the response of power electronics converters. This point and the characteristics of other transfer function models are discussed in appendix A.4.

4.3.2.2 Signals pre-processing

The following pre-processing actions have to be carried out on the measured dataset.

Off-set subtraction: When parametric identification of a transfer function is applied, the relationship between the input-output signals is assumed to be linear, as well as the output is assumed to be solely influenced by the input signal (plus noise). This is true in terms of dynamics as long as, under the proposed tests, only one input signal is perturbed. However, the signals are perturbed on a steady-state equilibrium point, which may be determined by additional effects.

For example, under a load step at constant input voltage, the output voltage is assumed to be solely influenced by the output current. However, at steady-state, the output voltage is determined by the reference control signal.

Consequently, the first pre-processing task consists in subtracting the steady-state value from both the measured input and output signals, before the step is done. This is expressed by (4-21), where $u_m(k)$ and $y_m(k)$ are the measured input and output signals, respectively; the subscript “*off*” denotes signals after offset subtraction, and uppercase names denote the steady-state of the signals, before the step is applied.

$$\begin{cases} u_{off}(k) = u_m(k) - U \\ y_{off}(k) = y_m(k) - Y \end{cases} \quad (4-21)$$

This way, both the input and the output signals of the model are zero before the step is applied, and the input-output dynamic relationship will be determined only by the transfer function model to identify.

Pre-filtering: Second, the signals may be optionally pre-filtered to minimize disturbances which are not modeled by the transfer function, such as switching ripple. In terms of frequency domain, pre-filtering acts as a weighting of the bandwidth of interest.

The pre-filter is defined by (4-22), where ‘ b_{lm} ’ and ‘ a_{ln} ’ are constant real coefficients.

$$L(q) = \frac{b_{l0} + b_{l1}q^{-1} + \dots + b_{lm}q^{-m}}{1 + a_{l1}q^{-1} + \dots + a_{ln}q^{-n}} \quad (4-22)$$

Both the input and the output signals have to be pre-filtered through the same pre-filter, as otherwise it would be included in the identified model. Hence, the pre-filtered signals (subscript ‘ p ’) would be defined as given by (4-23).

$$\begin{cases} u_p(k) = L(q) \cdot u_{off}(k) \\ y_p(k) = L(q) \cdot y_{off}(k) \end{cases} \quad (4-23)$$

As described in appendix A.4, pre-filtering may be seen as a way of fixing desired properties to the noise model. Suitable pre-filtering strategies are discussed in section 4.4.

4.3.2.3 Model order selection

Before running the fitting algorithm, the number of coefficients of the numerator and denominator of the transfer function has to be selected.

Starting from a low model order, several choices should be iteratively tested until acceptable identification results are obtained. A good first attempt can be done by looking at the waveform shape of the step response. For example, the overdamped step response shown in section 3.3.2 evidences the existence of two dominant real poles, meaning that a 2nd order transfer function could be a good starting point.

In many practical cases, 2nd to 4th order transfer functions yield good fitting results, as demonstrated later on.

4.3.2.4 Optimization algorithm

Following this, an optimization algorithm is executed to search for the coefficients of the transfer function model. A standard choice is to minimize the sum of squared prediction errors [68]. As explained in [68], the optimal estimation is obtained by minimizing the following cost function, where (N is the number of samples):

$$COF = \sum_{k=1}^N \frac{1}{H(q)} \cdot [y_p(k) - G(q) \cdot u_p(k)]^2 \quad (4-24)$$

If an output-error model (OE) is fitted, then $H(q) = 1$, so the cost function is the following one.

$$COF_{OE} = \sum_{k=1}^N [y_p(k) - G(q) \cdot u_p(k)]^2 \quad (4-25)$$

A variety of methods can be used to minimize COF_{OE} . In this thesis, Gauss-Newton is used. More details about this point are given in appendix A.4.

4.3.2.5 Validation

The quality of the fitting results is evaluated by comparing the model output $\hat{y}(k)$ and the measured, pre-processed output $y_p(k)$. In the case of an OE model, $\hat{y}(k)$ is given by (4-26).

$$\hat{y}(k) = G(q) \cdot u_p(k) \quad (4-26)$$

Along this thesis, the normalized root mean square error is used, which is given by (4-27) and is a typical merit function to evaluate fitting results.

$$fit\% = 100 \cdot \left(1 - \frac{\sqrt{\sum_{k=1}^N (y_p(k) - \hat{y}(k))^2}}{\sqrt{\sum_{k=1}^N (y_p(k) - \bar{y}_p)^2}} \right), \quad \bar{y}_p = \frac{1}{N} \sum_{k=1}^N y_p(k) \quad (4-27)$$

If poor fitting results are obtained, then either the model order should be re-adjusted or the pre-filter should be re-defined. The fitting results are evaluated by comparing the transient response of $\hat{y}(k)$ and $y_p(k)$.

4.3.2.6 Transformation to continuous time domain

Finally, the resulting discrete model can be transformed to continuous domain for the convenience of integration in system-level simulators. For example, the Tustin transformation can be applied. Tustin uses a first order approximation of the logarithmic relationship between the operator 's' and the operator 'z', as given by (4-28). Of course, other transformations such as zero-order-hold can be used instead.

$$G(s) = G(z) \Big|_{s=\frac{2z-1}{T_s z+1}} \quad (4-28)$$

On the other hand, the coefficients of $G(z)$ ($b_o \dots b_n, a_1 \dots a_m$) are the same that those of $G(q)$, as the shift operator 'q' is equivalent to 'z' in the Z domain (4-29).

$$u(k-n) = q^{-n}u(k) \Leftrightarrow Z(u(k-n)) = z^{-n}u(z) \quad (4-29)$$

The transformation results should be checked by comparing the frequency response of $G(s)$ with that of $G(z)$ for frequencies up to half the switching frequency.

4.3.2.7 Parametric identification in practice

Today, there are commercial tools that allow fitting a transfer function model straightforwardly, such as the System Identification Toolbox of Matlab [260]. This tool is used to apply parametric identification along this thesis. More specifically, (4-24) is optimized using the function 'oe' and the Gauss-Newton search method. The model validation is done using the function 'compare', which compares the model output with the measured, pre-processed output and quantifies the fit as given by (4-27). The transformation to continuous time domain can be done using the function 'Tustin' (Tustin method) or 'zoh' (zero-order-hold method) which are included in the Control System Toolbox of Matlab [261].

4.3.3 Cross-coupling effects

At this point, it is considered that only one input signals is disturbed at each time, so that every identified transfer function is “un-terminated”, i.e., is decoupled from the source and load dynamics. However, in real world, no ‘ideal’ voltage source or current sink exists. Consequently, v_i is disturbed under i_o steps due to the nonzero impedance of the DC source, namely Z_s . Similarly, i_o is disturbed under v_i steps due to the nonzero load admittance, namely Y_l .

Thereby, both the load and the source dynamics exhibit a certain coupling effect with the identified transfer functions. This problem is tackled in this section. Methods to analyze, to remove and to prevent those effects are presented.

4.3.3.1 Removal

In order to explain both the cross-coupling problem and the de-coupling method, the small-signal equivalent circuits, corresponding to the identification tests, are depicted in Fig. 4-16. $Z_s(s)$ represents the DC source impedance and $Y_l(s)$ represents the equivalent load admittance after the step. The DC-DC converter is represented by the small-signal g-parameters un-terminated model.

The first attempt to solve this problem was proposed in [148]. The idea was to express the ‘un-terminated’ transfer functions in terms of ‘terminated’ ones through the load-source impedances, which would be identified from additional experiments. However, this approach has some drawbacks. On the one hand, the relationship between un-terminated and measured transfer functions can be highly complex. On the other hand, identifying the load impedance and source admittances require additional experiments.

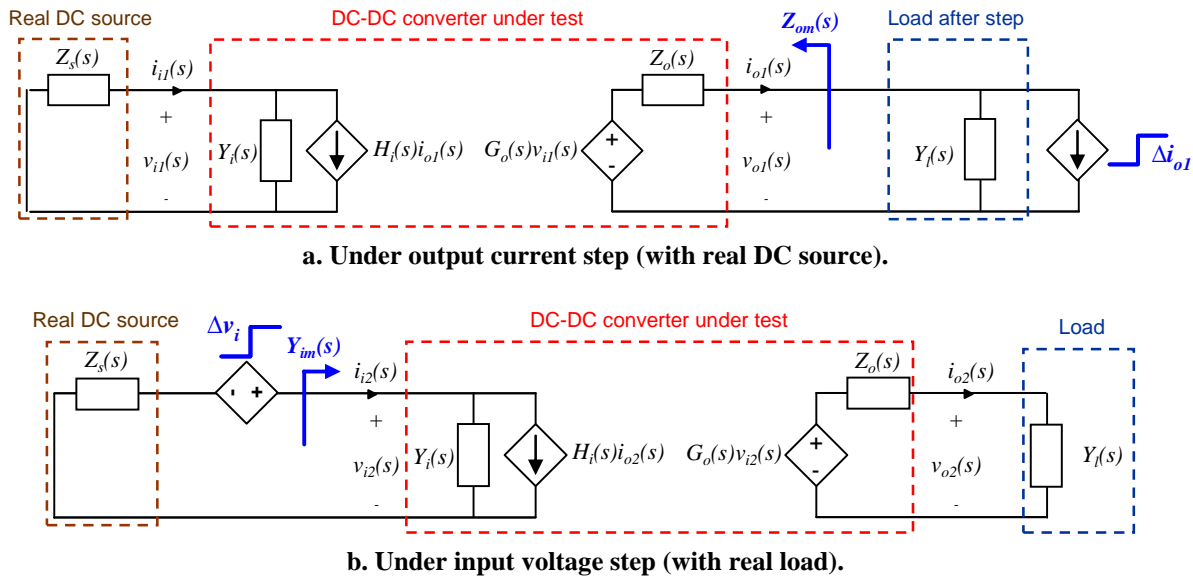


Fig. 4-16: Small-signal equivalent circuits having real DC source and load.

To overcome those drawbacks, an alternative method was proposed in [150]. The idea consists in expressing the relationship between ‘un-terminated’ and measured transfer functions through auxiliary transfer functions, namely Transimpedance ‘ $T_{rm}(s)$ ’ and Transconductance ‘ $T_{gm}(s)$ ’. Such transfer functions relate the cross-perturbed signals with the stepped ones. According to Fig. 4-16, those are defined as follows:

$$T_{rm}(s) = \frac{v_{i1}(s)}{i_{o1}(s)}, \quad T_{gm}(s) = \frac{i_{o2}(s)}{v_{i2}(s)} \quad (4-30)$$

This approach has two advantages. On the one hand, the mathematics is significantly simpler. On the other hand, no additional experiments are required to identify the auxiliary transfer functions, as the inputs for both ones are the stepped signals. From, Fig. 4-16a, the ‘terminated’, transfer functions can be expressed as a function of the un-terminated ones by means of $T_{rm}(s)$ as follows.

$$\begin{cases} v_{o1}(s) = G_o(s) \cdot v_{i1}(s) - Z_o(s) \cdot i_{o1}(s) & \Rightarrow \frac{v_{o1}(s)}{i_{o1}(s)} = -Z_{om}(s) = G_o(s) \cdot T_{rm}(s) - Z_o(s) \\ i_{i1}(s) = Y_i(s) \cdot v_{i1}(s) + H_i(s) \cdot i_{o1}(s) & \Rightarrow \frac{i_{i1}(s)}{i_{o1}(s)} = H_{im}(s) = H_i(s) + Y_i(s) \cdot T_{rm}(s) \end{cases} \quad (4-31)$$

Similarly, the following expressions can be derived from Fig. 4-16b.

$$\begin{cases} v_{o2}(s) = G_o(s) \cdot v_{i2}(s) - Z_o(s) \cdot i_{o2}(s) & \Rightarrow \frac{v_{o2}(s)}{v_{i2}(s)} = G_{om}(s) = G_o(s) - Z_o(s) \cdot T_{gm}(s) \\ i_{i2}(s) = Y_i(s) \cdot v_{i2}(s) + H_i(s) \cdot i_{o2}(s) & \Rightarrow \frac{i_{i2}(s)}{v_{i2}(s)} = Y_{im}(s) = Y_i(s) + H_i(s) \cdot T_{gm}(s) \end{cases} \quad (4-32)$$

By combining (4-31) and (4-32), the ‘terminated’ transfer functions can be expressed as a function of ‘un-terminated’ ones through a de-coupling matrix namely $[T(s)]$, which is comprised of the auxiliary transfer functions described above.

$$\begin{pmatrix} Y_{im}(s) \\ H_{im}(s) \\ G_{om}(s) \\ -Z_{om}(s) \end{pmatrix} = \underbrace{\begin{pmatrix} 1 & T_{gm}(s) & 0 & 0 \\ T_{rm}(s) & 1 & 0 & 0 \\ 0 & 0 & 1 & T_{gm}(s) \\ 0 & 0 & T_{rm}(s) & 1 \end{pmatrix}}_{[T(s)]} \cdot \begin{pmatrix} Y_i(s) \\ H_i(s) \\ G_o(s) \\ -Z_o(s) \end{pmatrix} \quad (4-33)$$

Then, the un-terminated transfer functions can be expressed as a function of the ‘terminated’ ones by inverting $[T(s)]$, as follows:

$$\begin{pmatrix} Y_i(s) \\ H_i(s) \\ G_o(s) \\ -Z_o(s) \end{pmatrix} = \underbrace{\frac{1}{1 - T_{gm}(s) \cdot T_{rm}(s)} \begin{pmatrix} 1 & -T_{gm}(s) & 0 & 0 \\ -T_{rm}(s) & 1 & 0 & 0 \\ 0 & 0 & 1 & -T_{gm}(s) \\ 0 & 0 & -T_{rm}(s) & 1 \end{pmatrix}}_{[T(s)]^{-1}} \cdot \begin{pmatrix} Y_{im}(s) \\ H_{im}(s) \\ G_{om}(s) \\ -Z_{om}(s) \end{pmatrix} \quad (4-34)$$

In [150], the decoupling matrix is first expressed non-parametrically as a function of frequency response measurements. After that, parametric identification is applied on the un-terminated frequency responses ($Y_i(j\omega)$, $H_i(j\omega)$, $G_o(j\omega)$ and $-Z_o(j\omega)$).

In this thesis, the method proposed in [150] is adapted to time domain. The de-coupling matrix $[T(s)]$ is directly expressed parametrically as a function of additional transfer function models, $T_{gm}(s)$ and $T_{rm}(s)$, which are identified as follows:

- $T_{rm}(s)$ is identified from an i_o step, considering i_o as the model input and v_i as the model output, and applying the method described in section 4.3.2.

- $T_{gm}(s)$ is identified from the measurements under a v_i step, considering v_i as the model input and i_o as the model output, and applying the method explained in section 4.3.2.

Consequently, **no additional tests are required to remove cross-coupling effects**. The additional requirement is to measure the cross-perturbed signals under the step identification tests. This is a key feature of the method.

4.3.3.2 Analysis

The inverse of $[T(s)]$ is relatively complex, yielding high order “un-terminated transfer functions” if every cross-coupling effect is taken into account. However, if the black-box model is comprised of high-order transfer functions, the simulation time could be excessively long. Therefore, in order to simplify $[T(s)]$, only the significant cross-coupling effects should be incorporated into it.

A simple method to evaluate the influence of the cross-perturbations on the identified transfer functions is described below. The idea consists in checking if the assumptions done at the beginning of the identification procedure are valid, i.e. the transient response of each output is only determined by the stepped input under each experimental test. If the assumptions are valid, the corresponding cross-coupling effect can be neglected, leading to simplifications into $[T(s)]$.

For instance, let consider the analysis of the cross-coupling effects on Z_{om} (see Fig. 4-16a). These effects will be negligible if the following condition holds:

$$\text{If } |G_o(s) \cdot v_i(s)| \ll |Z_o(s) \cdot i_o(s)| \text{ then } Z_{om}(s) \approx Z_o(s) \quad (4-35)$$

However, the analysis cannot be done just as given by (4-35), since neither frequency domain signals nor un-terminated transfer functions are available (until the de-coupling method is applied, which follows this analysis). Hence, the analysis is done using time-domain convolution and coupled transfer functions. The cross-coupling effects will be negligible if the following conditions are fulfilled (subscript ‘ p ’ denotes pre-processed measurements)^{4,5}.

$$\text{If } |G_{om}(q) \cdot v_{ip}(k)| \ll |Z_{om}(q) \cdot i_{op}(k)| \text{ then } Z_{om}(q) \approx Z_o(q) \quad (4-36)$$

As an illustrative example, let consider that a set of transfer functions for the output port has been identified, $Z_{om}(q)$ and $G_{om}(q)$. Signals $i_{op}(k)$ and $v_{ip}(k)$ are applied as inputs to the identified transfer functions (see Fig. 4-17). If $|v_{oG}(k)| \ll |v_{oZ}(k)|$ from the stepping time to the setting time, then the transient response of the output voltage can be assumed to depend only on $Z_{om}(q)$, that is, $v_{op}(k) \approx -Z_{om}(q)i_{op}(k)$. In that case, $Z_{om}(q) = Z_o(q)$, which simplifies the fourth row in (4-33) (i.e. $T_{rm}(s) = 0$ in the fourth row). The simplified de-coupling matrix is referred to as $[T_s(s)]$.

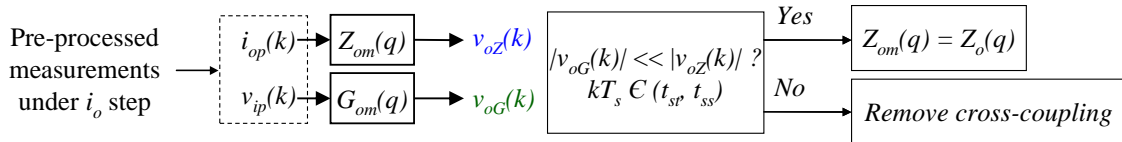


Fig. 4-17: Analyzing cross-coupling on $Z_o(q)$. t_{sp} : stepping time. t_{ss} : setting time. T_s : sampling time.

^{4,5} Rigorously speaking, the analysis should be done using un-terminated transfer functions. However, this is a qualitative analysis, so the derived conclusions are in general valid, as long as the terminated transfer functions are not highly different from the un-terminated ones.

Of course, this analysis can be skipped. However, in practice, usually some cross-coupling effects are negligible, meaning that the cross-coupling removal process can be significantly simplified and expedited. This analysis procedure is illustrated step by step in section 4.4.5.

4.3.3.3 Prevention

The above explained procedure is a complete solution to overcome the cross-coupling problem. However, for the sake of simplicity, the best solution is to prevent the cross-coupling effects, so that such procedure can be skipped.

Guidelines to minimize the cross-coupling effects are rather intuitive. Expressed in the continuous time domain, the cross-perturbation of v_i under a i_o step is caused by the DC bus impedance $Z_s(s)$ as expressed by (4-37).

$$v_i(s) = -Z_s(s) \cdot i_o(s) \quad (4-37)$$

Therefore, the lower the DC source impedance, the lower the cross-coupling effect. Following guidelines may be taken into account to minimize $Z_s(s)$:

- Try to minimize the impedance of the connection between the DC source and the input port of the converter. Reducing wires path and using twisting are some recommendations.
- Place external capacitor(s) close to the input port of the converter.

The cross-perturbation of i_o under a v_i step is caused by the load admittance $Y_l(s)$ as expressed by (4-38).

$$i_o(s) = Y_l(s) \cdot v_i(s) \quad (4-38)$$

Therefore, the lower the load admittance, the lower the cross-coupling effect. Following guidelines may be taken into account:

- Place an inductor connected in series with the load.
- If a resistor is used as a load and no dynamics dependence on I_o (operating point) is found, then the best choice is to make the steps at minimum load conditions (the higher the resistance, the lower the admittance).

4.3.3.4 Model order reduction

The un-terminated transfer functions, resulting from the de-coupling method explained above, could have excessively high order. In that case, a model order reduction method can be applied. A method based on ‘Balance Realization and Singular Perturbations’ [251], [252] is used in this thesis. This consists in transforming the transfer function to a state-space balanced form, and rearranging the system states in accordance to their contribution to the system dynamics. This way, the negligible state variables can be identified and removed, thus reducing the order of the system.

This method has been already applied for black-box modeling of DC-DC converters in [148] and [150]. In practice, it can be put into practice straightforwardly using the functions “*balreal*” and “*modred*” included in the Control System Toolbox of Matlab [261].

4.3.4 Parameterization of the large-signal black-box model

Once every un-terminated transfer function has been identified, the large-signal black-box model can be built. To do so, the static networks have to be characterized and the obtained transfer functions have to be post-processed.

4.3.4.1 Static networks characterization

The static networks are characterized from static tests, over the whole operating range, as follows:

- The static line and load regulation effects, represented by $v_{streg}(i_o, v_i)$, are parameterized from the static relationship between v_o , v_i and i_o .
- The efficiency η is characterized as a function of v_i and i_o .

4.3.4.2 Transfer functions post-processing

4.3.4.2.1 Static response subtraction

As explained in section 4.2.2, every dynamic network has null response at steady-state. Therefore every identified transfer function requires **subtraction** of its static response. Essentially, this is because the steady-state response of the identified (and un-terminated) transfer functions is given by the partial derivate of the static networks, as indicated by (4-4) and (4-5).

Such post-processing action can be expressed as follows. Note that if LLMN are used, the steady-state response of every transfer function should be subtracted.

$$\begin{cases} Y_{i0}(s) = Y_i(s) - Y_i(0) \\ G_{o0}(s) = G_o(s) - G_o(0) \\ H_{i0}(s) = H_i(s) - H_i(0) \\ Z_{o0}(s) = Z_o(s) - Z_o(0) \end{cases} \quad (4-39)$$

4.3.4.2.2 Gain readjustment (only gain-scheduled transfer functions)

If a gain-scheduled transfer function is applied (such as that shown in Fig. 4-6), then further post-processing actions have to be applied. Specifically, the DC gain of $H_{i0}(s)$ has to be normalized, yielding $H_{i0n}(s)$. For instance, in case of the back-current gain, it is done as follows:

$$H_{i0n}(s) = \frac{H_{i0}(s)}{H_i(0)} \quad (4-40)$$

On the other hand, if the simplified structure presented in Fig. 4-7 is applied, then the transfer function $H_{iL}(s)$ can be obtained from $H_{i0n}(s)$ as given by (4-16). Alternatively, it can be directly obtained from $H_i(s)$ as follows:

$$H_{iL}(s) = H_i(s) \cdot \frac{V_{ss}}{H_i(0)} \quad (4-41)$$

4.3.4.3 Soft-start and enabling networks

These networks are parameterized from experimental measurements of the soft-start profile or information provided in the datasheet.

4.3.5 Overview of the identification procedure

Fig. 4-18 depicts an overview of the proposed identification process. Different colors are used for signals obtained from different identification experiments.

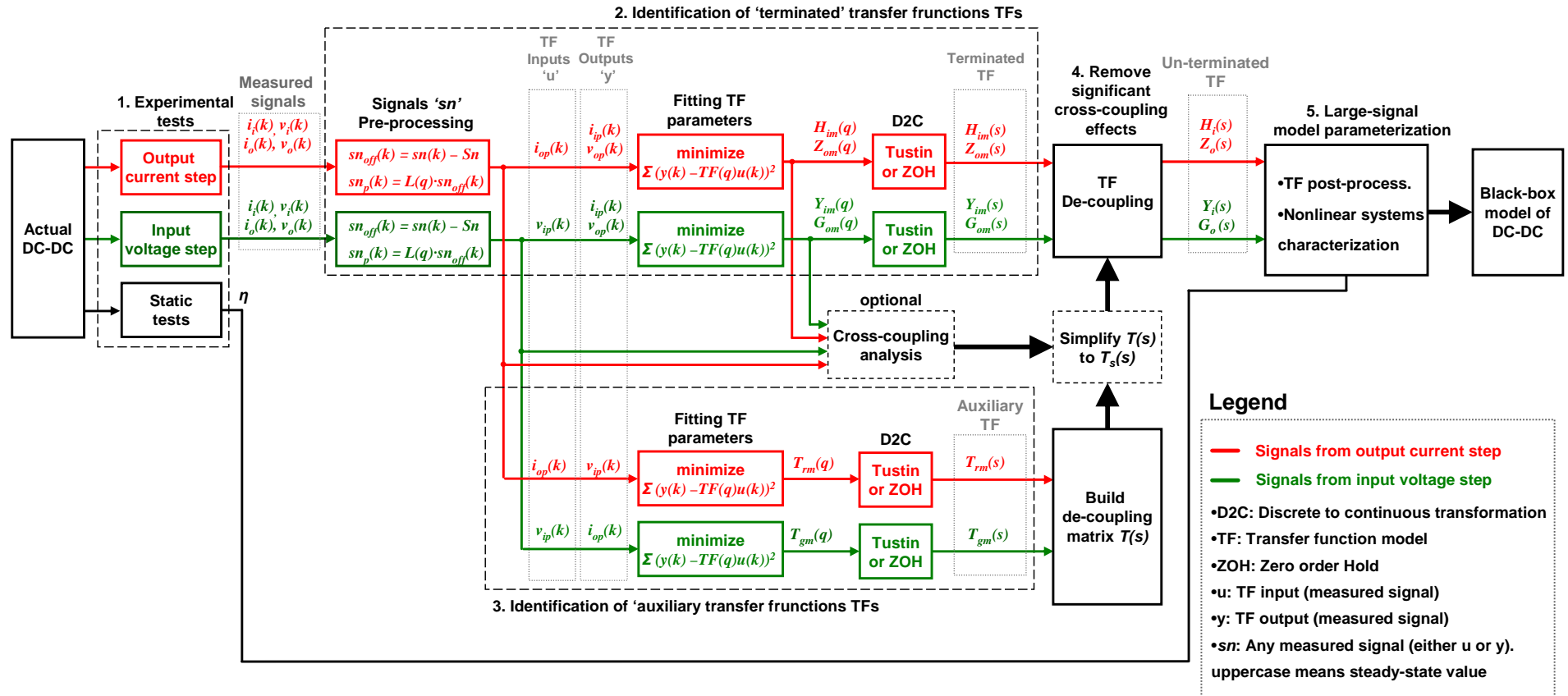


Fig. 4-18: Overview of the proposed identification process for large-signal black-box behavioral models of DC-DC converters with output voltage regulation.

4.4 Experimental results: modeling of a commercial buck converter

4.4.1 Introduction

In this section, a black-box model of a commercial buck converter is derived by making use of the proposed technique. No details about the internal elements of the converters are available, so this scenario demonstrates a real situation where the black-box modeling method would be applied. The followed procedure is depicted in Fig. 4-19^{4.6}, which has been already presented in chapter 3.

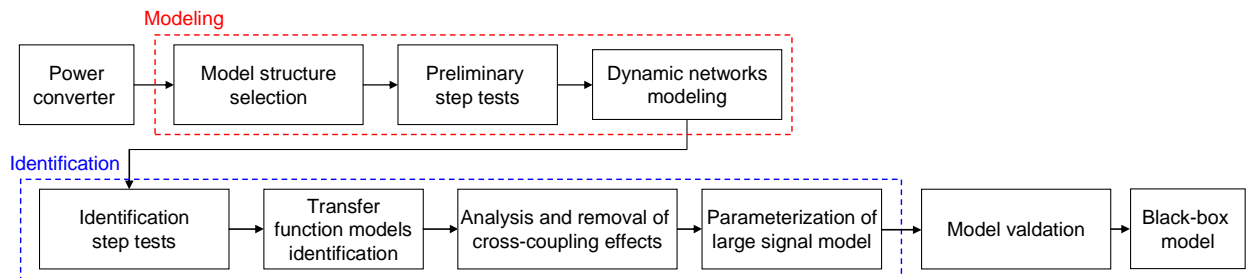


Fig. 4-19: Black-box modeling of a DC-DC converter with regulated output voltage.

The modeled converter is shown in Fig. 4-20 and the datasheet is found in [264]. It delivers regulated output voltage from a wide input voltage range. The maximum output current is 6 A and the switching frequency is $f_{sw} = 500$ kHz. The converter has been set to provide a regulated output voltage $V_o = 2.5$ V. The considered operating ranges are $V_i = [8$ V, 16 V] and $I_o = [2$ A, 6 A].



Fig. 4-20: Commercial DC-DC step down converter by Texas Instruments PTN78020W.

On the other hand, this converter requires external input-output capacitors. At the input port, a 100 μ F electrolytic capacitor has been connected in parallel with several ceramic capacitors, whose total capacitance is ≈ 16 μ F. At the output port, a 470 μ F electrolytic capacitor has been located. Later on, the impact of those capacitors on the dynamic response of the converter is shown through bode plots of the identified transfer functions.

4.4.2 Preliminary tests

The first task is to select the type of dynamic networks used to make up the model. A set of step tests are carried out on different operating points, in order to analyze the behavior of the converter from a qualitative point of view. This way, dynamic dependences on operating point can be analyzed. The experimental setup is depicted in Fig. 4-21. At the input port, the voltage source HP6012B is used to set the input voltage operating point V_i . At the output port, the resistor R_l sets the output current operating point I_o . The steps are applied as described below.

^{4.6} Note that ‘Model Validation’ refers in this figure to the comparison of the whole black-box model response to experimental measurements, once it has been completely parameterized. It is different from the validation of a single transfer function model, discussed in section 4.3.2.

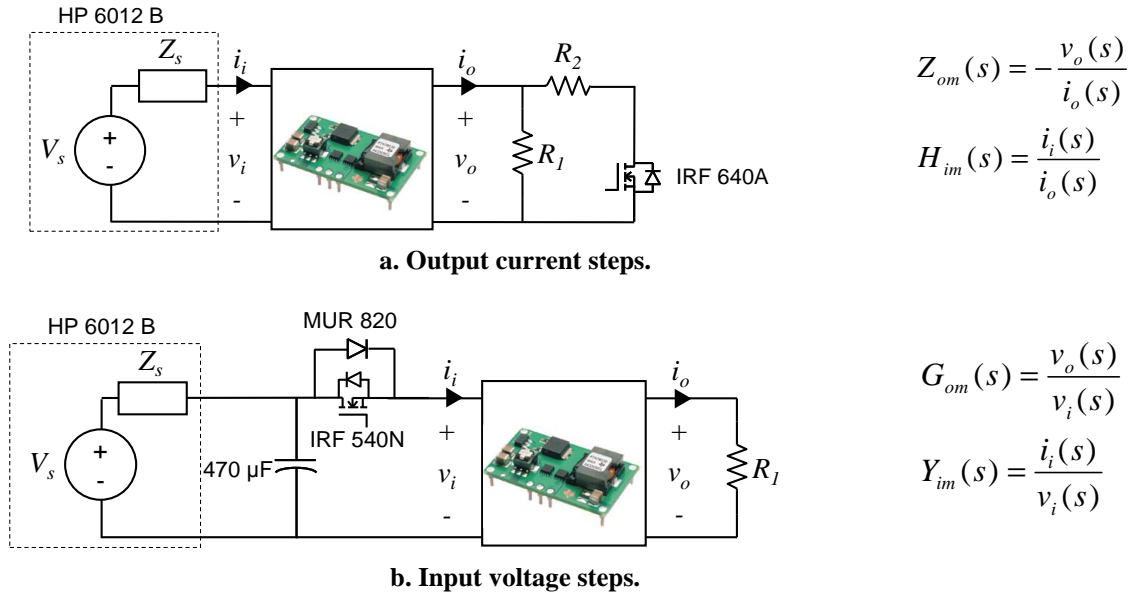


Fig. 4-21: Experimental setup.

- The output current i_o is stepped by switching a resistor R_2 .
- The input voltage v_i is stepped by switching a Mosfet connected in parallel with a single diode (voltage drop $V_d \approx 0.65$ V). A $470 \mu\text{F}$ capacitor has been located close to the switch in order to enhance the bus voltage stiffness, and consequently to increase the slew rate of Δv_i . Notice that the higher the slew rate, the higher the high frequency content of the stepped signal and therefore the higher the model identifiability at high frequency.

The measurements have been taken using a four channel oscilloscope TDS 5104 set in high resolution acquisition mode, voltage probes TEK 6139A and Hall Effect current probes TCP 202. The sampling frequency f_s is ten times the bandwidth of the system to be identified, according to that discussed in subsection 4.3.1.3. Since the maximum achievable frequency is assumed to be $f_{sw}/2 = 250$ kHz, f_s has been set to 2.5 MHz. The data acquisition mode has been set to “high-resolution-mode”^{4.7}.

4.4.2.1 Analysis of H_i and Z_o dependence on operating point

Firstly, the analysis of H_i and Z_o dependence on operating point, which is determined by V_i and I_o , is carried out as follows:

- The dependence on V_i is analyzed by applying the same i_o step at different V_i levels.
- The dependence on I_o is analyzed by applying i_o steps with fixed magnitude, over the full range of I_o , at constant V_i . That is, R_2 is kept constant and R_1 sets the desired I_o . The steps have relatively small-magnitude in order to ensure local linear operation.

4.4.2.1.1 Dependence on V_i

Fig. 4-22 shows the response of the converter to an output current step from 3.85 to 4.28 A ($\Delta i_o = 0.4$ A, 7% of the nominal I_o) at $V_i = 8$ V and $V_i = 12$ V. This yields the following conclusions:

^{4.7} In this acquisition mode, the oscilloscope samples data at maximum sampling rate (5GHz) and returns the averaged value over the selected sampling interval [265]. This way, high frequency noise and aliasing is prevented.

- The transient response of v_o is approximately equal in both cases, meaning that Z_o can be assumed to be independent of V_i .
- The transient response of i_i depends on V_i . The waveform shape is similar in both cases, but its amplitude is inversely proportional to V_i , approximately. This evidences the low-frequency CPL behavior of the converter and means that the static gain of H_i is inversely proportional to V_i .

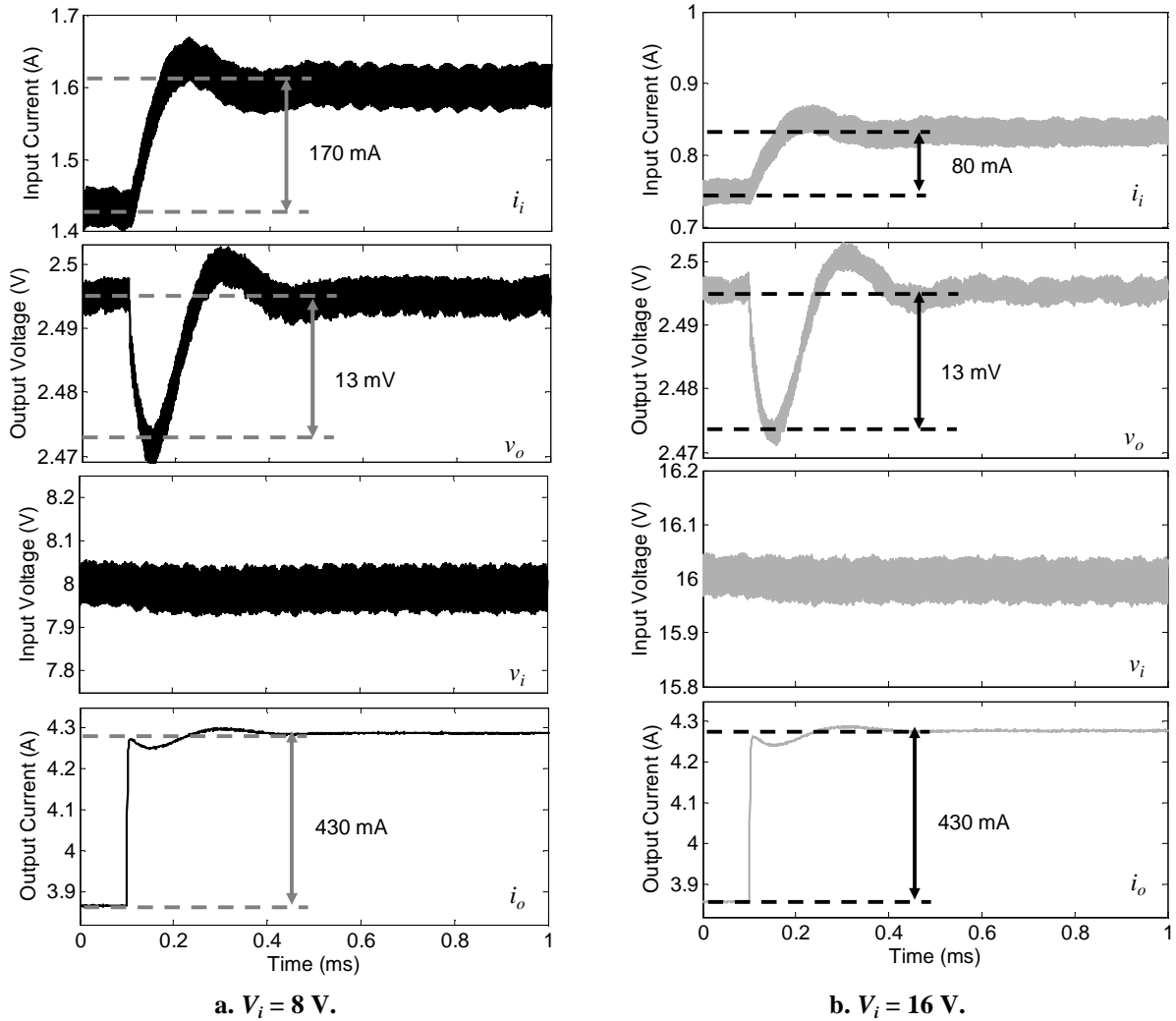


Fig. 4-22: Transient response under an output current step from 3.85 A to 4.28 A for different input voltage levels.

4.4.2.1.2 Dependence on I_o

Fig. 4-23 shows the response of the converter to i_o steps ($\Delta i_o = 0.4$ A) near the minimum and maximum I_o levels (2 A and 6 A, respectively), while V_i is set to the intermediate level (12 V). Both transient responses are very similar in both cases, meaning that **both Z_o and H_i can be assumed to be independent of I_o** . Higher ripple is found out in the second case because of the higher load current level.

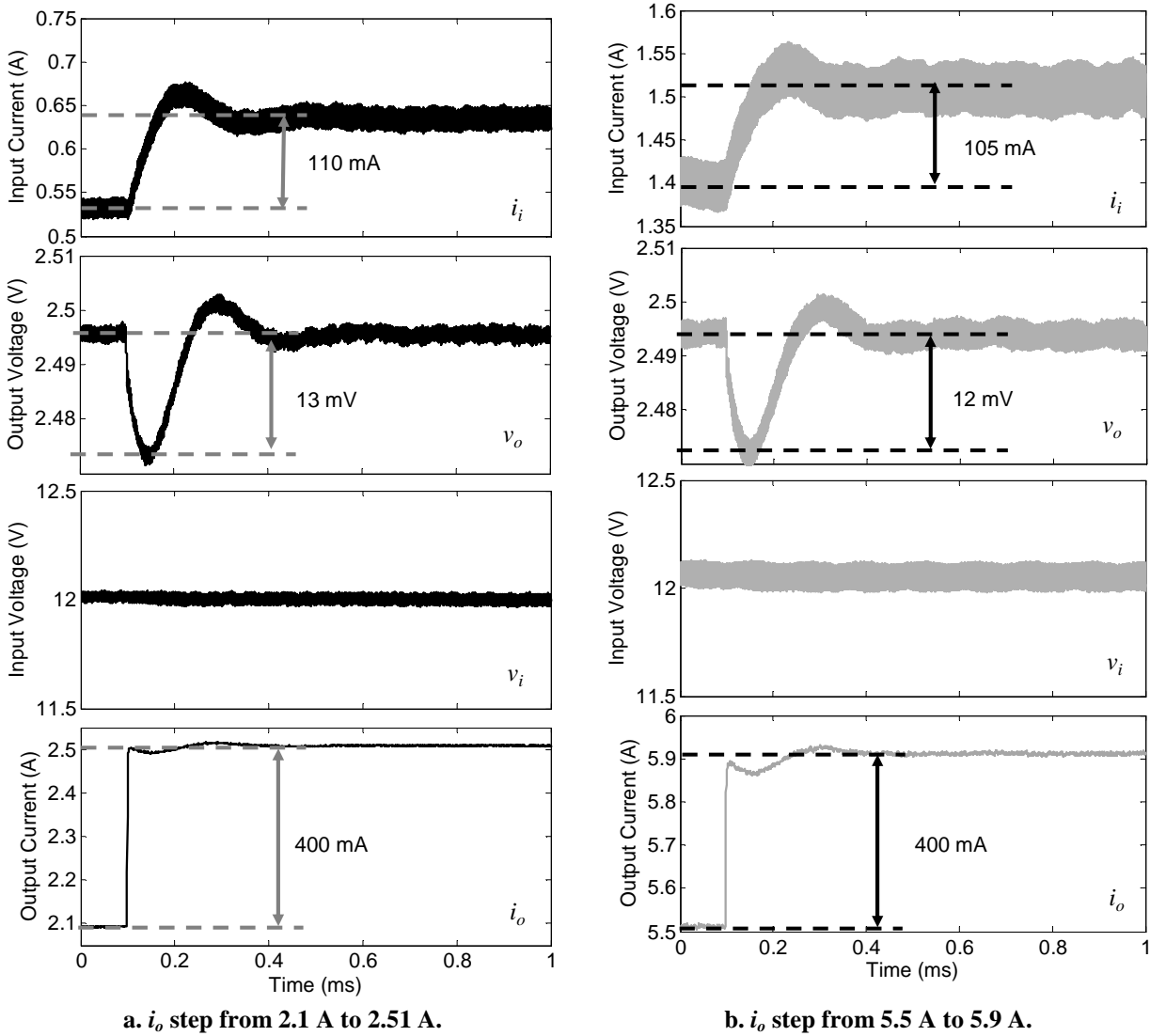


Fig. 4-23: Transient response under two output current steps with magnitude $\Delta i_o = 0.4$ A from different initial levels, both of them for $V_i = 12$ V.

4.4.2.2 Analysis of G_o and Y_i dependence on operating point

Secondly, the analysis of Y_i and G_o dependence on operating point is done.

- The dependence on V_i is analyzed by applying v_i steps on different V_i levels at constant I_o .
- The dependence on I_o is analyzed by applying v_i step with fixed magnitude, at different I_o levels, over the V_i operating range.

4.4.2.2.1 Dependence on V_i

Fig. 4-24 shows the response of the converter to v_i steps around the minimum and maximum V_i levels: 8 V and 16 V, respectively, whereas I_o is set to the intermediate level (4 A). The following conclusions are drawn:

- The transient response of v_o strongly depends on V_i , so that the higher V_i , the lower the v_o overshoot. Therefore, G_o depends on V_i .

- The transient response of i_i is similar in both cases, as it is essentially determined by the input filter of the converter at medium-high frequency. However, the variation of the steady-state value of i_i , i.e. ' ΔI_i ', depends on V_i , which is also related to the low-frequency CPL behavior of the converter. Therefore, Y_i depends on V_i at low-frequency.

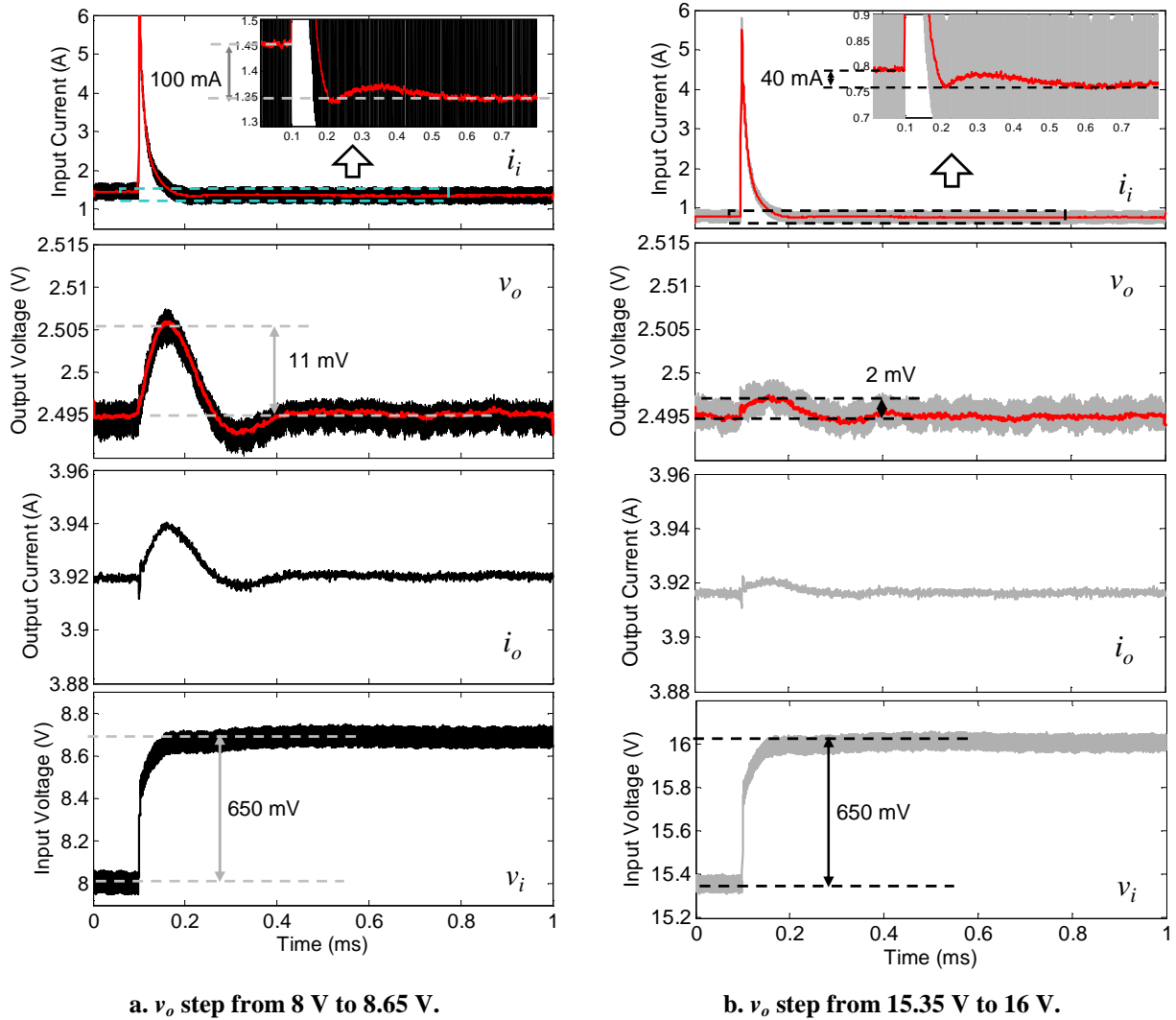


Fig. 4-24: Transient response under two input voltage steps with magnitude $\Delta v_i = 0.65$ V from different initial levels, both of them for $I_o = 3.92$ A.^{4,8}

4.4.2.2.2 Dependence on I_o

Fig. 4-25 shows the response of the converter to v_i steps on the intermediate V_i level at the maximum and minimum I_o levels, (2 A and 6 A). This leads to the following conclusions:

- The damping of v_o is lower in the second case, but this is slight and is essentially due to the use of a resistor to set the operating point of the converter. As a consequence, G_o is assumed to be independent of I_o .
- The transient response of i_i only differs in the variations of the steady-state value ΔI_i , which is again due to the low-frequency CPL behavior described above. Therefore, Y_i depends on I_o at low-frequency.

^{4,8} The averaged signals are obtained using a moving-average filter, which is described later on.

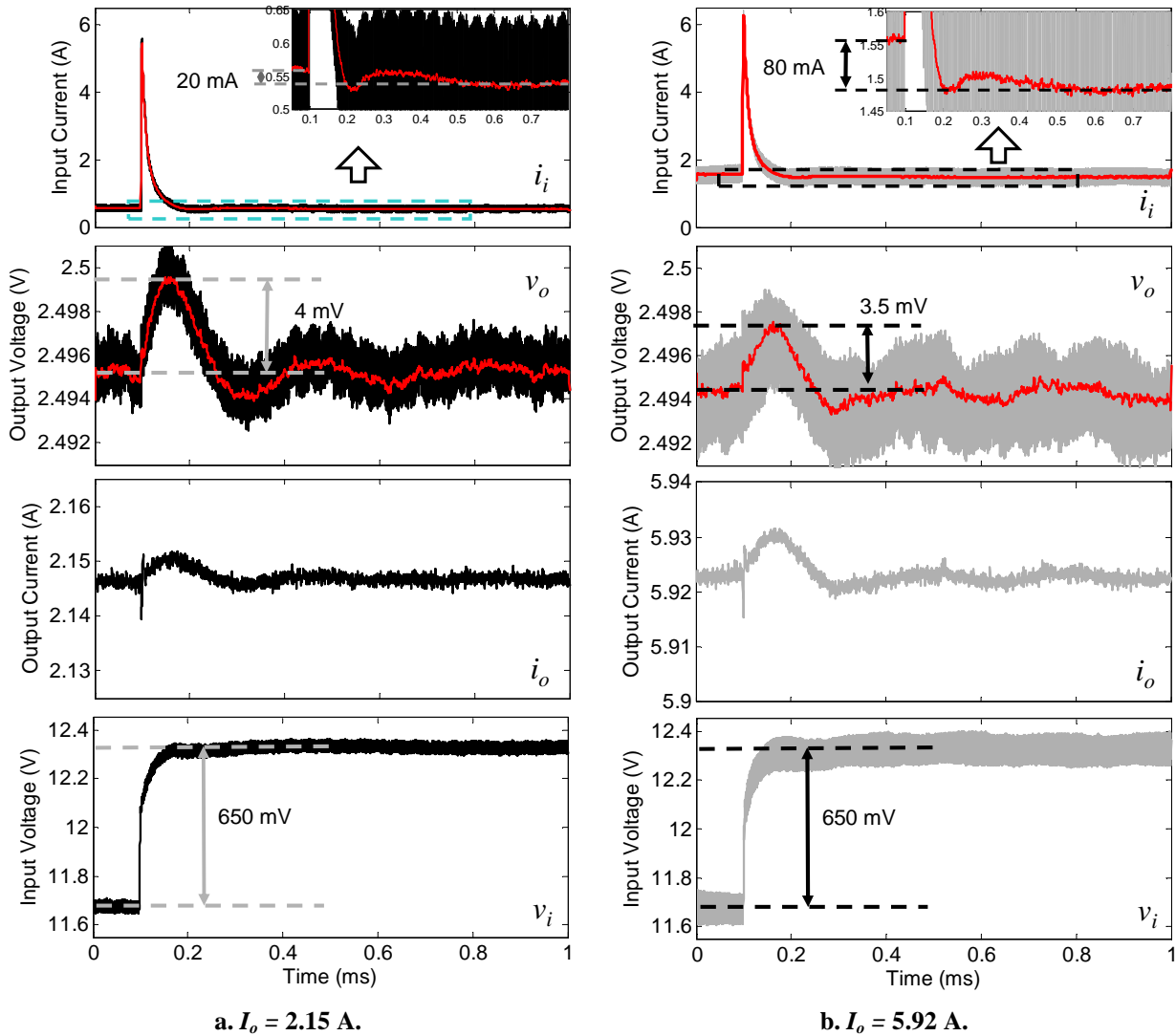


Fig. 4-25: Transient response under an input voltage step from 11.7 V to 12.3 V for different current levels.

4.4.2.3 Remarks on the analysis

It is important to note that this is a qualitative analysis of linearity, which in practice may provide sufficient information with regards to dynamic networks modeling. However, if a more accurate analysis of linearity is required, then local linear models should be identified around different operating points and their frequency responses should be compared to each other.

One reason why slight inaccuracy may exist in the analysis is the difference in the current waveforms, due to the fact that a resistor is used to set the operating point and to make the step. For example, consider the output current waveforms under resistive load switch-on shown in Fig. 4-23. Just after the step, the i_o waveform exhibits a certain oscillation that is proportional to v_o , so that $i_o = v_o/(R_1//R_2)$. Hence, it can be concluded that, the higher $R_1//R_2$, the closer the i_o waveform to an ideal step.

4.4.3 Dynamic networks modeling

Once the dynamic networks dependence on operating point has been analyzed, a proper model for each one is selected.

- The Z_o dependence on both V_i and I_o is negligible. Therefore, it can be assumed nearly linear and can be well modeled with a **single transfer function**.
- The static gain of H_i is inversely proportional to V_i . Therefore, a **gain-scheduled transfer function** is used to make it up.
- G_o depends on V_i , so that the higher V_i , the lower the gain of G_o . Although a gain-scheduled transfer function could be also a proper choice, a **LLMN** is used in this case for illustrative purposes. A range partitioning, consisting of three local linear models weighted through equispaced piece-wise linear functions, is used.
- Y_i depends on both V_i and I_o , but only at low frequencies. This is due to the low-frequency CPL behavior of the converter. Since this effect is already reproduced by the static networks, Y_i consists of a **single transfer function model**, corresponding essentially to the input filter of the converter.

The resulting model is shown in Fig. 4-26. The simplified structure introduced in section 4.2.4 has been considered, because the converter is modeled into the nominal working region and the static load-line regulation are very narrow and nearly linear (less than 1 mV/A and 1 mV/V, respectively).

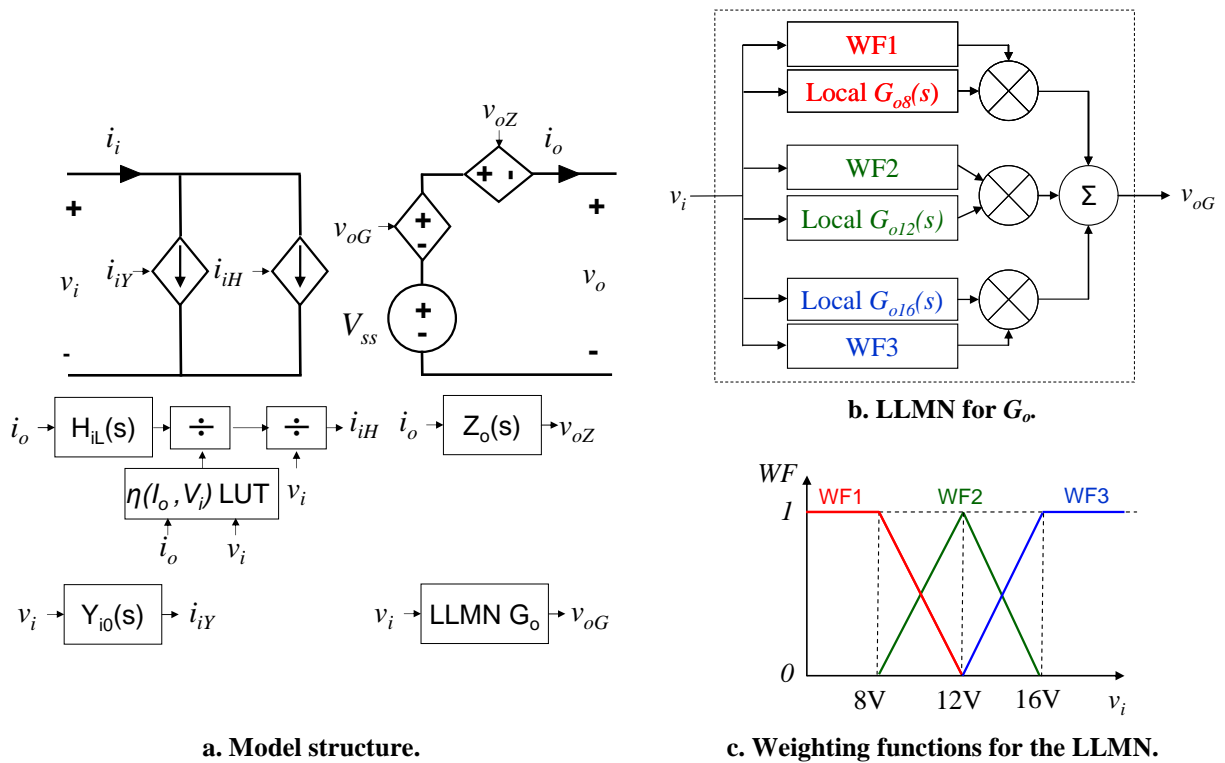


Fig. 4-26: Black-box model of the commercial converter PTN78020W by Texas Instruments for $V_i \in [8, 16]$ V and $I_o \in [2, 6]$ A.

4.4.4 Identification of terminated transfer functions

4.4.4.1 Transfer functions $H_{im}(s)$ and $Z_{om}(s)$

First, $Z_{om}(s)$ and $H_{im}(s)$ have been identified (note that subscript “ m ” denotes that the transfer functions are ‘terminated’ i.e. coupled with the load impedance). Since these transfer functions are

assumed to be independent of I_o , a larger output current step than those shown in the previous section has been applied. This way, the signal-to-noise ratio (SNR) is increased, meaning that better identification results are achieved.

The transient response of the converter to an i_o step from 3.3 A to 4.3 A at $V_i = 8$ V is shown in Fig. 4-27. A slew rate of $\Delta i_o \approx 400$ mA/ μ s has been achieved, which is high enough to obtain good fitting results up to approximately $f_{sw}/2$ (250 kHz), as will be demonstrated later on.

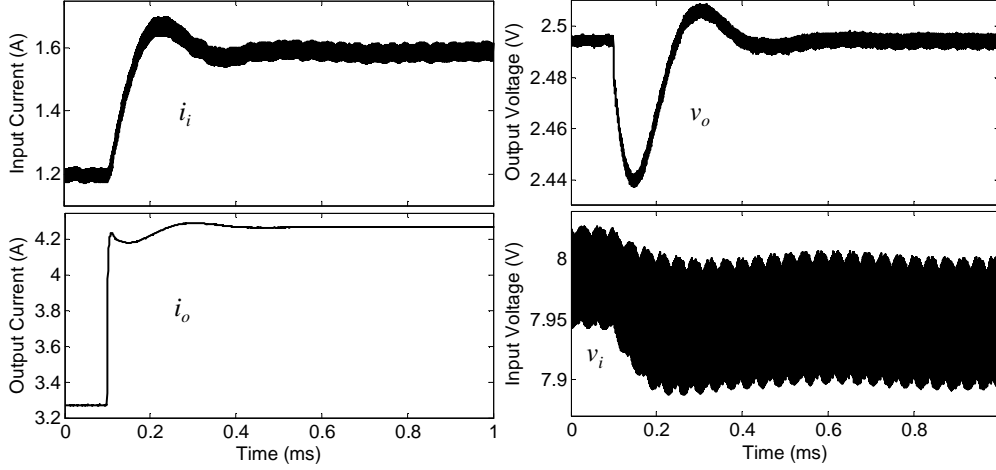


Fig. 4-27: Transient response of the commercial converter PTN78020W to a load current step from 3.3 A to 4.3 A at $V_i = 8$ V.

Before identifying a transfer function, the measured signals have to be pre-processed. As explained in subsection 4.3.2.2, it consists in subtracting the steady-state value and pre-filtering.

The moving average filter (MAF) [247], [248] is a simple and well suited smoothing filter. It is optimal for white noise filtering (fastest step response for a given reduction of white noise) and can be also applied to cancel harmonics [175]. The symmetrical form of MAF is given by (4-42), where M is the number of averaged samples. This non-causal form features zero-phase distortion (which simplifies the comparison of the filtered and the un-filtered signals) and requires M to be odd.

$$MAF(q) = \frac{1}{M} \sum_{n=-\frac{M-1}{2}}^{\frac{M-1}{2}} q^{-n} \quad (4-42)$$

The frequency response of MAF (magnitude) is given by (4-43), where M is the filter order and f_s the sampling frequency. From this expression one can find that every harmonic multiple of f_s/M is suppressed. Thus, since $f_s = 2.5$ MHz, choosing $M = 5$ leads to elimination of every harmonic resulting from the switching process, i.e. odd harmonics of the switching frequency.

$$|MAF(f)| = \frac{1}{M} \left| \frac{\sin(\pi \cdot M \cdot f \cdot f_s^{-1})}{\sin(\pi \cdot f \cdot f_s^{-1})} \right| \quad (4-43)$$

The 5th order MAF filter has been applied on the v_o waveform shown in Fig. 4-27. The filtered signal, v_{op} , has been simply obtained as follows.

$$v_{op}(k) = \frac{1}{5} (v_o(k-2) + v_o(k-1) + v_o(k) + v_o(k+1) + v_o(k+2)) \quad (4-44)$$

The transient response of v_o , before and after filtering is shown in Fig. 4-28, together with the Discrete Fourier Transform (DFT) and the frequency response of the MAF. Note that excellent rejection of the switching ripple is achieved while the average response of v_o is preserved. It is worth noting that the MAF represents, in discrete domain, the mathematical process used to derive classical average model [82]. Therefore, this may be seen as the ‘natural pre-processing method’ to transform the switching signal (time-variant process) into a continuous signal (time-invariant process).

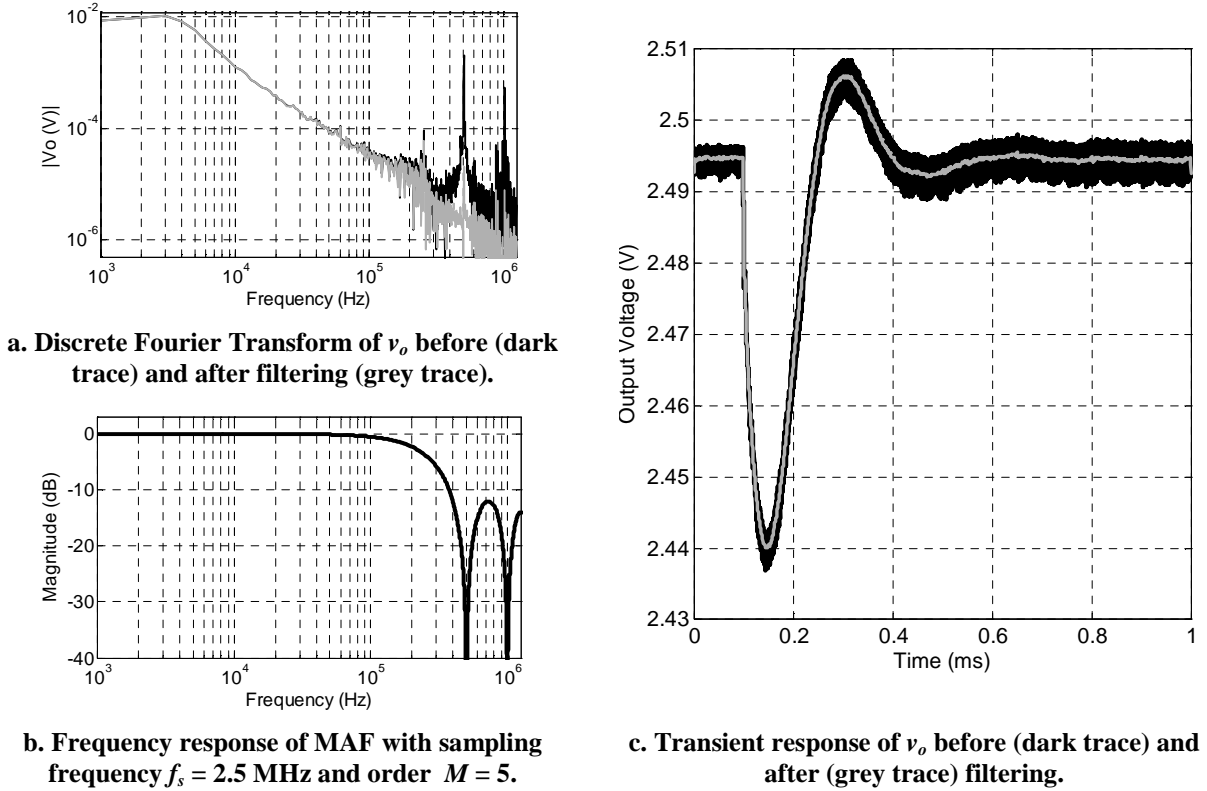


Fig. 4-28: Pre-filtering v_o with a moving average filter.

The fifth order MAF filter has been applied on the remaining signals. After that, the cost function (4-25) has been identified using the ‘*oe*’ function of Matlab. The order of both the numerator and the denominator has been iteratively increased until good fitting results have been achieved, i.e. until the identified system matches accurately the filtered output signal (v_o in case of Z_{om} and i_i in case of H_{im}).

The fitting results are shown in Fig. 4-29, where the identified model output is overlaid with the pre-filtered output using the Matlab function “*compare*”. Second and third order models yield good fitting results, as the model output fits accurately the average response of the pre-processed measurements. The fit is quantified as given by (4-27) resulting in values above 97% in both cases. The identified transfer functions are given by (4-45).

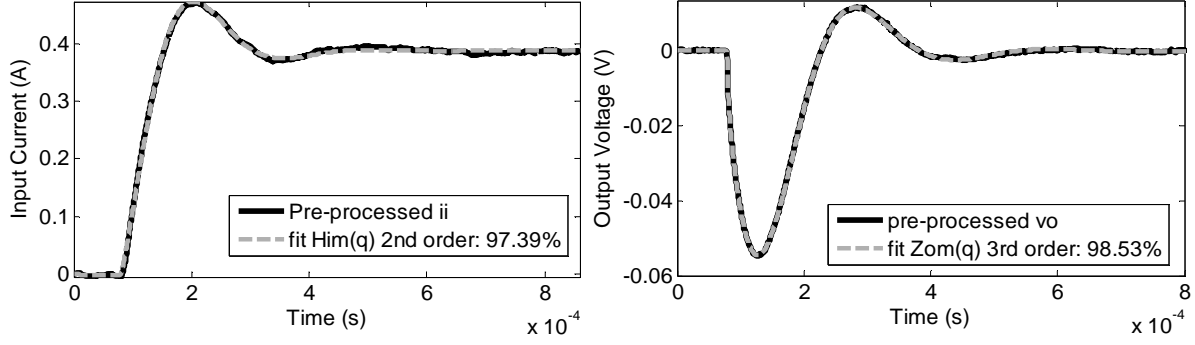


Fig. 4-29: Fitting results of $Z_{om}(q)$ and $H_{im}(q)$.

$$\begin{aligned} Z_{om}(q) &= \frac{-0.01591 + 0.03101q^{-1} - 0.0151q^{-2}}{1 - 2.052q^{-1} + 1.11q^{-2} - 0.0583q^{-3}} \\ H_{im}(q) &= \frac{0.002019 - 0.001984q^{-1}}{1 - 1.992q^{-1} + 0.9924q^{-2}} \end{aligned} \quad (4-45)$$

The identified transfer functions are converted from discrete domain to continuous domain using the ‘Tustin’ transformation. The resulting transfer functions are given by (4-46) in the Laplace domain.

$$\begin{aligned} Z_{om}(s) &= \frac{0.0147s^3 + 7.538 \cdot 10^4 s^2 + 9.518 \cdot 10^9 s + 5.057 \cdot 10^{11}}{s^3 + 4.462 \cdot 10^6 s^2 + 7.522 \cdot 10^{10} s + 2.323 \cdot 10^{15}} \\ H_{im}(s) &= \frac{0.001004s^2 + 5006s + 2.207 \cdot 10^8}{s^2 + 1.897 \cdot 10^4 s + 5.682 \cdot 10^8} \end{aligned} \quad (4-46)$$

4.4.4.2 Transfer functions $Y_{im}(s)$, $G_{o8m}(s)$, $G_{o12m}(s)$ and $G_{o16m}(s)$

Next, transfer function models for $Y_{im}(s)$ and the local models $G_{o8m}(s)$, $G_{o12m}(s)$ and $G_{o16m}(s)$, has been identified. Since G_o depends on V_i , small step magnitude ‘ Δv_i ’ is required. Therefore, a single diode has been used to make the step (see Fig. 4-21b).

Concerning I_o , the transfer functions are assumed to be independent of it. As a consequence the steps should be carried out at its minimum value ($I_o = 2$ A), in order to minimize the cross-coupling effects. Hence, $G_{o12m}(s)$ and $G_{o16m}(s)$ has been identified for $I_o = 2$ A. However, $G_{o8m}(s)$ has been identified for $I_o = 4$ A, in order to emphasize the cross-coupling effect and to validate the cross-coupling removal process. $Y_{im}(s)$ has been also identified for $I_o = 4$ A.

First, $G_{o8m}(s)$ and $Y_{im}(s)$ have been identified. The identification test is the same that was applied during the linearity analysis (Fig. 4-24a). The fitting results are illustrated in Fig. 4-30, where one can see that second and third order transfer functions yield good fitting results, as the fit is above 93% in both cases. The achieved slew rate was 115 mV/ μ s, which is high enough to obtain good fitting results up to half the switching frequency, as will be demonstrated later on.

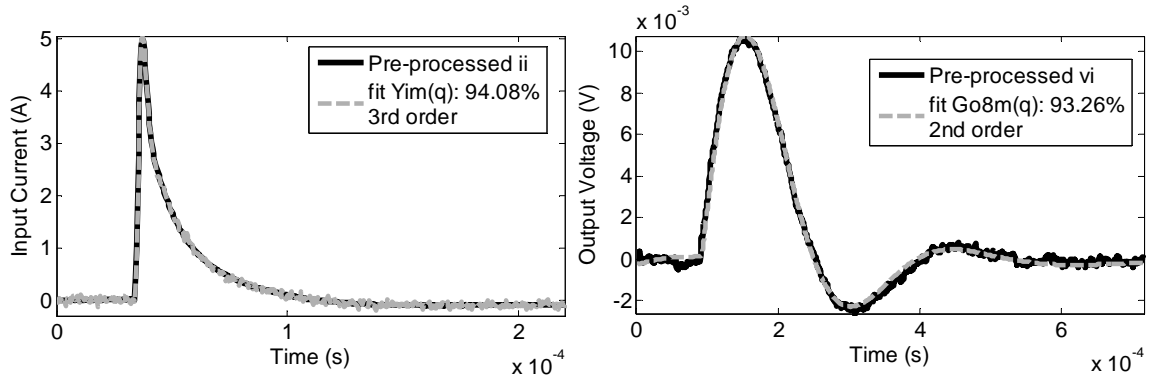


Fig. 4-30: Fitting results $G_{o8m}(q)$ and $Y_{im}(q)$.

The resulting transfer functions are given by (4-47) and (4-48) in discrete and continuous-time domain, respectively.

$$Y_{im}(q) = \frac{58.19 - 105.9q^{-1} + 47.67q^{-2}}{1 - 0.9477q^{-1} - 0.0284q^{-2} - 0.01089q^{-3}} \quad (4-47)$$

$$G_{o8m}(q) = \frac{0.0002831 - 0.0002831q^{-1}}{1 - 1.992q^{-1} + 0.9918q^{-2}}$$

$$Y_{im}(s) = \frac{110.9s^3 + 6.099 \cdot 10^8 s^2 + 2.757 \cdot 10^{14} s - 3.543 \cdot 10^{17}}{s^3 + 1.05 \cdot 10^7 s^2 + 2.683 \cdot 10^{13} s + 2.277 \cdot 10^{18}} \quad (4-48)$$

$$G_{o8m}(s) = \frac{1.421 \cdot 10^{-4} s^2 + 710.6s - 1.153 \cdot 10^5}{s^2 + 2.065 \cdot 10^4 s + 5.533 \cdot 10^8}$$

After that, transfer function models for $G_{o12m}(s)$ and $G_{o16m}(s)$ have been fitted. Step tests with magnitude $\Delta v_i \approx 0.65$ V have been applied around $V_i = 12$ V and $V_i = 16$ V for $I_o = 2$ A. The results are shown in Fig. 4-31.

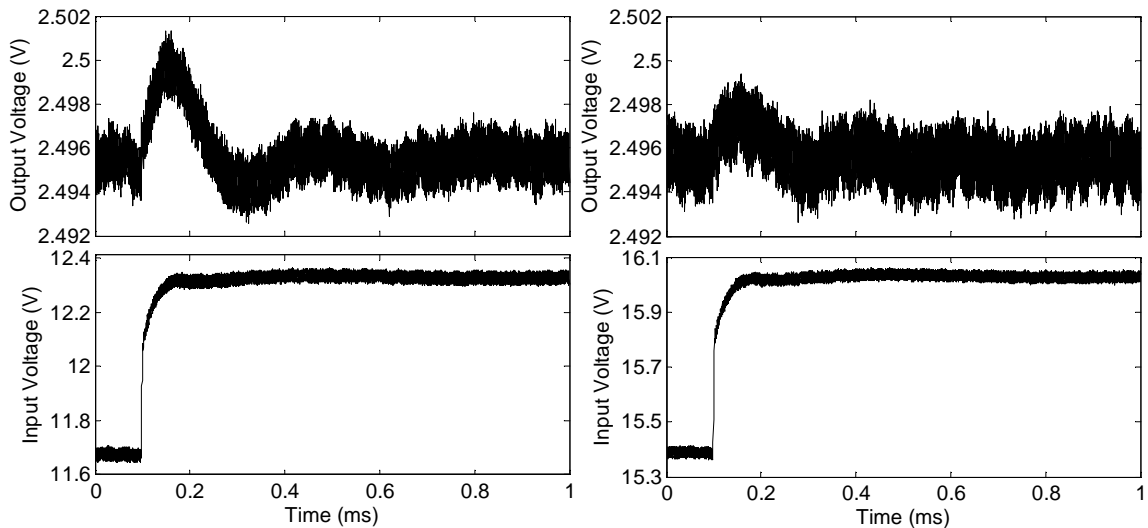


Fig. 4-31: Transient response of the commercial converter PTN78020W to input voltage steps from 11.7 V to 12.3 V and 15.4 V to 16 V at $I_o = 2$ A (only input-output voltages are shown).

The corresponding fitting results are depicted in Fig. 4-32. In this case the correlation is lower than in previous cases due to a lower SNR (the transient oscillation is much smaller). The identified transfer functions are given by (4-49) and (4-50) in discrete and continuous domain, respectively.

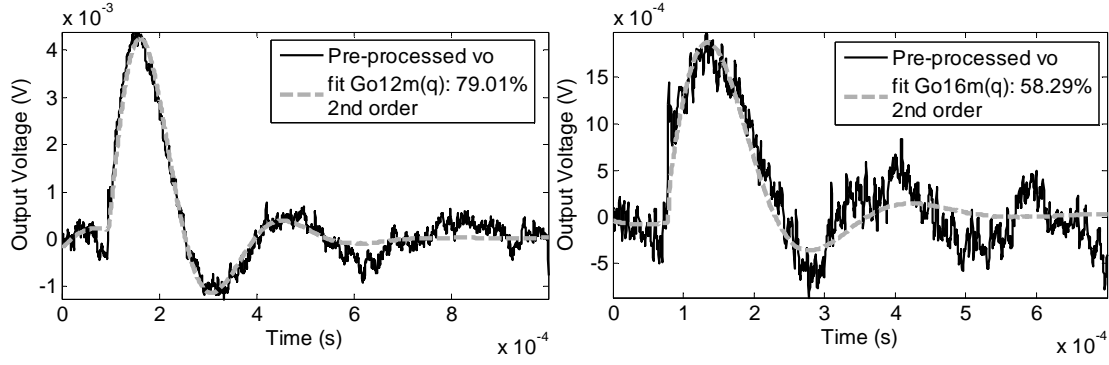


Fig. 4-32: Fitting results $G_{o12m}(q)$ and $G_{o16m}(q)$.

$$G_{o12m}(q) = \frac{0.0001025 - 0.0002025q^{-1}}{1 - 1.993q^{-1} + 0.9933q^{-2}}$$

$$G_{o16m}(q) = \frac{0.001031 - 0.002011q^{-1} + 0.0009804q^{-2}}{1 - 1.992q^{-1} + 0.9918q^{-2}} \quad (4-49)$$

$$G_{o12m}(s) = \frac{5.144 \cdot 10^{-5} s^2 + 257.2s + 1.889 \cdot 10^4}{s^2 + 1.693 \cdot 10^4 s + 5.177 \cdot 10^8}$$

$$G_{o16m}(s) = \frac{0.00101s^2 + 126.5s + 3.015 \cdot 10^4}{s^2 + 2.046 \cdot 10^4 s + 5.647 \cdot 10^8} \quad (4-50)$$

4.4.5 Analysis and removal of cross-coupling effects

4.4.5.1 Analysis and simplification of the de-coupling matrix

Once every ‘terminated’ transfer function has been identified ($Y_{im}(s)$, $H_{im}(s)$, $Z_{om}(s)$, $G_{o8m}(s)$, $G_{o12m}(s)$ and $G_{o16m}(s)$), the cross-coupling effects have to be analyzed, and the significant ones removed.

In order to figure out what effects are significant, convolution of the pre-processed inputs with the ‘terminated’ transfer functions is calculated, and the resulting responses are compared to each other (refer to section 4.3.3.2). The convolution has been obtained through simulation using Matlab Simulink [254]. The simulated schematics and resulting waveforms are depicted in Fig. 4-33 and discussed below. Note that the subscript ‘ p ’ denotes a pre-processed measurement (resulting from pre-filtering and offset subtraction).

- From Fig. 4-33a, the following conclusions are drawn:
 - $v_{oZ} \gg v_{oG}$ along the entire time window, (their maximum peak to peak oscillations are $\Delta v_{oZ} \approx 55$ mV and $\Delta v_{oG} \approx 0.3$ mV). Consequently, the cross-coupling effects on $Z_{om}(s)$ are negligible.
 - The signal i_{iY} is significant at the beginning of the transient. Therefore, the cross-coupling effects on $H_i(s)$ are significant. Specifically, $H_{im}(s)$ is coupled with both the source impedance $Z_s(s)$ and $Y_i(s)$ at high frequency. This fact has a simple explanation: v_i is perturbed at the beginning of the transient due to Z_s , so part of i_i flows through the input capacitor, which is related only to $Y_i(s)$.

- From Fig. 4-33b, it has been concluded that the cross-coupling effects are negligible on $Y_{im}(s)$ but significant on $G_{o8m}(s)$ (due to the load resistor).

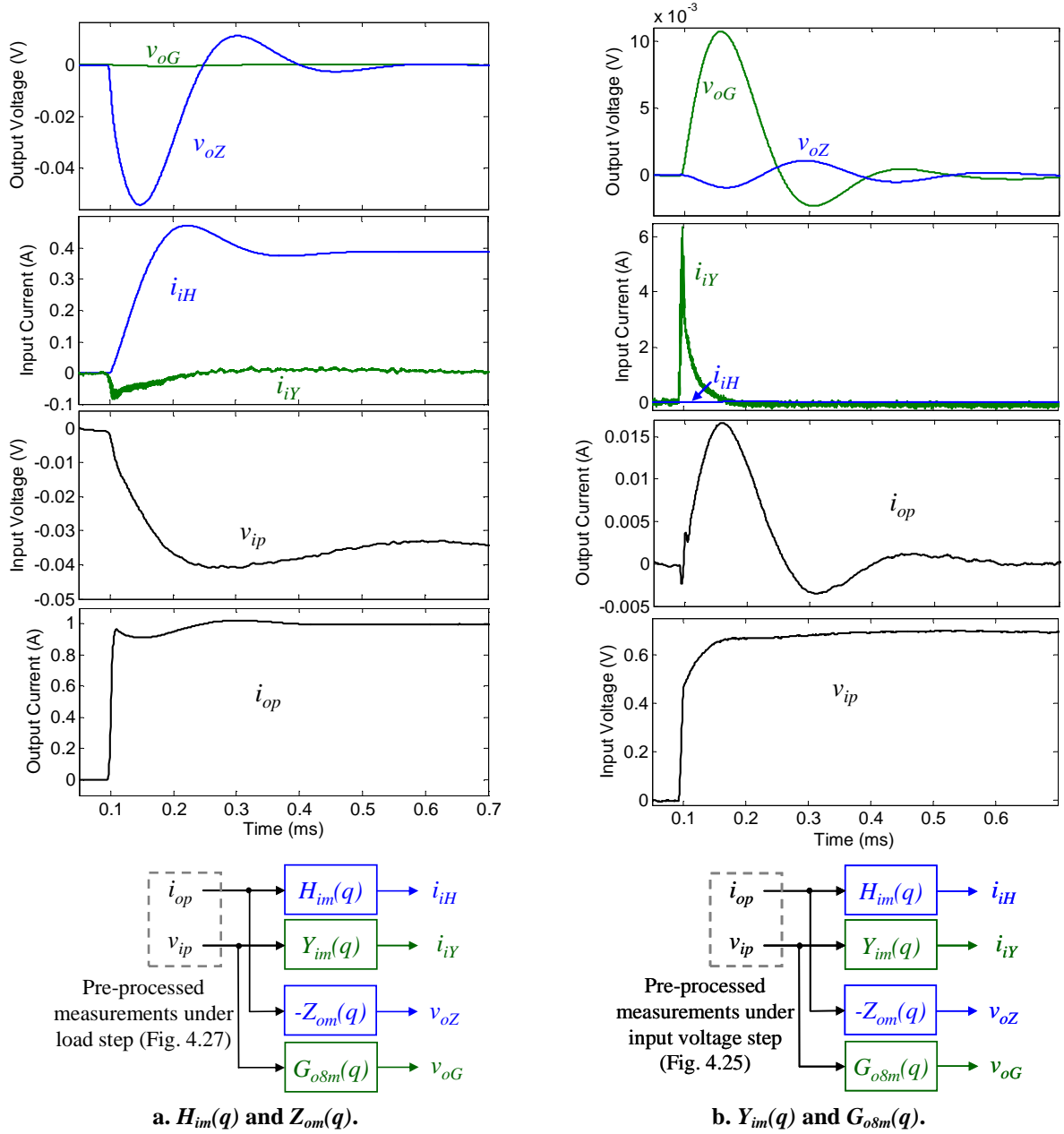


Fig. 4-33: Analysis of cross-coupling effects on identified transfer functions.

From the previous analysis the following approximations are done: $Y_i(s) = Y_{im}(s)$ and $Z_o(s) = Z_{om}(s)$. This simplifies the full decoupling matrix $[T(s)]$, given by (4-33), into $[T_s(s)]$, given by (4-51).

$$\begin{pmatrix} Y_{im}(s) \\ H_{im}(s) \\ G_{om}(s) \\ -Z_{om}(s) \end{pmatrix} = \underbrace{\begin{pmatrix} 1 & 0 & 0 & 0 \\ T_{rm}(s) & 1 & 0 & 0 \\ 0 & 0 & 1 & T_{gm}(s) \\ 0 & 0 & 0 & 1 \end{pmatrix}}_{[T_s(s)]} \begin{pmatrix} Y_i(s) \\ H_i(s) \\ G_o(s) \\ -Z_o(s) \end{pmatrix} \quad (4-51)$$

Then, the relationship between coupled and uncoupled transfer functions is the following one:

$$\begin{pmatrix} Y_i(s) \\ H_i(s) \\ G_o(s) \\ -Z_o(s) \end{pmatrix} = \underbrace{\begin{pmatrix} 1 & 0 & 0 & 0 \\ -T_{rm}(s) & 1 & 0 & 0 \\ 0 & 0 & 1 & -T_{gm}(s) \\ 0 & 0 & 0 & 1 \end{pmatrix}}_{[T_s(s)]^{-1}} \begin{pmatrix} Y_{im}(s) \\ H_{im}(s) \\ G_{om}(s) \\ -Z_{om}(s) \end{pmatrix} \quad (4-52)$$

It is important noticing that $[T_s(s)]^{-1}$ is much simpler than the full decoupling matrix $[T(s)]^{-1}$ given by (4-34). This clearly demonstrates the usefulness of the analysis described above.

4.4.5.2 Removal

The next task is to identify $T_{rm}(s)$ and $T_{gm}(s)$ from the pre-processed measurements shown in Fig. 4-33a and Fig. 4-33b, respectively. The fitting results are shown in Fig. 4-34. Good identification results have been achieved in both cases, as the model outputs are close to the pre-processed measurements. The obtained transfer functions in Laplace domain are given by (4-53).

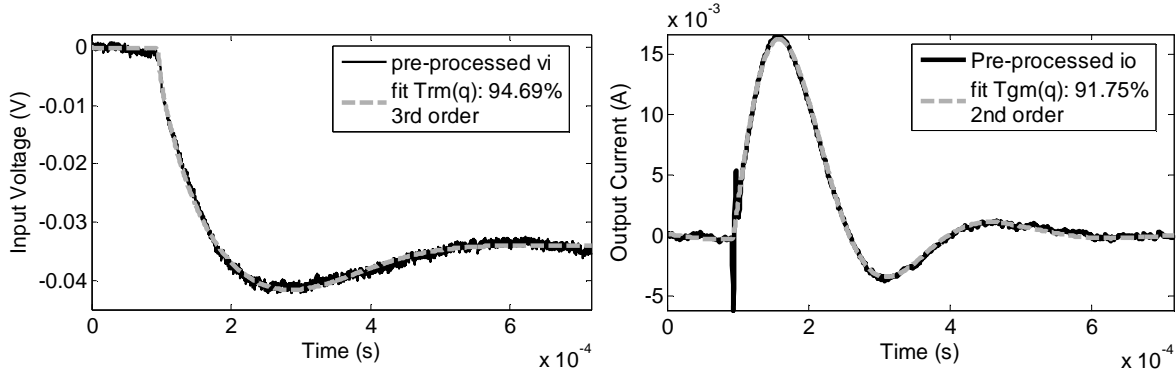


Fig. 4-34: Fitting results of $T_{rm}(q)$ and $T_{gm}(q)$.

$$T_{rm}(s) = \frac{-0.001271s^3 - 6547s^2 - 9.531 \cdot 10^8 s - 6.896 \cdot 10^{12}}{s^3 + 1.319 \cdot 10^6 s^2 + 2.453 \cdot 10^{10} s + 2.007 \cdot 10^{14}} \quad (4-53)$$

$$T_{gm}(s) = \frac{0.0002015s^2 + 1008s + 7.144 \cdot 10^4}{s^2 + 1.897 \cdot 10^4 s + 5.144 \cdot 10^8}$$

After that, (4-52) has been applied. The removal process is validated in Fig. 4-35. Using only ‘terminated’ transfer functions, significant deviations are evidenced between the sum of the convolution results and the preprocessed output signals. However, using the ‘un-terminated’ ones, good fit is observed.

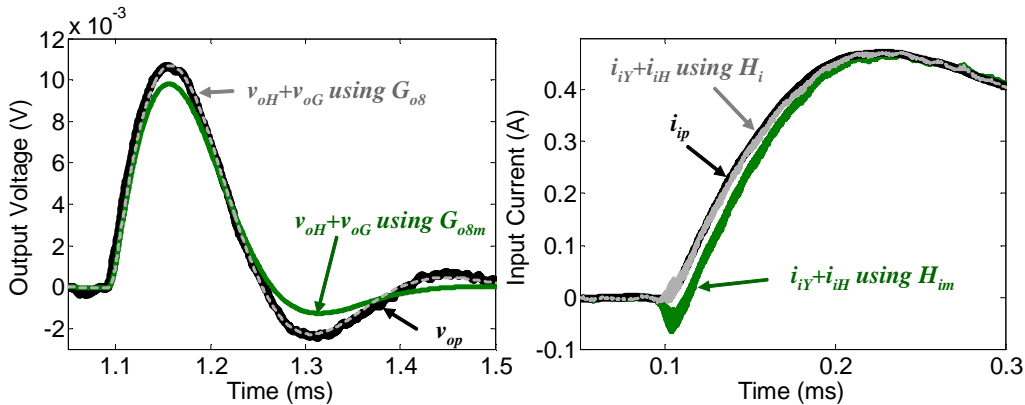


Fig. 4-35: Cross-coupling removal results.

Concerning $G_{o12m}(s)$ and $G_{o16m}(s)$, the cross-perturbations were found to be small and therefore where neglected. Hence, $G_{o12}(s) = G_{o12m}(s)$ and $G_{o16}(s) = G_{o16m}(s)$.

4.4.5.3 Model order reduction

The order of the decoupled transfer functions $H_i(s)$ and $G_{o8}(s)$, resulting from (4-52), is 7th and 8th respectively, which is relatively high. This is because they have been obtained from the combination of several transfer functions.

The model order reduction technique, presented in subsection 4.3.3.4, is next applied on both $H_i(s)$ and $G_{o8}(s)$. Firstly, the transfer functions are represented in a balanced state-space realization and then the vector of Hankel singular values is obtained. This vector represents the impact of each state-variable over the input-output model response. Then, the negligible ones can be detected and removed, thus reducing the model order. This task is easily carried out using the “*balreal*” function of Matlab, which receives as input the transfer function model and returns the balanced state-space realization and the Hankel singular values. The resulting values for H_i and G_{o8} are shown in Fig. 4-36 and discussed below.

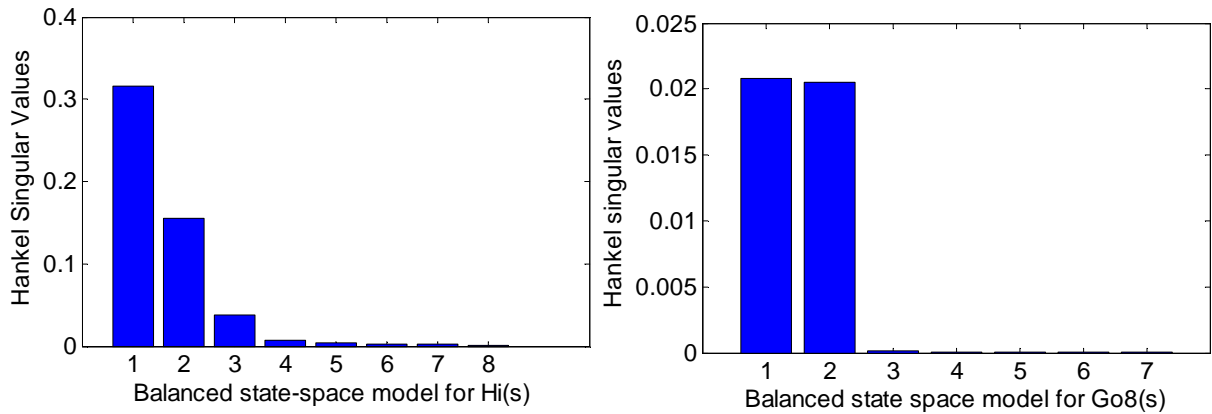


Fig. 4-36: Hankel singular values of the resulting $H_i(s)$ and $G_{o8}(s)$ from the decoupling process.

Concerning G_{o8} , two signal values are significant over the others. This means that only two state variables are significant, so model order reduction from 7th to 2nd can be carried out without changing the model response significantly. Regarding H_i , two are also the dominant state variables, although less difference is observed with respect to subsequent states.

Therefore, the order of both models has been reduced to two using the “*modred*” function. After that, the resulting state-space models have been represented again as transfer functions using the “*tf*” function. The transfer functions with reduced order are denoted with subscript ‘*r*’.

$$H_{ir}(s) = \frac{0.06192s^2 + 6568s + 1.96 \cdot 10^8}{s^2 + 1.66 \cdot 10^4 s + 5.116 \cdot 10^8}, \quad G_{o8r}(s) = \frac{3.606 \cdot 10^{-4} s^2 + 711.7s - 1.152 \cdot 10^5}{s^2 + 1.724 \cdot 10^4 s + 5.529 \cdot 10^8} \quad (4-54)$$

The results have been checked by comparing the frequency response of the transfer functions before and after model order reduction. As shown in Fig. 4-37, the frequency response of the reduced order transfer functions (subscript “*r*”) is very close to the original ones up to 50 kHz, approximately. Thereby, a substantial reduction of the model order has been successfully achieved whereas the dynamic response remains almost unchanged. If significant differences were found out within the bandwidth of interest, the “*modred*” function should be run again, but removing fewer state variables.

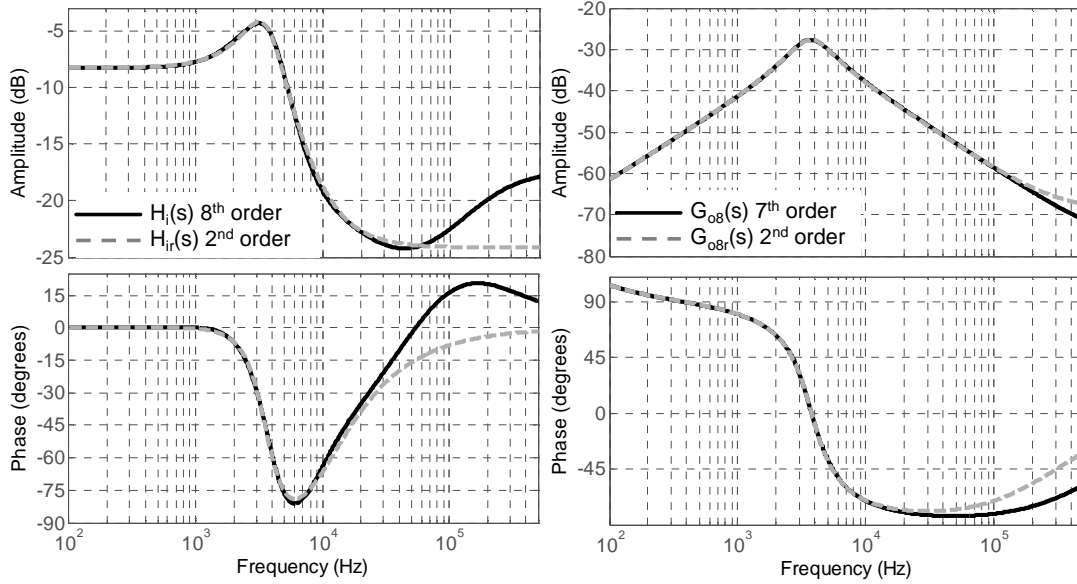


Fig. 4-37: Transfer functions $H_{iL}(s)$ and $G_{o8}(s)$ before and after model order reduction.

4.4.6 Parameterization of the large-signal model

Once the transfer function models have been identified, the large-signal model can be built.

- First, the efficiency has been characterized as a function of the operating point, yielding the graph shown in Fig. 4-38. The obtained data have been implemented using a 2-D look up table, which outputs the efficiency at any point through interpolation.
- Second, both $Y_i(s)$ and $H_{ir}(s)$ have been tuned to obtain the transfer functions $Y_{i0}(s)$ and $H_{iL}(s)$ as follows. Neither $G_o(s)$ nor $Z_o(s)$ have been post-processed, because the line-load static regulation is very narrow and nearly linear.

$$Y_{i0}(s) = Y_i(s) - Y_i(0) = \frac{110.9s^3 + 6.115 \cdot 10^8 s^2 + 2.799 \cdot 10^{14} s}{s^3 + 1.05 \cdot 10^7 s^2 + 2.683 \cdot 10^{13} s + 2.277 \cdot 10^{18}} \quad (4-55)$$

$$H_{iL}(s) = H_{ir}(s) \cdot \frac{2.495}{H_{ir}(0)} = \frac{0.4033s^2 + 4.278 \cdot 10^4 s + 1.276 \cdot 10^9}{s^2 + 1.66 \cdot 10^4 s + 5.116 \cdot 10^8}$$

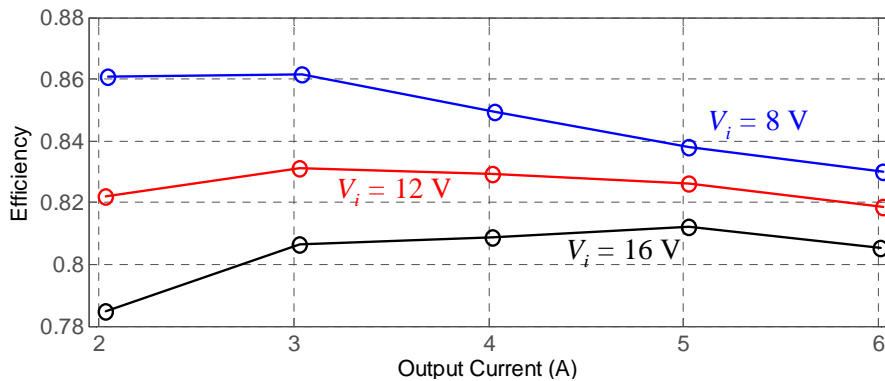


Fig. 4-38: Efficiency of PTN78020W as a function of I_o and V_i .

4.4.7 Validation

The proposed modeling and identification procedures have been validated as follows:

- First, the identification method of transfer function models has been validated. To do so, the frequency responses of the identified, ‘terminated’ transfer functions have been compared with frequency response measurements directly obtained from an AC sweep tests.
- Second, the cross-coupling removal process has been validated, and the usefulness of the prevention guidelines has been demonstrated. To do so, the cross-coupling effects have been experimentally minimized and ‘quasi’ un-terminated transfer functions have been identified. After that, the transfer functions resulting from the de-coupling process have been compared with the ‘quasi’ un-terminated ones.
- Third, the derived large-signal black-box model has been validated through comparison of simulation results and experimental measurements from a set of validation tests, different from those used for identification.

4.4.7.1 Identification of transfer functions: comparison with AC sweep results

The experimental setup used to measure both $Z_{om}(j\omega)$ and $H_{im}(j\omega)$ is shown in Fig. 4-39a. A variable-frequency current amplifier is used to draw sinusoidal perturbations on i_o , while the resistor R_l and the DC source set the operating point. The current amplifier has been implemented with bipolar transistors and operational amplifiers driven by a function generator, as shown in Fig. 4-39c. Thus, by making an AC frequency sweep on v_o , i_i and v_i , the sought frequency responses are obtained as follows:

$$Z_{om}(j\omega) = -\frac{v_o(j\omega)}{i_o(j\omega)} \quad H_{im}(j\omega) = \frac{i_i(j\omega)}{i_o(j\omega)} \quad (4-56)$$

The setup used to measure both $G_{osm}(j\omega)$ and $Y_{im}(j\omega)$ is shown in Fig. 4-39b. The current amplifier described above drawn sinusoidal current tones, which are translated into input voltage tones through a 2Ω resistor. The frequency responses are then obtained as follows:

$$G_{osm}(j\omega) = \frac{v_o(j\omega)}{v_i(j\omega)} \quad Y_{im}(j\omega) = \frac{i_i(j\omega)}{v_i(j\omega)} \quad (4-57)$$

The AC sweep tests could be carried out using other setups, as reported in [134], [144] and [147].

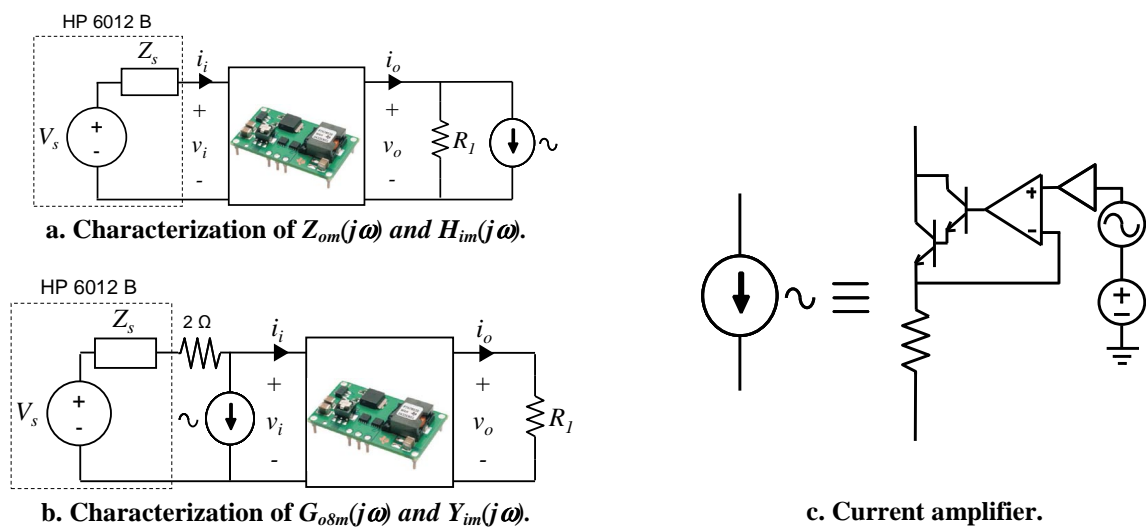


Fig. 4-39: AC sweep test: experimental setup.

Since this is a low-voltage converter, the magnitude of the output voltage is very low at some frequencies, meaning that the use of different data acquisition systems and probes may influence the result. Hence, in order to avoid uncertainties in the comparison, the response of the converter has been measured using the same oscilloscope and probes applied to record the step response. The frequency response has been characterized as follows.

- First, a dataset of input-output time waveforms has been recorded for each characterized frequency.
- Second, the magnitude and phase at each frequency has been obtained by applying the DFT on each dataset. The current amplifier has been set so that the magnitude of the input signals (i_o or v_i depending on the test) at each frequency is equal or lower than the magnitude of the steps applied for identification, thus ensuring local linear or nearly linear operation. The operating point is that previously considered to identify the transfer functions models.

The bode plots for $Z_{om}(j\omega)$ and $H_{im}(j\omega)$ are depicted in Fig. 4-40 and discussed below.

- Regarding $Z_{om}(j\omega)$, both frequency responses are very close to each other up to near $f_{sw}/2$, demonstrating the good performance of the proposed identification method. Note that the output impedance is dominated by the output capacitor impedance at high frequency, i.e. equivalent capacitance and equivalent series resistor (ESR). Hence, it could be estimated from the step test.
- Concerning $H_{im}(j\omega)$, a very good fit is observed up to 10 kHz, but discrepancies are noticed at higher frequencies in phase. Specifically, the frequency response obtained from AC sweep test exhibits non-minimum phase behavior at high frequency (phase drop), but the identified model does not. Those discrepancies may be expected, as long as the step signal has more energy at low frequency than at high frequency, then reducing the model identifiability at high frequency.

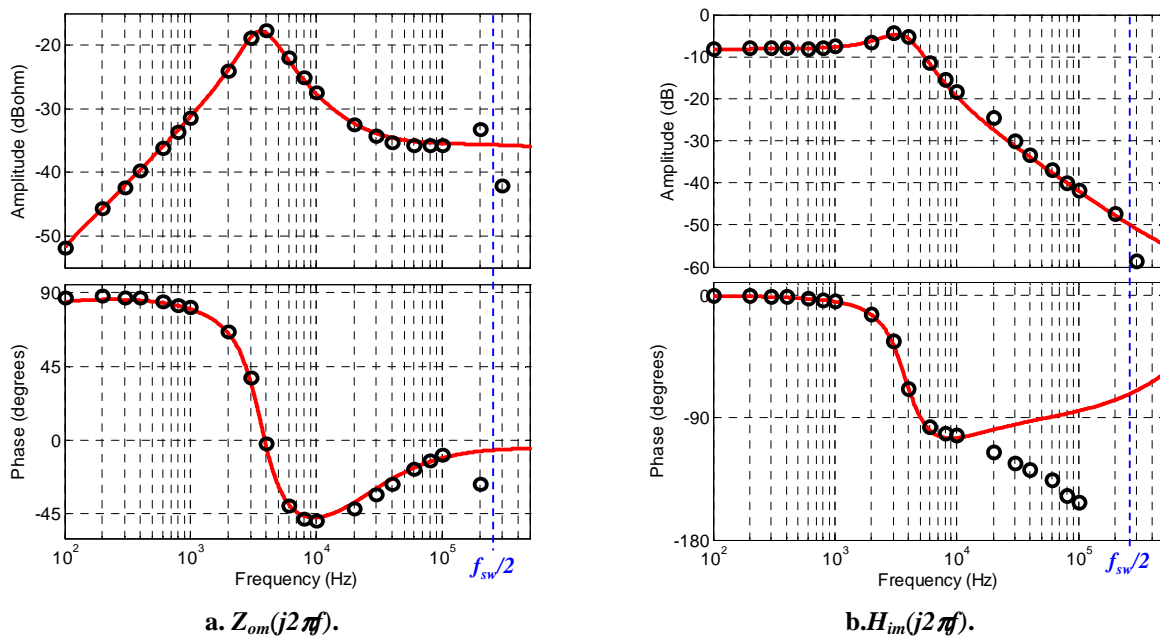


Fig. 4-40: Comparison of the AC sweep test results with the frequency response of the transfer functions $Z_{om}(s)$ and $H_{im}(s)$. Solid red line: Transfer functions. Dots: AC sweep test.

If a higher order model is identified for $H_{im}(s)$, the discrepancies in phase are alleviated. The result of increasing the model order is illustrated Fig. 4-41a. The initial part of the transient response is better fitted using a fifth order model, which results in less discrepancy with the AC sweep test measurements above 10 kHz, as shown in Fig. 4-41b. Nevertheless, those discrepancies at high frequency may be negligible from a practical point of view, due to the low-pass filter characteristic of $H_{im}(s)$.

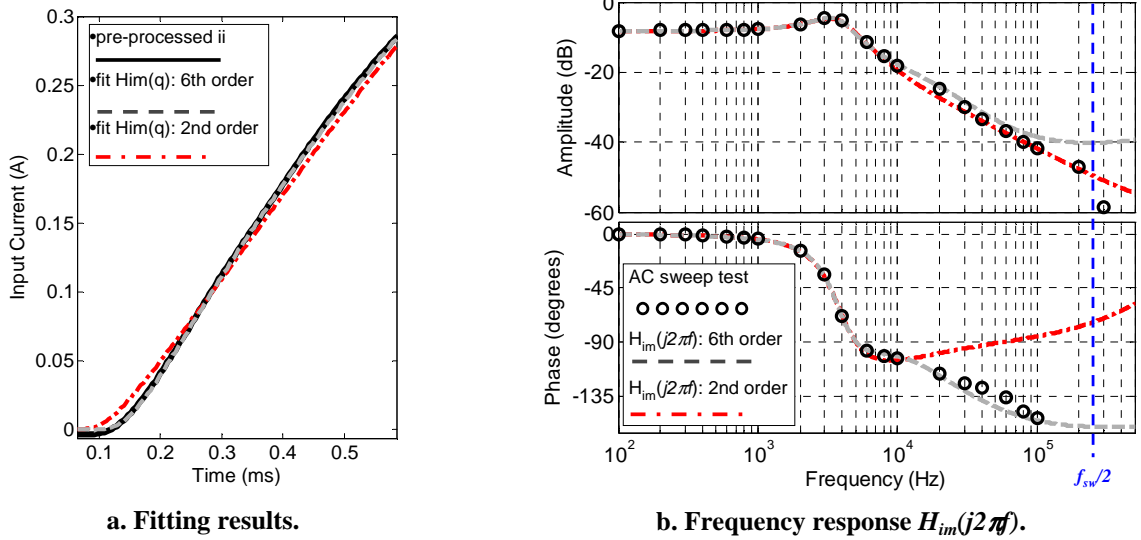


Fig. 4-41: Comparison of the AC sweep test results with the frequency response of $H_{im}(s)$ as a function of the model order.

The comparison corresponding to $Y_{im}(j\omega)$ and $G_{o8m}(j\omega)$ is depicted in Fig. 4-42 and discussed below.

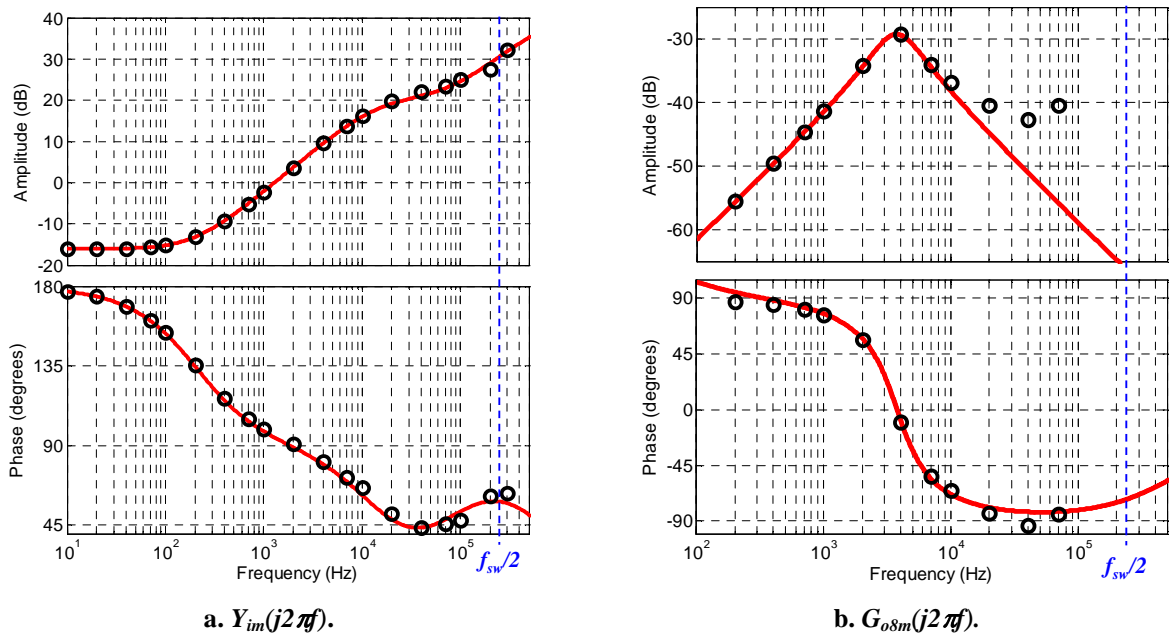


Fig. 4-42: Comparison of the AC sweep test results with the frequency response of the identified transfer functions $Y_{im}(j\omega)$ and $G_{o8m}(j\omega)$. Solid red line: Transfer functions. Dots: AC sweep test.

- Regarding $Y_{im}(j\omega)$, both frequency responses are very close to each other up to $f_{sw}/2$, which means, the input admittance has been accurately identified up to the maximum frequency

bandwidth of theoretical validity. Some interesting aspects are noticed in this bode plot. At low frequencies the CPL behavior is found, as $Y_{im}(j\omega)$ behaves as a negative incremental resistance whose admittance is $\approx -I_i/V_i = -1.4\text{A}/8\text{V} = -15.1\text{ dB}\angle 180^\circ$. As the frequency increases, $Y_{im}(j\omega)$ is dominated by the electrolytic capacitor. At the highest frequencies, the ceramic capacitors impedance is dominant (this is because the ceramic capacitors have lower ESR than electrolytic ones).

- In case of $G_{o8m}(j\omega)$, a good fit is observed up to 20 kHz. For higher frequencies the discrepancies are higher. It may be due to inaccuracy of the AC sweep test, since the measured oscillations was very low at those frequencies). Another reason would be inaccuracy of the transfer function model identification, since the SNR is relatively low.

4.4.7.2 Validation of the cross-coupling removal method and prevention guidelines

To validate the cross-coupling removal method and prevention guidelines, the identification tests have been repeated, but now preventing the cross-coupling effects as shown in Fig. 4-43 and described below:

- Cross-perturbations on v_i under i_o steps have been prevented by locating three 4.7 mF electrolytic capacitors close to the input port of the converter, thus reducing the source impedance.
- Cross-perturbations on i_o under v_i steps have been prevented by replacing the load resistor by an electronic load set in constant current mode.

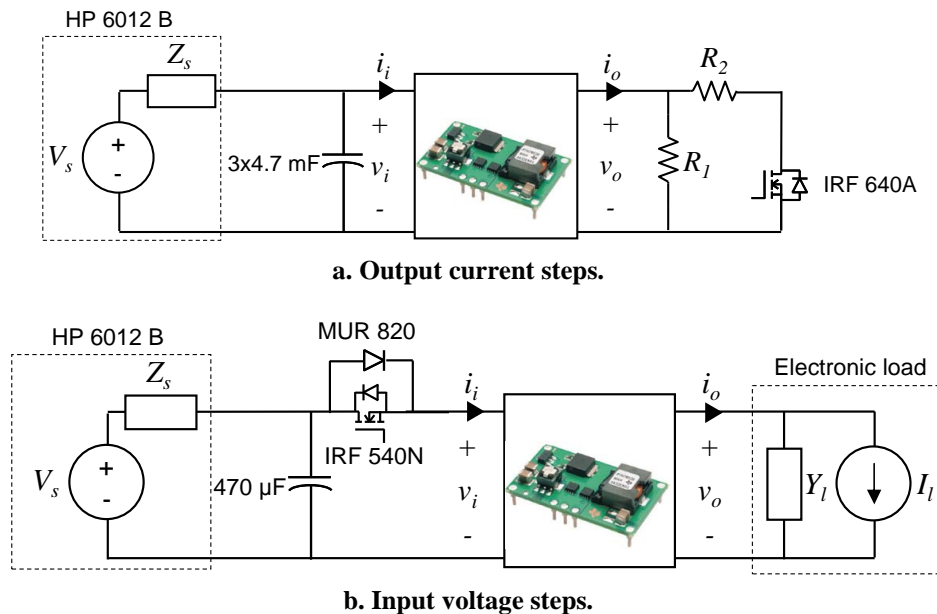


Fig. 4-43: Experimental setup with cross-coupling prevention.

The identification tests have been repeated, but now using this setup. The transient response of the converter to the i_o step, with and without cross-coupling prevention, is depicted Fig. 4-44. Only the signals affected by cross-coupling effects are shown. As can be seen, now the input voltage remains almost constant. Note that the input current ripple is significantly increased, due to the Z_s decrement.

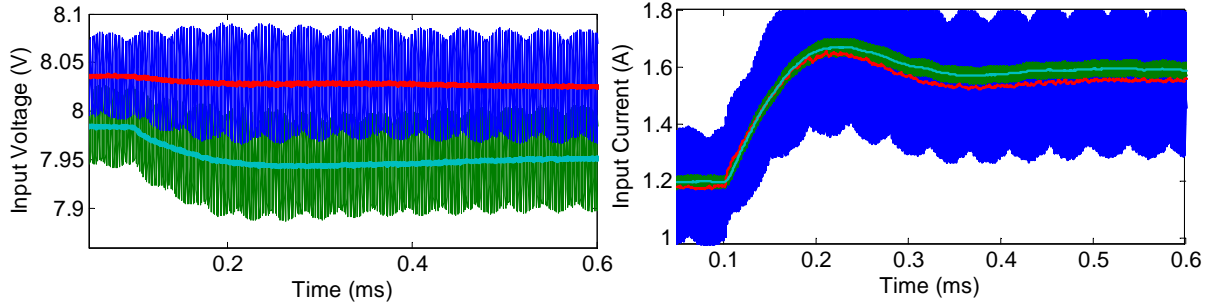


Fig. 4-44: Response of the converter to i_o step from 3.3 A to 4.3 A for $V_i = 8$ V. Blue lines: with cross-coupling prevention (averaged signals in red). Green lines: without cross-coupling prevention (averaged signals in cyan).

The response of the converter to the v_i step from 8 V to 8.65 V, with and without cross-coupling prevention, is shown in Fig. 4-45. The current now remains practically constant, which causes the v_o transient to be less damped.

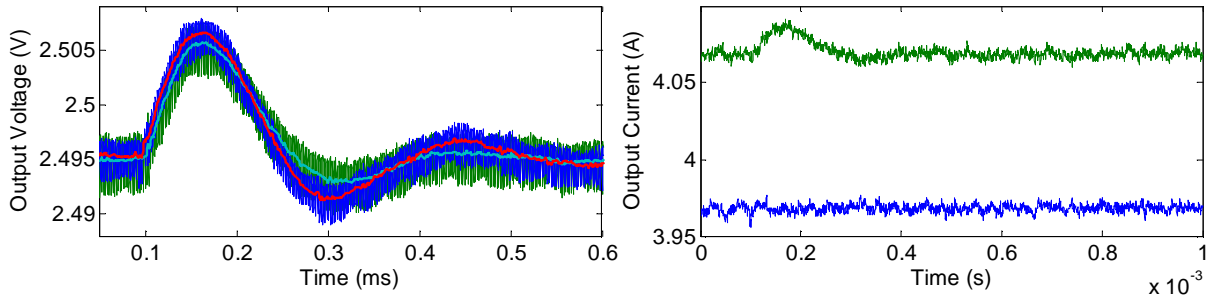


Fig. 4-45: Response of the converter to v_i step from 8.05 V to 8.65 V for $I_o = 4$ A. Blue lines: with cross-coupling prevention (averaged signals in red). Green lines: without cross-coupling prevention (averaged signals in cyan).

Transfer functions models have been identified after preventing the cross-coupling effect, corresponding to the $H_{iprev}(s)$ and $G_{o8prev}(s)$. The subscript ‘prev’ denotes cross-coupling prevention. The fitting results are shown in Fig. 4-46.

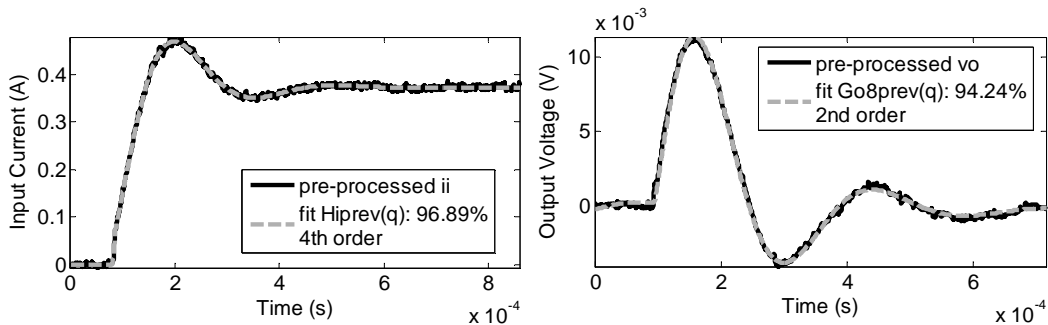


Fig. 4-46: Fitting results of $H_{iprev}(q)$ and $G_{o8prev}(q)$.

After transformation into continuous time domain, the cross-coupling effects on $H_{iprev}(s)$ and $G_{oprev}(s)$ have been evaluated. As shown in Fig. 4-47, those effects are now negligible. Consequently, the cross-coupling problem has been prevented.

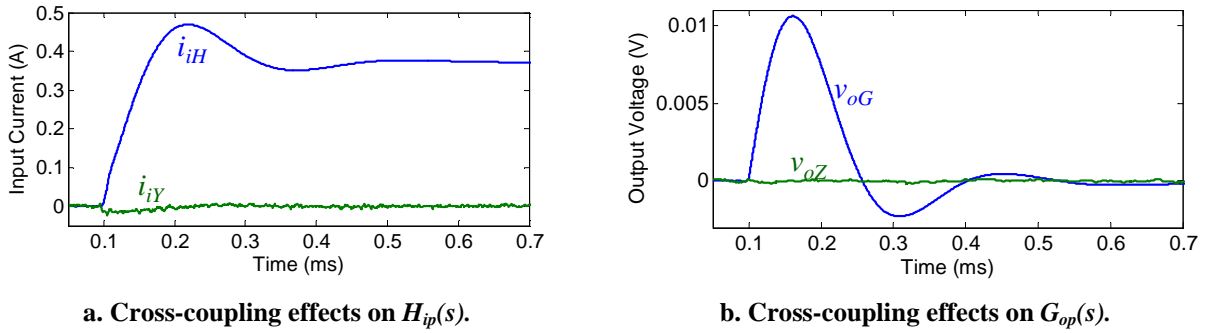


Fig. 4-47: Evaluation of cross-coupling effects after prevention.

Finally, the frequency responses of the ‘terminated’ transfer functions originally identified (subscript m), the ‘un-terminated’ ones (no subscript), and the ones with cross-coupling prevention (subscript ‘ $prev$ ’), are compared in Fig. 4-48. As can be seen, $G_{o8}(j\omega) \approx G_{o8prev}(j\omega)$ and $H_i(j\omega) \approx H_{iprev}(j\omega)$. Thus, the cross-coupling removal method has been validated, and the usefulness of the prevention guidelines has been demonstrated.

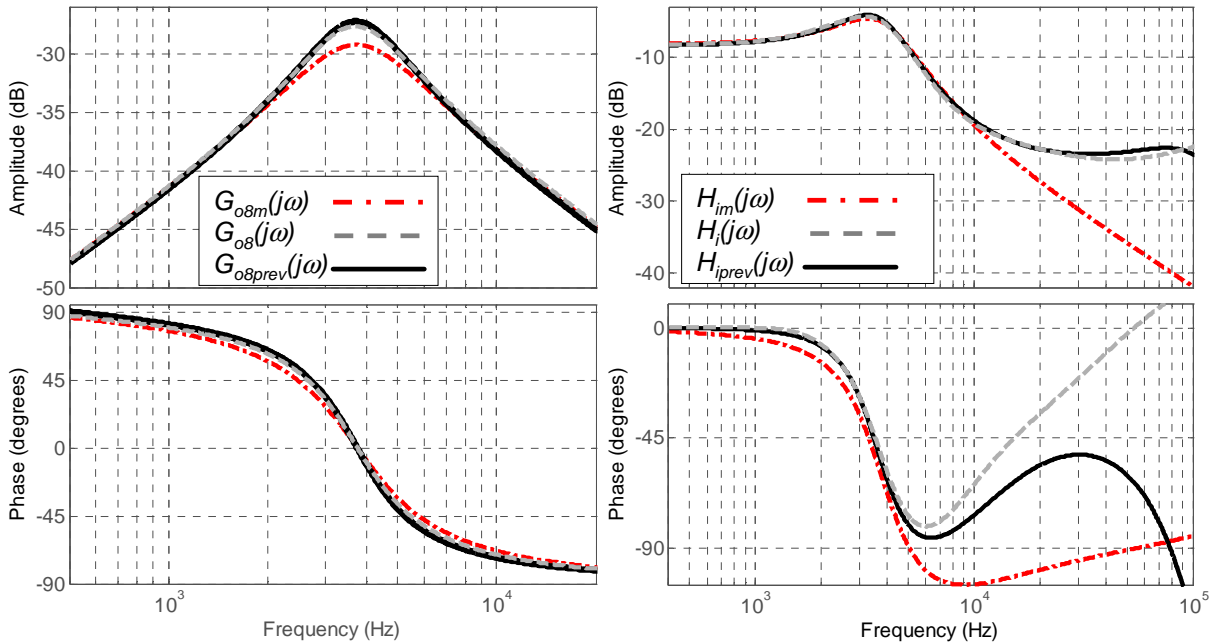


Fig. 4-48: Frequency response of transfer function models identified with cross-coupling effects (subscript ‘ m ’), after cross-coupling removal (no subscript) and with cross-coupling prevention (subscript ‘ $prev$ ’).

4.4.7.3 Validation of the large-signal black-box model

The black-box model of the commercial buck converter has been implemented in the circuit simulator PSIM [255]. A set of tests have been carried out both experimentally and by simulation, and the results from both tests have been compared. A capacitor bank has been located at the output of the voltage source, in order to reduce significantly the source impedance seen from the input port of the converter.

Four experimental tests have been carried out in order to carry out a complete validation of the modeling and identification methods.

4.4.7.3.1 Test 1. Large step increase and decrease in load

The first validation test consists of a large load step, from the minimum to near the maximum power level (see Fig. 4-49).

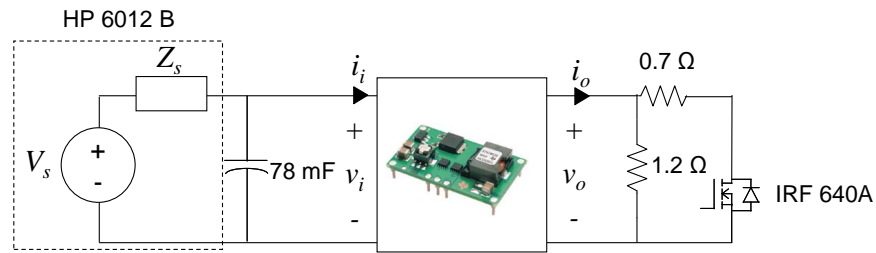


Fig. 4-49: Test 1. Large resistive load step under constant input voltage.

The results of the validation tests are depicted in Fig. 4-50. As can be seen, the model response is very close to the measured response, which yield the conclusions listed below:

- The assumptions about dynamics independence on I_o are valid.
- The un-terminated transfer functions $Z_o(s)$ and $H_i(s)$ have been properly obtained.
- The input-output dynamic power flow, taking into account efficiency, can be well modeled using the proposed structure.

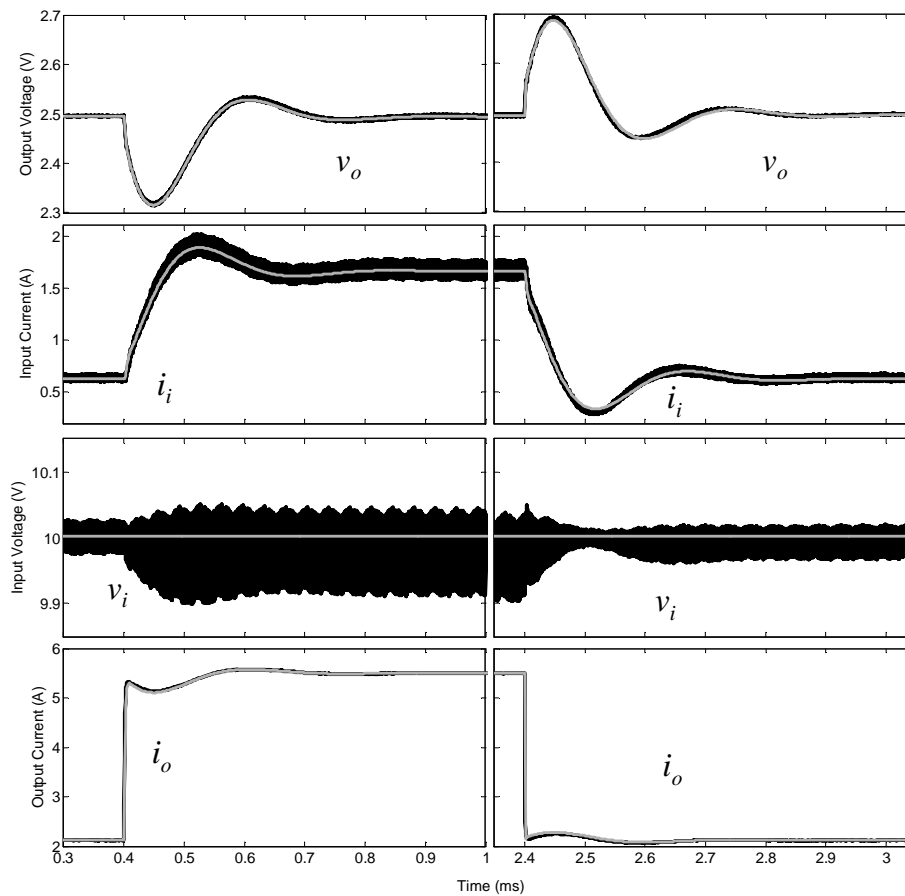


Fig. 4-50: Validation test 1. Comparison of experimental waveforms (dark traces) and simulation results (grey traces).

4.4.7.3.2 Test 2. Large step increase and decrease in input voltage

A large input voltage step has been applied by means of the experimental setup shown in Fig. 4-51. The Mosfet is connected in parallel to three diodes and is alternatively switched ‘on’ and ‘off’, while the converter supplies 13 W to a resistive load. The array of diodes has been simulated using a model that incorporates its I-V characteristic curve.

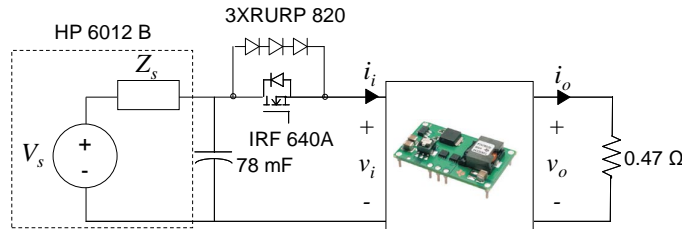


Fig. 4-51: Validation test 2. Large input voltage step.

The comparison between measurements and simulations is shown in Fig. 4-52 and discussed below.

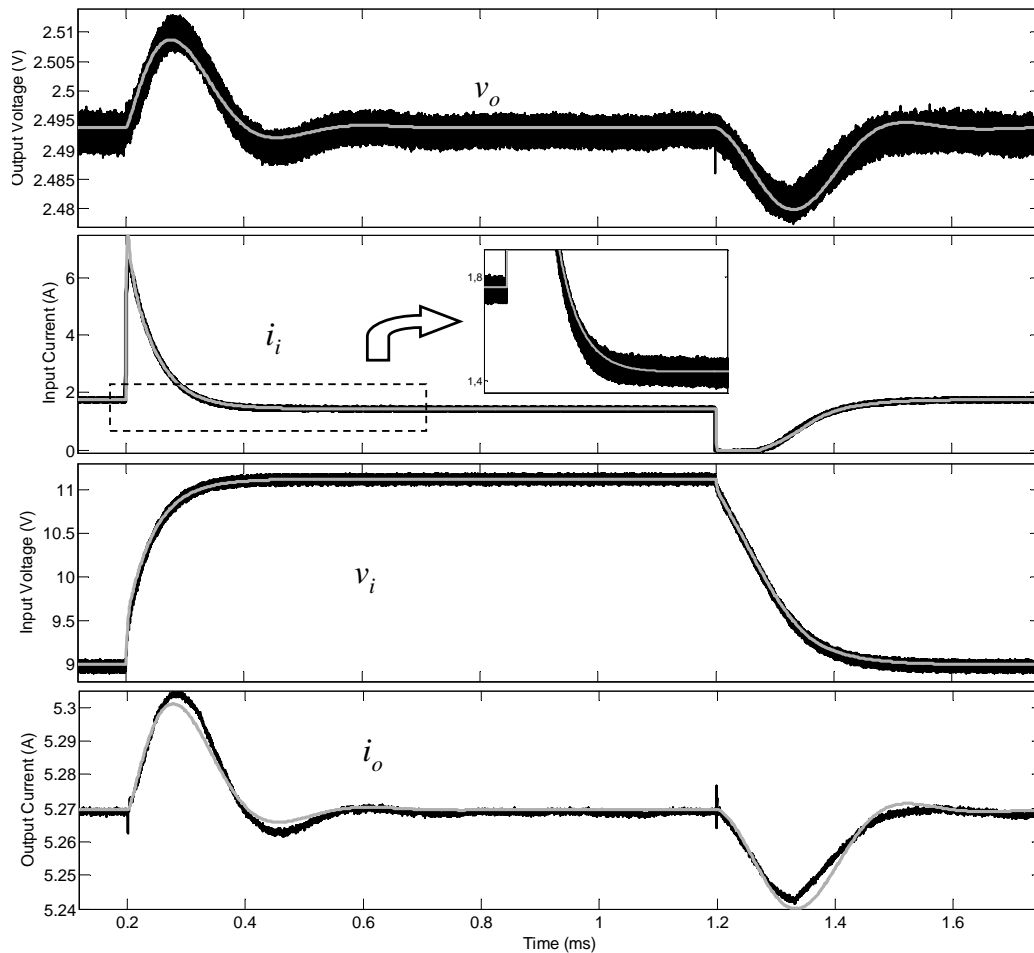


Fig. 4-52: Validation test 2. Comparison of experimental waveforms (dark traces) and simulation results (grey traces).

When the switch is turned on, a 2 V step in v_i is caused, whose slew rate of the step is lower than that under the identification test, because the Mosfet used in this case has a larger drain-to-source resistance. When the switch is turned off, the converter is initially disconnected from the power

source, so that v_i gradually decreases following a linear evolution. Such a decrease corresponds to the discharge of the input capacitor of the converter. Once the voltage drop upon the diodes exceeds the threshold voltage, current flows again through the input port.

From this test, the conclusions listed below have been drawn.

- The un-terminated transfer functions $Y_i(s)$, $G_{o8}(s)$ and $G_{o12}(s)$ have been properly obtained.
- The low-frequency CPL behavior of the converter is well modeled by means of the proposed model structure, as i_i decreases when v_i increases, so that the input-output power balance is maintained (see the zoomed part in the i_i plot).
- The LLMN for G_o can represent properly dynamics dependence on V_i . Fig. 4-53 shows the weighted output of the local transfer functions which compose the LLMN, where one can see how the v_o transient results from the combination of them.

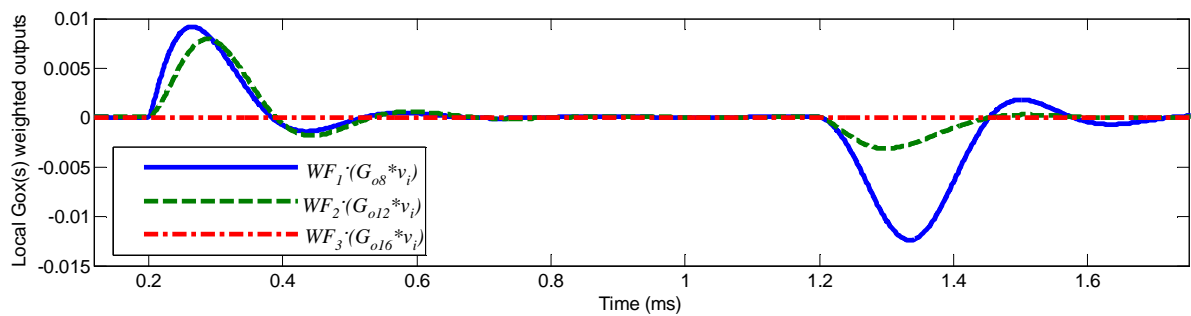


Fig. 4-53: Weighted response of the local linear models $G_{o8}(s)$, $G_{o12}(s)$ and $G_{o16}(s)$.

4.4.7.3.3 Test 3. Capacitive load step under weak DC bus

Previous validation tests have focused on large steps of only one input signal of the model (either v_i or i_o) while the perturbation of the other is much lower or null. However, for validation purposes, it may be interesting to **apply perturbations, different from steps, on both signals simultaneously**.

The next validation test consists in stepping a capacitive load, whereas an inductor is connected in series between the power source and the input port of the converter (see Fig. 4-54). When the Mosfet is switched ‘on’, a current peak is demanded by the capacitor. Compared to a resistive load step, this test emphasizes the high frequency components over the low frequency ones. Simultaneously, the input inductor resonates with the input capacitor of the converter, causing a large oscillation of v_i .

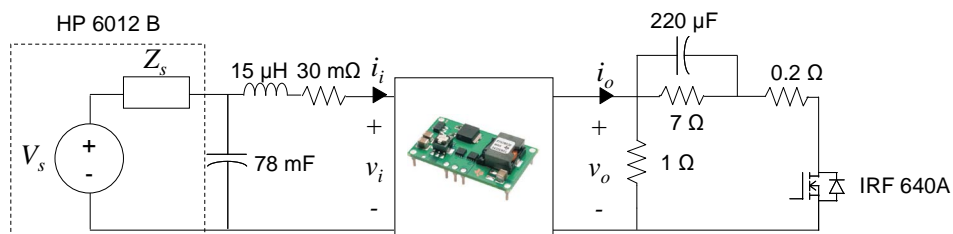


Fig. 4-54: Validation test 3. Large RC load step while fed from a weak DC bus.

The comparison between experimental and simulation results is given by Fig. 4-55. As shown, both the v_o undershoot and the oscillations at the input port are reproduced accurately. The conclusions listed below have been derived.

- The power converter reproduces the behavior of the system under simultaneous perturbation of the input signals, different from steps.
- The behavior at the input port under weak DC bus is well represented.

Both statements listed above corroborates that the un-terminated transfer function of the model has been properly validated.

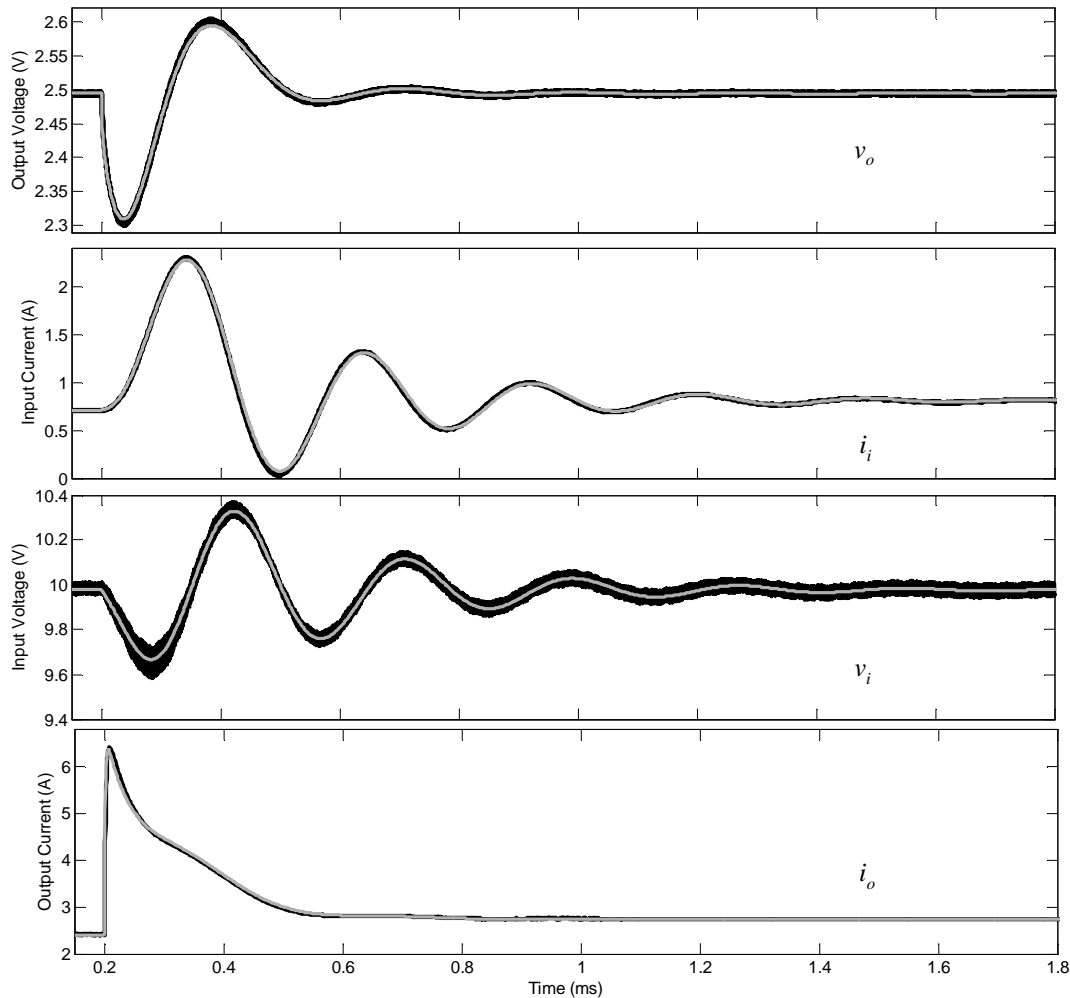


Fig. 4-55: Validation test 3. Comparison of experimental waveforms (dark traces) and simulation results (grey traces).

4.4.7.3.4 Test 4. Exponential current demand with series resistor at the input port

The final validation test consists in demanding an exponential load current profile, by means of the electronic load, whereas a series resistor is connected between the power source and the converter (see Fig. 4-56a). Compared to a step waveform, this test emphasizes the low frequency components. Moreover, large disturbances are simultaneously applied on both v_i and i_o . In this case, the output current profile is simulated using a controlled current source driven by a look-up-table.

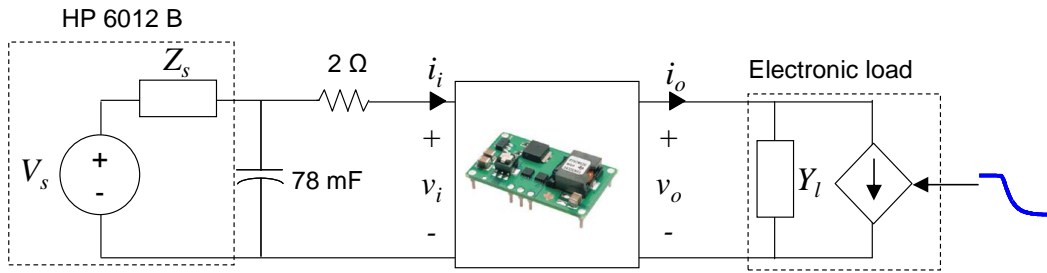


Fig. 4-56: Validation test 4. Experimental setup.

The comparison between experimental measurements and simulation results is depicted in Fig. 4-57. It is worth noticing that the slow constant time of i_o makes the transient response of v_o to be quite different from that measured under load steps. As can be seen, the response of v_o is accurately reproduced by the model. The i_i consumption is also well modeled in terms of statics and dynamics.

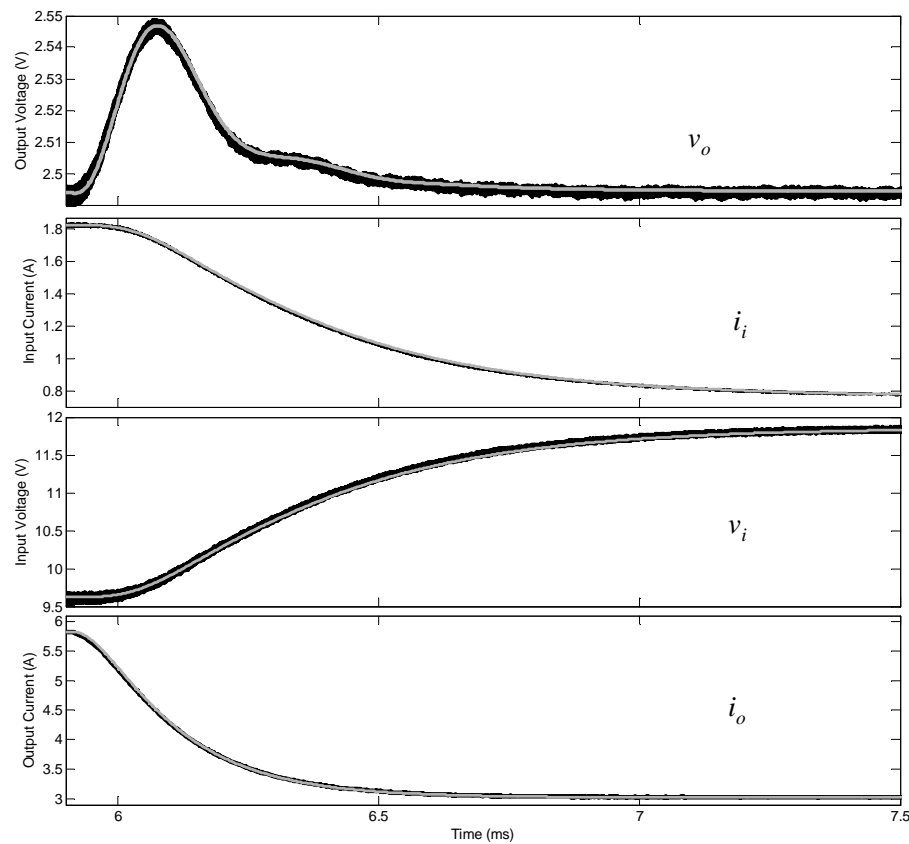


Fig. 4-57: Validation test 4. Comparison of experimental waveforms (dark traces) and simulation results (grey traces).

The conclusions that can be derived from this test are similar to those obtained from test 3. The model can represent simultaneous perturbations of both input signals, different from steps, meaning that the un-terminated transfer functions have been correctly obtained.

4.4.8 Summary

Throughout this section, a comprehensive illustration and validation of the proposed modeling and identification methods have been presented.

First, a large-signal black-box model of a commercial converter has been derived step-by-step.

- A comprehensive analysis of linearity within the considered working region has been carried out, from which guidelines for dynamic networks selection have been derived.
- Once the dynamic networks have been selected, ‘terminated transfer function models’ have been identified by means of step tests and a parametric identification algorithm. Following this, the cross-coupling effects have been analyzed and the significant ones have been removed. Later on, model order reduction has been applied on some of the un-terminated transfer functions. Finally, some of the transfer functions have been post-processed to build the large-signal model.

After that, a comprehensive validation has been carried out, covering the following aspects:

- The identification method, based on step tests and parametric identification, has been validated. To do so, the frequency response of the ‘terminated’ transfer functions has been compared to frequency responses directly measured by means of AC sweep tests.
 - In case of $Z_o(j\omega)$ and $Y_i(j\omega)$ accurate fit has been observed up to $f_{sw}/2$, which corroborates the good performance of the proposed technique.
 - In case of $G_o(j\omega)$ and $H_i(j\omega)$ accurate fit has been observed up to $f_{sw}/20$, but some disagreement has been evidenced for above frequencies. Such mismatching has been proven to be due to slight mismatching between the measured response and the fitted model response at the beginning of the transient, where the highest frequencies of the spectrum are dominant.
- The cross-coupling removal method and the prevention guidelines have been validated.
- Finally, both the large-signal black-box model and the experimental converter have been subjected to several large-signal tests, and the resulting waveforms have been compared to each other. It has been proven that the model can represent the large-signal behavior of the converter, under different load step types (capacitive load, resistive load and electronic load) and having stiff and weak DC buses. This has validated the good performance of the proposed modeling method, the conclusions derived from the linearity analysis, and the identification results of un-terminated transfer functions.

4.5 Experimental results: modeling of other commercial converters

In this section, the following commercial converters are modeled.

- Section 4.5.1: Forward converter by Murata.
- Section 4.5.2: Multistage AC/DC converter by Emerson (only the output port is modeled).

In both cases, the output current ranges from no-load to rated-load, and the operating point for the input voltage, V_i , is fixed (in case of the AC/DC converter, it means that the RMS value is fixed). Within the considered working region, these converters exhibit nonlinearities not presented by the buck converter modelled in section 4.4. Thus, the limitations of the proposed modeling approach can be explored.

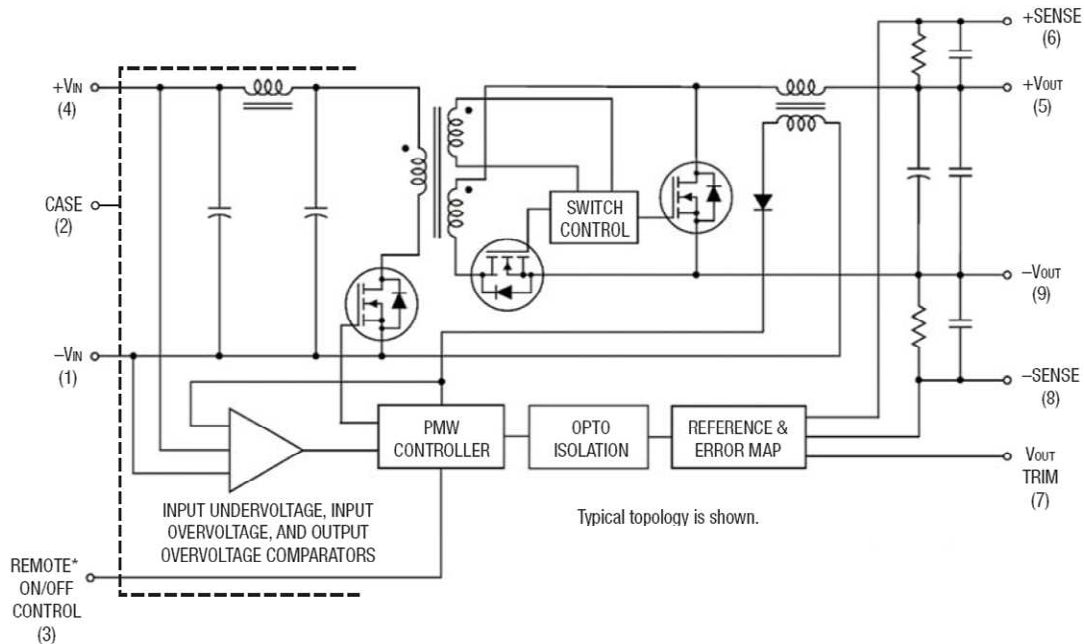
4.5.1 Forward converter

An isolated bus converter by Murata [257] (see Fig. 4-58) is modeled in this section. It consists of a synchronous forward topology. At the output, this converter provides regulated 12 V. At the input, it can be supplied from a DC bus ranging from 36 V to 75 V. The rated power is 150 W and the switching frequency is $f_{sw} \approx 335$ kHz.

The regulation stage comprises the integrated circuit UC3843A [258], which is a peak-current-mode PWM controller.



a. Image from datasheet.



b. Schematic (according to the datasheet, the left-side capacitor of the input filter is not present in the modeled unit).

Fig. 4-58: Commercial DC-DC isolated bus converter by Murata UCH-12/12.5-D48NB-C [257].

For modeling purposes, the load current ranges from no load (0 A) to rated load (12.5 A). Regarding the input voltage, the converter is assumed to be fed from a regulated 48 V bus, so $V_i = 48$ V. No additional input/output capacitors have been placed.

4.5.1.1 Preliminary tests: linearity analysis

The test bed, used for linearity analysis and model identification, is shown in Fig. 4-59.

- The output current steps (Fig. 4-59a) have been applied by switching a resistor R_2 , while R_1 sets the operating point. At the input port, a large capacitor bank has been implemented to minimize the cross-perturbation of v_i .
- The input voltage steps (Fig. 4-59b) has been applied by switching-on an array of three-diodes, yielding a voltage step with magnitude equal to 2 V, approximately. An electronic load has been used to set the operating point for the output current, I_o , so the cross-perturbation of it is minimized.

The data acquisition system is the same that has been used in section 4.4. The only different is that a differential probe Tektronix P5205 is used to measure the input voltage under i_o steps, and the output voltage under v_i steps. The sampling frequency is 2.5 MHz, which is approximately 7.5 times the switching frequency.

Only dynamics dependence on I_o is analyzed, because the input voltage operating point is only $V_i = 48$ V.

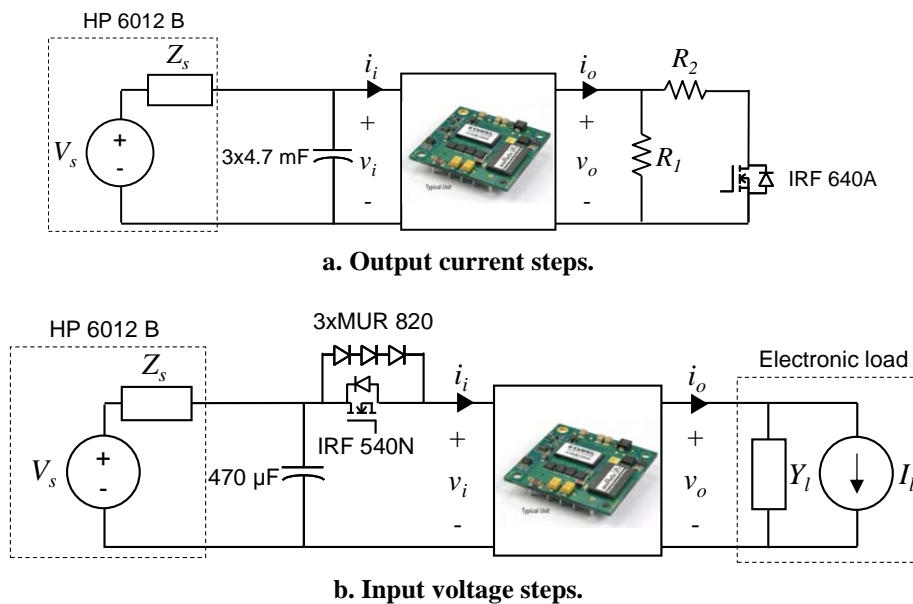


Fig. 4-59: Experimental setup, with cross-coupling prevention, for linearity analysis and model identification.

4.5.1.1.1 Analysis of H_i and Z_o dependence on I_o

The response of the converter under a set of load steps is shown in Fig. 4-60. The resistor R_2 is fixed at 33Ω , in order to have a fixed step magnitude equal to ≈ 350 mA. The operating point I_o is then gradually increased through R_1 . As may be seen, the response of the converter exhibits strong dependence on I_o at the lightest load levels. Within 0 A and 1 A, the response is nearly linear. However, between 1 A and 2 A the response strongly depends on I_o . Such dependence is evidenced not only on v_o but also on i_i , as they are related to each other through the input-output power balance. For current levels ranging from 2 A to 12.5 A, the response of the converter turns to be nearly linear.

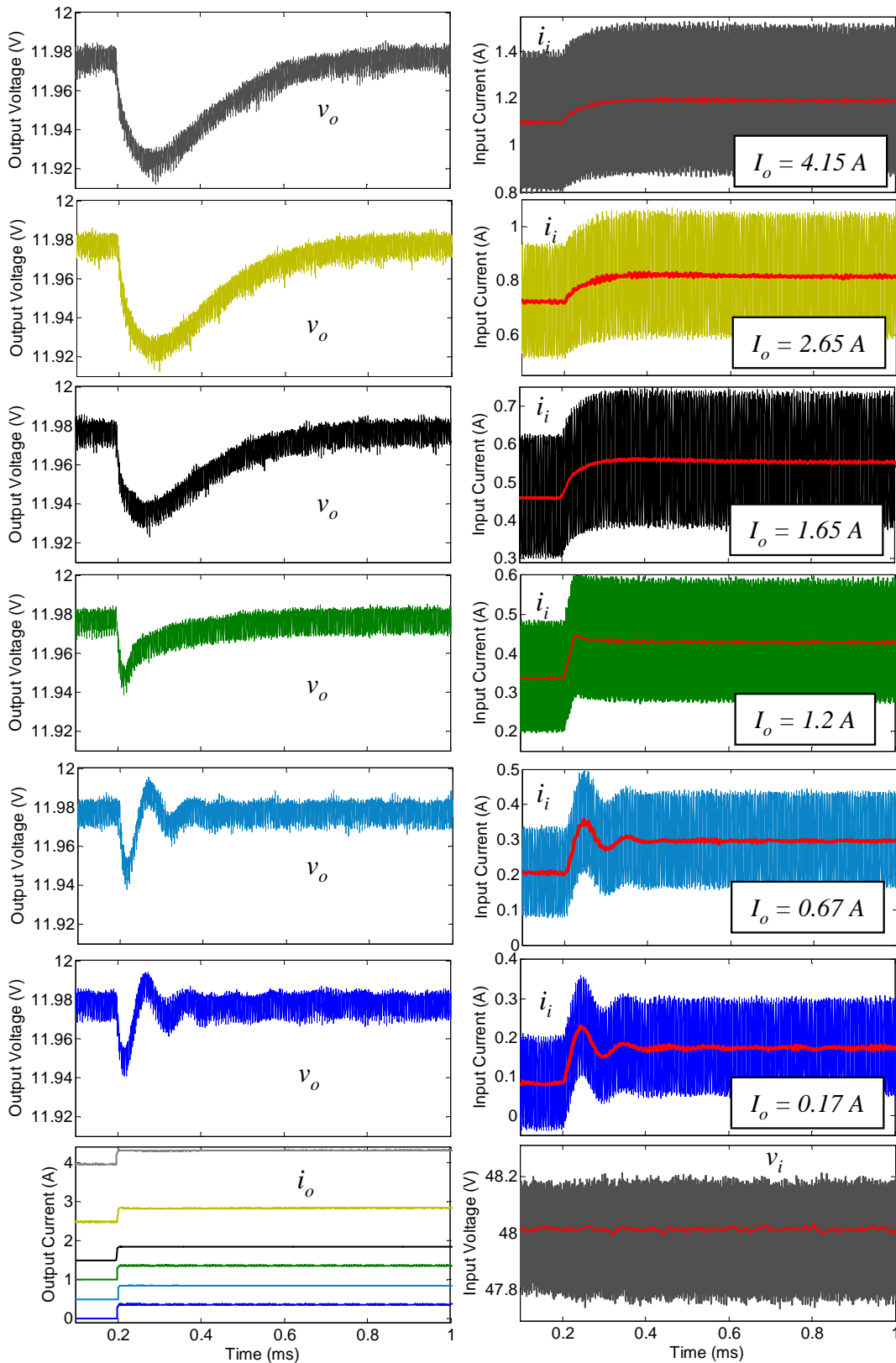


Fig. 4-60: Response of the forward converter under output current steps (averaged waveforms in red).

4.5.1.1.2 Analysis of Y_i and G_o dependence on I_o

The response of the converter under v_i steps at different I_o levels is depicted in Fig. 4-61. The input current exhibits an under-damped response. It can be noticed that, the higher the I_o level, the lower

the damping of the oscillation. On the other hand, the transient response of v_o exhibits a very small oscillation^{4,9}, meaning that the audiosusceptibility could be neglected in the model.

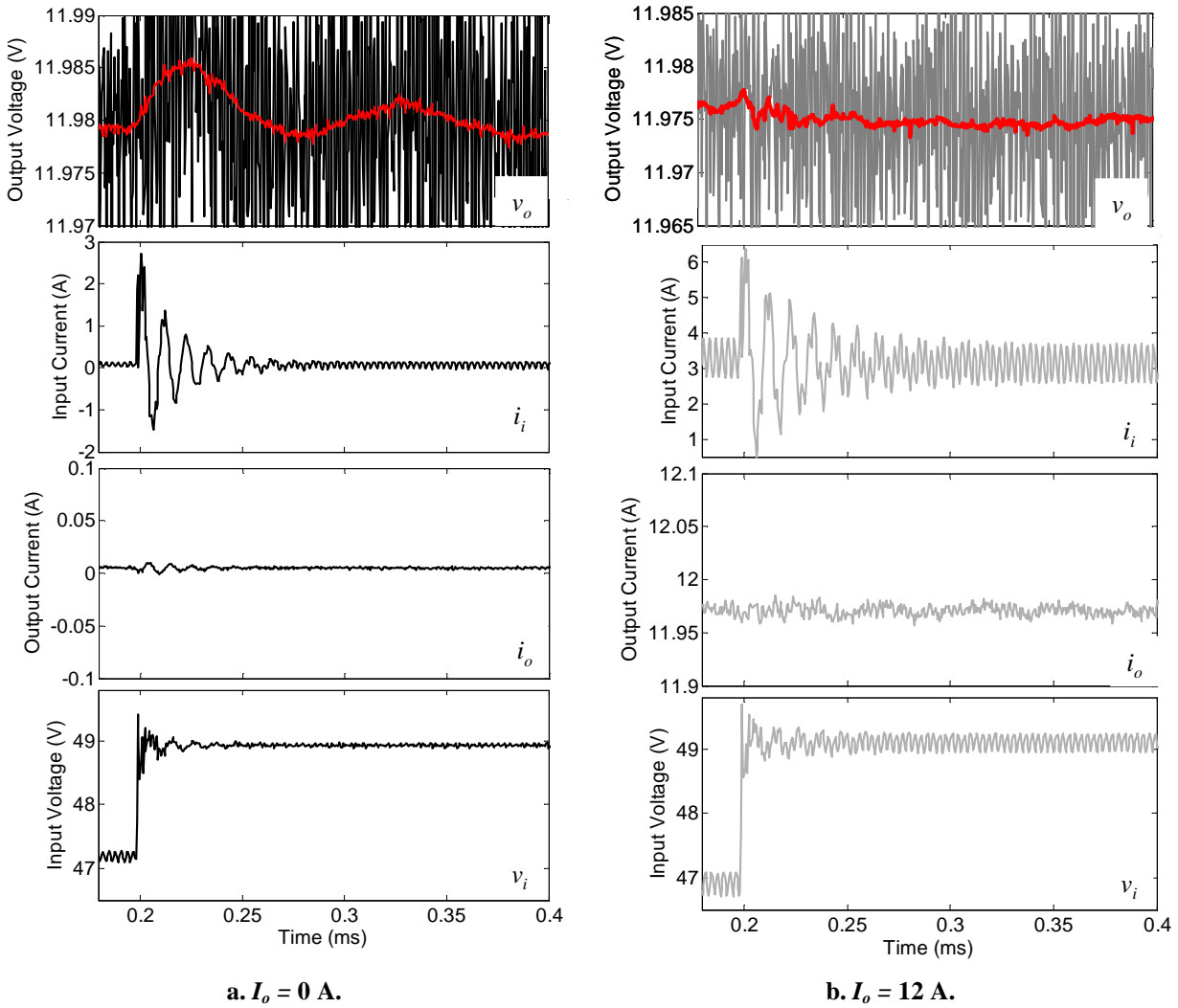


Fig. 4-61: Response of the forward converter under input voltage steps (averaged waveforms in red) for different current levels.

4.5.1.2 Dynamic networks modeling

According to the analysis above discussed, the dynamic networks have been built as follows:

- The output impedance has been modeled using a LLMN, in order to account for the dynamic dependence on I_o illustrated before. The range is narrowly partitioned for $I_o \in [0, 2]$ A, whereas a single transfer function is considered for $I_o \in [3, 12]$ A.
- The audiosusceptibility has been neglected, as it is very small.
- The back current gain has been modeled by means a LLMN, whose output is scaled as a function of the input voltage. This way, both the dynamic dependences on I_o and the CPL behavior are addressed. The range is partitioning is similar to that used for Z_o . However, two

^{4,9} Buck derived converters provided with peak current-mode-control (as the forward under study) allows achieving very low audiosusceptibility, as input voltage perturbations are rapidly compensated by the inner current controller.

local models are used for $I_o \in [3, 12]$ A, since there is a certain dependence on I_o within that range.

- The input admittance has been modeled by means of a LLMN, in order to reproduce the slight damping dependence on I_o discussed above. In this case, v_i is the input of the local linear models, but i_o drives the weighting functions.

The static load regulation is very narrow (less than 1 mV/A), so the simplified approach introduced in section 4.2.4 can be used. As a difference from the buck converter, the no-load current consumption is also modeled in this case. The derived model structure is depicted in Fig. 4-62.

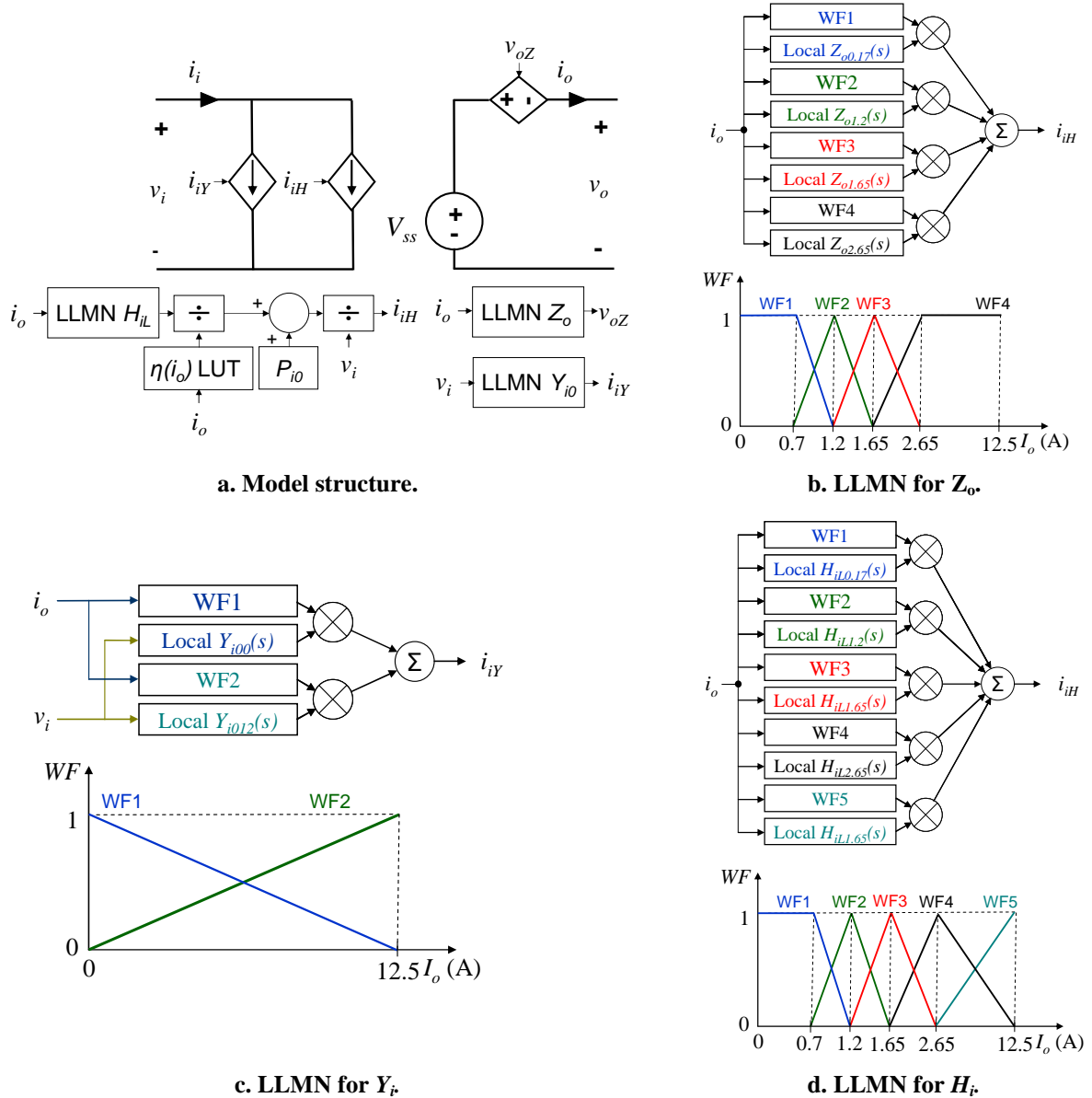


Fig. 4-62: Black-box model of the commercial forward converter UCH-12/12.5-D48NB-C by Murata for $V_i = 12$ V and $I_o \in [0, 12.5]$ A.

4.5.1.3 Model identification

4.5.1.3.1 Local linear models for Z_o and H_i

The local linear models corresponding to Z_o and H_i have been identified from the measurements shown in Fig. 4-60. Every signal has been pre-filtered using a 15th order MAF. This MAF yields rejection of every harmonic multiple of 166.7 kHz, which results in high attenuation of the switching frequency, which is approximately 335 kHz.

The transient responses shown in Fig. 4-60 have been used for model identification. After testing several step magnitudes, it was found that $\Delta i_o = 350$ mA results in nearly linear dynamic response while the SNR is reasonably high. The fitting results, corresponding to some local linear models, are depicted in Fig. 4-63. As can be seen, the identified model fits accurately the average response of the pre-processed measurements in all cases.

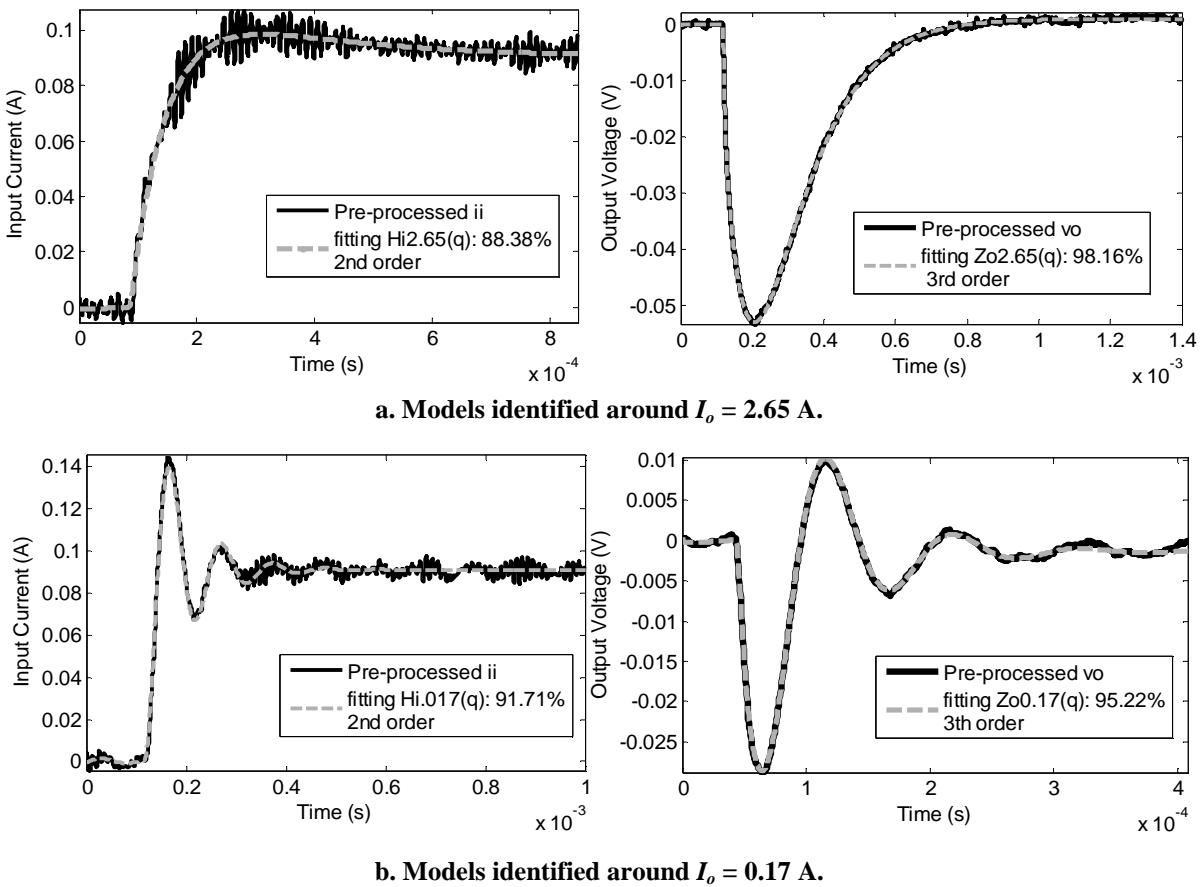


Fig. 4-63: Fitting results of some local linear models for H_i and Z_o .

The cross-coupling effects on the identified transfer functions have been found to be low enough, so that the identified transfer functions are assumed to be un-terminated.

The frequency response of the identified transfer functions is shown in Fig. 4-64 and Fig. 4-65. For illustrative purposes, the frequency response of transfer functions, identified on additional operating points, are plotted.

- Fig. 4-64 shows the frequency response of transfer functions identified at light load levels, ranging from 0 A to 2.65 A. The strong dependence on I_o is clearly noticed, as the frequency response changes abruptly around 1.4 A.

- Fig. 4-65 depicts the response of transfer function models identified at load levels ranging from 2.65 A to 12 A. As shown, the dynamic dependences on I_o are slight within this range.

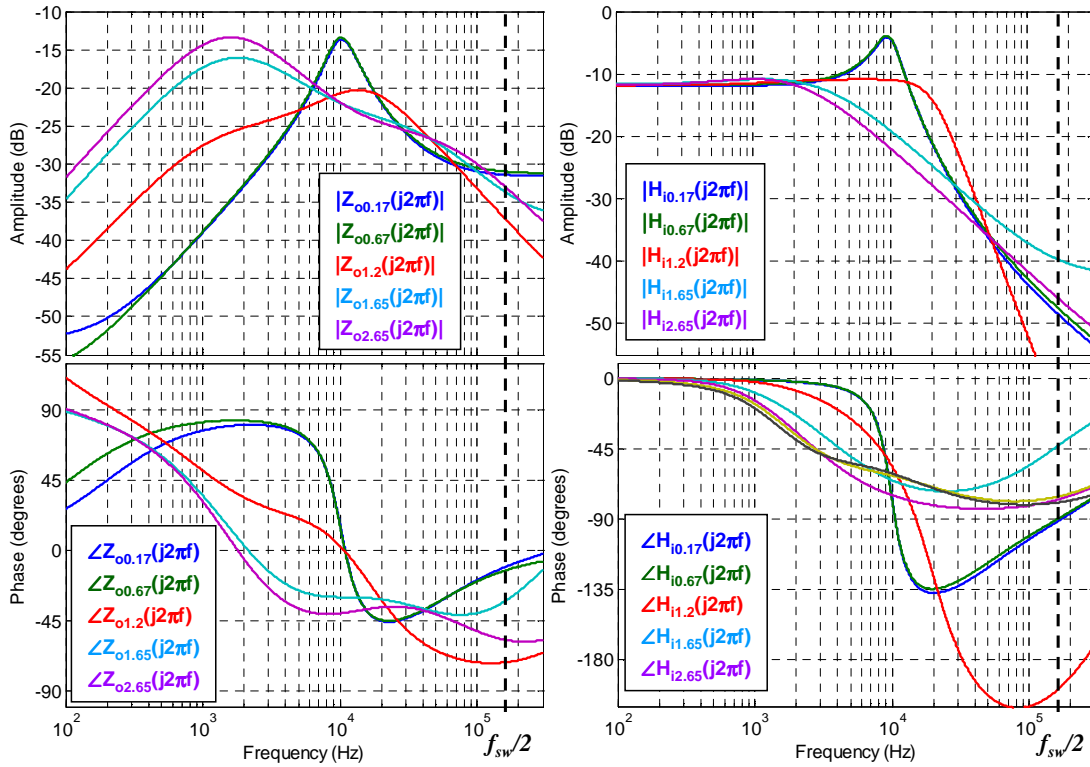


Fig. 4-64: Frequency response of $Z_o(j2\pi f)$ and $H_i(j2\pi f)$ at load levels from 0% to 20% of rated power.

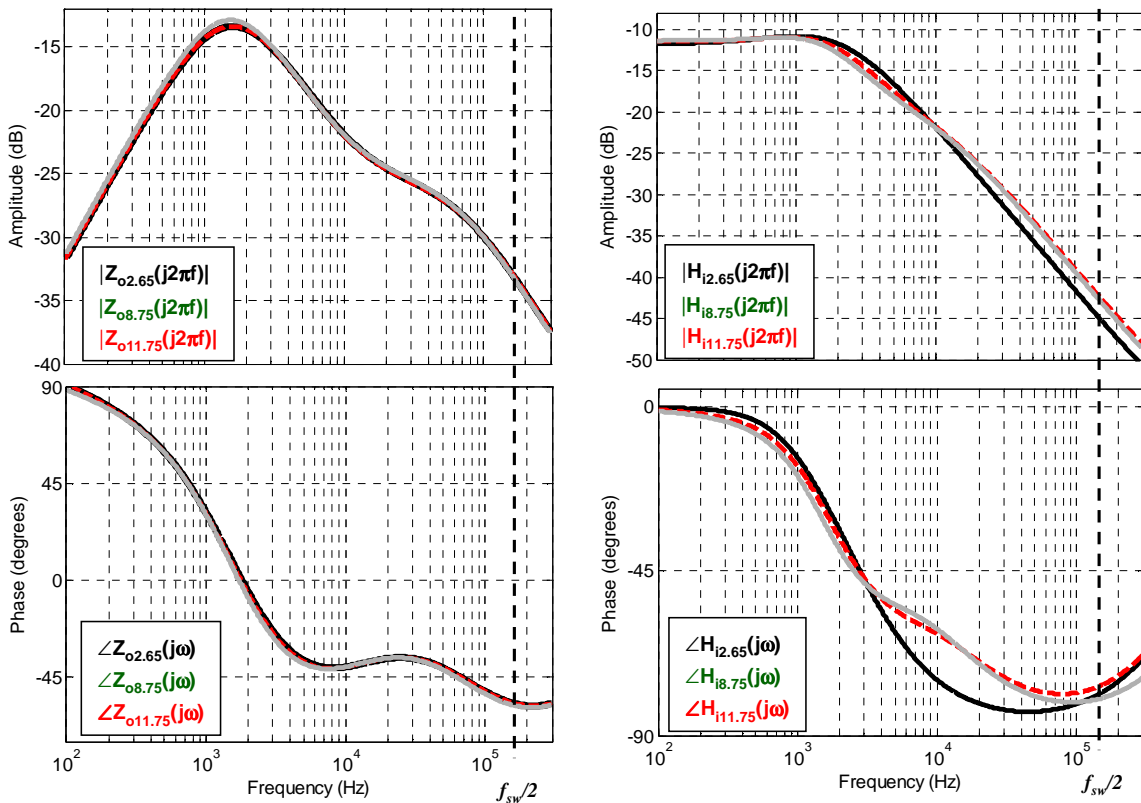


Fig. 4-65: Frequency response of $Z_o(j2\pi f)$ and $H_i(j2\pi f)$ at load levels from 20% to 100% of rated power.

4.5.1.3.2 Local linear models for Y_i

The fitting results corresponding to Y_i are illustrated in Fig. 4-66a. As can be seen, good fitting results of the average response has been obtained. The frequency response of the identified models is shown in Fig. 4-66b. At low frequency, the CPL behavior of the converter is evidenced, as the frequency response resembles a negative incremental resistance. The damping dependence on I_o can be clearly noticed in these plots.

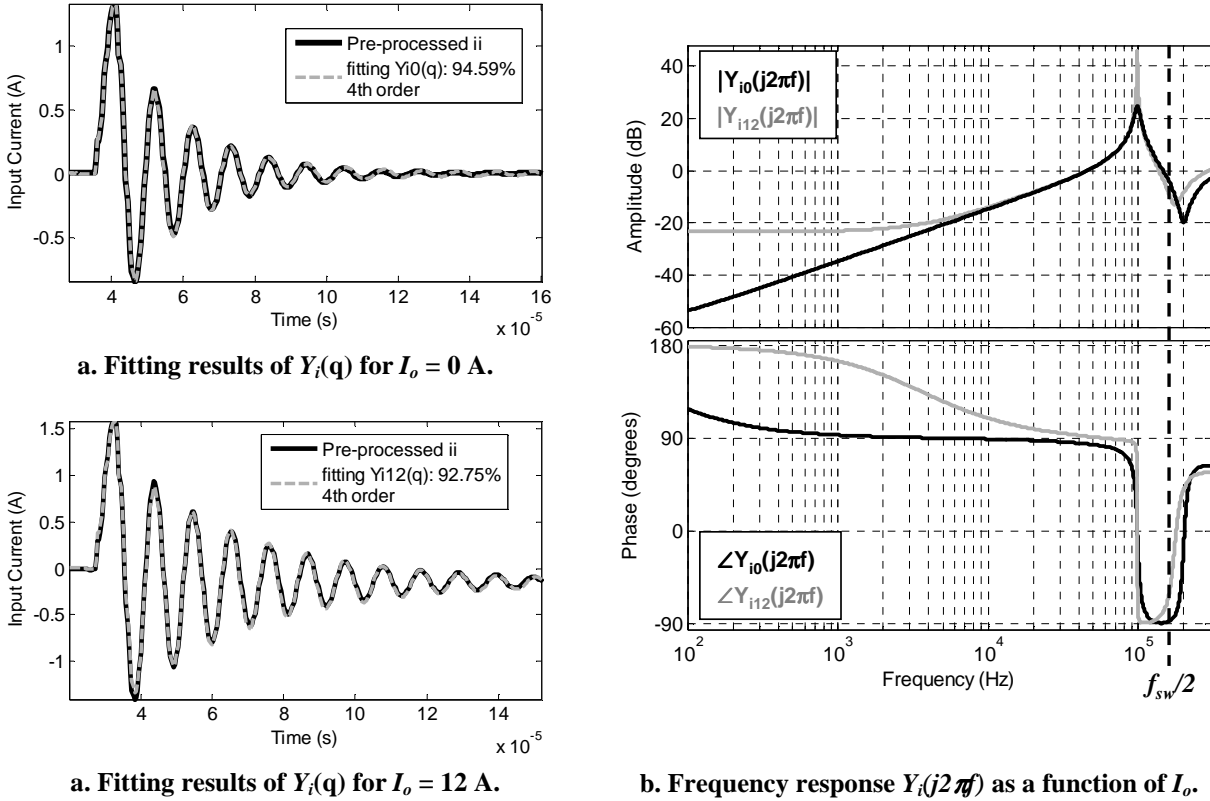


Fig. 4-66: Identification of $Y_i(q)$ and its frequency response for different values of I_o .

4.5.1.3.3 Building the large-signal model

Once the un-terminated transfer functions of the model have been identified, the large-signal model has been built. First, the efficiency of the converter, with and without considering no-load losses, has been characterized as a function of I_o . The resulting curves are depicted in Fig. 4-67. The no load losses are $P_{i0} = 3.2$ W.

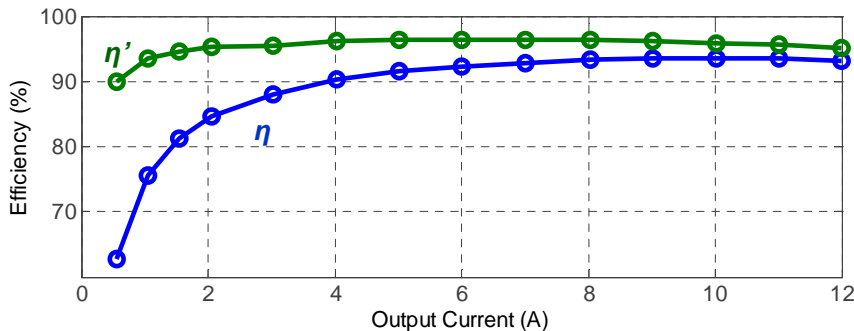


Fig. 4-67: Efficiency of the commercial forward converter, with (blue trace) and without considering no-load losses (green traces) as a function of I_o , for $V_i = 48$ V.

Following this, the following post-processing actions have been carried out on every local transfer functions into H_i and Y_i .

- The steady-state response of every local model into Y_i and Z_o has been subtracted, according to (4-40).
- The static gain of every local model into H_i has been readjusted as expressed by (4-41).

The resulting transfer functions are given below.

$$\begin{aligned}
 H_{iL0.17}(s) &= \frac{0.0357 \cdot s^2 + 187680 \cdot s + 4.6728 \cdot 10^{10}}{s^2 + 2.64 \cdot 10^4 \cdot s + 3.894 \cdot 10^9} \\
 H_{iL1.2}(s) &= \frac{8028 \cdot s^3 + 2.824 \cdot 10^{10} \cdot s^2 + 2.7288 \cdot 10^{16} \cdot s + 2.608 \cdot 10^{20}}{s^4 + 2.664 \cdot 10^5 \cdot s^3 + 3.473 \cdot 10^{10} \cdot s^2 + 2.307 \cdot 10^{15} \cdot s + 1.884 \cdot 10^{19}} \\
 H_{iL1.65}(s) &= \frac{0.3433 \cdot s^2 + 345120 \cdot s + 1.5864 \cdot 10^9}{s^2 + 2.899 \cdot 10^4 \cdot s + 1.322 \cdot 10^8} \\
 H_{iL2.65}(s) &= \frac{0.049 \cdot s^2 + 2.453 \cdot 10^5 \cdot s + 1.111 \cdot 10^9}{s^2 + 2.111 \cdot 10^4 \cdot s + 9.279 \cdot 10^7} \\
 H_{iL11.75}(s) &= \frac{-0.2 \cdot s^2 + 4.749 \cdot 10^5 \cdot s + 1.03 \cdot 10^{11}}{s^2 + 5.164 \cdot 10^5 \cdot s + 8.607 \cdot 10^9}
 \end{aligned} \tag{4-58}$$

$$\begin{aligned}
 Z_{o0.17}(s) &= \frac{0.01158 \cdot s^3 + 6.049 \cdot 10^4 \cdot s^2 + 1.308 \cdot 10^{10} \cdot s}{s^3 + 1.934 \cdot 10^6 \cdot s^2 + 6.892 \cdot 10^{10} \cdot s + 7.782 \cdot 10^{15}} \\
 Z_{o1.4}(s) &= \frac{0.002738 \cdot s^3 + 1.38 \cdot 10^4 \cdot s^2 + 5.299 \cdot 10^8 \cdot s}{s^3 + 1.603 \cdot 10^5 \cdot s^2 + 1.01 \cdot 10^{10} \cdot s + 5.809 \cdot 10^{13}} \\
 Z_{o1.65}(s) &= \frac{0.04897 \cdot s^2 + 3755 \cdot s}{s^2 + 2.41 \cdot 10^4 \cdot s + 1.266 \cdot 10^8} \\
 Z_{o2.65}(s) &= \frac{0.006549 \cdot s^3 + 3.329 \cdot 10^4 \cdot s^2 + 2.697 \cdot 10^9 \cdot s}{s^3 + 7.177 \cdot 10^5 \cdot s^2 + 1.381 \cdot 10^{10} \cdot s + 6.971 \cdot 10^{13}}
 \end{aligned} \tag{4-59}$$

$$\begin{aligned}
 Y_{i00}(s) &= \frac{10.82 \cdot s^4 + 3.191 \cdot 10^8 \cdot s^3 + 5.743 \cdot 10^{13} \cdot s^2 + 4.814 \cdot 10^{20} \cdot s}{s^4 + 9.892 \cdot 10^7 \cdot s^3 + 4.565 \cdot 10^{14} \cdot s^2 + 5.911 \cdot 10^{19} \cdot s + 1.668 \cdot 10^{26}} \\
 Y_{i012}(s) &= \frac{17.51 \cdot s^4 + 1.781 \cdot 10^8 \cdot s^3 + 4.194 \cdot 10^{13} \cdot s^2 + 2.235 \cdot 10^{20} \cdot s}{s^4 + 4.772 \cdot 10^7 \cdot s^3 + 2.141 \cdot 10^{14} \cdot s^2 + 1.912 \cdot 10^{19} \cdot s + 7.944 \cdot 10^{25}}
 \end{aligned} \tag{4-60}$$

4.5.1.4 Model validation

The model has been implemented in PSIM, and its response has been compared to that of the actual converter, under a set of validation experiments. The validation focuses on the behavior of Z_o and H_i , since they exhibit strong nonlinearities at light load and represent the major difference with respect to previous models. In all cases, the DC source has been modeled using an ideal voltage source, as the capacitor bank minimizes the impedance seen from the input port of the converter.

4.5.1.4.1 Validation test 1: Load current step from 4 A to 9 A

The first validation test is shown in Fig. 4-68. A large load step is applied while the input voltage is kept constant. The load current levels (from 4 A to 9 A) are within the nearly linear operating range of the converter.

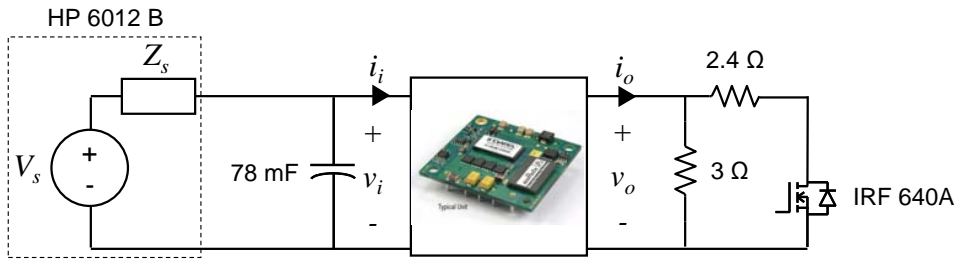


Fig. 4-68: Validation test 1. Large load current step from 4 A to 9 A.

The comparison between measurements and simulation results is shown in Fig. 4-69. As can be seen, the response of the converter is accurately reproduced by the model. This corroborates the nearly linear behavior of the converter for power levels above 25 %. The proper behavior of the gain-scheduled LLMN is also validated within the I_o range where the nonlinearities are relatively slight. Nevertheless, a slight oscillation under the load switch-off is noticed in i_i around 100 kHz. This is attributed to a slight disturbance of the input voltage, which is not predicted by the simulation (the input voltage is absolutely constant in the simulation) and was not captured during the identification process.

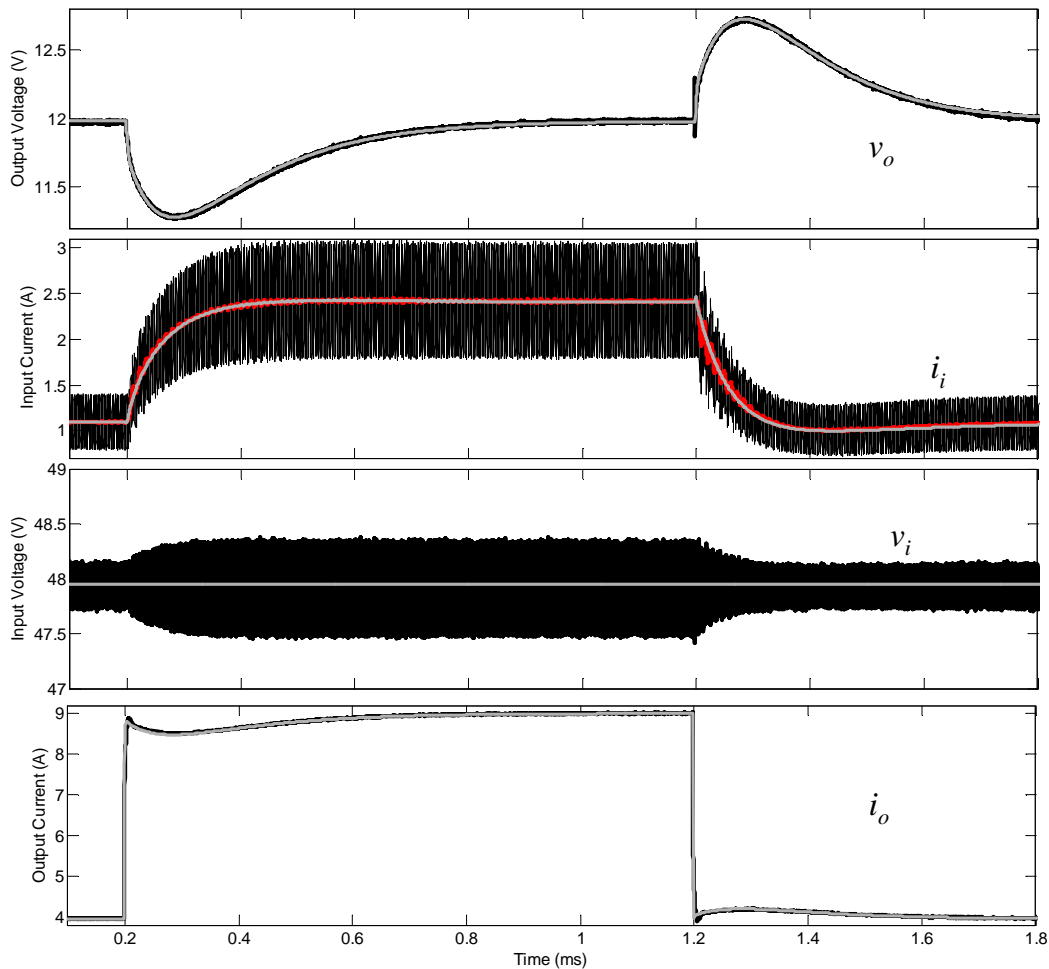


Fig. 4-69: Validation test 1. Experimental results (dark lines, averaged in red) compared to simulation results (grey lines).

4.5.1.4.2 Validation test 2: Load current step (using electronic load) from 0.5 A to 2.2 A

A narrower current step has been applied with the electronic load (see Fig. 4-70), but now at lighter load levels: from 0.5 A to 2.2 A. This way, the converter crosses a highly nonlinear region.

In that region, the dynamic response of the converter is strongly nonlinear.

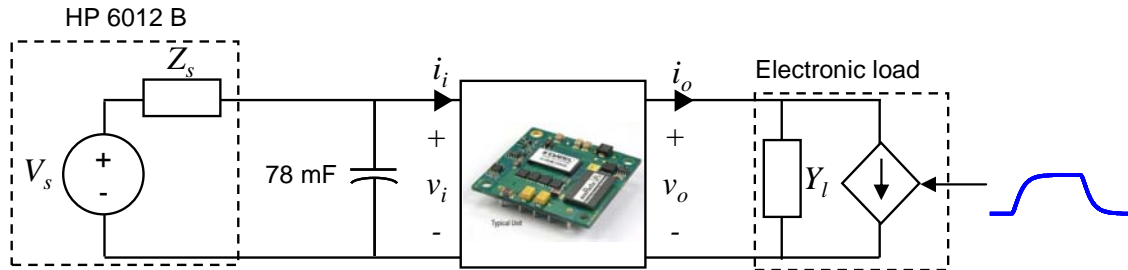


Fig. 4-70: Validation test 2. Load current step (using electronic load) from 0.5 A to 2.2 A.

The comparison between simulated waveforms and experimental measurements is shown in Fig. 4-71. As can be seen, the model fails to reproduce the transient response of the converter, although the static response is well predicted.

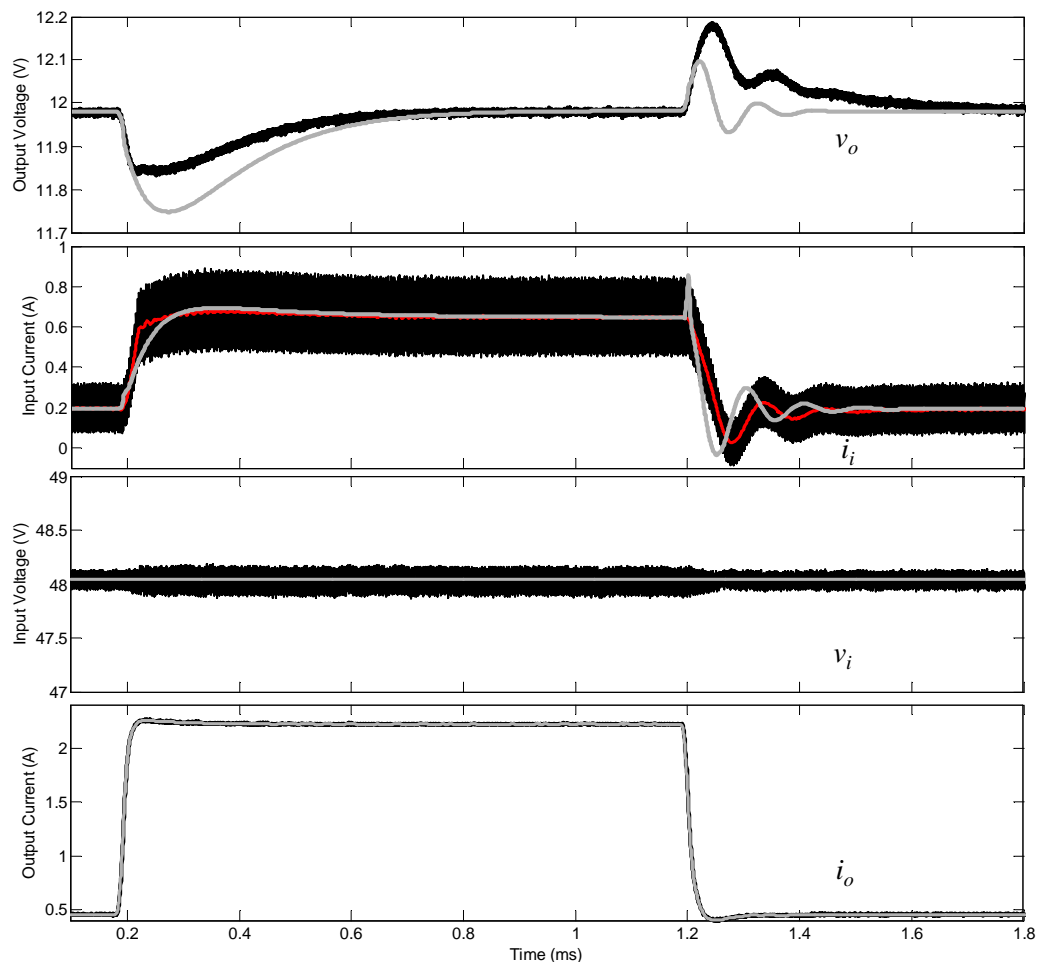


Fig. 4-71: Validation test 2. Comparison of experimental measurements (dark lines, averaged in red) and simulation results (grey lines).

The proposed modeling method fails because the dynamics of the converter changes non-smoothly near $I_o = 1.2$ A (see Fig. 4-64). In other words, the underlying dynamics is probably governed by

discontinuous differential equations. **As explained in [134], local linear model networks fail when the converter exhibits dynamic discontinuities.** Some reasons for having non-smooth dynamics are summarized below.

- The regulator dynamics is abruptly modified in a non-smooth manner.
- The conduction mode changes from CCM or DCM (or vice-versa). In such case, the dynamics of the inductor suddenly changes, so that one state variable is essentially lost. Note that such effect will be reflected on the input-output converter dynamics if single-loop control is used (VMC). However, if double loop control is used (consisting of inner inductor current loop), then the overall dynamics may only exhibits variations for frequencies above the BW of the current loop.

The author does not have available information about how the modeled forward converter works. One may think about variations in the conduction mode. However, if peak current mode control holds all the time, the dynamics should not change significantly (as the converter is essentially a programmed current source). Therefore, a possible reason could be that the dynamics of the control scheme is modified under light load conditions.

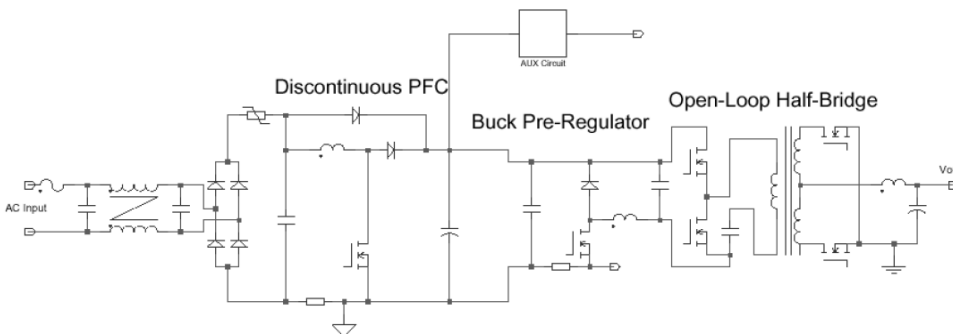
4.5.2 Multi-stage AC-DC converter (output port modeling)

In this section, the output port of an AC-DC power supply by Emerson [259] has been modeled. This power supply features universal 90-264 V AC input and 48 V DC regulated output. The rated power is 250 W.

A picture of the converter and its internal schematic are shown in Fig. 4-72. As can be seen, the power supply comprises three stages: the boost stage performs active power-factor correction, the buck stage provides fast regulation of the output voltage, and the half-bridge stage adds galvanic isolation.



a. Image from technical reference note.



b. Block diagram from technical reference note.

Fig. 4-72: Commercial PFC AC/DC converter LPS208-M by Emerson [259].

4.5.2.1 Preliminary tests: linearity analysis

Only the DC output port is modeled, so the model is simply comprised of a Thevenin one-port network, and the output impedance is the only dynamic network to be modeled. Hence, only the dynamic relationship between i_o and v_o has to be analyzed.

The test bed is depicted in Fig. 4-73a. The input port is tied to the utility grid, which features 220 V_{AC} and 50 Hz. The data acquisition system is that used in previous sections, and the sampling frequency has been set to five times the switching frequency, i.e. $f_s = 1$ MHz.

The response of the converter to several load steps, with a fixed magnitude equal to 0.5 A, but on different operating points, is shown in Fig. 4-73b. The dynamic relationship between v_o and i_o depends on the operating point, so that the higher I_o , the lower the voltage overshoot.

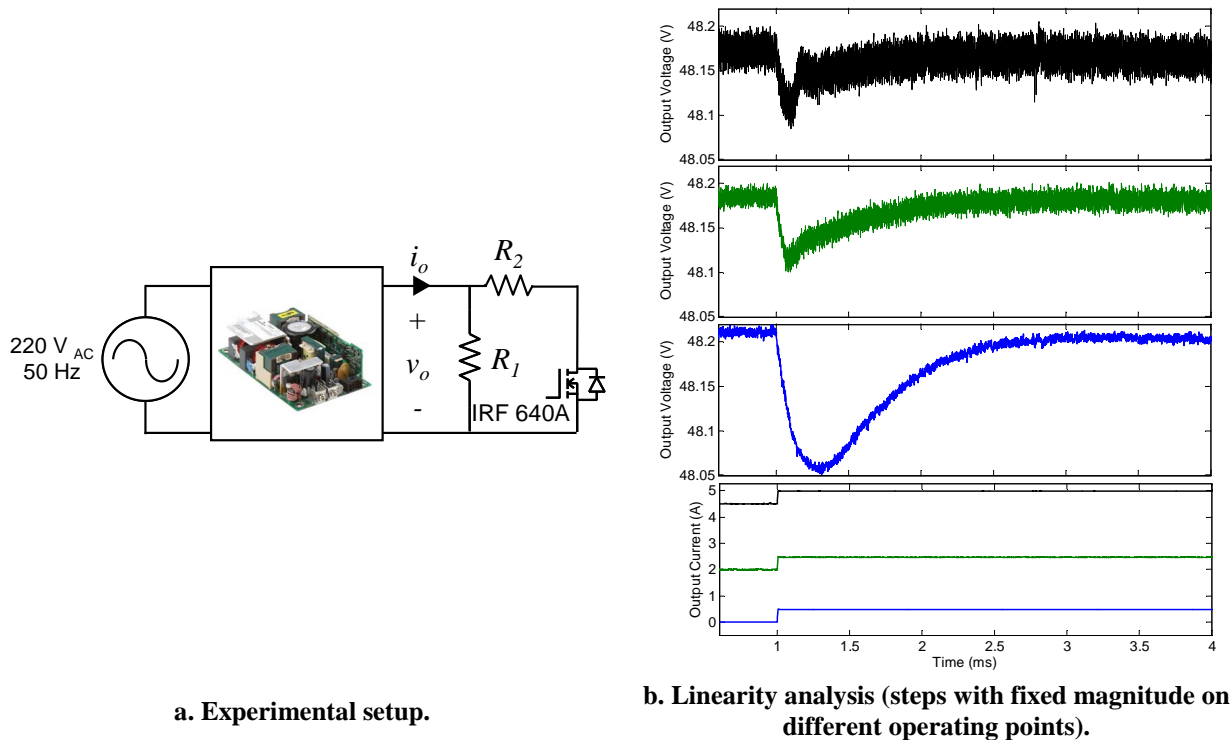


Fig. 4-73: Testing the response of the AC/DC converter to load current steps.

On the other hand, the static load regulation is higher than in previous converters, probably because the last power stage is un-regulated (see Fig. 4-72). The characterized curve is depicted in Fig. 4-74. It has been approximated by a linear function.

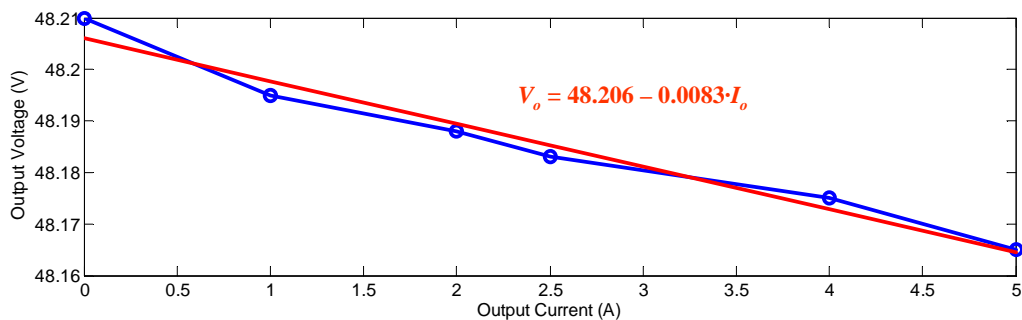


Fig. 4-74: Static load regulation. Measured curve and approximation through a linear function.

4.5.2.2 Dynamic networks modeling

According to the previous analysis, a LLMN has been used to build the output impedance and a linear function has been implemented to address the static regulation. The dynamic dependence on I_o is higher at light load levels, so the working region is more partitioned at light load levels. Four local linear models have been considered, as illustrated in Fig. 4-75.

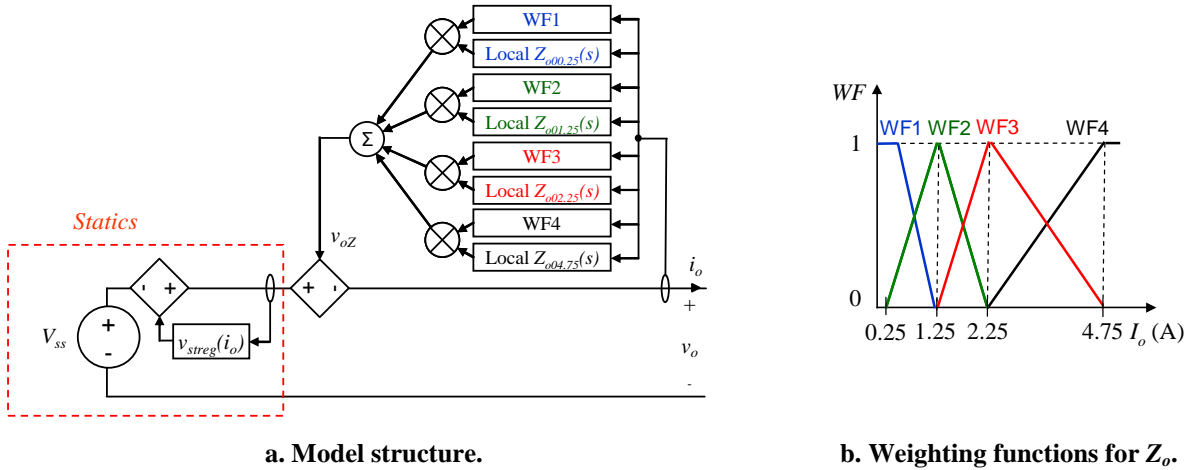


Fig. 4-75: Model for the output port of the AC-DC converter LPS208-M by Emerson for $V_i = 220 \text{ V}_{AC}$, 50 Hz and $I_o \in [0, 5] \text{ A}$.

The static load regulation corresponds to the following expression.

$$v_{streg}(i_o) = -0.083 \cdot i_o \quad (4-61)$$

4.5.2.3 Model Identification

As done in previous cases, the signals have been pre-filtered using a MAF. However, in this case a higher order has been used ($M = 21$) because v_o was found to contain significant harmonics not only at 200 kHz but also at lower frequencies, probably because the modeled power supply comprises several cascaded power stages. The fitting results of some local linear models are depicted in Fig. 4-76 and discussed below.

As can be seen, second models yield good results at light load (Fig. 4-76a), whereas third model models are required to fit the response at higher power levels (Fig. 4-76b). The reason for increasing the model order is that an oscillation, featured by conjugated complex poles, arises as the load increases. As can be seen in Fig. 4-76b, the oscillation is superimposed to a first order exponential evolution, which results in three-poles. The frequency response of every local linear model is shown in Fig. 4-76c.

As can be seen, the higher I_o , the lower the magnitude of Z_o for frequencies below 1 kHz. However, as a difference from the forward converter, the dynamic response changes smoothly. At high frequencies, all the models converge because the impedance is determined by the output capacitor(s).

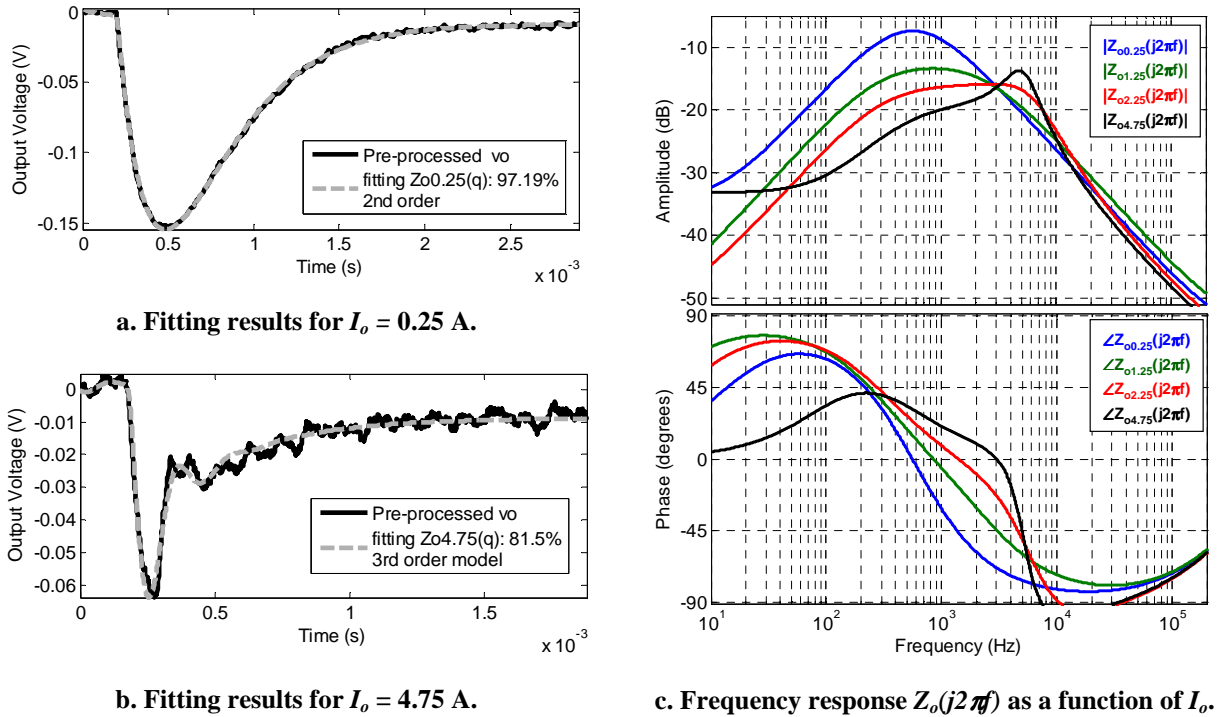


Fig. 4-76: Fitting results and frequency of local linear models for $Z_o(j2\pi f)$.

Once every transfer function model has been identified, its steady-state value has been subtracted, according to (4-39). The resulting transfer functions, implemented into the model, are given below.

$$\begin{aligned}
 Z_{o0.25}(s) &= \frac{2915 \cdot s}{s^2 + 7157 \cdot s + 1.277 \cdot 10^7} \\
 Z_{o1.25}(s) &= \frac{3786 \cdot s}{s^2 + 1.802 \cdot 10^4 \cdot s + 3.241 \cdot 10^7} \\
 Z_{o2.25}(s) &= \frac{2613 \cdot s^2 + 2.171 \cdot 10^8 \cdot s}{s^3 + 5.197 \cdot 10^4 s^2 + 1.491 \cdot 10^9 \cdot s + 2.755 \cdot 10^{12}} \\
 Z_{o4.75}(s) &= \frac{1680 \cdot s^2 + 9.718 \cdot 10^7 \cdot s}{s^3 + 2.267 \cdot 10^4 s^2 + 1.08 \cdot 10^9 s + 2.86 \cdot 10^{12}}
 \end{aligned} \tag{4-62}$$

4.5.2.4 Model validation

The model has been implemented in PSIM for validation purposes. Its response under a set of validation experiments have been compared to experimental measurements. The experimental setup, used for every validation test, is shown in Fig. 4-77. Different exponential current profiles, with different time constants and magnitudes, have been applied using the electronic load. The obtained results are discussed at the bottom of this section.

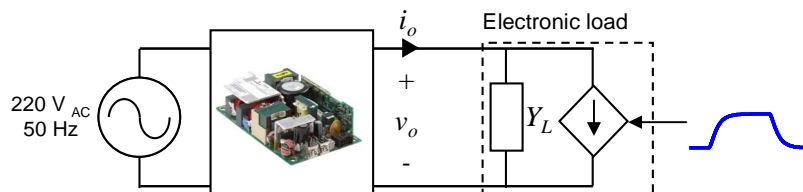


Fig. 4-77: Experimental setup for model validation.

Firstly, an exponential current ranging from 2.5 A to 3.5 A has been demanded. The variation of current is 20% of rated load, which is relatively narrow and corresponds to intermediate points between two local linear models (Fig. 4-75b). As shown in Fig. 4-78, the model response is close to the measured response.

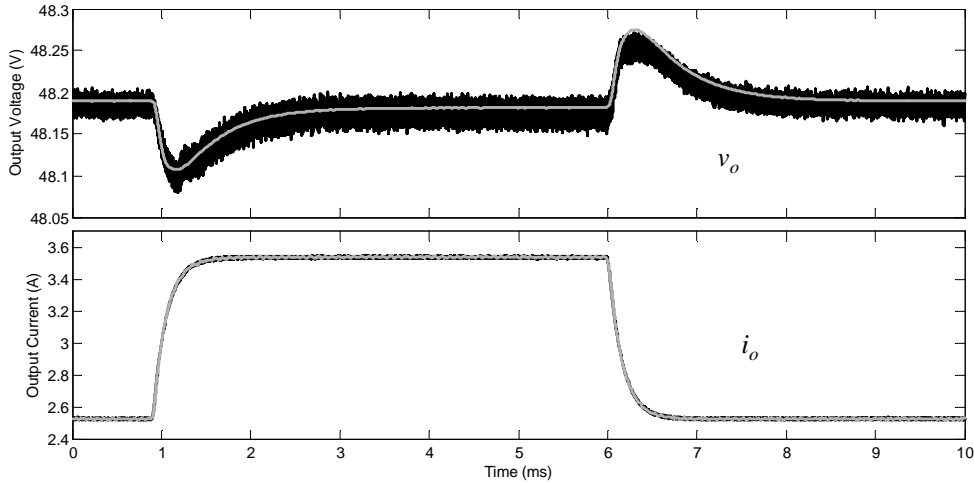


Fig. 4-78: Validation test 1. Experimental results (dark lines) compared to simulation results (grey lines).

Secondly, an exponential demand with similar magnitude but different initial value has been applied: from 1.5 A to 2.8 A. This way, the operating point changes from the second partition to the third partition of the range (see Fig. 4-75b). As can be seen, the model responds properly under the increase in load power, but significant mismatch is observed under decrease in power, even although the dynamics of this converter varies smoothly.

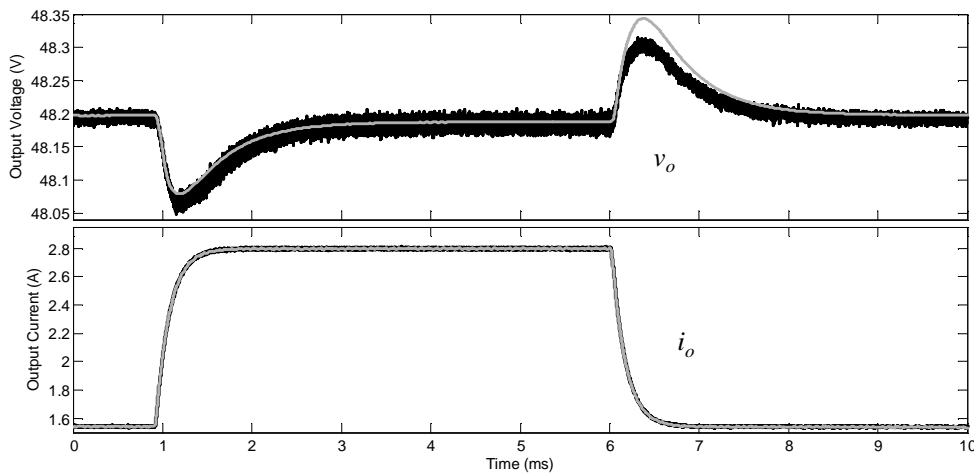


Fig. 4-79: Validation test 2. Experimental results (dark lines) compared to simulation results (grey lines).

Finally, a large current variation has been experimented: from 0.5 A to 5 A, which corresponds to the 86% of rated load. The simulation results and measurements are compared in Fig. 4-80. Largest differences between simulation results and measurements are observed in this case.

As demonstrated, the LLMN performs properly when relatively small-signal perturbations are applied, so that the behavior of the converter is nearly linear. However, this approach fails when large perturbations are applied. The reason is that nonlinearities are more significant under large perturbations, and the LLMN, which addresses nonlinear behavior as the combination of local linear model outputs, cannot predict them correctly.

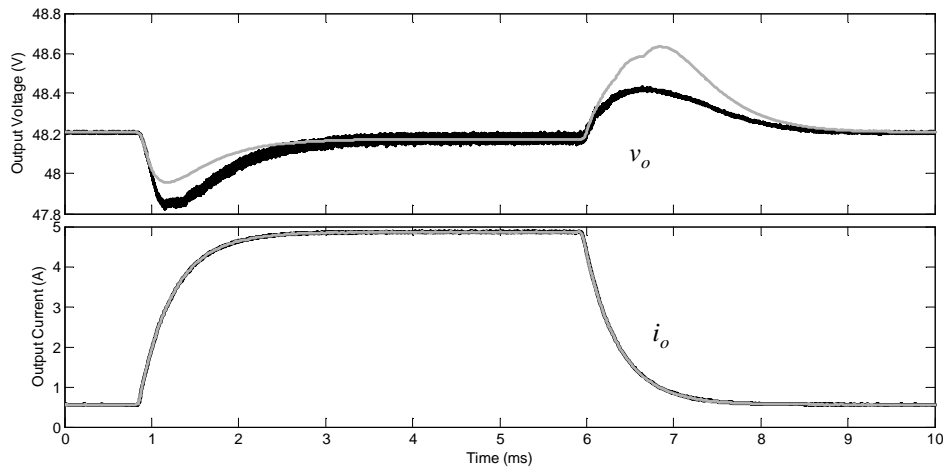


Fig. 4-80: Validation test 3. Experimental results (dark lines) compared to simulation results (grey lines).

Further discussion about the LLMN and possible improvements are discussed in the next section.

4.5.3 Discussion of results and introduction to model improvements

4.5.3.1 Limitations of local linear model networks based on local feedback

LLMNs, utilized throughout this chapter, return the ‘instantaneously weighted’ output of every local linear model. However, each model responds as a function of ‘internal states’, not as a function of the global state of the converter. Consequently, there is a **lack of ‘memory’ about influence of global states on the dynamics using this approach. The global state is not feedback into the local models.**

This issue is illustrated in Fig. 4-81, where a detail of Fig. 4-80, indicating the influence of each local model on the global response, is shown. As can be seen, after 6.6 ms, the response is only determined by the local models $Z_{o1.25}(s)$ and $Z_{o0.25}(s)$. Indeed, the response after 6.6 ms would be exactly the same, independently of how are the remaining local models. However, obviously, previous states have impact on the transient response.

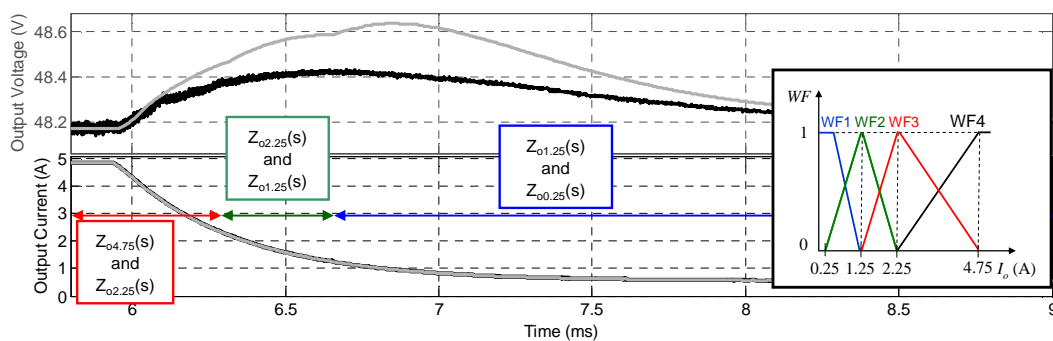


Fig. 4-81: Detail of waveforms shown in Fig. 4-82, where the influence of local linear models over the global response is shown.

4.5.3.2 Local linear model networks based on global feedback

An alternative to the LLMN based on local network consists in applying feedback of the global output into the local models, instead of the local outputs. The difference between local feedback and global feedback is illustrated in Fig. 4-83, where a LLMN, made up by two local linear discrete models, is implemented in both ways.

As can be seen in Fig. 4-83, the models are described in discrete domain by means of local polynomials $B_j(q)$ and $A_j'(q)$, which corresponds to the numerator and denominator of any local model 'j' and are defined as given by (4-63). Terms a_{ij} and b_{ij} represents the coefficients of the differential equation governing the local models, while m_j and n_j represents the denominator and numerator orders, respectively, of the local model 'j'.

$$B_j(q) = b_{0j} + b_{1j}q^{-1} + \dots + b_{m_j}q^{-m_j}; \quad A_j'(q) = a_{1j}q^{-1} + \dots + a_{n_j}q^{-n_j} \quad (4-63)$$

Then, by using local feedback, the relationship between the predicted local output $\hat{y}_j(k)$ and the input 'u' of each local model is defined as follows. As can be seen, the output of every local model is determined by current/past inputs and past local outputs.

$$\hat{y}_j(k) = -\sum_{i=1}^{n_j} a_{ij} \hat{y}_j(k-i) + \sum_{i=0}^{m_j} b_{ij} u(k-i) = B(q) \cdot u(k) - A(q) \cdot \hat{y}_j(k) \quad (4-64)$$

In contrast, using global feedback, the **output of every local model is determined by current/past inputs and global past outputs**. This is expressed by (4-65), where $\hat{y}(k)$ represents the global output.

$$\hat{y}_j(k) = -\sum_{i=1}^{n_j} a_{ij} \hat{y}(k-i) + \sum_{i=0}^{m_j} b_{ij} u(k-i) = B(q) \cdot u(k) - A(q) \cdot \hat{y}(k) \quad (4-65)$$

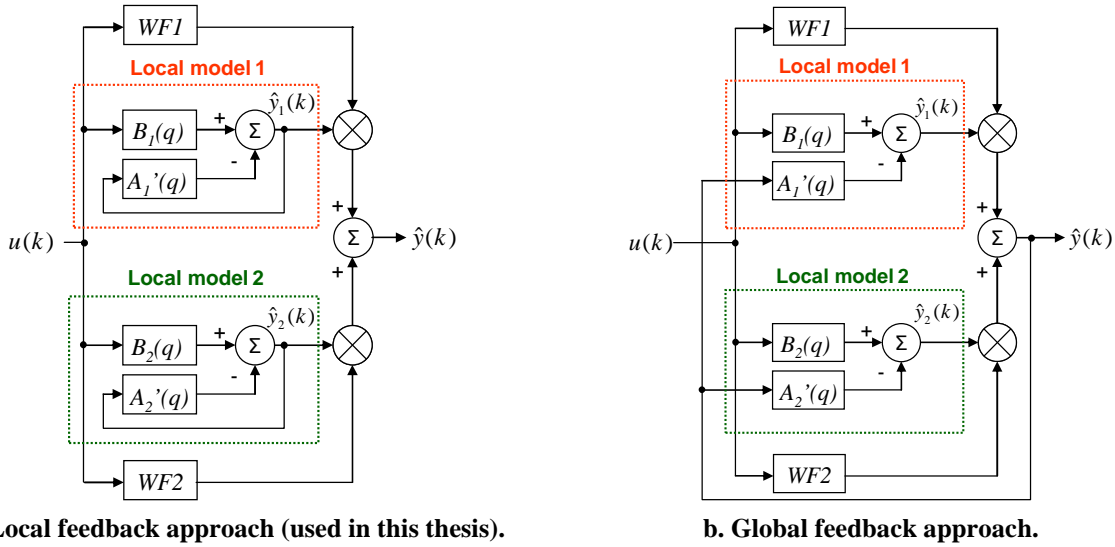


Fig. 4-83: Possible implementation of nonlinear structures made up by weighted local linear models.

Local linear model networks featuring local feedback and global feedback are discussed in [68].

To illustrate how the global feedback works, the model of the AC/DC converter, shown in Fig. 4-75, has been transformed back to discrete domain and implemented using discrete differential equations and global feedback (similarly to Fig. 4-83b, but having four local models). The validation test shown in Fig. 4-80 has been run again, and the response of the black-box model, using global feedback, has been compared with the model response based on local feedback, and with the experimental waveforms. The results are shown in Fig. 4-84, where it can be seen that global feedback yields better results.

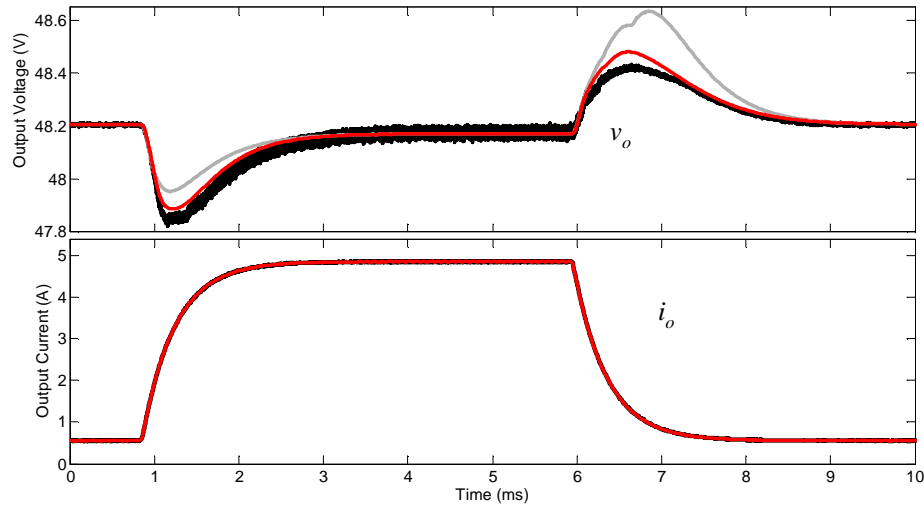


Fig. 4-84: Validation test for AC-DC converter model: comparison of experimental measurements (dark traces) with model response using local feedback (grey), and global feedback (red).

Nevertheless, additional considerations have to be taken in mind when using global feedback. Some of them are listed below.

- LLMNs with local feedback are stable if every local model is stable, but this is not necessarily true for models with global feedback. Stability with global feedback is discussed in [68].
- In order to implement LLMNs with global feedback into a simulator, the discrete differential equation has to be build, instead of using transfer function model blocks.

On the other hand, this modeling approach has some limitations. For example, the response under very fast change of operating point is very similar to that using local feedback, because the output is the only global state variable that makes influence on the local models. This is illustrated in Fig. 4-85, where the response of the AC-DC converter to a resistive load step is compared to the response of the black-box model, using both local feedback and global feedback. After the load switch-on, the response is immediately determined by the local model $Z_{o04.75}(s)$. Then, since the global output and the local output are almost equal, both approaches yield similar error.

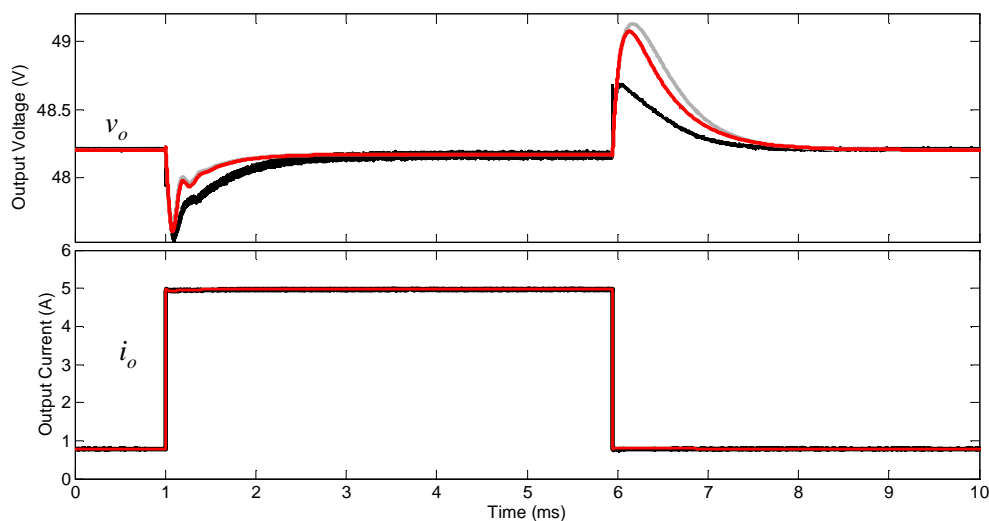


Fig. 4-85: Validation test for AC-DC converter model, consisting in stepping a resistive load: comparison of experimental measurements (dark traces) with model response using local feedback (grey traces), and global feedback (red traces).

4.5.3.3 Weighted state-space model

An alternative to global feedback consists in building a common state-space structure for all the local models, so that the parameters are weighted as a function of operating point [74], [170].

Consider the time varying state-space model defined by the following expression (in continuous time domain), where parameters of 'A', 'B', 'C' and 'D' are a function of the input, 'u', and/or the state space variables, 'x'.

$$\begin{cases} \dot{x} = A(x, u) \cdot x + B(x, u) \cdot u \\ y = C(x, u) \cdot x + D(x, u) \cdot u \end{cases} \quad (4-66)$$

Then, a large-signal nonlinear model may be build by linearization of the state-space model on different operating points, and combination of the linearized models using weighting functions, as given by (4-67), where 'N' is the number of local model and 'A_j', 'B_j', 'C_j' and 'D_j' comprise the state-space coefficients of the local linear model 'j'.

$$\begin{cases} \dot{x} = \sum_{j=1}^N WF_j(x, u) \cdot (A_j \cdot x + B_j \cdot u) \\ y = \sum_{j=1}^N WF_j(x, u) \cdot (C_j \cdot x + D_j \cdot u) \end{cases} \quad (4-67)$$

Compared to the approaches shown above, the state-variables are shared by all the local models. However, the same model structure is also shared. This means that **every local model must have the same number of poles and zeroes, and smooth variations of them within the working range must hold (smooth dynamic variations with operating point)**. Therefore, the AC-DC converter may not be well modeled by using this approach because the dynamics is described by a third order model at rated load, whereas second order models are used at light load.

Nevertheless, the aim of this section is only to discuss possible improvements to the LLMN model used along this thesis. A deep analysis of those alternative networks exceeds the objectives of this thesis and is a matter of future work. A comparison between different LLMN realizations is described in [74].

4.6 Experimental results: modeling of a DC distributed power system

Finally, all the modeled converters have been put together to make up the DC distributed power system shown in Fig. 4-86. This architecture is based on an intermediate-regulated bus and may emulate a scaled power system for telecommunications [3], [8]. The system comprises three differentiated stages, which are explained below.

- At the first stage, the multi-stage AC/DC converter by Emerson is used as the 'Front-end converter' (modeled in section 4.5.2). It is tied to the mains and provides 48 V_{DC} at the output.
- At the second stage, the forward converter by Murata is used as the 'Bus converter' (modeled in section 4.5.1) and provides regulated 12 V_{DC} to the intermediate bus.
- At the third stage, the system is comprised of the following subsystems.

- The buck converter by Texas Instruments is used as a POL converter (modeled in section 4.4) and supplies tightly regulated low-voltage to a dedicated, variable load (e.g. analog and digital devices), which is emulated using resistors.
- A buck-boost converter, by Texas Instruments, is also applied as a POL converter (the model is given in appendix A.2) to provide $-3 V_{DC}$ to other variable load, also emulated using resistors.
- Additional resistors that represent other loads.

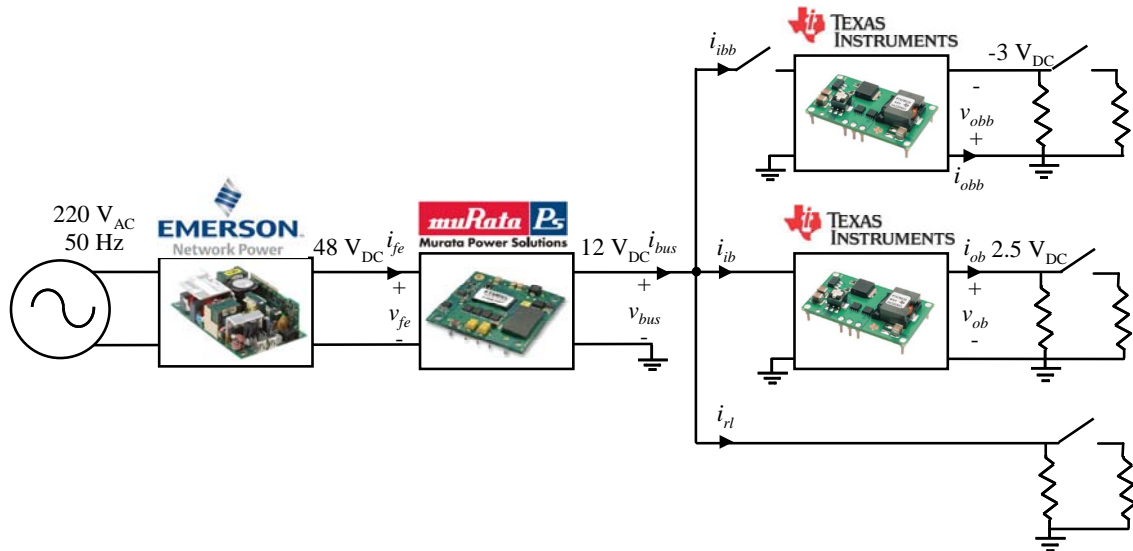


Fig. 4-86: DC distributed power system for system-level validation of black-box models.

This architecture comprises the parallel and series connection of black-box models for power converters from a variety of manufacturers. Thus, the usefulness of the models to carry out system-level simulations can be explored. Every switch in Fig. 4-86 has been implemented using MOSFETs.

4.6.1 System-level test 1: Step decrease in point-of-load power

The experimental setup corresponding to the first test is depicted in Fig. 4-87. The load power supplied by the buck is stepped from 14.5 W to 5 W (65 % of rated power), while the buck-boost supplies 9 W and an additional 28 W resistive load is tied to the intermediate bus.

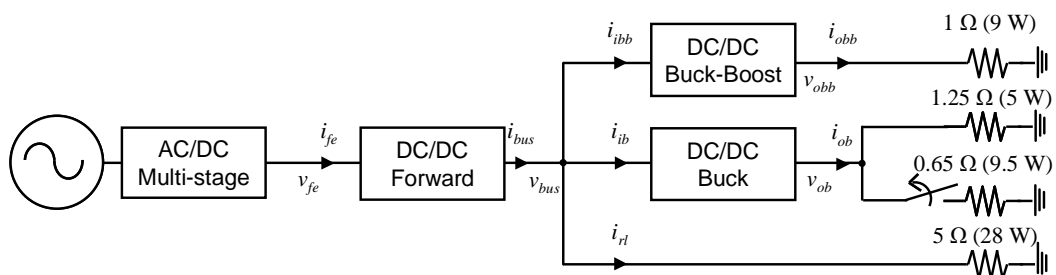


Fig. 4-87: system-level test 1. Step decrease in point-of load converter power.

The comparison between experimental measurements and simulation results is shown in Fig. 4-88. As can be seen, the transient response and static response of every measured signal is successfully predicted. Every voltage overshoot and setting time is predicted with a high degree of accuracy, meaning that the models can be used to determine whether the integrated system fulfill

dynamic requirements under transients or not. This is an important issue concerning power quality, as described in chapter 1, section 1.3. From the static point of view, the black-box models allow predicting the current consumption by the subsystems and, consequently, **the global energy efficiency can be studied.** The high switching ripple exhibited by i_{fe} and v_{fe} is due to the absence of filters throughout the system.

Note that both the forward and the AC/DC converters models work properly, despite some limitations of them were evidenced in previous sections. This is because the forward converter is operating within the nearly linear region (the output power is above 25% of rated load) and the AC/DC converter is subjected to a relatively small perturbation ($\Delta i_{fe} \approx 5\%$ of rated load).

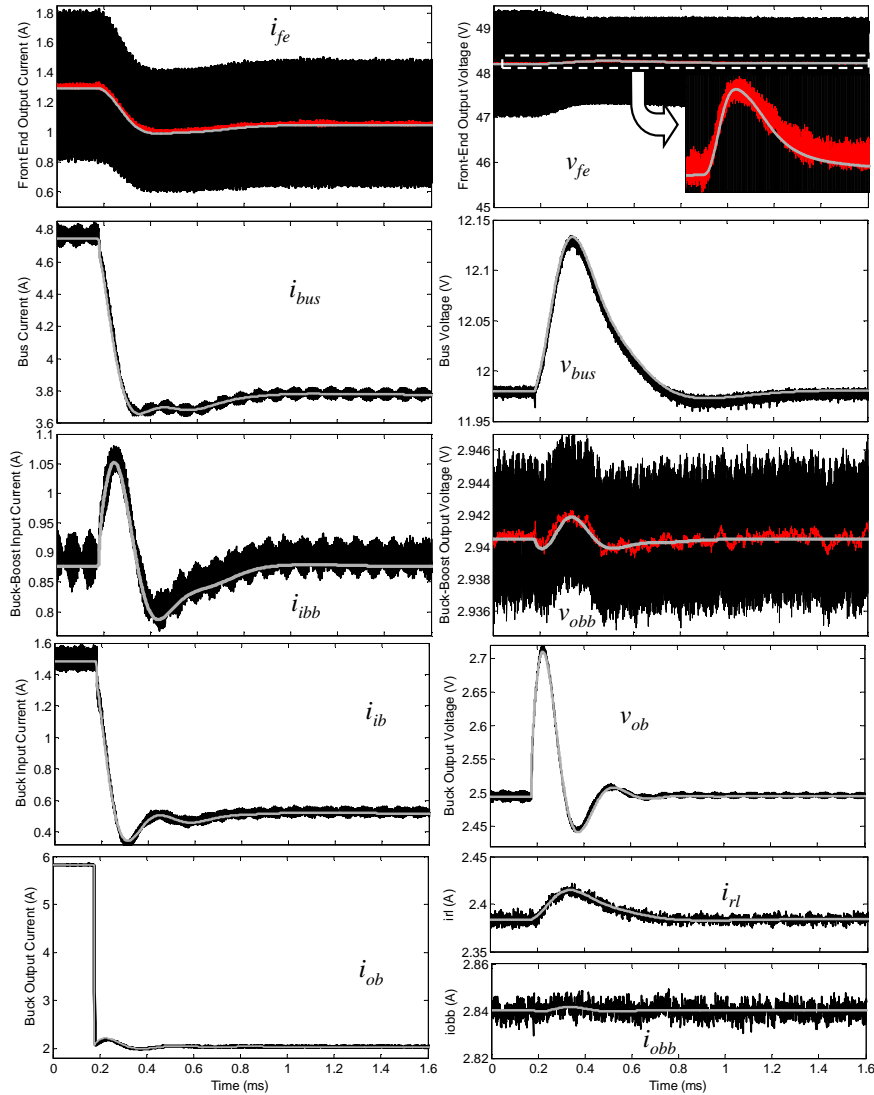


Fig. 4-88: System-level test 1. Comparison of experimental measurements (dark lines, averaged in red) and simulation results (grey lines).

4.6.2 System-level test 2: Step increase in intermediate-bus power

As the second validation test, a step increase in the intermediate bus power is applied using a resistive load, as shown in Fig. 4-89. The bus power is suddenly increased from 37.5 W to 85.5 W, which means a 33% step of rated load power.

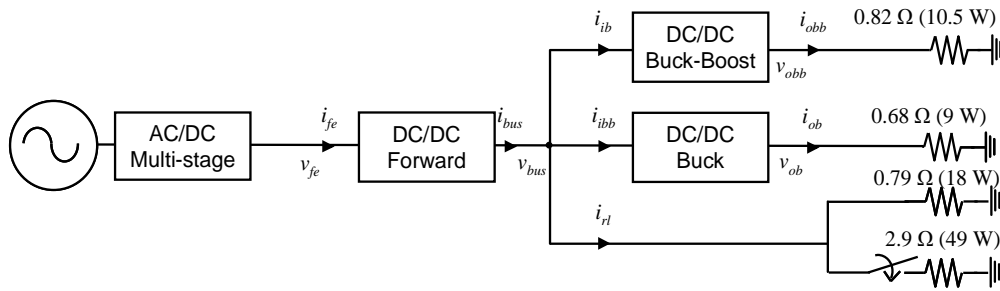


Fig. 4-89: System-level test 2. Large step increase in intermediate bus power.

The validation results are shown in Fig. 4-90. Again, the response of every voltage and current is accurately predicted, which corroborates the statements indicated above. Some deviation is observed in v_{fe} , which may be expected, as the LLMN for the front-end converter is inaccurate under relatively large i_{fe} steps.

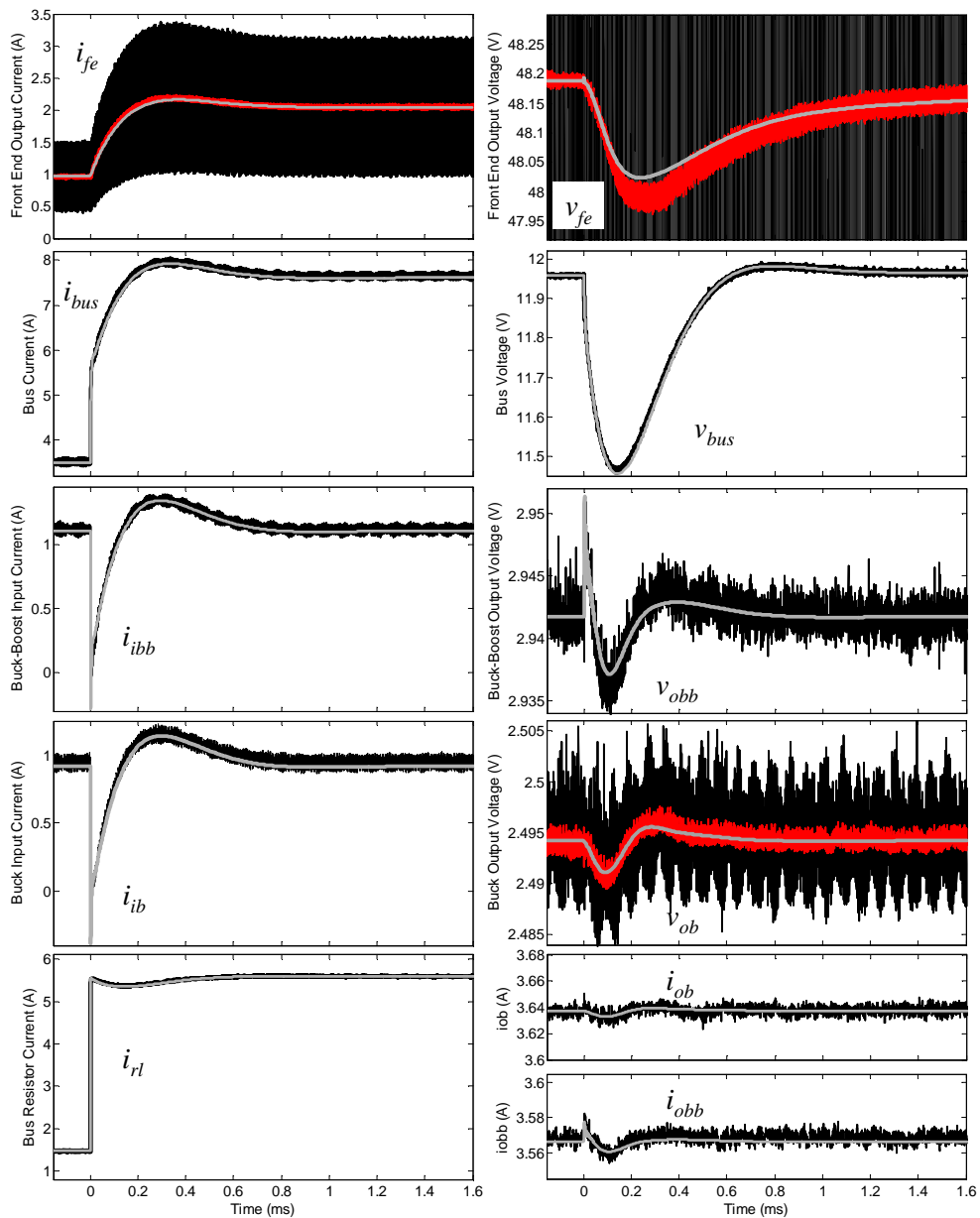


Fig. 4-90: System-level test 2. Comparison of experimental measurements (dark lines, averaged in red) and simulation results (grey lines).

Notice in Fig. 4-90 that, at the beginning of the transient, both i_{ib} and i_{ibb} evidence a sudden transient decrease. This is because the switched load is initially supplied in part by the input capacitors of the POL converters, which in this case are relatively large. Such a transient distribution of current throughout the intermediate bus is well predicted by the black-box models. It is also worth highlighting how the load step is reflected at the output port of the POL converters, and how this effect is also well predicted through simulation.

4.6.3 System-level test 3: Dynamic interaction of subsystems

As a third test, an RL cell (0.12Ω , $10.3 \mu\text{H}$) has been located between the front-end converter and the bus-converter. This cell may emulate a long interconnection wire and stresses the dynamic interactions between the front-end converter and the bus converter. To analyze such interactions, several steps in intermediate bus power have been tested, as depicted in Fig. 4-91.

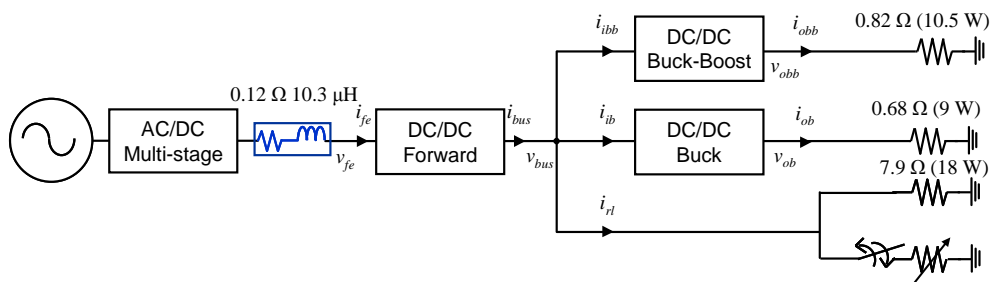


Fig. 4-91: System-level test 3. Step increase and decrease in intermediate bus power, with a series RL cell interconnected between the front-end converter and the bus converter.

4.6.3.1 Step increase and decrease in bus power from 37.5 W to 85.5 W and back

The first step corresponds to the power levels experimented in the test 2: from 37.5 W to 85.5 W and back (33% of rated bus power). The results are shown in Fig. 4-92.

As can be seen, both v_{fe} and i_{fe} exhibits a large oscillation. The oscillation frequency is 29 kHz, approximately, and corresponds to the resonance occasioned by the input filter of the bus converter and the added inductor. Although the system remains stable, such an oscillation evidences a degradation of the phase margin at the interface between both converters.

However, the oscillation is not reflected in the intermediate bus. This is due to the low audiosusceptibility of the bus converter. As pointed out in section 4.5.1, the forward converter is provided with a peak-current controller, which rapidly compensates any perturbation of v_{fe} .

The oscillation is well predicted through simulation, although some slight differences are noticed, which are probably due to the following reasons.

- The use of LLMNs to make up both the output impedance of the front-end converter and the input admittance of the bus converter. As discussed along section 4.5, those are only an approximation to the true nonlinear dynamics, meaning that some mismatch may be expected.
- Slight imprecision in the identification of the output impedance and/or the input admittance of the involved converters.

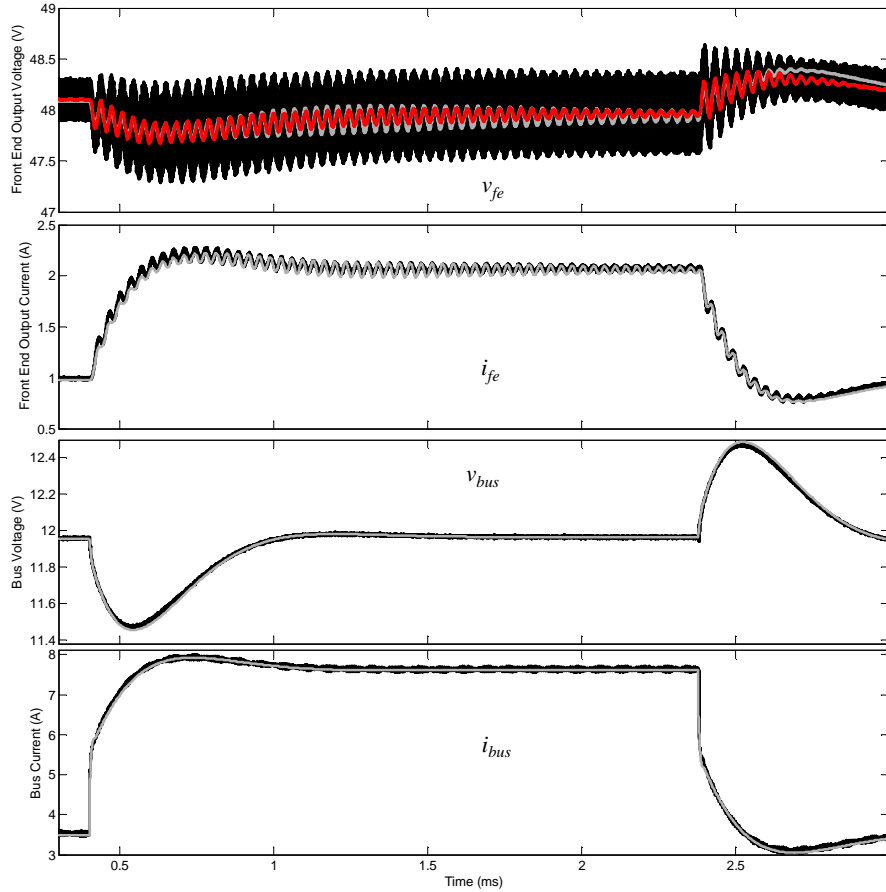


Fig. 4-92: System-level test 3.1. Comparison of experimental measurements (dark lines, averaged in red) and simulation results (grey lines).

4.6.3.2 Step increase and decrease in bus power from 37.5 W to 110 W and back

Following, the magnitude of the power step has been increased. Now the power is stepped from 37.5 W to 110 W (50% of rated bus power). The results are shown in Fig. 4-93.

As can be seen in Fig. 4-93, a large oscillation is found after the step increase. However, as a difference from the previous case, the oscillation is gradually amplified following an exponential evolution, which evidences an unstable situation. As soon as the bus power is decreased back to 37.5 W, the system becomes stable again. Such an unstable situation is caused by the CPL behavior of the regulated converter which, from the small-signal point of view, behaves as a negative incremental resistor.

This phenomenon was introduced in chapter 1 and can be explained by applying the Nyquist criteria on the return ratio $L(s)$ defined by (4-68), where $Z_{ofe}(s)$, $Z_{RL}(s)$ and $Y_{ibus}(s)$ denote the output impedance of the front-end converter, the RL cell impedance and the input admittance of the bus converter, respectively. As the bus power increases, $Y_{ibus}(s)$ also increases at low-frequency, so that the Nyquist stability criterion is violated when a certain threshold level is reached. This is explained in detail in appendix 0.

$$L(s) = \left(Z_{ofe}(s) + Z_{RL}(s) \right) \cdot Y_{ibus}(s), \quad Y_{ibus}(0) \approx -I_{fe} \cdot V_{fe}^{-1} \quad (4-68)$$

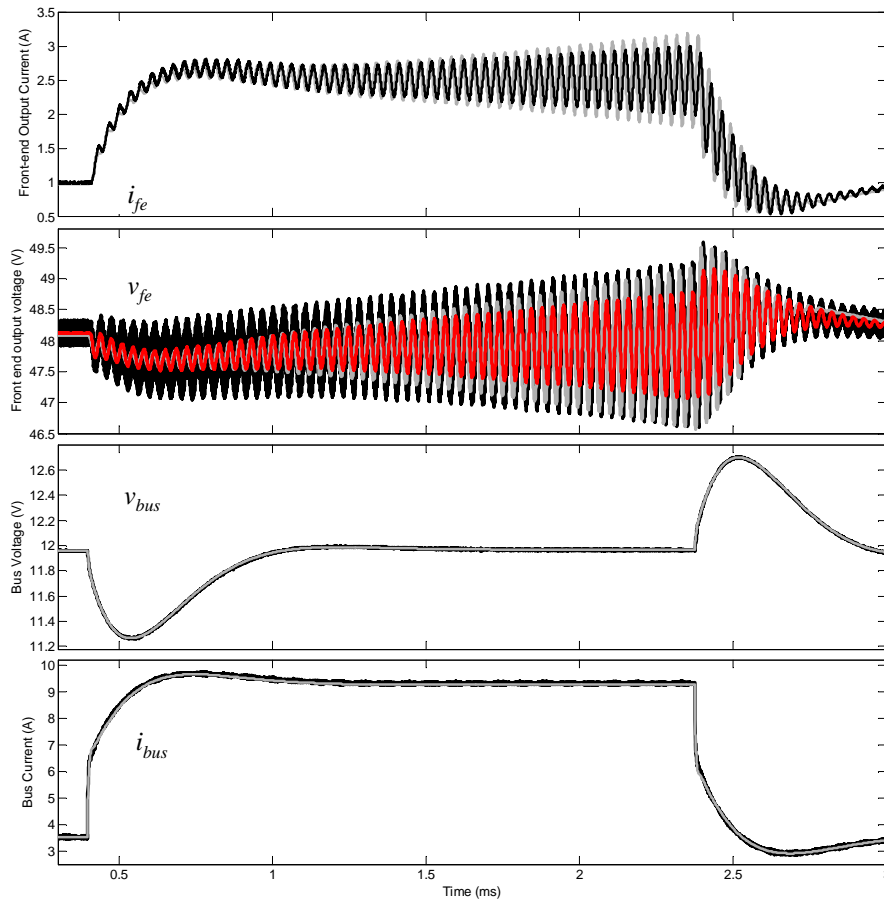


Fig. 4-93: system-level test 3.2. Comparison of experimental measurements (dark lines, averaged in red) and simulation results (grey lines).

As can be seen, the instability is predicted by the black-box models, as they address the CPL behavior. Some differences in magnitude as noticed, which are attributed to slight imprecision of the black-box model and slight inaccuracy in the identification process. Nevertheless, the measurement equipment and slight error in the modeling of the wires impedance may also be the reason why such difference exists.

Additionally, the maximum bus power, for which the system is stable, has been investigated. Experimentally, the system exhibits instability for bus power levels above 98 W, but the simulated system becomes unstable for bus power levels above 105 W, approximately. Such difference is relatively small (less than 10%), and is attributed to the reason pointed out above.

From this test a key conclusion is drawn: **the black-box model can be used to predict subsystem interactions and, consequently, for system-level stability assessment.** This is a key point, as the system-designer can determine problematic working conditions by simulation, which alleviates the experimental work and means both cost saving and time saving. Moreover, this helps during the design of damping networks to prevent instability. As a practical example, consider that the analyzed system represents a real situation in which the interconnection wires have large inductance. The black-box models may allow the system designer to determine, by simulation, the damping network to be placed in front of the bus converter.

4.6.4 System-level test 4: Hot-swap of a point-of-load converter

The final test consists in hot-swapping a POL converter (the buck-boost converter) to the intermediate bus. The experimental setup is depicted in Fig. 4-94.

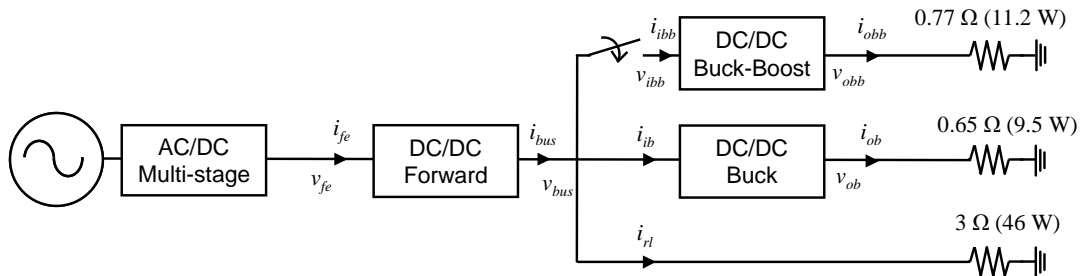


Fig. 4-94: System-level validation test 4: hot swap connection of the buck-boost converter.

This DC-DC converter features soft-start functionality, which is shown in Fig. 4-95. Once v_{ibb} input voltage level falls within the working range (time t_0), the soft-start system drives the output voltage of the converter so that it rises gradually from zero to the nominal value. Note that a large current peak appears when the input voltage is stepped. This is the so-called ‘inrush current’ and corresponds to the input capacitor charge.

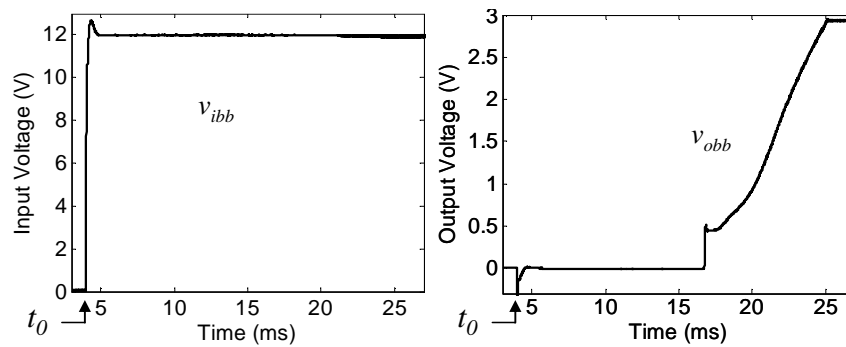


Fig. 4-95: Measured soft-start of the buck-boost converter with resistive load at the output.

The measured soft-start profile has been incorporated into the model by using the approach described in section 4.3.4.3. The comparison between experimental waveforms and simulation results is depicted in Fig. 4-96. As can be deduced, **the proposed soft-start network allows reproducing accurately the soft-start profile**. This is because the slew rate of v_o is slow compared to the time constants associated to the converter dynamics. However, note that the simulated i_{ibb} is lower than the measured one at the beginning of the transient. This fact may be expected, as the efficiency is implemented only as a function of I_{obb} (which assumes that V_{obb} is always equal to -3 V). However, during the soft-start, v_{obb} is lower, which implies a lower efficiency because the difference between v_{ibb} and v_{obb} is higher. Consequently, the real efficiency is lower than predicted by the model. In fact, as v_{obb} approaches the nominal value, the simulated current is closer to the measured one.

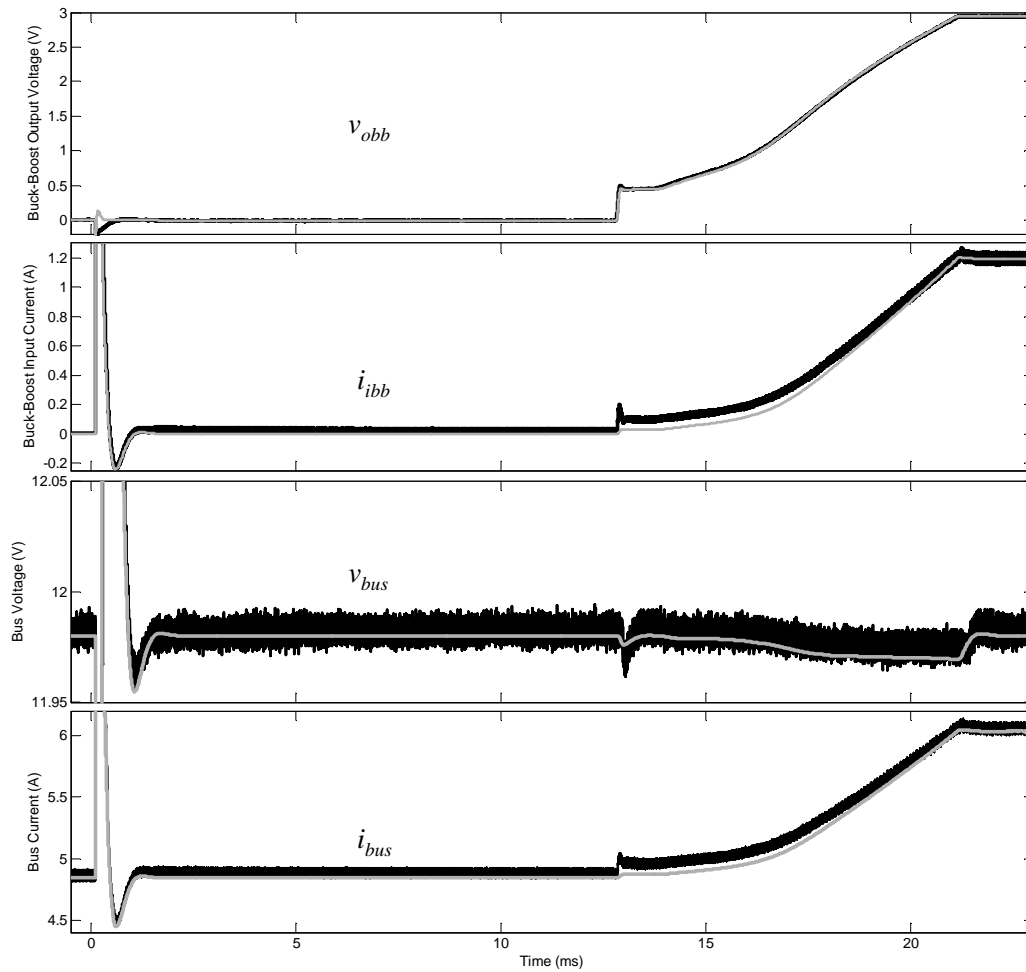


Fig. 4-96: System-level validation test 4. Comparison of experimental measurements (dark lines, averaged in red) and simulation results (grey lines).

A detail of the initial transient, corresponding to a time interval between 0.1 ms and 0.8 ms, is shown in Fig. 4-97. This corresponds to the inrush current demanded by the input filter of the buck-boost converter, whose peak is quite large (approximately 60 A), and is supplied by both the output capacitor of the bus converter and the input capacitor of the buck converter. **The inrush current is well predicted by the model**, as well as the current transient at the input port of the other converters.

It is worth noting that the inrush current causes a large v_{bus} undershoot (20%, approximately). This is accurately predicted by the model and may be quite important in practice, as it may trip under-voltage protections. Nevertheless, in real systems the inrush current is usually limited either by a dedicated circuit [262], or by the switch, e.g., if solid state power controllers (SSPC) are used (refer to chapter 1, section 1.2).

Nevertheless, some mismatch is also observed. Concerning the front-end voltage, it can be seen that, although the model reproduces the low-frequency transient, there is a high-frequency oscillation (67 kHz) which is not accurately predicted by the model. It probably corresponds to the resonance of the parasitic inductance of the wires (approximated to 1 μH in the model) with the input filter of the converter, and is attributed to model inaccuracy. Regarding, the buck-boost voltage, a large mismatch is observed. This may be expected, as long as the black-box model is parameterized under nominal operation of the converter, but at this time the converter is off.

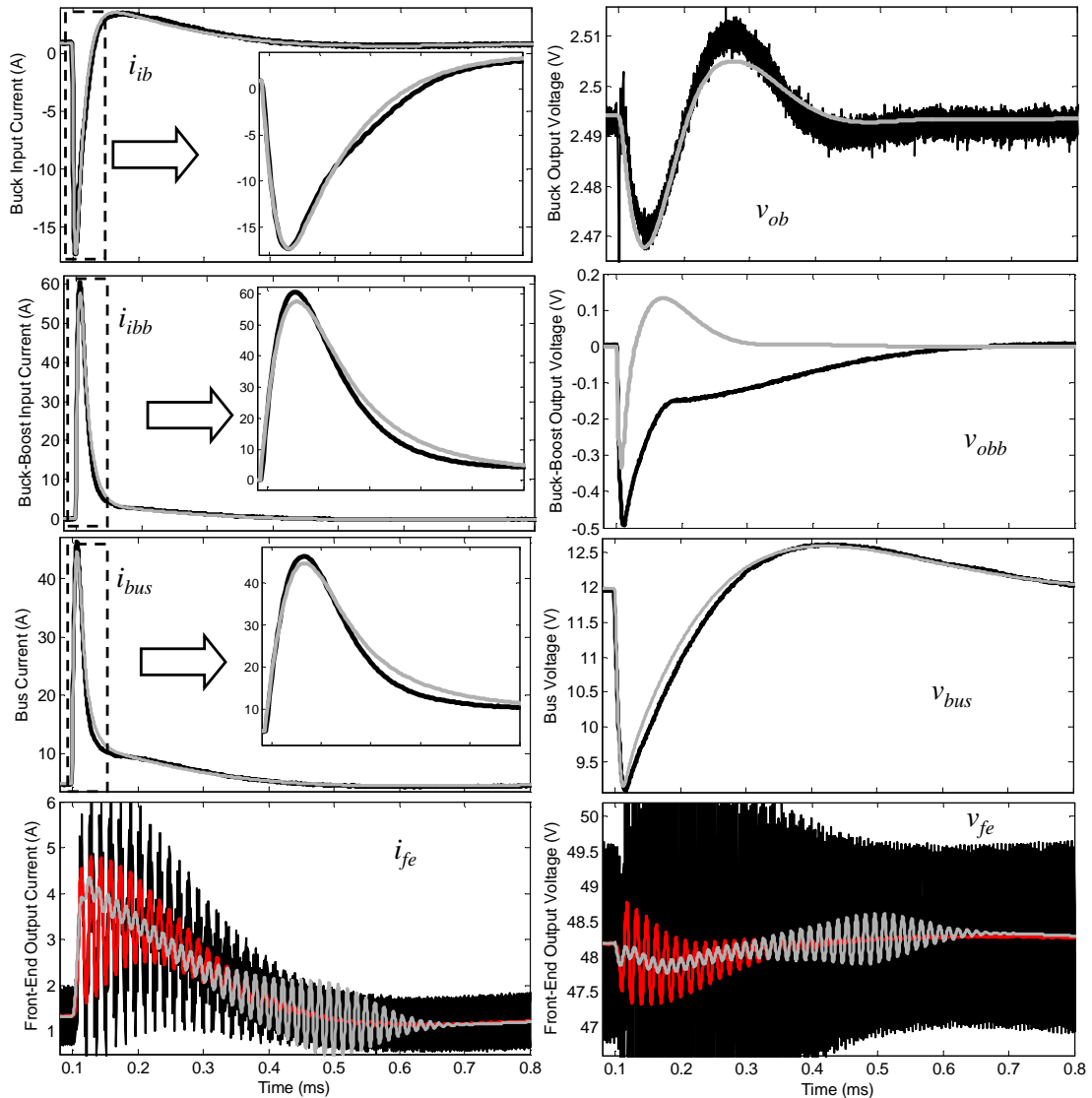


Fig. 4-97: System-level validation test 4. Detail of the initial transient. Comparison of experimental measurements (dark lines, averaged in red) and simulation results (grey lines).

4.7 Conclusions

In this chapter, **extension to the existing black-box model of DC-DC converters with output voltage control, and a novel identification method based on transient response analysis, has been proposed as original contributions.** The proposed method is based on a set of simple experimental tests and the use of parametric identification algorithms. A summary of contributions and main conclusions is given below.

- The existing black-box model has been complemented with additional features, such as soft-start networks.
- The **identification step tests** have been presented and practical implementation has been discussed.
- The use of **parametric identification techniques** has been described in detail to identify transfer function models.

- **An existing frequency-domain-based method, to remove the cross-coupling effects** of the identified models with the load/source dynamics, **has been adapted to time domain**. In addition, a novel **analysis method of the cross-coupling effects** has been presented. Thus, one can determine which effects are negligible, and then remove only the significant ones.
- The parameterization of the large-signal black-box model from the identified transfer function models has been described.
- A comprehensive validation of the proposed method has been carried out by means of a **commercial buck converter**. Both the identification method and the cross-coupling analysis and removal techniques have been proven to exhibit good performance. Moreover, a comparison between the frequency response of the identified transfer functions and results from an AC sweep has demonstrated the good performance of the proposed identification technique. Finally, the resulting model has been validated through a set of validation tests. The good agreement between simulations and measurements has corroborated the good performance of the modeling method.
- Following this, the method has been also applied to other commercial converters: a **forward converter and a multistage AC/DC converter** (only the output port has been modeled in the last case). The proposed method has been proven to work properly on those converters. Moreover, limitations of the black-box models to deal with nonlinear behavior under large-signal perturbations have been discussed, and possible solutions to this have been introduced.
- Finally, all the modeled converters have been interconnected to make up a **DC distributed power system**. The model capabilities to carry out system-level simulations have been demonstrated. It has been proven that the models can predict current and voltage transients under variations in load, global system-efficiency and system-level instability due to dynamic interactions of subsystems. Their capabilities to reproduce the inrush current and the soft-start profile, during a hot-swap of a power converter, have been also demonstrated.

5 Black-box modeling of Three-Phase Voltage Source Inverters with Output Voltage Control

5.1	Introduction.....	149
5.2	Model description: balanced conditions	149
5.2.1	Converter description	149
5.2.2	Model basis: definition of interface signals	150
5.2.3	The synchronous ‘d-q’ reference frame	151
5.2.4	Model structure	153
5.2.4.1	Small-signal approach	153
5.2.4.2	Large-signal approach	154
5.2.4.3	Model simplification: merge static and dynamic networks	155
5.2.4.4	Soft-start and enabling networks	157
5.3	Model identification.....	158
5.3.1	Experimental tests	158
5.3.1.1	Output current steps (d coordinate)	160
5.3.1.2	Output current steps (q coordinate)	160
5.3.1.3	Input voltage step	161
5.3.1.4	Setting the d-q operating point for the load current.....	161
5.3.2	Park’s transformation (AC signals only).....	162
5.3.3	Cross-coupling effects.....	163
5.3.3.1	Removal.....	163
5.3.3.2	Analysis.....	165
5.3.3.3	Prevention.....	166
5.3.4	Parameterization of large-signal black-box model.....	167
5.3.5	Overview of the identification procedure.....	167
5.4	Simplifying the modeling and identification of the output impedance	169
5.4.1	Linear properties	169
5.4.2	Orthogonal properties.....	170
5.4.3	Limitations	172
5.5	Simulation results.....	173
5.5.1	Introduction and system description.....	173
5.5.2	Modeling	175
5.5.2.1	Linearity analysis	175
5.5.2.2	Dynamic networks selection.....	177
5.5.3	Identification	178
5.5.3.1	Resistive load step.....	179
5.5.3.2	Capacitive load step.....	181
5.5.3.3	Input voltage step	183
5.5.4	Validation.....	184

5.5.4.1	Validation test 1. Large inductive load step	185
5.5.4.2	Validation test 2. Nonlinear load	186
5.5.4.3	Validation test 3. Disturbed DC bus	187
5.5.5	Summary	188
5.6	Experimental results.....	189
5.6.1	Introduction and system description	189
5.6.2	Modeling	190
5.6.2.1	Preliminary tests: linearity analysis	190
5.6.2.2	Dynamic networks modeling	192
5.6.3	Identification	193
5.6.3.1	Step tests and identification of transfer function models.....	193
5.6.3.2	Analysis and removal of cross-coupling effects	197
5.6.3.3	Discussion on identification results	198
5.6.3.4	Parameterization of dynamic networks	200
5.6.3.5	Parameterization of the soft-start functionality and the enabling network	200
5.6.4	Validation.....	202
5.6.4.1	Validation test 1: Input voltage step down	202
5.6.4.2	Validation test 2: Large RL load step	203
5.6.4.3	Validation test 3: Hot swap of the VSI to the DC bus	205
5.6.5	Summary	207
5.7	Modeling unbalanced conditions: first approach	207
5.7.1	Basic concepts: symmetrical components and d-q-0 transformation.....	207
5.7.2	Extensions of the black-box model	210
5.7.2.1	Three-wire system	210
5.7.2.2	Four-wire system	210
5.7.3	Identification of zero-sequence impedance.....	213
5.7.4	Simulation results.....	213
5.7.4.1	Three-wire system	213
5.7.4.2	Four wire system (only VSI with delta-star transformer).....	215
5.8	Conclusions.....	218

5.1 Introduction

Emerging technologies such as more/all electric aircrafts, naval ships and smart-grids are leading to the introductions of three-phase AC and hybrid AC/DC distributed power systems. Those systems rely on power electronics converters such as three-phase AC-DC and DC-AC converters. Hence, system-level behavioral models of them are required.

As explained in section 2, the first approach to system-level modeling of AC-DC and DC-AC converters has been recently reported [153]. However, the reported models are linear and can only represent the small-signal behavior of the converter under balanced-conditions. Moreover, no experimental identification method of such models has been yet reported.

In this chapter, **a large-signal black-box modeling method of three phase VSIs provided with output voltage regulation, as well as a novel identification method based on transient response to step tests, is presented as original contribution.**

Similarly to DC-DC converters, the proposed modeling method is based on input-output g-parameters network. The identification of the black-box model relies on step tests and parametric identification algorithm. The simplicity of the experimental procedure is one of the most remarkable features of the proposed method. The chapter is organized as follows.

- **Section 5.2** describes the proposed black-box model.
- **Section 5.3** presents the identification procedure, consisting of the experimental tests and the use of parametric identification techniques. Also, the cross-coupling problem is tackled in this section.
- **Section 5.4** analyzes a particular implementation of the modeled converter: the VSI with capacitive input filter and linear control strategy. This implementation exhibits several remarkable properties which simplify the modeling and identification procedure.
- **Sections 5.5 and section 5.6** presents a comprehensive illustration and validation of the proposed method through simulation results and experimental results, respectively.
- **Section 5.7** tackles the modeling of the three-phase VSI under un-balanced conditions. Both three-wire and four-wire systems are considered.

5.2 Model description: balanced conditions

5.2.1 Converter description

A generic diagram of the modeled converter is shown in Fig. 5-1 and described below. Elements represented by dashed line are optional.

- **DC-DC front-end converter (optional):** this converter is sometimes used to boost the input voltage and/or provide galvanic isolation through a high-frequency transformer.
- **Power stage:** The power stage is comprised of the following elements.
 - **Input filter:** comprised of a capacitor and sometimes a series inductor.

- **Switching bridge:** typically comprised of IGBTs.
- **Output filter:** comprised of a LC cell. A low-frequency transformer is sometimes used to provide galvanic isolation and/or boost the output voltage.
- **Control stage:** The control stage comprises the next parts.
 - **Modulator:** Typical schemes are Space Vector Modulation and selective harmonic elimination, among others.
 - **Voltage and (optionally) current regulator:** The regulators command the modulator so that the output voltage follows the reference signal V_{ref} . The control scheme can be comprised of an inner current loop plus and outer voltage loop, or only the voltage loop. The regulator stage can be implemented in either stationary frame ($a-b-c$ or $\alpha-\beta$) or $d-q$ frame. Those reference frames are reviewed later on.

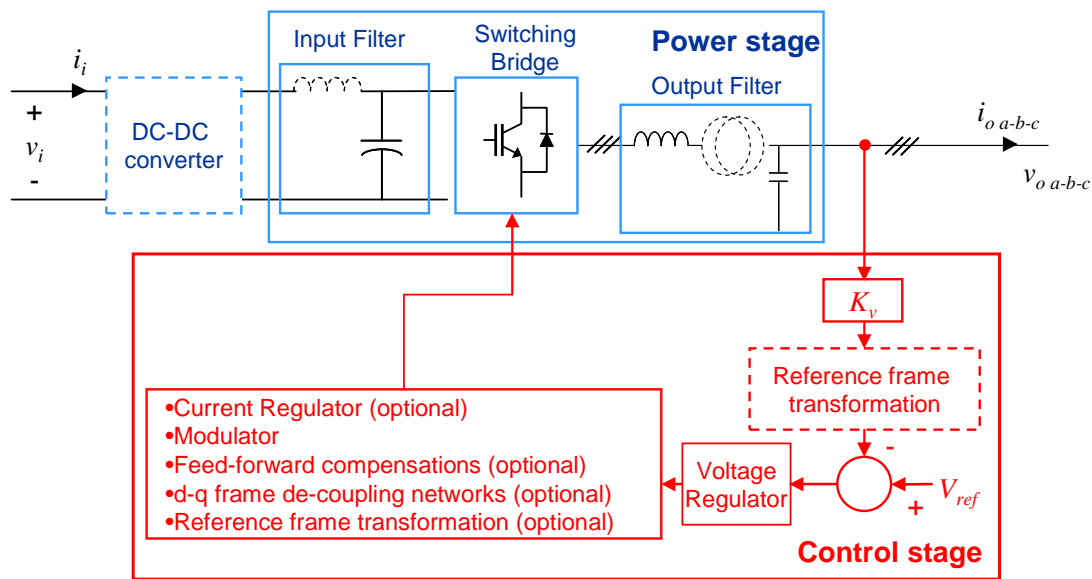


Fig. 5-1: Three phase Voltage Source inverter with LC output filter and voltage regulation.

5.2.2 Model basis: definition of interface signals

As explained in chapter 3, the first task in black-box modeling is to determine the interface signals of the modeled subsystem, and to sort them into model inputs and model outputs. By having a look at the system-level functionality of the converter, the following conclusions can be drawn.

- At the output port, the converter behaves as a regulated AC voltage source, so that the output current i_o is determined by the active and reactive load power.
- At the input port, the converter behaves as a current sink, so that the input current i_i is determined by the load active power and the input voltage v_i .

Therefore, the system-level behavior of this converter resembles that of DC-DC converters modeled along chapter 4. Consequently:

- The AC output currents i_{oa} , i_{ob} , i_{oc} and DC input voltage v_i are the model inputs.
- The AC output voltage v_{oa} , v_{ob} , v_{oc} and DC input current i_i are the model outputs.

Hence, the model interface is that shown in Fig. 5-2.

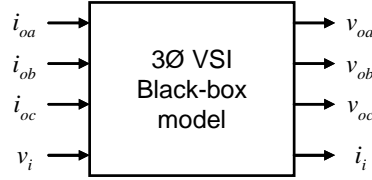


Fig. 5-2: System-level model of the three phase VSI with regulated output voltage.

The main difference from DC-DC converters is the AC interface at the output port. Instead of having a single output voltage and a single output current, there are three AC voltages and currents. AC signals are time-variant at steady-state; therefore a ‘constant operating point’ cannot be defined. That problem is overcome by making use of the Park’s transformation, or ‘ a - b - c ’ frame to ‘ d - q ’ frame transformation. By means of this, a three-phase balanced sinusoidal system can be ‘instantaneously’ mapped into two DC signals, called ‘ d ’ and ‘ q ’, without any loss of information. This transformation is well known and is briefly reviewed in the next point.

5.2.3 The synchronous ‘ d - q ’ reference frame

Consider a set of three balanced sinusoidal signals s_a , s_b and s_c , which are featured by same magnitude, same angular fundamental frequency ‘ ω_o ’ and are shifted 120 degrees. Then, the sum of them at any instant of time is null.

$$s_a + s_b + s_c = 0 \quad (5-1)$$

According to that constraint, such a set of three-phase signals can be transformed into two orthogonal signals by the linear transformation given by (5-2). This is the so-called ‘Clarke transformation’, or ‘ a - b - c to α - β ’ transformation [175]. The resulting signals s_α , s_β are featured by same magnitude as the a - b - c signals and are shifted 90 degrees.

$$\begin{pmatrix} s_\alpha \\ s_\beta \end{pmatrix} = \frac{2}{3} \cdot \begin{pmatrix} 1 & -\frac{1}{2} & -\frac{1}{2} \\ 0 & \frac{\sqrt{3}}{2} & -\frac{\sqrt{3}}{2} \end{pmatrix} \cdot \begin{pmatrix} s_a \\ s_b \\ s_c \end{pmatrix} \quad (5-2)$$

This transformation has a meaningful geometrical interpretation. The three phase signals (s_a , s_b and s_c) can be represented as a vector rotating at angular frequency ‘ ω_o ’ in a three dimensional space, so that the projection of the vector onto the three-axes gives the instantaneous value of the signals. This reference frame is referred to as ‘ a - b - c frame’ (see Fig. 5-3).

As long as the signals fulfill (5-1), the vector is actually lying within a bi-dimensional plane. Consequently, the system can be transformed into a bi-dimensional space, defined by two orthogonal axes, as defined by (5-2). The resulting reference frame is the so-called ‘ α - β frame’.

Within α - β frame, the signals s_α , s_β are represented through a set two orthogonal, stationary axes, and a vector rotating at synchronous frequency. However, if those axes rotate at the same speed as the vector, then the projection of the vector result in two DC signals. In plain words, a rotating vector in a stationary frame results in a stationary vector in a rotating frame [175]. This transformation can be done through the orthogonal matrix given by (5-3), where $\theta = \omega_o \cdot (t - t_0)$ and t_0 is the reference time.

$$\begin{pmatrix} s_d \\ s_q \end{pmatrix} = \begin{pmatrix} \cos \theta & \sin \theta \\ -\sin \theta & \cos \theta \end{pmatrix} \cdot \begin{pmatrix} s_\alpha \\ s_\beta \end{pmatrix} \quad (5-3)$$

The resulting signals, s_d s_q , are said to be mapped into ‘ d - q frame’. The reference time ‘ t_0 ’ allows setting the relative position of the d - q axes with respect to the vector.

Fig. 5-3 illustrates the concepts discussed above. The reference time ‘ t_0 ’ has been selected so that $s_\beta(t_0) = 0$. Thereby, the projection onto the ‘ q ’ axis is null, i.e. $s_q = 0$. The reference time ‘ t_0 ’ will play a critical role during the identification process, as will be discussed later on.

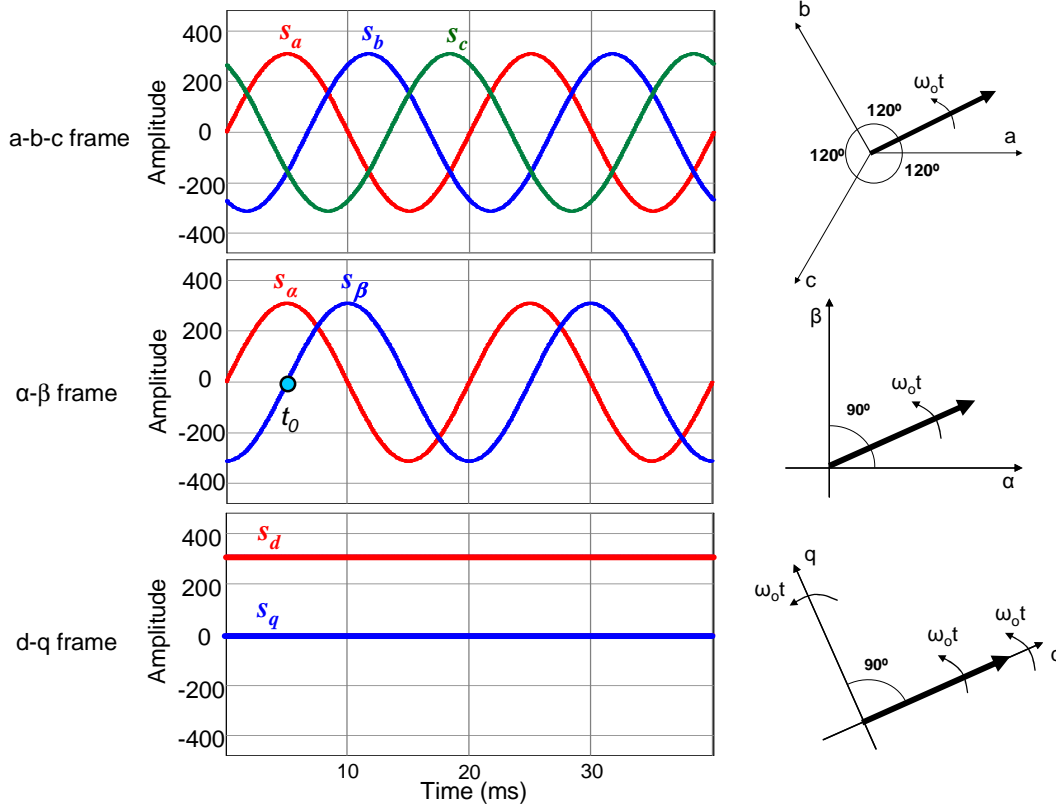


Fig. 5-3: Three phase balanced signals represented into a - b - c frame, a - β frame and d - q frame.

Both reference frame transformations, defined by (5-2) and (5-3), can be merged into a single one as expressed by (5-4). Three-phase signals can be directly converted from a - b - c frame to d - q frame using this linear transformation^{5.1}. This is the so-called ‘Park’s Transformation’ [177]-[179]^{5.2}.

$$\begin{pmatrix} s_d \\ s_q \end{pmatrix} = \frac{2}{3} \cdot \begin{pmatrix} \cos \theta & \cos\left(\theta - \frac{2 \cdot \pi}{3}\right) & \cos\left(\theta + \frac{2 \cdot \pi}{3}\right) \\ -\sin \theta & -\sin\left(\theta - \frac{2 \cdot \pi}{3}\right) & -\sin\left(\theta + \frac{2 \cdot \pi}{3}\right) \end{pmatrix} \cdot \begin{pmatrix} s_a \\ s_b \\ s_c \end{pmatrix} \quad (5-4)$$

On the other hand, the inverse transformation from d - q frame to a - b - c frame is defined as follows.

^{5.1} The a - b - c to d - q transformation is linear time-variant. As a consequence, a linear dynamic system into a - b - c frame is also linear into d - q frame, but the system dynamics is affected by the transformation.

^{5.2} The transformation given (5-4) is said to be ‘amplitude invariant’, meaning that the amplitude of the vector mapped into d - q and a - b - c frame is the same. Alternative definitions, such as the ‘power invariant’ one, are also widely applied. They differ from each other by a constant factor $(3/2)^{1/2}$.

$$\begin{pmatrix} s_a \\ s_b \\ s_c \end{pmatrix} = \begin{pmatrix} \cos \theta & -\sin \theta \\ \cos\left(\theta - \frac{2 \cdot \pi}{3}\right) & -\sin\left(\theta - \frac{2 \cdot \pi}{3}\right) \\ \cos\left(\theta + \frac{2 \cdot \pi}{3}\right) & -\sin\left(\theta + \frac{2 \cdot \pi}{3}\right) \end{pmatrix} \cdot \begin{pmatrix} s_d \\ s_q \end{pmatrix} \quad (5-5)$$

5.2.4 Model structure

5.2.4.1 Small-signal approach

As illustrated above, a three phase balance system can be mapped by means of two DC signals into d - q frame, so it is possible to define a constant operating point. Hence, those techniques already described for black-box modeling of DC-DC converters can be adapted to the three-phase VSI. Moreover, thanks to the linear properties of the Park's transformation (or a - b - c to d - q frame transformation), linearity of the VSI is retained when mapped into d - q frame.

The model is internally represented in d - q coordinates, so that the d - q output voltage and input current are model outputs, whereas d - q output current and input voltage are model inputs. This leads, to a three-port g-parameters network, consisting of two output ports, one for each d - q channel, and one input port. In terms of small-signal, it can be represented by the linear model shown in Fig. 5-4^{5.3}. Since this is a three-input, three-output network, up to nine transfer function models are required to model all those relationships between the inputs and the outputs: four transfer functions for the output impedance ($Z_{odd}(s)$, $Z_{odq}(s)$, $Z_{oqd}(s)$ and $Z_{oqq}(s)$), two ones for the audiosusceptibility ($G_{od}(s)$ and $G_{oq}(s)$), two for the back-current-gain ($H_{id}(s)$ and $H_{iq}(s)$) and one for the input admittance ($Y_i(s)$).

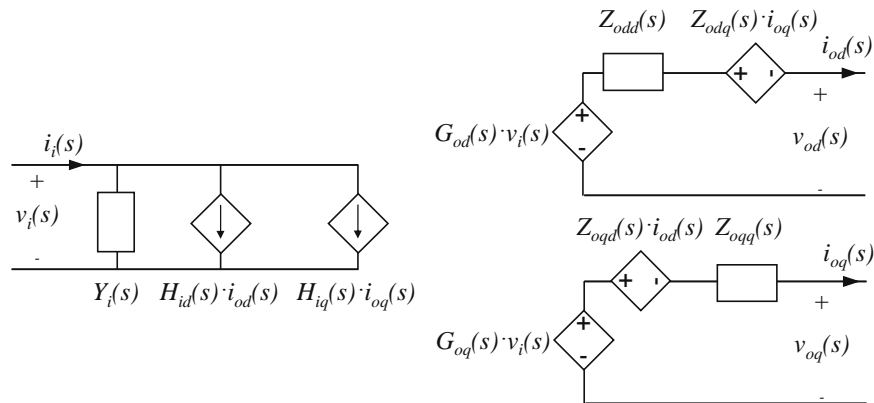


Fig. 5-4: Small-signal d-q black-box model of three phase VSIs with regulated output voltage (Laplace domain).

This model has been recently shown in [153]. However, it requires to be extended in order to carry out large-signal time domain simulations. Indeed, as the model is described in d - q coordinates, it cannot be interfaced with other three phase subsystems and loads, unless also mapped into the d - q frame.

^{5.3} Note that this model would be also valid to model a single-input two-outputs DC-DC converter. This clearly illustrates the equivalency between black-box models for three-phase VSI into d-q and DC-DC converters.

5.2.4.2 Large-signal approach

To address large-signal behavior, the model shown in Fig. 5-5 is proposed.

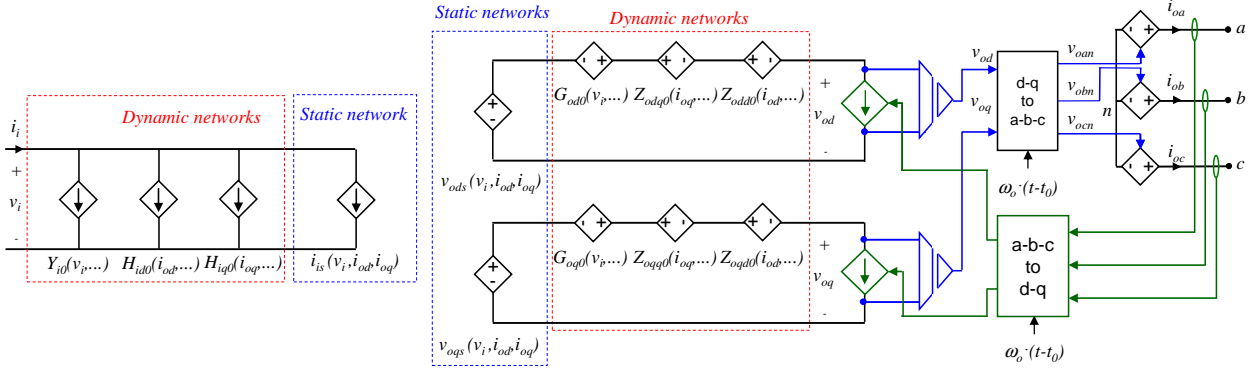


Fig. 5-5: Large-signal black-box model of three phase VSIs with regulated output voltage.

Compared to the small-signal model, the following modifications have been carried out.

- **Static networks are added at the input and the output port**, which address the static behavior of the input current, i_{is} , and the d - q output voltage, v_{ods} and v_{oqs} , as a function of model inputs. By means of such networks, the static line-load regulation is represented, as well as the input-output power transfer, including constant-power-load behavior. From a general point of view, these networks can be expressed as follows.

- The output static networks can be expressed as given by (5-6). V_{ssd} and V_{ssq} denote the nominal output voltage, which will be determined by the control action as well as the d - q axes setting through the reference time ' t_0 ' (refer to section 5.2.3). On the other hand, v_{stregd} and v_{stregq} represents effect related to the static load and line regulation, i.e. steady-state voltage dependence on load current and input voltage levels.

$$\begin{cases} v_{ods}(v_i, i_{od}, i_{oq}) = V_{ssd} + v_{stregd}(v_i, i_{od}, i_{oq}) \\ v_{oqs}(v_i, i_{od}, i_{oq}) = V_{ssq} + v_{stregq}(v_i, i_{od}, i_{oq}) \end{cases} \quad (5-6)$$

- The input static network addresses the input-output power balance. The active power and reactive power are defined into d - q frame as given by (5-7). At the input port, only load active power flow is reflected^{5.4}, so i_{is} is defined as given by (5-8), where η denotes efficiency. Note that this network also represents the constant-power-load behavior of the regulated VSI, since v_i is inversely proportional to i_{is} under constant active load power.

$$\begin{cases} p_o = \frac{3}{2} \cdot (v_{od} \cdot i_{od} + v_{oq} \cdot i_{oq}) \\ q_o = \frac{3}{2} \cdot (v_{oq} \cdot i_{od} - v_{od} \cdot i_{oq}) \end{cases} \quad (5-7)$$

$$i_{is}(v_i, i_{od}, i_{oq}) = \frac{3}{2} \cdot \frac{v_{osd}(v_i, i_{od}, i_{oq}) \cdot i_{od} + v_{osq}(v_i, i_{od}, i_{oq}) \cdot i_{oq}}{v_i \cdot \eta(v_i, i_{od}, i_{oq})} \quad (5-8)$$

^{5.4} Reactive power corresponds to energy that is flowing through phases, but does not mean power consumption. Therefore, at steady-state, it is not directly reflected at the input port (only indirectly due to any power loss variation).

- **Each transfer function is replaced by a dynamic network that can be either linear or nonlinear.** Such dynamic networks can be built using a transfer function model, a gain-scheduled transfer function or a LLMN. Those are applied in a similar manner as described in chapter 4 for DC-DC converters. Details about them can be found in section 4.2.3, and application examples on three-phase VSIs will be illustrated in section 5.5 and section 5.6. Note that every dynamic network is denoted with subscript ‘0’, meaning null static response.
- **Reference frame transformation blocks are added in order to interface the ‘ d - q ’ network with the rest of the system,** which normally is mapped into ‘ a - b - c ’ frame. They work as follows.
 - On the one hand, the d - q voltage is measured, mapped into the d - q frame by (5-5), and outputted through three controlled voltage sources. If the line-neutral voltage is measured during model parameterization, those sources should be connected as a star, as shown below. If the line-line voltage is considered, delta connection would be used.
 - On the other hand, the a - b - c current is measured, mapped into d - q frame by (5-4) and inputted into the model through two controlled current sources.

The proposed extension to large-signal modeling is an original contribution of this thesis.

5.2.4.3 Model simplification: mergin static and dynamic networks

The proposed model can be significantly simplified under some circumstances, which are typically fulfilled by VSIs with tightly regulated output voltage.

Consider that the static line and load regulation are narrow, so that $v_{stregd} \ll V_{ssd}$ and $v_{stregq} \ll V_{ssq}$ within the working range of interest. If the a - b - c to d - q transformation is set so that $V_{oq} \approx 0$, then the output power can be rewritten as follows, at steady-state. This is done by an adequate selection of the time instant ‘ t_0 ’, as illustrated in Fig. 5-3.

$$\begin{cases} P_o|_{V_{oq} \approx 0} \approx \frac{3}{2} \cdot (V_{od} \cdot I_{od}) \\ Q_o|_{V_{oq} \approx 0} \approx -\frac{3}{2} \cdot (V_{od} \cdot I_{oq}) \end{cases} \quad (5-9)$$

Thus, if $V_{oq} \approx 0$, then I_{od} is related to the active power delivered to the AC load, whereas I_{oq} is related to the reactive power circulating through the load. Hence, the input current at steady-state can be simply defined as follows.

$$i_{is}(v_i, i_{od}, i_{oq}) \approx \frac{3}{2} \cdot \frac{V_{ssd} \cdot i_{od}}{v_i \cdot \eta(v_i, i_{od}, i_{oq})} \quad (5-10)$$

Such simplification has important consequences in terms of dynamics. As can be deduced from (5-9), the input-output power transference is directly related to I_{od} . Hence, the following conclusions are drawn:

- H_{id} represents the power transfer from the input to the output port, as well as transient variations of energy stored into the reactive components (i.e. inductors and capacitors) under active power transients.
- H_{iq} is essentially related to transient variations of energy stored into the reactive components of the VSI under reactive power transients.

Further simplifications can be done on the model. As H_{id} is the only component related to input-output power transfer, its behavior will be similar to that of H_i for DC-DC converters (refer to chapter 4). Due to this, the low-frequency gain of H_{id} will be inversely proportional to V_i and η , making the gain-scheduled transfer function a suitable approach to build it (see the upper part of Fig. 5-6). If a gain-scheduled transfer function is used, the scheduling function GS will be defined as follows.

$$GS(i_{od}, i_{oq}, v_i) = \frac{\partial i_{is}}{\partial i_{od}} \approx \frac{3}{2} \cdot \frac{V_{ssd}}{v_i \cdot \eta(v_i, i_{od}, i_{oq})} \cdot \left[1 - \underbrace{\frac{i_{od}}{\eta(v_i, i_{od}, i_{oq})} \cdot \left(\frac{\partial \eta(v_i, i_{od}, i_{oq})}{\partial i_{od}} \right)}_{eff} \right] \quad (5-11)$$

If the second addend in (5-11) is neglected (i.e. $eff \ll 1$), then the small-signal response of the 'whole' H_{id} can be expressed as follows.

$$\begin{aligned} H_{id}(s) &= \left. \frac{i_i(s)}{i_{od}(s)} \right|_{i_{oq}(s)=0, v_i(s)=0} = \frac{\partial i_{is}(I_{od}, I_{oq}, V_i)}{\partial I_{od}} + GS(I_{od}, I_{oq}, V_i) \cdot H_{id0n}(s) \approx \\ &\approx \frac{3}{2} \cdot \frac{V_{ssd}}{V_i \cdot \eta(V_i, I_{od}, I_{oq})} \cdot (H_{id0n}(s) + 1) \end{aligned} \quad (5-12)$$

In that case, the static input network and the back-current gain can be merged into a single network, as shown at the bottom part of Fig. 5-6. Moreover, if the static line and load regulation are not only very narrow but also nearly linear, the transfer function models into the output impedance and audiosusceptibility can directly incorporate them (this is the reason why subscript '0' is not utilized in Fig. 5-6). This simplification is very similar to that presented for DC-DC converters in section 4.2.4.

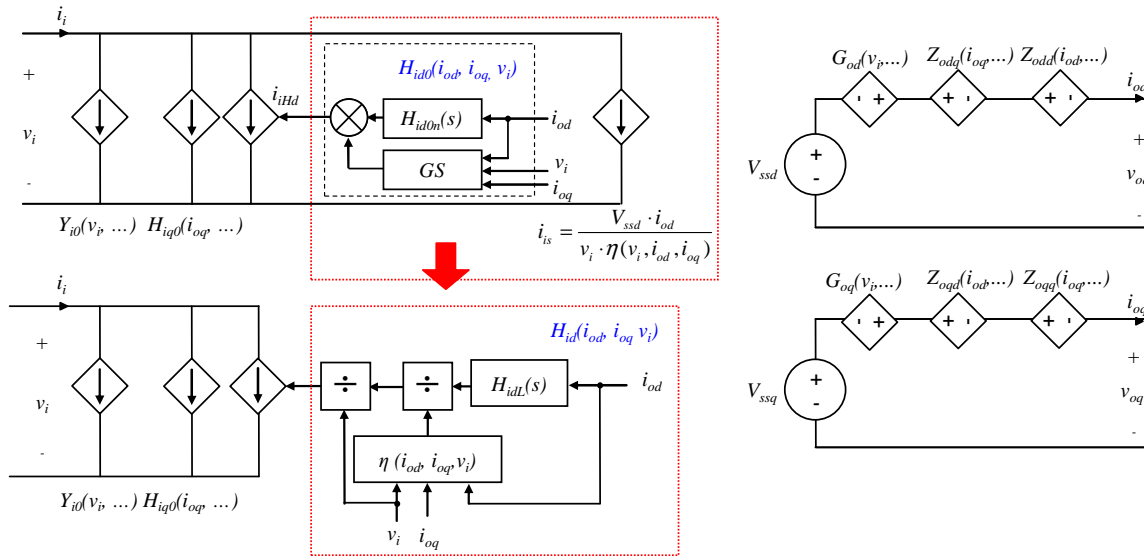


Fig. 5-6: Simplifying the black-box model of the three-phase VSI in case of nearly constant V_{od} , V_{oq} .

The relationship between $H_{idL}(s)$ and $H_{id0n}(s)$ is given by the following expression.

$$H_{idL}(s) = \frac{3}{2} \cdot V_{ssd} \cdot (H_{id0n}(s) + 1) \quad (5-13)$$

On the other hand, similar simplification can be derived in case the no-load losses are incorporated into the model. This is done in a similar manner as previously described for DC-DC converters (refer to section 4.2.4). The resulting simplified model is shown in Fig. 5-7, where P_{i0} represents the no load losses and η' represents the efficiency after subtracting them, as defined by (5-14).

$$\eta' = \frac{P_o}{P_i - P_{i0}} \quad (5-14)$$

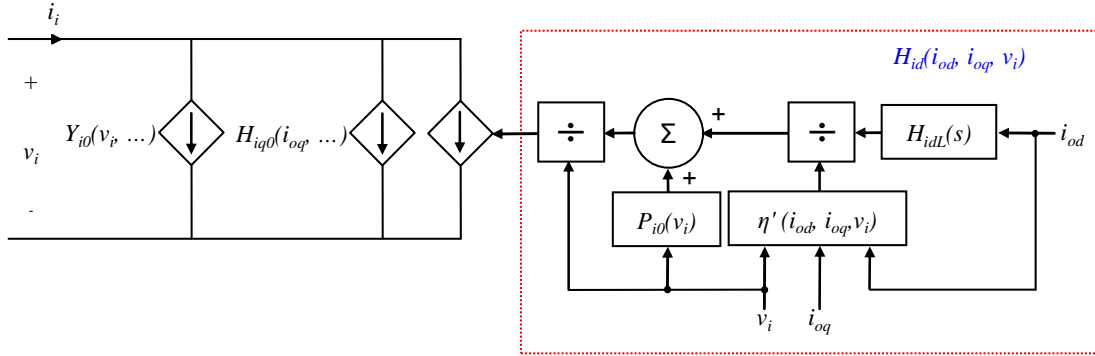


Fig. 5-7: Simplifying the black-box model of the three-phase VSI including no load losses.

5.2.4.4 Soft-start and enabling networks

Similarly to DC-DC converters, three-phase VSI are provided with ‘soft-start’ functionalities so that, once the VSI is enabled, the output voltage gradually increases from zero to the nominal value by following a preset starting profile. To enable the VSI, the input voltage must fall within the working range of the converter and the converter must be activated through an ‘on/off’ signal.

The g-parameters model for three-phase VSI can be easily provided with this kind of functionalities, in a similar way as explained in chapter 4 for DC-DC converters. The soft-start network can be implemented as depicted in Fig. 5-8.

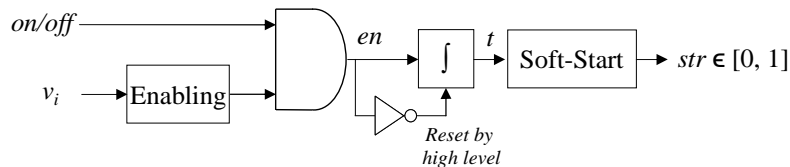


Fig. 5-8: Soft-start and enabling networks.

- The block ‘Enabling’ is comprised of logic blocks and outputs a binary signal ‘1’ or ‘0’ as a function of v_i . Thus, if the input voltage falls within the working range of the VSI and the activation signal of the converter ‘on/off’ is set to ‘1’, then the signal ‘en’ is set to ‘1’.
- Once the signal ‘en’ toggles from ‘0’ to ‘1’, a counter (resettable integrator) is started. It drives the block ‘Soft-start’. This block stores the soft-start profile and outputs the signal ‘str’ as a function of time ‘t’. Note that such a soft-start profile is normalized, so that the signal ‘str’ is equal to ‘1’ when the VSI has reached the nominal operation conditions. If a linear profile is used (which is commonly used) then the ‘soft-start’ block simply includes a constant factor.

The signal ‘str’ is used to scale the d - q output voltage resulting from the d - q output networks of the model. Such a signal is used to scale also the output of H_{id} , in order to account for the input-output power balance of the converter. Fig. 5-9 shows the modifications to be done in the large-signal model of the VSI, in order to include the soft-start capabilities.

Note that this approach is appropriate as long as the time constants associated to the soft-start are much slower than the closed-loop time constants under nominal operation, so that the dynamics of the black-box model does not make influence on the response during the soft-start process. Practical implementations of the enabling network will be seen in section 5.6.

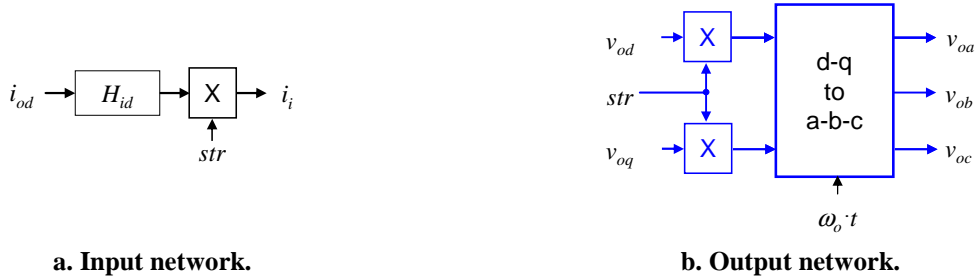


Fig. 5-9: Modifications on the input-output networks to be driven by the soft-start networks.

5.3 Model identification

At the moment, no whole identification method of black-box models for three phase VSIs has been reported in the literature. **The first identification method is proposed in this section as original contribution.**

The identification procedure relies on those concepts described in chapters 4. The process consists of a set of sequential tasks, as depicted in Fig. 5-10. The parametric identification of transfer functions is applied in the same way as described in chapter 4, so the reader is referred to section 4.4 for a detailed about it.

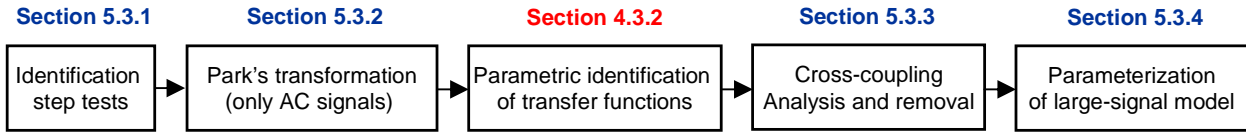


Fig. 5-10: Identification procedure of the large-signal black-box model for a three-phase VSI

5.3.1 Experimental tests

As introduced in chapter 3, the idea behind the identification method consists in stepping one input signal while the other ones are kept constant. If the step magnitude is designed so that local linear (or nearly linear) behavior is kept, then the input-output dynamics can be explained by the small-signal model shown in Fig. 5-4. It can be mathematically expressed as follows into Laplace domain.

$$\begin{pmatrix} i_i(s) \\ v_{od}(s) \\ v_{oq}(s) \end{pmatrix} = \begin{pmatrix} Y_i(s) & H_{id}(s) & H_{iq}(s) \\ G_{od}(s) & -Z_{odd}(s) & -Z_{odq}(s) \\ G_{oq}(s) & -Z_{oqd}(s) & -Z_{oqq}(s) \end{pmatrix} \cdot \begin{pmatrix} v_i(s) \\ i_{od}(s) \\ i_{oq}(s) \end{pmatrix} \quad (5-15)$$

Once the small-signal model described by (4-17) has been identified, some transfer functions are post-processed to build the large-signal one.

As the model is featured by three-input signals, three step tests have to be carried out.

1. i_{od} step while both i_{oq} and v_i are kept constant.
2. i_{oq} step while both i_{od} and v_i are kept constant.

3. v_i step while both i_{od} and i_{oq} are kept constant.

This way, the transient response of each output signal depends on only one transfer function under each test. A conceptual approach to the identification process is depicted in Fig. 5-11.

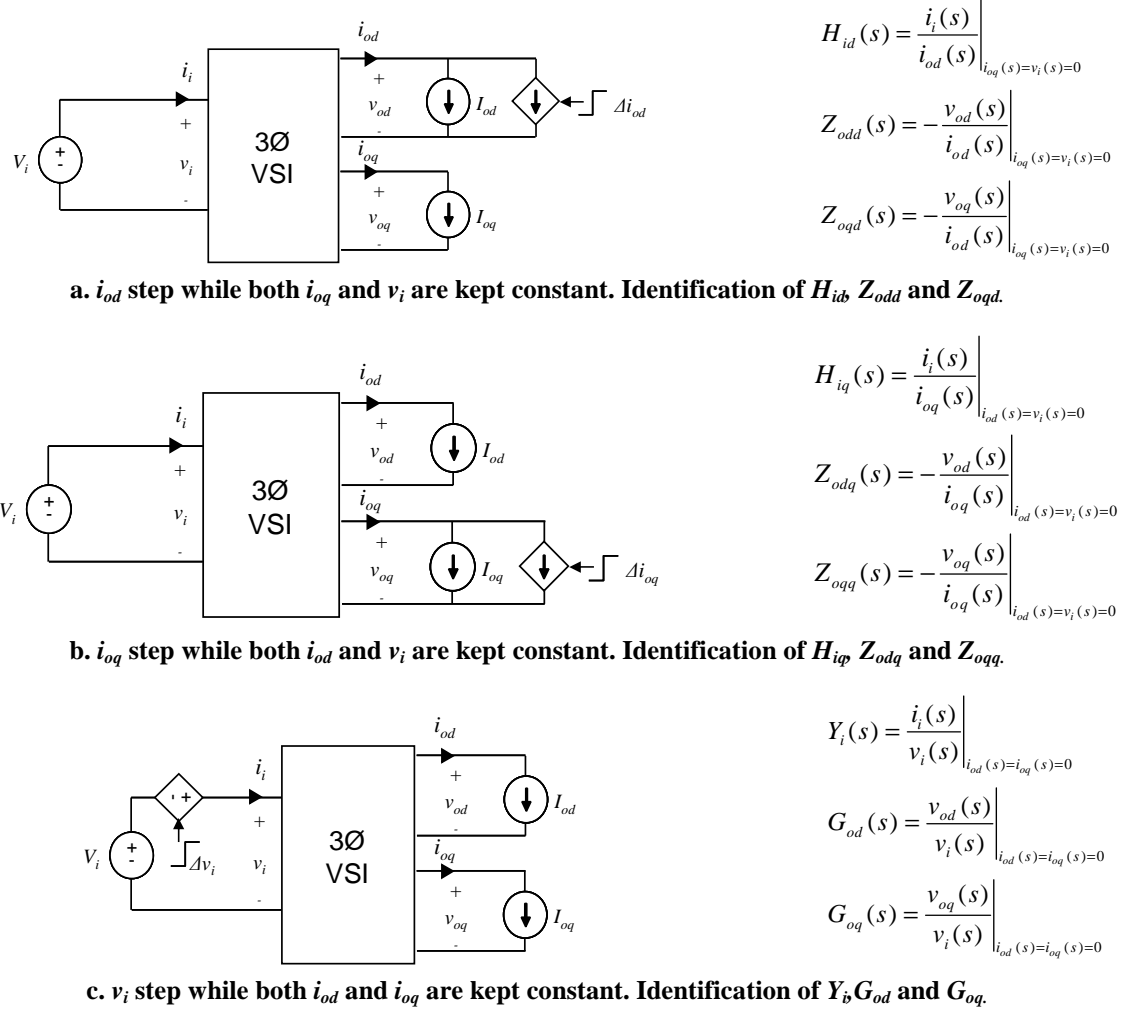


Fig. 5-11: Identification experiments of black-box models for three phase VSI with regulated output voltage.

By looking at Fig. 5-11, one may wonder about the following question: *how can only one i_{od} - q coordinate be stepped, while the other is kept constant?*

The answer to this question is figured out from the analysis of ‘instantaneous power’ mapped into d - q frame, which has been previously defined by (5-7). As indicated by (5-9), if the a - b - c to d - q transformation is set so that $V_{oq} = 0$, then the active and reactive power are proportional to I_{od} and I_{oq} , respectively. **Consequently, if the Park’s transformation is set so that $V_{oq} = 0$, active power steps will be reflected as i_{od} steps, whereas reactive power steps will be reflected as i_{oq} steps**, as indicated in (5-16). This is the key idea behind the proposed identification method.

$$\begin{cases} \Delta p_o \approx \frac{3}{2} \cdot V_{od} \cdot \Delta i_{od} \\ \Delta q_o \approx -\frac{3}{2} \cdot V_{od} \cdot \Delta i_{oq} \end{cases} \quad (5-16)$$

Practical implementations of the proposed tests are described in the following sections.

5.3.1.1 Output current steps (d coordinate)

Active power steps are reflected as i_{od} steps, so this can be simply done by switching a balanced resistive load ' R_2 ', as illustrated in Fig. 5-12.

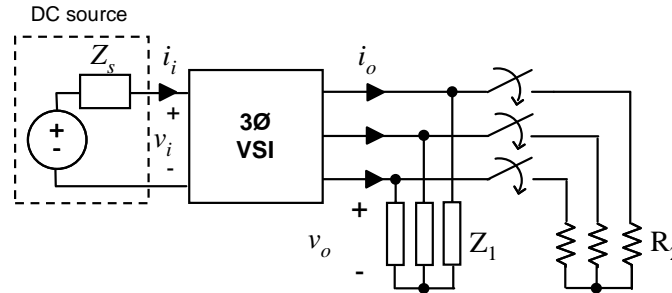


Fig. 5-12: stepping i_{od} by means of a resistive load switch-on (switch-off is also valid).

At the input port, the operating point of the input voltage V_i is set by a DC source. At the output port, the operating point of the output current I_{od} and I_{oq} is set through balanced impedance, namely Z_1 . The magnitude of the step is given by (5-17).

$$\Delta i_{od} \Big|_{V_{oq}=0} = \frac{V_{od}}{R_2}, \quad \Delta i_{oq} \Big|_{V_{oq}=0} = 0 \quad (5-17)$$

From this test, $Z_{odd}(s)$, $Z_{oqd}(s)$ and $H_{id}(s)$ are identified.

5.3.1.2 Output current steps (q coordinate)

To make an i_{oq} step, a reactive load (either inductive or capacitive) may be stepped (either switched 'on' or 'off'). Possible solutions are discussed below.

- Inductive load steps.
 - An inductive load switch-on may limit the slew-rate of the stepped current coordinate. Moreover, if the inductive load has associated a significant resistive component, both i_{od} and i_{oq} would be stepped.
 - An inductive load switch-off may cause a large and harmful transient over-voltage upon the switch.
- Capacitive load steps.
 - A capacitive load switch-on may cause a large transient over-current.
 - A **capacitive load switch off** means an i_{oq} step down with high slew rate. Neither over-current nor over-voltage is caused, so this is **the selected choice** (see Fig. 5-13).

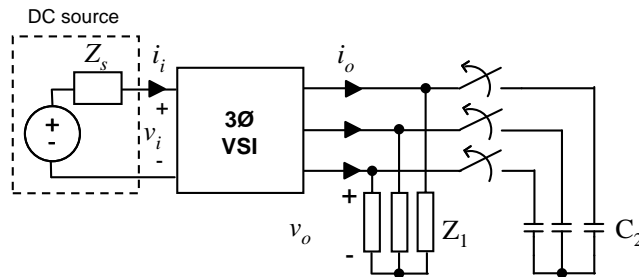


Fig. 5-13: stepping i_{oq} by means of a capacitive load switch-off.

It is important to note that the capacitor C_2 should fulfill with the capacitive reactive power range allowed by the converter. Since the output of the considered VSI is capacitive, placing an excessively high capacitor at the output may change significantly the voltage control loop. Thereby, it may lead to an unstable situation.

The DC source sets V_i , while Z_l in parallel with C_2 determines I_{od} and I_{oq} . The magnitude of the step is given by (5-18). From this test, $Z_{oqq}(s)$, $Z_{odq}(s)$ and $H_{iq}(s)$ are identified.

$$\Delta i_{od} \Big|_{V_{oq}=0} = 0, \quad \Delta i_{oq} \Big|_{V_{oq}=0} = -\omega_o \cdot C_2 \cdot V_{oq} \quad (5-18)$$

5.3.1.3 Input voltage step

The input voltage step can be applied in a similar way to exposed in chapter 4. Suitable solutions are depicted in Fig. 5-14 and are described below.

- The circuit shown in Fig. 5-14a is based on the connection of an array of diodes in parallel with a switch. When the switch is turned on, a positive voltage step is applied at the input of the converter. The step magnitude is given by (5-19), where n is the number of diodes and V_d is the voltage drop per diode.

$$\Delta v_i = n \cdot V_d \quad (5-19)$$

- The circuit shown in Fig. 5-14b relies on the use of a resistor to cause a voltage drop, instead of the diodes. In this case, the magnitude of the step depends on the input current of the converter as given by (5-20), where R_d denotes the resistance of the resistor.

$$\Delta v_i = R_s \cdot I_i \quad (5-20)$$

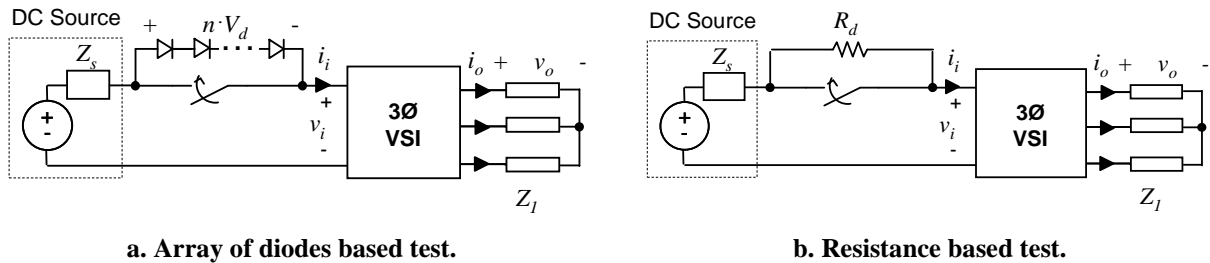


Fig. 5-14: practical implementations of the v_i step test.

In both cases, the achieved slew-rate is determined by the sum of the source impedance Z_s and the switch impedance. The operating points V_i and I_{od} , I_{oq} are determined by the DC source and the impedance Z_l , respectively. Concerning data recording, guidelines to select the total time and the sampling time has been indicated in section 4.3.1.3.

5.3.1.4 Setting the d-q operating point for the load current

The operating point of the load current, I_{od} and I_{oq} , is determined by the $d-q$ frame load admittance. Below, relationship between the load parameters mapped into $a-b-c$ and $d-q$ frame is presented.

Consider a three-phase load admittance defined by the matrix $[Y_l(s)]_{abc}$.

$$\begin{pmatrix} i_{oa} \\ i_{ob} \\ i_{oc} \end{pmatrix} \cdot \underbrace{\begin{pmatrix} Y_{laa}(s) & 0 & 0 \\ 0 & Y_{lbb}(s) & 0 \\ 0 & 0 & Y_{lcc}(s) \end{pmatrix}}_{[Y_l(s)]_{abc}} \cdot \begin{pmatrix} v_{oa} \\ v_{ob} \\ v_{oc} \end{pmatrix} \quad (5-21)$$

This admittance can be mapped into d - q frame as expressed by (5-22).

$$\begin{pmatrix} i_{od} \\ i_{oq} \end{pmatrix} \cdot \underbrace{\begin{pmatrix} Y_{l_{dd}}(s) & Y_{l_{dq}}(s) \\ Y_{l_{qd}}(s) & Y_{l_{qq}}(s) \end{pmatrix}}_{[Y_l(s)]_{dq}} \cdot \begin{pmatrix} v_{od} \\ v_{oq} \end{pmatrix} \quad (5-22)$$

Under balanced conditions, i.e. $Y_{laa}(s) = Y_{lbb}(s) = Y_{lcc}(s)$, following relationship between a - b - c admittance and d - q admittance holds. Such relationship is obtained by applying the transformation reported in [199].

$$\begin{cases} Y_{l_{dd}}(s) = Y_{l_{qq}}(s) = \frac{Y_{laa}(s + j\omega_o) + Y_{laa}(s - j\omega_o)}{2} \\ Y_{l_{dq}}(s) = -Y_{l_{qd}}(s) = j \frac{Y_{laa}(s + j\omega_o) - Y_{laa}(s - j\omega_o)}{2} \end{cases} \quad (5-23)$$

Then, the steady-state relationships are obtained by particularizing (5-24) for $s = 0$. Typical configurations for the load and related d - q operating points are depicted in Fig. 5-15. Pure resistive and capacitive loads are simply obtained by simplifying these equations.

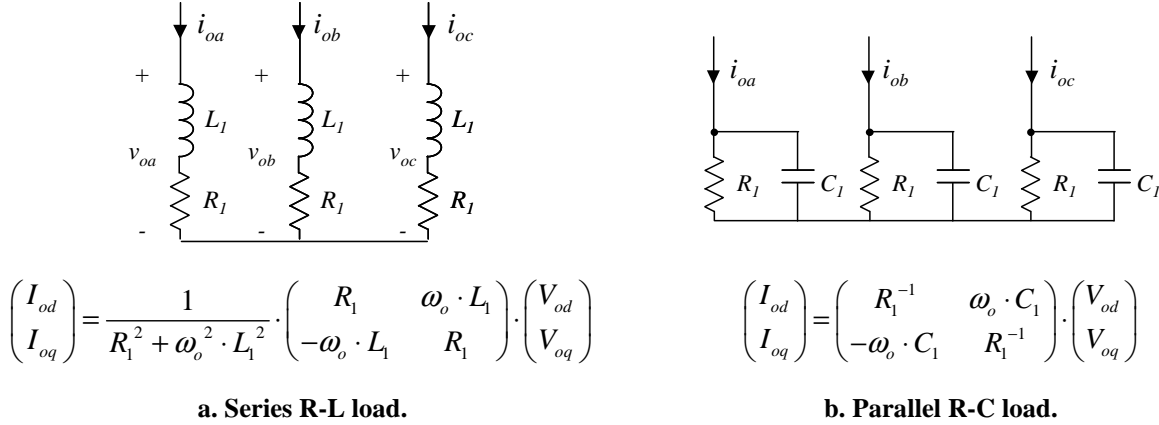


Fig. 5-15: Some load configurations and corresponding d - q operating point.

5.3.2 Park's transformation (AC signals only)

Once the transient response of the converter has been measured, the AC signals have to be mapped into d - q frame, so that $V_{oq} = 0$. V_{oq} is set to zero through a proper selection of the reference time ' t_0 ', as follows.

1. Apply the a - b - c frame to a - β frame transformation (5-2) on the measured voltage.
2. Find out the time instant where $v_{o\beta} = 0$ (before the step is applied). It corresponds to ' t_0 '.

This process has been illustrated in Fig. 5-3. Once ' t_0 ' has been determined, the Park's transformation (5-4) is applied on the measured a - b - c voltage and current by using $\theta = \omega_o \cdot (t - t_0)$ as the

transformation angle. Following this, transfer function models are identified by following the process described in chapter 4, section 4.3.2.

5.3.3 Cross-coupling effects

Ideally, the transient response under each identification tests is determined by only one transfer function, since only one input signal is stepped (Fig. 5-11). However, in a real scenario, the other signals would be also disturbed due to the following reasons.

- The DC bus impedance $Z_s(s)$ will cause undesired cross-perturbations of v_i during output current steps.
- The d - q frame load admittance, $[Y_l(s)]_{dq}$, will cause undesired perturbations on i_{oq} during the resistive load steps, on i_{od} during the capacitive load steps, and on both i_{od} and i_{oq} during the input voltage steps.

Hence, both the load and the source dynamics exhibit a certain coupling effect with the identified transfer functions. Methods to remove, to analyze and to prevent them are described in this section.

5.3.3.1 Removal

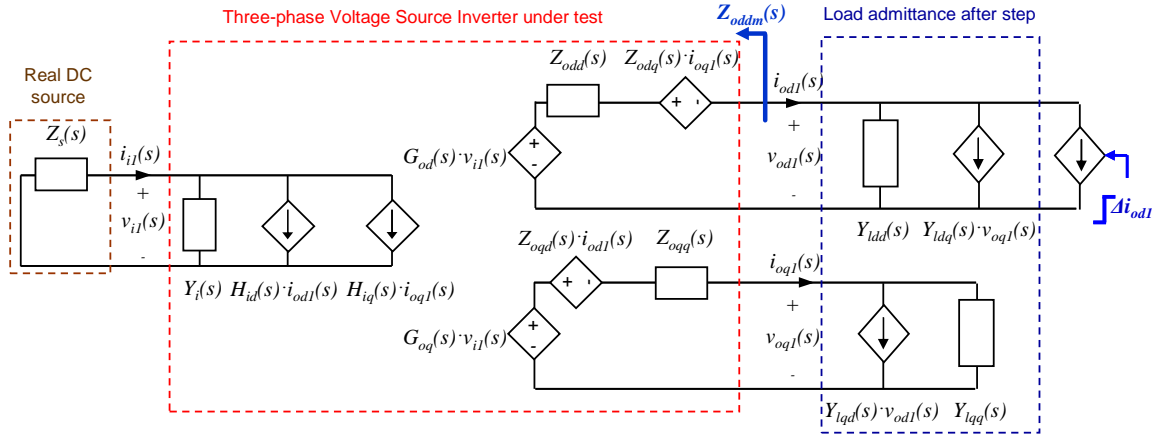
In order to explain both the cross-coupling problem and the de-coupling method, the small-signal d - q ‘terminated’ equivalent circuits, corresponding to the identification tests, are shown in next page (Fig. 5-16).

The load admittance, $[Y_l]$, corresponds to that just after applying the step test. Hence, under resistive switch-on (Fig. 5-16a) it corresponds to $[Y_l] = [Z_l]^{-1} + [R_2]^{-1}$, but under capacitive switch-off (Fig. 5-16b) it only corresponds to $[Y_l] = [Z_l]^{-1}$.

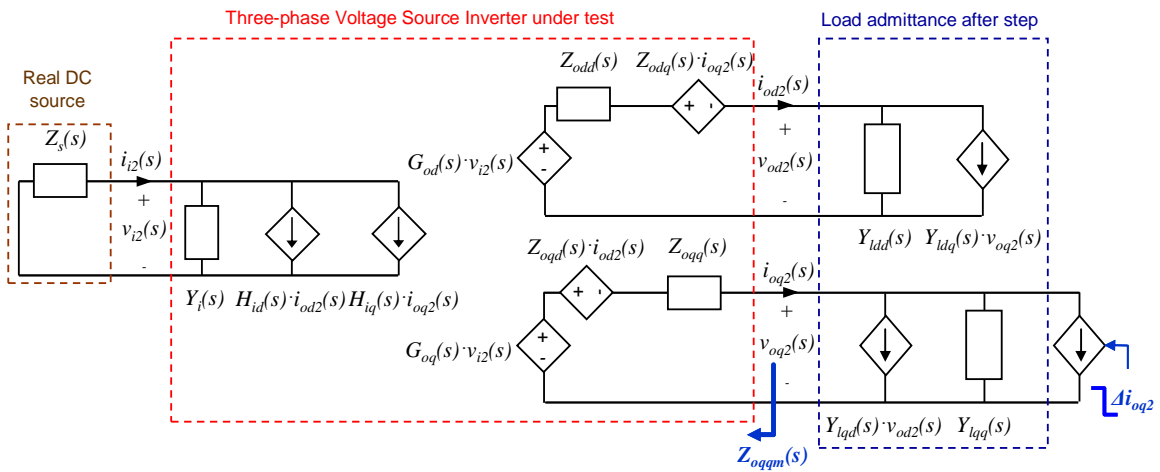
The cross-coupling effects are evidenced in Fig. 5-16. For instance, consider Fig. 5-16a. Due to the non-zero $[Z_s]$ and $[Y_l]$, both i_{oq} and v_i are perturbed under a i_{od} step, meaning that the identified impedance from measurements, $Z_{oddm}(s)$, differs from the un-terminated (sough) one, $Z_{odd}(s)$, because it is ‘cross-coupled’ with both Z_s and $[Y_l]$ through the input port and the q -channel of the output port.

To address this problem, the method originally proposed in [150], for DC-DC converters, have been extended to the three-phase VSI into d - q frame. The idea consists in expressing the relationship between the ‘terminated’ transfer functions, identified directly from measurements (subscript ‘ m ’), and the un-terminated ones through six auxiliary transfer functions. Such transfer functions relate the cross-perturbed signals with stepped ones (two ones per test) and are defined as follows.

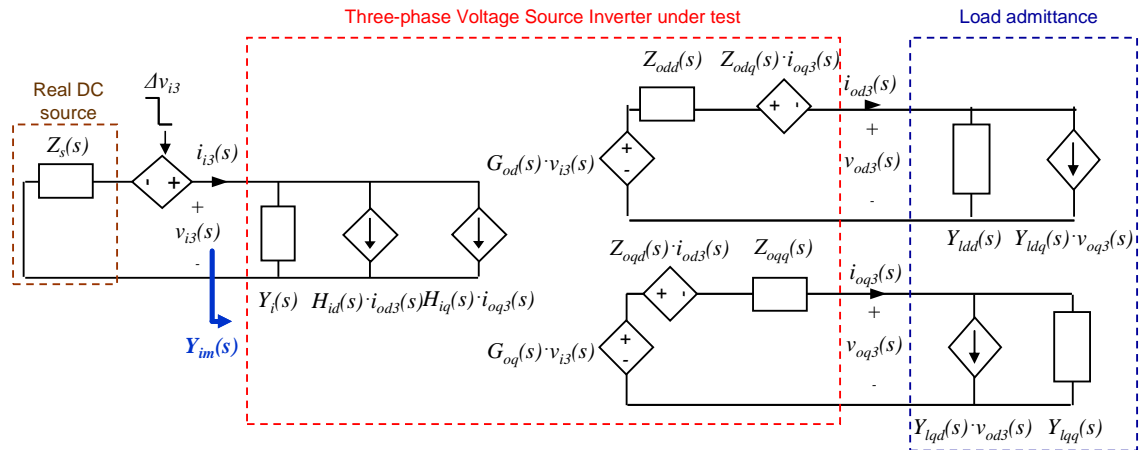
$$\left\{ \begin{array}{l} T_{iqdm}(s) = \frac{i_{oq1}(s)}{i_{od1}(s)}, \quad T_{rdm}(s) = \frac{v_{i1}(s)}{i_{od1}(s)} \Rightarrow \text{cross - perturbations under } i_{od} \text{ step} \\ T_{idqm}(s) = \frac{i_{od2}(s)}{i_{oq2}(s)}, \quad T_{rqm}(s) = \frac{v_{i2}(s)}{i_{oq2}(s)} \Rightarrow \text{cross - perturbations under } i_{oq} \text{ step} \\ T_{gdm}(s) = \frac{i_{od3}(s)}{v_{i3}(s)}, \quad T_{gqm}(s) = \frac{i_{oq3}(s)}{v_{i3}(s)} \Rightarrow \text{cross - perturbations under } v_i \text{ step} \end{array} \right. \quad (5-24)$$



a. Equivalent circuit under resistive load switch-on (Fig. 5-12), where $[Y_l(s)]_{dq} = [Z_l(s)]_{dq}^{-1} + [R_2(s)]_{dq}^{-1}$.



b. Equivalent circuit under capacitive load switch-off (Fig. 5-13), where $[Y_l(s)]_{dq} = [Z_l(s)]_{dq}^{-1}$.



c. Equivalent circuit under input voltage step (Fig. 5-14), where $[Y_l(s)]_{dq} = [Z_l(s)]_{dq}^{-1}$.

Fig. 5-16: Small-signal d-q ‘terminated’ equivalent circuit for the identification tests of a three-phase VSI^{5.5}.

By means of those auxiliary transfer functions, the ‘terminated’ transfer functions can be related to the ‘un-terminated’ ones in a simple manner. To illustrate this, consider again the circuit shown in Fig. 5-16a. The voltage v_{od1} can be expressed as a function of terminal signal and un-terminated transfer functions as follows.

^{5.5} Note that any balanced impedance can be mapped into d-q frame as explained in section 5.3.1.4.

$$v_{od1}(s) = G_{od}(s) \cdot v_{i1}(s) - Z_{odd}(s) \cdot i_{od1}(s) - Z_{odq}(s) \cdot i_{oq1}(s) \quad (5-25)$$

By dividing both sides by i_{od1} , the following expression is obtained.

$$\frac{v_{od1}(s)}{i_{od1}(s)} = -Z_{oddm}(s) = G_{od}(s) \cdot T_{rdm}(s) - Z_{odd}(s) - Z_{odq}(s) \cdot T_{iqdm}(s) \quad (5-26)$$

Thus, the identified transfer function from measurements, Z_{oddm} , is directly expressed as a function of un-terminated ones through the auxiliary transfer functions defined in the first row of (5-24). By following a similar procedure, every identified transfer function can be expressed as a function of un-terminated ones by a de-coupling matrix $[T(s)]$, as given by (5-27).

$$\begin{pmatrix} Y_{im}(s) \\ H_{idm}(s) \\ H_{iqm}(s) \\ G_{odm}(s) \\ -Z_{oddm}(s) \\ -Z_{odqm}(s) \\ G_{oqm}(s) \\ -Z_{oqdm}(s) \\ -Z_{oqqm}(s) \end{pmatrix} = \underbrace{\begin{pmatrix} 1 & T_{gdm}(s) & T_{gqm}(s) & 0 & 0 & 0 & 0 & 0 & 0 \\ T_{rqm}(s) & 1 & T_{iqdm}(s) & 0 & 0 & 0 & 0 & 0 & 0 \\ T_{rdm}(s) & T_{idqm}(s) & 1 & 0 & 0 & 0 & 0 & 0 & 0 \\ 0 & 0 & 0 & 1 & T_{gdm}(s) & T_{gqm}(s) & 0 & 0 & 0 \\ 0 & 0 & 0 & T_{rqm}(s) & 1 & T_{iqdm}(s) & 0 & 0 & 0 \\ 0 & 0 & 0 & T_{rdm}(s) & T_{idqm}(s) & 1 & 0 & 0 & 0 \\ 0 & 0 & 0 & 0 & 0 & 0 & 1 & T_{gdm}(s) & T_{gqm}(s) \\ 0 & 0 & 0 & 0 & 0 & 0 & T_{rqm}(s) & 1 & T_{iqdm}(s) \\ 0 & 0 & 0 & 0 & 0 & 0 & T_{rdm}(s) & T_{idqm}(s) & 1 \end{pmatrix}}_{[T(s)]} \begin{pmatrix} Y_i(s) \\ H_{id}(s) \\ H_{iq}(s) \\ G_{od}(s) \\ -Z_{odd}(s) \\ -Z_{odq}(s) \\ G_{oq}(s) \\ -Z_{oqd}(s) \\ -Z_{oqq}(s) \end{pmatrix} \quad (5-27)$$

Then, the un-terminated transfer functions are expressed as a function of the terminated ones just by inverting $[T(s)]$. The six transfer functions into $[T(s)]$ are identified as follows.

- $T_{iqdm}(s)$ and $T_{rdm}(s)$ are identified from an i_{od} step, considering i_{od} as the model input and i_{oq} , v_i as the model outputs, respectively.
- $T_{iqdm}(s)$ and $T_{rqm}(s)$ are identified from an i_{oq} step, considering i_{oq} as the model input and i_{od} , v_i as the model outputs, respectively.
- $T_{gdm}(s)$ and $T_{gqm}(s)$ are identified from a v_i step, considering v_i as the model input and i_{od} , i_{oq} as the model outputs, respectively.

Again, notice that **no additional identification tests are required to parameterize $[T(s)]$** . The only requirement is to measure the cross-perturbed signals, under each identification test, and to identify the additional transfer functions listed above.

However, the resulting inverse matrix, $[T(s)]^{-1}$, is complex if every transfer function is incorporated into it. That may yield very high order transfer functions. However, in practice, some of the cross-coupling effects are usually negligible, so $[T(s)]$ could be simplified if only the significant cross-coupling effects are incorporated into it.

A preliminary analysis of the cross-coupling effects allows determining which effects are negligible, so that the corresponding rows in (5-30) can be simplified. As explained in the previous chapter, the simplified matrix is referred to as $[T_s(s)]$.

5.3.3.2 Analysis

The cross-coupling effects are evaluated in a similar way as described in section 4.3.3.2. The idea is to check if the original conditions stated at the beginning of the identification process are valid, i.e. the transient response of each model output depends on only one model input under each test (see

Fig. 5-11). For instance, let consider the analysis of the cross-coupling effects on Z_{oddm} (see Fig. 4-17). Convolution of the pre-processed measurements (subscript 'p'), under its identification test (i_{od} step), with the transfer functions, into the d-channel output port, has to be evaluated. The results listed below can be obtained.

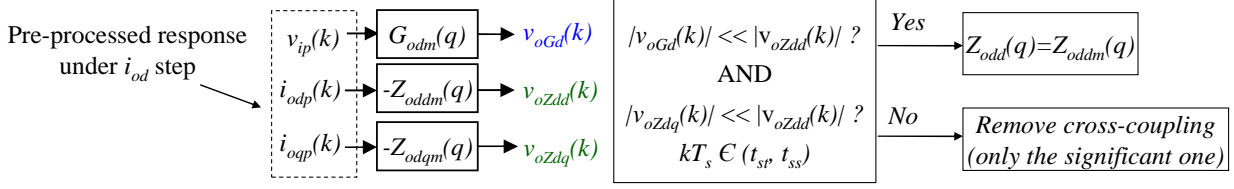


Fig. 5-17: Analyzing cross-coupling on $Z_{oddm}(q)$. t_{st} : stepping time. t_{ss} : setting time. T_s : sampling period.

- **Both** $|v_{oGd}(k)| \ll |v_{oZdd}(k)|$ **and** $|v_{oZdq}(k)| \ll |v_{oZdd}(k)|$. In this case the cross-coupling effects are negligible. Hence, $Z_{odd}(q) \approx Z_{oddm}(q)$, meaning that $T_{iqdm}(s) = 0$ and $T_{rdm}(s) = 0$ in the fifth row of (5-27).
- **Only** $|v_{oGd}(k)| \ll |v_{oZdd}(k)|$. Then, $T_{rdm}(s) = 0$ in the fifth row of (5-27), but $T_{iqdm}(s)$ must be considered.
- **Only** $|v_{oZdq}(k)| \ll |v_{oZdd}(k)|$. Then, $T_{iqdm}(s) = 0$ in the fifth row of (5-27), but $T_{rdm}(s)$ must be considered.
- **Neither** $|v_{oGd}(k)| \ll |v_{oZdd}(k)|$ **nor** $|v_{oZdq}(k)| \ll |v_{oZdd}(k)|$. Both cross-coupling effects are significant, so the fifth row of (5-27) has to be maintained unchanged.

A similar procedure is followed for the remaining transfer functions.

5.3.3.3 Prevention

In order to simplify the de-coupling procedure as much as possible, the best solution is to prevent the cross-coupling effects during the experimental part. Guidelines to prevent such effects are deduced from Fig. 5-16 and are described below.

5.3.3.3.1 Cross-perturbations under output current steps

The cross-perturbation of v_i is caused by the DC bus impedance Z_s and can be expressed as follows.

$$v_i(s) = -Z_s(s) \cdot i_i(s) \quad (5-28)$$

Therefore, **the lower Z_s , the lower the cross-coupling effect**. Reducing wires paths and placing external capacitor(s) close to the input port of the VSI are some guidelines to minimize Z_s .

The cross-perturbation of i_{oq} , under a resistive load-switch on, can be expressed as given by (5-29), where Y_{lqd} , Y_{lqd} correspond to the load admittance (after stepping R_2), expressed in d - q coordinates

$$i_{oq}(s) = Y_{lqd}(s) \cdot v_{od}(s) + Y_{lqq}(s) \cdot v_{oq}(s) \quad (5-29)$$

Similarly, the cross-perturbation of i_{od} can be expressed as

$$i_{od}(s) = Y_{lqd}(s) \cdot v_{od}(s) + Y_{lqq}(s) \cdot v_{oq}(s) \quad (5-30)$$

Thus, the lower the load admittance (after the step) $[Y_l(s)]_{dq}$, the lower the cross-perturbation effects. Hence, **the cross-coupling effect is lower under load switch-off and is fully avoided if a load switch-off is done to no load conditions (i.e. $Y_l = 0$)**. As a consequence, if the dynamics

dependence on I_{od} and I_{oq} is negligible, the best choice is to perform load switch-off to minimum load conditions.

5.3.3.3.2 Cross-perturbations under input voltage steps

In this case the cross-perturbations are only due to the load admittance. According to (5-29) and (5-30), the lower the load level the lower the cross-perturbations. Therefore, if dynamics dependence on I_{od} and I_{oq} is negligible, the best choice is to perform the step at minimum load conditions.

5.3.4 Parameterization of large-signal black-box model

At this point, a linear structure has been identified such as that shown in Fig. 5-4. To build a large-signal model, the following actions are carried out, i.e.:

- Characterization of the static networks, including efficiency, load and line regulation and no load losses.
- Post-processing of un-terminated transfer functions, including the following actions:
 - Static response subtraction. Examples are shown below.

$$Y_{i0} = Y_i(s) - Y_i(0), H_{i0} = H_i(s) - H_i(0), \text{ etc.} \quad (5-31)$$

- Gain readjustment, only for gain-scheduled transfer functions. An example is shown below for the case of H_{id0n} (see Fig. 5-6, top part).

$$H_{id0n}(s) = H_{id0}(s) \cdot H_{id}(0)^{-1} \quad (5-32)$$

If one of the simplified structures shown in Fig. 5-6 (bottom part) and Fig. 5-7 is used, then the following equation should be applied.

$$H_{idL}(s) = H_{id}(s) \cdot V_{ssd} \cdot H_{id}(0)^{-1} \quad (5-33)$$

- Parameterize soft-start profile and enabling networks from manufacturer's data or measurements.

More details about each task are described in detail in section 4.3.4 on DC-DC converters, and are applied in an analogous manner to this case.

5.3.5 Overview of the identification procedure

Fig. 5-18 depicts an overview of the proposed identification process. Different colors are used for signals obtained from different identification experiments.

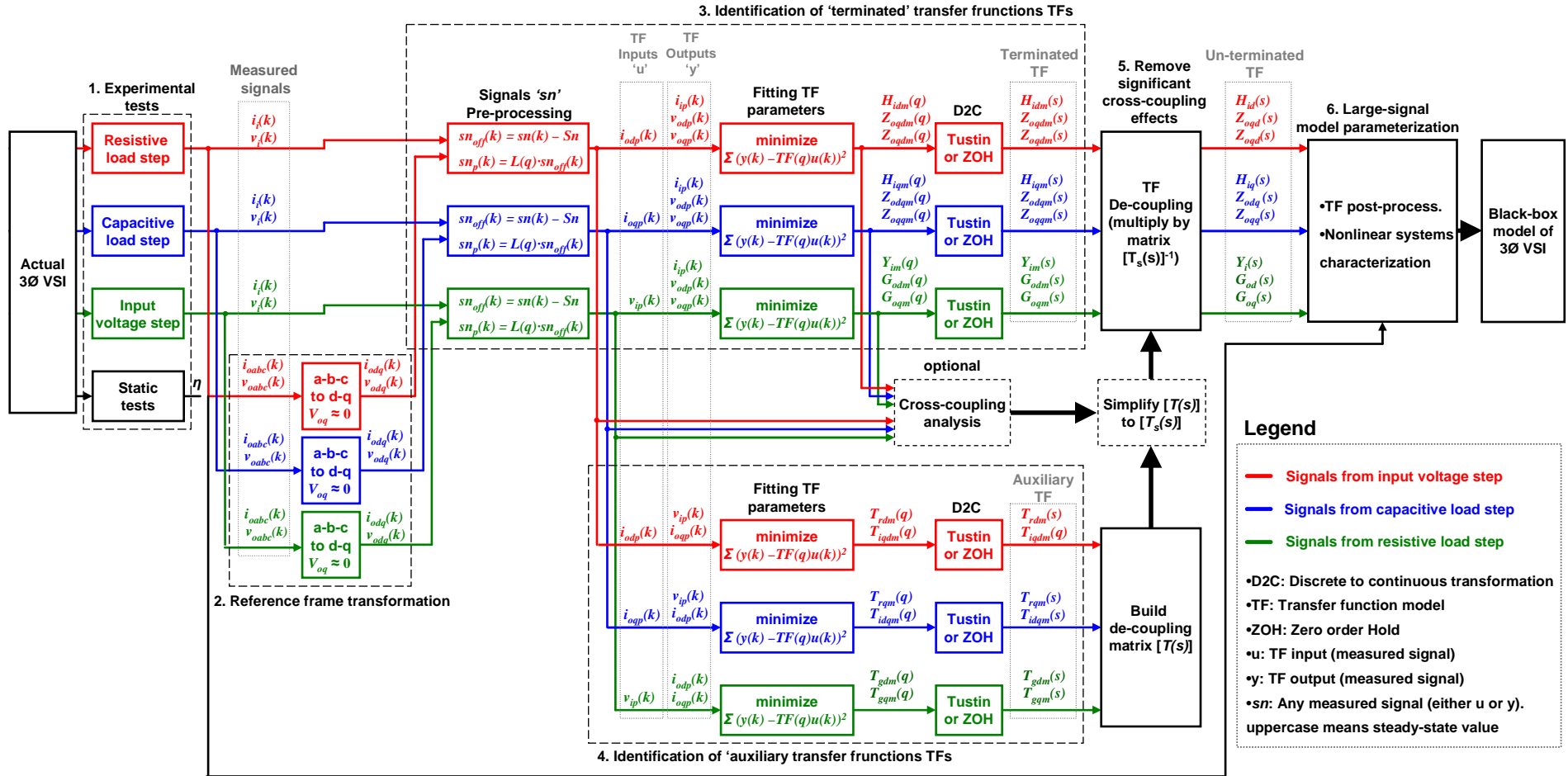


Fig. 5-18: Overview of the proposed identification process for large-signal black-box behavioral models of three-phase (3Ø) voltage source inverters (VSIs).

5.4 Simplifying the modeling and identification of the output impedance

The presented black-box modeling method covers any VSI structure such as that presented in Fig. 5-1. If the modeled converter is absolutely tackled as a black-box (i.e. there is no information about its internal structure), then a comprehensive analysis of linearity should be carried out over the full operating range, due to the relatively large number of interface signals and transfer functions involved in the modeling.

However, there is a power stage configuration which is typically applied in industry: **the three phase VSIs provided with input capacitive filter** [180]-[192]. This topology features the dynamic properties listed below, which allows simplifying both the modeling and identification procedure of the output impedance. It is worth remarking that the output impedance plays a critical role in terms of stability analysis. For instance, if stability analysis of an AC bus is required, they would be the only required transfer functions to identify.

- This topology features **linear properties at the output port**, so the output impedance is independent of I_{od} , I_{oq} . Therefore, if the power stage configuration is known in advance, then the analysis of linearity can be alleviated.
- If the VSI is provided with a **linear regulation scheme of the instantaneous voltage**, the **output impedance features orthogonal properties**. Such a type of control is widely used [180]-[192]. Thanks to the orthogonal properties, **only a single resistive load step is required to identify the output impedance**. This is of special interest if the modeling focuses on the three-phase AC port and the input port is not a matter of interest. For example, if the **stability of a three-phase AC bus** is studied.

5.4.1 Linear properties

The power stage under consideration is shown in Fig. 5-19. The linear regulation scheme performs linear operation on the measured AC signals and commands the modulator block. Although not shown, the switching bridge could comprise a four leg for neutral path connection or more levels in high voltage applications, as well as a low-frequency transformer.

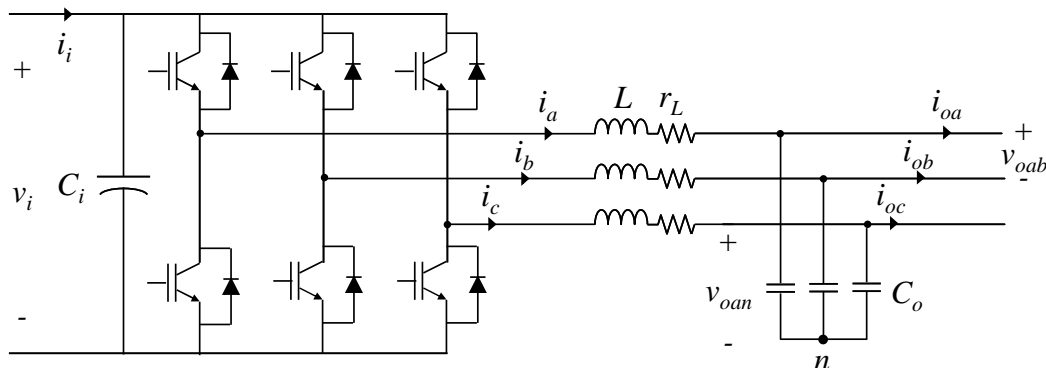


Fig. 5-19: Power stage of a three-leg, three-phase VSI with capacitive input filter (plant only).

By averaging the switching bridge, the equivalent circuit shown in Fig. 5-20 is obtained.

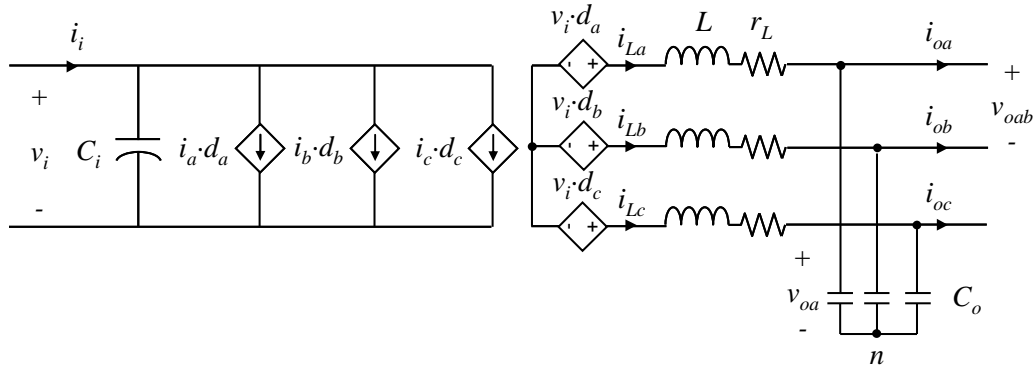


Fig. 5-20: a-b-c frame large-signal average model of the VSI (plant only).

The average model can be mapped into d - q frame by applying the Park's transformation (5-4) on the differential equations governing the plant dynamics. This yields the well known model shown in Fig. 5-21 [100], [177], [178], where both v_{od} and v_{oq} corresponds to d - q frame mapping of the AC line-neutral voltage and ω_o corresponds to the fundamental angular frequency. As can be seen, the d - q frame model is linear but cross-coupling between the d - q coordinates comes up. This results from the linear time-variant nature of the Park's transformation.

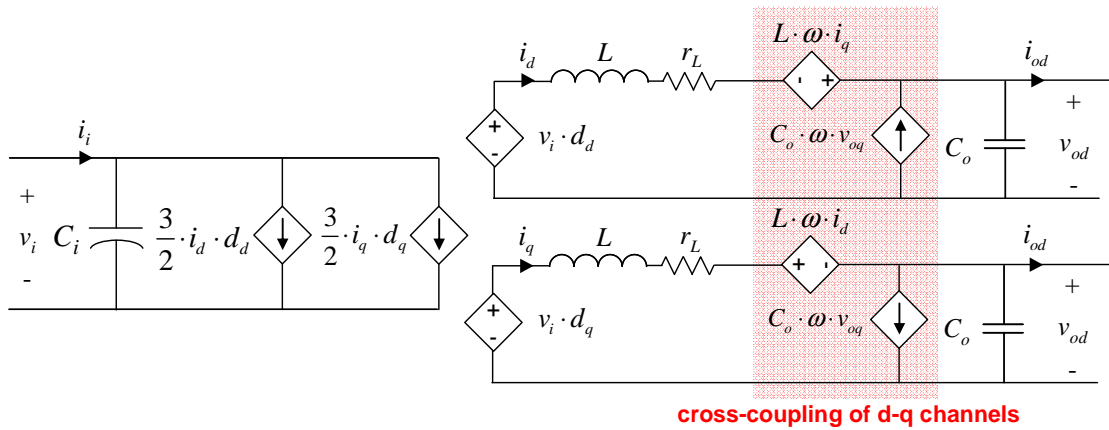


Fig. 5-21: d - q frame large-signal average model of the VSI (plant only).

As can be seen, the averaging process results in controlled sources, both at the input port and at the output port. Those sources depend on the multiplication on time-varying signals and therefore are responsible for the converter nonlinearity. However, at the output port, the nonlinearity is due to the input voltage multiplied by the duty cycle. Therefore, from analysis of this circuit, the following conclusions can be drawn.

- **L.1. The output impedance (Z_{odd} , Z_{odq} , Z_{oqd} and Z_{oqq}) is independent of I_{od} and I_{oq} .**

Essentially, this is because the output port of the average model is linear if v_i is kept constant. This statement is valid as long as no dynamics dependence on I_{od} , I_{oq} is introduced by the regulation.

5.4.2 Orthogonal properties

Further analysis of the d - q average model (Fig. 5-21) yields interesting observations. Consider that V_i is kept constant, so the output network is linear. Analysis of the node at the AC capacitor link and the mesh over the inductor results in (5-34) and (5-35), respectively, into Laplace domain.

$$V_i \cdot \begin{pmatrix} d_d(s) \\ d_q(s) \end{pmatrix} = \begin{pmatrix} Z_L(s) & -\omega_o \cdot L \\ \omega_o \cdot L & Z_L(s) \end{pmatrix} \cdot \begin{pmatrix} i_d(s) \\ i_q(s) \end{pmatrix} + \begin{pmatrix} v_{od}(s) \\ v_{oq}(s) \end{pmatrix} \quad (5-34)$$

$$\begin{pmatrix} i_d(s) \\ i_q(s) \end{pmatrix} = \begin{pmatrix} i_{od}(s) \\ i_{oq}(s) \end{pmatrix} + \begin{pmatrix} Y_{Co}(s) & -\omega_o \cdot C_o \\ \omega_o \cdot C_o & Y_{Co}(s) \end{pmatrix} \cdot \begin{pmatrix} v_{od}(s) \\ v_{oq}(s) \end{pmatrix} \quad (5-35)$$

As can be seen, every matrix into those expressions is featured by equal diagonal terms, whereas the off-diagonal terms only differ from each other by a minus sign. Hence, any of them can be expressed as follows, where m_a and m_b are any complex number.

$$[M] = \begin{pmatrix} m_a & -m_b \\ m_b & m_a \end{pmatrix} \quad (5-36)$$

M can be rewritten as follows, where $\det(M) = m_a^2 + m_b^2$.

$$[M] = \sqrt{\det(M)} \cdot \underbrace{\frac{1}{\sqrt{\det(M)}} \cdot \begin{pmatrix} m_a & -m_b \\ m_b & m_a \end{pmatrix}}_{[M_o]} \quad (5-37)$$

It is easy to verify that M_o fulfills the following equality (' T ' is the transposition operator).

$$[M_o^T] = [M_o^{-1}] \quad (5-38)$$

Consequently, $[M_o]$ is an orthogonal matrix [253]. Orthogonal matrixes feature the following properties (among others), which are of interest in this thesis.

- P_1 : Multiplication and summation of orthogonal matrixes result in other orthogonal matrix.
- P_2 : Inverting an orthogonal matrix yields other orthogonal matrix.

If the VSI is featured by a linear regulation scheme, then the output impedance will be linear. Moreover, if the regulation scheme can be expressed in terms of orthogonal matrixes, the output impedance will be determined by multiplication, summation and inversion of orthogonal matrixes into Laplace domain. Therefore, it will be orthogonal.

In practice, three-phase linear, vector regulation schemes usually comprise the same regulators for every controlled coordinate. That scenario results in regulation schemes determined by orthogonal matrixes, regardless of the reference frame. In those cases, the following statement applies.

- **O.1. The output impedance of three-phase VSIs with a linear and orthogonal control scheme feature orthogonal properties, meaning that $Z_{odd}(s) = Z_{oqq}(s)$ and $Z_{odq}(s) = -Z_{oqo}(s)$.**

This fact has a simple explanation. The α - β to d - q transformation (5-3) is linear, time-variant and orthogonal. Therefore, any linear, orthogonal system into α - β frame results in a linear, orthogonal system into d - q frame. However, the poles and zeroes into α - β frame are different from those into d - q frame.

From statement 'O.1.', the following statement follows.

- **O.2. If the output impedance of the VSI is linear and features orthogonal properties, no reactive power step is required to identify it. Therefore, a single resistive load step is sufficient.**

It is important to point out that 'linear control scheme' refers herein to schemes relying on linear relationship between the AC measured voltages and currents. Therefore, **orthogonal properties**

apply to linear, ‘vector’ control schemes but not to ‘scalar’ control schemes, such as RMS control or amplitude control [190], [191], [193]. Although those strategies are usually based on linear PI regulators, nonlinear operations are carried out on the AC voltage measurements to get the amplitude or RMS level. Therefore:

- **O.3. Orthogonal properties hold if the regulation scheme relies on linear operations on the AC measured voltages and currents.**

However, there are some exceptions to this rule. VSIs provided with inner fast nonlinear current control (such as hysteresis control or adaptive predictive control) and outer linear voltage control also features orthogonal output impedance. Those schemes usually feature an outer loop whose dynamics is much slower than that of the inner loop. As a consequence, below the time constant of the inner closed-loop, the reference current i_{ref} can be assumed to be proportional to the inductor current by a constant factor K_{cc} (see Fig. 5-22). In that case, the VSI essentially behaves as a programmable current source feeding the AC capacitor and the load, so the global dynamics of the regulation stage can be assumed to be linear, and then orthogonal properties also apply.

Table 5.1 illustrates some ‘vector’ and ‘scalar’ control schemes for three-phase VSIs, where R_v and R_i denotes LTI regulators, such as *PI* or *PR* regulators. For each case, whether the output impedance features orthogonal properties or not is indicated.

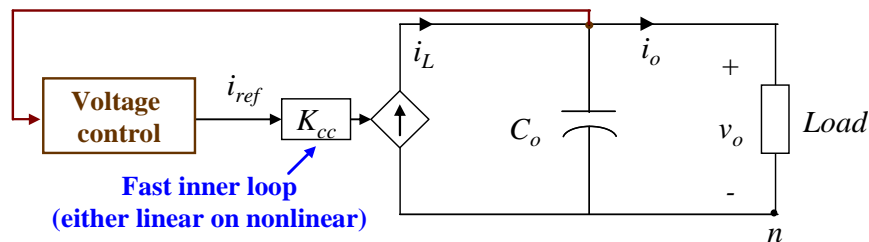


Fig. 5-22: simplified equivalent circuit of a VSI with fast inner current controller and a much slower outer voltage controller (only one phase is shown)

Of course, the orthogonal properties are not restricted only for those strategies, but also any linear, ‘vector’ strategy with symmetrical control parameters, that is, control strategies without the indicated feed-forward, decoupling networks or inner loops.

A three-phase VSI that fulfill the aforementioned requirements is evaluated through simulation in section 5.5 and analyzed theoretically in appendix A.1.2, thus illustrating the orthogonal properties herein described.

5.4.3 Limitations

Note that **this study assumes that the filter is absolutely balanced and neglects modulation dead-time effect on the VSI dynamics.** Consequently, modulation dead-time, tolerance in filter components, and other non-idealities have not been considered. Those may cause the output impedance to deviate from the orthogonal behavior, as well as a certain dependence on I_{od} and I_{oq} may arise. As demonstrated in [102], [194], such deviations from orthogonal behavior and dependences on operating point, can be evidenced specially in open-loop inverters at low-frequency.

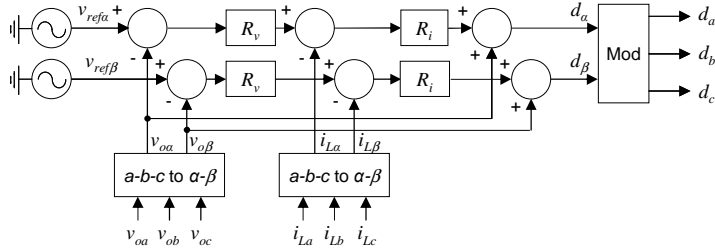
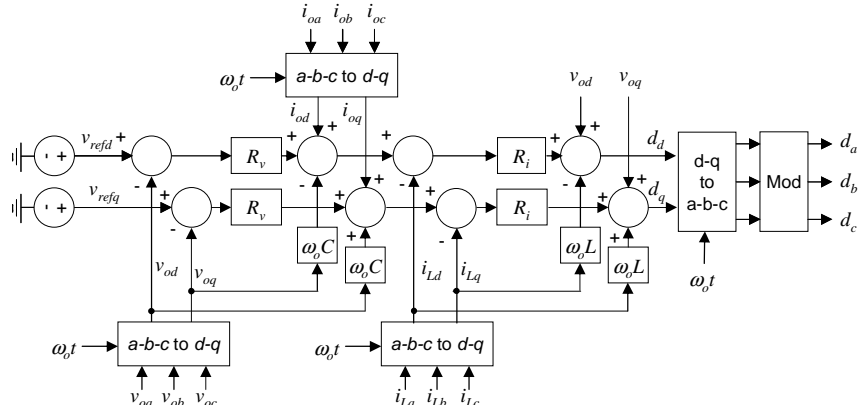
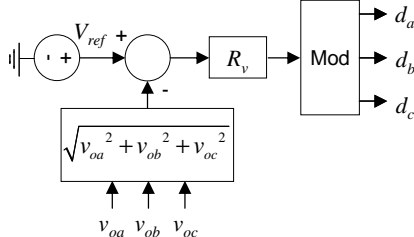
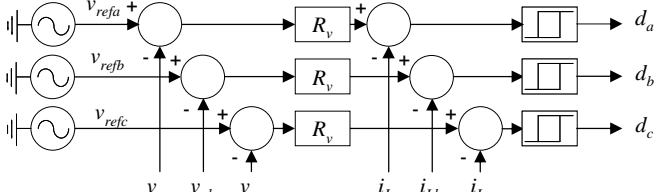
Control scheme	Is Z_o orthogonal?
	$Z_{odd}(s) = Z_{oqq}(s)$ $Z_{odq}(s) = -Z_{oqd}(s)$
a. α-β frame double-loop control with “back EMF de-coupling” [189].	YES
	$Z_{odd}(s) = Z_{oqq}(s)$ $Z_{odq}(s) = -Z_{oqd}(s)$
b. d-q frame double-loop control with d-q decoupling networks, load current feed-forward and “back EMF de-coupling” [182], [183].	YES
	$Z_{odd}(s) \neq Z_{oqq}(s)$ $Z_{odq}(s) \neq -Z_{oqd}(s)$
c. Magnitude controller (scalar controller) [190], [193].	NO
	$Z_{odd}(s) = Z_{oqq}(s)$ $Z_{odq}(s) = -Z_{oqd}(s)$
d. a-b-c frame double-loop control based on hysteresis current control [187].	YES

Table 5.1: Examples of control schemes for VSI and related orthogonal properties.

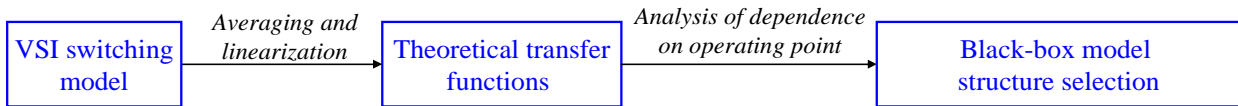
5.5 Simulation results

5.5.1 Introduction and system description

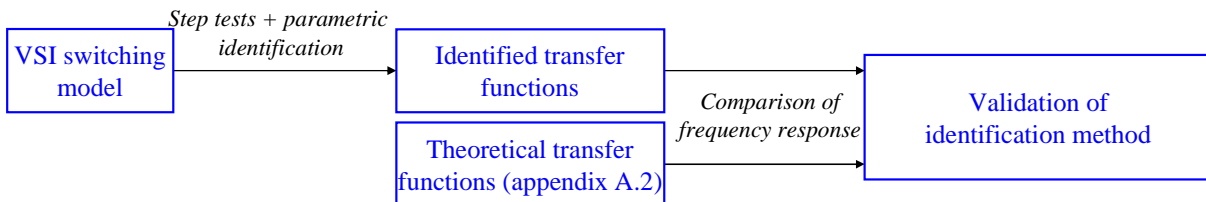
In this section, the proposed methods are illustrated and validated through simulation results.

- The identification process is illustrated and validated by comparing the frequency response of the identified transfer functions with the theoretical ones.
- The dynamic properties of VSIs, discussed in section 5.4, are demonstrated.
- The large-signal black-box model is validated through comparison of its response and the switching model response under a variety of large signal tests.

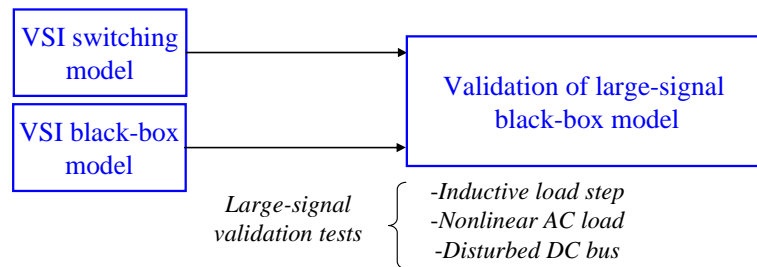
The followed procedure is illustrated in Fig. 5-23. In this section, the selection of the black-box model structure relies on a theoretical analysis. Other modeling aspects, such as the analysis of linearity and the cross-coupling problem, are experimentally tackled in the next section.



a. Black-box model structure selection (section 7.5.1).



b. Validation of identification method (section 7.5.2).



c. Validation of black-box model (section 7.5.3).

Fig. 5-23: Validation procedure through simulation results.

A three phase VSI has been modeled and simulated using PSIM (switching model). Its schematic is depicted in Fig. 5-24 and described below. It corresponds to that shown in Table 5.1a. More details are provided in appendix A.1.2.

- **General specification:** The VSI features $V_i = 750 \text{ V} \pm 10\%$, $V_o = 220 \text{ V RMS}$ line-neutral, $f_o = 50 \text{ Hz}$ and $f_{sw} = 12 \text{ kHz}$. The rated power is 7.5 kVA and the minimum power factor is 0.75 (inductive load) and 0.95 (capacitive load). It is intended to supply linear loads as well as a nonlinear load rated at 3.75 kW.
- **AC and DC filters:** The AC filter is comprised of 0.5 mH inductors ($\approx 0.008 \text{ pu}$) and 30 μF capacitors ($\approx 0.18 \text{ pu}$)^{5,6}. The inductor losses are emulated by a 100 m Ω series resistor. The input filter is comprised of a 2.2 mF electrolytic capacitor whose ESR = 40 m Ω .
- **Control stage:** The control stage is implemented in α - β frame and is comprised of an inner current loop, based on a PI compensator, and an outer voltage loop based on a PR compensator

^{5,6} Base impedance is $3 \cdot (220 \text{ V}_{\text{RMS}})^2 / 7.5 \text{ kVA} = 19.4 \Omega$.

[181]. The inner and outer loops feature 2 kHz and 500 Hz crossover frequency, respectively, both of them having 50° phase margin. This reference frame has been selected in order to illustrate how a VSI controlled into a stationary frame is modeled into the synchronous $d-q$ frame. Every signal is sampled two times per switching period, as suggested in [189], resulting in a sampling frequency $f_s = 24$ kHz. No quantization effects have been modeled. The unit delay, placed in front of the modulator, accounts for the one-cycle transport delay [189].

- **Modulation:** A triangle carrier based implementation of the continuous space-vector pulse width modulation (CSVPWM) has been utilized, where the zero sequence detection is based on the minimum magnitude test [195]. For the sake of simplicity, no dead time has been simulated.

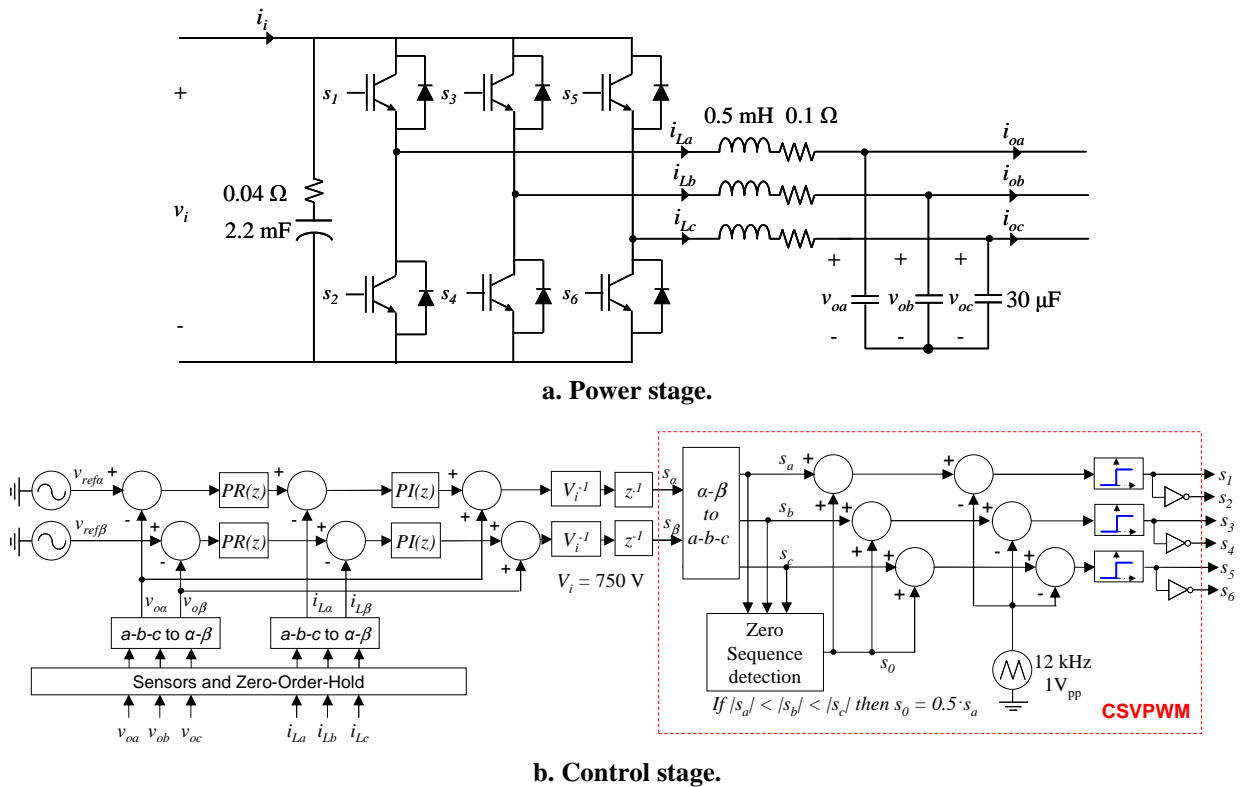


Fig. 5-24: Three-phase VSI simulated in PSIM (switching model).

5.5.2 Modeling

5.5.2.1 Linearity analysis

The selection of the black-box model structure relies on a theoretical analysis of the simulated VSI. Every transfer function, corresponding to the small-signal g-parameters model (see Fig. 5-4) has been derived (details are given in appendix A.1.2). This analysis allows deciding which type of dynamic network is appropriated for each case (i.e. single transfer function, gain-scheduled transfer function or LLMN). First, the $d-q$ frame working range is determined.

- **Output current range:** This is obtained from the active and reactive power ranges and the operating point of the output voltage, which is fixed. Since $V_{oq} \approx 0$ V, then V_{od} corresponds to the peak value of the phase-neutral voltage, i.e. $220 \cdot \sqrt{2}$ V. By using (5-9), the following operating range is obtained: $I_{od} \in [0, 16]$ A and $I_{oq} \in [-11, 5]$ A.

- **Input voltage rage:** The operating range is relatively narrow ($\pm 10\%$ of nominal voltage). Consequently, no dependences on V_i are considered, so $V_i = 750$ V.

Fig. 5-25 depicts the frequency response of the four transfer functions corresponding to the output impedance, i.e., $Z_{odd}(s)$, $Z_{odq}(s)$, $Z_{oqd}(s)$ and $Z_{oqq}(s)$. Since the input filter is capacitive, those transfer functions are independent of both I_{od} and I_{oq} . Moreover, the orthogonal properties are evident, as $Z_{odd}(j\omega) = Z_{oqq}(j\omega)$ and $Z_{odq}(j\omega) = -Z_{oqd}(j\omega)$. This is because the regulation scheme is linear and the parameters of all regulators are the same.

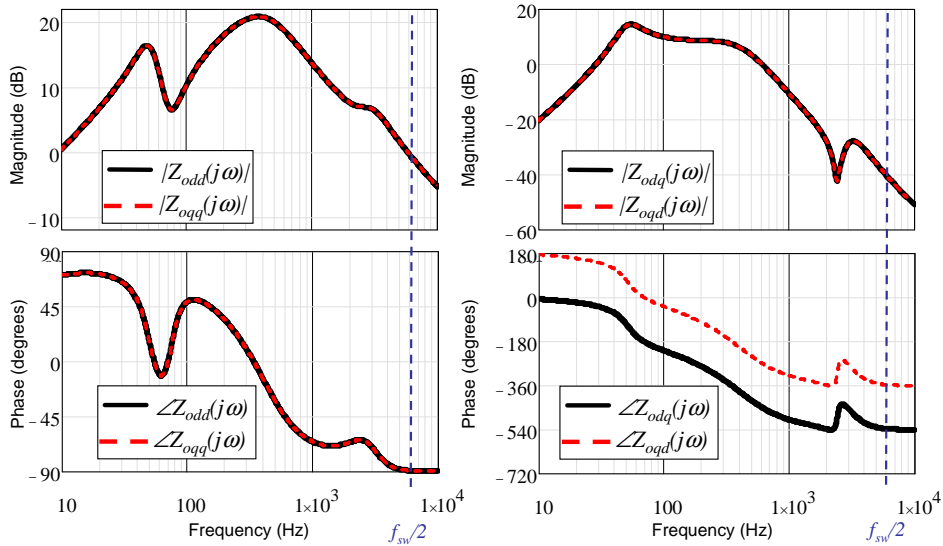


Fig. 5-25: Frequency response of the output impedance.

Fig. 5-26 shows the frequency response of $G_{od}(s)$ and $G_{oq}(s)$, evaluated on two I_{od} and I_{oq} boundary levels. Negligible dependence is found out.

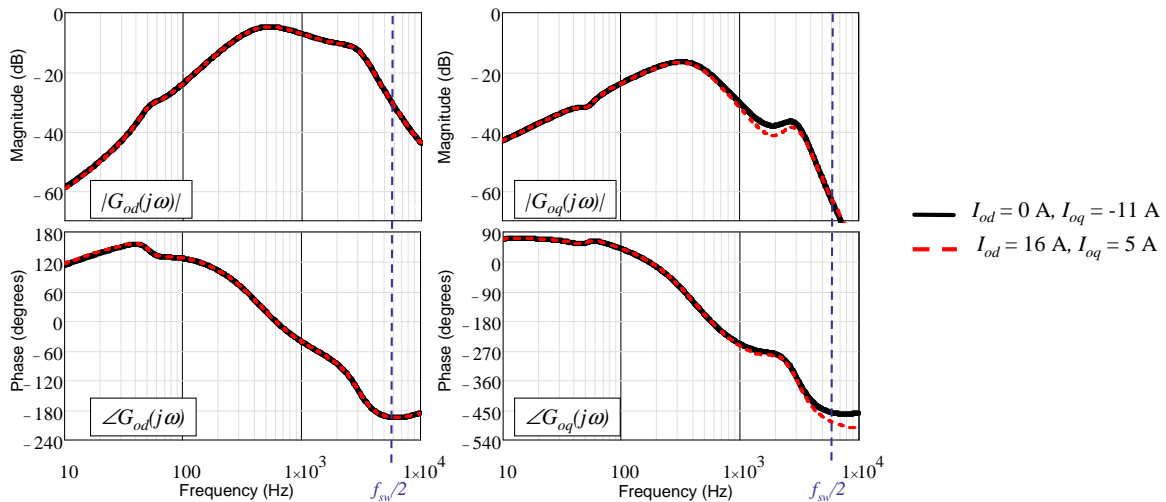


Fig. 5-26: Frequency response of the audiosusceptibility.

The frequency response of the back-current gain is depicted in Fig. 5-27. In this case, three boundary levels for the couple (I_{od}, I_{oq}) have been selected, so that the dynamic dependence on each current coordinate is analyzed separately. As can be seen, $H_{id}(s)$ depends only on I_{od} (dependence on I_{oq} is negligible), whereas $H_{iq}(s)$ depends on both I_{od} and I_{oq} . It is worth noticing that $H_{iq}(j\omega) < H_{id}(j\omega)$ for almost all frequencies (largest differences are found at low-frequency). This is

due to the fact that, as stated in section 5.2.4.2, $H_{id}(s)$ essentially accounts for dynamic variations of energy stored in the AC filter, whereas $H_{iq}(s)$ accounts not only for such a variations but also for power transferred from the input port to the AC load (because $V_{oq} = 0$).

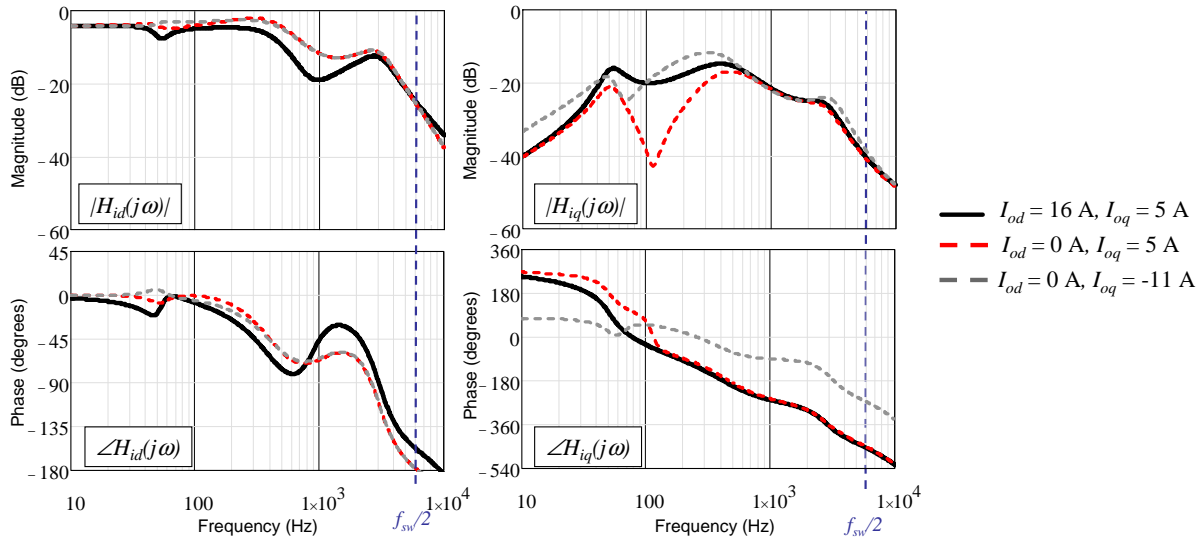


Fig. 5-27: Frequency response of the back-current gain.

Finally, the frequency response of the input admittance is plotted in Fig. 5-28 as a function of the operating point. As can be seen, it essentially behaves as a negative resistor in parallel with the input capacitor over the whole operating range.

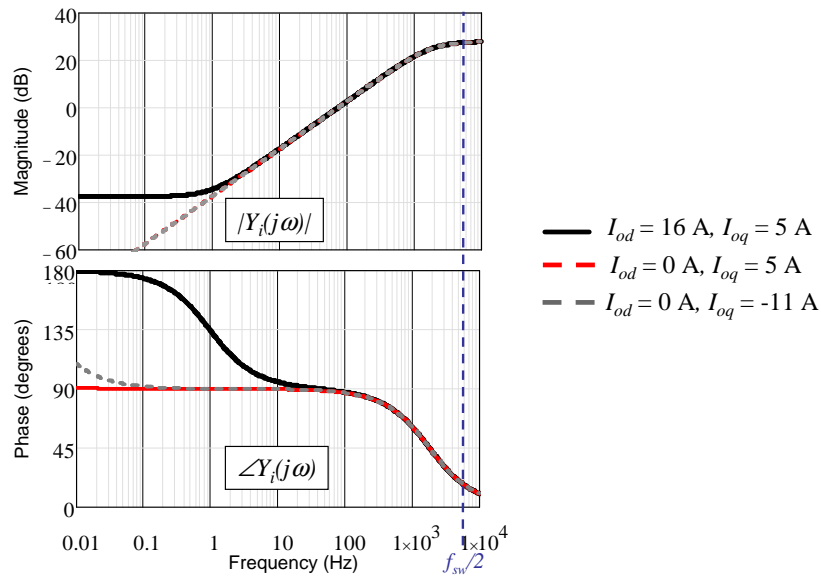


Fig. 5-28: Frequency response of the input admittance.

5.5.2.2 Dynamic networks selection

From the previous analysis, the model structure shown in Fig. 5-29 has been selected. It is justified below.

- **Z_{odd} , Z_{odq} , Z_{oqd} and Z_{oqq} :** A single transfer function is appropriate, as the impedance is independent of both I_{od} and I_{oq} . Moreover, the modeled VSI features orthogonal properties at the output port, so $Z_{odd}(s) = Z_{oqq}(s)$ and $Z_{odq}(s) = -Z_{oqd}(s)$.

- G_{od}, G_{oq} : A single transfer function is also a suitable choice, since the dynamic dependences on I_{od} and I_{oq} have been found to be negligible.
- H_{id} : Since the static regulation is almost perfect, the simplified structure shown in Fig. 5-6 is adopted. This accounts for the CPL behavior at low frequency. However, significant dynamic dependence on I_{od} has been found out so, instead of a single transfer function, a LLMN, whose output is scaled as a function of the input voltage, is used. As the nonlinearity is not very pronounced, the LLMN is only comprised of two local models, corresponding to $I_{od} = 0$ A and $I_{od} = 16$ A, respectively. Note that the efficiency is very high in this simplified example (the switches are ideal) so it is not explicitly added in the model.
- H_{iq} : This dynamic network depends on both I_{od} and I_{oq} . However, as $|H_{iq}(j\omega)| \ll |H_{id}(j\omega)|$ for all ω , it is not incorporated into the model for the sake of simplicity. Nevertheless, in order to validate completely the identification procedure, it will be identified.
- Y_i : It is modeled as a single transfer function, corresponding to the input filter. As explained before, this is because the CPL behavior, associated to the low-frequency negative resistance evidenced in Fig. 5-28, is already modeled by H_{id} .

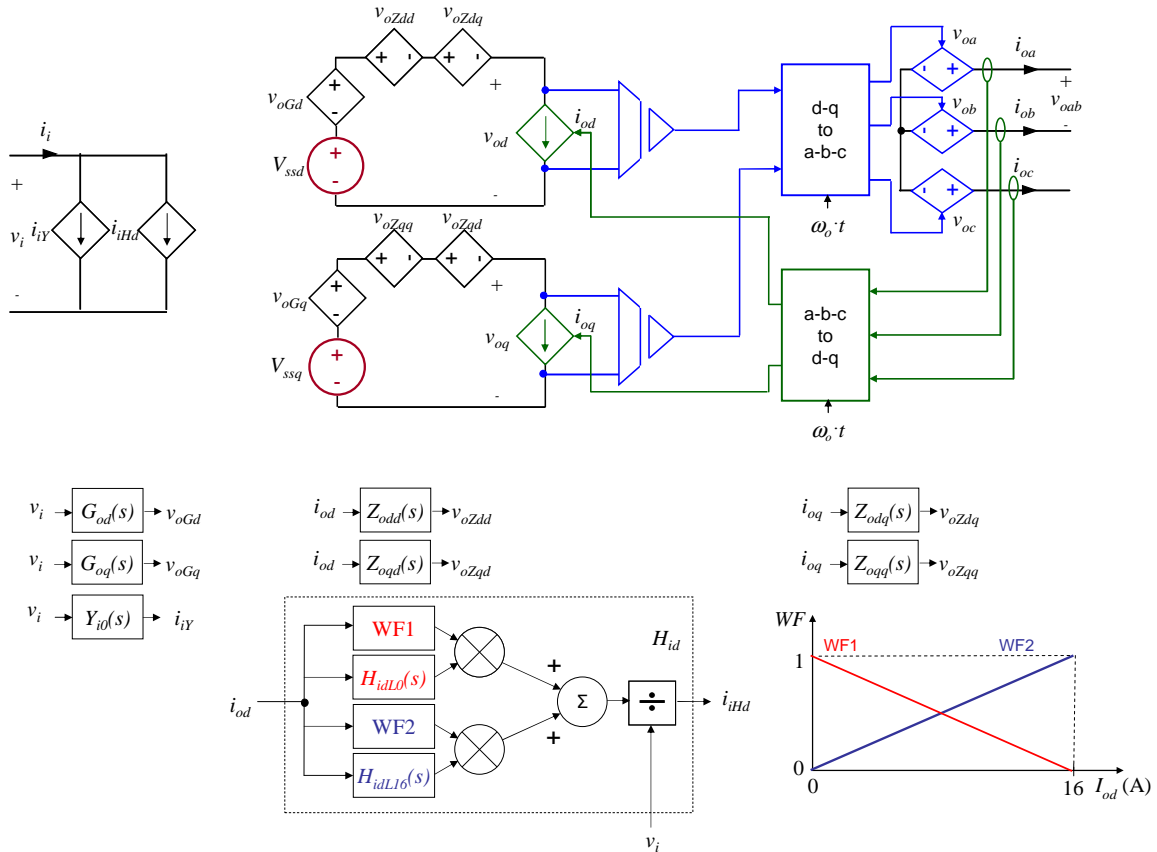


Fig. 5-29: Black-box model of the simulated VSI.

5.5.3 Identification

Once the model structure has been determined, the transfer functions into the model are identified. The DC power supply has been modeled as an ideal voltage source in series with a 5 m Ω resistance and a 1.5 μ H inductance. Such impedance is very small and does not make influence on the system dynamics, so no significant cross-perturbations of v_i are caused.

5.5.3.1 Resistive load step

First, a resistive load step has been applied from 1.8 kW to no load conditions. It corresponds to $R_2 = 80 \Omega$ line-neutral and $Z_l = \infty$ in Fig. 4-13. The sampling frequency has been set to a high value ($f_s = 100 \cdot f_{sw}$) in order to avoid aliasing^{5.7}. Later on, the obtained signals are pre-filtered and decimated.

The resulting waveforms are shown in Fig. 5-30. As can be seen, by setting the a - b - c to d - q transformation as proposed (i.e. $V_{oq} = 0$), the resistive load step results in stepping i_{od} . Moreover, since the step has been done to no-load conditions, cross-perturbations of the non-stepped current coordinate (i_{oq}) are absolutely prevented, as justified in section 5.3.3.3.

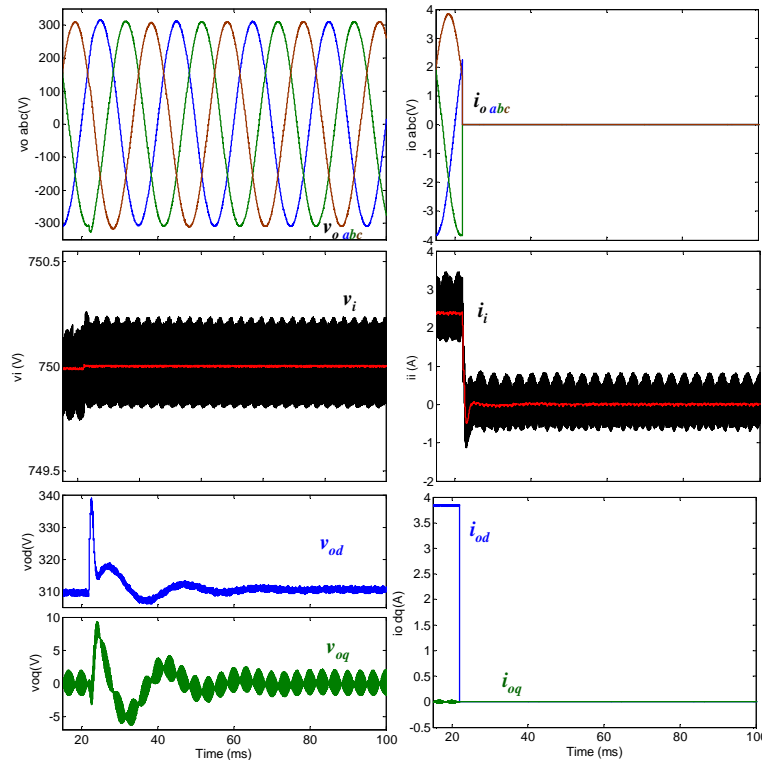


Fig. 5-30: Transient response of the simulated VSI to resistive load step from 1.8 kW to no-load (averaged signals in red).

Following this, $Z_{odd}(s)$, $Z_{odq}(s)$ and $H_{id0}(s)$ have been identified. It is important to remember that the parametric identification algorithms returns discrete transfer functions (defined as a function of operator ‘ q ’), which are later converted to continuous time domain. Note also that un-terminated transfer functions are directly obtained. This is because neither i_{oq} nor v_i have been disturbed, so no cross-coupling effects are caused.

Before applying the fitting algorithms, the signals have been filtered through MAF over a switching period. This way, the switching harmonics have been largely attenuated. After that, decimation has been applied as follows.

- In case of $H_{id0}(q)$, decimation by a factor 1/20 has been used (this results in a equivalent sampling frequency $f_s = 5 \cdot f_{sw}$).

^{5.7} This process is similar to that applied by the Tektronix oscilloscopes used in this thesis, when operating in high-resolution mode.

- In case of $Z_{odd}(q)$ and $Z_{oqd}(q)$, decimation by a factor 1/100 has been selected (equivalent $f_s = f_{sw}$). This is because the setting time of v_{od} and v_{oq} is larger due to a low frequency oscillation. Utilization of such a decimation factor results in better trade-off between high-frequency information, fitting performance and model order.

The coefficient of the transfer function has been fitted using the ‘oe’ function. The fitting results, evaluated using the function ‘compare’, are shown in Fig. 5-46. As can be seen, 5th and 6th order transfer functions yield accurate fits.

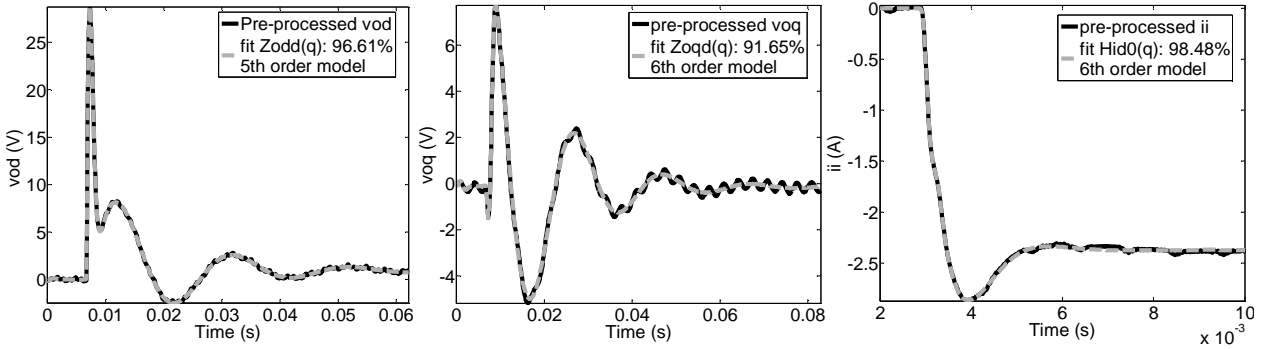
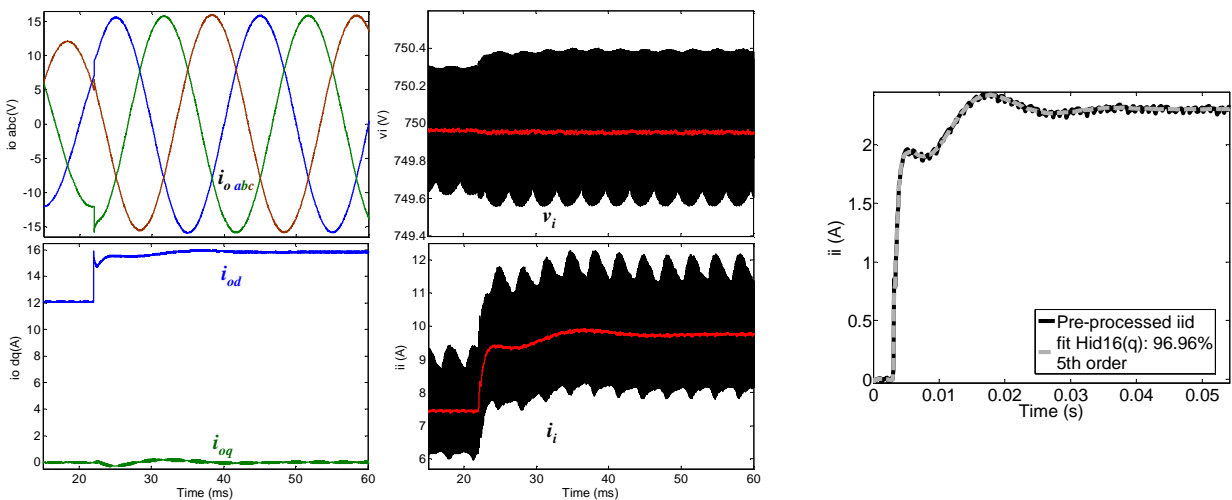


Fig. 5-31: Fitting results of Z_{ods} , Z_{oqd} and H_{id0} .

Note that a slight 300 Hz oscillation is found out in v_{oq} . This corresponds to low-frequency 5th and 7th harmonics mapped into d - q frame. Those harmonics do not play an important role in this simulated example, but they would be more important in other circumstances. A more detailed discussion about this is given in the experimental results section.

Following this, a resistive load switch-on has been applied from 5.7 kW to 7.5 kW, in order to identify $H_{id16}(s)$. The waveforms of interest are depicted in Fig. 5-32a. As a difference from the previous test, cross-perturbations of i_{oq} are caused, due to the non-null load after the step. However, it is negligible because $|H_{iq}(j\omega)| \ll |H_{id}(j\omega)|$ for all ω (see Fig. 5-27). The fitting results of $H_{id16}(q)$ are shown in Fig. 5-32b. In this case, the resulting sampling frequency after decimation is $f_s = f_{sw}$.



a. Transient response of the simulated VSI to resistive load step from 5.7 kW to 7.5 kW (averaged signals in red).

b. Fitting results of H_{id16} .

Fig. 5-32: Experimental tests and fitting results corresponding to the identification of $H_{id16}(q)$.

Finally, the performance of the identification method has been evaluated through comparison of the frequency response of the theoretical transfer functions and the identified ones (see Fig. 5-33). In all cases, very accurate fitting results are evidenced up to ≈ 1 kHz, which is high enough taking into account the dynamics timescale of the simulated VSI. It is important to point out that the step signal emphasizes low-frequencies over high-frequencies, and this is because, in general, certain deviation is observed at high frequencies.

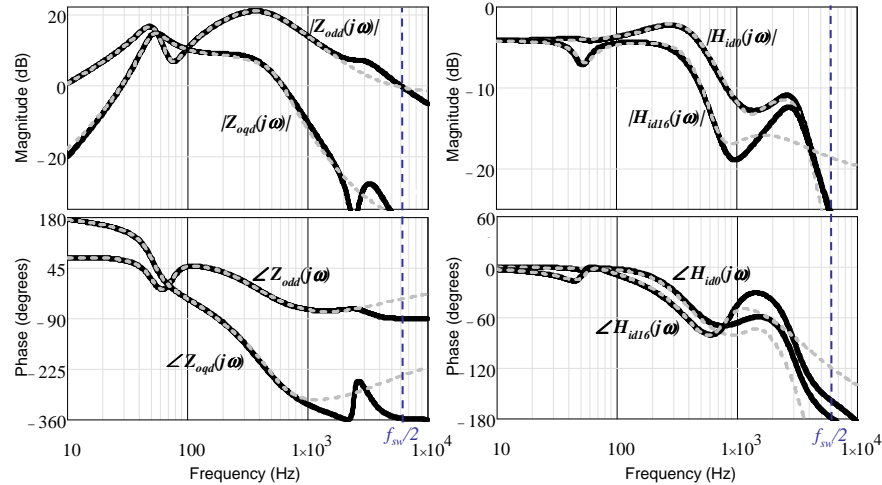


Fig. 5-33: Comparison of identified transfer functions (dashed grey lines) and theoretical ones (solid black traces) from the resistive load steps.

5.5.3.2 Capacitive load step

After that, a capacitive load disconnection has been carried out from 1.8 KVAR to no-load conditions. It corresponds to $C_2 = 40 \mu\text{F}$ line-neutral and $Z_l = \infty$ in Fig. 5-13.

It is important to remark that the switched capacitor must fall within the capacitive load range allowed by the VSI, as otherwise stability problems may come up. Fig. 5-52 shows the resulting waveforms.

As can be seen, the output current exhibits large switching ripple content. This is because the switching harmonics of the inductor current are shared among both the capacitive load and the AC filter capacitor. Compared to the previous resistive load step, shown in Fig. 5-30, the following observations can be done.

- The transient response of v_{oq} is equal to that of the previous v_{od} , whereas v_{od} exhibits symmetry over the time axis with respect to the previous v_{oq} . This is a clear indicator of the orthogonal properties exhibited by the tested VSI.
- The transient response of i_i exhibits much smaller magnitude than the previous one, which evidences that $|H_{i_q}(j\omega)|$ is much lower than $|H_{i_d}(j\omega)|$ mainly at low-frequency.

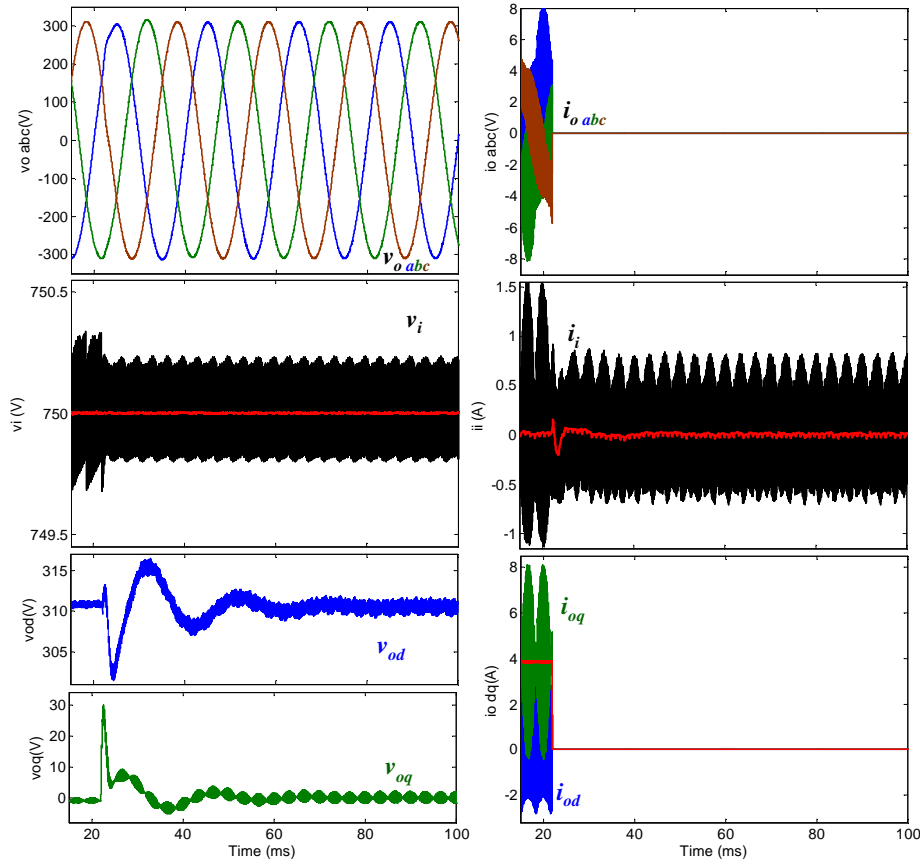


Fig. 5-34: Transient response of the simulated VSI to capacitive load step from 1.8 kVar to no-load (averaged signals in red).

Following this, transfer function models corresponding to $Z_{oqq}(s)$, $Z_{odq}(s)$ and $H_{iq}(s)$ have been identified. Actually, due to the orthogonal properties, it is not necessary to identify any impedance transfer function from this test. Nevertheless, $Z_{oqq}(s)$ and $Z_{odq}(s)$ are herein identified in order to carry out a complete evaluation of the proposed identification method.

The fitting results are shown in Fig. 5-35^{5.8}. As can be seen, highly accurate results have been achieved in case of $Z_{odd}(q)$ and $Z_{oqq}(q)$, as the correlation is above 93%. In case of $H_{iq}(q)$, the correlation is lower, but this is because the signal to noise ratio (SNR) is relatively high. Nevertheless, the average response of the pre-processed i_i is well fitted by the identified model.

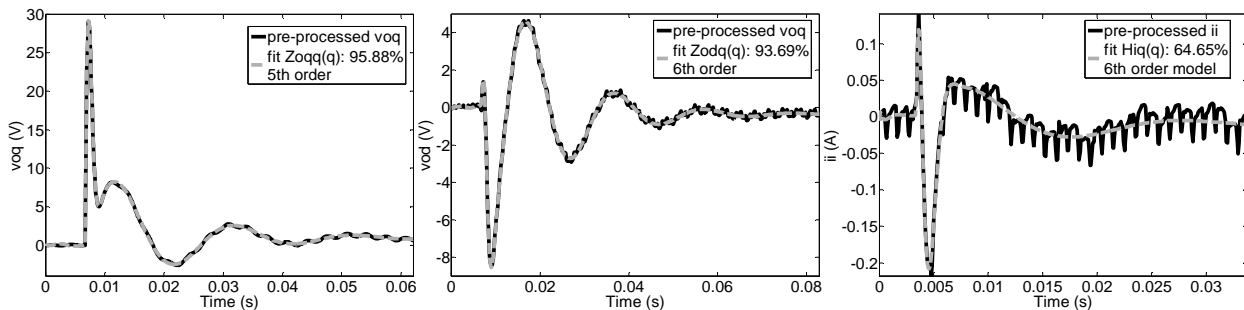


Fig. 5-35: Fitting results of Z_{oqq} , Z_{odq} and H_{iq} .

The theoretical transfer functions are compared to the identified ones in Fig. 5-36. As can be seen, accurate results have been achieved for both $Z_{oqq}(s)$ and $Z_{odq}(s)$ up to ≈ 1 kHz. In case of $H_{iq}(s)$, larger

^{5.8} Every signal has been averaged over one switching period, followed by decimation by a factor 1/100.

differences are observed, which are attributed to the strong $H_{iq}(s)$ dependence on I_{oq} . To illustrate that, the theoretical frequency response corresponding to both the initial and the final values of i_{oq} have been plotted (that is, $I_{oq} = 4$ A and $I_{oq} = 0$ A).

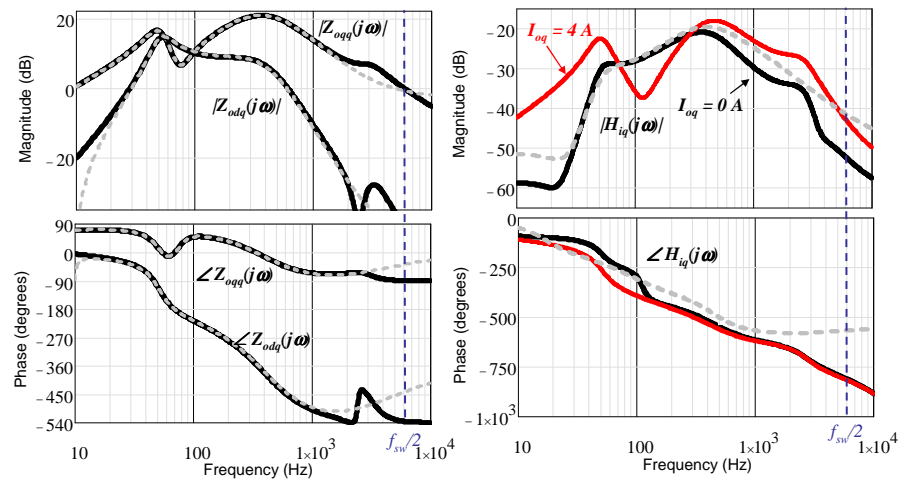


Fig. 5-36: Comparison of identified transfer functions (dashed grey lines) and theoretical ones (solid traces) from the capacitive load switch-off.

5.5.3.3 Input voltage step

Finally, the input voltage step has been applied to identify the remaining transfer functions. In order to prevent cross-perturbations of the current, the step has been carried out at no load conditions. On the other hand, a 5 % step magnitude has been chosen to keep nearly linear local conditions. The step has been carried out by using an array of diodes in parallel with a Mosfet (Fig. 5-14a), whose internal resistance is 20 mΩ.

Fig. 5-37 shows the simulation results. As can be noticed, the dynamic response under the v_i step is much faster than that under load steps. This is because the audio-susceptibility of the VSI is essentially determined by the inner current loop.

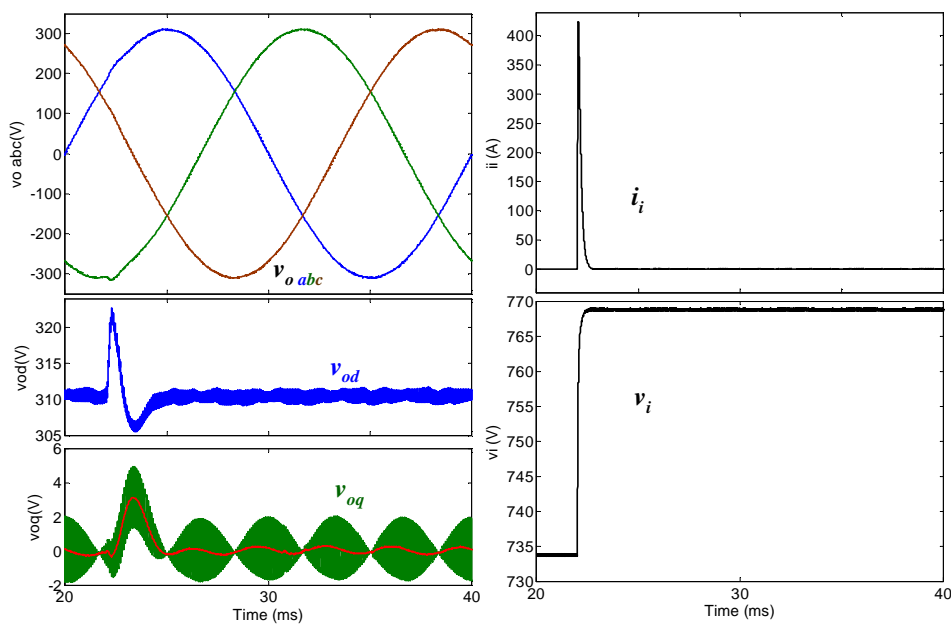


Fig. 5-37: Transient response of the simulated VSI to an input voltage step at no load conditions (averaged signals in red).

The identification results are evaluated in Fig. 5-38. Accurate fittings have been achieved, as the correlation is above 96% in all cases. In this case decimation was done by a factor 1/20, yielding an equivalent sampling frequency $f_s = 5 \cdot f_{sw}$. The comparison of theoretical and identified transfer functions is shown in Fig. 5-39. The identified and the theoretical frequency responses are quite similar, being particularly close in case of $Y_i(j\omega)$ and $G_{od}(j\omega)$.

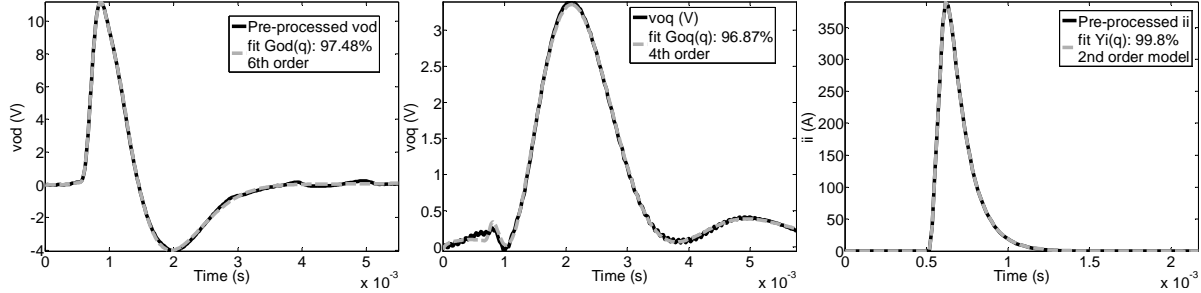


Fig. 5-38: Fitting results of G_{od} , G_{oq} and Y_i .

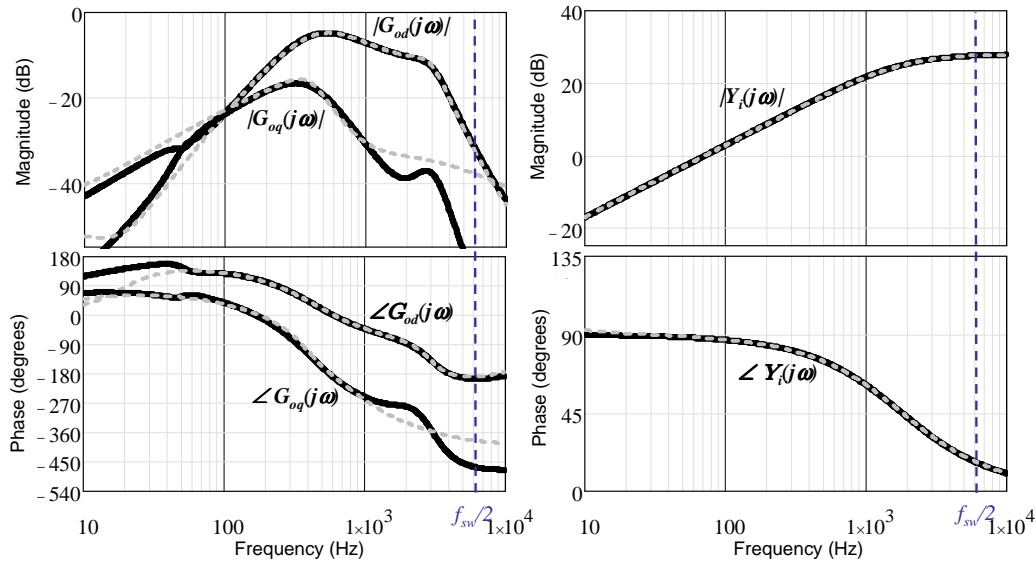


Fig. 5-39: Comparison of identified transfer functions (dashed grey lines) and theoretical ones (solid black traces) from the input voltage step.

As a conclusion, the **proposed identification method, based on step tests and parametric identification, has been illustrated and proven to be a simple and effective solution.**

Finally, the identified transfer functions, corresponding to the input port, have been post-processed according to (5-31) and (5-33), yielding the transfer functions that compose the large-signal black-box model.

5.5.4 Validation

For validation purposes, both the black-box model and the switching model have been subjected to a variety of large signal tests, and the resulting responses have been compared to each other. It is important to remark that the validation tests are different from the identification ones. This allows validating the following aspects.

- The model addresses the large-signal average behavior of the three-phase VSI.

- The un-terminated transfer functions into the black-box model have been properly identified.

5.5.4.1 Validation test 1. Large inductive load step

Firstly, a large RL load step, from no-load to rated power, has been applied. This way, both i_{od} and i_{oq} are simultaneously perturbed in a large signal sense. Moreover, the slew rate of both coordinates is severely limited by the inductive part of the load. Additionally and V_i has been decreased to 700 V and a series RL cell has been located at the input port, in order to perturb v_i simultaneously. The simulated test is depicted in Fig. 5-40.

The resulting waveforms are shown in Fig. 5-41. As can be seen, the black-box model response is very close to the switching model response. The fit is very accurate in case of the output voltage, which **corroborates both the linear and the orthogonal properties of the output impedance**. However, **slight deviations are observed in the input current**. Such a deviation is attributed to the H_{id} dependence on I_{od} , which is just roughly approximated by the LLMN.

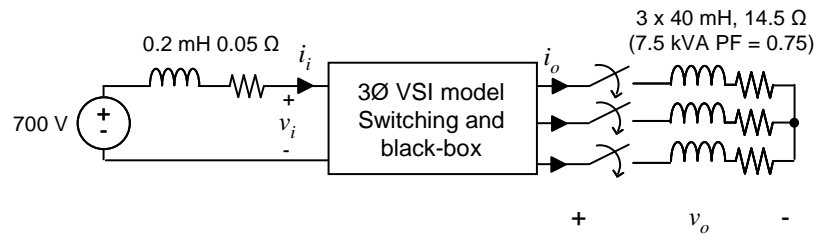


Fig. 5-40: Validation test 1. Large RL step load with series RL cell at the input.

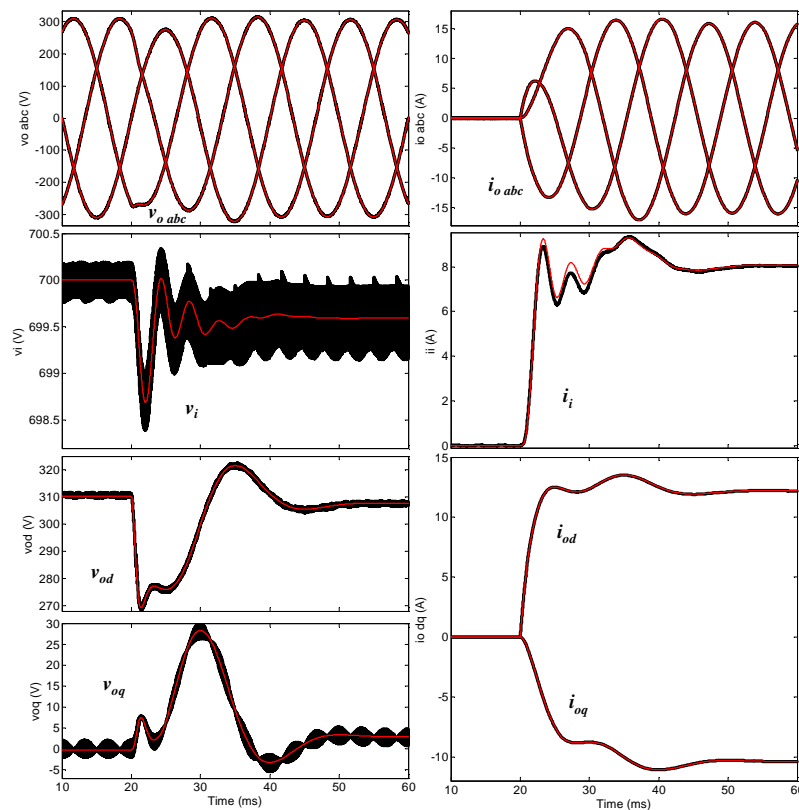


Fig. 5-41: Validation test 1. comparison of switching model response (dark lines) and black-box model response (red lines).

5.5.4.2 Validation test 2. Nonlinear load

As a second validation test, a nonlinear load, consisting of a diode bridge provided with LC output filter, has been located at the output port in parallel with a linear load (see Fig. 5-42). Initially, the power delivered to the nonlinear load is low (only 500 W), but this power is stepped up to 3.75 kW after some milliseconds. This causes a large distortion of the output current due to low frequency harmonics (5^{th} , 7^{th} , 11^{th} , 13^{th} , etc.) [193]. Moreover, a RL cell, different from that used before, has been located at the input port, and the input voltage has been increased up to 800 V.

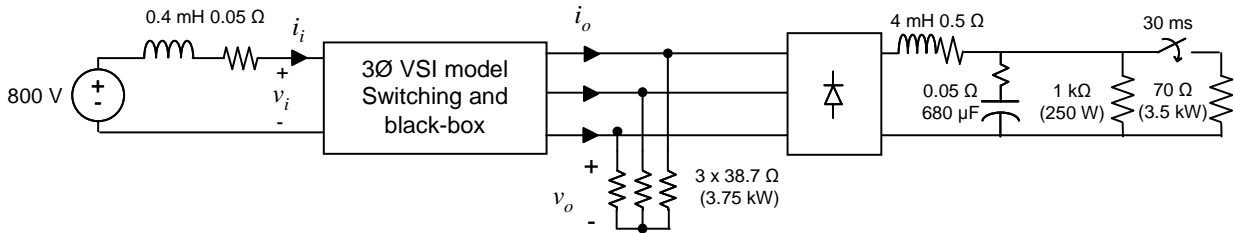


Fig. 5-42: Validation test 2. Step increase in nonlinear load power.

The simulation results are shown in Fig. 5-43 and discussed below.

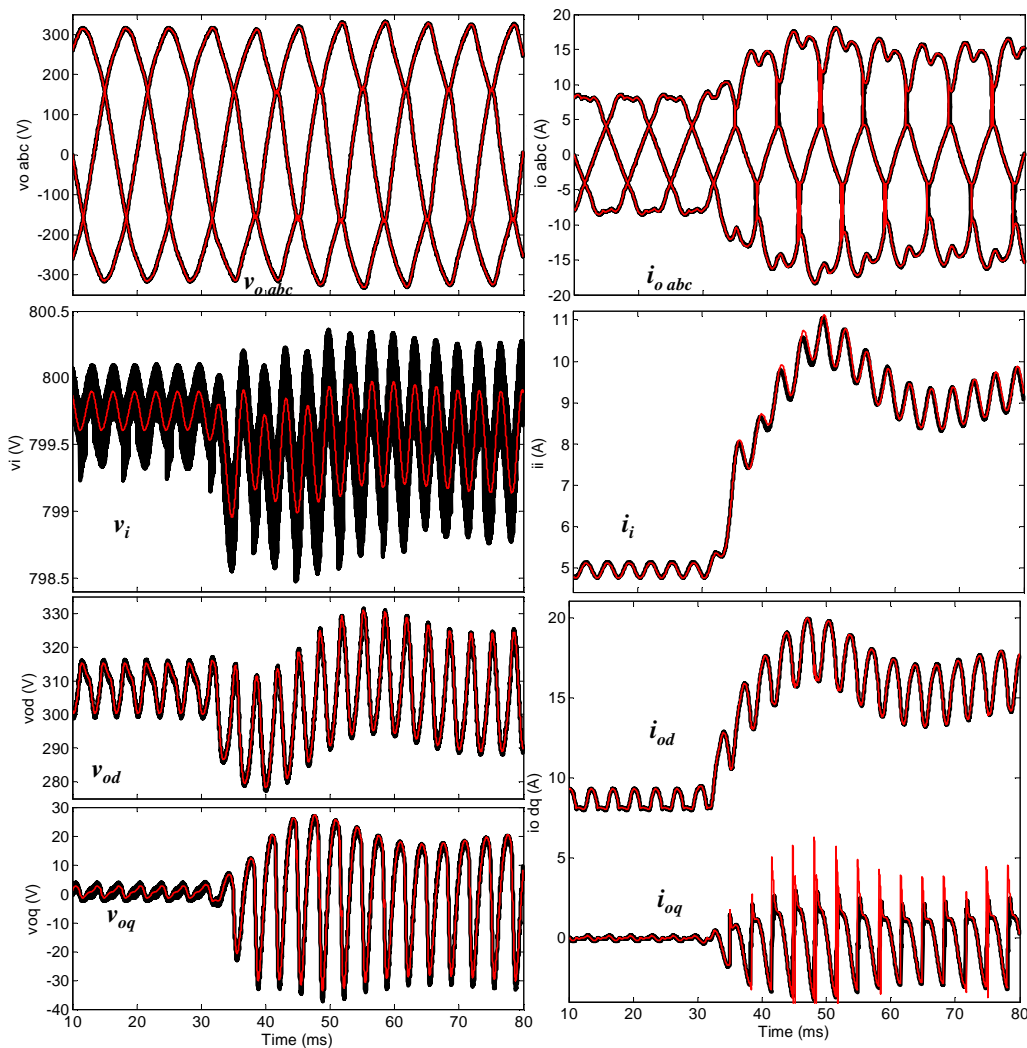


Fig. 5-43: Validation test 2. Comparison of switching model response (dark lines) and black-box model response (red lines).

The output voltage and input current is distorted due to the harmonics drawn by the nonlinear load. In fact, v_{od} and v_{oq} exhibits a dominant harmonic at 300 Hz, which corresponds to both the negative sequence 5th harmonic and the positive sequence 7th harmonics, mapped into d - q frame. Such a 300 Hz oscillation means an active power oscillation and is therefore reflected in i_i .

At the beginning of the simulation, the harmonic distortion is relatively slight. After the nonlinear load power is increased (30 ms), the distortion is significantly increased. As can be seen, **the black-box model predicts accurately not only the new voltage and current distortion, but also the transient evolution of them.**

5.5.4.3 Validation test 3. Disturbed DC bus

The final validation test consists in disturbing the input DC bus with low frequency harmonics. This way, the predicting capabilities of the model under distorted DC bus can be evaluated.

The DC bus has been modeled as a 750 V_{DC} source in series with AC sources corresponding to 50 Hz, 150 Hz, 250 Hz and 350 Hz. The magnitudes of the AC sources have been set to 15 V_p, 10 V_p, 8 V_p and 5 V_p, respectively. This results in large v_i oscillation between 700 V and 800 V. Additionally, a load switch-off is applied at 20 ms. Such a large distortion may not be realistic, but put the simulated VSI into challenging conditions and therefore allows evaluating the predicting capabilities of the black-box model. The test is illustrated in Fig. 5-44.

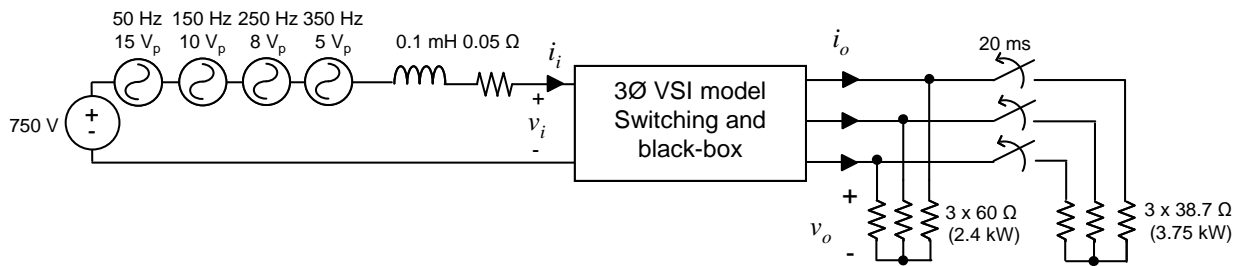


Fig. 5-44: Validation test 3. Step increase in nonlinear load power.

The comparison between the switching model response and the black-box model response is shown in Fig. 5-45. As can be seen, the oscillation of the DC bus is reflected at the output voltage through the audiosusceptibility. The input current also exhibits large oscillation, essentially corresponding to the power flowing through the input capacitor. **The black-box model addresses both the steady-state distortion of every signal but also the transient evolution after the load is switched-off.**

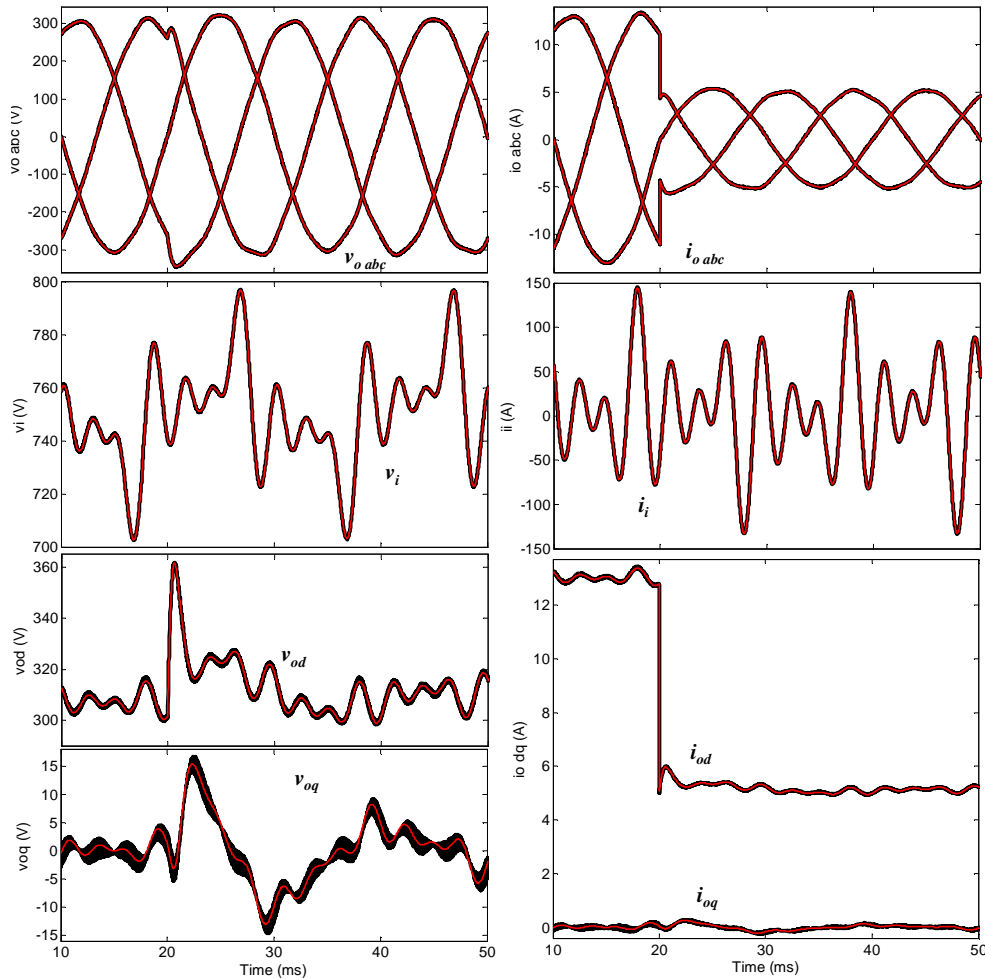


Fig. 5-45: Validation test 3. Comparison of switching model response (dark lines) and black-box model response (red lines).

5.5.5 Summary

In this section, the modeling and identification methods have been validated. The properties for the output impedance, discussed in section 5.4, have been evaluated as well.

- A VSI provided with linear control of the ‘instantaneous’ AC waveform, into α - β frame, has been analytically modeled into d-q frame using small-signal techniques. The properties of the output impedance, regarding linearity and orthogonally, have been corroborated.
- From the small-signal analysis, a suitable large-signal behavioral black-box model structure has been deduced, comprised of transfer function models and a gain-scheduled LLMN. The gain-scheduled LLMN addresses both the low-frequency CPL behavior of the VSI and the input-output power transference.
- The model has been completely identified by applying step tests. The performance of the identification method has been evaluated by comparing the frequency response of the identified transfer functions with those derived theoretically. Good agreement was found, although slight differences were observed at high frequency (above 1/10 the switching frequency).
- Finally, both the black-box model and the switching model have been subjected to large signal tests (large passive load steps, nonlinear load steps and DC bus with large distortion). The good

agreement between the switching model response and the black-box model response has demonstrated the good performance of the proposed solution, at least under the tested control scheme.

5.6 Experimental results

5.6.1 Introduction and system description

In this section, the proposed method is experimentally validated. As a difference from the simulated case study, no details about the internal elements of the converter are available. Therefore, the black-box model is completely derived only by making use of measurements. Issues not tackled in the previous section, such as the experimental analysis of linearity and the cross-coupling problem, are herein discussed. Moreover, other concerns such as noise measurements and low-frequency harmonics are also tackled.

The modeled three-phase VSI (see Fig. 5-46) is oriented to more-electric-aircraft systems and complies with the MIL-STD-704F aircraft regulation [263]. The converter features three phase regulated output voltage $V_o = 115$ V AC line-neutral at 400 Hz, and input voltage ranging from 250 V_{DC} to 280 V_{DC}. The rated power is 5 kVA and the power factor ranges from 0.95 (capacitive) to 0.75 (inductive).



Fig. 5-46: Three phase 5 kVA Voltage Source Inverter by Ingeniería Viesca S.L.

The VSI is implemented in a test bed of a MEA power system by EADS, which is described in [16], [17]. The experimental system under study, which is part of the whole test bed, is depicted in Fig. 5-47. It consists of a 40 kW line-commutated rectifier, which delivers power from the 3 \emptyset utility grid to a 270 V_{DC} DC bus, and a three-phase loads bank comprised of balanced resistive, inductive and capacitive loads.

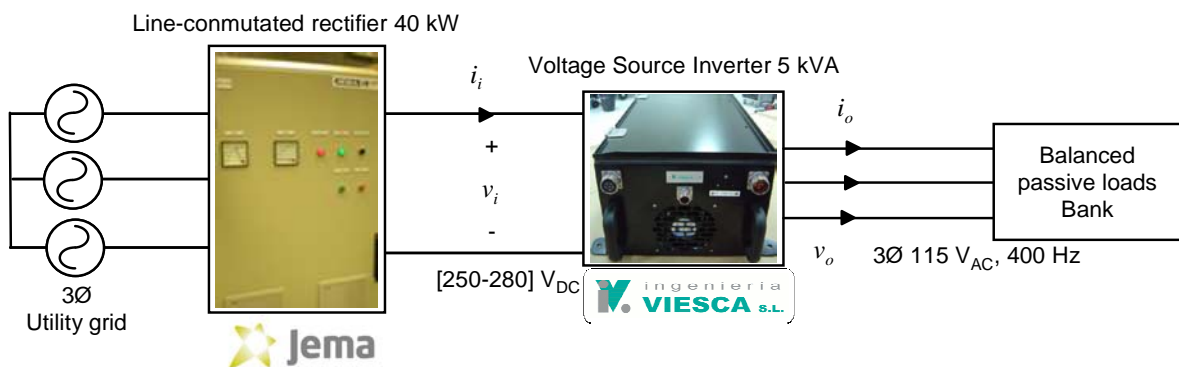


Fig. 5-47: Schematic of experimental system (part of a MEA test bed).

The data acquisition equipment consists of two synchronized Tektronix oscilloscopes MSO4104 and TDS5104, working in high resolution mode. The sampling frequency was set to a relatively high value, $f_s = 1$ MHz. Later on, after checking that $f_{sw} \approx 20$ kHz, the measurements were re-sampled to 100 kHz (five times f_{sw}). In all cases, the line AC current i_o , the line-neutral AC voltage v_o , the DC current i_i and the DC voltage v_i have been measured.

5.6.2 Modeling

5.6.2.1 Preliminary tests: linearity analysis

First, the dynamics dependence on the operating point has been evaluated, in order to select either a linear or a nonlinear approach for each dynamic network.

The allowed voltage range for the 270 V_{DC} bus is narrow, according to MIL-STD-704-F (from 250 V to 280 V at steady state). Hence, for the sake of simplicity, no dynamic systems dependence on the input voltage operating point, V_i , has been considered. Therefore, only dependences on the output current, I_{od} , I_{oq} have been evaluated.

The analysis of H_{id} , Z_{odd} , Z_{oqd} dynamics dependence on I_{od} is illustrated in the following paragraphs. This analysis has been carried out by stepping a 1.1 kW fixed resistive load, ‘ R_2 ’, while different initial active power levels were set by ‘ Z_1 ’ (refer to Fig. 4-13). Every load step has been performed using mechanical contactors.

Fig. 5-48 shows the response of the VSI to a resistive load step from 3.3 kW to 4.4 kW. As can be seen, stepping a resistive load means stepping i_{od} . However, notice that v_{od} and v_{oq} exhibit a significant ripple which may affect not only the identification process but also the analysis of linearity. This ripple is not only due to the switching harmonics but also to low-frequency harmonics, and deserves a discussion.

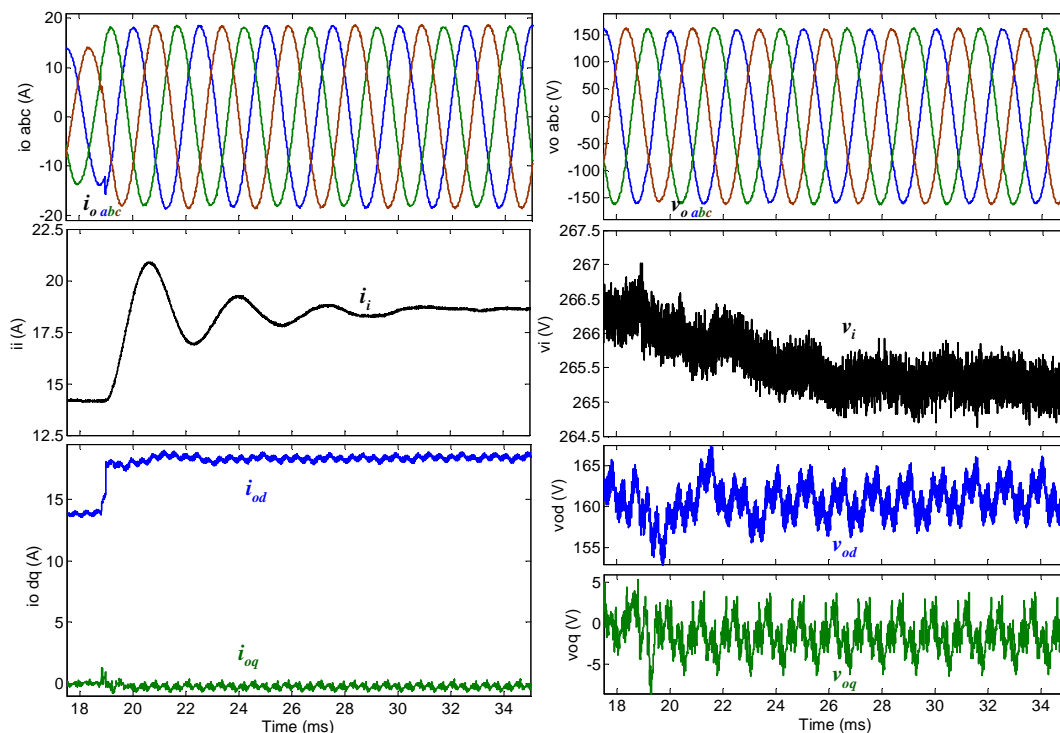


Fig. 5-48: Transient response of the VSI to a resistive load step from 3.3 kW to 4.4 kW ($R_1 = 11\Omega$).

Fig. 5-49a shows the DFT of V_{od} (steady-state). As can be seen, such a ripple is mainly due to even harmonics of the fundamental frequency. This is because odd harmonics into the a - b - c frame are reflected as even harmonics into the d - q frame. The most relevant low-frequency harmonics are found out at 800 Hz and 2400 Hz. This fact may be expected. 800 Hz corresponds to negative-sequence at the fundamental frequency due to a slight voltage unbalance ($\approx 1\%$). 2400 Hz corresponds to the d - q representation of the negative-sequence 5th harmonic combined with the positive-sequence 7th harmonic. Those are due to dead-times and other non-idealities. On the other hand, the dominant switching harmonic is found out at 19.2 kHz.

Therefore, selective harmonic cancellation filters are well suited to pre-filter the d - q signals. The MAF is a simple smoothing filter which not only exhibits a fast step response but also can be used to perform selective cancellation of even harmonics, as has been discussed in chapter 4. Through an adequate selection of the averaging window, the low-frequency harmonics can be cancelled out at the expense of less model identifiability within the filtered bandwidth. The frequency response of MAF (magnitude) is reminded below. More details can be found in section 4.4.4.1.

$$|MAF(f)| = \frac{1}{M} \left| \frac{\sin(\pi \cdot M \cdot f \cdot f_s^{-1})}{\sin(\pi \cdot f \cdot f_s^{-1})} \right| \quad (5-39)$$

From this expression one can find that every harmonic multiple of f_s/M is suppressed, where M is the number of averaged samples. Thus, since $f_s = 100$ kHz, choosing $M = 125$ leads to cancellation of every harmonic multiple of 800 Hz (see Fig. 5-49b). The use MAF to cancel out low-frequency harmonics is reported in [175].

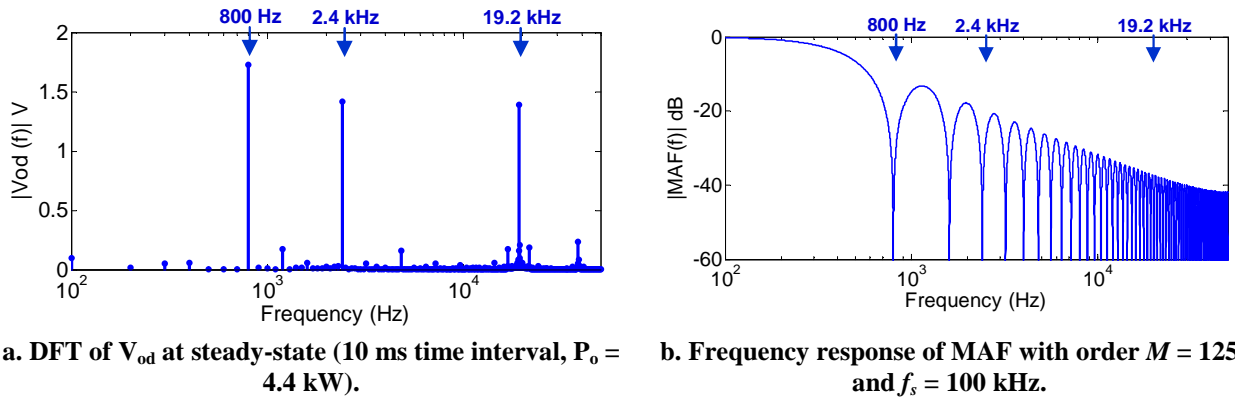


Fig. 5-49: Spectral analysis of the steady-state output voltage (d channel) and frequency response of suggested MAF filter for harmonic cancellation.

The filter performance is illustrated in Fig. 5-50, where the v_{od} waveforms before and after filtering are shown. MAF provides high harmonics and noise rejection while preserving the low-frequency transient evolution, although the model identifiability above 800 Hz is reduced. Note that a symmetric MAF form has been used, so that phase shift is prevented.

Therefore, this filter has been subsequently applied on the AC voltage to carry out the linearity analysis. Alternative filtering strategies, such as cascaded Notch filters [248], may be also used in order to better preserve the dynamics above 800 Hz, at the expense of less noise smoothing.

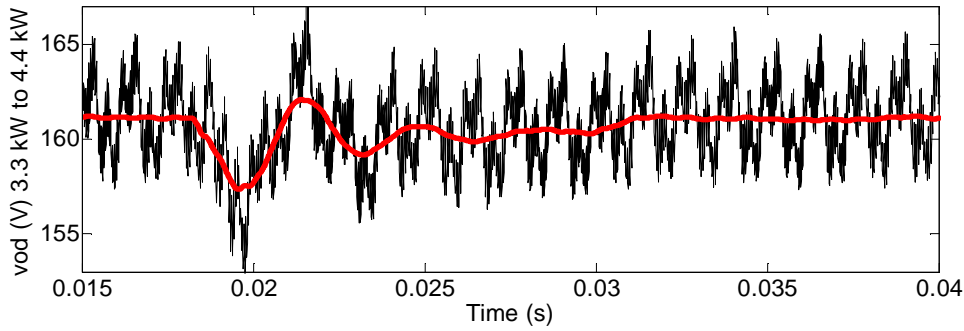


Fig. 5-50: Output voltage v_{od} pre-filtering through MAF with $M = 125$.

In Fig. 5-51, the transient response shown above (Fig. 5-48) is compared with the transient response to a step from 1.1 kW to 2.2 kW. As can be seen, there is a slight relationship between I_{od} and the damping of i_i and v_{od} , so that the higher I_{od} , the higher the damping. It is also worth noticing that, as a difference from the simulated case, V_{od} and V_{oq} slightly depends on I_{od} (in terms of statics).

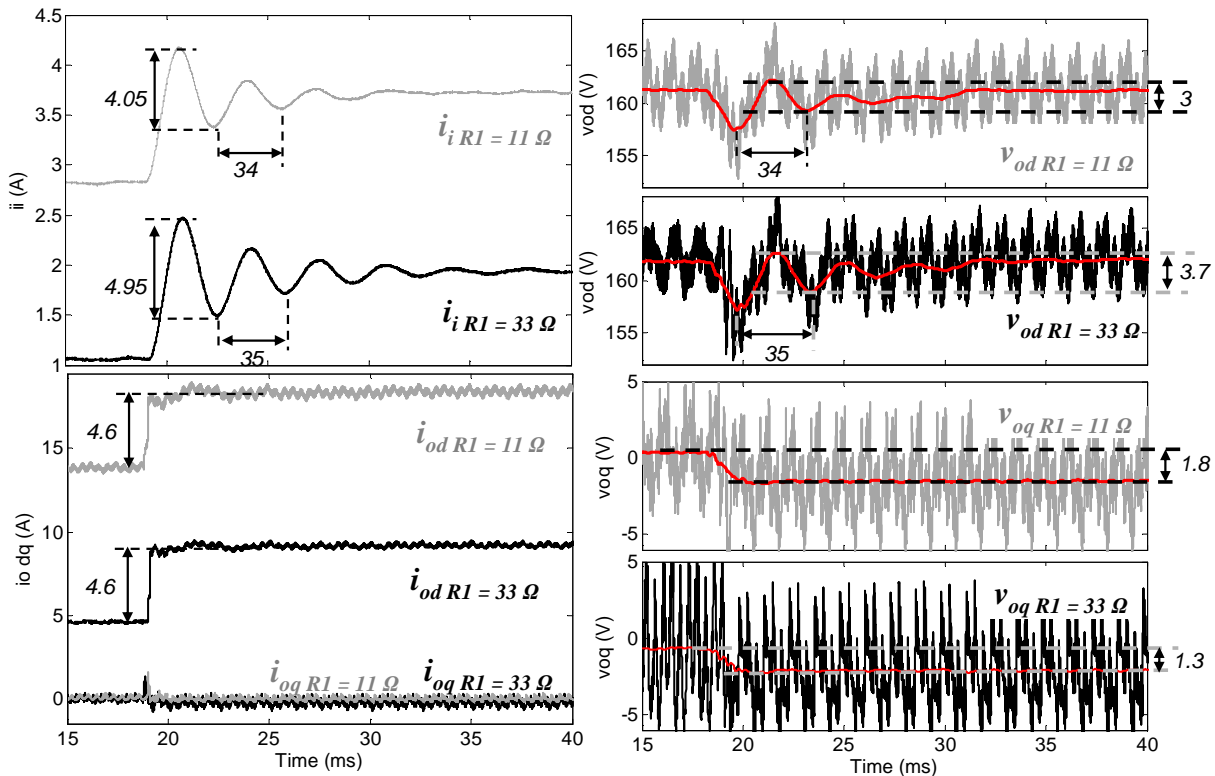


Fig. 5-51: Comparison of transient response to load steps from 1.1 kW to 2.2 kW (black traces) and from 3.3 kW to 4.4 kW (grey traces). Signals pre-filtered through MAF with $M=125$ in red.

The other dynamic networks have been considered independent of I_{od} . On the other hand, the dynamic systems dependence on I_{oq} has been also neglected. Those assumptions are validated later on in section 5.6.4.

5.6.2.2 Dynamic networks modeling

According to the previous analysis, every dynamic system has been simply modeled using a single transfer function except H_{id} , which has been made up using a gain-scheduled transfer function, in order to account with the constant-power-load behavior of the VSI. Then, the resulting black-box model structure that depicted in Fig. 5-52. A trade-off between simplicity and accuracy has been considered when choosing it.

Concerning the static load and line regulation, it was found to be slight, and has been approximated in a linear manner for simplicity. Hence, they are directly incorporated into the linear d-q models for the output impedance and the audiosusceptibility.

Additionally, enabling and soft-start networks have been added (parameterized later on).

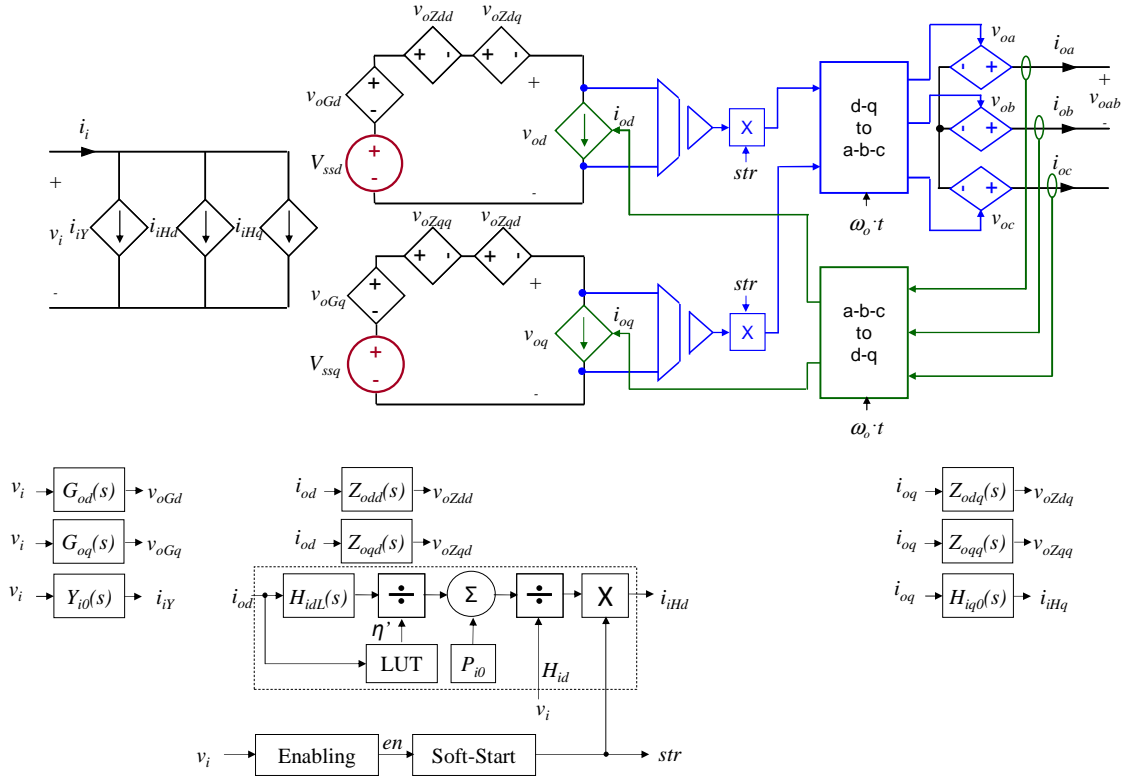


Fig. 5-52: Black-Box model of the experimental VSI.

5.6.3 Identification

5.6.3.1 Step tests and identification of transfer function models

5.6.3.1.1 Resistive load steps

First, a resistive load step from 2.3 kW to 4.5 kW has been carried out. This test is preferred instead of those shown above because the step magnitude is larger and the SNR is improved. The resulting transient waveforms are depicted in Fig. 5-53. The $a-b-c$ to $d-q$ transformation has been set so that $V_{oq} = 0$ V after the step, that is, $P_o = 4.5$ kW and $Q_o = 0$ KVAR, which correspond to $I_{od} = 18.5$ A and $I_{oq} = 0$ A. As can be seen, this results in an i_{od} step. Consequently, $Z_{oddm}(q)$, $Z_{oqdm}(q)$ and $H_{idm}(q)$ can be identified^{5.9}.

The identification results are evaluated in Fig. 5-54, where the pre-processed experimental output is compared to the response of the identified transfer function (subjected to the pre-processed experimental input). This is done by using the Matlab function ‘compare’ (more details about the pre-processing and the validation process are given in section 4.3.2). As can be seen, relatively low model orders (1st to 3rd order) yields accurate fits of the pre-processed experimental response.

^{5.9} The obtained transfer functions are denoted with the subscript “m” because cross-perturbations of both i_{oq} and v_i have been caused under this test. Those are analyzed later on.

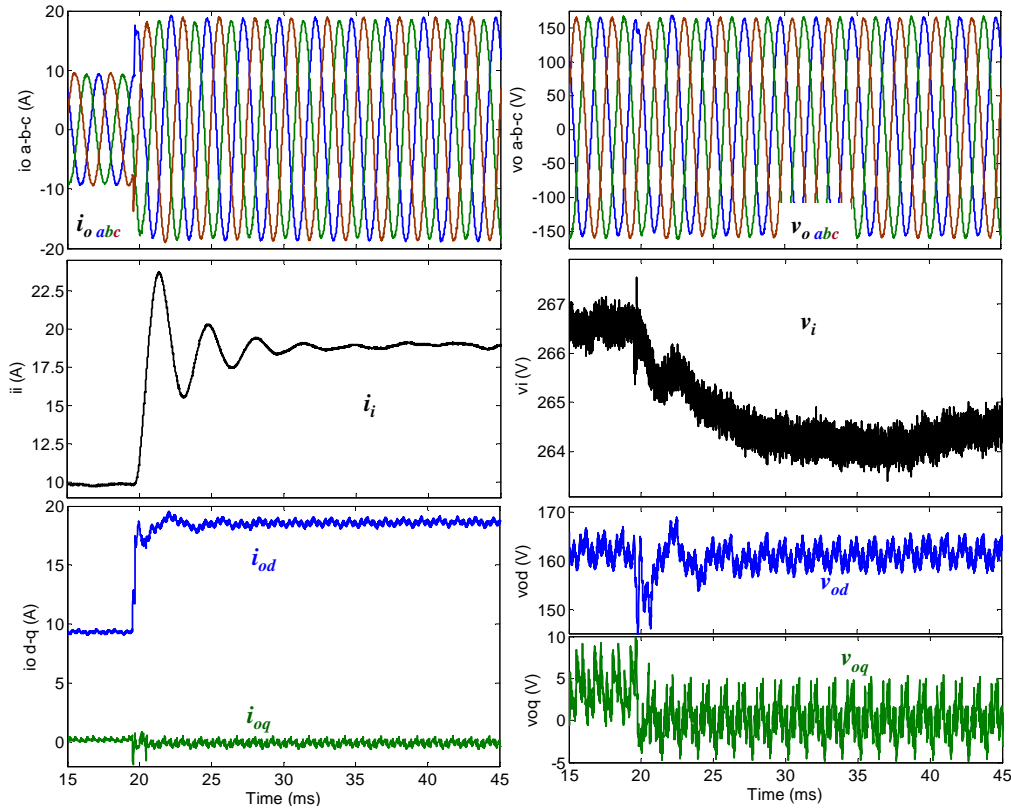


Fig. 5-53: Transient response to resistive load step from $P_o=2.3$ to 4.5 kW, $Q_o=0$ kVAR.

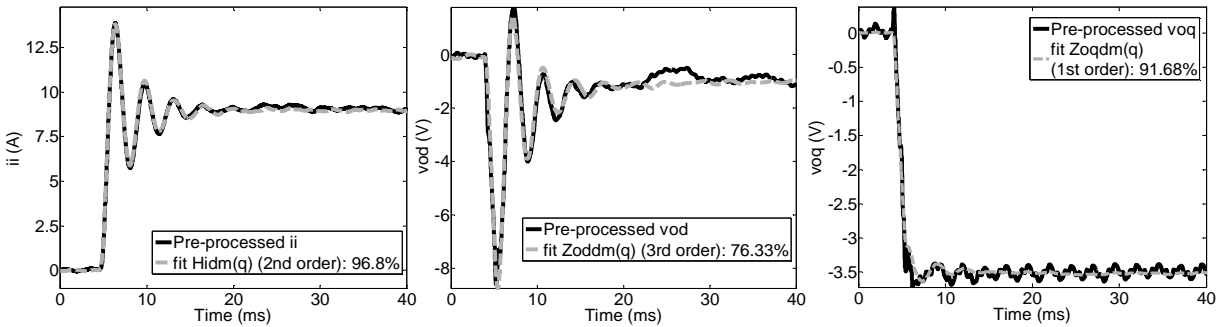


Fig. 5-54: Fitting results of H_{idms} , Z_{oddm} and Z_{odqm} .

5.6.3.1.2 Capacitive load steps

A capacitive load disconnection from 1.5 kVAR to 0 kVAR has been carried out while the active power is $P_o = 4.5$ kW. Note that the active and reactive power levels, after the test, are the same than those after the resistive load step. This ensures that, according to the synchronization done before, $V_{oq} = 0$ V after the step, so that the cross-perturbations of i_{oq} are minimized.

The transient waveforms are shown in Fig. 5-55. As can be seen, the capacitive step is mapped into d - q frame as an i_{oq} step while the perturbation of i_{od} is much lower. Hence, $Z_{odqm}(q)$, $Z_{oqqm}(q)$ and $H_{iqm}(q)$ can be identified.

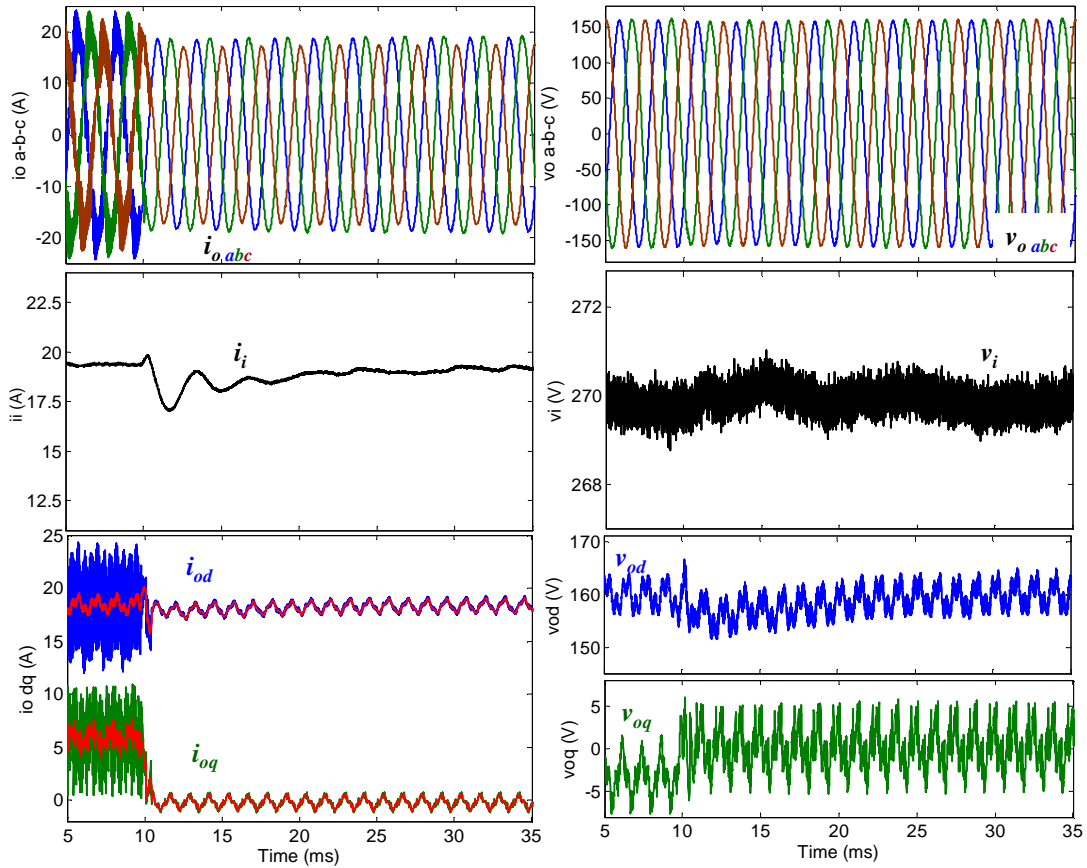


Fig. 5-55: Transient response to capacitive load step from $Q_0=1.5$ kVar to 0 kVar. $P_o = 4.5$ kW. Averaged signals in red.

At this point, one may wonder why both steps were not done to no-load condition, instead of choosing $P_o = 4.5$ kW as the final power level. If the step were done to no-load condition, the cross-perturbations of the non-stepped coordinates would have been nullified, as justified in section 5.3.3. However, the possible combinations of capacitive and resistive load were constrained in the aircraft test-bed, so that the capacitive load can be stepped only if a resistive load is enabled.

The fitting performance and the selected model orders are depicted in Fig. 5-56. As can be seen, good fitting results have been achieved using low-order models.

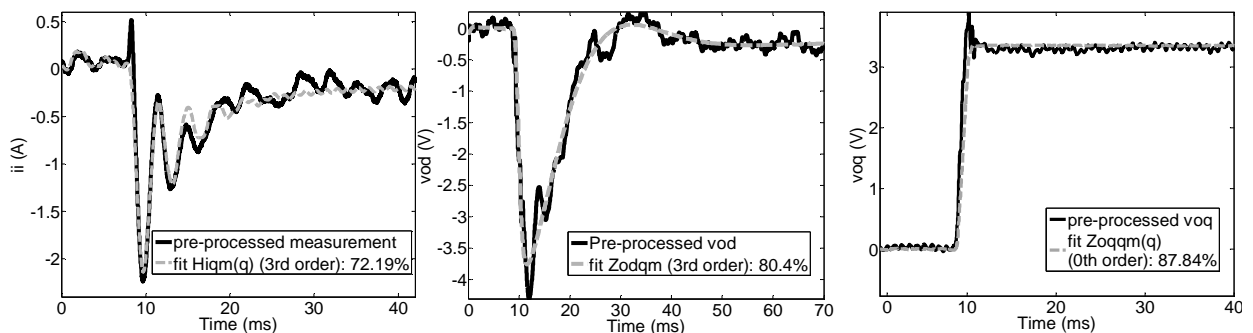


Fig. 5-56: Fitting results of H_{iqm} , Z_{odqm} and Z_{oqqm}

5.6.3.1.3 Input voltage step

An input voltage step has been carried out by means of the setup shown in Fig. 5-14a. Fig. 5-57 shows a picture of the piece of equipment used to carry out the step. This implementation allows a

flexible selection of the number of diodes to be connected in series. Hence the magnitude of the step is easy to set over a wide range.

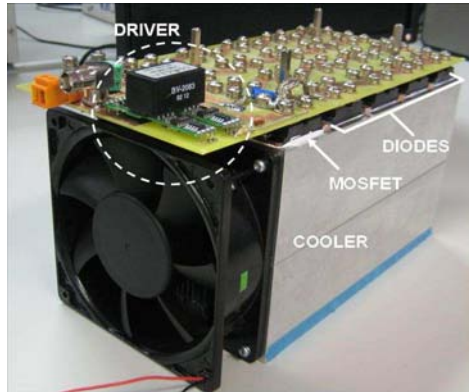


Fig. 5-57: Piece of equipment used to carry out input voltage steps, consisting of an array of diodes in parallel with a solid state switch.

The test has been performed at no-load condition, so the cross-perturbations of i_{od} and i_{oq} have been prevented. The measured response is depicted in Fig. 5-58. Notice the very high slew rate of v_i achieved with the proposed setup. Note also that i_i responds as a second-order under-damped system, which evidences the existence of an input L-C filter. In fact, this is probably the reason why a slight dynamics dependence on the I_{od} was found out in section 5.6.2.1.

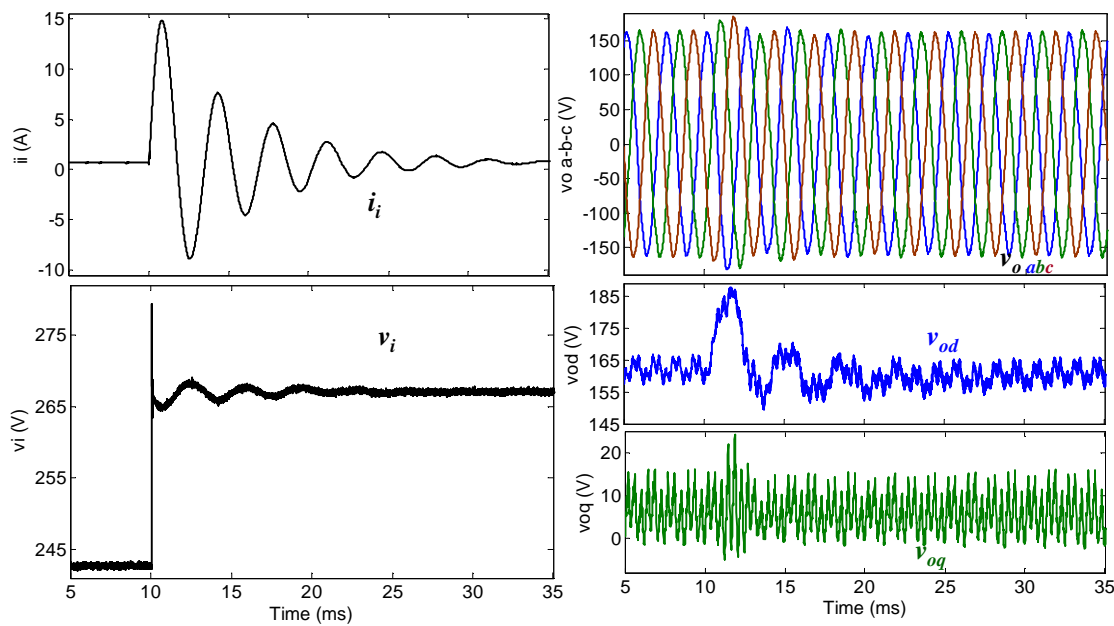


Fig. 5-58: Transient response to input voltage step (no-load condition).

Fig. 5-59 depicts the transient waveforms fitting (after filtering through MAF) for $G_{od}(q)$, $Y_i(q)$ and $G_{oq}(q)$. It can be concluded that $G_{oq}(q)$ could have been neglected, without significant loss of accuracy, because $v_{oq} \ll v_{od}$ along the entire time window.

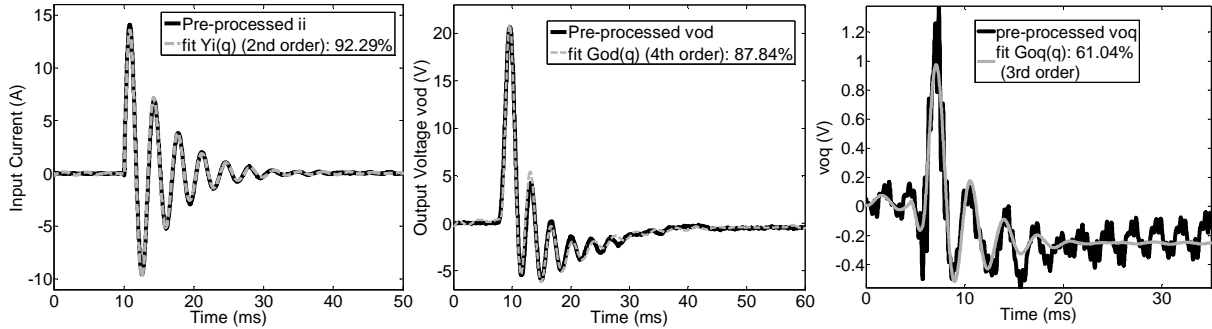
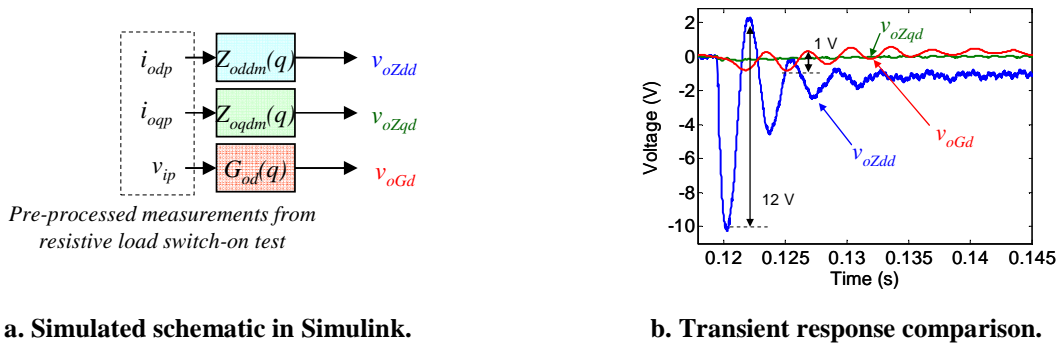


Fig. 5-59: Fitting results of Y_i , G_{od} and G_{oq} .

5.6.3.2 Analysis and removal of cross-coupling effects

The cross-perturbation effects have been evaluated following the process described in 5.3.3.2. Convolution of the measured pre-processed signals (subscript 'p') and the identified transfer functions is applied, and the resulting responses are compared to each other.

Fig. 5-60 depicts the analysis of cross-coupling effects on $Z_{oddm}(s)$. The input signals correspond to the resistive load step shown in Fig. 5-53 (after pre-processing). As can be seen, $v_{oZdd} \ll v_{oZqd}$ and $v_{oZdd} \ll v_{oGd}$ along the entire time window. Hence, the cross-perturbation effects are negligible, so $Z_{odd}(s) = Z_{oddm}(s)$.

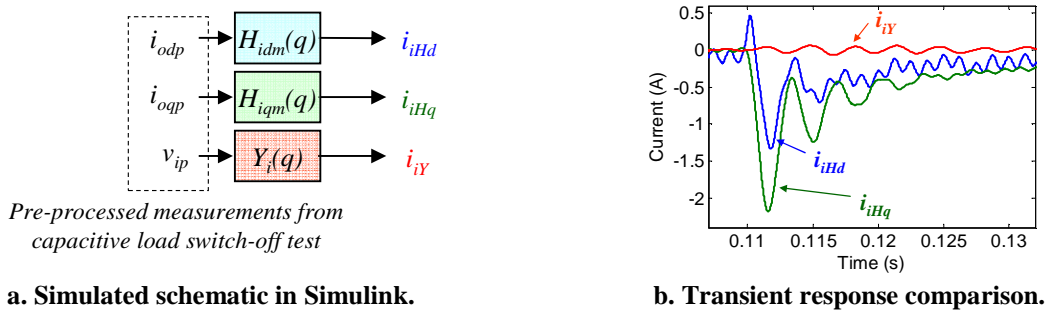


a. Simulated schematic in Simulink.

b. Transient response comparison.

Fig. 5-60: Evaluating the cross-coupling effects on Z_{oddm} .

Following a similar procedure, the cross-coupling effects on the other transfer functions have been found to be negligible, except for H_{iqm} . As Fig. 5-61 shows, the cross-perturbations of i_{od} makes significant influence on i_i and, consequently, has to be removed.



a. Simulated schematic in Simulink.

b. Transient response comparison.

Fig. 5-61: Evaluating the cross-coupling effects on H_{iqm} .

Since the cross-coupling effect on H_{iqm} is the only significant one, the decoupling matrix " $T_s(s)$ " is comprised of only one transfer function, so the inverse matrix is very simple.

$$[T_s(s)] = \begin{pmatrix} 1 & 0 & 0 & 0 & 0 & 0 & 0 & 0 & 0 \\ 0 & 1 & 0 & 0 & 0 & 0 & 0 & 0 & 0 \\ 0 & T_{idqm}(s) & 1 & 0 & 0 & 0 & 0 & 0 & 0 \\ 0 & 0 & 0 & 1 & 0 & 0 & 0 & 0 & 0 \\ 0 & 0 & 0 & 0 & 1 & 0 & 0 & 0 & 0 \\ 0 & 0 & 0 & 0 & 0 & 1 & 0 & 0 & 0 \\ 0 & 0 & 0 & 0 & 0 & 0 & 1 & 0 & 0 \\ 0 & 0 & 0 & 0 & 0 & 0 & 0 & 1 & 0 \\ 0 & 0 & 0 & 0 & 0 & 0 & 0 & 0 & 1 \end{pmatrix} \rightarrow [T_s(s)]^{-1} = \begin{pmatrix} 1 & 0 & 0 & 0 & 0 & 0 & 0 & 0 & 0 \\ 0 & 1 & 0 & 0 & 0 & 0 & 0 & 0 & 0 \\ 0 & -T_{idqm}(s) & 1 & 0 & 0 & 0 & 0 & 0 & 0 \\ 0 & 0 & 0 & 1 & 0 & 0 & 0 & 0 & 0 \\ 0 & 0 & 0 & 0 & 1 & 0 & 0 & 0 & 0 \\ 0 & 0 & 0 & 0 & 0 & 1 & 0 & 0 & 0 \\ 0 & 0 & 0 & 0 & 0 & 0 & 1 & 0 & 0 \\ 0 & 0 & 0 & 0 & 0 & 0 & 0 & 1 & 0 \\ 0 & 0 & 0 & 0 & 0 & 0 & 0 & 0 & 1 \end{pmatrix} \quad (5-40)$$

Then, the “un-coupled” transfer function $H_{iq}(s)$ is simply derived as

$$H_{iq}(s) = -T_{idqm}(s) \cdot H_{idm}(s) + H_{iqm}(s) \quad (5-41)$$

The fitting results of T_{idqm} are depicted in Fig. 5-62a, showing that it has been properly fitted. The performance of the removal process is evaluated in Fig. 5-62b, where the simulated input current is compared to the measured one i_i before and after removing the cross-coupling effects. As can be seen, the sum of the transfer function outputs, after cross-coupling removal, matches the measured current, so the cross-coupling effects have been effectively removed.

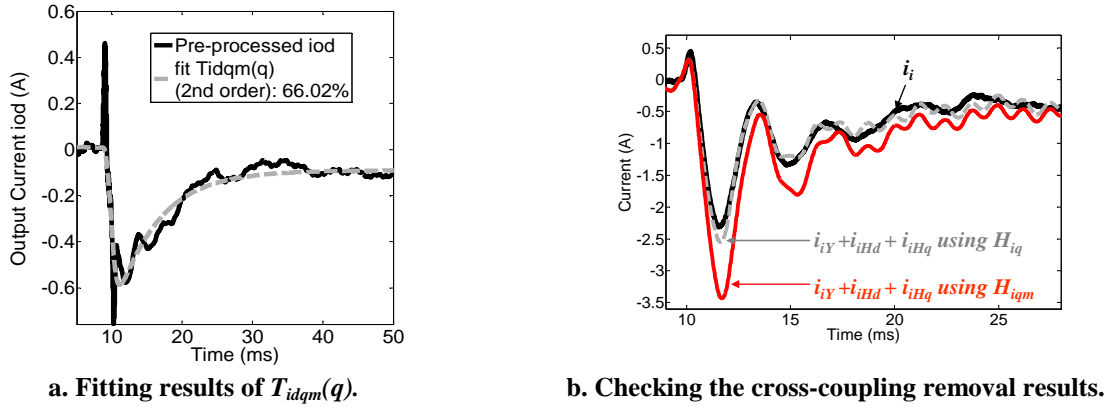


Fig. 5-62: Removing cross-coupling effects from H_{igq} .

5.6.3.3 Discussion on identification results

The frequency response of the un-terminated transfer functions, related to the input port of the model, is depicted in Fig. 5-63 and discussed below.

- $Y_i(j\omega)$ evidences the existence of an LC input filter whose cut-off frequency is ≈ 300 Hz. Note that, as the identification test was carried out at no-load conditions, no low frequency CPL behavior is observed.
- $H_{id}(j\omega)$ and $H_{iq}(j\omega)$ exhibit a resonance at the cut-off frequency of the input filter. This is related to the input-output power transference. Moreover, $|H_{id}(j\omega)| \gg |H_{iq}(j\omega)|$ for $f < f_{sw}/2$. This is because $H_{id}(s)$ accounts for the i_i response under active power changes at the AC side, which means power being delivered from the input to the output port. However, $H_{iq}(s)$ accounts only variations of energy stored in the under reactive power changes. Those are much smaller and are only slightly reflected at the DC side. Indeed, $H_{iq}(s)$ could be neglected for the sake of a simpler model.

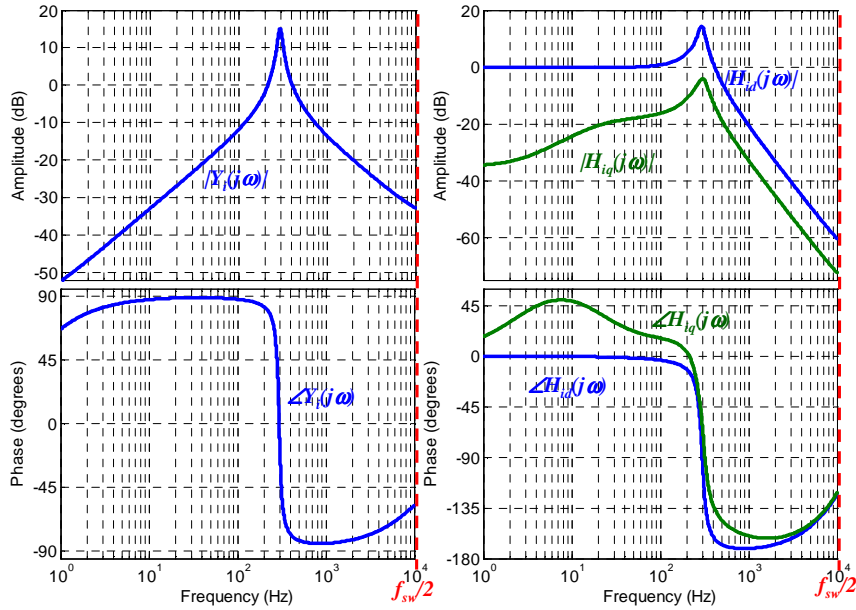


Fig. 5-63: Frequency response of $Y_i(j\omega)$, $H_{id}(j\omega)$ and $H_{iq}(j\omega)$.

The frequency response of the transfer functions related to the output port are depicted in Fig. 5-64 and discussed below.

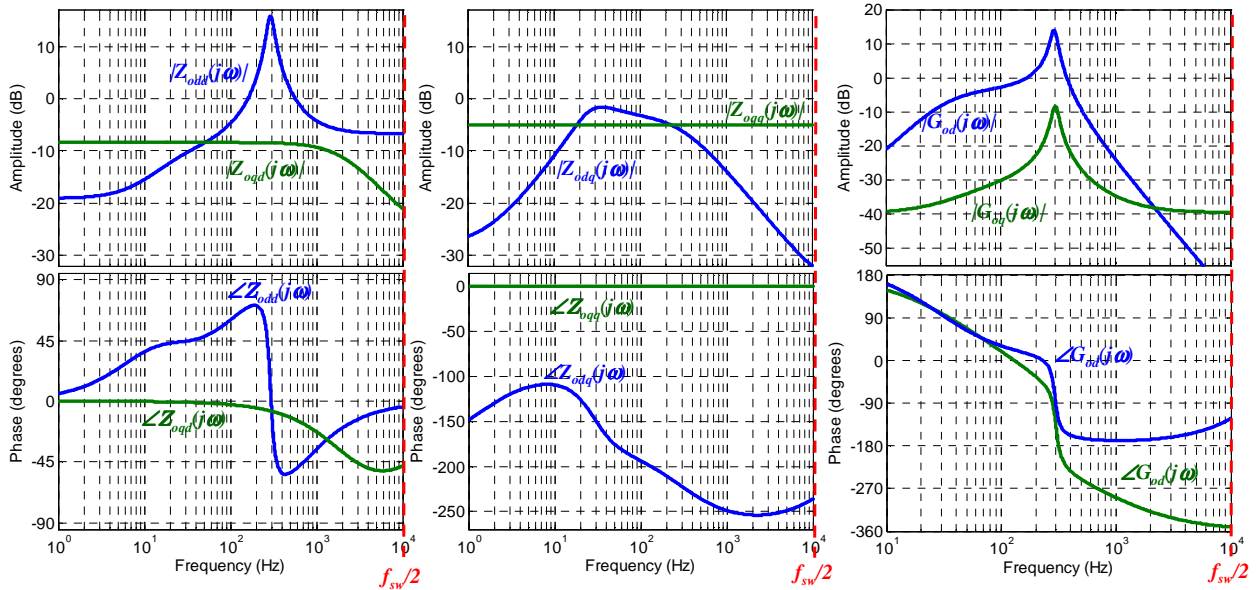


Fig. 5-64: Frequency response of $Z_{odd}(j\omega)$, $Z_{odq}(j\omega)$, $Z_{oqd}(j\omega)$, $Z_{oqq}(j\omega)$, $G_{od}(j\omega)$, $G_{oq}(j\omega)$.

- $Z_{odd}(j\omega)$ exhibits a resonance at the cut-off frequency of the DC filter. This is because $Z_{odd}(s)$ is closely related to the AC voltage magnitude response under active power changes, which means power processed by the DC filter. As a consequence, the DC filter dynamics is clearly reflected at the AC side. However, $Z_{odq}(j\omega)$ does not exhibit the 300 Hz resonance because it is related to the VSI dynamics under reactive power changes, which are only slightly reflected at the DC side of the VSI.
- $Z_{oqq}(j\omega)$ and $Z_{oqd}(j\omega)$ exhibits a nearly flat response. It demonstrates that, as a difference from the simulated VSI, the output impedance does not exhibit orthogonal properties. The reason why orthogonal properties do not hold could be the type of control scheme. As indicated in section 5.4.2, orthogonal properties are not found under magnitude control or RMS control.

- Both $G_{od}(j\omega)$ and $G_{oq}(j\omega)$ exhibits a resonance at 300 Hz, because both transfer functions relates the output voltage with the input voltage and, as a consequence, the DC filter is implicated. However, $|G_{od}(j\omega)| \gg |G_{oq}(j\omega)|$, because $G_{oq}(s)$ essentially represents phase displacements in the AC voltage under input voltage changes, which are small.

Note that most of the discussion has been related to DC side filter. However, high frequency dynamic effects which may be expected to be observed, such as the AC filter dynamics, are not observed in the identified transfer functions. This is probably because of the reduced identifiability of the model above 800 Hz due to the use of step signals as well as the pre-filtering actions.

5.6.3.4 Parameterization of dynamic networks

Once every transfer function model has been identified, the dynamic network for H_{id} has been tuned. First, the power losses at no-load condition have been obtained, resulting in $P_{i0} = 250$ W. Second, the efficiency with and without considering no-load losses, namely η and η' respectively, have been characterized as given by (5-14). The obtained results are plotted in Fig. 5-65, where one may notice that η' is approximately constant over the whole operating range. Therefore, it has been modeled as a constant factor $\eta' = 0.955$ for the sake of simplicity.

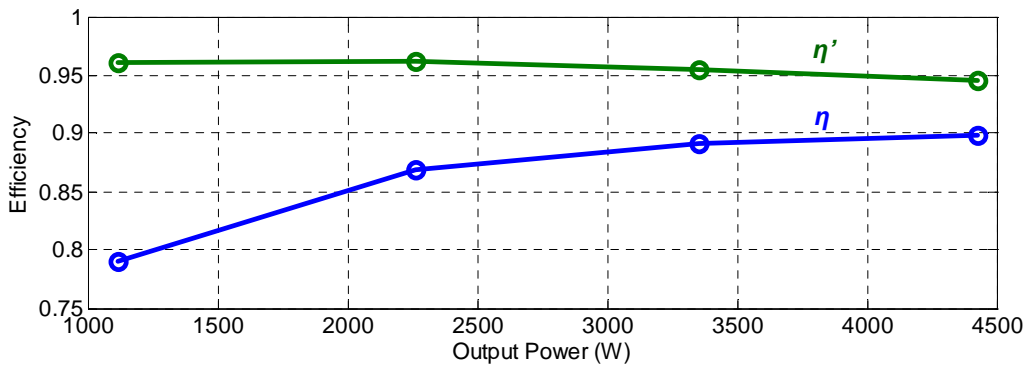


Fig. 5-65: Global efficiency η and efficiency without considering no-load losses η' .

Second, the transfer functions $Y_i(s)$, $H_{id}(s)$ and $H_{iq}(s)$ have been tuned as discussed in section 5.3.4, resulting in the transfer functions for the model $Y_{io}(s)$, $H_{idL}(s)$ and $H_{iq0}(s)$. No post-processing actions have been carried out on the transfer functions at the output port (i.e. output impedance and audiosusceptibility), as they directly incorporate the static line and load regulation.

5.6.3.5 Parameterization of the soft-start functionality and the enabling network

Finally, the soft-start functionality of the VSI has been modeled. First, the enabling network has been parameterized from information provided by the manufacturer. In this case, the enabling/disabling functionality includes and hysteresis band. Its operation is illustrated in Fig. 5-66a and described below.

Consider that the VSI is initially disabled. If v_i falls within the range $[E_l, E_h]$, then the VSI will be enabled. Once the VSI is enabled, it will not be disabled unless v_i either decreases below D_l or increases above D_h . The enabling function with hysteresis can be implemented using simple logic consisting of four comparators, two set-reset flip-flops and one ‘AND’ gate, as depicted in Fig. 5-66b.

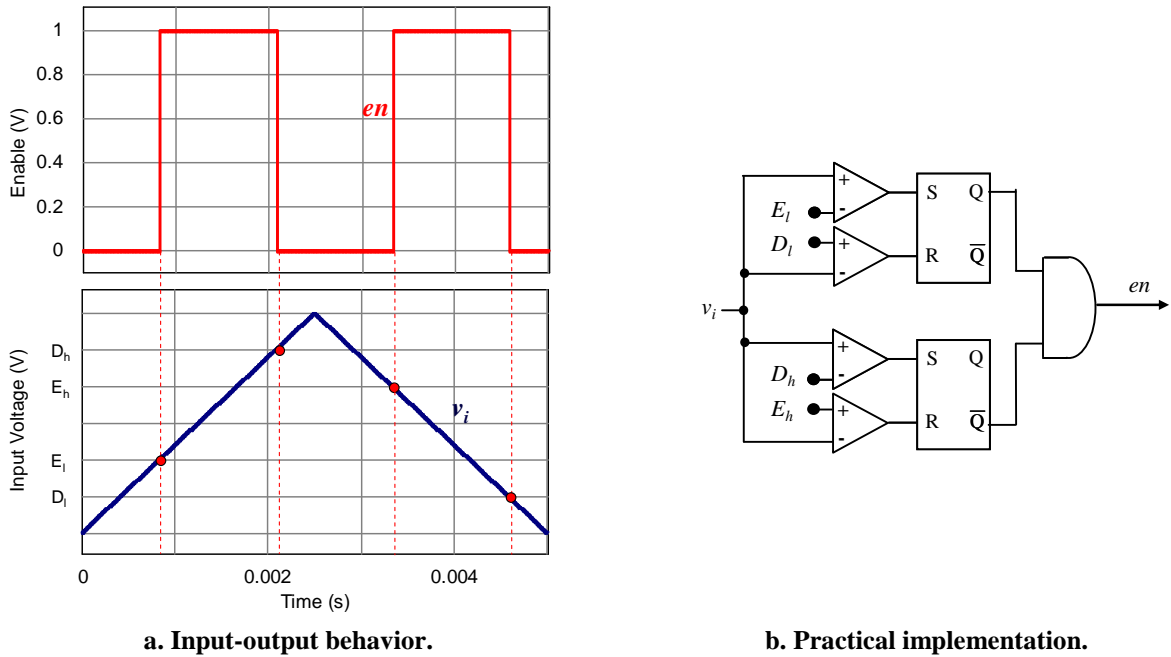


Fig. 5-66: Modeling the enabling functionality.

Second, the soft-start profile has been experimentally tested. This has been done by hot swapping the VSI to the DC bus at no load condition. The measured response is depicted in Fig. 5-67. As can be seen, the AC voltage rises following a nearly linear trajectory. The rise time has been found out to be $t_0 = 1.67$ s and independent of the load current.

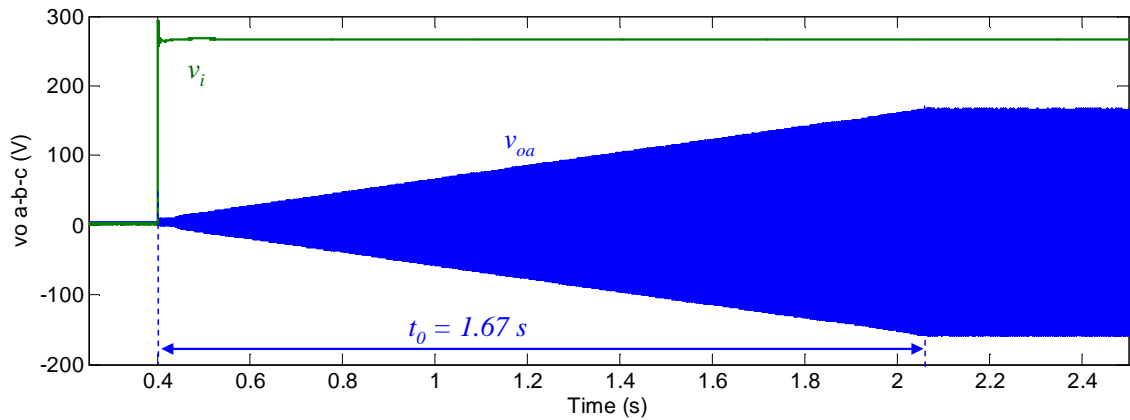


Fig. 5-67: Soft-start of the VSI.

This profile can be simply modeled using a resettable integrator cascaded to a gain block equal to t_0^{-1} and a saturation block which limits the output to '1' (see Fig. 5-68). Thus, when the signal v_{ss} reaches '1', the output voltage reaches steady-state condition.

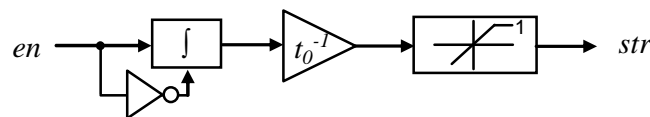


Fig. 5-68: Modeling the soft-start functionality.

At this point, the large-signal black-box model shown in Fig. 5-52, has been completely parameterized.

5.6.4 Validation

The identified model has been implemented in the circuit simulator PSIM for validation purposes. The validation consists in comparing the response of the black-box model and the response of the actual VSI under several electrical tests.

5.6.4.1 Validation test 1: Input voltage step down

First, an input voltage step-down has been performed through the experimental test shown in Fig. 5-69a. The step has been carried out switching off the Mosfet connected in parallel with the array of diodes, while the VSI delivers 2.3 kW to a resistive load.

The input voltage v_i has been simulated using a controlled voltage source driven by a LUT, which outputs the measured waveform as a function of time. This way, both the experimental VSI and the black-box model has been subjected to the same v_i perturbation. On the other hand, the load has been emulated using ideal resistors. The simulated schematic is depicted in Fig. 5-69b.

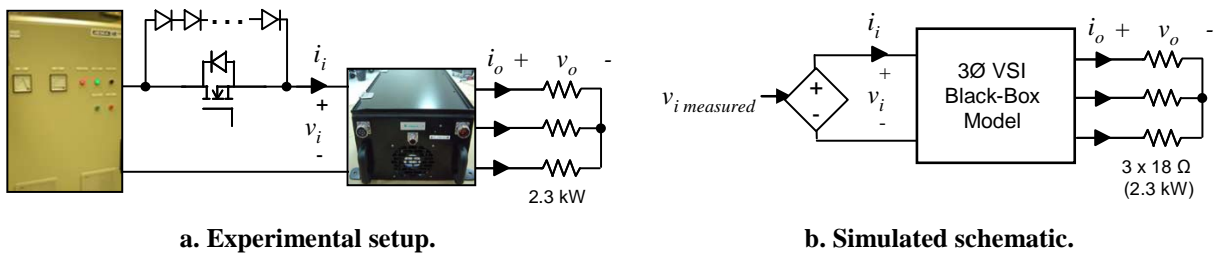


Fig. 5-69: Validation test 1.

The comparison results are plotted in Fig. 5-70. The conclusions listed below have been drawn.

- The black-box model reproduces both the static and the dynamic behavior of three phase VSIs accurately. Notice that the CPL behavior of the converter at low-frequency is well modeled (i.e. at steady-state the input current increases after the input voltage decreases). Note that a slight mismatch is found in the steady-state value (≈ 350 mA), which is attributed to the simplifications done in the efficiency modeling (η was modeled as a constant factor, refer to section 5.6.3.4).
- The model has been accurately identified. This fact is particularly evidenced for $Y_{io}(s)$ and $G_{od}(s)$, which dominates the transient response under this test.

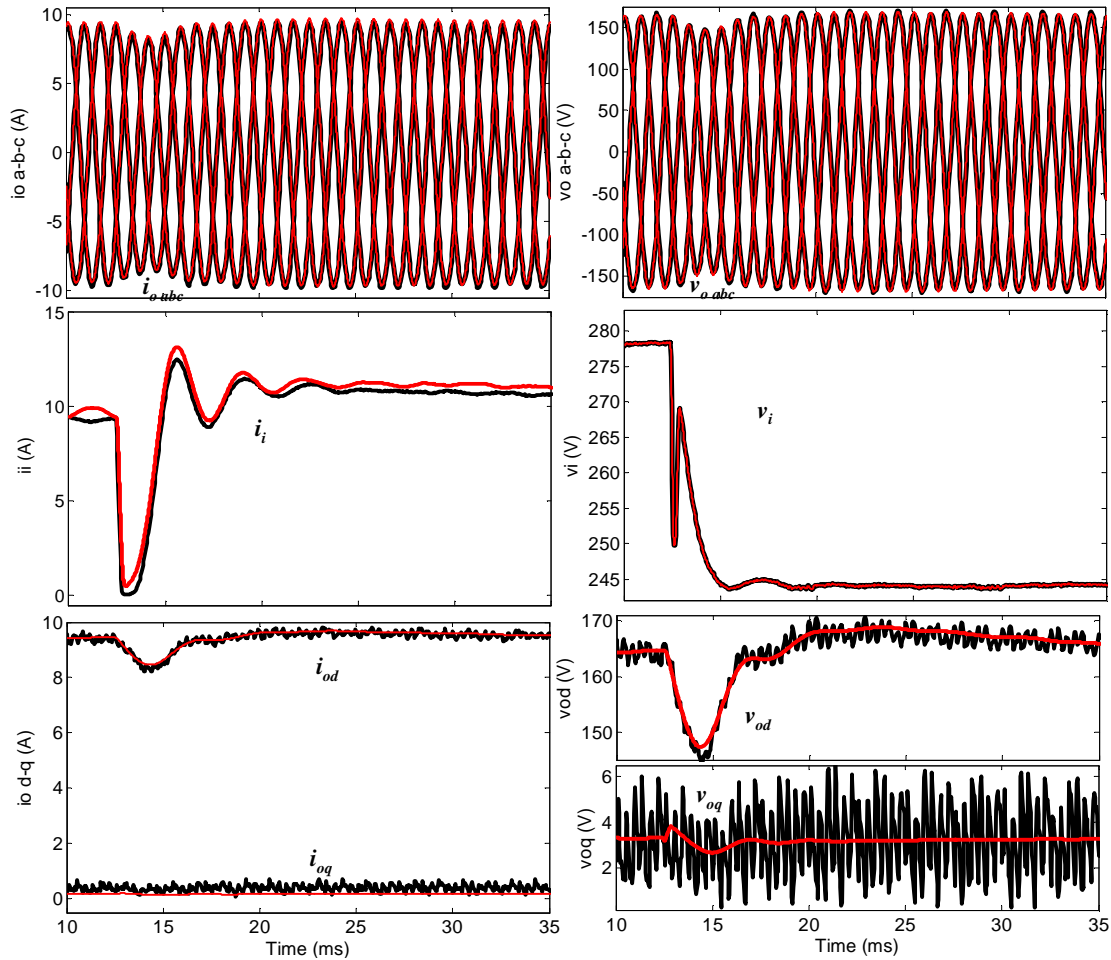


Fig. 5-70: Validation test 1. Comparison of experimental response (dark lines) and black-box model response (red lines).

5.6.4.2 Validation test 2: Large RL load step

Second, an inductive load step from 0 KVA to 5 kVA, $\cos\phi=0.7$ and back has been tested (see Fig. 5-71a). The load has been switched using solid-state relays, so the load is switched-off when the inductor is de-energized. In this case, a black-box model of the line-commutated rectifier has been derived by making use of the technique described in Chapter 4. Therefore, this test permits validating the model performance when interconnected with other black-box models (Fig. 5-71b).

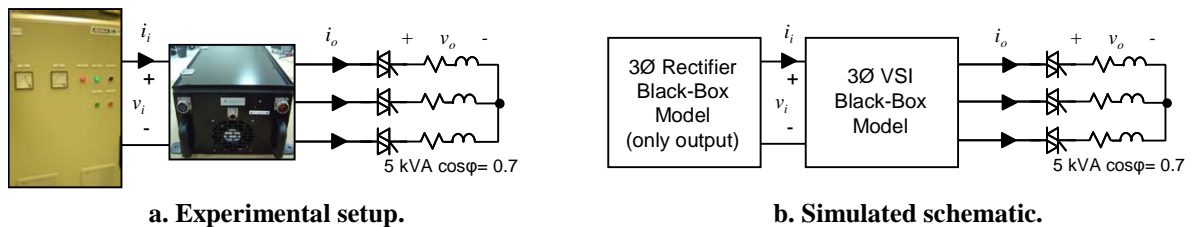


Fig. 5-71: Validation test 2.

The rectifier is working in discontinuous conduction mode because of the light load level (from 0% to 10%). As a consequence the output impedance has been found out to be dependant of current, so a LLMN approach has been used to make it up. The LLMN model consists of two local linear models corresponding to the maximum and minimum I_i level under this test (see Fig. 5-72).

Since the VSI dynamics is much faster than the rectifier dynamics, the output impedance of the rectifier has been well identified from the measured v_i and i_i waveforms.

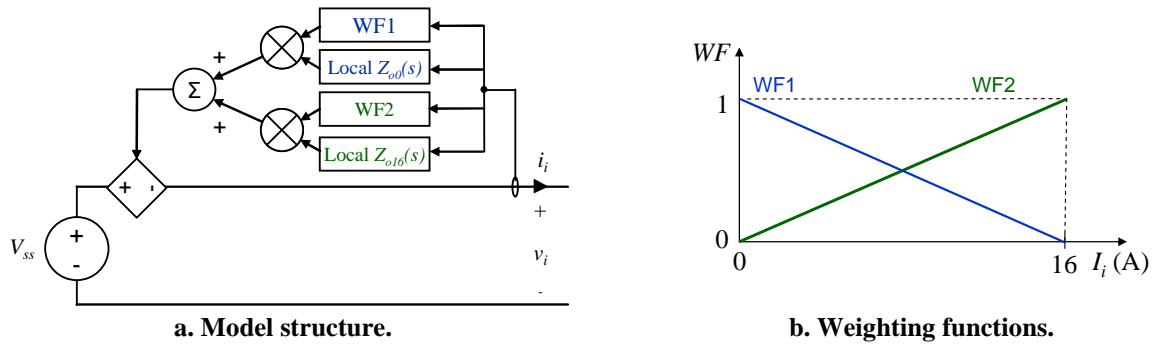


Fig. 5-72: Black-box model for the output port of the line-commutated rectifier (power level ranging from 0 kW to 4 kW).

The comparison of the simulation results and the experimental response, under load switch-on and switch-off, are depicted in Fig. 5-73 and Fig. 5-74, respectively. The results are discussed below.

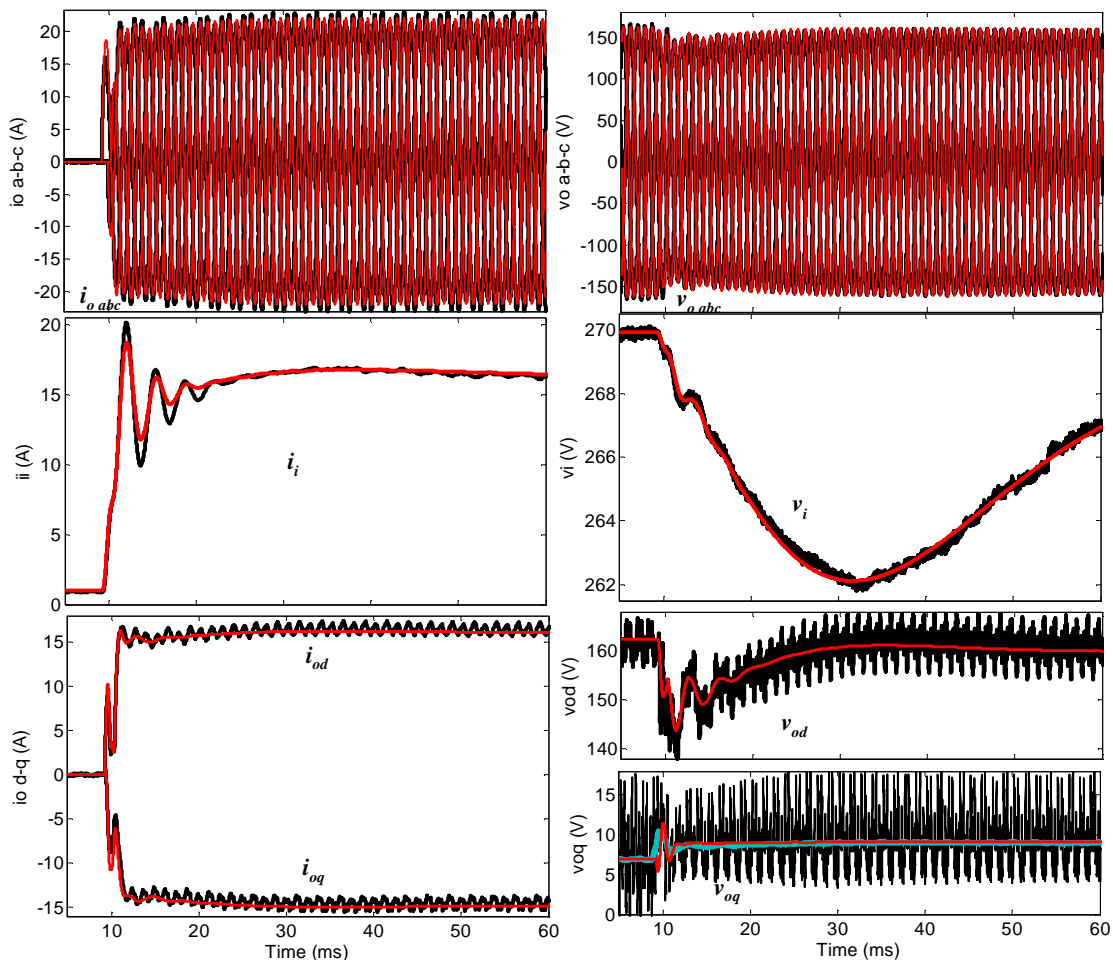


Fig. 5-73: Validation test 2a. Comparison of experimental response (dark lines) and black-box model response (red lines). Filtered experimental response (using MAF) corresponds to cyan traces.

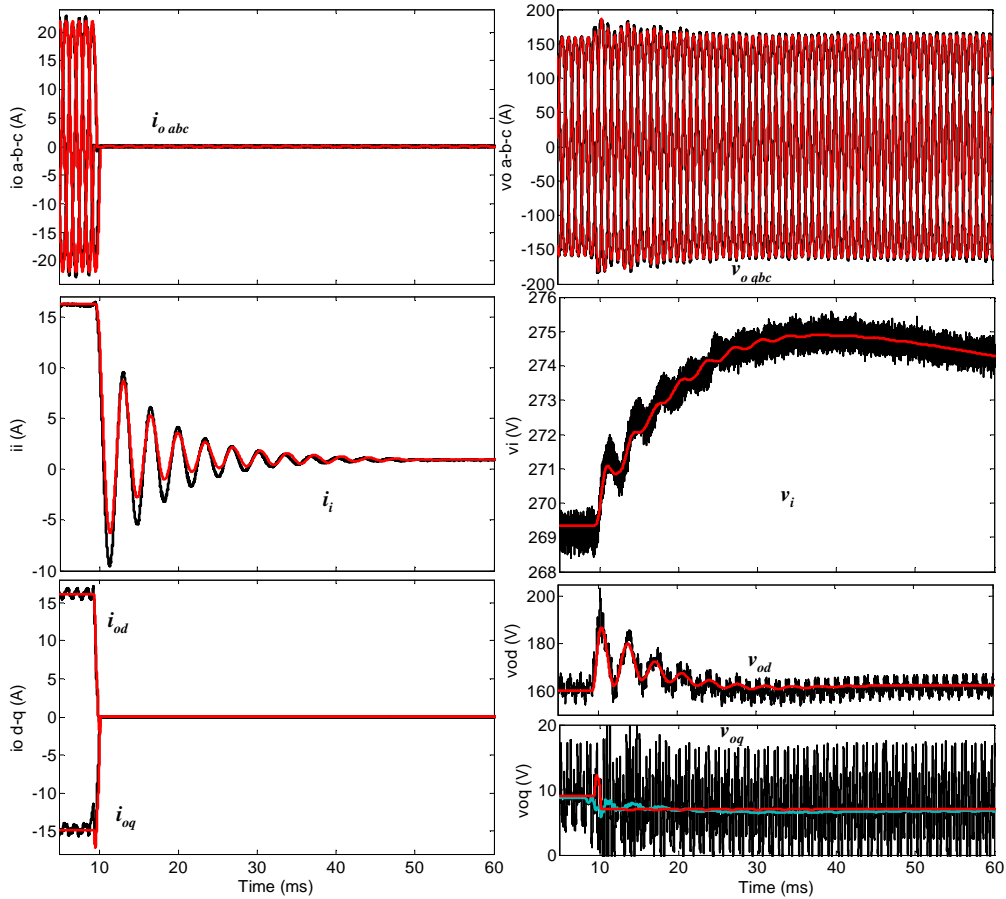


Fig. 5-74: Validation test 2b. Comparison of experimental response (dark lines) and black-box model response (red lines)..Filtered experimental response (using MAF) corresponds to cyan traces.

- The model performs properly when implemented in a virtual test bed.
- At the output port, the low-frequency average behavior of the output voltage is well reproduced by the model, under simultaneous excitation of i_{od} and i_{oq} . This corroborates the appropriateness of the proposed modeling method as well as the good performance of the identification method. This is particularly true for $Z_{odq}(s)$, $Z_{oqd}(s)$, $Z_{oqq}(s)$, $Z_{odd}(s)$, which dominates the response of the output voltage under this test.
- At the input port, the current consumption is well reproduced, although slight mismatch has been found out under transient conditions. As demonstrated in section 5.6.2.1, the VSI dynamics depends slightly on I_{od} but, for the sake of simplicity, such dependence has not been incorporated into the model.

5.6.4.3 Validation test 3: Hot swap of the VSI to the DC bus

Finally, a hot swap of the VSI to the DC bus has been tested while a 4.6 kW resistive load is tied at the output port (see Fig. 5-75). The aim of this test is to validate the proposed soft-start and enabling networks, as well as to evaluate the capability of the model to predict the inrush current.

The comparison between experimental and simulated waveforms is shown in Fig. 5-76. As can be seen, both the input current consumption and the output voltage evolution are accurately predicted. Note that the input current follows a quadratic evolution, due to the fact that the output voltage increase linearly with time, and consequently, the power increases quadratically.

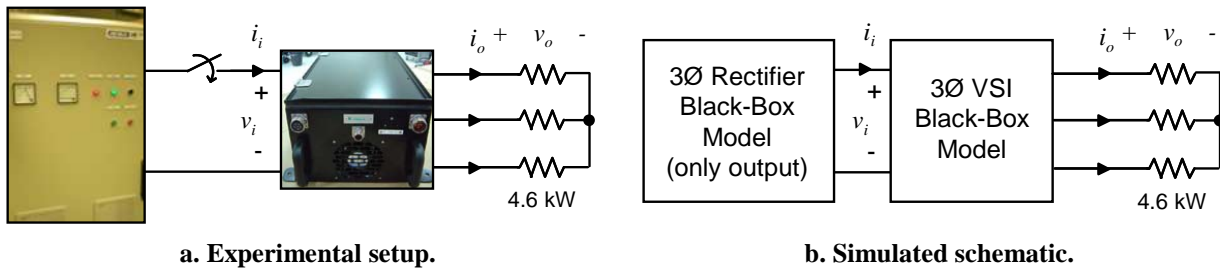


Fig. 5-75: Validation test 3.

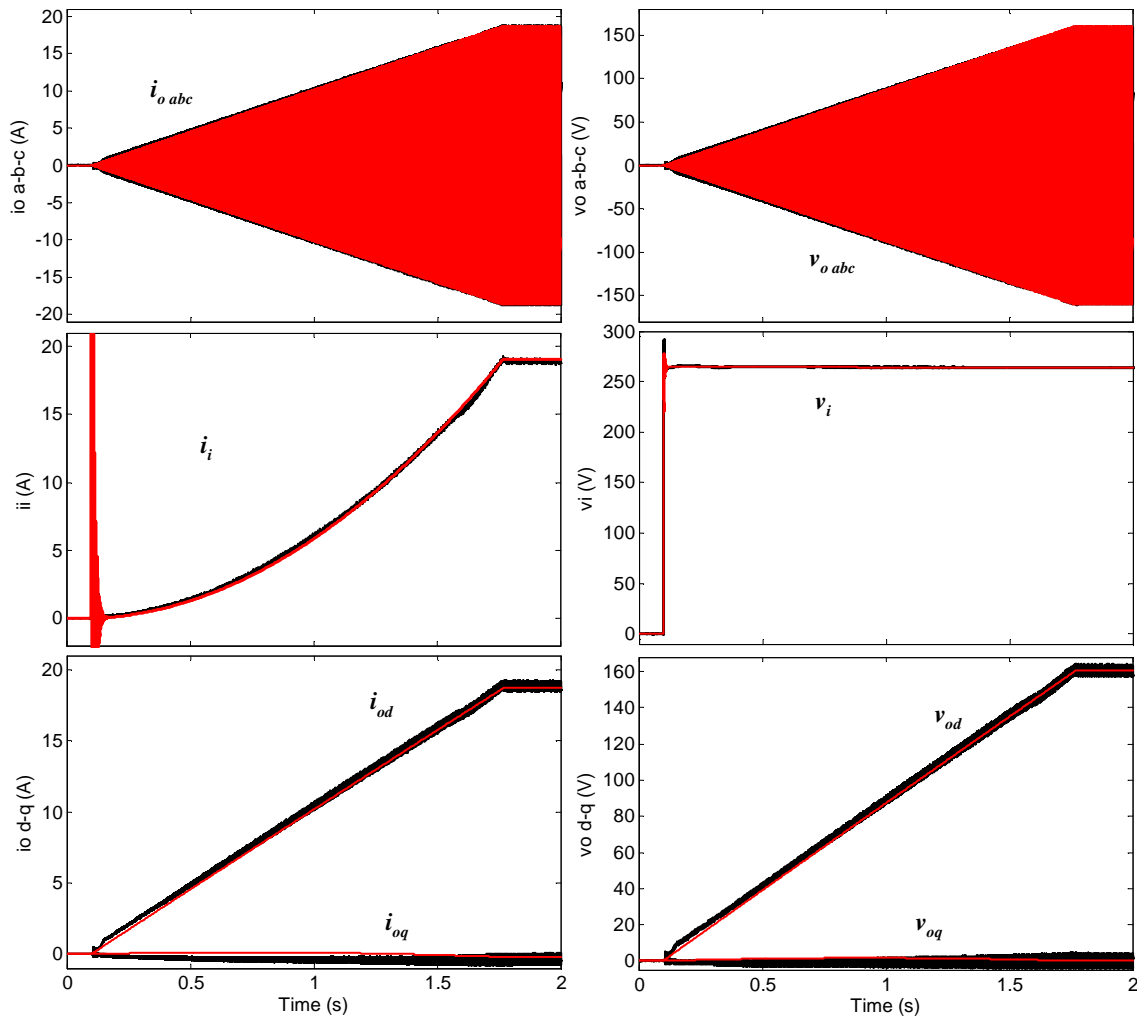


Fig. 5-76: Validation test 3. Comparison of experimental response (dark lines) and black-box model response (red lines).

A detail of the inrush current is shown in Fig. 5-77. Although the oscillation frequency is well predicted, large mismatching between the measured and the simulated waveforms is observed. Such a mismatching is attributed to the strong nonlinearities exhibited by the actual VSI at the beginning of the transient, which are probably due to saturation of the inductor filter. If the current is high enough so that the magnetizing flux exceeds the saturation threshold, the incremental permeability of the inductor decreases suddenly. Consequently, the current exhibits a large transient peak. Such an effect is not predicted by the black-box model, as the input admittance is modeled using a linear approach, that is, the inductance of the filter is assumed to be constant.

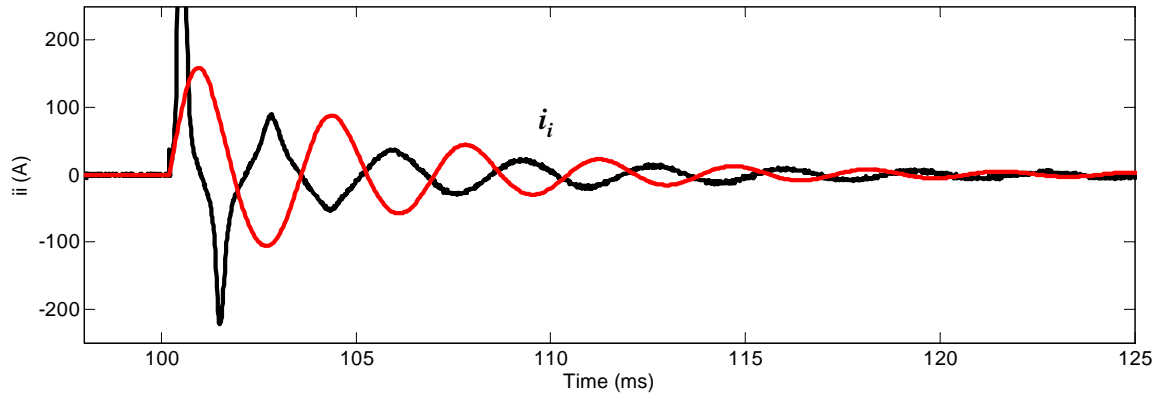


Fig. 5-77: Detail of the i_i under a hot swap to the DC bus: measured (black trace) and simulated (red trace).

5.6.5 Summary

In this section, a comprehensive experimental validation of the proposed modeling and identification procedures for three-phase balanced VSI has been presented. The tested VSI complies with MIL-STD regulation, was manufactured by a company and was tested into a test bed for a MEA. Therefore, this represents a realistic situation where the proposed methodologies could be applied.

- The proposed identification procedure has been put into practice experimentally. Issues such as low-frequency harmonics filtering and cross-coupling effects, which were not addressed in the simulation part, have been tackled. A simple pre-filtering has been proposed, which allows for accurate fitting results at low-frequency, at the expense of less accuracy for frequencies above the pre-filtered low-frequency harmonics. The cross-coupling analysis and removal procedure has been also illustrated and validated.
- The black-box model has been validated experimentally by comparing the model response with experimental measurements under large-signal transient tests. The model has been found to represent properly the large-signal behavior of the VSI, both in stand-alone and integrated with a source subsystem in a system-level simulation. Slight mismatching due to linearity assumptions and simplifications in the input-output power balance has been detected and justified. Despite such slight differences, a trade-off between simplicity and prediction accuracy is achieved.

5.7 Modeling unbalanced conditions: first approach

At this point, the three-phase VSI has been analyzed under balanced conditions. However, unbalanced conditions can be found out due to single phase loads.

In this section, the modeling under unbalanced conditions is introduced, both in case of three-wire and four-wire systems. The model capabilities to cope with unbalanced situations are explored and further extensions of the model to account for neutral current are proposed.

5.7.1 Basic concepts: symmetrical components and d-q-0 transformation

To understand the concepts behind an unbalanced situation, let us review the decomposition into symmetrical components. This was firstly proposed by Fortescue [196] and states that any set of

three-phase unbalanced signals can be decomposed as the sum of three sets of balanced signals, so-called sequences. The first set is so-called positive sequence \vec{I}_p and rotates at the same direction as the signals do. The second one is so-called negative sequence \vec{I}_n and rotates in the opposite direction. The third one is so-called zero-sequence \vec{I}_0 and comprises three signals which are equal in phase and magnitude. This decomposition is mathematically expressed by (5-42), where $a = e^{j2\pi/3}$.

$$\begin{pmatrix} \vec{I}_p \\ \vec{I}_n \\ \vec{I}_0 \end{pmatrix} = \frac{1}{3} \begin{pmatrix} 1 & a & a^2 \\ 1 & a^2 & a \\ 1 & 1 & 1 \end{pmatrix} \begin{pmatrix} \vec{I}_a \\ \vec{I}_b \\ \vec{I}_c \end{pmatrix} \quad (5-42)$$

Fig. 5-78 illustrates the decomposition of a three-phase unbalanced system into positive sequence, negative sequence and zero sequence. In case of balanced systems, only positive-sequence is found. In case of three-phase three-wire unbalanced systems, both positive-sequence and negative-sequence exist. Finally, in case of three-phase four-wire unbalanced systems, all sequences can be found. This is because the zero-sequence is found when the sum of a - b - c signals is different from zero, which can occur in four-wire system.

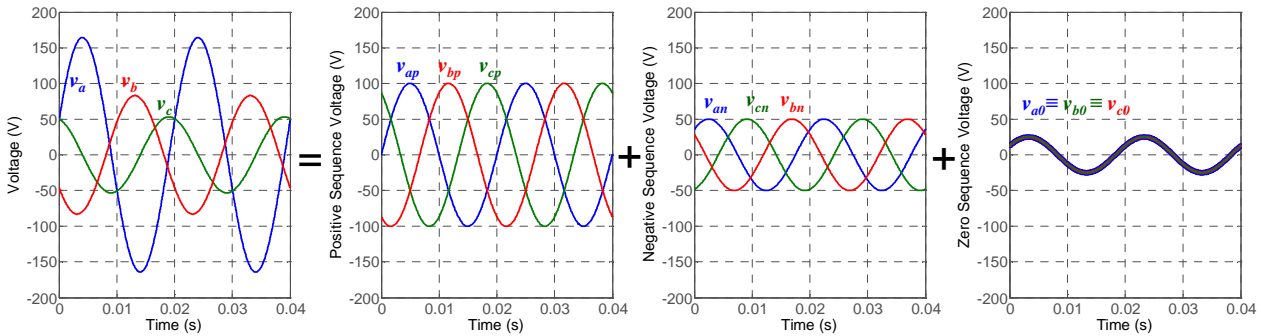


Fig. 5-78: Symmetrical components decomposition of three-phase unbalanced signals.

The symmetrical components has a clear interpretation in the ‘ d - q ’ frame. To show this, let’s consider the simple case shown in Fig. 5-79, where a balanced three-phase AC voltage source is feeding a set of resistive loads. Initially, the load is absolutely balanced, so the d - q components are DC signals. However, at $t = 0.02$ s an unbalanced load is switched-on and, consequently, the current turns to be unbalanced. This is reflected into d - q frame as an oscillation at two-times the fundamental frequency, which corresponds to negative sequence.

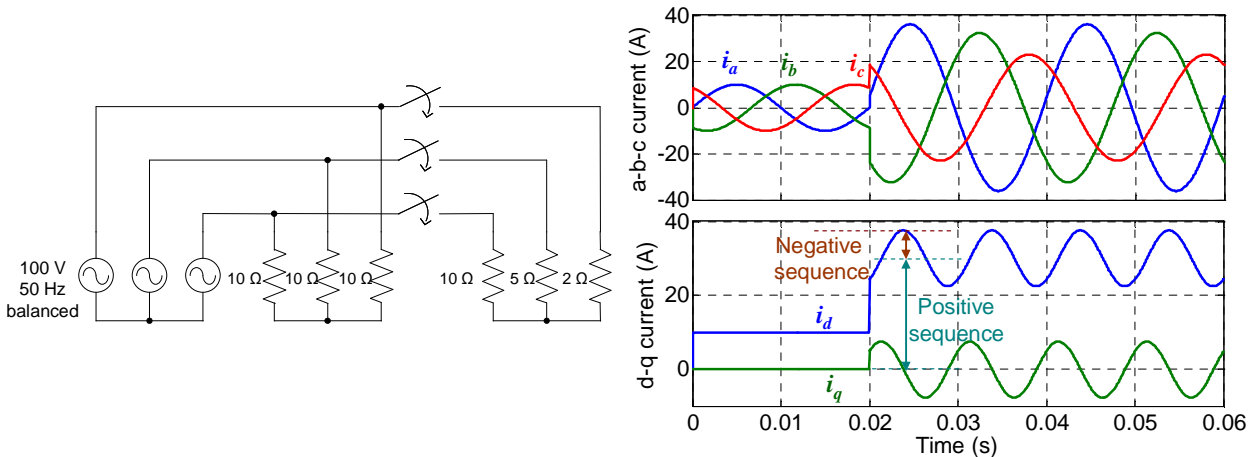


Fig. 5-79: From balanced to un-balanced conditions in a three-phase three-wire system.

The oscillation is observed because, in terms of space vectors, the negative sequence vector rotates in the opposite direction as the positive sequence vector does. Hence, if the d - q transformation rotates in the same direction as the positive sequence, then the positive sequence components are mapped as DC signals, whereas the negative sequence components are mapped as AC signals whose frequency is two times the rotating frequency. In this case there is no zero-sequence current because there is no neutral path and the constraint (5-1) holds (i.e. the sum of a - b - c signals is zero).

However, in case of four-wire systems and un-balanced conditions, there is neutral current so the constraint (5-1) does not hold. Therefore, the three-phase system cannot be fully represented only in terms of two signals. The a - b - c to d - q transformation has to be complemented with an additional coordinate, named ‘0’, which corresponds to the zero-sequence.

The ‘ a - b - c ’ to ‘ d - q -0’ transformation is given by (5-43) [177], [178]. As can be seen, the ‘0’ coordinate is related to the ‘ a - b - c ’ coordinates through constant factors, in other words, they hold a LTI relationship. In contrast, d - q components hold a LTV relationship with a - b - c components.

$$\begin{pmatrix} s_d \\ s_q \\ s_0 \end{pmatrix} = \frac{2}{3} \begin{pmatrix} \cos \theta & \cos\left(\theta - \frac{2 \cdot \pi}{3}\right) & \cos\left(\theta + \frac{2 \cdot \pi}{3}\right) \\ -\sin \theta & -\sin\left(\theta - \frac{2 \cdot \pi}{3}\right) & -\sin\left(\theta + \frac{2 \cdot \pi}{3}\right) \\ \frac{1}{2} & \frac{1}{2} & \frac{1}{2} \end{pmatrix} \begin{pmatrix} s_a \\ s_b \\ s_c \end{pmatrix}, \quad \theta = \omega_0 \cdot (t - t_0) \quad (5-43)$$

The inverse transformation is given by (5-44).

$$\begin{pmatrix} s_a \\ s_b \\ s_c \end{pmatrix} = \begin{pmatrix} \cos \theta & -\sin \theta & 1 \\ \cos\left(\theta - \frac{2 \cdot \pi}{3}\right) & -\sin\left(\theta - \frac{2 \cdot \pi}{3}\right) & 1 \\ \cos\left(\theta + \frac{2 \cdot \pi}{3}\right) & -\sin\left(\theta + \frac{2 \cdot \pi}{3}\right) & 1 \end{pmatrix} \begin{pmatrix} s_d \\ s_q \\ s_0 \end{pmatrix}, \quad \theta = \omega_0 \cdot (t - t_0) \quad (5-44)$$

The zero sequence components are mapped into a subspace that is orthogonal to the d - q subspace, and both of them are de-coupled [200]. To illustrate the impact of the zero-sequence in four wire systems, the schematic simulated above has been considered again, but now having a neutral wire. As illustrated in Fig. 5-80, when the step load is applied zero-sequence current comes up at 50 Hz, which corresponds to one third the neutral current.

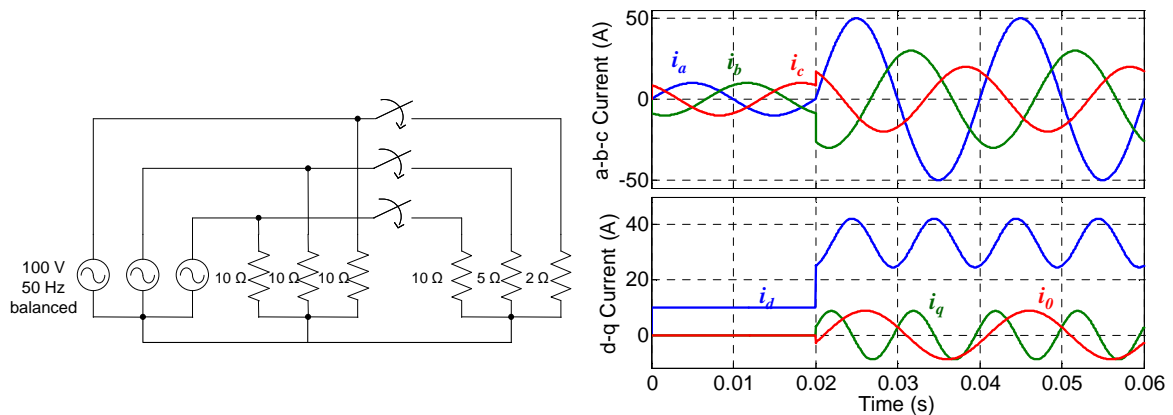


Fig. 5-80: From balanced to un-balanced conditions in a three-phase four-wire system.

5.7.2 Extensions of the black-box model

5.7.2.1 Three-wire system

In case of three-wire systems, the constraint (5-1) holds, i.e., the sum of three-phase signals is null. Hence the system is fully represented in terms of the ‘ d - q ’ coordinates, so the black-box model shown in Fig. 5-5 does not require further extension. To represent properly the steady-state behavior of the system under unbalanced load, it is important that the transfer functions of the model are accurately identified at two times the fundamental frequency. This is because the negative sequence is mapped into ‘ d - q ’ frame as an oscillation at two times the fundamental frequency (see Fig. 5-79).

5.7.2.2 Four-wire system

In case of four-wire systems, the zero-sequence components must be incorporated in the black-box model in order to address unbalanced conditions. There are several methods to tie the neutral wire to the VSI. The way the neutral current path is closed has impact on the way the zero sequence can be incorporated in the black-box model. Typical configurations of four-wire three-phase VSI are briefly described below and a first approach to address one of them is described.

First of all, it is important to remark that, since d - q components and zero-sequence components are de-coupled, **no modifications have to be done on the d - q output networks to address zero-sequence components.**

5.7.2.2.1 Delta-star transformer

A typical solution relies on the use of a zero-sequence trapping transformer, such as a delta-star transformer, as shown in Fig. 5-81. The neutral wire is tied to the mid-point of the star, in the secondary side. As a consequence, any load zero-sequence is trapped within the delta and does not flow into the DC side of the VSI. This solution is simple, robust and results in small zero-sequence output voltage as long as the leakage inductance of the transformer is low, as demonstrated below. However, the low-frequency transformer is a bulky component. This approach is widely used in several applications, such as ground power units for airplanes [184], [185] and auxiliary power systems for railways [193], where galvanic isolation is required.

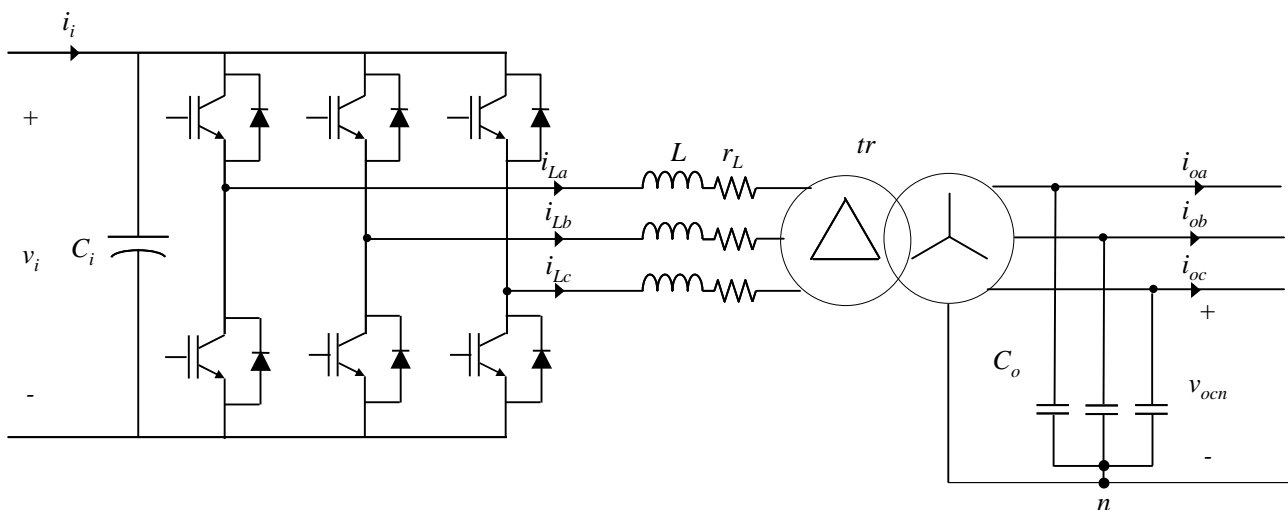


Fig. 5-81: Four wire VSI configuration based on delta-triangle transformer.

The zero-sequence equivalent circuit is shown in Fig. 5-82. It corresponds to the transformer model in parallel with the AC capacitor, where subscript ‘*l*’ denotes leakage inductance and ‘*m*’ denotes magnetizing inductance. The primary of the transformer is short-circuited, as the zero-sequence is trapped by the delta [192], [197].

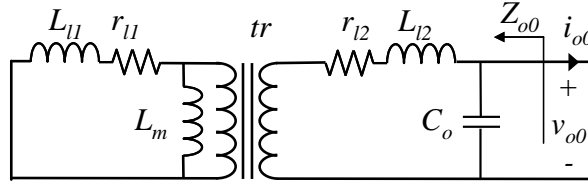


Fig. 5-82: Equivalent zero-sequence circuit in case of neutral wire tied to a delta-star transformer.

As can be seen the zero-sequence output impedance, Z_{o0} , is linear. Moreover, since typically $L_m \gg L_{l1}$ then this impedance can be approximated as given by (5-45). From this expression it follows that the lower the leakage inductance, the lower the zero-sequence impedance.

$$Z_{o0}(s) \approx \frac{(s \cdot L_{l1} + r_{l1}) \cdot tr^2 + s \cdot L_{l2} + r_{l2}}{1 + s \cdot C_o \cdot [(s \cdot L_{l1} + r_{l1}) \cdot tr^2 + (s \cdot L_{l2} + r_{l2})]} \quad (5-45)$$

The zero-sequence can be incorporated into the black-box model just by adding an additional network for the ‘*O*’ coordinate, as shown in Fig. 5-83 (extensions are highlighted in blue). As can be seen, the ‘*O*’ network only comprises one transfer function model, corresponding to the output impedance. The neutral point is tied to the mid-point of the star formed by the ‘*a-b-c*’ voltage controlled sources. This way, each voltage source corresponds to each phase-neutral voltage at the secondary of the transformer. Note that, since the delta of the transformer prevents the zero-sequence current from flowing into the DC side, no additional elements have to be added in the input network of the model.

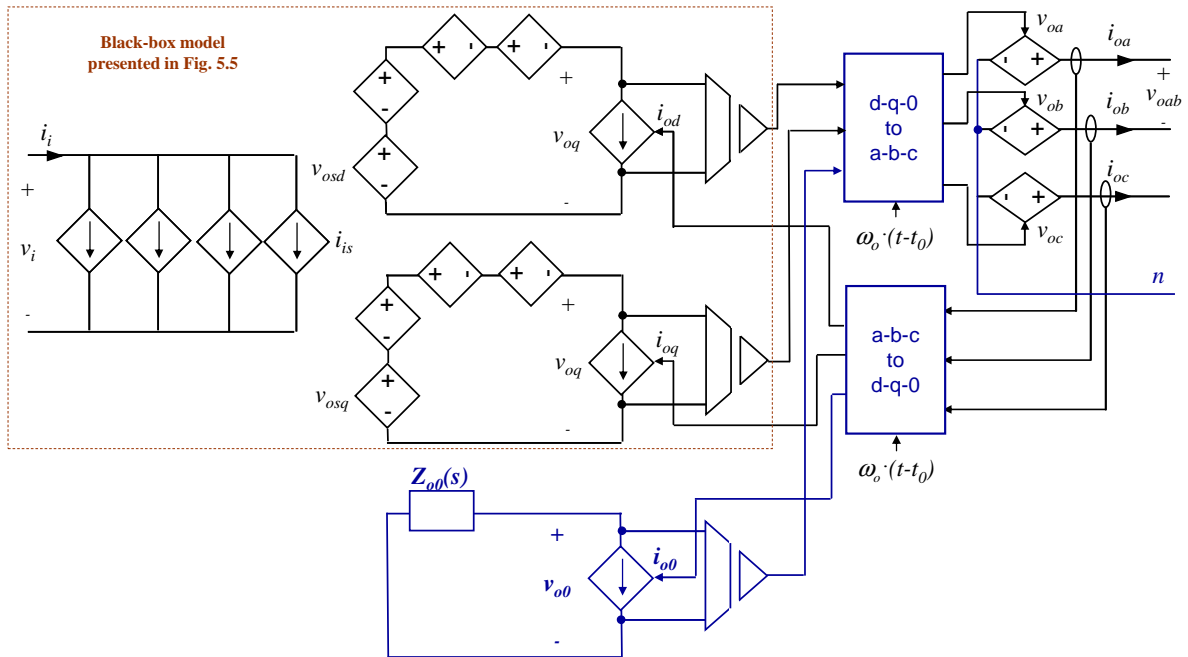


Fig. 5-83: Black-box model of a three-phase four-wire VSI with neutral wire tied to the delta-star transformer.

It is important noting that the dynamics of the AC filter remains unchanged when mapping it into zero-sequence components, because the relationship between them is LTI, as indicated above. It is also worth remarking that, if the model is intended to represent balanced conditions, the '0' network can be neglected because no neutral current will flow.

5.7.2.2.2 Alternative four-wire VSI configurations

Another approach to provide a path for the neutral current is to split the DC link capacitor into two and connect the neutral wire to the mid point of the capacitors, as shown in Fig. 5-84.

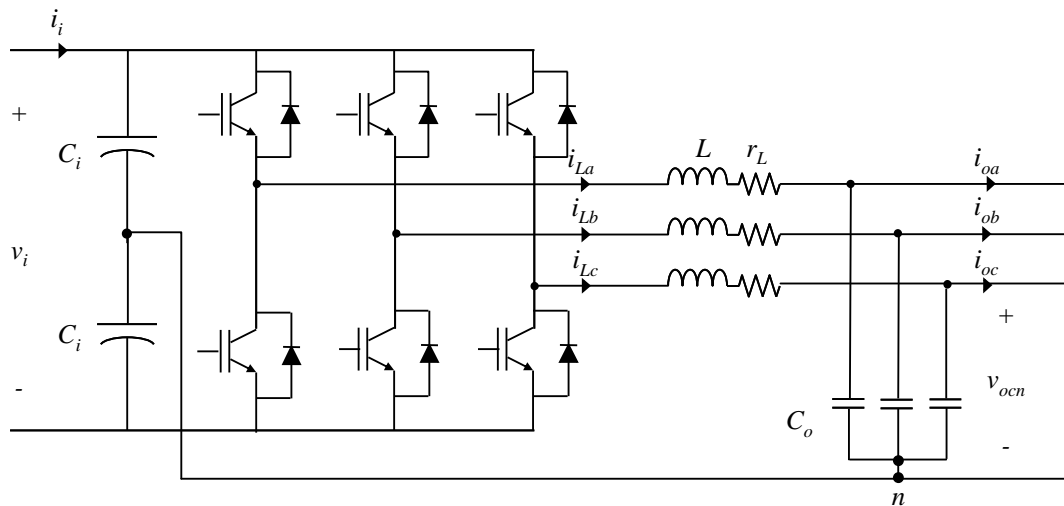


Fig. 5-84: Four wire VSI configuration based on split DC link capacitor.

This is a simple passive solution, but requires huge DC link capacitors to achieve acceptable input voltage oscillation under unbalanced conditions due to the neutral current flowing through them. Another drawback is a lack of the DC link voltage utilization, as the maximum modulation index within linear region is lower [178].

An active alternative consists in adding an additional leg to the VSI switching bridge and tying the neutral wire to the mid point of the leg, as shown in Fig. 5-85.

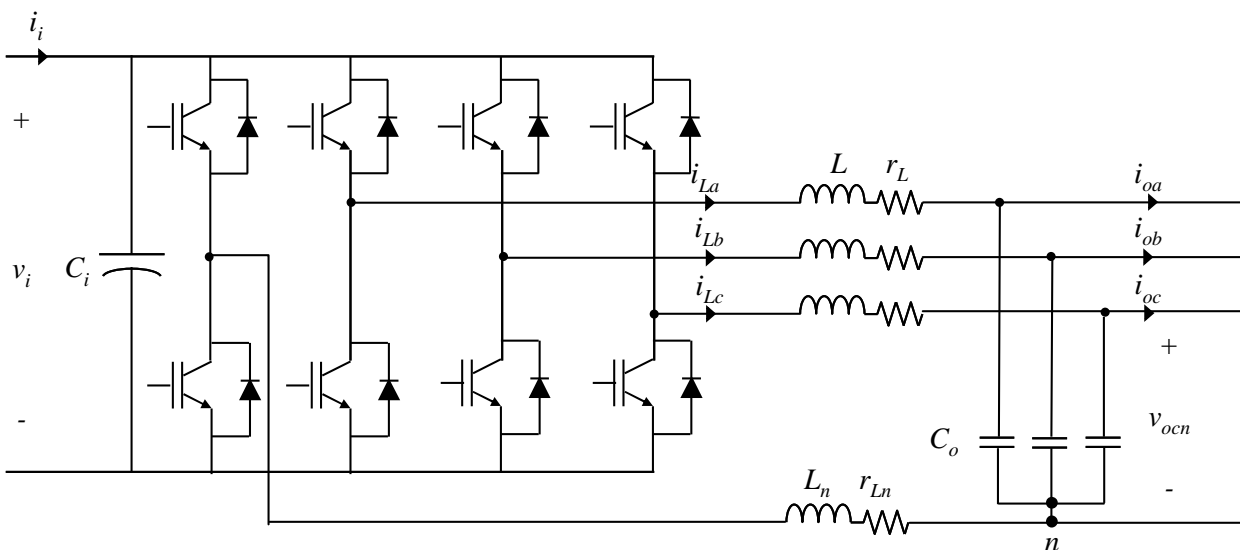


Fig. 5-85: Four-wire VSI configuration based on four-leg power stage.

This way, the neutral current can be controlled through the added switches and higher utilization of the DC link voltage can be achieved [177], [178], [183]. However, there are more switching devices and additional EMI problems may come up due to the switched neutral point. An additional inductor can be added in the neutral path to reduce the switching ripple content of the neutral current.

In those cases the zero-sequence will be reflected also in the DC side. However, the way the black-box model should be extended has not been studied yet and is a matter of future research.

5.7.3 Identification of zero-sequence impedance

The zero sequence comes up only under unbalanced situations. Therefore, it can be stepped just by making a load step from balanced to unbalanced conditions, as shown in Fig. 5-86.

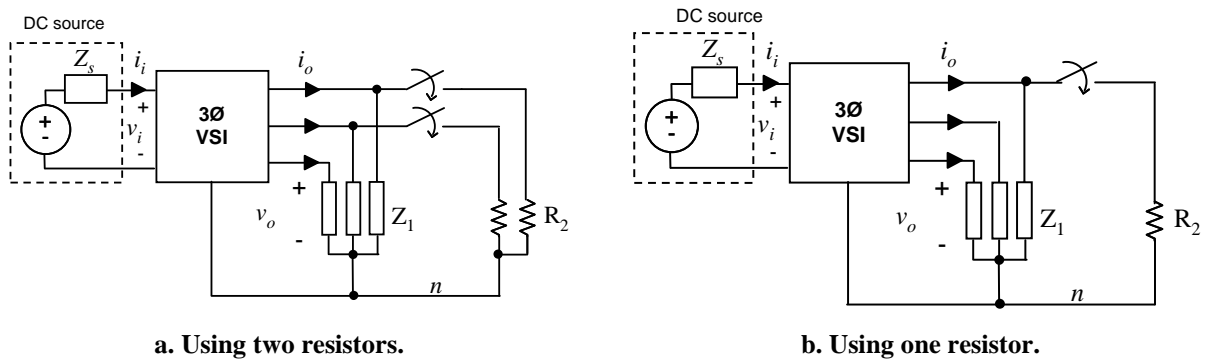


Fig. 5-86: Experimental tests for identification of zero-sequence network.

However, as a difference from the d - q signals under balanced conditions, the zero-sequence oscillates at steady-state (at the fundamental frequency). As a consequence, the transient response of the zero-sequence current and voltages, v_{o0} and i_{o0} must be filtered using a Notch filter to remove the steady-state oscillation. This way, the signal is constant before and after the step, so parametric identification can be readily applied. A second-order Notch filter has the following form (continuous time realization), where ω_c and B are the notching frequency and the bandwidth, respectively.

$$L(s) = \frac{s^2 + \omega_c^2}{s^2 + B \cdot s + \omega_c^2} \quad (5-46)$$

5.7.4 Simulation results

The predicting capabilities of the black-box model, under unbalanced conditions, are analyzed by simulation in this section. Both three-phase and four-wire systems are considered.

5.7.4.1 Three-wire system

The case study is the same that has been tackled in section 5.5. The schematic of the VSI and the corresponding black-box model are shown in Fig. 5-24 and Fig. 5-29, respectively. Both the switching model and the black-box model have been subjected to a resistive load step from balanced to unbalanced conditions, as shown in Fig. 5-87. As can be seen, 2 kW load are switched but only in the phase 'a' and the phase 'c'.

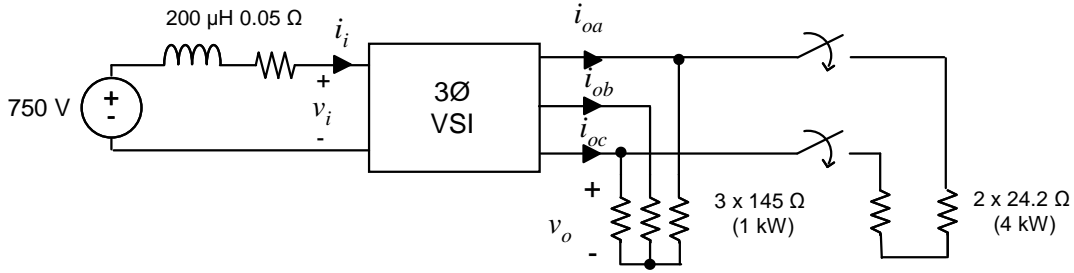


Fig. 5-87: Validation test. Load step from balanced to un-balanced conditions in a three-wire VSI.

The resulting waveforms are depicted in Fig. 5-88. The d - q model already identified in section 5.5 matches the switching model response under unbalanced conditions. Only a slight mismatch is observed in the input current, which is attributed to the slight $H_{id}(s)$ dependence on I_{od} . Therefore, in case of three-wire systems, the d - q model shown Fig. 5-5 can reproduce the large-signal behavior of the VSI both under balanced and unbalanced conditions.

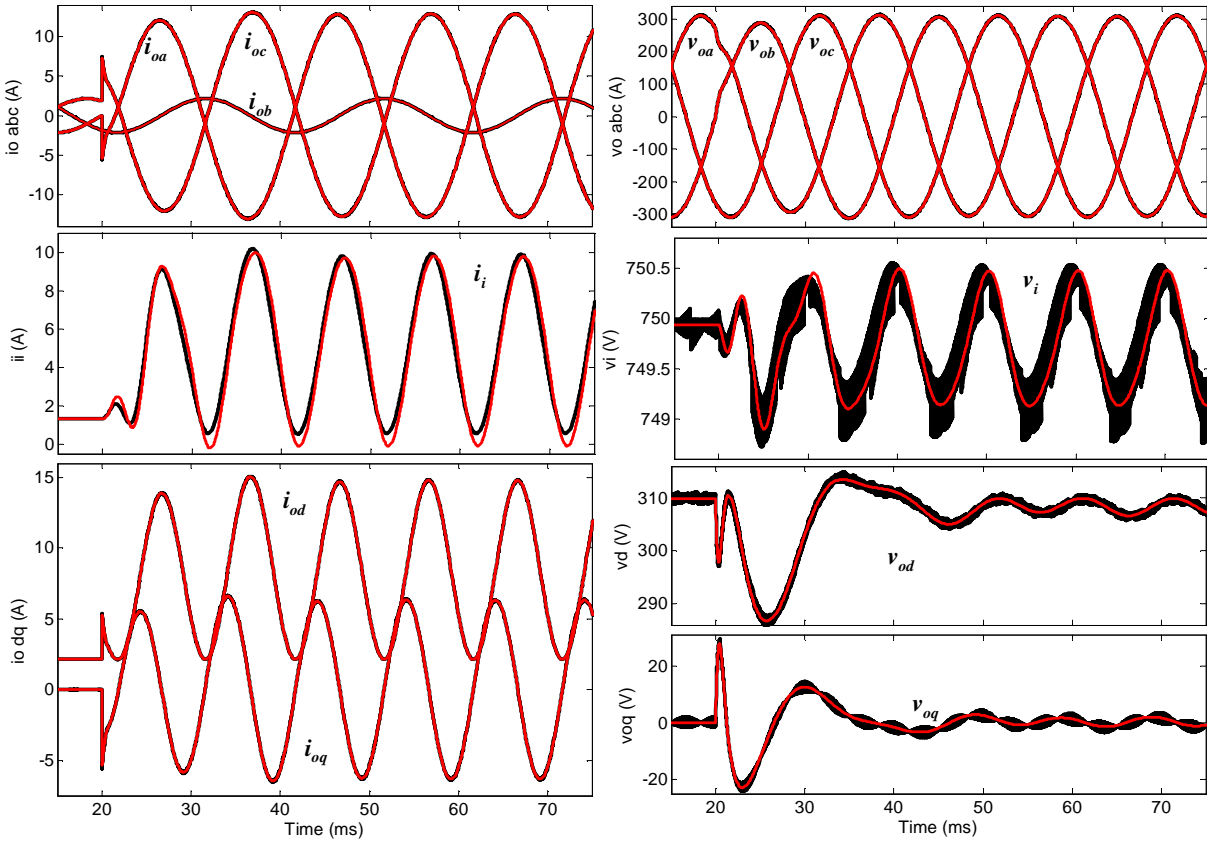


Fig. 5-88: Validation test. Comparison of switching model response (dark traces) and black-box model response (red traces)

The steady-state behavior of the VSI deserves a more detailed analysis. The PR regulator, implemented in stationary frame (either a - b - c or α - β), makes the output voltage to remain practically balanced, as it compensates both the positive and the negative sequence [198], [199]. Such a property is evidenced in the output impedance at 100 Hz. The d - q voltage at 100 Hz can be expressed as

$$\begin{cases} V_{od}(2j\omega_o) = -Z_{odd}(2j\omega_o) \cdot I_{od}(2j\omega_o) - Z_{odq}(2j\omega_o) \cdot I_{oq}(2j\omega_o) \\ V_{oq}(2j\omega_o) = -Z_{oqd}(2j\omega_o) \cdot I_{od}(2j\omega_o) - Z_{oqq}(2j\omega_o) \cdot I_{oq}(2j\omega_o) \end{cases} \quad (5-47)$$

Notice in Fig. 5-88 that the currents at 100 Hz are shifted 90°, so they can be expressed as

$$\vec{I}_{oq}(2j\omega_o) = j \cdot \vec{I}_{od}(2j\omega_o) \quad (5-48)$$

Therefore, the voltage oscillation at 100 Hz will be null if the following equalities are fulfilled.

$$\begin{cases} Z_{odq}(2j\omega_o) = j \cdot Z_{odd}(2j\omega_o) \\ Z_{oqd}(2j\omega_o) = -j \cdot Z_{oqq}(2j\omega_o) \end{cases} \quad (5-49)$$

As shown in Fig. 5-89, at 100 Hz the impedances are approximately equal in magnitude and approximately shifted 90°. This is the reason why the unbalanced is reflected only as a slight oscillation in the d - q voltage, at steady-state. They are not fulfilled at all because a certain damping was provided at 50 Hz in the PR regulator (refer to appendix A.1.2).

Therefore, from this analysis it follows that, **in order to reproduce properly the response of the VSI under unbalanced conditions, the transfer functions of the model must be accurately identified at two times the fundamental frequency.**

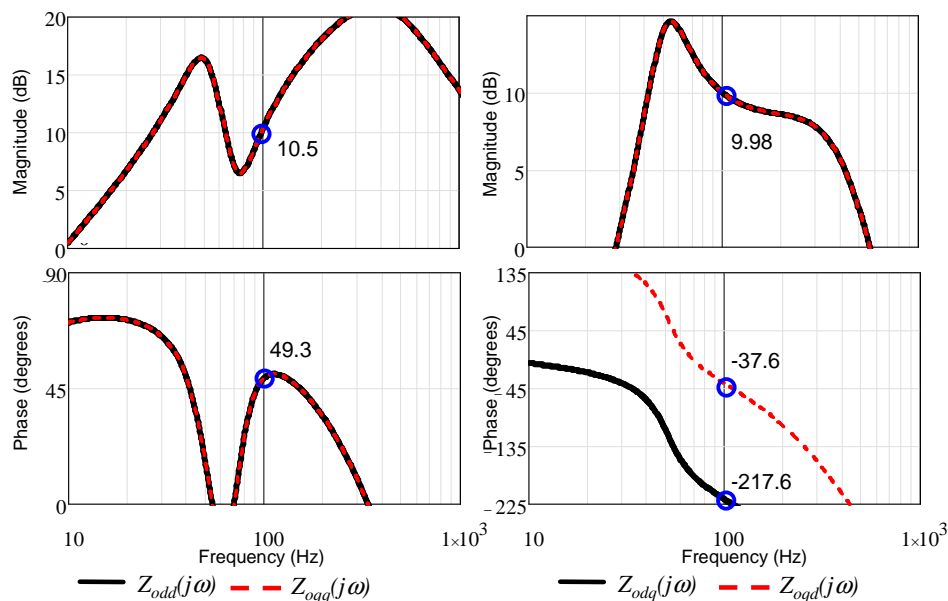
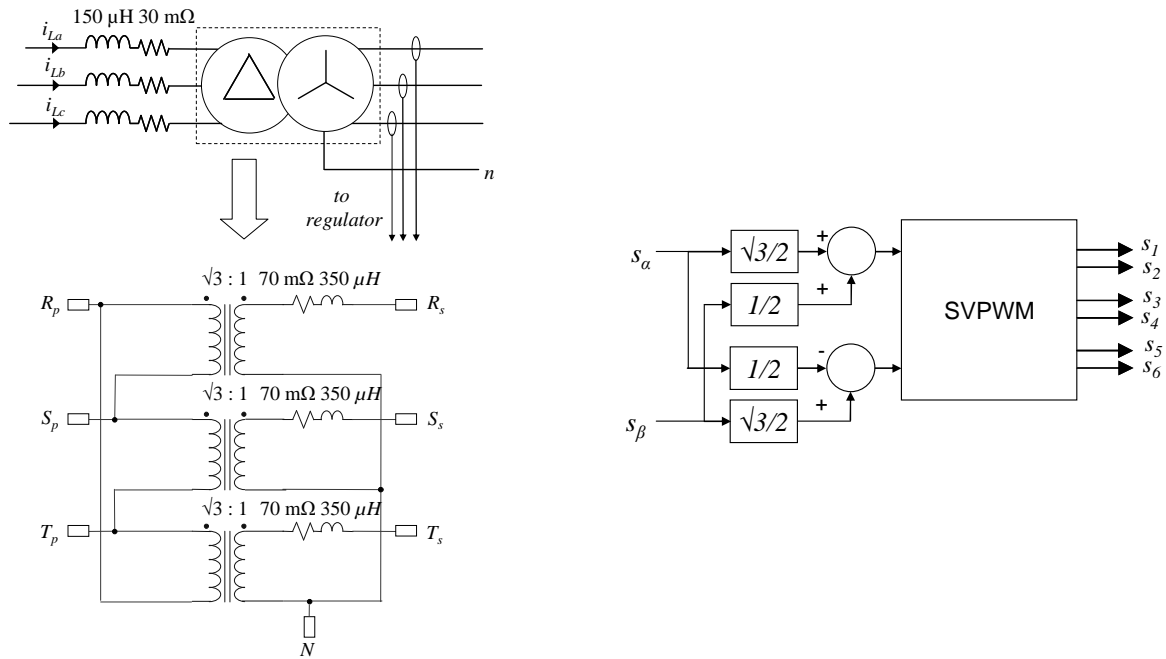


Fig. 5-89: Frequency response of the output impedance within d - q , remarking the response at 100 Hz.

5.7.4.2 Four wire system (only VSI with delta-star transformer)

In order to validate the modeling concepts described in section 5.7.2.2, the VSI simulation model studied in section 5.5 (see Fig. 5-24) has been provided with a delta-star transformer. It has been done so that the d - q dynamics remains unchanged. The modifications are listed below and are illustrated in Fig. 5-90.

- The transformation ratio of the line-line voltage is one and the magnetizing inductance has been assumed to be infinite.
- The previous AC inductor impedance has been shared between the new one and the equivalent series impedance of the transformer.
- The transformer introduces a 30° phase shift between the primary and the secondary currents. Therefore, the input signals of the modulator have been linearly combined so that such a phase shift is compensated. On the other hand, the current sensors have been moved to the secondary side.



a. Power stage modifications (Fig. 5-24a).

b. Control stage modifications (Fig. 5-24b).

Fig. 5-90: Modifications done in the simulated VSI when adding a delta-triangle transformer.

As explained before, the model has to be complemented with the ‘0’ sequence output impedance, which is identified by applying a load step from balanced to unbalanced conditions.

To do this, the experiment shown in Fig. 5-86b has been carried out, where Z_1 is comprised of three 145 Ω resistors (1 kW total power) and R_2 is comprised of a single 24.2 Ω resistor, (2kW power) tied to the phase ‘a’. The resulting waveforms are shown in Fig. 5-91. A large oscillation is found out in the zero-sequence voltage, which corresponds to the resonance between the leakage inductance of the transformer and the output capacitor. In fact, that oscillation contains the dynamic information from which the zero-sequence impedance will be identified.

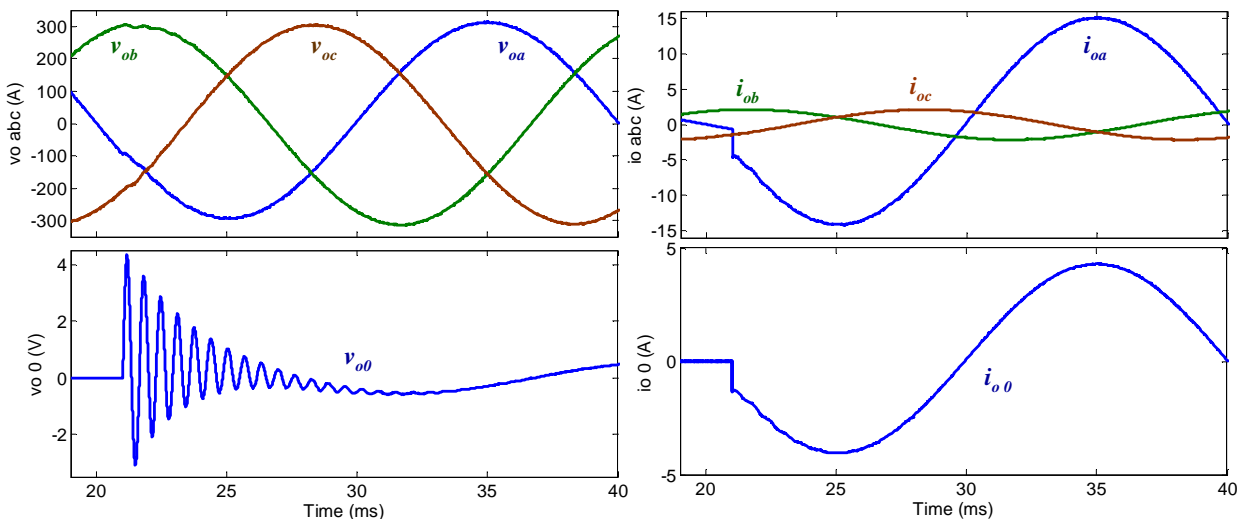


Fig. 5-91: Transient response of the four-wire VSI under a load step from balanced to unbalanced conditions.

The Notch filter has been designed using the Matlab function ‘*iirnotch*’, including in the Filter Design Toolbox. Both the center frequency and the bandwidth are 50 Hz (quality factor is 1)^{5.10}.

Both the filter frequency response and the filtering results are depicted in Fig. 5-92. Note that the high-frequency transient oscillation is preserved in the filtered-signals, while the 50 Hz steady-state oscillation is removed. No further pre-processing actions have been required.

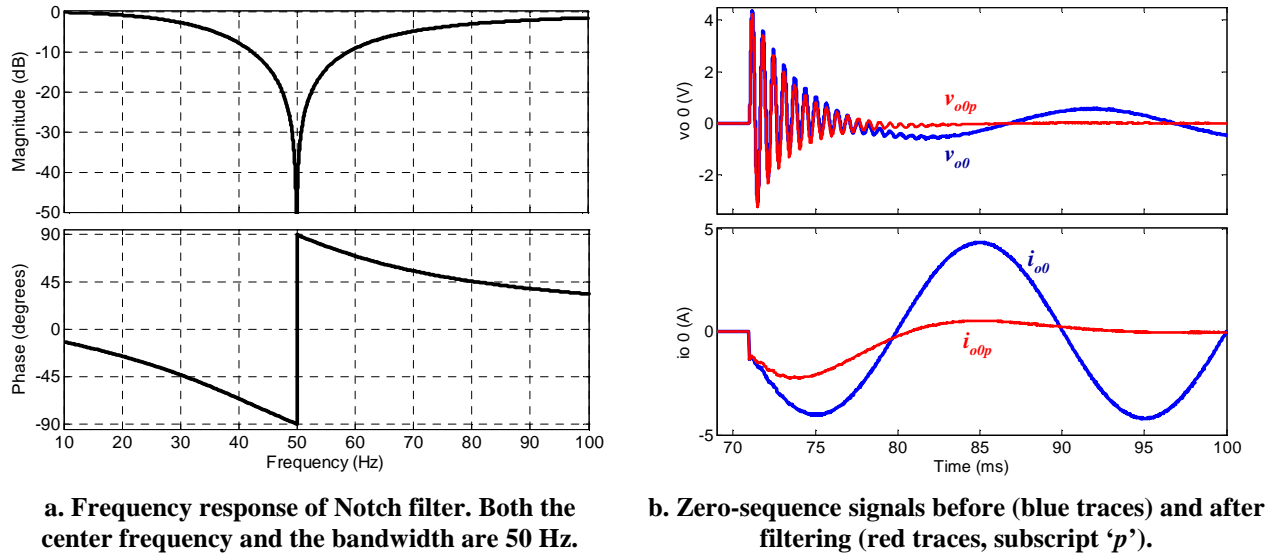


Fig. 5-92: Filtering the zero-sequence components through a Notch filter.

The fitting results of the zero-sequence impedance (using the function ‘*oe*’) are depicted in Fig. 5-93a. A second order model, corresponding to the leakage inductance of the transformer and the AC filter capacitor, yields an accurate fit. A comparison of the frequency response of the identified model and the theoretical transfer function, (5-45), is given in Fig. 5-93b. Both frequency responses match. This validates both the theoretical analysis of the zero-sequence impedance and the proposed identification method.

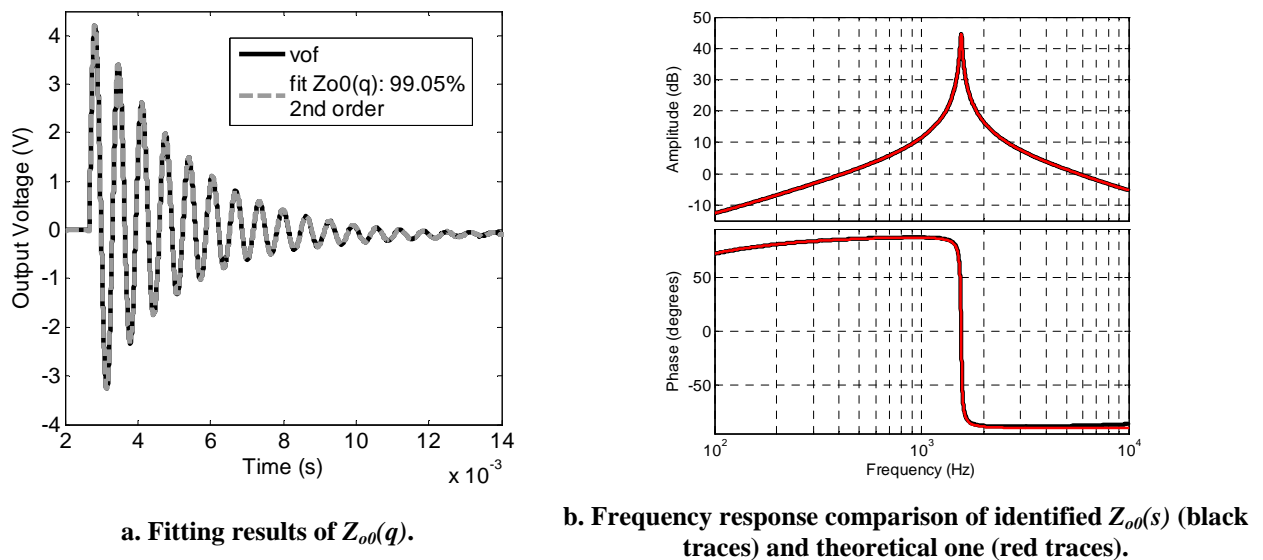


Fig. 5-93: Identifying the zero-sequence.

^{5.10} The higher the quality factor of the Notch filter, the longer the setting time of the filtered signal.

Finally, the proposed four-wire extended black-box model has been validated. The validation test is the same that has been considered in the previous section, (Fig. 5-87), but now a neutral wire is tied between the mid point of the load and the power converter. The comparison between the switching model response and the black-box model response is shown in Fig. 5-94. The good agreement between the responses of both models validates the proposed extensions of the black-box model to handle zero-sequence components.

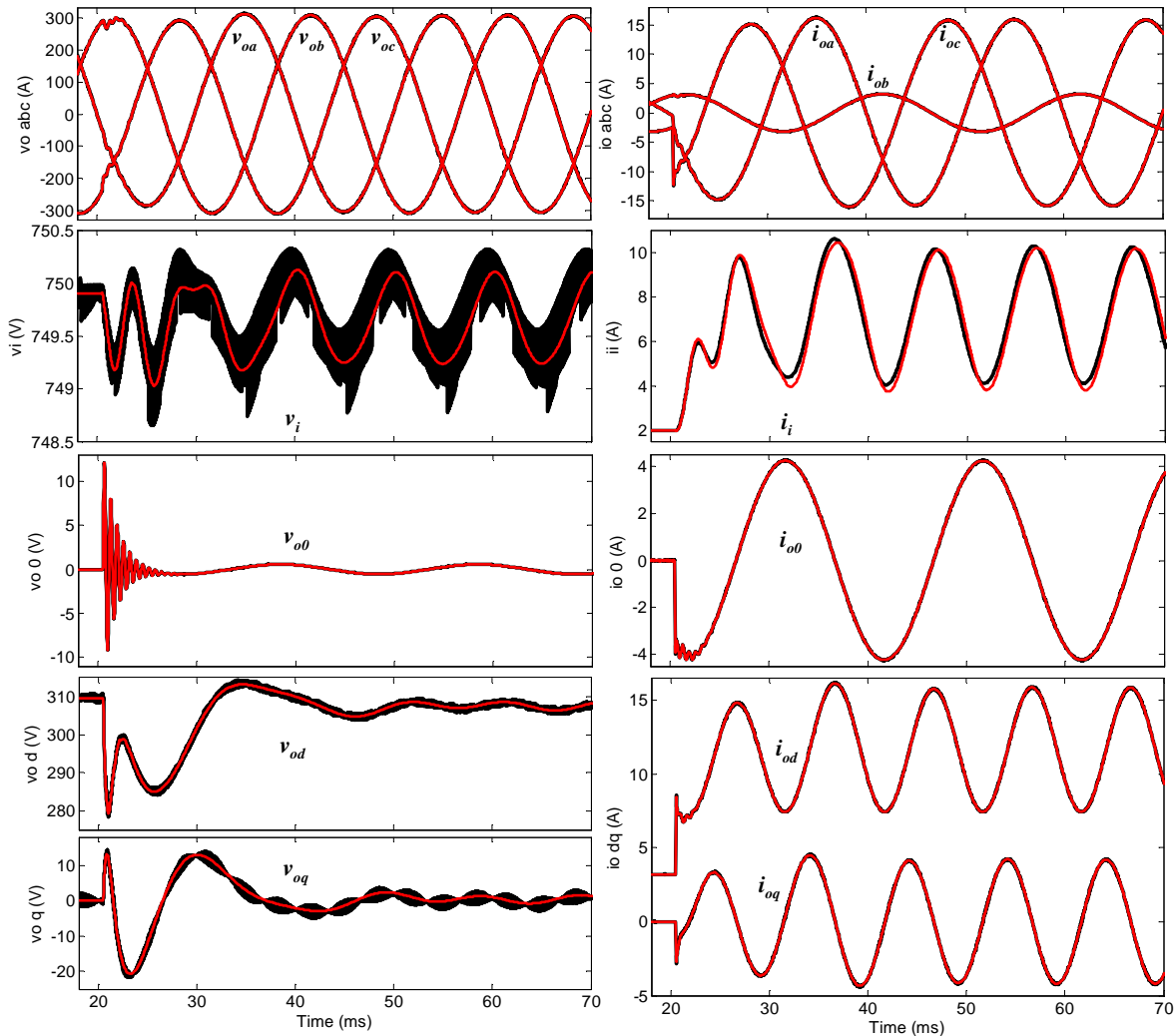


Fig. 5-94: Validation test. Comparison of switching model response (dark traces) and black-box model response (red traces).

5.8 Conclusions

In this chapter, a novel large-signal black-box modeling and identification method of three-phase voltage source inverters, based on transient response under step tests, has been proposed as original contribution.

- The model consists on a g-parameters network, implemented in d - q coordinates. The input network consists of a Norton circuits and the output networks consists of Thevenin circuits (one for each coordinate). Transformation blocks are implemented to interface the d - q model with the rest of the AC bus (supposed to be described in a - b - c coordinates). The model is made up using transfer function models and nonlinear static functions and is capable of reproducing

the large-signal behavior of the converter. More specifically, in this thesis, starting from an existing small-signal model, an extension to large-signal modeling has been proposed.

- The identification method is based on the transient response of the converter under a set of very simple tests: an active power step (resistive load step), a reactive power step (capacitive load disconnection) and an input voltage step. After that, parametric identification algorithms are applied to obtain transfer function models from the step response. Finally, cross-coupling effects with the load-source subsystems are analyzed and removed (if necessary), yielding un-terminated transfer functions. Finally, in order to make up the large-signal model, some additional post-processing actions are carried out on the un-terminated transfer functions.
- Some dynamic properties of the three-phase VSI have been described which simplifies the modeling procedure. Such properties apply when the input filter is capacitive and no DC-DC front-end converter is used, which is a common case. Moreover, if the regulation scheme is linear and all coordinates are regulated with the same parameters, then the output impedance of the VSI features orthogonal properties.
- The modeling and the identification procedure, as well as the aforementioned dynamic properties, have been validated through both simulation results and experimental measurements. A comprehensive discussion of the obtained results has been presented as well. On the one hand, the black-box model is able to reproduce with high accuracy the large-signal behavior of the three-phase VSI. On the other hand, the model parameters can be accurately identified using the proposed technique. Nevertheless, the use of the step as excitation signal may reduce the model identifiability at high frequency.
- Finally, the behavior of the black-box model under unbalanced conditions has been discussed. It has been demonstrated that, in case of three-wire systems, the $d-q$ frame based model is able to reproduce unbalanced conditions. However, in case of four-wire systems, the model has to be extended with an additional zero-sequence network. First solutions to this has been provided and validated through simulation results.

6 Black-box modeling of a fuel cell power supply based on DC-DC converter with input current control

6.1	Introduction.....	223
6.2	Model description.....	224
6.2.1	Description of the modeled subsystem.....	224
6.2.2	Model structure	224
6.2.2.1	Small-signal approach	224
6.2.2.2	Large-signal approach	225
6.3	Model identification.....	228
6.3.1	Identification step tests.....	228
6.3.1.1	Reference signal step.....	229
6.3.1.2	Output voltage step.....	229
6.3.1.3	Output current step.....	230
6.3.1.4	Practical considerations	231
6.3.2	Cross-coupling effects.....	232
6.3.2.1	Removal.....	232
6.3.2.2	Analysis.....	232
6.3.2.3	Prevention.....	233
6.3.3	Transfer functions post-processing	233
6.3.4	Overview of the identification procedure.....	233
6.4	Experimental results.....	235
6.4.1	Subsystem description.....	235
6.4.2	Preliminary tests: linearity analysis.....	236
6.4.3	Dynamic networks modeling	238
6.4.4	Identification of transfer functions	238
6.4.4.1	Transfer function $G_{refm}(s)$	238
6.4.4.2	Transfer function $Y_o(s)$	239
6.4.5	Analysis and removal of crosscoupling effects.....	241
6.4.5.1	Analysis	241
6.4.5.2	Removal.....	241
6.4.5.3	Model order reduction	242
6.4.6	Parameterization of the large-signal model.....	242
6.4.7	Model validation	243
6.4.7.1	Test 1. Large reference signal step at maximum output voltage	243
6.4.7.2	Test 2. Large reference signal step and battery bus power step	244
6.4.7.3	Test 3. Resistive load step	245
6.4.7.4	Test 4. Triangular reference signal with resistive load.....	246
6.5	Conclusions.....	247

6.1 Introduction

Novel power distribution systems for on-board applications comprise a wide variety of energy sources and storage components, including engines, batteries, super capacitors and fuel cells (FCs) (refer to section 1.2.2). As a consequence, DC-DC converters with control strategies, different from output voltage control, are required.

For instance, consider the system shown in Fig. 6-1, which comprises a DC-DC converter that delivers power from a FC to a battery bus. This may represent the APU for a MEA or the drive train system for an electric vehicle introduced in chapter 1 (Fig. 1.4 and Fig. 1.7, respectively). In such systems, the average power is supplied by the FC whereas the battery covers the peak power demands. As the bus voltage is imposed by the battery, a DC-DC converter with input-current control is used to perform direct regulation of the power delivered from the fuel cell to the bus.

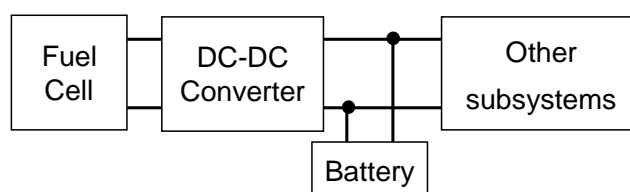


Fig. 6-1: Fuel cell based power supply tied to a battery bus.

However, at the moment, existing modeling techniques focus on either un-regulated converters, or converters with output voltage control. These approaches are not appropriate in this case, because a power converter with output voltage control behaves essentially as a voltage source, whereas a converter with input current control essentially behaves as a power source. As a consequence of such qualitative difference, a different black-box modeling approach is required.

This chapter proposes a black-box modeling and identification technique for subsystems comprised of a DC-DC converter with input current control, cascaded to a FC. The DC-DC converter is hereinafter referred to as ‘Power Conditioning Unit’ (PCU). The modeling and identification method features similar characteristics as those presented in previous chapter:

- The proposed model reproduces the large-signal low-frequency behavior of the subsystem comprised of the fuel cell in series with the PCU, in terms of its input-output signals.
- The identification procedure is based on the step response of the converter.

The chapter is organized as follows:

- Section 6.2: The proposed black-box model is described.
- Section 6.3: The identification method is explained.
- Section 6.4. The method is illustrated and validated by making use of a commercial DC-DC converter specifically designed for fuel cell power conditioning.

6.2 Model description

6.2.1 Description of the modeled subsystem

The modeled subsystem is shown in Fig. 6-2. The converter is controlled with an inner current loop, which regulates the current being subtracted from the fuel cell. The reference signal for that loop, namely i_{ref} , is set by an external control unit as a function of the power system requirements [25], [26], [203], [206].

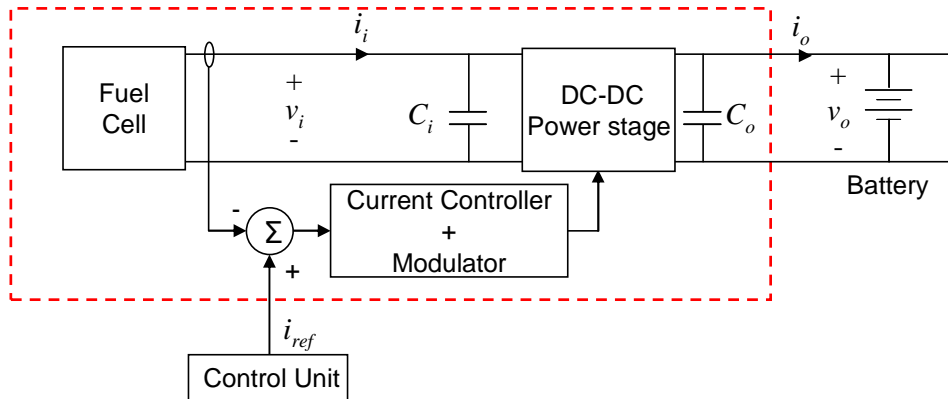


Fig. 6-2: Diagram of the modeled subsystem (dashed by red line).

6.2.2 Model structure

6.2.2.1 Small-signal approach

In order to determine a proper model structure, the input-output signals of the subsystems have to be determined and sorted as model inputs and outputs.

The modeled subsystem comprises not only the PCU but also the FC. Hence, the only interface signals are i_{ref} , v_o and i_o . As a difference from previous models, the output voltage is determined by an external subsystem (in this case a battery bus), so the best choice is to model the output port as a Norton network, so that v_o is a model input and i_o is a model output. On the other hand, i_{ref} is also a model input because it is imposed by an external subsystem (the control unit).

Therefore, the black-box model is a two-input one-output network, as shown in Fig. 6-3. In terms of small-signal, the input-output dynamic relationship can be represented by two transfer functions, which are described below.

- $Y_o(s)$ corresponds to the output admittance of the converter and models the dynamic relationship between i_o and v_o .
- $G_{ref}(s)$ models the dynamic relationship between i_o and i_{ref} . Since i_{ref} drives i_i , it represents the closed-loop control transfer function (i.e. $i_i(s)/i_{ref}(s)$) cascaded to the relationship $i_o(s)/i_i(s)$.

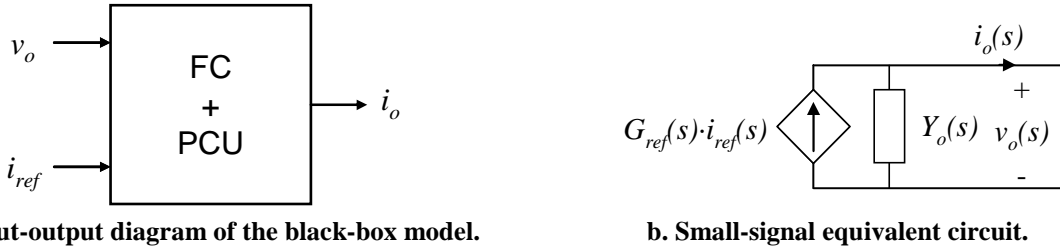


Fig. 6-3: Proposed black-box model: basic approach.

6.2.2.2 Large-signal approach

To address large-signal behavior, the small-signal structure is complemented with a static network that represent the static behavior of the subsystem $i_{os}(v_o, i_{ref})$. On the other hand, the transfer function models ($G_{ref}(s)$ and $Y_o(s)$) are replaced by more general dynamic networks, namely $G_{ref0}(v_o, \dots)$ and $Y_{o0}(i_{ref}, \dots)$, that can be either linear or nonlinear, and whose response at steady-state is null (meaning of subscript ‘0’). The resulting large-signal model is shown in Fig. 6-4. The dynamic networks are modeled as described in previous chapters, i.e. by using transfer functions, gain scheduled transfer functions and LLMNs (refer to section 4.2.3).

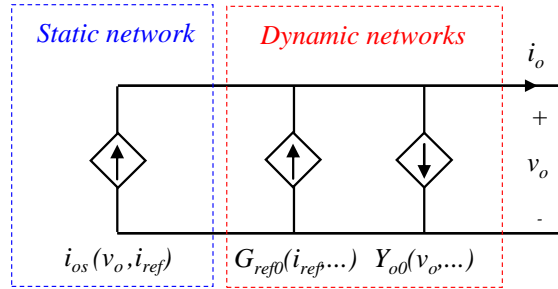


Fig. 6-4: Large-signal model of a FC power supply based on DC-DC converter with input current control.

Under small-signal perturbations, the large-signal model is related to the small-signal one through the following expressions:

$$Y_o(s) = Y_{o0}(s) - \frac{\partial i_{os}(V_o, I_{ref})}{\partial V_o}, \quad G_{ref}(s) = G_{ref0}(s) + \frac{\partial i_{os}(V_o, I_{ref})}{\partial I_{ref}} \quad (6-1)$$

Below, a static analysis is described, from which some guidelines for implementing the dynamic networks are derived.

6.2.2.2.1 Static network modeling

The static relationship between the input-output variables can be derived from a power balancing as given by (6-2), where η denotes the efficiency of the converter and is a function of operating point.

$$V_o \cdot I_o = V_i \cdot I_i \cdot \eta(V_o, I_i, V_i) \quad (6-2)$$

The relationship between V_i and I_i can be expressed as a function of the inner resistance ‘ R_{fc} ’ and the open-circuit voltage ‘ V_{ofc} ’ of the FC as expressed by (6-3), where R_{fc} is a nonlinear function of current, but nearly linear within ohmic region [207]-[269]. This is illustrated in Fig. 6-5, where the static I-V curve of a polymer electrolyte membrane (PEM) fuel cell is shown (blue line).

$$V_i = V_{ofc} - R_{fc}(I_i) \cdot I_i \quad (6-3)$$

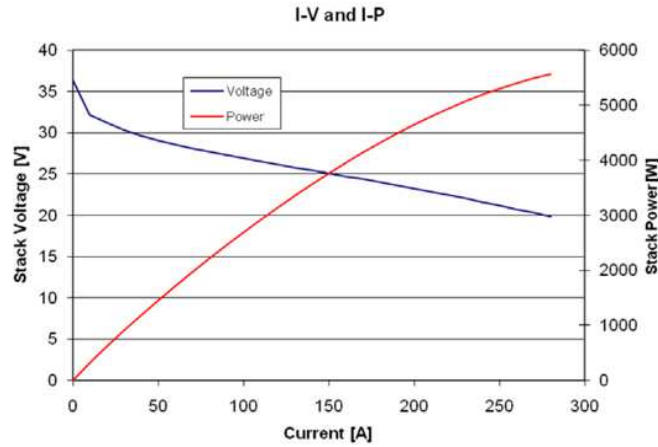


Fig. 6-5: Static response of a PEM FC [269].

On the other hand, the current controller is usually provided with integral action, so that the sensed FC current (i_i) tracks i_{ref} at steady-state. Taking into account the sensor gain and other scaling factors, the input current can be expressed as a function of the reference current through a linear relationship as given by (6-4), where α_1 and α_2 are constant factors.

$$I_i = \alpha_1 + \alpha_2 \cdot I_{ref} \tag{6-4}$$

Combining (6-2), (6-3) and (6-4), the following expression is derived, where the nonlinear static input-output relationship is evidenced.

$$I_o = i_{os}(V_o, I_{ref}) = \frac{\eta(V_o, I_{ref})}{V_o} \cdot \left(V_{ofc} \cdot (\alpha_1 + \alpha_2 \cdot I_{ref}) - R_{fc}(I_{ref}) \cdot (\alpha_1 + \alpha_2 \cdot I_{ref})^2 \right) = \frac{P_o}{V_o} \tag{6-5}$$

Such a nonlinear static relationship is also reflected in the low-frequency dynamic behavior of the subsystem. Taking this result into account, suitable options for the modeling of G_{ref0} and Y_{o0} are described below.

6.2.2.2.2 Modeling G_{ref0}

According to (6-5), the static gain of G_{ref0} will depend on V_o and I_{ref} . If this is the dominant nonlinearity, G_{ref0} can be well approximated by a gain-scheduled transfer function, as shown in Fig. 6-6^{6.1}. The scheduling function (GS) is mathematically defined as follows.

$$GS(i_{ref}, v_o) = \frac{\partial i_{os}(i_{ref}, v_o)}{\partial i_{ref}} \tag{6-6}$$

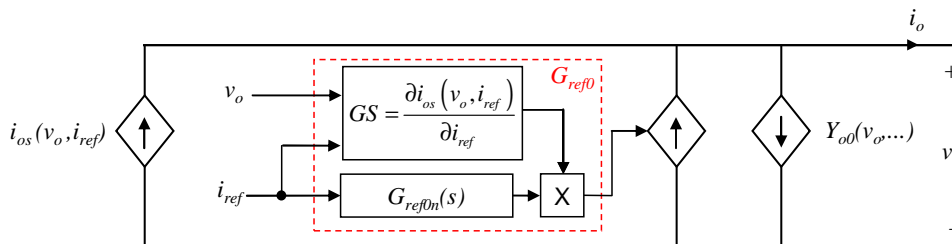


Fig. 6-6: Modeling G_{ref0n} as a gain-scheduled transfer function.

^{6.1} Notice that, as explained in chapter 4, subscript ‘0’ means null response at steady-state and subscript ‘n’ means normalized gain.

By applying small-signal perturbations on i_{ref} , the small-signal transfer function given by (6-7) is obtained. This equation shows that the function GS corresponds to the static gain of $G_{ref}(s)$ in the small-signal model. Therefore, the dynamic relationship between i_{ref} and i_o is equally scaled at all frequencies. Note that $|G_{ref0n}(0)| = 0$, as the statics is addressed by the network i_{os} .

$$G_{ref}(s) = \underbrace{G_{ref0n}(s) \cdot GS(I_{ref}, V_o)}_{G_{ref0}(s)} + \frac{\partial i_{os}(I_{ref}, V_o)}{\partial I_{ref}} = (G_{ref0n}(s) + 1) \cdot GS(I_{ref}, V_o) \quad (6-7)$$

More details about gain-scheduled transfer functions can be found in section 4.2.3.3.

However, if additional dynamic dependence on operating point is observed, then a LLMN should be used instead of a gain-scheduled transfer function. Details about LLMNs are found in section 4.2.3.2.

6.2.2.2.3 Modeling Y_{o0}

According to (6-5), I_o is inversely proportional to V_o . Therefore, for frequencies well below the cross-over frequency of the control loop (f_c), i_i is approximately constant if i_{ref} is kept constant and, consequently, P_o is also approximately constant. **As a consequence the subsystem behaves as a ‘constant-power-source’ P_o at the output port** (see Fig. 6-7)^{6.2} and the low-frequency output admittance can be expressed as follows.

$$I_o = \frac{P_o}{V_o} \Rightarrow Y_o(s)|_{s \rightarrow 0} = -\frac{\partial I_o}{\partial V_o} = \frac{P_o}{V_o^2} = \frac{I_o}{V_o} \quad (6-8)$$

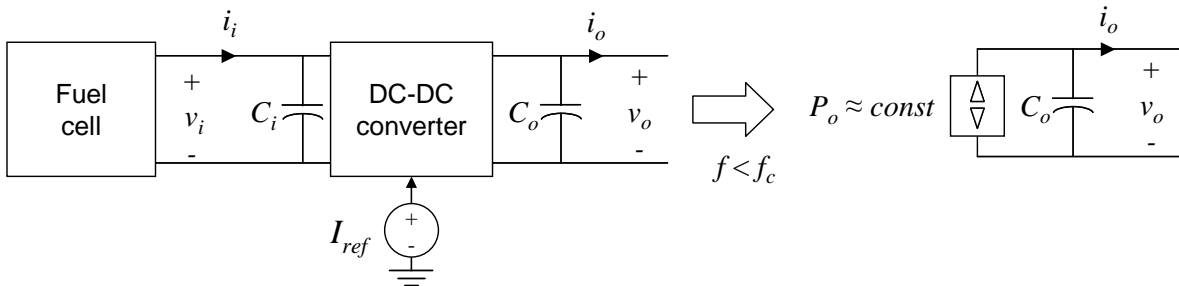


Fig. 6-7: Equivalent model of the PCU for frequencies below the cross-over frequency of the control loop, f_c .

As the frequency increases, the equivalent model shown at the right part of Fig. 6-7 is less accurate, but the influence of the output capacitor ‘ C_o ’ on $Y_o(s)$ increases. In fact, in many practical cases, for frequencies above f_c , the admittance is essentially determined by ‘ C_o ’. In those cases, $Y_o(s)$ is well approximated as follows.

$$Y_o(s) = -\frac{\partial i_{os}(I_{ref}, V_o)}{\partial V_o} + Y_{o0}(s) = \frac{I_o}{V_o} + s \cdot C_o \quad (6-9)$$

The constant power source is already represented by the static network $i_{os}(v_o, i_{ref})$. Then, the output admittance of the large-signal model can be well approximated by a single transfer function in many practical cases (see Fig. 6-8). Otherwise, if additional dependence on operating point is observed, a LLMN approach could be applied.

^{6.2} This statement is valid for frequencies low enough so that the variation of energy stored if the reactive components of the converter (inductors and capacitors) are negligible compared to the energy transferred from the input to the output port.

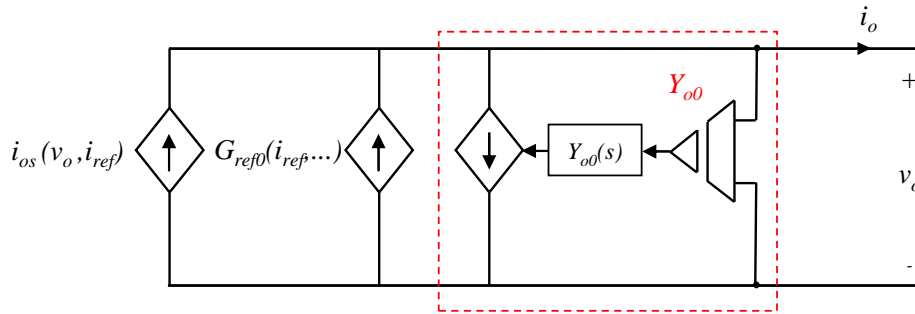


Fig. 6-8: Modeling the output admittance through a single transfer function.

Practical implementation of the networks shown in Fig. 6-6 and Fig. 6-8 will be shown in section 6.4, together with bode plots of the related transfer functions.

6.3 Model identification

The identification procedure consists of a set of sequential tasks:

- Firstly, identification step tests are applied, so that local linear behavior is maintained.
- Secondly, transfer function models are identified from the measured response.
- Thirdly, cross-coupling effects are analyzed and removed (if required).
- Finally, the obtained un-terminated transfer functions are post-processed to parameterize the dynamic networks and build the large-signal model.

The procedure is depicted in Fig. 6-9, where the section of the chapter corresponding to each task is indicated. The parametric identification of transfer functions is applied in the same way as described in section 4.3.2, so the reader is referred to it for more details.

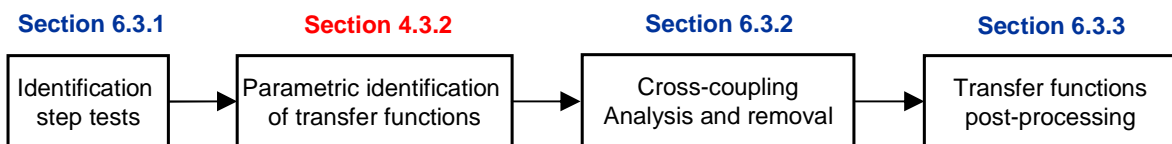


Fig. 6-9: Identification procedure of the black-box model for the fuel cell power conditioning unit.

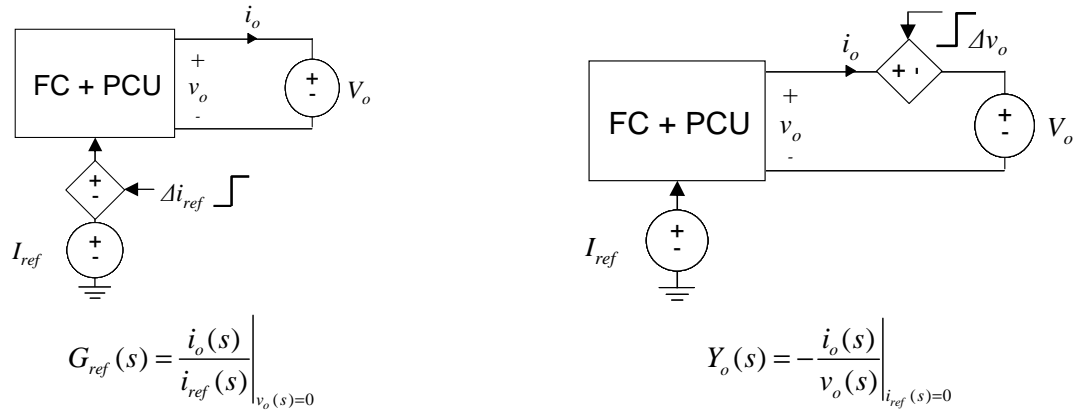
6.3.1 Identification step tests

The identification method relies on applying several step tests so that, under each test, only one input signal is stepped while the other remains constant. The step magnitude has to be sufficiently small so that local linear behavior is maintained. The local small-signal relationship between the model output and the model inputs can be derived from analysis of Fig. 6-3b, yielding (6-10).

$$i_o(s) = \begin{pmatrix} G_{ref}(s) & -Y_o(s) \end{pmatrix} \begin{pmatrix} i_{ref}(s) \\ v_o(s) \end{pmatrix} \quad (6-10)$$

The inputs are i_{ref} and v_o , so the following experimental tests should be applied (see Fig. 6-10).

- Reference signal step while the output voltage is kept constant, from which $G_{ref}(s)$ is identified.
- Output voltage step while the reference signal is kept constant, from which $Y_o(s)$ is identified.



a. i_{ref} step while v_o is constant. Identification of G_{ref} . b. v_o step while i_{ref} is constant. Identification of Y_o .

Fig. 6-10: Proposed identification tests. Conceptual approach.

However, as the PCU exhibits capacitive output, the voltage step may result in a large current peak transient that would be harmful to the experimental devices. An alternative consists in applying an output current step, so that the output impedance of the PCU, $Z_o(s)$, is identified. Then the output admittance is just obtained as $Y_o(s) = Z_o(s)^{-1}$. This alternative test is illustrated in Fig. 6-11. Note that, as I_{ref} sets the power delivered by the FC, the output power P_o is constant under the test.

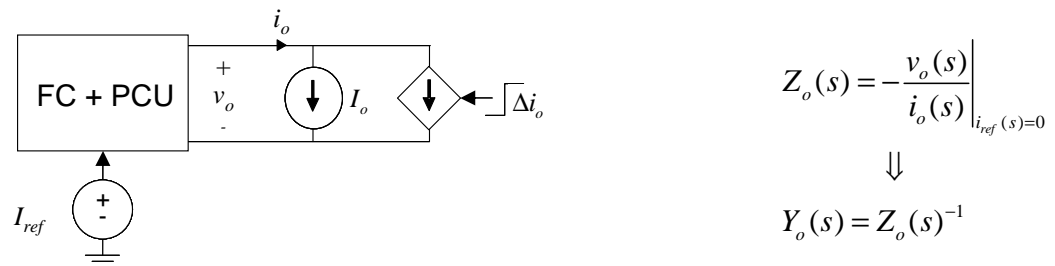


Fig. 6-11: Alternative test for identification of Y_o . Conceptual approach.

Practical implementations of those tests are described below.

6.3.1.1 Reference signal step

The reference signal can be stepped by means of a signal generator while the output voltage is kept constant by using an electronic load set in constant-voltage mode or a battery bus (see Fig. 6-12).

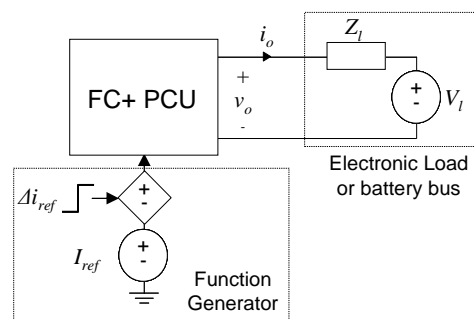


Fig. 6-12: i_{ref} step while v_o is kept constant. Identification of G_{ref} .

6.3.1.2 Output voltage step

The output voltage can be stepped through the experimental tests shown in Fig. 6-13, which are similar to those presented in chapter 4 and 5 to step the input voltage. The idea is to locate either a set

of diodes or a resistor in series between the PCU and the electronic load (or battery), so that a voltage drop Δv_o is caused between them. A switch is connected in parallel so that, when the switch is turned on, the voltage drop is translated from the series element to the output of the converter.

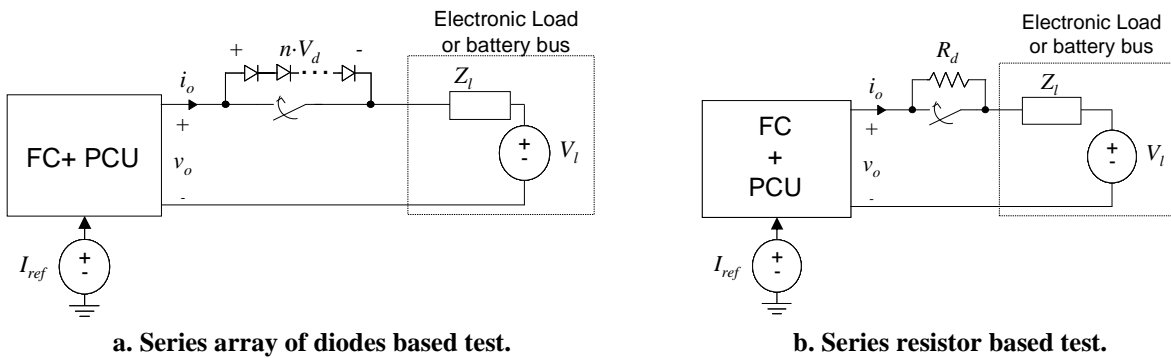


Fig. 6-13: v_o step while i_{ref} is kept constant. Identification of Y_o .

In this case, the step is negative, as i_o flows from the converter to the electronic load. If n diodes are used, then the magnitude of the step is that given by (6-11) (V_d is the voltage drop per diode).

$$\Delta v_o = -n \cdot V_d \quad (6-11)$$

Otherwise, if a resistor R_d is applied, then the magnitude of the step is that expressed by (6-12). This is expressed as a function of the output power P_o , which is constant under the test. V_l corresponds to the initial value for the output voltage.

$$\Delta v_o = -\frac{P_o}{V_l} \cdot R_d \quad (6-12)$$

6.3.1.3 Output current step

As above mentioned, i_o steps can be applied instead of v_o steps in order to identify Y_o . This allows avoiding the large current peak that may be induced in a PCU with capacitive output. Output currents steps are easy to apply using either resistors or an electronic load working in current transient mode, as shown in Fig. 6-14.

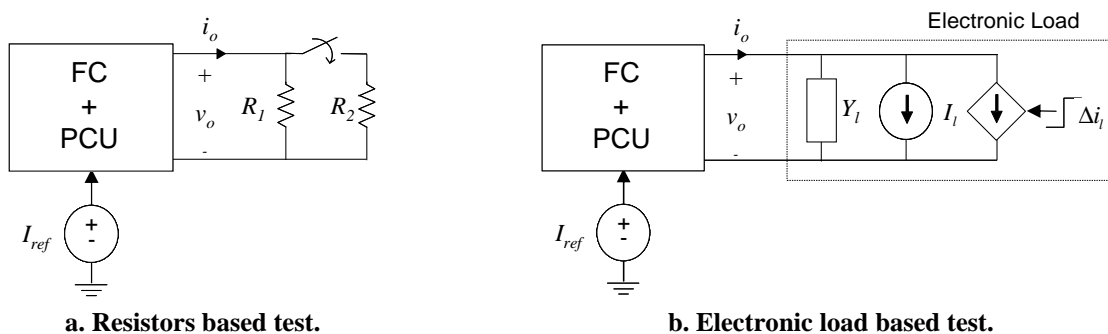


Fig. 6-14: i_o step while i_{ref} is kept constant. Identification of Z_o , from which Y_o is obtained.

- If a resistive load ' R_2 ' is switched-on, then i_o increases and v_o decreases (P_o is constant). R_1 can be calculated as given by (6-13), where V_{oi} denotes the initial value of the output voltage. The resistor R_2 can then be expressed as a function of the desired initial and final voltage levels (V_{oi} and V_{of} , respectively), as given by (6-14).

$$R_1 = \frac{V_{oi}^2}{P_o} \quad (6-13)$$

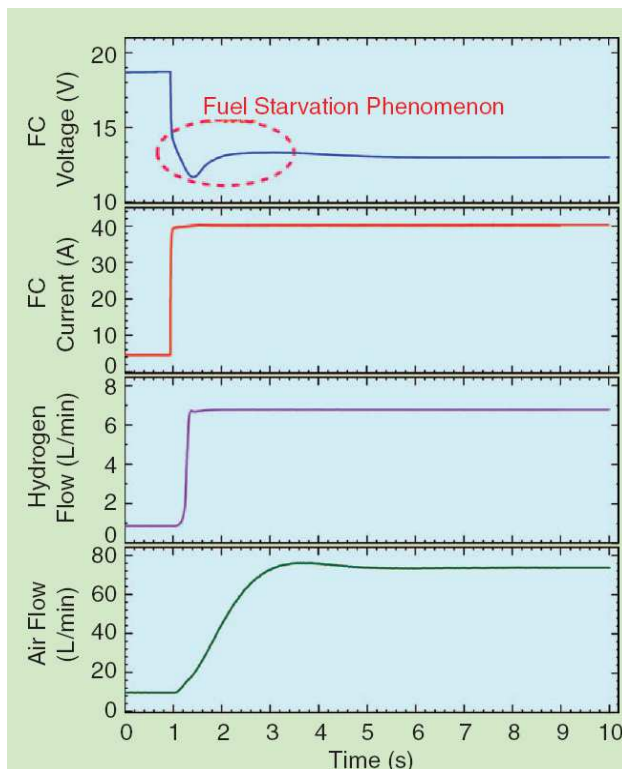
$$\begin{cases} V_{oi}^2 = P_o \cdot R_1 \\ V_{of}^2 = P_o \cdot R_1 \parallel R_2 \end{cases} \Rightarrow R_2 = R_1 \cdot \left(\frac{R_1 \cdot P_o}{V_{of}^2 - V_{oi}^2} - 1 \right) = \frac{V_{oi}^2}{P_o} \cdot \left(\frac{V_{oi}^2}{V_{of}^2 - V_{oi}^2} - 1 \right) \quad (6-14)$$

- If the step is carried out using an electronic load, then V_{oi} and V_{of} are related to I_l and ΔI_l as expressed by (6-15).

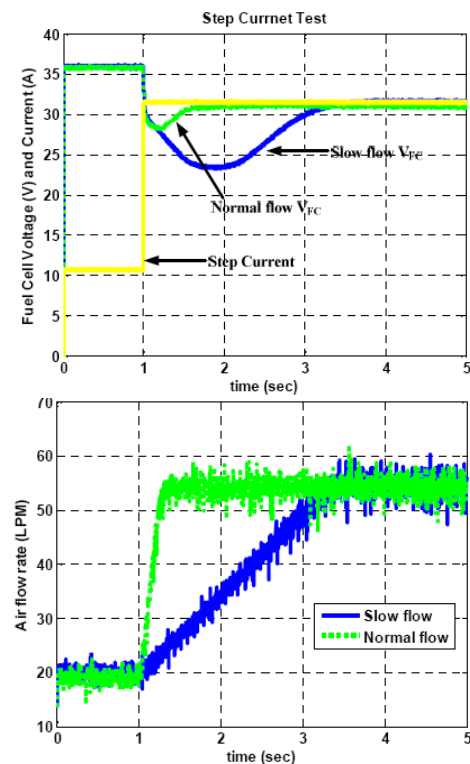
$$I_l = \frac{P_o}{V_{oi}}, \Delta I_l = P_o \cdot \left(\frac{1}{V_{of}} - \frac{1}{V_{oi}} \right) \quad (6-15)$$

6.3.1.4 Practical considerations

In practical application, the slew-rate of i_{ref} may be limited by the external control unit in order to respect constraints of the FC. If the slew rate is excessively high, then a lack of air flow may be caused, resulting in a nonlinear response of the FC featured by a large voltage undershoot. This phenomenon, so-called ‘Starvation effect’, may damage the FC and should be avoided. Hence, the applied slew rate of i_{ref} may be limited to the maximum one achievable in the intended application. Fig. 6-15 shows the transient response of the FC voltage to current steps, under lack of air flow, reported in the literature [26], [207], [209]. As can be seen, under low air flow, relatively large under-voltage is evidenced.



a. Response to output current step of a 500 W PEM FC reported in [209].



b. Response to output current step of a 1000 W PEM FC reported in [207].

Fig. 6-15: Examples of transient response of PEM FCs to current steps, under lack of air flow.

6.3.2 Cross-coupling effects

At this point, the identification procedure assumes that only one input signal is disturbed under each test, while the other remains absolutely constant. This is true under v_o or i_o steps, as i_{ref} should be normally well isolated from the power signals. However, under i_{ref} steps, v_o is disturbed due to the electronic load (or battery) impedance. Therefore, cross-coupling effects are caused only on $G_{ref}(s)$.

6.3.2.1 Removal

The small-signal ‘terminated’ equivalent circuit, corresponding to the reference signal step (Fig. 6-12), is shown in Fig. 6-16.

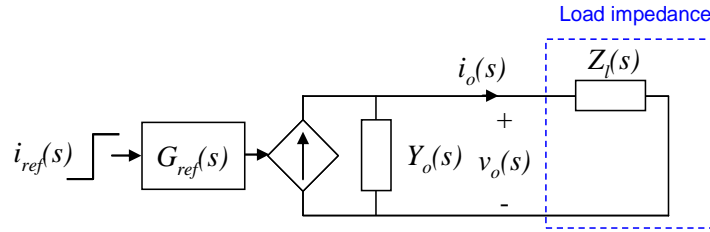


Fig. 6-16: Small-signal terminated equivalent circuit of the FC+PCU subsystem under reference signal step.

Expressions to remove the cross-coupling effect are simple to obtain. The dynamic response of the output current would depend on both $G_{ref}(s)$ and $Y_o(s)$, as given by (6-16).

$$i_o(s) = G_{ref}(s) \cdot i_{ref}(s) - Y_o(s) \cdot v_o(s) \quad (6-16)$$

By dividing both sides by i_{ref} , the following expression results, where $G_{refm}(s)$ represents the ‘terminated’ transfer function identified from the measured terminal signals, i_o and i_{ref} . $T_{rm}(s)$ models the cross-perturbations effects on v_o .

$$\frac{i_o(s)}{i_{ref}(s)} = G_{refm}(s) = G_{ref}(s) - Y_o(s) \cdot \underbrace{\frac{v_o(s)}{i_{ref}(s)}}_{T_{rm}(s)} \quad (6-17)$$

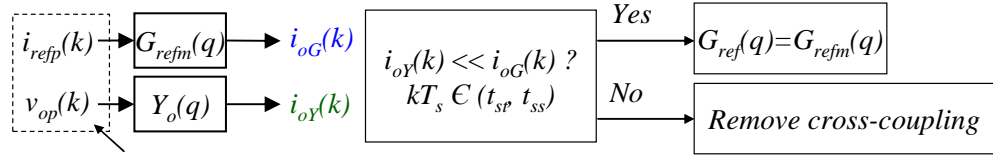
Rearranging (6-17), the ‘un-terminated’ TF, $G_{ref}(s)$, is obtained as

$$G_{ref}(s) = G_{refm}(s) + Y_o(s) \cdot T_{rm}(s) \quad (6-18)$$

$T_{rm}(s)$ is identified from the i_{ref} step, considering i_{ref} as the input and v_o as the output. After that, model order reduction can be optionally applied, as discussed in chapter 4, if the order of the resulting transfer function is excessively high.

6.3.2.2 Analysis

The analysis method, which is analogous to that presented in chapters 4, section 4.3.3.2, is illustrated in Fig. 6-17. The pre-processed measurements (subscript ‘ p ’) under an i_{ref} transient, are convoluted with the corresponding transfer functions identified from measurements, $G_{refm}(q)$ and $Y_o(q)$, resulting in $i_{oG}(k)$ and $i_{oY}(k)$, respectively. Then, if $i_{oY}(k) \ll i_{oG}(k)$, the assumptions done at the beginning of the identification process are valid (the transient response essentially depends on G_{ref}) and the cross-coupling effect can be neglected. Otherwise, it should be removed.



Pre-processed measurements under i_o step

Fig. 6-17: Analyzing cross-coupling on $G_{ref}(q)$. t_{st} : stepping time. t_{ss} : setting time. T_s : sampling period.

6.3.2.3 Prevention

The cross-perturbation of v_o under i_{ref} steps is due to a non-zero electronic load impedance, $Z_l(s)$, and can be expressed as

$$v_o(s) = -Z_l(s) \cdot i_o(s) \tag{6-19}$$

Therefore, the lower the electronic load impedance, the lower the cross-coupling effect. To minimize $Z_l(s)$, external capacitor(s) should be located close to the output port of the PCU.

6.3.3 Transfer functions post-processing

As explained in previous chapters, the steady-state of the identified transfer functions have to be subtracted, as the static response is already reproduced by the static network i_{os} . Such a post-processing action can be expressed as follows:

$$Y_{o0}(s) = Y_o(s) - Y_o(0), \quad G_{ref0}(s) = (G_{ref}(s) - G_{ref}(0)) \tag{6-20}$$

Note that, if a gain-scheduled approach is used to make up G_{ref0} , gain normalization is also required, as follows:

$$G_{ref0n}(s) = \frac{G_{ref0}(s)}{G_{ref}(0)} \tag{6-21}$$

6.3.4 Overview of the identification procedure

An overview of the identification process is depicted below. Since two identification approaches have been presented to identify the output admittance Y_o , two figures are shown: Fig. 6-18 corresponds to identification based on output voltage steps, and Fig. 6-19 corresponds to identification based on output current steps.

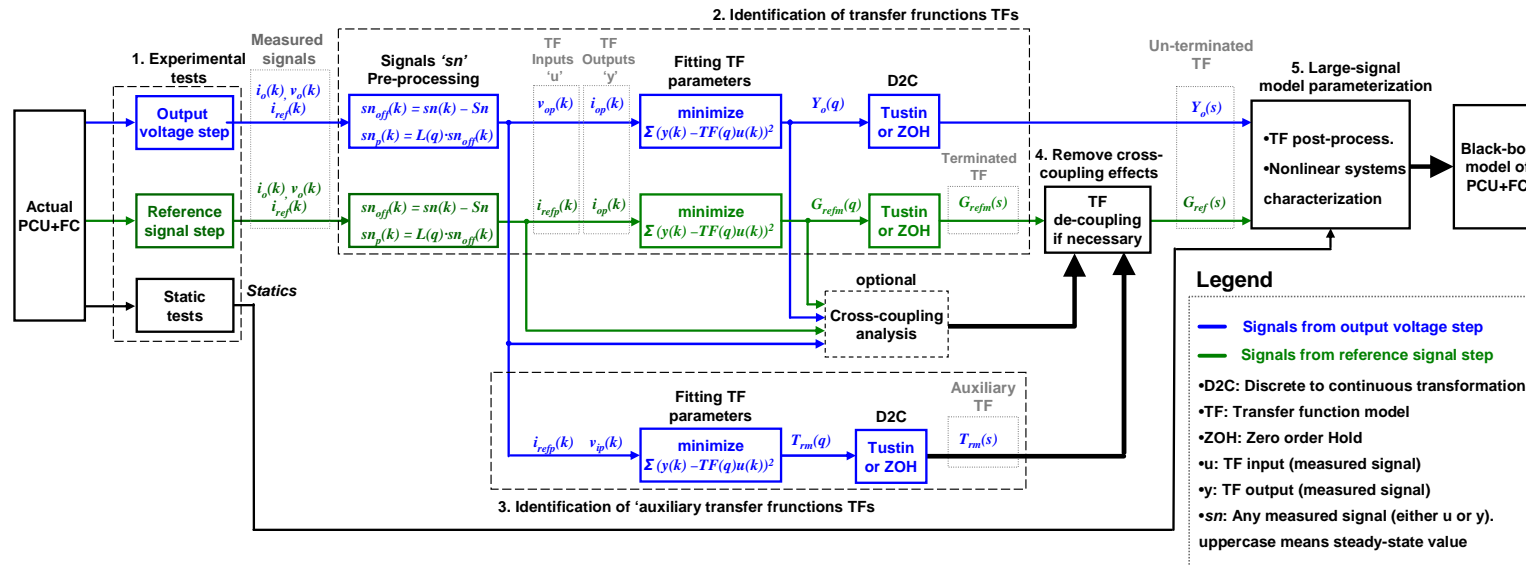


Fig. 6-18: Overview of the identification process for behavioral modeling of subsystem comprised of a FC+PCU. Identification based on output voltage steps.

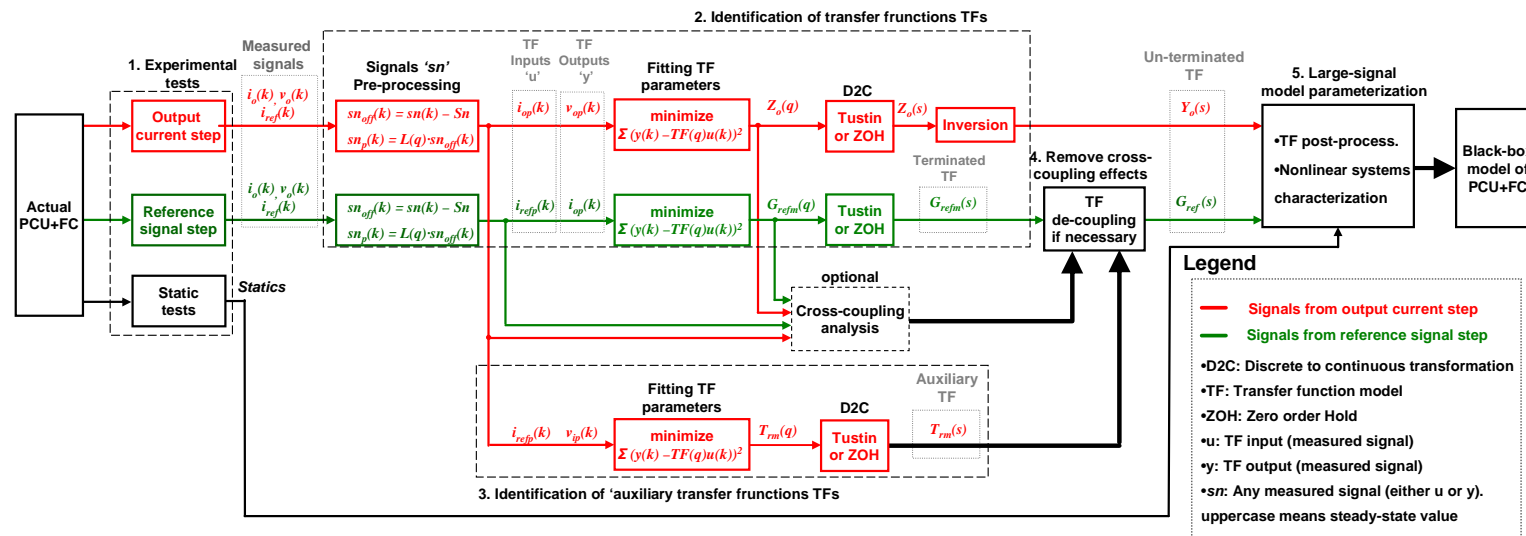


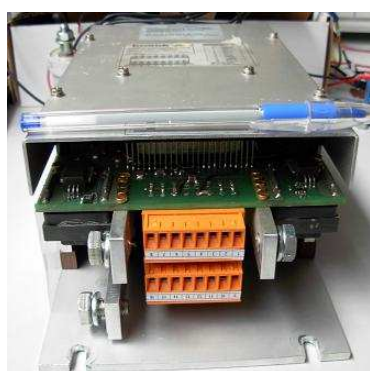
Fig. 6-19: Overview of the identification process for behavioral modeling of subsystem comprised of a FC+PCU. Identification based on output current steps.

6.4 Experimental results

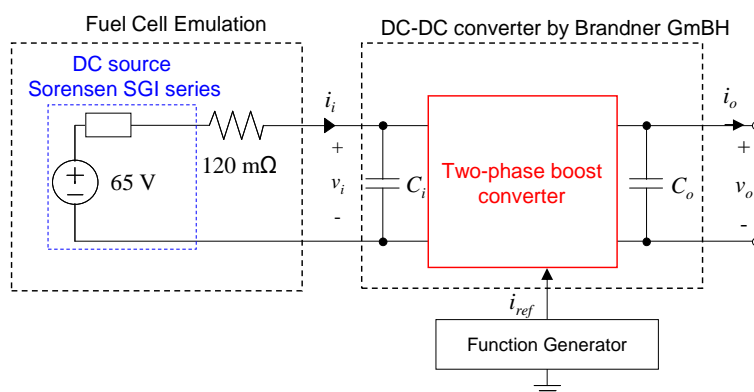
6.4.1 Subsystem description

An actual 4kW DC-DC converter, specifically designed for FC power conditioning by Brandner GmbH (see Fig. 6-20a), has been modeled through the proposed method. This converter is intended to power a 72 V electric vehicle battery bus. It consists of a two-phase boost topology provided with input current control. This topology is widely used in those applications where the FC voltage is lower than the battery bus voltage [203]-[206].

The FC has been emulated by means of a DC power supply connected in series with a power resistor. The resistor emulates constant internal resistance of the FC, which is valid within ohmic region (see Fig. 6-5). A diagram of the modeled subsystem is shown in Fig. 6-20b. The considered working range is defined by an output power range $P_o \in [1 \text{ kW}, 4 \text{ kW}]$ and $V_o = 72 \text{ V} \pm 10\%$.



a. 4 kW DC-DC converter by Brandner GmbH.



b. Diagram of the experimental setup.

Fig. 6-20: Experimental subsystem under study.

Using this experimental setup, the following assumptions have been considered.

- The FC operates only within ohmic region, where the internal resistance is nearly constant.
- The low-frequency dynamics of the FC [207]-[210] is neglected. This may result in a low-frequency transient overlaid to the transient response of the converter.
- Using a real FC, such slew rate is usually limited to avoid damaging the FC. Since starvation phenomenon is not emulated, no limitation in the i_{ref} slew rate has been considered. Thus, the capabilities of the proposed approach to model the converter dynamics can be evaluated in a more complete way.

The followed modeling and identification procedure is that applied systematically in previous chapters. It is reminded in Fig. 6-21. This diagram is explained in detail in section 3.4.1.

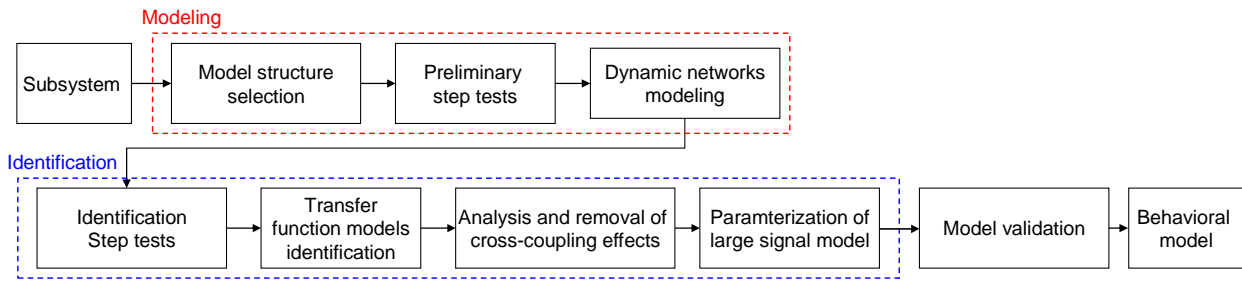


Fig. 6-21: Black-box modeling procedure.

Every measurement has been carried out by using a Tektronix Oscilloscope MSO4104 equipped with a hall-effect current probe TEK-TCPA300 and voltage probe TEK-P5050. The sampling frequency has been set to five times the switching frequency, that is, 1 MHz, according to the guidelines described in section 4.3.1.3.

6.4.2 Preliminary tests: linearity analysis

The considered structure of the model is that shown in Fig. 6-4, which is made up by the dynamic networks G_{ref} and Y_o and the static network i_{os} .

In this section, the dynamic behavior of the PCU is analyzed from a qualitative point of view, in order to select suitable dynamic networks to make up both G_{ref} and Y_o . The static network is built up in section 6.4.6.

The experimental setups are depicted in Fig. 6-22. As the working range of V_o is relatively narrow, only dynamics dependence on I_{ref} is evaluated.

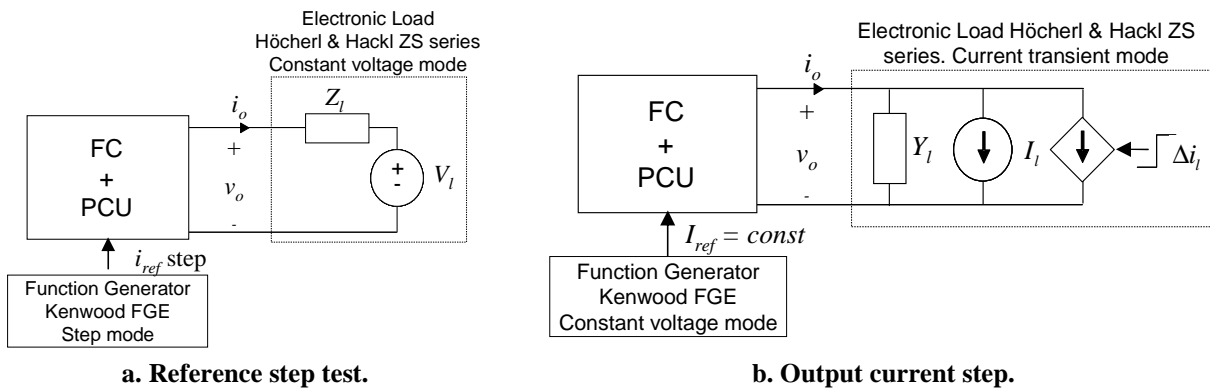


Fig. 6-22: Step tests. Experimental setups.

Fig. 6-23 shows the transient response of the PCU under two reference signal steps with equal magnitude but from different operating points. Both i_o waveforms exhibit similar shape, but different magnitude. This evidences a $G_{ref}(s)$ dependence on I_{ref} mainly on the static gain. Note also that v_o is disturbed, resulting in cross-coupling effects that will be analyzed later on.

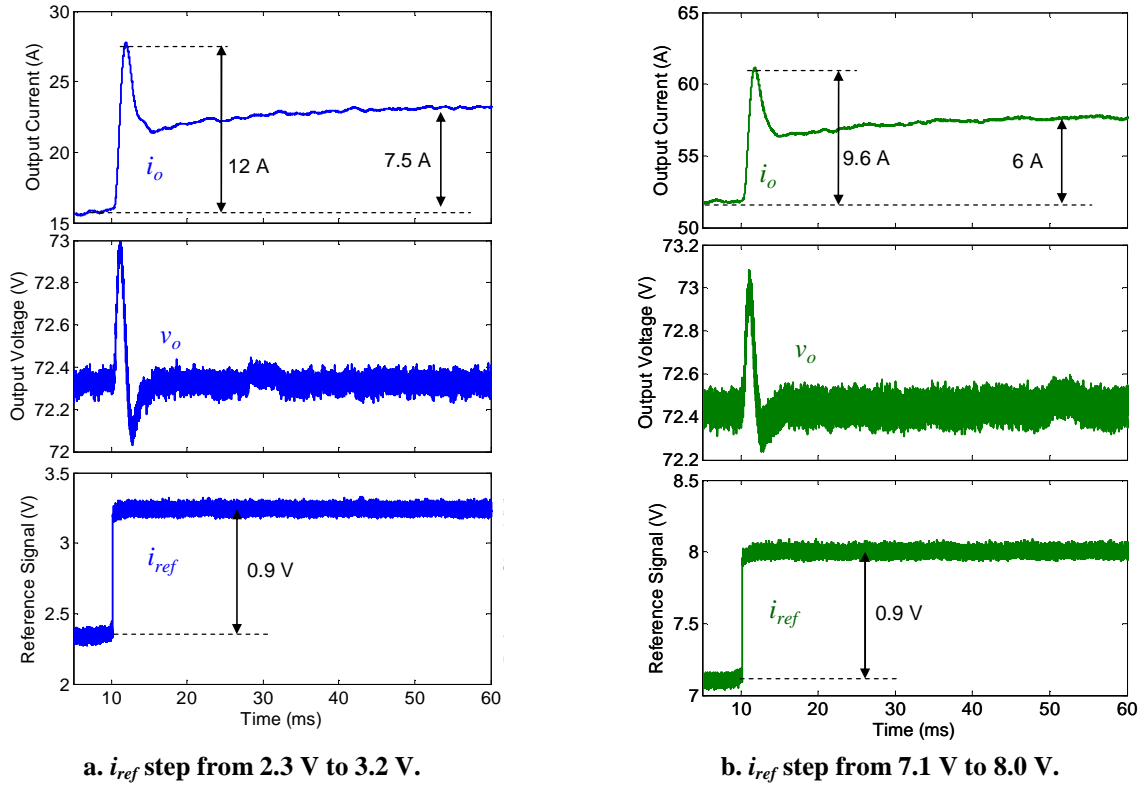


Fig. 6-23: Transient response of the FC + PCU to reference signal steps.

Fig. 6-24 shows the response of the PCU to output current steps with similar magnitude at two different I_{ref} levels. The constant-power source behavior of the subsystem is evidenced: as the current increases the voltage decreases, so that the output power remains nearly constant at steady-state.

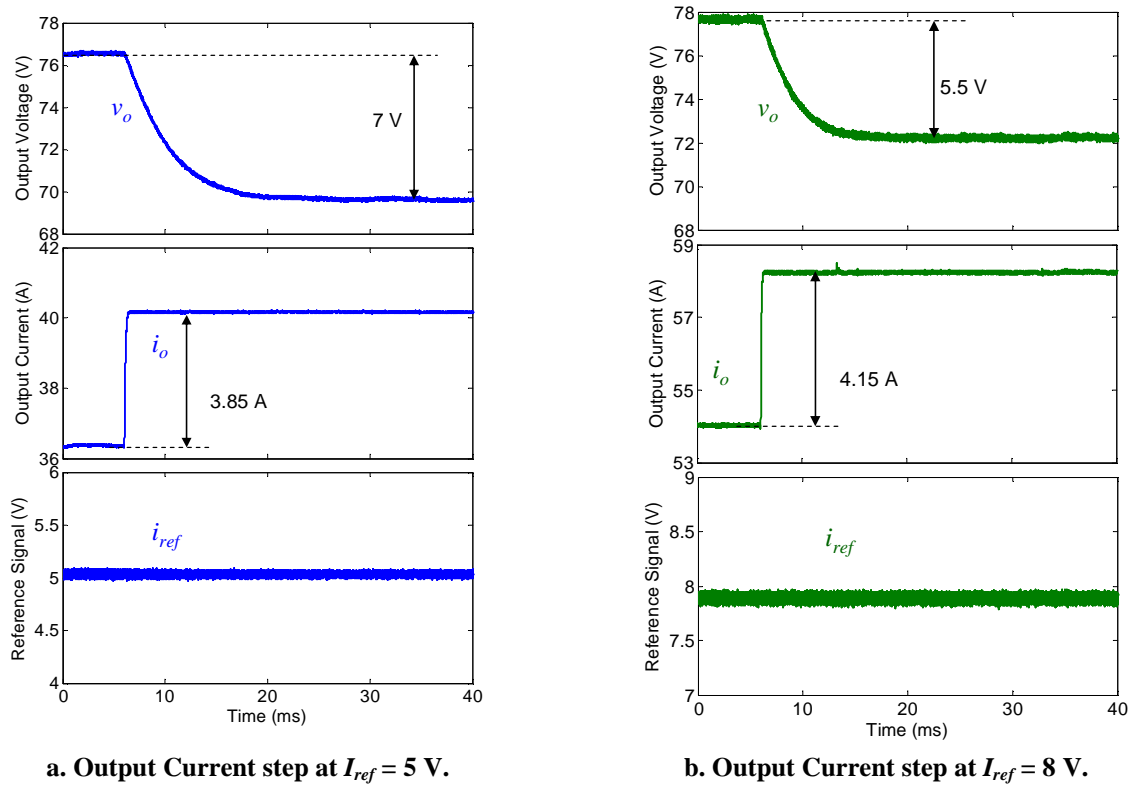


Fig. 6-24: Transient response of the FC + PCU to output current steps.

In both cases, the output voltage evidences a first-order exponential evolution. Therefore, $Y_o(s)$ is essentially determined by the output capacitor C_o in parallel with a positive incremental resistor (corresponding to a constant power source). Note that there is no cross-perturbation of i_{ref} , as expected.

6.4.3 Dynamic networks modeling

From the previous analysis, the following conclusions have been drawn:

- G_{ref} can be well modeled by a transfer function $G_{ref0n}(s)$, whose gain is scheduled by GS .
- Y_o can be well modeled using a transfer function model, $Y_{o0}(s)$, corresponding essentially to the output capacitor admittance. The constant-power-source behavior is already modeled by the static function i_{os} .

Therefore, the resulting model structure is that depicted in Fig. 6-25.

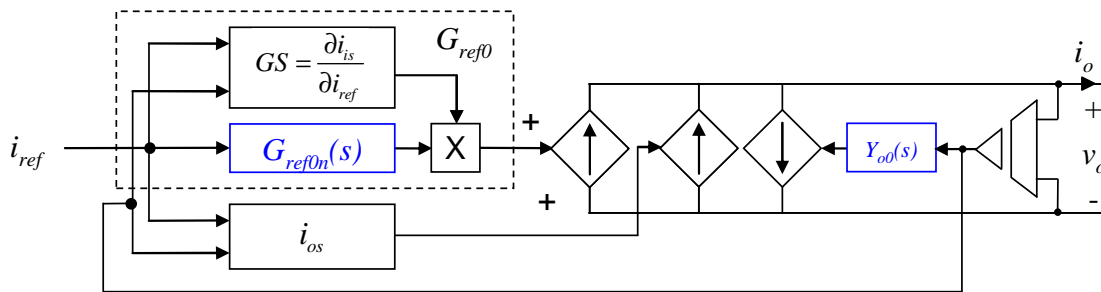


Fig. 6-25: Black-box model of the FC + PCU by Brandner GmbH for $I_{ref} \in [2-8]$ V.

6.4.4 Identification of transfer functions

6.4.4.1 Transfer function $G_{refm}(s)$

The transfer function $G_{refm}(s)$ has been identified using the Matlab function ‘*oe*’, as done in previous chapters. Before doing so, the measured waveforms have been decimated from 1 MHz to 50 kHz, because the dynamic timescale of the converter (setting time equal to 40 ms) is much slower than the switching period (5 μ s). Otherwise, the amount of data would be excessively large and may result in worse model estimation, as discussed in section 4.3.1.3.

The Matlab function ‘*resample*’ has been used to decimate the data. This function applies an anti-aliasing filter. No further pre-filtering actions have been required.

Transfer function models have been identified on two different operating points, in order to illustrate the low-frequency dynamic nonlinearities. The transient responses shown in Fig. 6-23 have been used to identify the model. The fitting results are evaluated using the function *compare* (details are given in section 4.4) in Fig. 6-26. Sixth order models yield good fitting results, as the fit is above 96% in both cases. To make up the black-box model, the transfer function corresponding to $I_{ref} = 7.5$ V is used, i.e. $G_{refm}(s) \equiv G_{ref7.5m}(s)$.

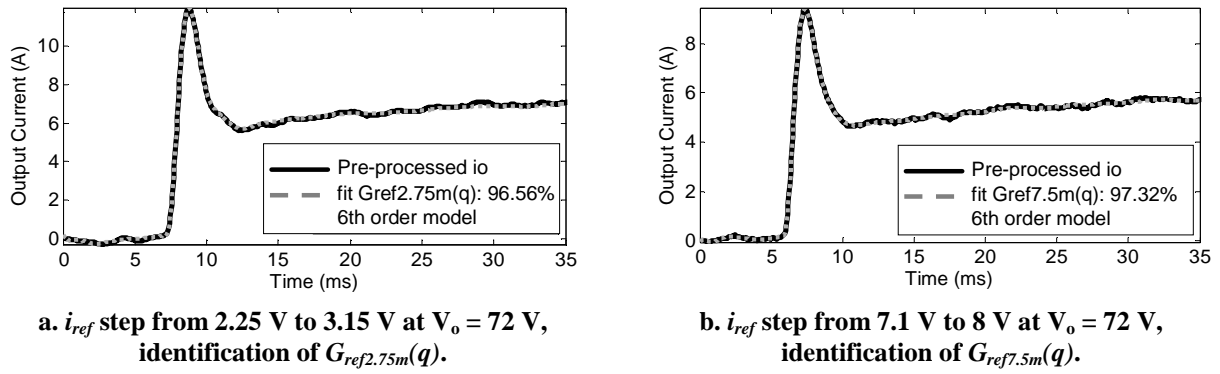


Fig. 6-26: Fitting results of $G_{ref0}(s)$ on two different operating points from i_{ref} steps.

In addition, the performance of the identification method has been evaluated by comparing the frequency response of the identified transfer functions with results from an AC sweep test. The AC sweep test setup and the comparison are depicted in Fig. 6-27. Main conclusions are listed below.

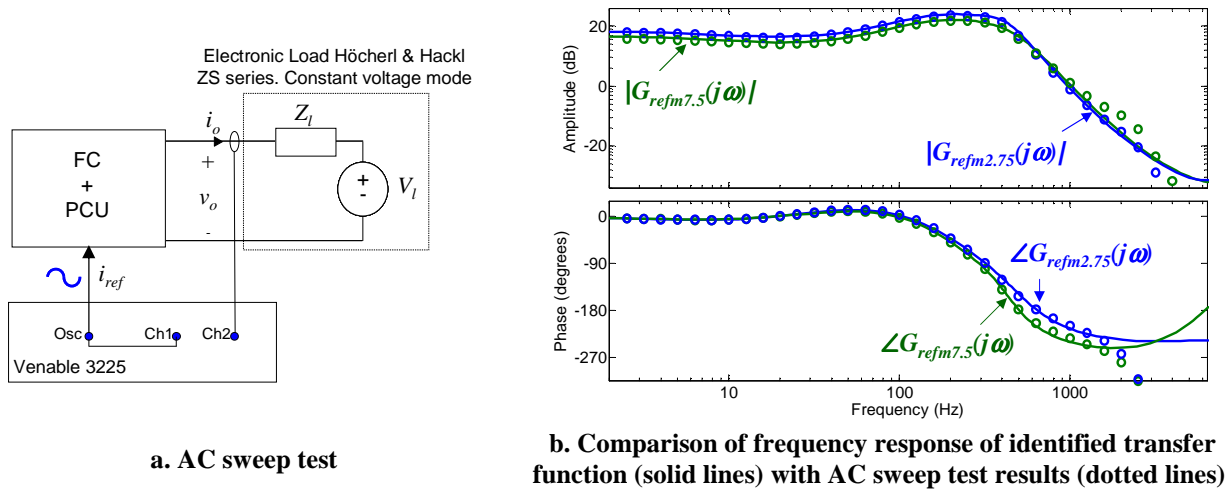


Fig. 6-27: Validation of identification results of $G_{refm}(s)$ at $I_{ref} = 2.75$ V and $I_{ref} = 7.5$ V.

- The frequency responses of the identified transfer functions match the results from the AC sweep tests up to 1 kHz, which is sufficiently high taking into account the dynamic timescale of the converter. Hence, the good performance of the identification method has been corroborated.
- The dynamics dependence on I_{ref} is mainly reflected at low-frequency. Below 1 kHz, the transfer functions differ from each other in terms of the static gain, approximately. This demonstrates the appropriateness of the gain-scheduled model.

6.4.4.2 Transfer function $Y_o(s)$

Following this, the output admittance of the model has been identified. First, transfer function models, corresponding to the output impedance of the converter $Z_o(q)$, has been identified from both transient responses shown Fig. 6-24. The achieved slew rate of i_o is ≈ 0.0315 A/ μ s, which is high enough taking into account the dynamic timescale of the converter. As depicted in Fig. 6-28, 2nd order models result in accurate models fit. The subscript corresponds to the reference signal level.

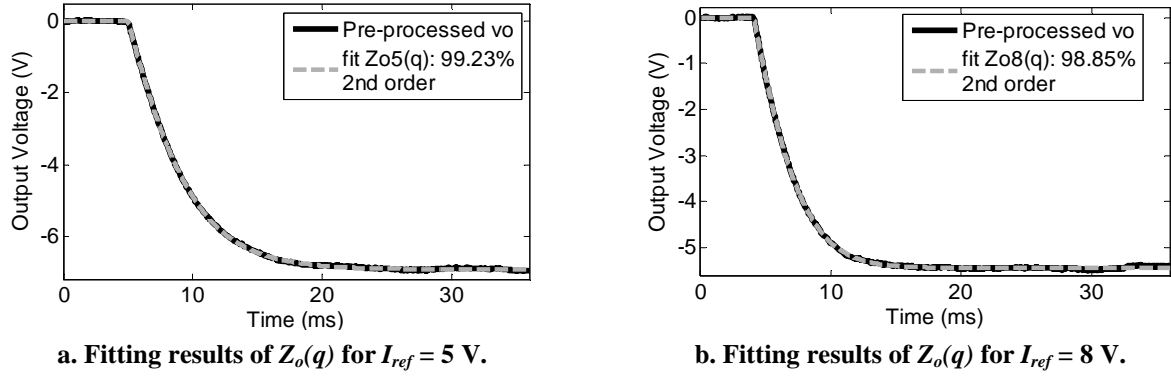


Fig. 6-28: Fitting results of $Z_o(q)$ on different I_{ref} levels.

After that, those impedances have been converted from discrete domain to continuous time domain. Finally, the output admittance has been obtained as $Y_{o5}(s) = Z_{o5}(s)^{-1}$ and $Y_{o8}(s) = Z_{o8}(s)^{-1}$. The frequency response of both transfer functions is compared in Fig. 6-29 and discussed below.

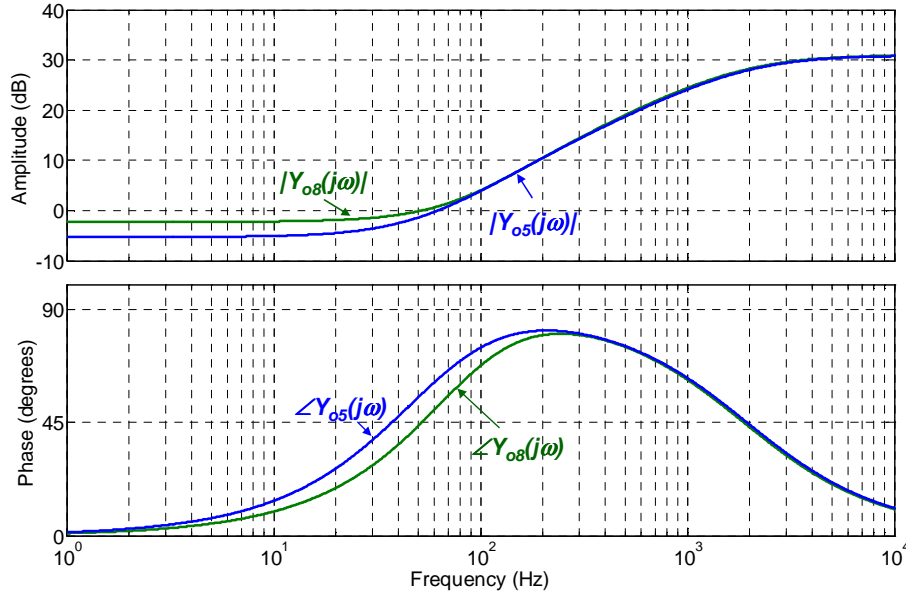


Fig. 6-29: Frequency response of $Y_o(s)$ as a function of I_{ref} .

As can be seen, they merge above 100 Hz, where $Y_o(j\omega)$ is dominated by the output capacitor. Below 100 Hz, the frequency response resembles a positive resistance, whose admittance is I_o/V_o . This corresponds to the low-frequency constant-power source behavior of the converter. Assuming constant P_o , it can be derived from (6-5) as follows.

$$I_o = \frac{P_o}{V_o} \Rightarrow Y_o(s) \Big|_{s \rightarrow 0} = -\frac{\partial I_o}{\partial V_o} = \frac{P_o}{V_o^2} = \frac{I_o}{V_o} \quad (6-22)$$

Indeed, expression (6-23) is verified, where I_{o5} , V_{o5} , I_{o8} and V_{o8} correspond to the intermediate level of the waveforms depicted in Fig. 6-24 (the subscript indicates the I_{ref} value).

$$Y_{o5}(0) = 0.55 \approx \frac{I_{o5}}{V_{o5}} = \frac{38 \text{ A}}{73 \text{ V}} = 0.52, \quad Y_{o8}(0) = 0.77 \approx \frac{I_{o8}}{V_{o8}} = \frac{56 \text{ A}}{75 \text{ V}} = 0.74 \quad (6-23)$$

This corroborates the analysis of linearity exposed in section 6.4.2, as well as the appropriateness of a single transfer function model for making up Y_o . For modeling purposes, the transfer function corresponding to $I_{ref} = 8$ V has been selected, i.e. $Y_o(s) \equiv Y_{o8}(s)$.

6.4.5 Analysis and removal of crosscoupling effects

6.4.5.1 Analysis

As evidenced in Fig. 6-23, cross-perturbations of v_o are caused under i_{ref} steps, resulting in cross-coupling effects between the identified transfer function, G_{refm} , and the electronic load impedance, Z_l . Therefore, this effect has to be analyzed and removed if necessary.

The analysis results are shown in Fig. 6-30. As can be seen, i_{oY} is significant at the beginning of the transient, so the cross-coupling effect on $G_{refm}(s)$ is significant and has to be removed.

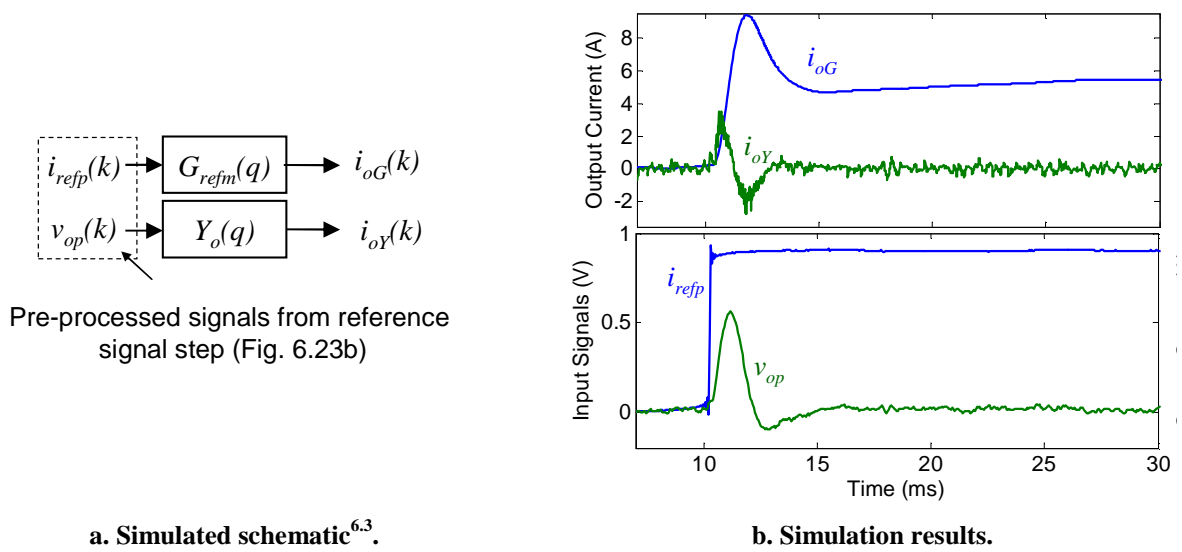


Fig. 6-30: Analysis of cross-coupling effects.

6.4.5.2 Removal

To remove the cross-coupling effect, the auxiliary transfer function $T_{rm}(s)$ has been identified from the transient responses of v_{op} and i_{refp} shown in Fig. 6-30b. The fitting results are depicted in Fig. 6-31a, where one can see that a fourth order model yields accurate fitting results. Following this, $G_{ref}(s)$ has been obtained using (6-18).

Finally, the removing results have been evaluated by simulating the schematic shown in Fig. 6-31b. The sum of the transfer function outputs is compared with the measured and pre-processed output, i_{op} . The comparison is depicted in Fig. 6-31c. As can be seen, if the ‘terminated’ transfer function is considered, i.e. $G_{refm}(s)$, the resulting signal deviates from i_{op} . However, if $G_{refm}(s)$ is replaced by the ‘un-terminated’ one, $G_{ref}(s)$, such a deviation is corrected. Therefore the cross-coupling effect has been properly eliminated.

^{6.3} Rigorously speaking, both transfer functions should correspond to the same operating point, as the cross-coupling removal process relies on local small-signal LTI models. However, $Y_{o8}(q)$ and $G_{ref7.5m}(q)$ have been identified at $I_{ref} = 8$ V and $I_{ref} = 7.5$ V, respectively. Nevertheless, such a difference is relatively small and its impact is negligible.

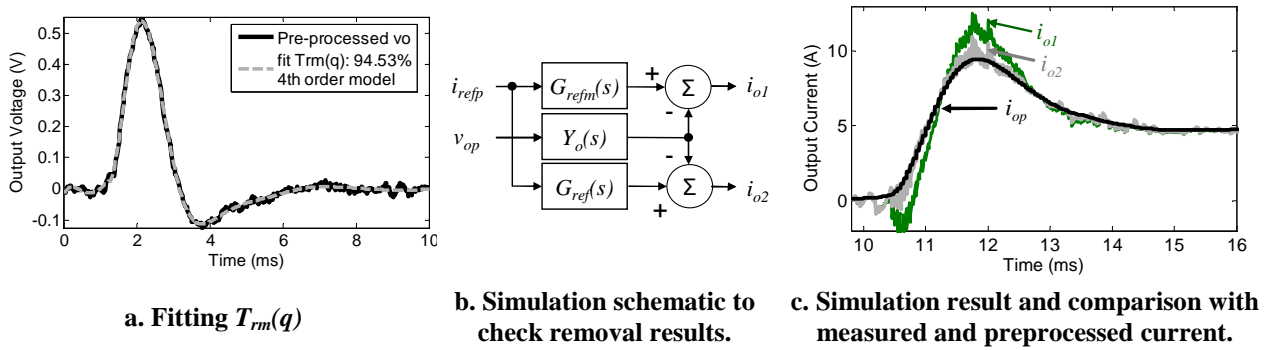


Fig. 6-31: Removing cross-coupling effects and checking results.

6.4.5.3 Model order reduction

The order of the ‘un-terminated’ transfer function, $G_{ref}(s)$, is relatively high (12th order). Therefore, model-order reduction has been applied using the Matlab functions ‘*modred*’ and ‘*balreal*’, in a similar way as described in chapter 4. This yields a 6th order transfer function, referred to as $G_{refr}(s)$. Fig. 6-32 compares the frequency responses of the ‘terminated’ transfer function, $G_{refm}(s)$, the ‘un-terminated’ one, $G_{ref}(s)$, and the ‘reduced-order’ one, $G_{refr}(s)$. The conclusions are listed below.

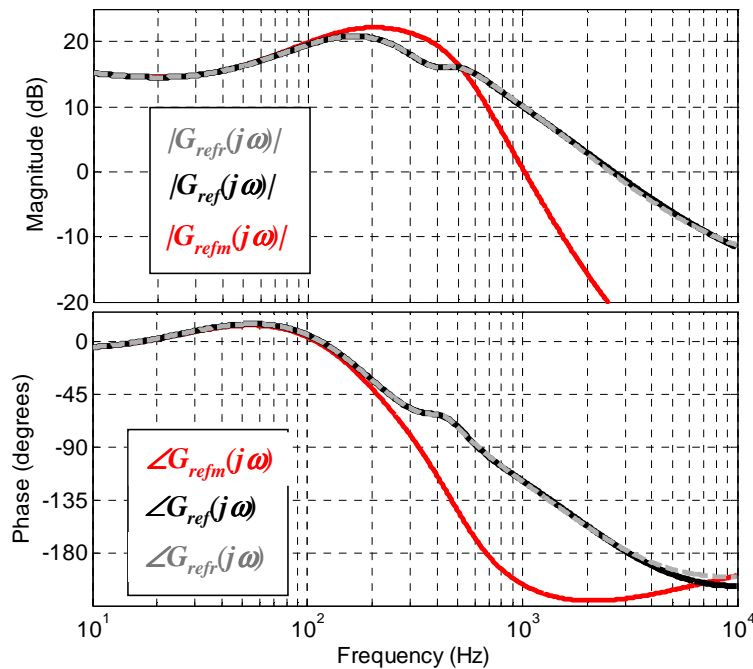


Fig. 6-32: Frequency response of $G_{refm}(s)$ (6th order), $G_{ref}(s)$ (12th order) and $G_{refr}(s)$ (6th order).

- The cross-coupling effect makes significant influence on the ‘terminated’ transfer function above 100 Hz.
- A substantial model-order reduction of the ‘un-terminated’ transfer function has been achieved, whereas the frequency response remains almost unchanged up to 10 kHz.

6.4.6 Parameterization of the large-signal model

At this point, un-terminated transfer functions $G_{ref}(s)$ and $Y_o(s)$ has been obtained, from which the transfer functions of the model, $G_{ref0n}(s)$ and $Y_{o0}(s)$, have been post-processed as given by (6-20) and

(6-21). Note that $G_{ref}(s)$ is used instead of $G_{ref}(s)$ into (6-20) because model-order reduction has been applied.

$$\begin{cases} G_{ref0n}(s) = \frac{-1.03s^6 - 1.44 \cdot 10^4 s^5 - 1.43 \cdot 10^7 s^4 - 8.7 \cdot 10^{10} s^3 + 5.8 \cdot 10^{13} s^2 - 2.21 \cdot 10^{16} s}{s^6 + 1.31 \cdot 10^4 s^5 + 4.38 \cdot 10^7 s^4 + 1.3 \cdot 10^{11} s^3 + 1.65 \cdot 10^{14} s^2 + 1.03 \cdot 10^{17} s + 5.42 \cdot 10^{18}} \\ Y_{o0}(s) = \frac{0.9782s^2 + 693.1s}{0.0281s^2 + 359.8s + 3.337 \cdot 10^5} \end{cases} \quad (6-24)$$

Finally, the static functions have been parameterized. Fig. 6-33 shows the static relationship between I_o and I_{ref} at $V_o = 72$ V. As can be seen, a second order polynomial fits it properly.

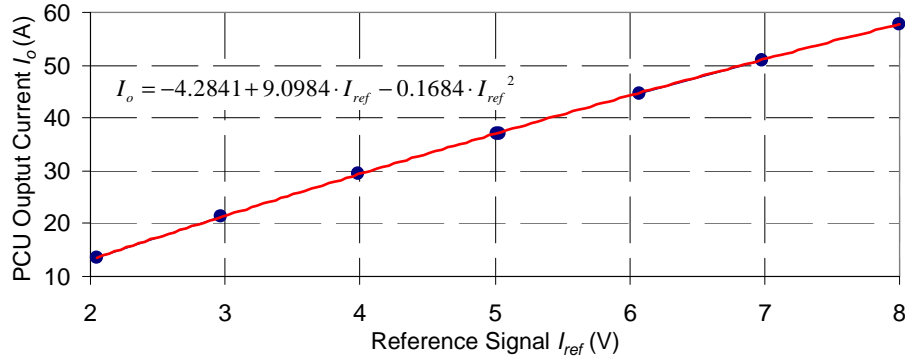


Fig. 6-33: Fitting the steady-state response of the converter by a second-order polynomial.

Hence, the following expressions for the static network i_{is} and GS have been obtained. Note that the polynomial coefficients are multiplied by v_o because both functions incorporates a division by v_o .

$$\begin{cases} i_{os}(i_{ref}, v_o) = \frac{K_0 + K_1 \cdot i_{ref} + K_2 \cdot i_{ref}^2}{v_o} \\ GS(i_{ref}, v_o) = \frac{\partial i_{os}(i_{ref}, v_o)}{\partial i_{ref}} = \frac{K_1 + 2 \cdot K_2 \cdot i_{ref}}{v_o} \end{cases} \quad (6-25)$$

$K_0 = -4.2841 \cdot 72 = 308$, $K_1 = 9.0984 \cdot 72 = 655$, $K_2 = -0.1684 \cdot 72 = -12.1$

Thus, the large-signal black-box model shown in Fig. 6-25 has been completely parameterized.

6.4.7 Model validation

The derived black-box model has been implemented in the circuit simulator PSIM for validation purposes [255]. The response of the model has been compared to the response of the actual converter under a variety of validation tests, different from those used for model identification.

6.4.7.1 Test 1. Large reference signal step at maximum output voltage

The first test consists in making a large i_{ref} step, while the output voltage is set to its maximum considered value ($V_o = 80$ V). The experimental setup and simulated schematic are depicted in Fig. 6-34. As model inputs, the measured signals v_o and i_{ref} have been applied by using controlled sources. The signals have been re-sampled using the Matlab function 'resample', which also applies anti-aliasing filtering.

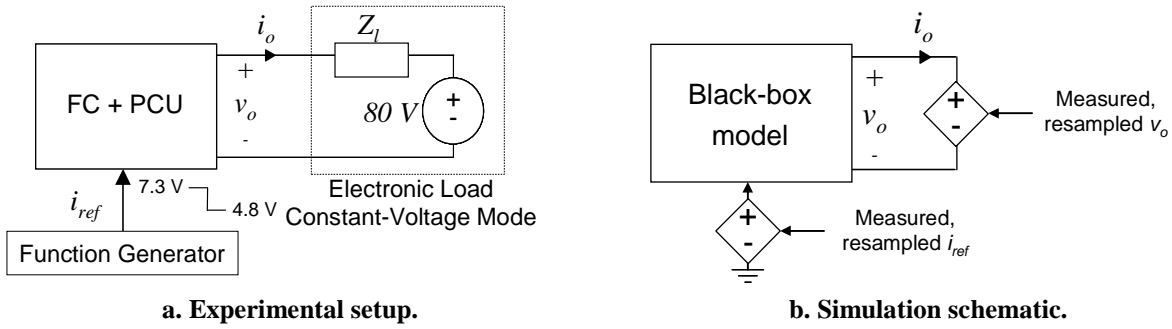


Fig. 6-34: Validation test 1. Large reference step under constant output voltage.

Fig. 6-35 depicts the comparison of experimental measurements and simulation results. Although a certain mismatch is observed at the beginning of the transient, a good fitting is observed. This demonstrates the good performance of the model and, more specifically, the appropriateness of the gain-scheduled model, summed to the static function, used to make up G_{ref} .

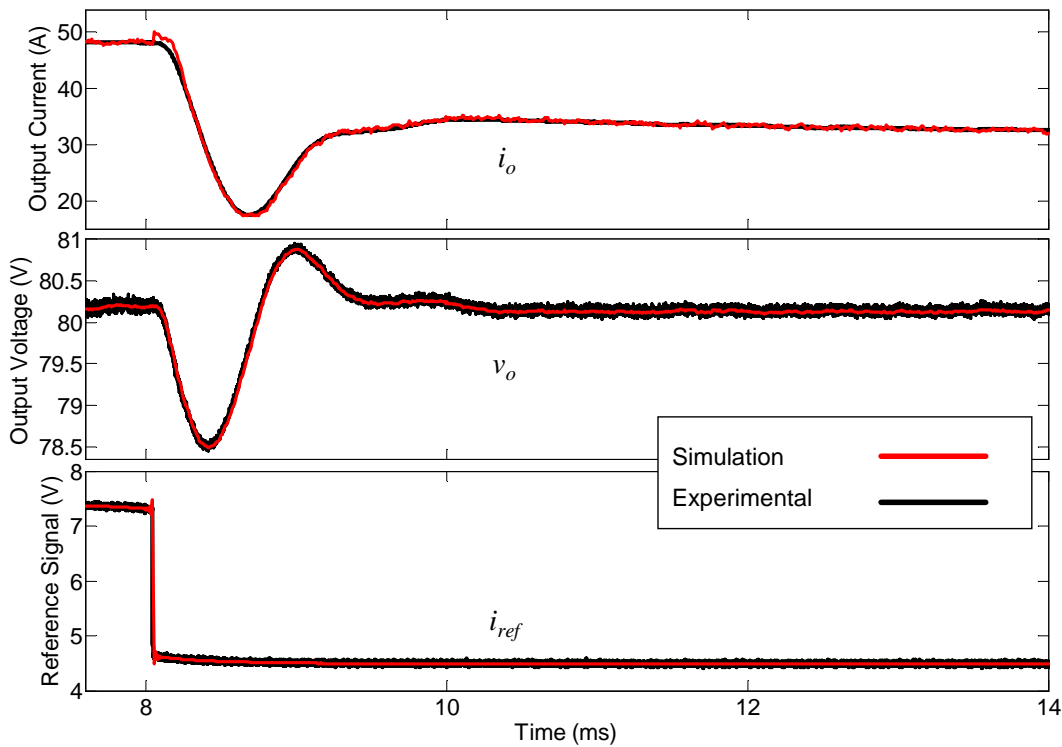


Fig. 6-35: Validation test 1. Comparison between experimental measurements and simulation results.

6.4.7.2 Test 2. Large reference signal step and battery bus power step

The second test consists in applying a large load load current step (25 A) while the output voltage is maintained close to 72 V, through a set of batteries by Saft (see Fig. 6-36). This test reproduces conditions similar to those that may be found on an actual on-board power system. In addition, a reference signal step-up is applied. Both the measured v_o and i_{ref} have been applied as model inputs by using controlled voltage sources driven by a look-up-table.

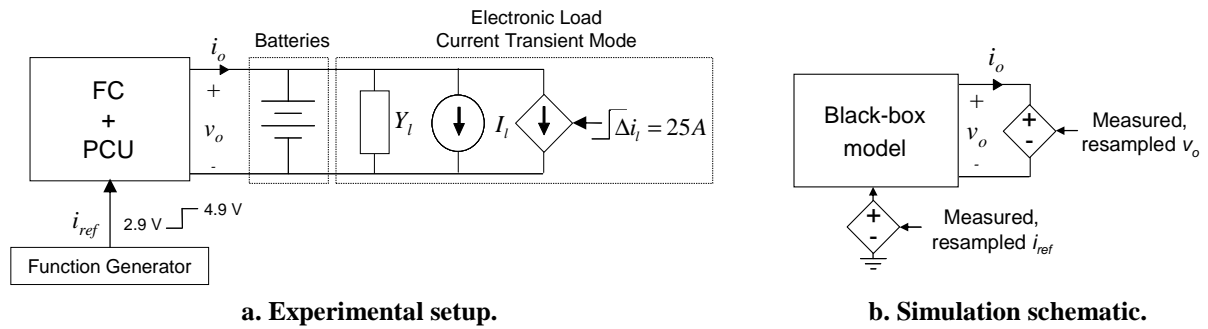


Fig. 6-36: Validation test 2. Reference signal step followed by battery bus power step.

The comparison is depicted in Fig. 6-37, from which the following conclusions are drawn:

- The v_o transient is different from that measured under the validation test 1. In this case, the model also matches the measured i_o under the i_{ref} step. As a consequence, the cross-coupling effects have been properly removed from the identified transfer functions.
- The i_o transient under the bus power step is also well modeled, which evidences that the output admittance of the converter has been well modeled and identified.

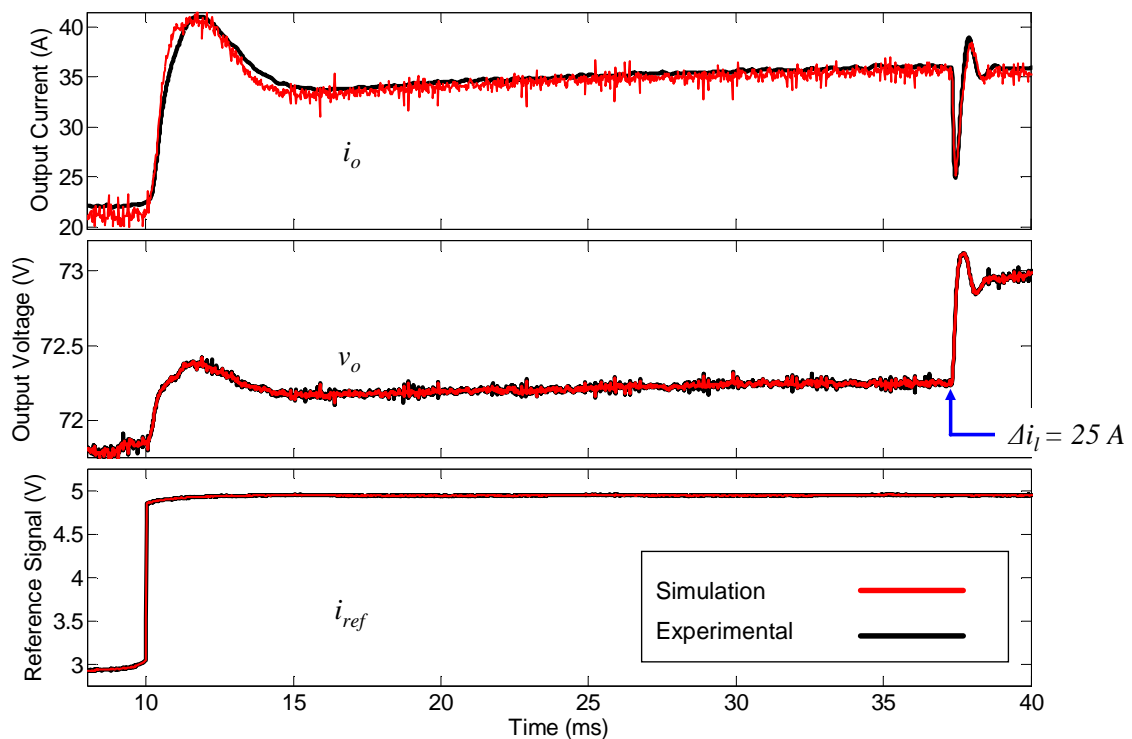


Fig. 6-37: Validation test 2. Comparison between experimental measurements and simulation results.

6.4.7.3 Test 3. Resistive load step

The third validation test consists in stepping a resistive load at constant i_{ref} (see Fig. 6-38). In this case, the loads and the function generator have been modeled using resistors and a DC source, respectively.

As shown in Fig. 6-39, the simulation results match the measured waveforms. Notice how the model reproduces the constant-power-source behavior of the converter under constant reference signal (the current decreases if the voltage increases, at steady-state).

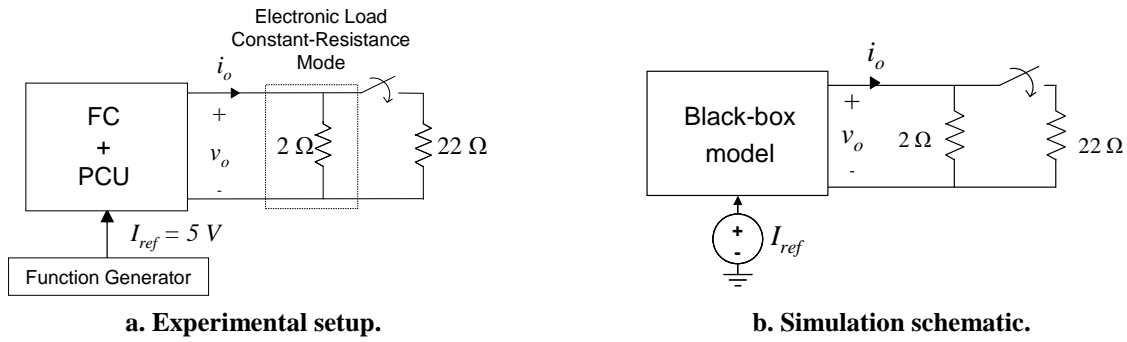


Fig. 6-38: Validation test 3. Resistive load step at constant reference signal.

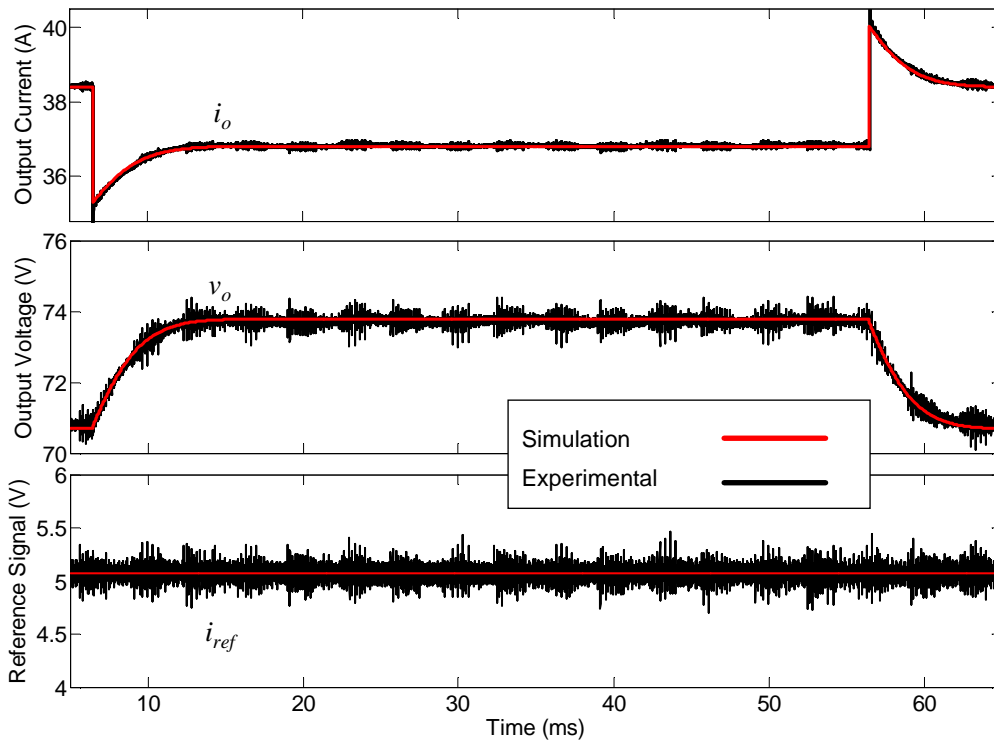


Fig. 6-39: Validation test 3. Comparison between experimental measurements and simulation results.

6.4.7.4 Test 4. Triangular reference signal with resistive load

Finally, a triangular waveform with large magnitude and ≈ 60 Hz has been applied as reference signal, while a resistor has been placed at the output of the converter (see Fig. 6-40).

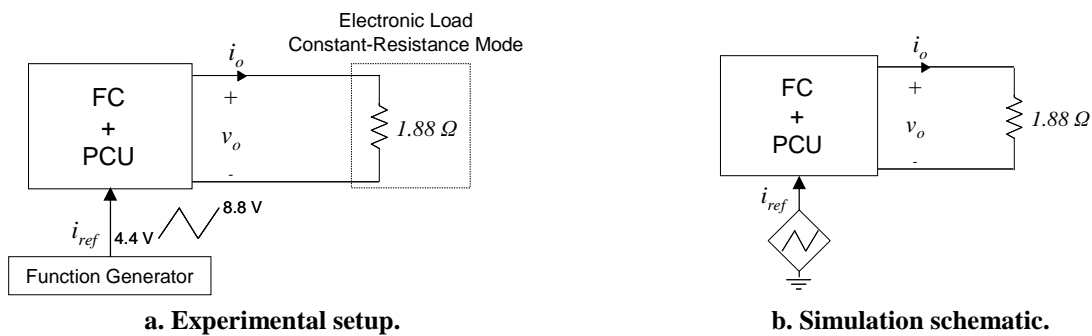


Fig. 6-40: Validation test 4. Triangular reference waveform with resistive load.

This is a challenging test, since both v_o and i_{ref} are simultaneously disturbed in a large-signal sense. Moreover, such disturbances are very different from those used to identify the model. Again, the loads have been modeled using ideal resistances, while the function generator has been modeled an ideal triangular source.

The comparison between simulation results and measurements is depicted in Fig. 6-41. As can be seen, the model response is very close to the measured waveforms. This further corroborates the good performance of the proposed model to carry out large signal simulations, as well as the identification methodology of un-terminated transfer functions.

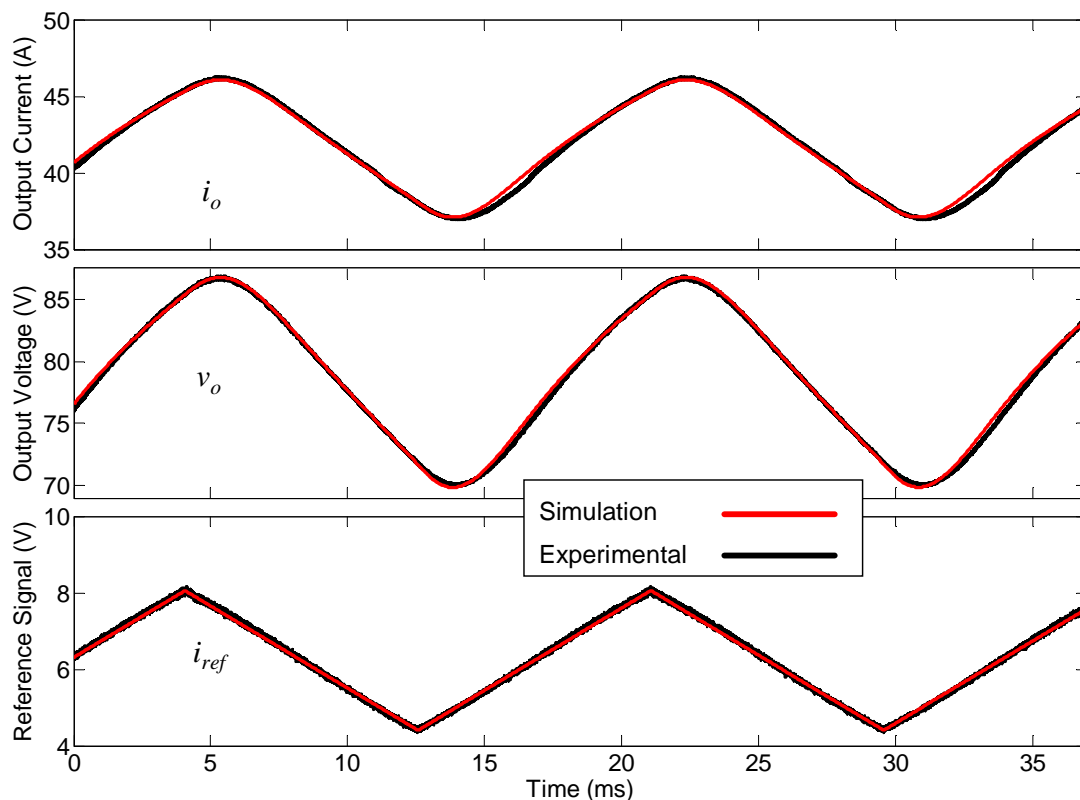


Fig. 6-41: Validation test 4. Comparison between experimental measurements (dark lines) and simulation results (dark lines).

6.5 Conclusions

In this chapter, as an original contribution, a black-box modeling method of DC-DC converters with input current control, cascaded with fuel cells, has been proposed. This kind of subsystem is applied in power distribution systems where the fuel cell supplies a battery bus (e.g. some architectures of auxiliary power units for the more-electric-aircraft and electric-vehicles). The main conclusions are summarized below:

- The model reproduces the behavior of the power conditioning unit at the output port and comprises two dynamic networks, so that the output current is modeled as a function of the reference control signal and the output voltage.
- The model is able to reproduce the large-signal low frequency behavior of the power converter, in a similar way to conventional average models do.

- The identification method is based on simple step tests.
- This type of converters has been proven to behave as a power source at the output port. Therefore, the proposed approach is also valid to model power supplies based on DC-DC converters with input voltage control.
- A step-by-step application of the modeling procedure, on a commercial converter specifically designed for fuel-cells, has been presented. The good agreement between simulation results and experimental measurements, under a variety of tests, has validated the proposed methodology.
- However, at this point, the experimental validation has been carried out by using a FC emulation consisting of a DC source in series with a power resistor. Future work should be carried out by using an actual FC in order to evaluate the influence of the FC dynamics on the output current response.

7 Black-box modeling of Solar Array Simulators for Spacecraft

7.1	Introduction.....	251
7.2	Electrical behavior of solar arrays and comparison with solar array simulators	253
7.2.1	Static behavior.....	253
7.2.2	Dynamic behavior	253
7.2.3	Frequency response comparison	254
7.3	Model description.....	256
7.3.1	Small-signal approach	256
7.3.2	Extension to large signal	256
7.3.2.1	Simplifying the large-signal model: local linear region of the I-V curve.....	257
7.4	Model identification	257
7.4.1	Identification step tests.....	258
7.4.2	Large-signal model parameterization	259
7.5	Experimental results	260
7.5.1	Modeling	260
7.5.2	Identification	261
7.5.2.1	Experimental tests	261
7.5.2.2	Transfer functions fitting.....	262
7.5.3	Validation	263
7.5.3.1	Comparison with AC sweep test results	263
7.5.3.2	Comparison with experimental measurements under small and large signal perturbations	264
7.5.4	Summary	266
7.6	Analysis of dynamic interactions between a solar array simulator and a power conditioning and distribution unit for spacecraft.....	266
7.6.1	Operating models and dynamic behavior of the solar array regulator	266
7.6.2	Experimental system description	267
7.6.3	Experimental analysis	268
7.6.4	Prediction of dynamic interactions using black-box models.....	270
7.7	Conclusions.....	272

7.1 Introduction

Sunlight is a primary energy source for spacecraft power systems. It is converted to electrical energy by means of photovoltaic solar arrays (SAs). Nowadays, triple-junction Gallium-Arsenide (3JGaAs) SAs are applied in spacecraft applications [239]-[246]. Compared to silicon based SAs for terrestrial applications, 3JGaAs SAs achieve higher efficiency at the expense of a higher cost. Current 3JGaAs photovoltaic cells achieve efficiencies around 30% [239]. A solar wing for spacecraft based on 3JGaAs cells is depicted in Fig. 7-1.



Fig. 7-1: Solar wing of spacecraft (Alphabus) made up by 3JGaAs cells. Photo reported in [241].

The energy fed from the SA is delivered to the power distribution system of the spacecraft by means of the so-called power conditioning and distribution unit (PCDU). Fig. 7-2 depicts a PCDU architecture based on regulated DC bus, which will be discussed more in depth later on. A solar array regulator (SAR) is located in front of the SA and typically consists of either a switching shunt regulator or a PWM converter [48], [242].

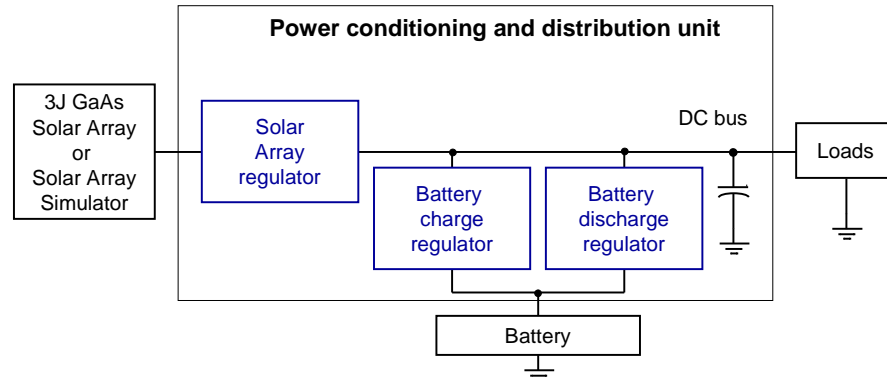


Fig. 7-2: Power distribution system for spacecraft based on regulated bus architecture.

However, emulation in the laboratory of the environmental conditions in outer space (irradiance, temperature, etc.) requires complex and expensive experimental equipment. Consequently, during spacecraft integration and tests, system integrators typically make use of solar array simulators (SASs) instead of the actual SA. SASs are commercial hardware devices capable of emulating the I-V curve of a SA for different environmental conditions [243]-[244], thus offering flexibility and allowing a much simpler test bed.

SASs represent the I-V curve of actual SAs accurately. However, the dynamic response is usually different. This fact plays an important role, since **the dynamic response of the SAS may influence the dynamic behavior of the PCDU** under certain conditions. This may lead to wrong conclusions about system performance in outer space.

In order to introduce the problem of dynamic interactions, the system shown in Fig. 7-2 is considered. As a difference from terrestrial applications (where the SAR typically tracks the maximum-power-point MPP of the SA), in spacecrafts sometimes there is more power available in the SA than is demanded by the PCDU. Under that circumstance, the SAR does not perform maximum-power-point-tracking (MPPT), but it **performs DC bus voltage regulation** and delivers only the required load power from the SA to the DC bus. Consequently, the **SAR behaves as a constant power load (CPL)** at the input port, which **may lead to instability** if the SAS impedance is excessively high (as described in chapter 1).

Summarizing, under certain operation modes of the PCDU, the dynamic response of the SAS plays a critical role. Indeed, the PCDU could be unstable when supplied by a SAS but stable when supplied by a 3JGaAs SA, or vice-versa. Fig. 7-3 illustrates this problem.

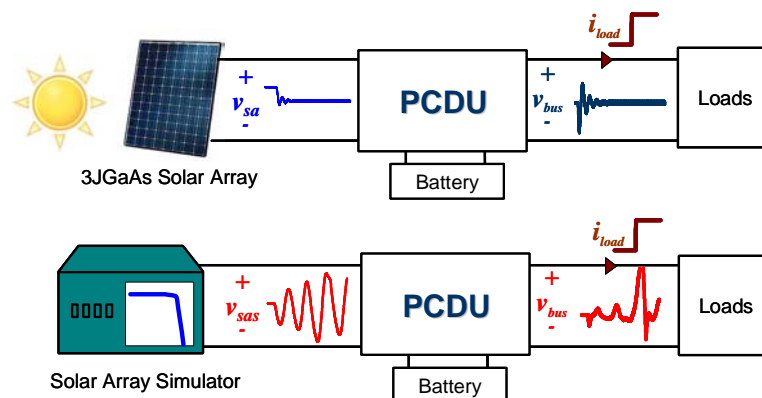


Fig. 7-3: Illustration of dynamic interactions between the SASs and the PCDU as a potential source of system-level stability problems.

Therefore, black-box modeling can be a useful technique to analyze dynamic interactions between SAS and PCDU. If a model of the SAS is available, the response of the PCDU when a SAS is used instead of an actual SA can be directly evaluated through simulation^{7.1}. This may lead to both cost saving and time saving.

In this chapter, a black-box modeling and identification method of SASs is presented, and applied to analyze dynamic interactions with PCDUs. It is organized as follows:

- Section 7.2 briefly describes the electrical behavior of actual SAs and SASs, describing main similarities and differences. A comparison between the frequency response of commercial SASs and the frequency response of 3JGaAs solar arrays is shown.
- Section 7.3 describes the proposed black-box model for the solar array simulator.
- Section 7.4 presents the identification procedure, which relies on the time domain response of the SAS under step tests. Practical implementation of the tests are described and discussed.
- Section 7.5 presents a validation of the modeling and identification methods. This is carried out by making use of a commercial SAS specifically designed for spacecraft applications. The SASs are shown to be highly nonlinear systems, in terms of static response and dynamic response. Therefore, this is a challenging case that allows exploring the performance of the modeling and identification methods discussed along this thesis.

^{7.1} Note that accurate models of 3JGaAs SAs have been already reported in the literature [241].

- Finally, in section 7.6, the dynamic interactions between SASs and PCDUs are analyzed. First, this problem is described and experimentally demonstrated by making use of different commercial SASs. After that, the dynamic interactions are evaluated by making use of the developed black-box models.

7.2 Electrical behavior of solar arrays and comparison with solar array simulators

7.2.1 Static behavior

A photovoltaic SA generates current from incident light through a photoelectric process [245]. A typical I-V static curve of a SA is depicted in Fig. 7-4a. This is defined by the short-circuit current I_{sc} , open-circuit voltage V_{oc} and maximum power point (MPP) voltage V_{mpp} and current I_{mpp} . The MPP splits the curve into two regions, so-called ‘voltage region’ (voltage higher than V_{mpp}) and ‘current region’ (voltage lower than V_{mpp}).

The static behavior of SAs has been widely studied in the literature and can be well explained by the model shown in Fig. 7-4b [245]. The constant current source I_{pv} corresponds to the current generated by incident light and $I_s(V)$ corresponds to the current through the Shockley diode. R_s and R_p represent the parallel and series equivalent resistances of the SA, including harness and wires.

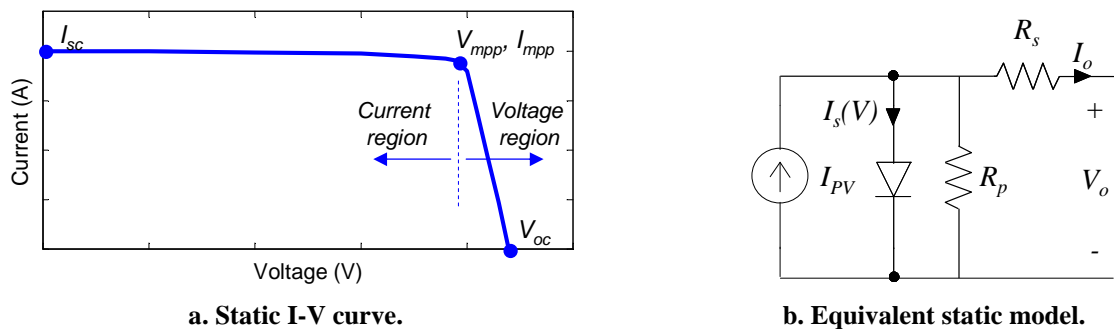


Fig. 7-4: Static behavior of a SA, well emulated by a SAS.

SASs can emulate this type of curves accurately. Typically, SASs allow defining the I-V curve in several ways. Two typical ones are described below:

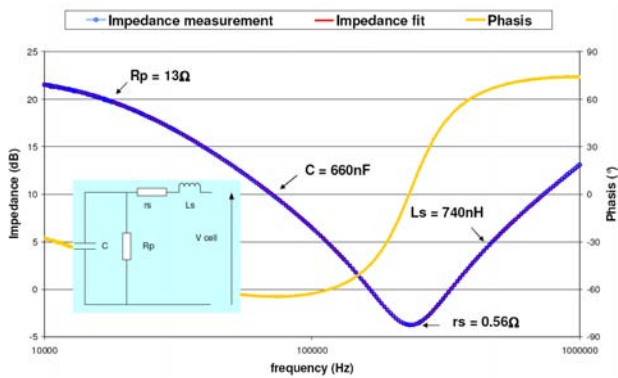
- The user defines several discrete points of the I-V curve. Then any point at the curve is obtained through linear interpolation of given points.
- The user defines the I_{sc} , V_{oc} , V_{mpp} and I_{mpp} . Then the I-V curve is approximated by using an analytical expression.

Moreover, SASs oriented to spacecraft power systems also allow programming time-varying I-V curves, in order to emulate time-varying environmental conditions. This way, periodical orbital cycles featured by eclipse and sunlight semi-periods can be tested.

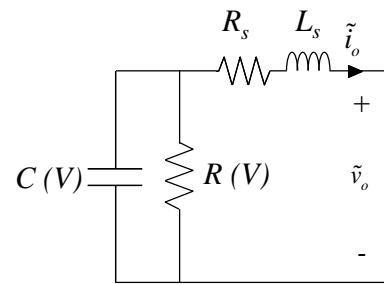
7.2.2 Dynamic behavior

The dynamic behavior of a SA is well described by parasitic capacitors and inductances. The frequency response of a 3JGaAs cell and a small-signal equivalent circuit are shown in Fig. 7-5.

- At low frequency it exhibits resistive behavior, essentially corresponding to the inverse slope of the I-V curve.
- At medium frequencies, the parasitic capacitance of the SA is noticed, which is much higher in 3JGaAs cells than in Si cells. Essentially, the parasitic capacitance is due to the so-called ‘space-charge’ and ‘diffusion’ capacitances. Both of them are a function of voltage (and environmental conditions), so that the higher the voltage the higher the capacitance [241]-[242].
- At high frequency, the impedance of the harness and the wires, R_s and L_s dominates the SA impedance.



a. Frequency response of a 3JGaAs SA reported in [241].



b. Equivalent small-signal model.

Fig. 7-5: Small-signal response of a SA, not well emulated by a SAS.

The dynamic response of the SA in general differs from that exhibited by a commercial SAS, since the latter is determined by the internal electronics and control algorithms.

7.2.3 Frequency response comparison

Below, the frequency response of commercial SASs is compared to that of a 3JGaAs SA. The selected SASs, hereinafter referred to as SAS1 and SAS2, are typically used in the space sector and are made by different manufacturers. A similar I-V curve has been programmed in both SAS and their frequency response has been characterized through an AC sweep test for several operating points.

The experimental setup used to carry out the AC sweep is shown in Fig. 7-6. A variable-frequency current amplifier is used to draw sinusoidal perturbations on the output current of the SAS, i_o , while the resistor R_1 sets the operating point within the I-V curve. By making an AC frequency sweep on v_o and i_o with a network analyzer, the SAS small-signal impedance has been characterized.

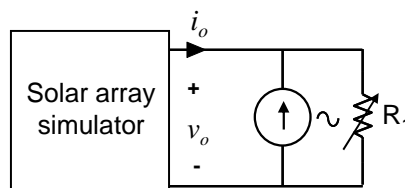


Fig. 7-6: Experimental setup for small-signal dynamic characterization of solar array simulators.

The 3JGaAs SA has been simulated in Pspice using a large-signal model (experimentally validated) of the cell 3G-28 by Azur-Space GmbH [268], which is reported in [241]. A simplified diagram of the model, which illustrates its basic functionalities, is depicted in Fig. 7-7. I_{sc} is the short-circuit current, the diode accounts for the current decrement as the voltage increases, and $C(V)$ models the parasitic capacitance as a function of the voltage. Neither wires nor harness impedance has been modeled (R_s and L_s in Fig. 7-5b).

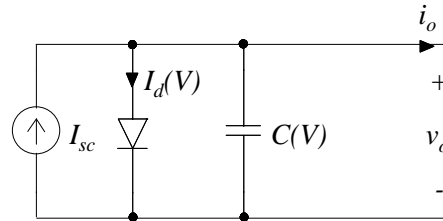


Fig. 7-7: Simplified diagram of the 3JGaAs cell model [241].

Several cells have been combined in series and parallel connection, in such a way that an I-V curve, similar to that programmed in the SASs, has been obtained.

The frequency response of both SASs and the simulated SA are compared in Fig. 7-8 for several operating points. Significant qualitative differences are observed in the dynamic response. For example, SAS1 exhibits a resonance within voltage region that is not exhibited by an actual SA. SAS2 does not exhibit such a resonance, but the phase lies below 90° within current region, while the phase of the SA does not. The importance of these differences and, specifically, the resonance of SAS1 within voltage region, are demonstrated in section 7.6.

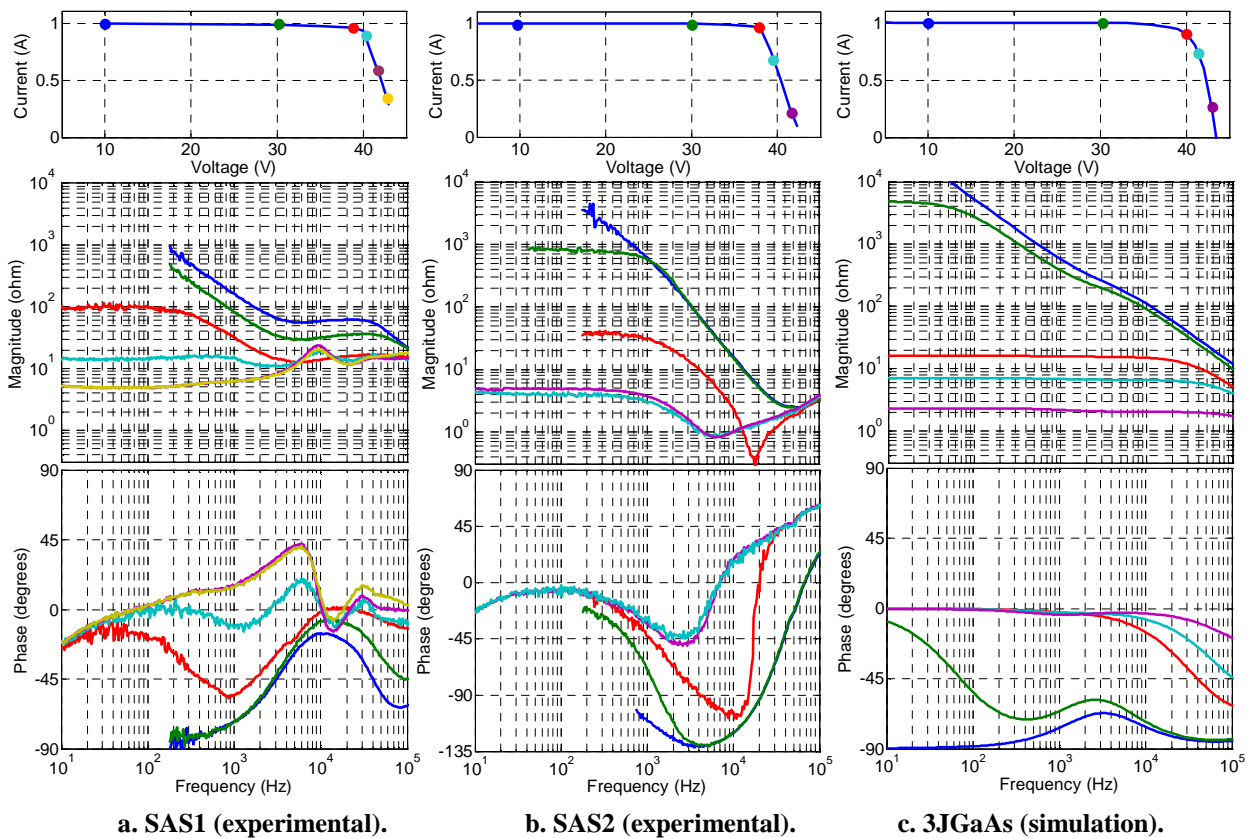


Fig. 7-8: Comparison between frequency responses of two commercial solar array simulators (a, b) and the simulation model of a 3JGaAs solar array (c).

7.3 Model description

7.3.1 Small-signal approach

The SAS is a one-port network, where the output voltage and currents, i_o and v_o , are the interface signals with the rest of the systems. Therefore, those are the input-output signals of the model.

In order to split the interface signals into model input and output, the terminal behavior of the SAS is considered. As reviewed in section 7.2.1, the I-V curve of a SAS (and a SA) can be split into current region and voltage region (see Fig. 7-4a):

- **Within the voltage region**, the SAS behavior is closer to that of a voltage source. Consequently, i_o should be the input and v_o should be the output. Then, the small-signal input-output behavior is determined by the output impedance of the SAS $Z_o(s)$.
- **Within the current region**, it is closer to that of a current source. Hence, v_o should be the input and i_o the output, so the small-signal input-output behavior is determined by the output admittance, $Y_o(s)$.

Such structures are illustrated in Fig. 7-9. They are related to each other, as $Z_o(s) = Y_o(s)^{-1}$.



Fig. 7-9: Small-signal black-box models for a SAS.

7.3.2 Extension to large signal

To address large-signal behavior, the small-signal model is modified as follows:

- A static network is added to model the static I-V curve of the SAS. It is denoted as $i_{os}(v_o)$ for the Norton network and $v_{os}(i_o)$ for the Thevenin network.
- $Z_o(s)$ and $Y_o(s)$ are replaced by dynamic networks, namely Z_{o0} and Y_{o0} , which has null response at steady-state. Such dynamic networks can be implemented using a transfer function, a gain-scheduled transfer function or a LLMN (details are given in chapter 4.2.3). Whether a linear or a nonlinear network should be used depends on the particular behavior of the modeled SAS within the considered I-V curve region. Practical examples will be illustrated in subsequent sections.

The resulting large-signal model structures are depicted in Fig. 7-10. The relationship between the small-signal model and the large-signal model is given by the expressions listed below.

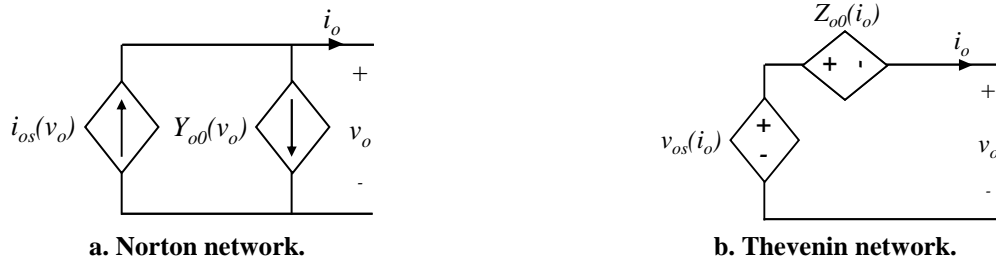


Fig. 7-10: Large-signal black-box models for a SAS.

$$\begin{cases} -\frac{i_o(s)}{v_o(s)} = Y_o(s) = Y_{o0}(s) - \frac{\partial i_{os}(V_o)}{\partial V_o} \\ -\frac{v_o(s)}{i_o(s)} = Z_o(s) = Z_{o0}(s) - \frac{\partial v_{os}(I_o)}{\partial I_o} \end{cases} \quad (7-1)$$

Note that, if the whole I-V curve is considered, both structures may be valid but, due to the very high impedance usually exhibited by SASs within current region, the Norton approach is better suited, in terms of simulation speed and robustness.

7.3.2.1 Simplifying the large-signal model: local linear region of the I-V curve

If a local region of the I-V curve is modeled, so that the local slope of the curve is approximately constant and the dynamics is nearly linear within it, then the models shown in Fig. 7-10 can be simplified to those shown in Fig. 7-11, which consist of a single transfer function, corresponding to either $Y_o(s)$ or $Z_o(s)$ and a DC source, corresponding to either the short-circuit current I_{sc} or the open-circuit voltage V_{oc} (i.e. the model output under null input).

Note that these models are equal to the small-signal ones (Fig. 7-9) plus the DC sources corresponding to I_{sc} and V_{oc} . Since the static response is also linear, the transfer functions can directly incorporate the DC impedance or admittance of the SAS, thus simplifying the implementation.

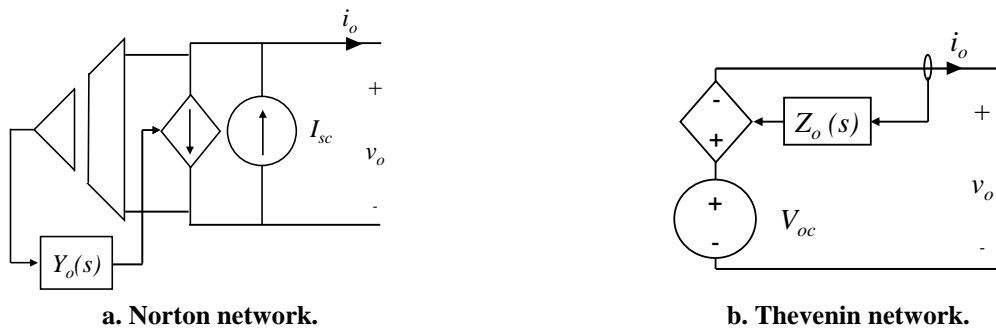


Fig. 7-11: Black-box linear model of SAS (valid for local linear region of the I-V curve).

7.4 Model identification

The identification method relies on the same concepts shown in previous chapters:

- First, steps are carried out so that the behavior of the system is nearly linear.
- Second, transfer function models are identified from the step responses.
- Finally, the large-signal model is parameterized.

The identification procedure is illustrated in Fig. 7-12. This section focuses on the identification test and the parameterization of the large-signal model. The reader is referred to section 4.4 for details about the parametric identification procedure.

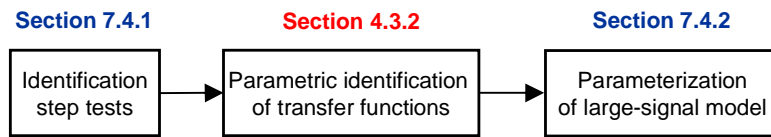


Fig. 7-12: Identification procedure of the black-box model for solar array simulators.

Note that, as a difference from the identification of black-box model for other converters, no cross-coupling effect occurs. This is because the model of the SAS has a single input.

7.4.1 Identification step tests

Within current region the SAS behaves as a current source. Hence, v_o should be the stepped signal, so that an admittance model $Y_o(s)$ is identified. Equivalently, i_o should be the stepped signal within voltage region, so that an impedance model $Z_o(s)$ is identified. Such tests are depicted in Fig. 7-13, from a conceptual point of view.

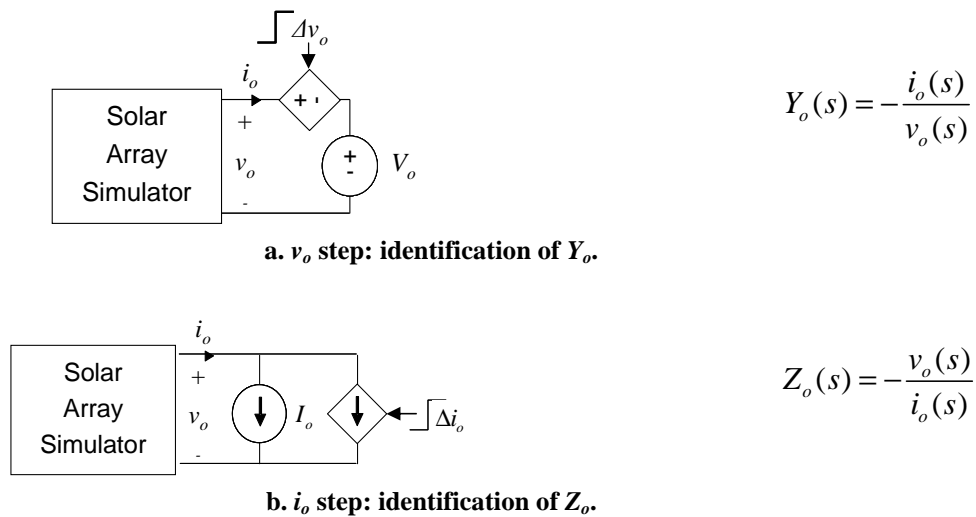


Fig. 7-13: Proposed identification tests: conceptual approach.

Experimental implementations of those tests are depicted in Fig. 7-14. The first one (Fig. 7-14a) is based on two resistive loads, so the step is applied by switching on/off R_2 . The second one (Fig. 7-14b) is based of an array of diodes connected in parallel with a switch, so the step is applied when the diodes are short-circuited. In both cases, R_1 is used to set the operating point.

Both tests can be applied to make steps within both I-V curve regions. Nevertheless, it is worth noting that, within current region, the array of diodes based test allows setting the step magnitude straightforwardly, as it corresponds to the voltage drop across the diodes.

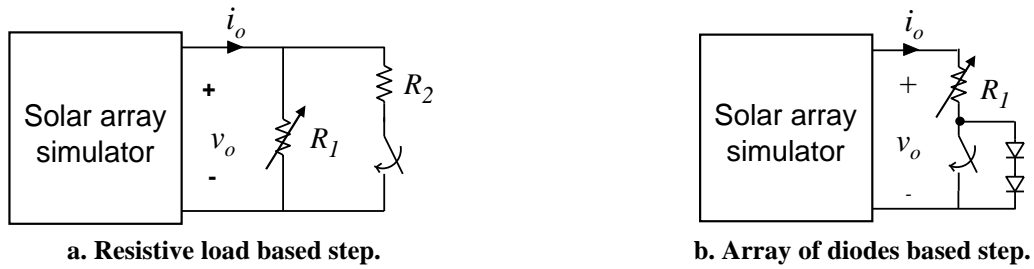


Fig. 7-14: Practical setups to make voltage steps within current region and current steps within voltage region.

7.4.2 Large-signal model parameterization

To build a large-signal model of the SAS, the static I-V curve is characterized, and the identified transfer functions are post-processed to obtain the dynamic network Y_{o0} or Z_{o0} (if the simplified structures shown in Fig. 7-11 are applied, no post-processing actions are required).

The post-processing tasks are similar to those explained in previous chapters. On the one hand, the static response of the identified transfer functions has to be subtracted, as expressed in (7-2). Note that, if a LLMN is used, they correspond to any local linear model.

$$\begin{cases} Y_{o0}(s) = Y_o(s) - Y_o(0) \\ Z_{o0}(s) = Z_o(s) - Z_o(0) \end{cases} \quad (7-2)$$

If a gain-scheduled transfer function is applied, then the transfer function also requires gain normalization. Details can be found in section 4.3.4.2.

On the other hand, if a model for the whole I-V curve is sought, then further considerations have to be taken into account. As explained in section 7.3.2, a Norton network may be considered to model the entire I-V curve. Doing so means that admittance local models are required not only for current region but also for voltage region. However, according to the above explanation, impedance models are identified within voltage region. Admittance model can be obtained within voltage region as follows:

- **Inverting impedance models.** This method has the disadvantage that unstable models can result, in case the identified impedance model has non-minimum phase (i.e. it has zeroes in the right half plane), unless the numerator is constrained to have zeroes only on the left-half plane.
- **Identify directly an admittance model within voltage region.** This can be done by considering the stepped signal (i_o) as the model output instead of input, when applying the parametric identification. The differences between considering the stepped signal as input or output have not been studied in depth in this thesis, and they are a matter of future work^{7.2}.

^{7.2} Some observations are herein pointed out. Swapping the input and the output may have important consequences if an equation-error type of model is identified, such as ARX or ARMAX. This is because the identified noise model shares the denominator with the process model. However, if a model belonging to the class of output-error models is identified, such as OE or BJ, the noise model and process model are independent.

Along this thesis OE is used, but the consequences of identifying an admittance model, instead of inverting an impedance one, have not been studied in depth. Nevertheless, after some preliminary analysis, it has been observed that both approaches yield similar results.

7.5 Experimental results

A black-box model of SAS1 for operation within the whole I-V curve has been derived through the proposed procedure. The programmed I-V curve is the same that has been characterized in section 7.2.3.

7.5.1 Modeling

The nonlinear behavior of SAS1 within the whole I-V requires a nonlinear modeling approach, so the Norton network depicted in Fig. 7-10 has been applied. A LLMN has been selected to make up the dynamic network Y_{o0} .

In order to select a proper model partitioning, the dynamic response plotted in Fig. 7-8a has been analyzed. As can be seen, within current region, the magnitude of the impedance decreases smoothly as the current increases. However, abrupt dynamics variations can be noticed near the MPP, as the operating point moves from current region to voltage region. Within the voltage region the dynamics dependence on operating point is quite slight and is only noticed in the damping of the resonance near 10 kHz. Therefore, two local models within current region (for $V_o = 1$ V and $V_o = 30$ V), one model for the MPP ($V_o = 39$ V) and one model within the voltage region ($V_o = 41$ V) have been selected, weighted through piece-wise linear functions. On the other hand, the static network has been implemented by means of a LUT and linear interpolation. The model implementation is shown in Fig. 7-15.

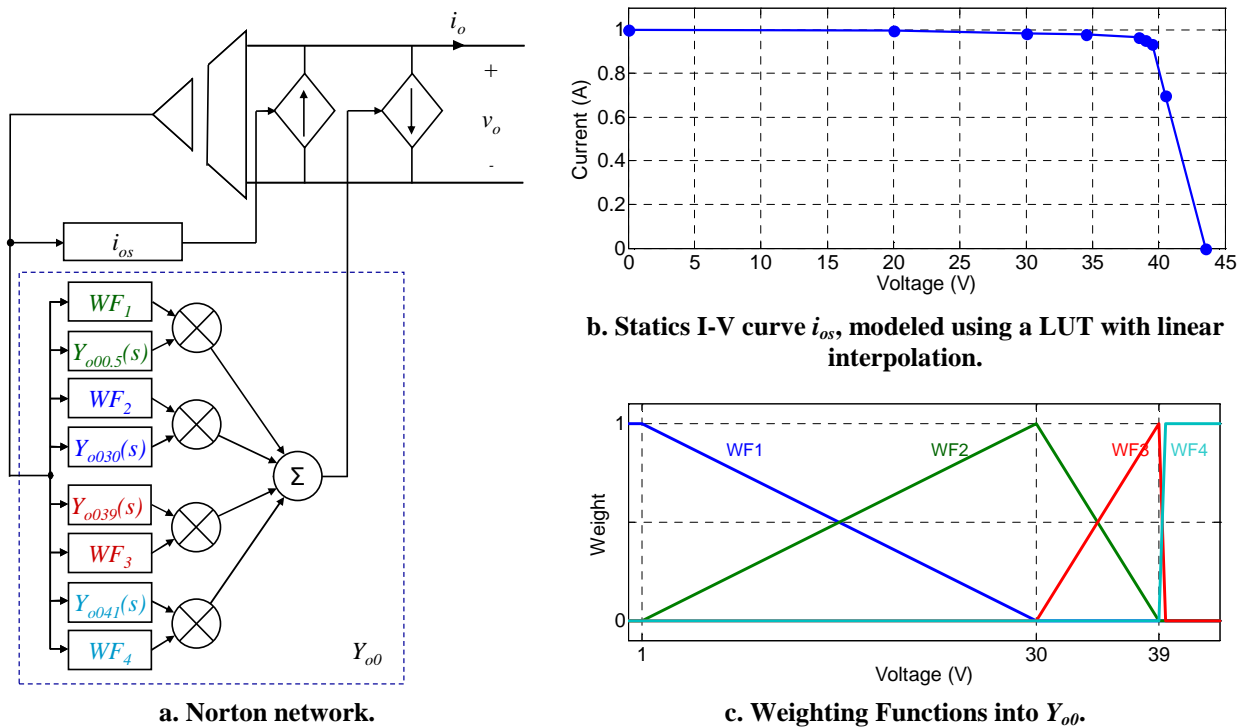


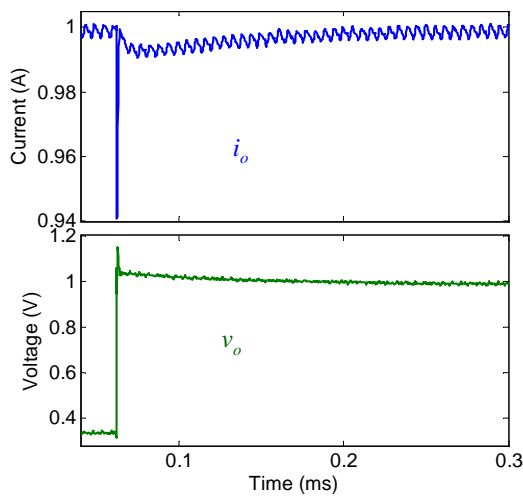
Fig. 7-15: Black-box model of the experimental SAS referred to as ‘SAS1’.

7.5.2 Identification

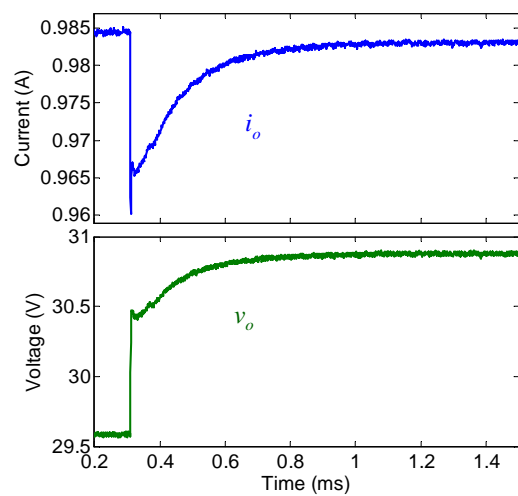
7.5.2.1 Experimental tests

The SAS is a highly nonlinear piece of equipment, so it is a challenging dynamic system to identify through step tests. In order to keep local linear behavior, small steps have been applied on different operating points by means of the diodes-based setup shown in Fig. 7-14b. The transient response has been measured by using a Tektronix oscilloscope MSO4104, a current probe TEK-TCPA300 and a voltage probe TEK-P5050.

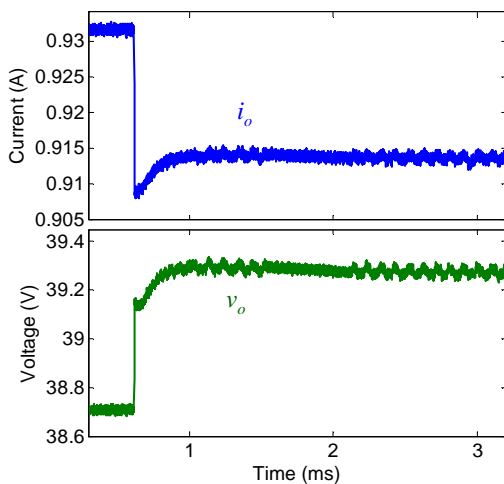
The resulting waveforms are depicted in Fig. 7-16. Within current region (1 V, 30 V), v_o is stepped because the I-V curve is flat, i.e. the behavior of the SAS resembles a current source. Within voltage region (41 V), i_o is stepped because the SAS behavior is closer to that of a voltage source than a current source. Around the MPP (39 V), both magnitudes are stepped.



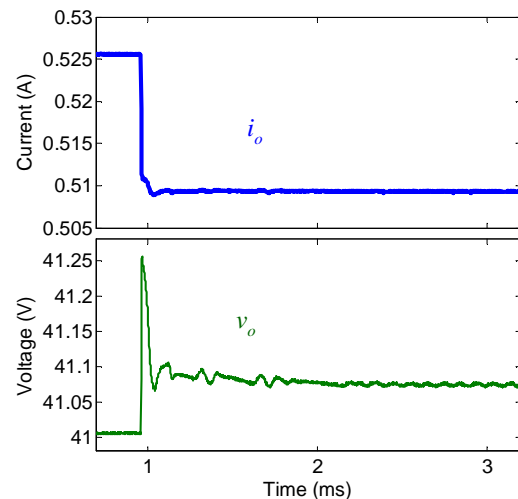
a. Response around 0.5 V (current region).



b. Response around 30 V (current region).



b. Response around 39 V (MPP).



d. Response around 41 V (voltage region).

Fig. 7-16: Transient response of SAS1 under step tests, carried out through the array of diodes based setup (Fig. 7-14b), for several operating points.

7.5.2.2 Transfer functions fitting

The local transfer function models have been identified by applying the parametric identification method described in section 4.4, using the Matlab function ‘*oe*’. The fitting results, evaluated by means of the Matlab function ‘*compare*’, are plotted in Fig. 7-17. As can be seen, the average behavior of the waveform is properly fitted in all cases.

In all cases, the stepped signals has been the transfer function input, so two admittance models have been identified within current region and one impedance model has been identified within voltage region. Around the MPP, both v_o and i_o are stepped, so any of them may be taken as the model input. In this example, i_o has been selected as the input, so an impedance model has been also identified for the MPP.

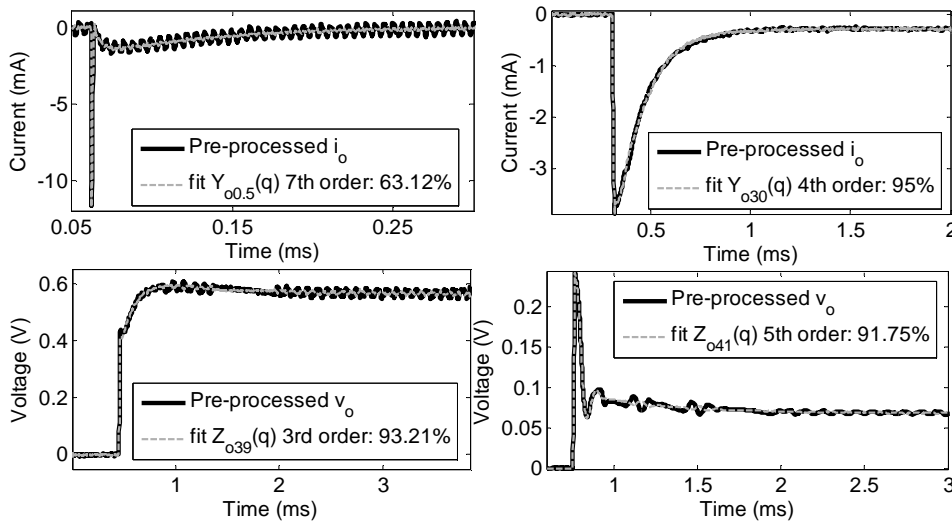


Fig. 7-17: Transient response of SAS1 under step tests, carried out through the array of diodes based setup (Fig. 7-14b), for several operating points (indicated in the subscript of each transfer function name).

The resulting transfer functions, after conversion into continuous time domain, are given by (7-3).

$$\left\{ \begin{array}{l} Y_{00.5}(s) = \frac{-0.1 \cdot s^7 - 1.6 \cdot 10^6 \cdot s^7 + 6.6 \cdot 10^{12} \cdot s^5 + 4.5 \cdot 10^{20} \cdot s^4 + 2.6 \cdot 10^{27} \cdot s^3 + 4.3 \cdot 10^{32} \cdot s^2 + 8.2 \cdot 10^{37} \cdot s + 1.4 \cdot 10^{40}}{s^7 + 7.9 \cdot 10^7 \cdot s^7 + 1.3 \cdot 10^{15} \cdot s^5 + 8.5 \cdot 10^{21} \cdot s^4 + 3.3 \cdot 10^{28} \cdot s^3 + 4.0 \cdot 10^{34} \cdot s^2 + 6.7 \cdot 10^{39} \cdot s + 8.0 \cdot 10^{43}} \\ Y_{030}(s) = \frac{0.05 \cdot s^4 + 1.7 \cdot 10^5 \cdot s^3 + 7.0 \cdot 10^{10} \cdot s^2 + 4.3 \cdot 10^{15} \cdot s + 1.9 \cdot 10^{18}}{s^4 + 2.9 \cdot 10^6 \cdot s^3 + 3.2 \cdot 10^{12} \cdot s^2 + 1.7 \cdot 10^{17} \cdot s + 1.7 \cdot 10^{21}} \\ Z_{039}(s) = \frac{19 \cdot s^3 + 10.0 \cdot 10^5 \cdot s^2 + 1.2 \cdot 10^{10} \cdot s + 1.1 \cdot 10^{13}}{s^3 + 6.0 \cdot 10^4 \cdot s^2 + 3.6 \cdot 10^8 \cdot s + 3.4 \cdot 10^{11}} \\ Z_{041}(s) = \frac{3.9 \cdot s^5 + 4.5 \cdot 10^7 \cdot s^4 + 6.3 \cdot 10^{12} \cdot s^3 + 5.3 \cdot 10^{17} \cdot s^2 + 8.5 \cdot 10^{21} \cdot s + 1.1 \cdot 10^{25}}{s^5 + 2.2 \cdot 10^6 \cdot s^4 + 4.4 \cdot 10^{11} \cdot s^3 + 2.3 \cdot 10^{16} \cdot s^2 + 1.3 \cdot 10^{21} \cdot s + 2.7 \cdot 10^{24}} \end{array} \right. \quad (7-3)$$

Following this, the impedance models have been inverted to implement the model. Finally, every admittance model has been post-processed according to (7-2). The resulting ones are given by (7-4).

$$\left\{ \begin{array}{l} Y_{000.5}(s) = \frac{-0.1 \cdot s^7 - 1.6 \cdot 10^6 \cdot s^7 + 6.4 \cdot 10^{12} \cdot s^5 + 4.5 \cdot 10^{20} \cdot s^4 + 2.6 \cdot 10^{27} \cdot s^3 + 4.3 \cdot 10^{32} \cdot s^2 + 8.1 \cdot 10^{37} \cdot s}{s^7 + 7.9 \cdot 10^7 \cdot s^7 + 1.3 \cdot 10^{15} \cdot s^5 + 8.5 \cdot 10^{21} \cdot s^4 + 3.3 \cdot 10^{28} \cdot s^3 + 4.0 \cdot 10^{34} \cdot s^2 + 6.7 \cdot 10^{39} \cdot s + 8.0 \cdot 10^{43}} \\ Y_{0030}(s) = \frac{0.05 \cdot s^4 + 1.6 \cdot 10^5 \cdot s^3 + 6.7 \cdot 10^{10} \cdot s^2 + 4.1 \cdot 10^{15} \cdot s}{s^4 + 2.9 \cdot 10^6 \cdot s^3 + 3.2 \cdot 10^{12} \cdot s^2 + 1.7 \cdot 10^{17} \cdot s + 1.7 \cdot 10^{21}} \\ Y_{0039}(s) = \frac{0.39 \cdot s^3 + 2.8 \cdot 10^5 \cdot s^2 - 1.1 \cdot 10^7 \cdot s}{19.1 \cdot s^3 + 10.0 \cdot 10^5 \cdot s^2 + 1.2 \cdot 10^{10} \cdot s + 1.1 \cdot 10^{13}} \\ Y_{0041}(s) = \frac{0.065 \cdot s^5 - 8.5 \cdot 10^6 \cdot s^4 - 1.0 \cdot 10^{12} \cdot s^3 - 1.0 \cdot 10^{17} \cdot s^2 - 7.0 \cdot 10^{20} \cdot s}{3.9 \cdot s^5 + 4.5 \cdot 10^7 \cdot s^4 + 6.3 \cdot 10^{12} \cdot s^3 + 5.3 \cdot 10^{17} \cdot s^2 + 8.5 \cdot 10^{21} \cdot s + 1.1 \cdot 10^{25}} \end{array} \right. \quad (7-4)$$

7.5.3 Validation

The proposed modeling and identification procedures have been validated as follows:

- First, the frequency responses of the identified admittance models have been compared with frequency response measurements directly obtained through AC sweep tests.
- Second, the large-signal black-box model has been validated through comparison of simulation results and experimental measurements under a set of large-signal validation tests, different from those used for model identification.

7.5.3.1 Comparison with AC sweep test results

The comparison is done in terms of impedances, so both $Y_{0.5}(j\omega)$ and $Y_{30}(j\omega)$ have been inverted. The results are shown in Fig. 7-18 and discussed below.

- $Y_{0.5}(j\omega)^{-1}$, $Y_{30}(j\omega)^{-1}$: The frequency response of the identified models is close to the AC sweep test results, although a slight mismatch is observed. Such a mismatch is probably due to the nonlinear behavior of the SAS within current region. Notice that $Y_{0.5}(j\omega)^{-1}$ has been improperly characterized below 100 Hz through the AC sweep, which is due to the fact that SASs typically exhibit low-frequency high impedance at low voltage, where the I-V curve is very flat. Hence, the induced sinusoidal perturbations on i_o are very small and, consequently, a current probe with very high resolution would be required. It is worth noting that this is not a problem if steps are applied to characterize the SAS impedance.
- $Z_{30}(j\omega)$: Some mismatch is observed, mostly in phase. This is attributed to the highly nonlinear behavior of the SAS near the MPP.
- $Z_{41}(j\omega)$: Both frequency responses are very close. Note that the dynamic nonlinearities are quite slight within voltage region, which makes easier the identification task through steps.

The conclusion is that the model of the SAS can be properly identified by means of the step tests. However, in those regions where the dynamic behavior exhibits abrupt variations with the operating point, such as around the MPP in the case study, the step test based method exhibits limited accuracy.

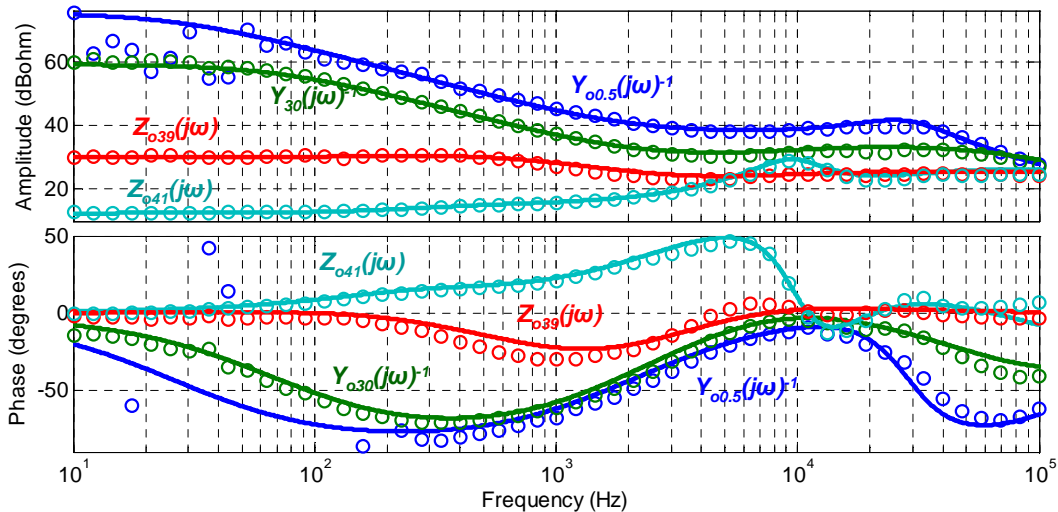


Fig. 7-18: Comparison of frequency response measured through AC sweep test (dots) with frequency response of the identified transfer function models (solid lines) as a function of the operating point.

7.5.3.2 Comparison with experimental measurements under small and large signal perturbations

7.5.3.2.1 Validation test 1. Small magnitude steps within current region

Firstly, two resistive load steps (small magnitude) have been tested, within current region, by means of the experimental setup shown in Fig. 7-14a. The first one has been carried out around 30 V, which is the operating point corresponding to a local LTI model. The second one has been done far from any local LTI model (15 V). The validation results are shown in Fig. 7-19 and discussed below.

- Step around 30 V: The model response is very close to the measured response. The high accuracy is due to the fact that the step is done around a local model of the LLMN.
- Step around 15 V: In this case a certain mismatching between the model response and the measured response is observed. This is because the model is operating far from any local LTI model, and this approach only approximates the true nonlinear dynamics as the combination of local linear models (in this test, the combination of the models at 0.5 V and 30 V). Nevertheless, the differences are relatively small, meaning that the setting time and voltage undershoot are sufficiently well predicted. Then, this test demonstrates the appropriateness of the LLMN under relatively small disturbances and continuous dynamics (smooth dynamic variation as the operating point varies). In fact, such a difference may be reduced if the number of LLMN is increased.

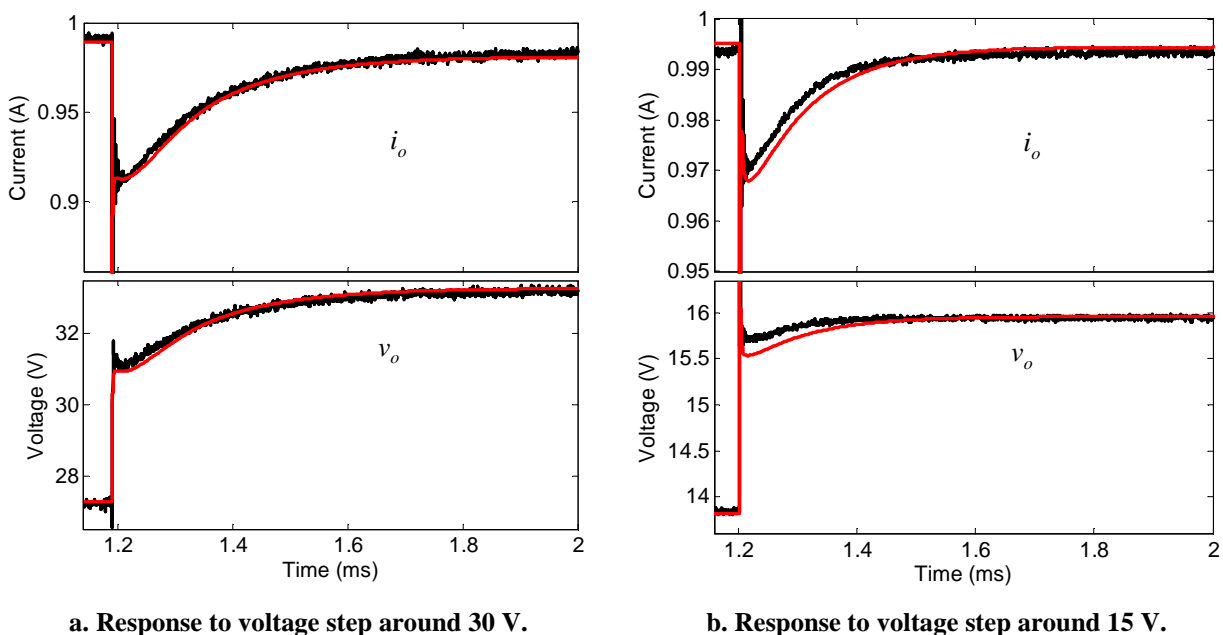


Fig. 7-19: Comparison between model response (red traces) and experimental measurements (black traces) under small magnitude steps within current region.

7.5.3.2.2 Validation test 2. Small magnitude steps within voltage region, near the MPP

Secondly, a resistive load has been switched ‘off and ‘on’ within voltage region, near the MPP. The validation results are plotted in Fig. 7-20 and discussed below.

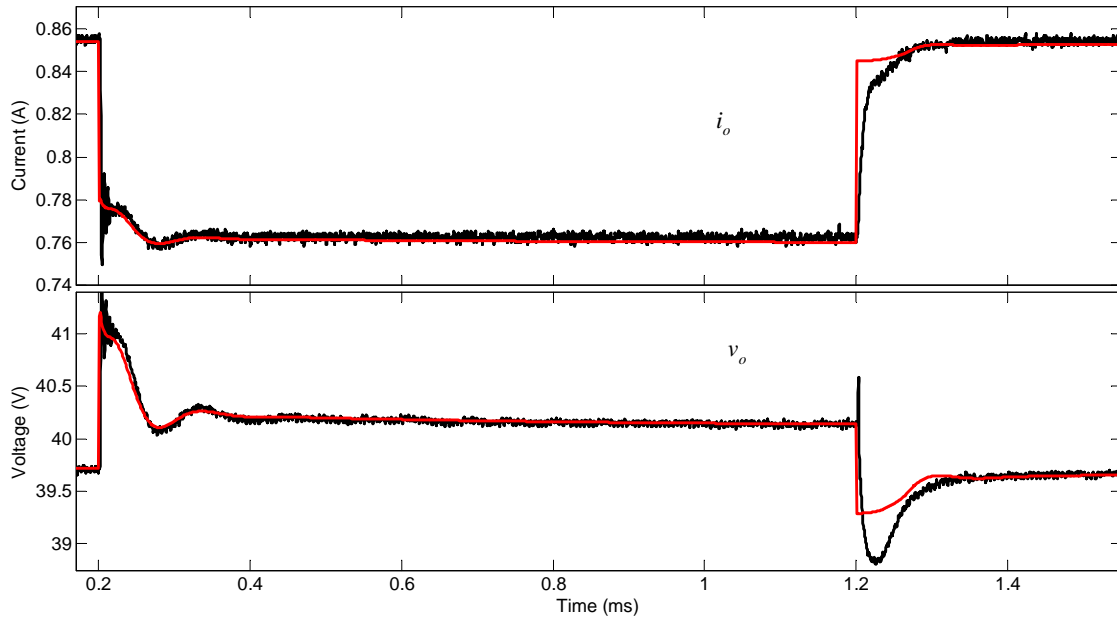


Fig. 7-20: Comparison between model response (red traces) and experimental measurements (black traces) under small magnitude steps within voltage region.

As can be seen, under a step-down in current the model reproduces properly the response of the SA (the slight mismatch is attributed to the linearity assumptions). However, under a current step-up, significant differences are observed. This is because the SAS lies over the boundary of the MPP and the voltage region, which has been found to be a highly nonlinear zone (see Fig. 7-8a). This test evidences the limitations of the LLMN, which does not perform properly if the dynamics changes abruptly with the operating point (in this case, the results are not necessarily better in the number of local models is increased).

7.5.3.2.3 Validation test 3. Large magnitude steps

Thirdly, the response of the model to large magnitude steps has been analyzed (see Fig. 7-21).

- The first one corresponds to a load step from short-circuit to 30 V. This electrical requirement is similar to that applied in sequential switching shunt regulators [44], [45], [242], where each SA section is either connected to the DC bus or shunted. As shown in Fig. 7-21a, less accuracy than before is achieved, because the true SAS is nonlinear, whereas the model response essentially corresponds to that of the local model for 30 V.
- The second test consists in applying a large step from voltage region to current region. This requirement is found in PCDUs based on PWM converters, when the control mode of the solar array regulator (SAR) changes from bus voltage (or bus current) regulation to MPPT [49]. As depicted in Fig. 7-21b, the dynamic behavior is not properly modeled, again because the SAS dynamics changes abruptly and LLMNs do not perform properly in this case.

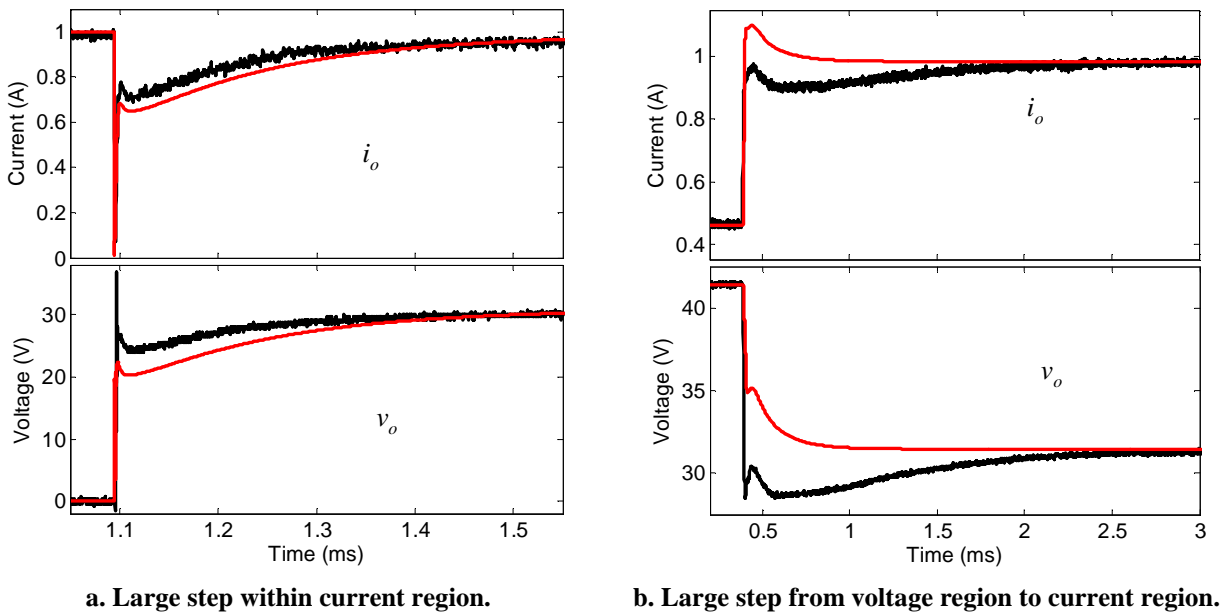


Fig. 7-21: Comparison between model response (red traces) and experimental measurements (black traces) under large magnitude steps.

7.5.4 Summary

From this experimental study, the following conclusions have been drawn:

- The proposed black-box model, consisting of a nonlinear static function summed to a LLMN, has been proven to predict the dynamic response of the real SAS under relatively small perturbations, so that the dynamics is nearly linear or the nonlinearities are smooth. However, the model fails to predict the dynamic response under large-signal perturbations that imply non-smooth variations of the dynamic behavior (such as jumps from voltage region to current region).
- The local LTI models are well identified through the proposed step tests.

7.6 Analysis of dynamic interactions between a solar array simulator and a power conditioning and distribution unit for spacecraft

7.6.1 Operating models and dynamic behavior of the solar array regulator

In this section, the problem of dynamic interactions between SAR and PCDUs is tackled. The effectiveness of the black-box models of SAS for prediction of such interactions through simulation is demonstrated as well.

The analysis is herein focused on regulated bus architectures based on PWM converters. Fig. 7-2 depicts the structure of this type of PCDU [43], [46]-[48]. It is comprised of three types of converters: the solar array regulator (SAR), the battery charge regulator and the battery discharge regulator.

A simplification of the system shown in Fig. 7-2 is depicted in Fig. 7-22, where a high-level diagram of the control structure for the SAR is illustrated. The control mode of the SAR is determined as a function of the power distribution system requirements as described below.

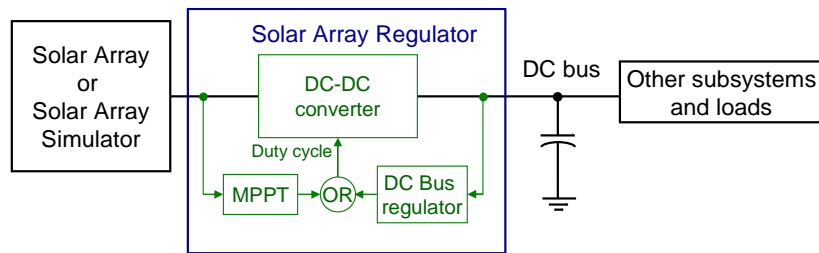


Fig. 7-22: High-level control scheme of a solar array regulator for a spacecraft PCDU based on regulated bus.

- If the power available at the solar array exceeds the power demand from the PCDU (including the load power and the battery recharge power), then the SAR takes control over the DC bus voltage, so its duty cycle is determined by the DC Bus regulator.
- If the power available at the solar array is lower than the power demand from the PCDU, e.g. during eclipse, then the SA is operated at the MPP in order to deliver the maximum power available at the SA to the PCDU. Therefore, the duty cycle of the SAR is driven by the MPPT.

The dynamic characteristics of the SAR at the input port are the key point behind the dynamic interactions problem with the SAS. Those are closely related to control mode as follows^{7.3}:

- **MPPT control:** Either the input voltage v_i or the input current i_i of the SAR is controlled, in order to operate at the MPP of the I-V curve. If v_i is controlled, then the SAS behaves as a “constant voltage load” at low frequencies. If i_i is controlled, the SAS behaves as a “constant current load”. Dynamically, this is a favorable situation, so stability issues should not be a concern [64]^{7.4}. Nevertheless, it is worth pointing out that an improper dynamic response of the SAS may yield to degradation of the MPPT tracking performance [49].
- **DC bus voltage control:** The output voltage v_{bus} of the SAR is controlled, so the SAR behaves as a CPL at low frequencies, that is to say, i_i is inversely proportional to v_i if the output power is kept constant. As demonstrated in chapter 4, this is an unfavorable situation in terms of stability, as the CPL means an incremental negative resistor from the small-signal point of view. Hence, stability problems could come up [54], [64]. Thereby, this section focuses on this operation mode. It is worth pointing out that such an unfavorable situation is also found in case of un-regulated bus architectures, where the bus current is controlled by the SAR instead of the bus voltage [47] and, consequently, it also exhibits CPL behavior at the input port.

7.6.2 Experimental system description

The PWM boost converter described in [46] has been used as a SAR. Boost-type converters are becoming a matter of interest concerning new high-voltage bus based architectures of PCDUs for spacecrafts [50], [51]. The system configuration is depicted in Fig. 7-23, which corresponds to that of regulated bus architectures when there is no battery power flow. The SAR comprises an inner

^{7.3} In the following explanation, the load is assumed to be constant in all cases.

^{7.4} This operating mode has not been studied in depth in this work

inductor current loop plus an outer voltage loop, which keeps v_o tightly regulated to 28 V. A resistors bank is used to perform load power step, from which the dynamic response of the system can be analyzed. The maximum tested power is 28 W.

Two commercial SASs, namely SAS2 and SAS3, have been used to feed the SAR. SAS2 has been already characterized in section 7.2.3 (see Fig. 7-8b). SAS3 is made by the same manufacturer as SAS1 (see Fig. 7-8a), although it is a different version, and both of them feature similar dynamics. The I-V curve is characterized by $I_{sc} = 2\text{ A}$, $V_{oc} = 21.3\text{ V}$, $V_{mpp} \approx 19\text{ V}$ and $I_{mpp} \approx 1.95\text{ A}$.

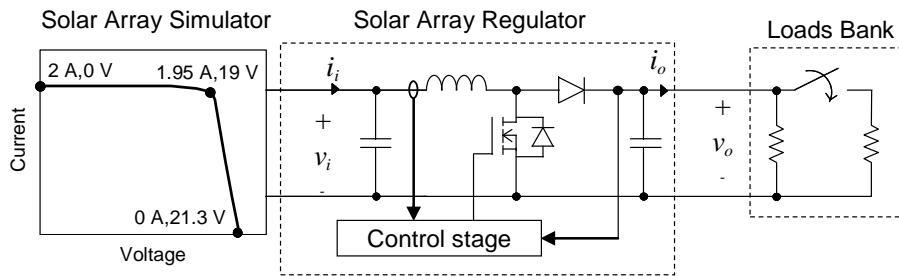


Fig. 7-23: System under experimental study.

The SAS is operated within the voltage region. This is a typical working region under the considered control mode [48], [49]. The frequency response of SAS2 and SAS3 is shown in Fig. 7-24. Similarly to SAS1, SAS3 exhibits a large resonance peak (in this case above 5 kHz), whereas SAS2 features a nearly linear flat response up to 10 kHz.

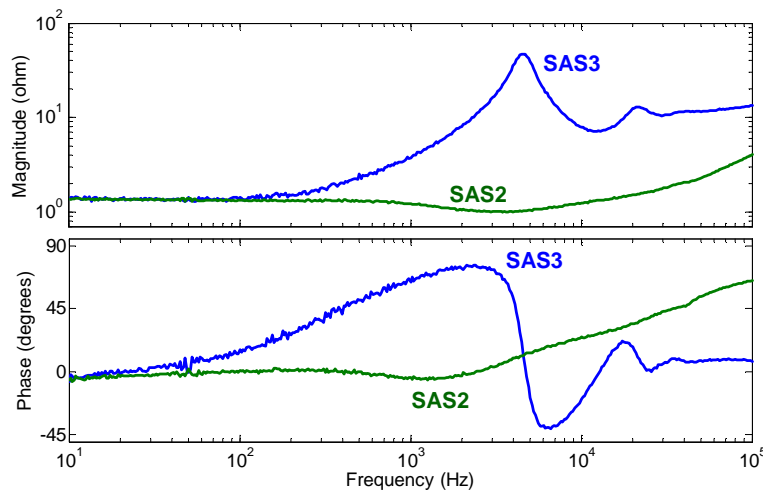


Fig. 7-24: Frequency response of SAS2 and SAS3 within voltage region.

As demonstrated later on, such a resonance may cause significant dynamic interactions between the SAS and the SAR which may even lead to unstable situations.

7.6.3 Experimental analysis

The system has been subjected to several load steps, and the dynamic response using SAS2 has been compared to that using SAS3. Fig. 7-25 shows the response of the system under a step up in load from 5 W to 12 W and back.

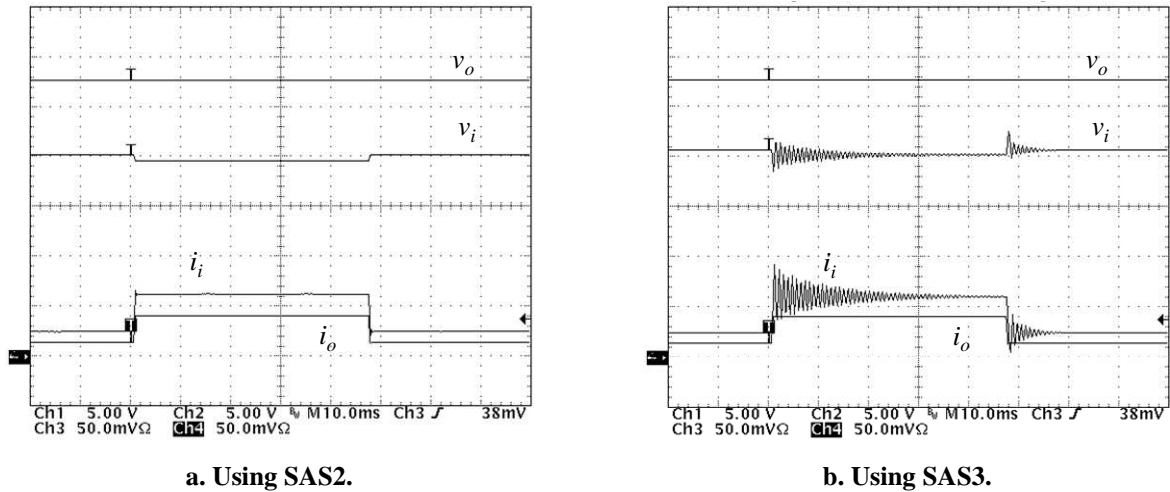


Fig. 7-25: Transient response of the SAR under a resistive load step from 4.5 W to 12 W and back.

As can be seen in Fig. 7-25, the system is stable in both cases but, if SAS3 is used, large oscillation is found out. This is caused by the resonance peak exhibited by the impedance of SAS3 that degrades significantly the dynamics, not only at the interface between the SAS and the SAR, but also at the DC bus. Fig. 7-26 shows a detail of the response under the step up in load power. If SAS2 is used, the setting time is about 0.6 ms. However, this setting time is more than 50 times higher if SAS3 is used.

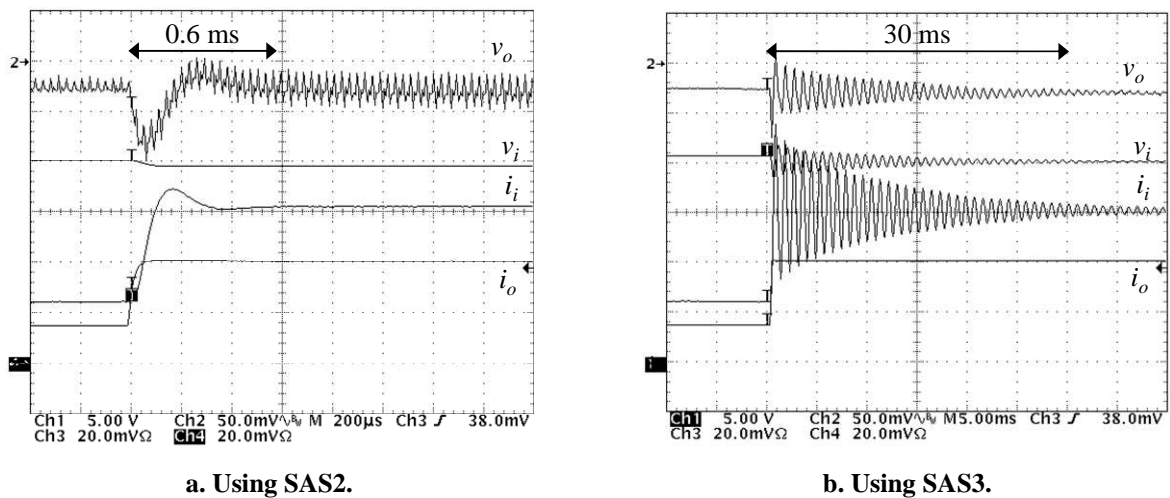


Fig. 7-26: Detail of the transient response of the SAR under a resistive load step from 4.5 W to 12 W.

The impact of the SAS dynamics on the DC bus performance has been also investigated in frequency domain. The output impedance magnitude of the SAR is plotted in Fig. 7-27 for load power equal to 4.5 W. As can be seen in Fig. 7-27, a large peak is found out near 1 kHz if SAS3 is used. Due to such a peak, the DC bus impedance may not comply with the highly demanding power quality requirements for spacecrafts dictated by the standards [267]^{7.5}.

^{7.5} Note that this is a ‘terminated’ output impedance of the SAR, as the SAS makes influence on it.

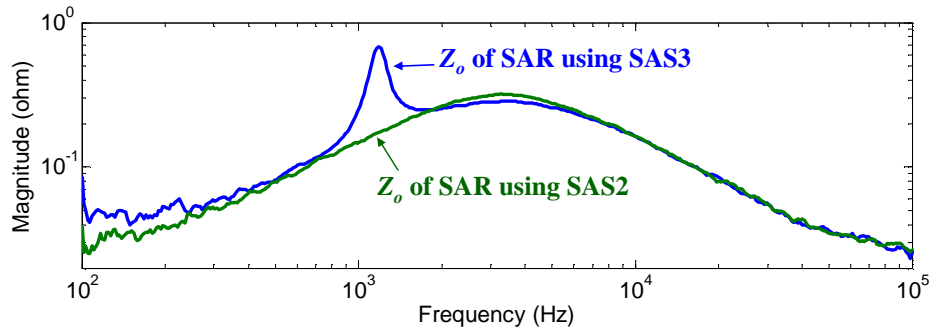


Fig. 7-27: ‘Terminated’ output impedance magnitude of the SAR for load power equal to 4.5 W.

After that, a larger load step has been tested: from 5.6 W to 28 W. As shown in Fig. 7-28, no oscillations are found if SAS2 is used. However, if SAS3 is applied instead, the system becomes unstable after the load is switched on.

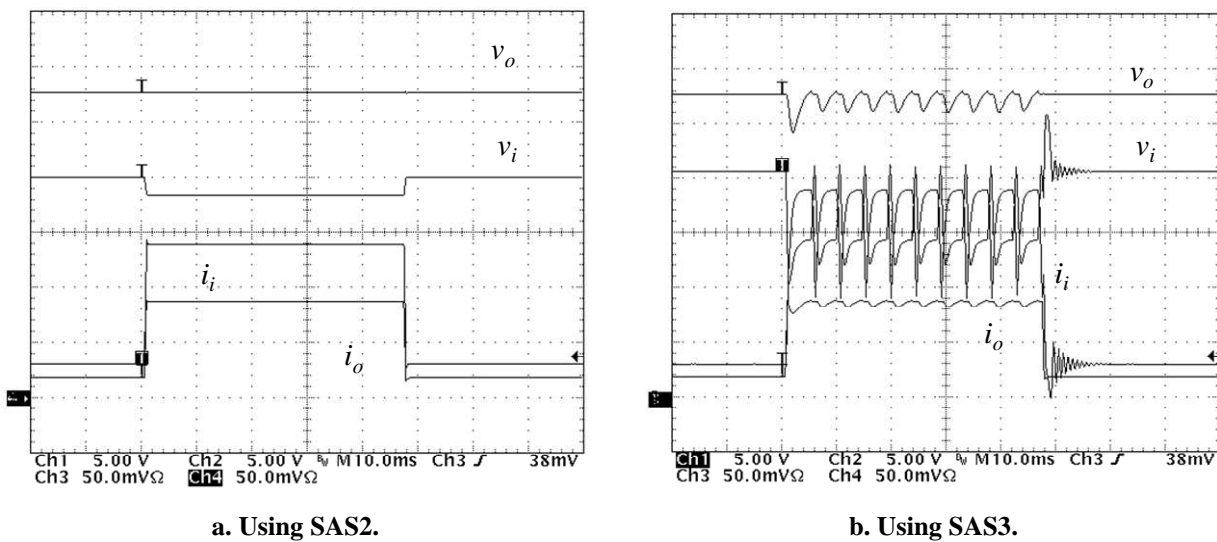


Fig. 7-28: Transient response of the SAR under a resistive load step from 4.5 W to 28 W and back.

The conclusion is that the SAS dynamics can strongly influence the dynamic performance of the PCDU when the SAR performs bus voltage regulation. Due to this, the PCDU may not comply with the standards on DC bus power quality when using a SAS, whereas it may comply when using the real SA. Even further, the system may be unstable when using a SAS, whereas it may be stable when using the real SA.

A theoretical analysis and prediction of such interactions, through input-output impedance models of the SAR and the SAS, respectively, is presented in appendix 0.

7.6.4 Prediction of dynamic interactions using black-box models

The capability of the black-box model to predict the dynamic interaction has been investigated. The SASs exhibits a nearly linear behavior within the region of interest, i.e. voltage region (see Fig. 7-8). Hence, a linear approach, consisting of a Thevenin network, has been chosen as the model structure (see Fig. 7-11). On the other hand, a switching model has been used for the boost converter. The simulation schematic is depicted in Fig. 7-29.

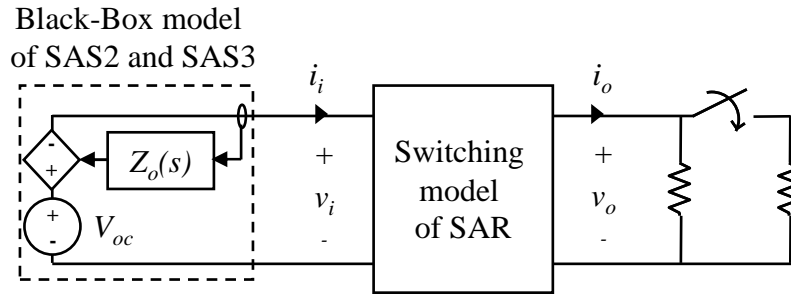


Fig. 7-29: Simulation schematic for analysis of dynamic interactions.

The system response under resistive load steps has been simulated in PSIM. Step increase in load has been simulated from 4.5 W to 12 W and from 12 W to 28 W, which are the power levels evaluated experimentally in Fig. 7-26 and Fig. 7-28. The results are shown in Fig. 7-30 and discussed below.

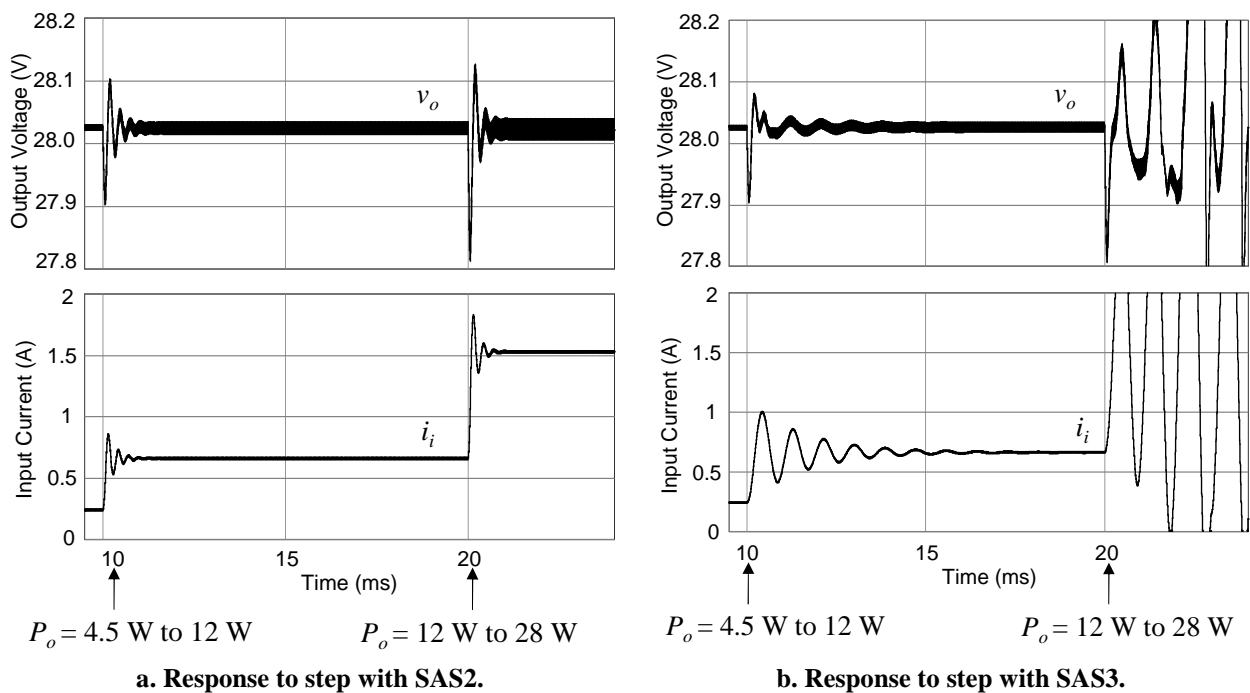


Fig. 7-30: Transient response of the SAR under a resistive load step from 4.5 W to 28 W and back.

As shown in Fig. 7-30, the system is stable after both steps if the model of SAS2 is used. However, when using SAS3, the input current exhibits a larger oscillation after the first step, and become unstable after the second step. This is in agreement with the experimental findings so, as a conclusion, **the black-box modeling technique proposed in this section can be used to analyze the problem of interactions straightforwardly through simulation.**

In both cases, the differences between simulated (Fig. 7-30) and experimental waveforms (Fig. 7-26 and Fig. 7-28) are mainly attributed to difference between the switching model of the SAR and the real converter.

7.7 Conclusions

In this chapter, as an original contribution, a black-box modeling method of solar array simulators (SASs) has been proposed. The aim is to predict, by simulation, differences in the dynamic performance of a distribution system when it is tested using a SAS instead of a real SA, proven that the dynamic behavior of SAS currently used by industry is different from that of real SA (based on 3JGaAs PV cells).

- The black-box model is comprised of a static network (which stores the I-V curve) and a dynamic network which can be either linear or nonlinear. Simplified linear approaches have been proposed, well suited if the SAS is intended to address behavior only on a nearly linear local region.
- The LTI models into the black-box model are identified by applying step tests, so that local linear behavior is kept, followed by parametric identification.
- The proposed black-box modeling technique has been applied to derive a model of a commercial SAS typically used in the space industry. It has been demonstrated that **the model allow predicting the static behavior accurately. The dynamic behavior is well predicted under relatively small-perturbations, so that the dynamic response is nearly linear, or smoothly nonlinear.** However, within region of the I-V curve where strong dynamic nonlinearities are found out (e.g. near the MPP in the case study), the mode fails to predict the dynamic response of the SAS.
- Finally, the problem of dynamic interactions has been experimentally tackled. It has been demonstrated that, in case of PCDU architectures based on regulated bus and PWM converters, **the dynamic interactions may play a critical role when the solar array regulator (SAR) regulates the bus voltage.** The black-box modeling technique can be used to predict such interaction problem due to the following reasons:
 - Under bus voltage regulation, the SAS is operated within a single region. Therefore, the dynamics varies smoothly as the operating point changes.
 - The dynamic interactions between SAS and SAR (including instability) are well predicted by small-signal theory, using linearized models of the SAS and the SAR. **As the black-box model for SASs is accurate under local linear operation, it can be used to address the dynamic interactions problem.**

It is worth noting that such a problem of dynamic interactions between SASs and SARs may not be restricted only to spacecrafts. Specifically, it may be also a concern in micro-grid systems partially based on PV generation [38], [39], which presents some similarities with the PCDU studied in this chapter. Under islanding operation, the SA will not operate in MPPT if the SA power exceeds the load power demand. As a consequence, the SAR may exhibits CPL behavior at the input port if its output current (or voltage) is regulated. This may lead to the problem of dynamic interactions and instability herein discussed and proven.

8 Grey-Box Modeling of a Switched Reluctance Starter-Generator

8.1	Introduction.....	275
8.2	The switched reluctance starter/generator: basic concepts	276
8.2.1	Principle of operation	276
8.2.2	Control strategy	277
8.2.2.1	Operation as a Starter	277
8.2.2.2	Operation as a Generator	278
8.3	Proposed modeling and identification method.....	279
8.3.1	Basic approach	279
8.3.2	Modeling and identification for the generator operation.....	280
8.3.2.1	Generator network structure	280
8.3.2.2	Identification	281
8.3.3	Modeling and identification for the starter operation.....	283
8.3.3.1	Starter network structure	283
8.3.4	Identification	285
8.3.4.1	Power balance block.....	285
8.3.4.2	Speed dynamics block	286
8.4	Experimental results	287
8.4.1	System description	287
8.4.2	Generator operation.....	288
8.4.2.1	Estimation of C_{bus} and R_{Cbus}	288
8.4.2.2	Identification of $R_v H_v$ and τ	290
8.4.2.3	Incorporating clamping functions CF.....	292
8.4.2.4	Remarks on dynamics dependence on operating point	293
8.4.2.5	Model validation under operation as a generator	294
8.4.3	Starter operation	297
8.4.3.1	Power balance block.....	297
8.4.3.2	Closed loop speed transfer function $G_\omega(s)$	298
8.4.3.3	Load torque transfer function $G_T(s)$	299
8.4.3.4	Model validation under operation as a starter	301
8.5	Conclusions.....	305

8.1 Introduction

As explained in chapter 2, the more-electric-aircraft (MEA) concept is leading to an increase in onboard electrical equipment to drive aircraft subsystems that have conventionally been supplied by pneumatic, hydraulic or mechanical means. The starter-generator is a key enabling technology of the MEA for providing engine starting and powering onboard loads and actuators. The switched reluctance machine (SRM) is one of the candidate technologies for future engine-embedded starter/generators due to its simple structure, robustness, and fault tolerance [211]-[216]. Besides the MEA, the SRM is also a candidate for starter/alternators for hybrid electric vehicles and wind turbine applications [219]-[221].

As a difference from converters and subsystems addressed in previous chapters, the switched reluctance starter/generator (SRSG) is a bidirectional subsystem. To start the aircraft engine the starter/generator operates as a motor and draws power from the auxiliary power unit (APU), accelerating the gas turbine to ground idle. Once the engine is running, the machine operates as a generator and supplies power to the system.

At the moment, existing modeling approaches for SRSGs focus on a detailed description of the electromagnetic behavior of the machine and switching behavior of the converter [218], [222]-[230]. Therefore these models are not well suited for system-level analysis. To address this lack of models, a system-level behavioral modeling technique for a SRSG is proposed in this chapter. Its characteristics are similar to those featured by models presented in previous chapters.

- Parameterization based on straightforward transient response measurements.
- Simple representation of relationships between average terminal waveforms, leading to manageable system simulation times.
- The internal structure of the SRSG is not included, thereby protecting confidential data.

However, the approach followed in this chapter is different. The proposed model may be referred to as a “grey-box”, since represents partially some inner elements of the SRSG, as well as prior knowledge about the SRSG can be readily used to parameterize in part the model. Moreover, as a difference from previous models, neither a Thevenin network nor a Norton network is used to make up the model.

The chapter is structured as follows.

- Section 8.2 describes briefly the basis of the switched reluctance machine (SRM) as well as control strategies for the SRSG.
- Section 8.3 presents the proposed modeling and identification approach.
- Section 8.4 illustrates and validates the proposed approach through experimental results, which has been obtained on a 30 kW SRSG for aerospace.
- The main conclusions and contributions are discussed in section 8.5.

8.2 The switched reluctance starter/generator: basic concepts

8.2.1 Principle of operation

The aim of this section is to describe briefly the working principle of the SRM. For illustrative purposes, the explanation is focused on the SRM structure depicted in Fig. 8-1. This SRM is made up by a stator with 6 poles and a rotor with 4 poles (denoted as 6/4), both of them made of laminated steel^{8.1}. The coils around the stator poles are connected to form each phase windings. The absence of windings on the rotor allows high temperature operation as well as high rotational speed. The stator windings corresponding to phase 'a' are highlighted in Fig. 8-1a.

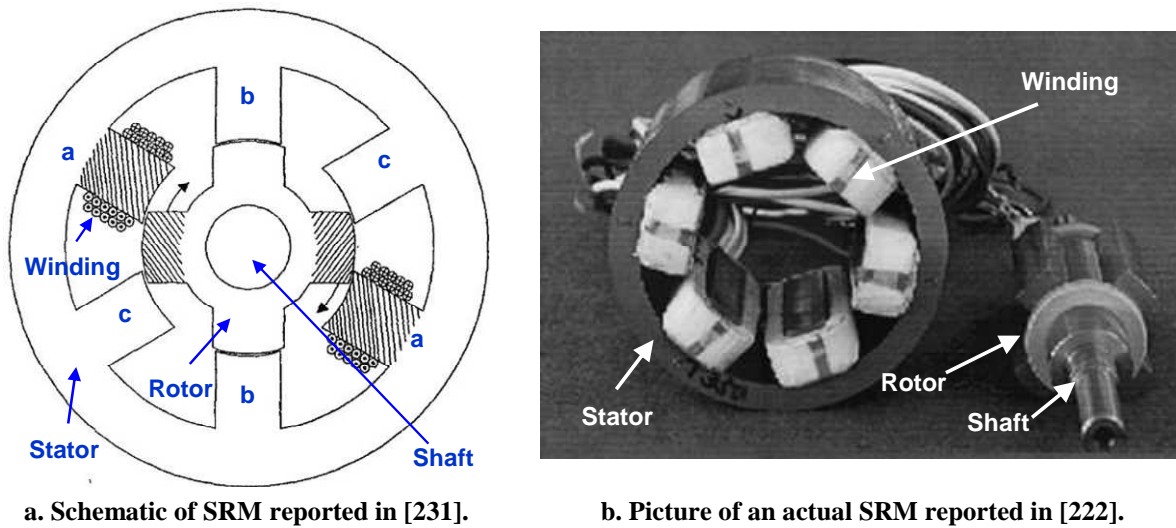


Fig. 8-1: A 6 stator poles and 4 rotor poles (6/4) SRM.

As stated in [232]-[233], a SRM can be defined as a *machine in which torque is produced by the tendency of its moveable part to move to a position where the inductance of the excited winding is maximized*. A continuous production (generator) or consumption (motor) of power is achieved by proper control of the current through the windings by means of a power converter. Among several topologies, the asymmetric inverter is a typical choice [213], [215], [218], [227], [231], [234], [235]. A three-phase asymmetric inverter for a 6/4 SRM is shown in Fig. 8-2.

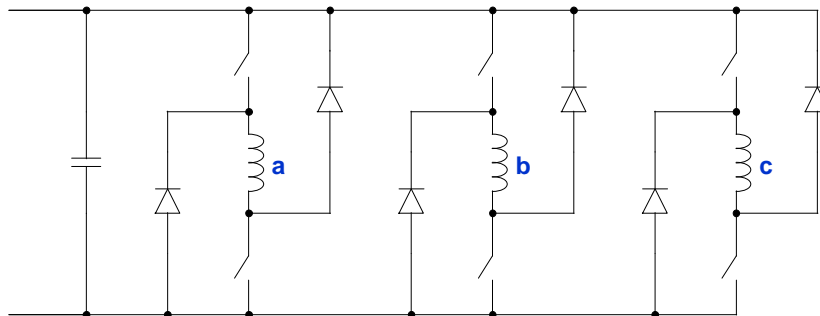


Fig. 8-2: Three-phase asymmetrical converter for a 6/4 SRM.

^{8.1} SRMs can be also comprised of a different number of rotor and stator poles, i.e. 8/6, 12/8, 24/16, etc.

The working principle of the SRM is illustrated in Fig. 8-3, where idealized phase inductance and phase current profiles are depicted as a function of rotation angle. A description of the operating principle is given below.

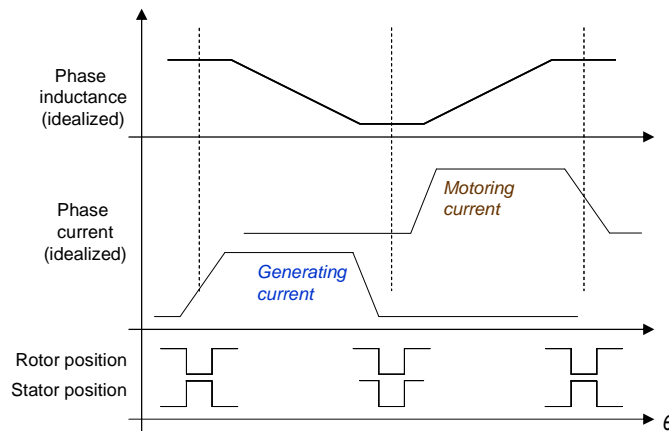


Fig. 8-3: Idealized phase inductance and phase current of a SRM.

- Under motoring operation, phase current makes the rotor poles to align with the stator poles. Then, each phase is excited before the rotor poles come into alignment with the stator poles, so torque is applied to the rotor in the direction of rotation. As can be seen in Fig. 8-3, when motoring the phase inductance increases if current is flowing.
- Under generator operation, torque is applied opposing rotation. Then, each phase is excited as the rotor poles move through the aligned position. As depicted in Fig. 8-3, when generating the phase inductance decreases if current is flowing.

A detailed description about the principle of operation of the SRM can be found in [232]-[234].

8.2.2 Control strategy

Among several control options for this machine [211]-[213], [215], [227], [231], [232], [234]-[238], the following description will be focused on SRSG for aerospace where the control target is speed when motoring and DC voltage when generating.

8.2.2.1 Operation as a Starter

The starting process of a gas turbine for aerospace application, which is considered for validation purposes later on, is depicted in Fig. 8-4. The SRM accelerates the engine emulator to approximately 3,500 rpm against constant drag torque. The torque on the SRM then reduces as the engine has been ignited and accelerates up to ground idle speed. The SRM is disconnected from the DC bus at $t = 28$ s as the engine is then self-sustaining. Starting profiles of gas turbines are found in [211], [213], [215].

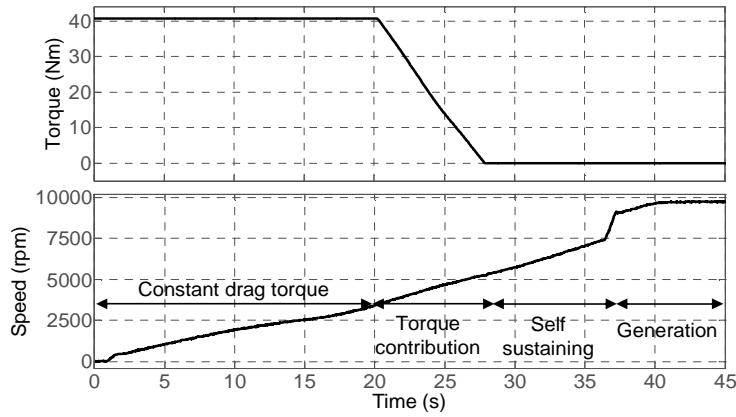


Fig. 8-4: Starting process of a gas engine for aerospace.

In order to carry out the starting process, the rotation speed of the SRM is regulated through a regulation loop such as that shown in Fig. 8-5. The speed of the spool ω is measured (sensor gain K_ω) and compared to a reference speed signal ω_{ref} which commands the starting profile. The output, v_{com} , of speed regulator R_ω passes to the ‘Driver’ to set the commutation angles and current control levels used to command the power electronics. ω_{ref} is the speed reference from the engine starter and K_ω represents the speed sensor.

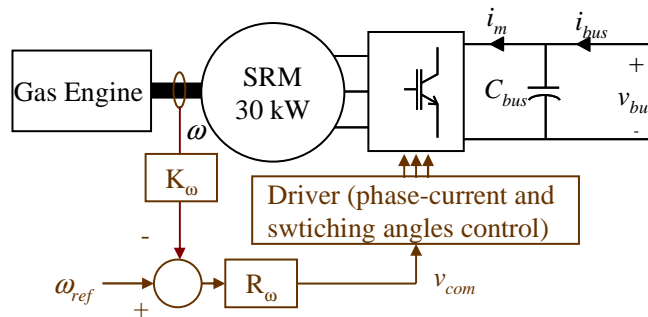


Fig. 8-5: Control scheme of a SRM for aerospace during starting of a gas engine.

8.2.2.2 Operation as a Generator

Once the SRM has been started, the engine can deliver power to the DC bus. Then the control target turns to be the DC bus voltage. A block diagram of the control structure of a SRSG in generator mode is shown in Fig. 8-6. The error between the bus voltage v_{bus} and the reference signal v_{ref} passes through the voltage regulator R_v , forming signal v_{com} , which, along with the machine speed ω , commands the ‘Driver’ to set the power electronics switching pattern.

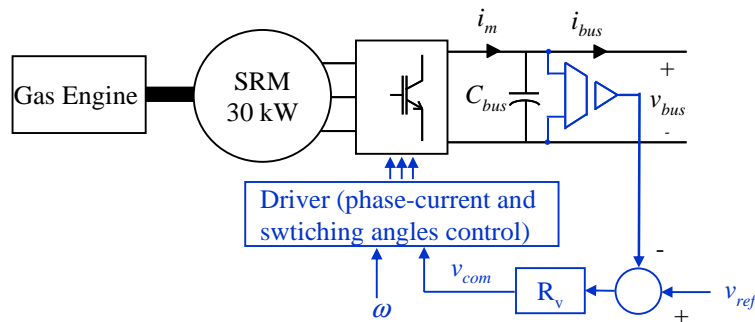


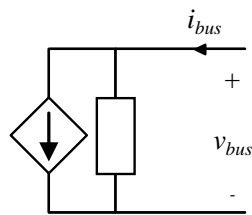
Fig. 8-6: Control scheme of a SRM for aerospace during generating process.

8.3 Proposed modeling and identification method

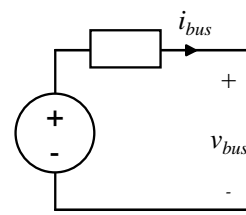
8.3.1 Basic approach

As a difference from converters and subsystems modeled in previous chapters, this is a bidirectional subsystem. As a consequence, depending on the operating mode, the SRSRG behaves at the DC terminal in a different way. This is described below and illustrated in Fig. 8-7.

- During starting process, the SRSRG takes power from the DC bus to accelerate the gas turbine. In other words, it behaves as a current sink.
- During generating process, the SRSRG regulates the bus voltage and delivers power from the gas engine to the bus. In plain words, it behaves as a voltage source.



a. Starting process: Current sink.



b. Generating process: Voltage source.

Fig. 8-7: Possible black-box model structures for the starter-generator.

In this chapter, a different approach has been chosen to make up the behavioral model. By looking at the circuits shown in Fig. 8-5 and Fig. 8-6, the following conclusions can be derived:

- When generating, the control stage sets the current delivered by the machine, i_m , to minimize the error between v_{ref} and v_{bus} .
- When motoring, the control stage sets the current demanded by the machine, i_m , in order to accelerate it as commanded by ω_{ref} .

Consequently, the power stage may be modeled as a controlled current source in parallel with the DC bus capacitor, leading to the model structure shown in Fig. 8-8. Such a current source essentially models the average current delivered or demanded by the SRM, denoted as i_m .

The model shown in Fig. 8-8 is comprised of two networks, one for the operation as a generator and the other for the operation as a starter. A high level description of both networks is given below.

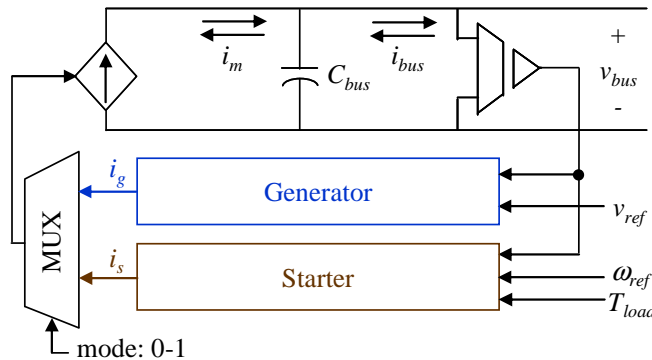


Fig. 8-8: Proposed grey-box starter/generator model.

- The generator network outputs averaged machine current under generating operation, denoted as i_g , as a function of the reference voltage signal v_{ref} and the bus voltage v_{bus} ^{8.2}.
- The starter network computes the averaged current demanded by the machine when starting, which is denoted as a i_s . Such a demand is determined by the load torque T_{load} , the reference speed ω_{ref} and the bus voltage v_{bus} .

This modeling approach is referred to as “grey box” because the model partially represents the inner structure of the SRSG and any prior knowledge about parameters such as C_{bus} or the regulator tuning / architecture can be readily used to partially parameterize the model. Compared to previous black-box approaches, this model features the following characteristics:

- The same electrical circuit is used to model both the starting and the generating operations.
- Clamping or anti-windup functions provided into the voltage regulators can be easily incorporated into the model. This is an important point because the dynamic behavior of the experimental SRSG, modeled in this chapter, is strongly determined by such functions.

A detailed description about each network as well as the identification procedure is described in next sections.

8.3.2 Modeling and identification for the generator operation

8.3.2.1 Generator network structure

A detail of the generator network structure is depicted in Fig. 8-9. The bus voltage is compared to the reference signal in a similar manner as done in the actual SRSG. The resulting error signal is the input to the block T_v , which contains the following elements.

- Voltage regulation block VR , comprising a linear proportional-integral term R_v , and any special functions such as clamping or anti-windup, denoted as “ CF ”.
- H_v which represents the dynamic relationship between v_{com} and i_m , including the driver and power stage. This is assumed to be LTI, and can be approximated by a first order transfer function in practice [217], [236].
- ‘Delay τ ’ accounts for any transport delay, in case it is significant.

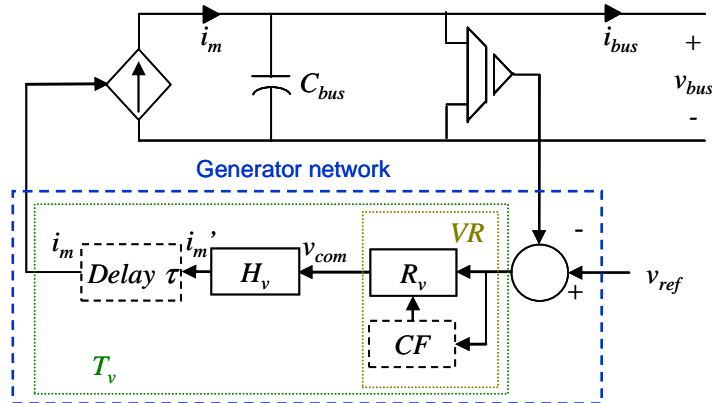


Fig. 8-9: Detail of the generator network.

^{8.2} Note that ω is not an input for the generator network, so one may think that this is not in agreement with Fig. 8-6. However, mechanical speed transients are relatively slow compared to the electrical transients so its impact upon v_{bus} is negligible.

This modeling approach allows accounting for nonlinear dynamics related to clamping or anti-windup functions through the network CF . However, dynamic dependences on operating point cannot be represented, as R_v and H_v are LTI networks^{8.3}.

8.3.2.2 Identification

The generator network is identified from the transient response of the SRSG under a step in load current i_{bus} . This can be done by switching a resistive load, as shown in Fig. 8-10.

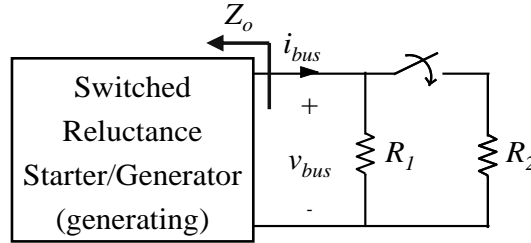


Fig. 8-10: Detail of the generator network.

From the transient response of v_{bus} and i_{bus} , every parameter of the model is identified by following the sequential process illustrated in Fig. 8-11. This is explained below step by step.

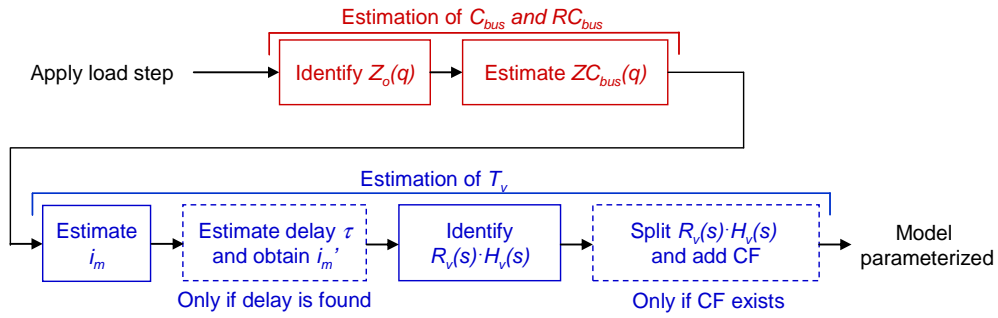


Fig. 8-11: Flowchart of the generator network identification.

8.3.2.2.1 Estimation of C_{bus} and R_{Cbus}

By applying a small-signal perturbation to i_{bus} in the model while v_{ref} is kept constant, the expression (8-1) for the output impedance is obtained, where $T_v(s)$ is a linear representation of the block T_v in the Laplace domain (the CF block is disabled) and is given by (8-2). $e^{-\tau s}$ corresponds to the loop delay.

$$-\left. \frac{v_{bus}(s)}{i_{bus}(s)} \right|_{v_{ref}(s)=0} = Z_o(s) = \frac{1}{ZC_{bus}(s)^{-1} + T_v(s)} \quad (8-1)$$

$$T_v(s) = R_v(s)H_v(s)e^{-\tau s} \quad (8-2)$$

As can be seen, $Z_o(s)$ corresponds to the parallel connection of the bus capacitor impedance, $ZC_{bus}(s)$, with $T_v(s)^{-1}$. $Z_o(s)$ can therefore be used to estimate the bus capacitance and parasitic resistance (if significant).

To identify the output impedance, the transient waveforms v_{bus} , i_{bus} under the load step are measured. After that, such measurements are post-processed, as explained in section 4.3.2, and the

^{8.3} Although H_v may be represented by a LLMN to represent any dynamics dependence on operating point, its use into the proposed model for SRSG has not been studied in detail in this thesis. Nevertheless, the experimental SRSG modeled in section 8.4 exhibits slight dynamics dependence on operating point, which may be neglected for the sake of simplicity.

coefficients of a transfer function for the output impedance $Z_o(q)$ are obtained by applying a parametric identification algorithm. If an OE model is identified, the cost function to minimize is the following, where subscript 'p' denotes post-processed signal.

$$COF = \sum_{k=1}^N \left(v_{busp}(k) - Z_o(q) \cdot i_{busp}(k) \right)^2 \quad (8-3)$$

According to (8-1), at high frequencies $Z_o(j\omega) \approx ZC_{bus}(j\omega)$ so, once $Z_o(q)$ has been identified, C_{bus} and RC_{bus} can be approximated from inspection of the bode plot.

8.3.2.2.2 Estimation of T_v

Once $ZC_{bus}(s)$ has been identified, $T_v(s)$ could be directly obtained as:

$$T_v(s) = Z_o(s)^{-1} - ZC_{bus}(s)^{-1} \quad (8-4)$$

However, using (8-4) has some drawbacks. On the one hand, an unstable transfer function is obtained for $T_v(s)$ if a non-minimum phase transfer function is identified for $Z_o(s)$. On the other hand, the transfer function $T_v(s)$ may exhibit un-realistic poles and zeroes at high frequency unless $ZC_{bus}(s)$ matches exactly $Z_o(s)$ at high frequency.

An alternative method that overcomes those problems is described below. By looking at the generator model (Fig. 8-9), it can be deduced that, under linear operation, $T_v(s)$ is dynamically related to the average machine current $i_m(s)$ as:

$$T_v(s) = - \frac{i_m(s)}{v_{bus}(s)} \Bigg|_{v_{ref}(s)=0} \quad (8-5)$$

Therefore, if the machine current i_m is estimated, a transfer function model can be identified for $T_v(s)$ by applying parametric identification. $i_m(k)$ can be estimated as given by (8-6).

$$i_m(k) = ZC_{bus}(q)^{-1} \cdot v_{bus}(k) + i_{bus}(k) \quad (8-6)$$

Before identifying $T_v(s)$, any transport delay τ in the loop can be determined by visual inspection of $i_m(k)$ (as illustrated later on). If a delay is apparent, then it can be subtracted by shifting the estimated machine current as follows, where i_m' is the shifted current and f_s is the sampling frequency.

$$i_m'(k) = i_m(k + \tau \cdot f_s) \quad (8-7)$$

Following this, a transfer function model for the product of $R_v(s)H_v(s)$ can be identified from i_m' and v_{bus} .

$$R_v(s)H_v(s) = - \frac{i_m'(s)}{v_{bus}(s)} \Bigg|_{v_{ref}(s)=0} \quad (8-8)$$

Finally, in case the regulator is provided by any clamping or anti-windup function (CF), the identified transfer function (8-8) can be split into a transfer function for the *Driver* and machine dynamics, i.e. $H_v(s)$, and a transfer function for the regulator. Then the regulator can be provided with the aforementioned functions CF . This requires to know in advance some properties about the regulator dynamics and the functions CF . Nevertheless, in many practical cases the voltage regulator is a PI type, so $H_v(s)$ and $R_v(s)$ can be split by taking into account that the lowest pole and zero will be related to the PI regulator.

8.3.3 Modeling and identification for the starter operation

8.3.3.1 Starter network structure

The proposed model for the starter operation is depicted in Fig. 8-12. Essentially this network is based on a power balance between mechanical and electrical power. The model comprises the following blocks:

- Speed dynamics: This block return the machine speed ω as a function of the commanded reference ω_{ref} and the load torque T_{load} .
- Power balance: This block estimates the electrical power demanded by the machine P as a function of the mechanical power. P is then divided by the bus voltage, yielding the average current consumed by the machine, i_m . Each block is described in detail below.

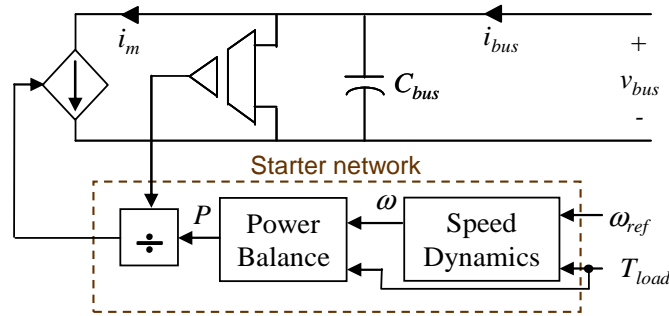


Fig. 8-12: Starter network: basic schematic.

8.3.3.1.1 Power balance block

The instantaneous electrical power is obtained by first calculating the electromagnetic torque T_{elec} using (8-9), where J is the total moment of inertia, B is the friction coefficient and ω is the speed. T_{elec} corresponds to averaged torque over a revolution cycle.

$$T_{elec} = T_{load} + J \frac{d\omega}{dt} + B\omega \quad (8-9)$$

The mechanical power P_m is calculated using (8-10).

$$P_m = \omega T_{elec} \quad (8-10)$$

Then, combining (8-9) and (8-10), P_m can be expressed as a function of ω and T_{load} .

$$P_m = \omega T_{load} + J \omega \frac{d\omega}{dt} + B\omega^2 \quad (8-11)$$

Equation (8-11) corresponds to the electromechanical power transfer, but not all the electrical power demanded from the DC bus is transferred to the load. Part of it is dissipated in the switching bridge and the coils, and other part is stored in the windings as electromagnetic energy. This can be mathematically expressed by means of the power balance given by (8-12), where $P_{loss-elec}$ corresponds to the electrical losses and dE_L/dt denotes the rate of change of stored electromagnetic energy in the SRM (averaged over one cycle).

$$P = v_{bus} \cdot i_m = P_m + P_{loss-elec} + \frac{dE_L}{dt} \quad (8-12)$$

Within one cycle, part of the energy transferred from the DC bus is stored in the machine as electromagnetic energy but, concerning variations of the averaged electromagnetic energy over one cycle, it is null, i.e. $dE_L/dt=0$. This is because, in case of conventional SRM, the current flowing through each winding decreases to zero within each revolution cycle [211], [232]-[234], [237], so, at the beginning of each cycle, such a stored energy is always zero. Therefore, there is no state variable related to it.

This is illustrated in Fig. 8-13. The current starts rising from zero within each cycle, so all the energy stored in the windings is returned to the source, and consequently $dE_L/dt=0$. Dynamically, this effect is analogous to that of DC-DC converters operating in DCM, where the inductor is lost as a state-variable because its current decreases to zero within a switching period [96]^{8.4}.

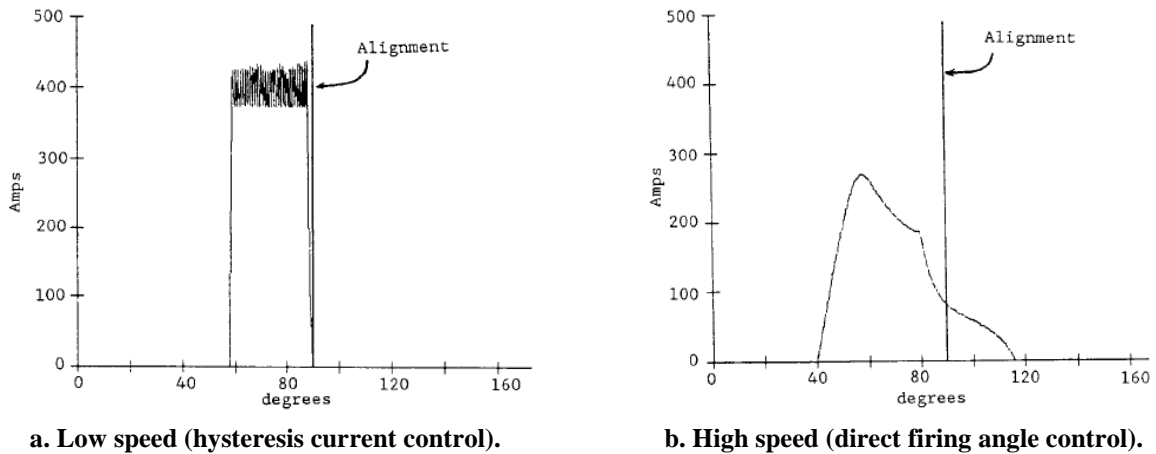


Fig. 8-13: Phase current of a SRM reported in [211].

Taking that into account, (8-11) can be substituted into (8-12), yielding (8-13):

$$P = \left[\omega \left(T_{load} + J \frac{d\omega}{dt} \right) + P_{loss-total} \right] \quad (8-13)$$

$P_{loss-total}$ is the total power losses of the SRS and can be expressed as:

$$P_{loss-total} = B\omega^2 + P_{loss-elec} \quad (8-14)$$

8.3.3.1.2 Speed dynamics block

The small signal dynamics of the speed controller are represented by the block diagram in Fig. 8-14, where the mechanical dynamics are again assumed to be described by (8-9). $R_\omega(s)$ and $K_\omega(s)$ represent the dynamics of the speed regulator and the speed sensor, respectively (see Fig. 8-6).

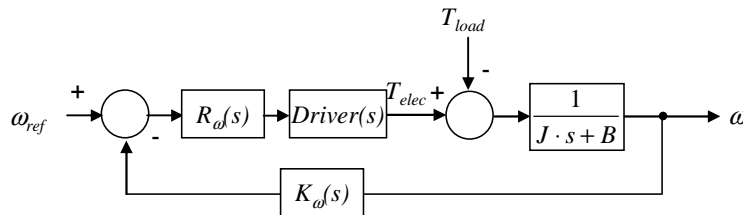


Fig. 8-14: Small-signal model of the speed control loop.

^{8.4} Nevertheless, it has been demonstrated that the inductor makes some influence on the DC-DC converters dynamics also in DCM [238], but only at high frequency (above one tenth of the switching frequency, approximately)

From Fig. 8-14, the relationship between ω , T_{load} and ω_{ref} can be expressed as given by (8-15), where $G_{\omega}(s)$ is the closed-loop transfer function of the speed regulation and $G_T(s)$ is the closed-loop relationship between T_{load} and ω . Compared to DC-DC converters modeled in chapter 4, $\omega(s)$, $G_T(s)$ and $T_{load}(s)$ are analogous to the output voltage, the output impedance and the output current, respectively.

$$\omega(s) = G_{\omega}(s)\omega_{ref}(s) - G_T(s)T_{load}(s) \quad (8-15)$$

The resulting model for the starter network is depicted in Fig. 8-15. Note that, although the speed dynamics is expressed in terms of transfer functions, both $G_{\omega}(s)$ and $G_T(s)$ could be replaced by a LLMN if a significant dynamics dependence on operating point is found.

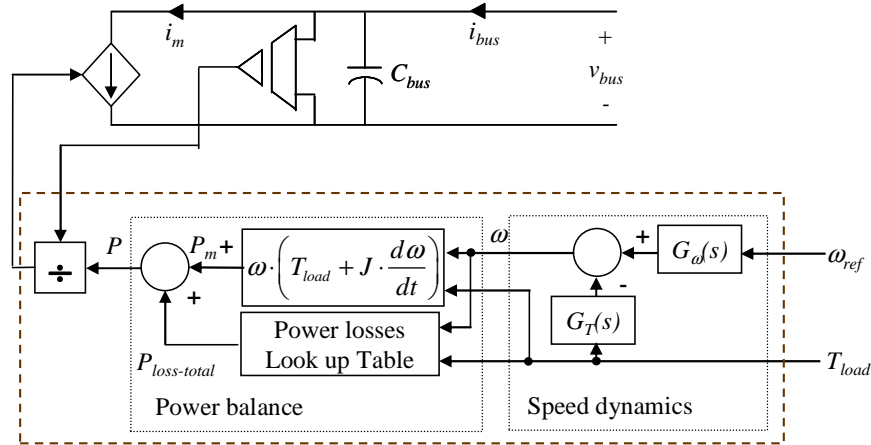


Fig. 8-15: Detail of the starter network.

8.3.4 Identification

Again, the parameterization procedure is based on time domain measurements and parametric identification methods.

8.3.4.1 Power balance block

The total moment of inertia J can be identified from a constant acceleration test, as depicted in Fig. 8-16a, whereas the mechanical load torque is kept constant.

The instantaneous drop in bus current, Δi_{bus} , as the machine attains its final speed, is assumed to represent the accelerating power at the final speed (see Fig. 8-16b). From (8-13), just before arriving to the final speed level (point 'a') the machine current i_m can be expressed as:

$$i_{m-a} = \frac{1}{v_{bus}} \cdot \left[\omega \left(T_{load} + J \frac{d\omega}{dt} \right) + P_{loss-total} \right] \quad (8-16)$$

Once the machine arrives steady-state (point 'b'), $d\omega/dt = 0$, so i_m is defined as:

$$i_{m-b} = \frac{1}{v_{bus}} \cdot \left[\omega \cdot T_{load} + P_{loss-total} \right] \quad (8-17)$$

Assuming that $P_{loss-total}$ is similar for points 'a' and 'b', and considering that $\Delta i_{bus} \approx \Delta i_m$ (as the mechanical time constants are much slower than the electrical ones), the total moment of inertia J may be estimated as given by (8-18).

$$J \approx \frac{\Delta i_{bus} v_{bus}}{\omega_f \frac{d\omega}{dt}} \quad (8-18)$$

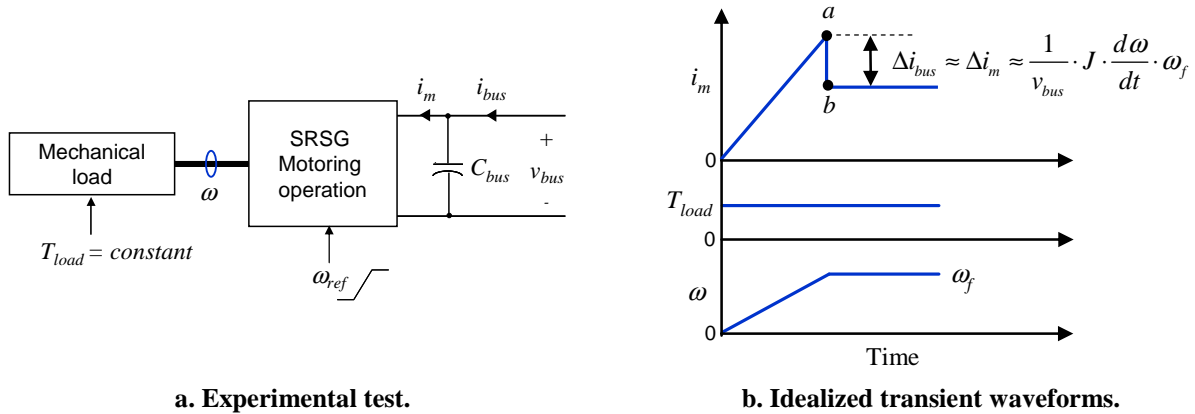


Fig. 8-16: Proposed estimation method of the total moment of inertia J .

On the other hand, the power losses are simply characterized from the difference between the input electrical power and the output mechanical power, as given by (8-19), over the operating range of the SRSG at steady-state ($d\omega/dt=0$).

$$P_{loss_total}(T_{load}, \omega) = i_{bus} \cdot v_{bus} - T_{load} \cdot \omega \quad (8-19)$$

8.3.4.2 Speed dynamics block

The transfer functions $G_\omega(s)$ and $G_T(s)$ are identified from step tests, in a similar manner as has been described in previous chapters. The speed dynamics network has two inputs (ω_{ref} and T_{load}) and one output (ω). Therefore, two step tests are required:

- **Test 1:** The signal ω_{ref} is stepped while T_{load} is kept constant. Then, $G_\omega(s)$ can be identified from the transient response of ω and ω_{ref} , as indicated in Fig. 8-17a.
- **Test 2:** The mechanical load torque T_{load} is stepped while ω_{ref} is kept constant. Then, $G_T(s)$ can be identified from the transient response of ω and T_{load} , as indicated in Fig. 8-17b.

The actual system may have limitations in the achievable slew rate of ω_{ref} and/or T_{load} . In that case, both signals should be incremented at the maximum slew rate.

The transfer function models are identified from the measured transient response by applying a parametric identification technique. Details are given in section 4.4. If an OE model is identified, the cost functions to minimize are the following, where subscript ‘ p ’ denotes ‘pre-processed’ (details are given in section 4.3.2.2).

$$COF = \sum_{k=1}^N (\omega_p(k) - G_\omega(q) \omega_{refp}(k))^2 \quad (8-20)$$

$$COF = \sum_{k=1}^N (\omega_p(k) - G_T(q) (-T_{loadp}(k)))^2 \quad (8-21)$$

Note that, if a LLMN is used, then several step tests should be applied on different operating points in order to identify local transfer functions.

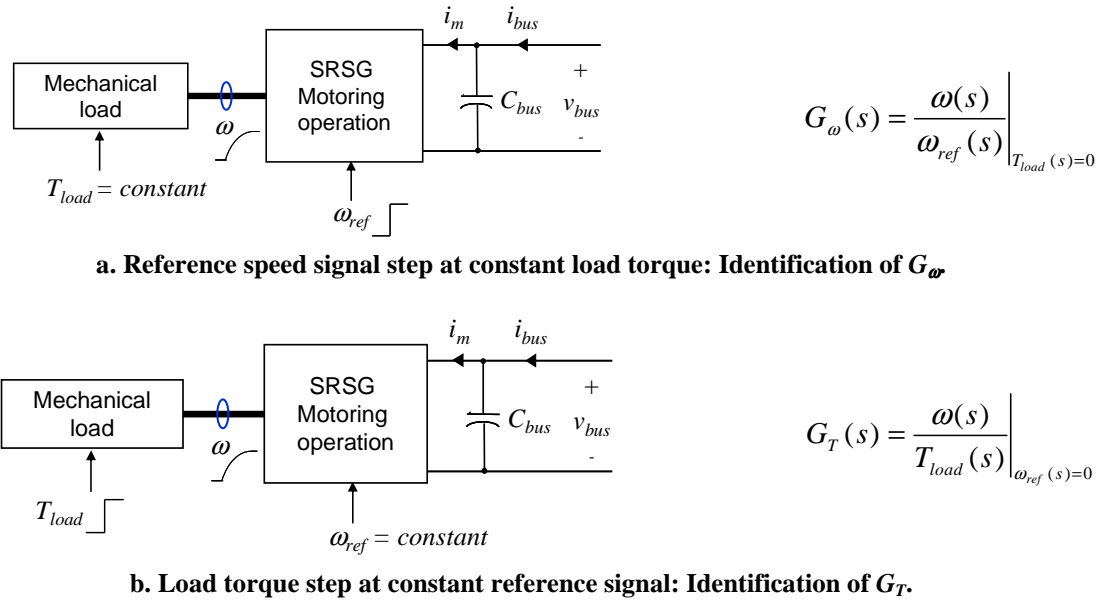


Fig. 8-17: Proposed identification tests of the speed dynamics network.

8.4 Experimental results

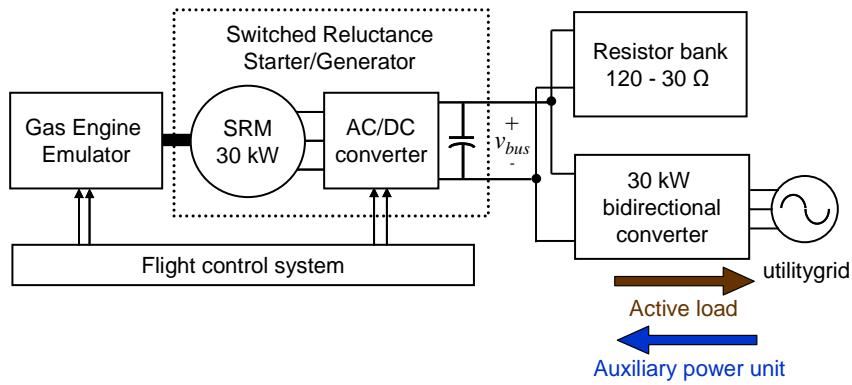
8.4.1 System description

An experimental SRSG has been modeled by using the proposed approach. The experimental system under consideration is shown in Fig. 8-18. This system is part of an electric power network evaluation facility that uses a combination of real hardware and hardware in the loop, and allows investigating new aerospace systems in a safe and controlled environment. Details about the full system are given in [14].

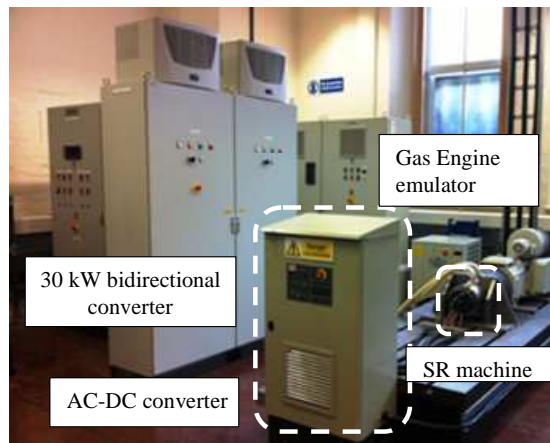
The system comprises a commercial SRSG that is driven by an engine emulator, as well as a 30 kW resistor bank and a 30 kW bidirectional converter. Every subsystem is connected to a 540 V DC bus.

- During starting of the gas engine emulator, the bidirectional converter acts as an APU and regulates the DC bus as well as supplies power to the SRSG.
- Once the gas engine emulator is generating, the bidirectional converter acts as an active load, operating in either constant current or constant power mode. The DC bus is regulated by the SRSG, which supplies a maximum of 30 kW over a speed range of 7,000 rpm to 15,000 rpm.

The gas engine emulator is a 115 kW, 15,000 rpm, bidirectional induction machine drive system and is commanded by a flight control system (FCS) which contains a generic thermodynamic and mechanical gas engine model. The model takes environmental data, throttle position and electrical power off-take as inputs and outputs torque when the SRSG is motoring, and speed when the SRSG is generating.



a. Schematic.



b. Picture.

Fig. 8-18: Experimental system under study.

8.4.2 Generator operation

The procedure described in section 8.3.2.2 has been applied to the actual SRSG under generating operation. The measurements have been carried out using an oscilloscope Tektronix DPO7000C series equipped with a current probe TEK-TCPA300 and a differential voltage probe TEK-P5205. The signals have been sampled at $t_s = 50 \mu s$ rate using high resolution mode.

8.4.2.1 Estimation of C_{bus} and R_{Cbus}

Fig. 8-19 shows the transient response of the SRSG to a 5 kW resistive load step (no clamping functions are activated under this test, so nearly linear behavior is ensured).

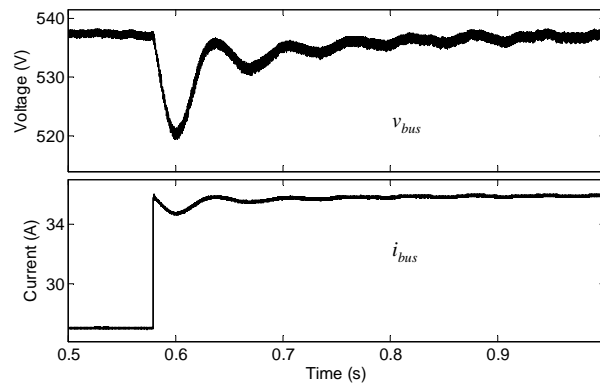


Fig. 8-19: SRSG response under a load step from 15 kW to 20 kW at constant speed $n_m = 7,000$ rpm.

As can be seen in Fig. 8-19, the transient response of v_{bus} exhibits an oscillation superimposed to a slow exponential evolution. This suggests fitting a third order transfer function for the output impedance. Since the dynamics timescale of the generator is much slower than the sampling time ($50 \mu s$), the transient signals have been re-sampled to $200 \mu s$ before fitting the model.

As shown in Fig. 8-20, a third order model yields good fitting results of the averaged response. The fitting results have been evaluated using the Matlab function *compare* (more details are given in section 4.4). The resulting transfer function, after transformation to continuous time domain, is given below.

$$Z_o(s) = \frac{0.028s^3 + 140.6s^2 + 1.064 \cdot 10^4 s + 4782}{s^3 + 44.6s^2 + 8587s + 8.21 \cdot 10^4} \quad (8-22)$$

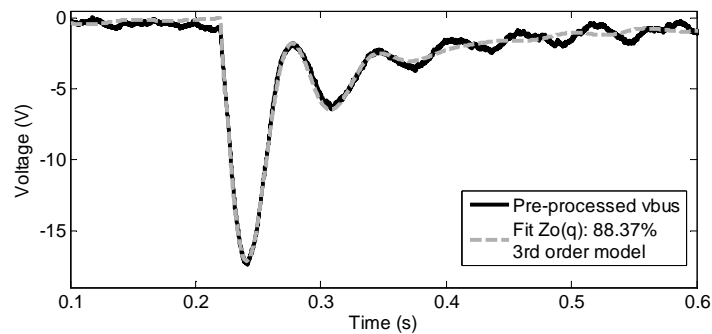


Fig. 8-20: Fitting results of $Z_o(q)$.

According to (8-1), by analyzing $Z_o(j\omega)$ at high frequencies, $ZC_{bus}(s)$ can be estimated. The frequency response of $Z_o(j\omega)$ is plotted in Fig. 8-21, where one can notice a low frequency pole at ≈ 1.6 Hz plus two complex conjugate poles at ≈ 14 Hz. It has been found that $ZC_{bus}(s)$ can be approximated by a capacitance of 7.2 mF in series with a 28 m Ω resistor. As shown in Fig. 8-21, such capacitor impedance matches the identified output impedance accurately.

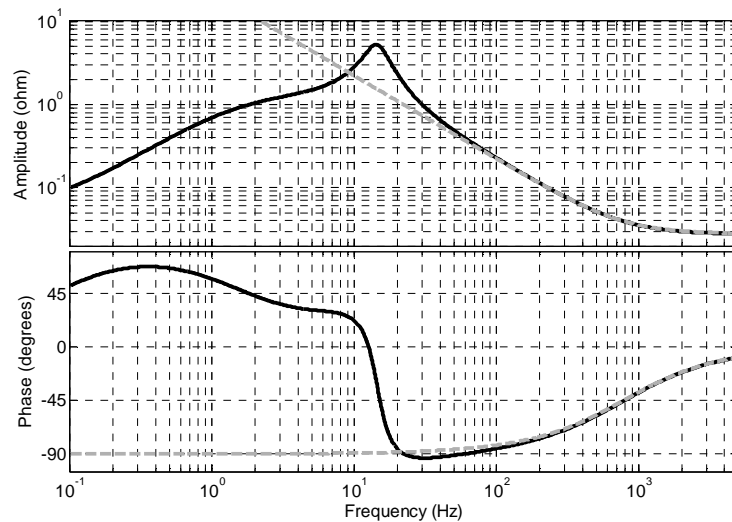


Fig. 8-21: Frequency response of the identified output impedance $Z_o(j\omega)$ (dark solid line) and the estimated output capacitor $ZC_{bus}(j\omega)$ (grey dashed line).

8.4.2.2 Identification of $R_v H_v$ and τ

Once the bus capacitor impedance has been identified, the machine current i_m has been estimated from the measured v_{bus} and i_{bus} as given by (8-6). The estimated i_m is shown in Fig. 8-22. It exhibits a large amount of high frequency ripple due to the low impedance of the capacitor at high frequency.

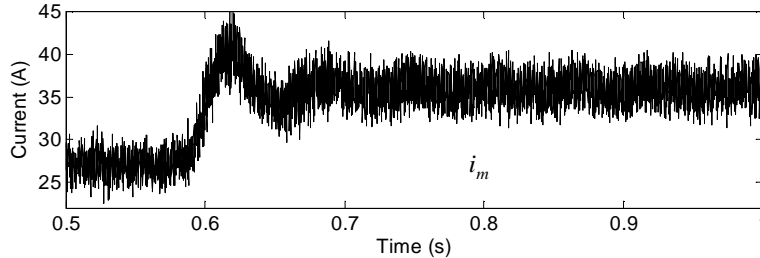


Fig. 8-22: Estimated machine current i_m .

A transport delay of approximately 8 ms is apparent between the load step and the beginning of the transient response of i_m as shown in Fig. 8-23.

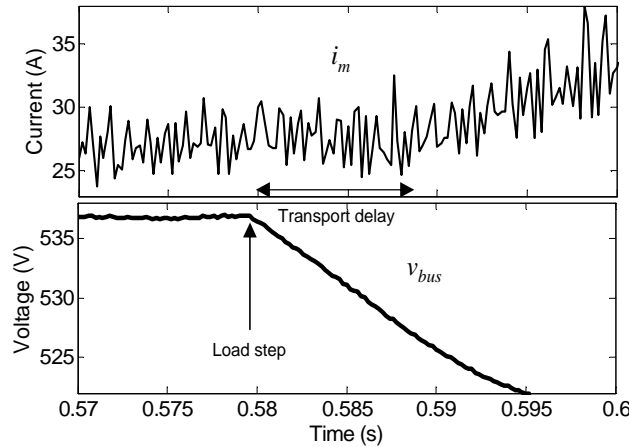


Fig. 8-23: Transport delay between the load switching and the beginning of the i_m transient response.

Hence, if $T_v(s)$ is identified directly from i_m and v_{bus} , then it will include the delay. An alternative approach is to shift the estimated machine current, as given by (8-7), yielding i_m' . Then, from the transient response of v_{bus} and i_m' , a transfer function model corresponding to $R_v(s)H_v(s)$ can be identified. Both i_m' and v_{bus} have been pre-filtered using a moving average filter of 25 samples, in order to attenuate the high frequency ripple. The results are depicted in Fig. 8-24, where it is shown that the average behavior of the pre-processed i_m' is accurately fitted by a third order transfer function.

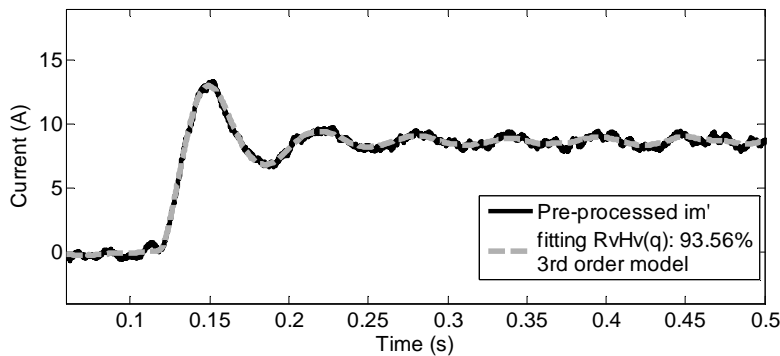


Fig. 8-24: Fitting results of $R_v(q)H_v(q)$.

The resulting transfer function after transformation into continuous time domain is given by (8-23) and its frequency response is shown in Fig. 8-25, where some properties of the regulator, such as the low-frequency integrator, are apparent.

$$R_v(s)H_v(s) = \frac{0.2933s^3 + 2987s^2 + 5.38 \cdot 10^5 s + 4.622 \cdot 10^6}{s^3 + 9288s^2 + 5.81 \cdot 10^5 s + 9.176 \cdot 10^4} \quad (8-23)$$

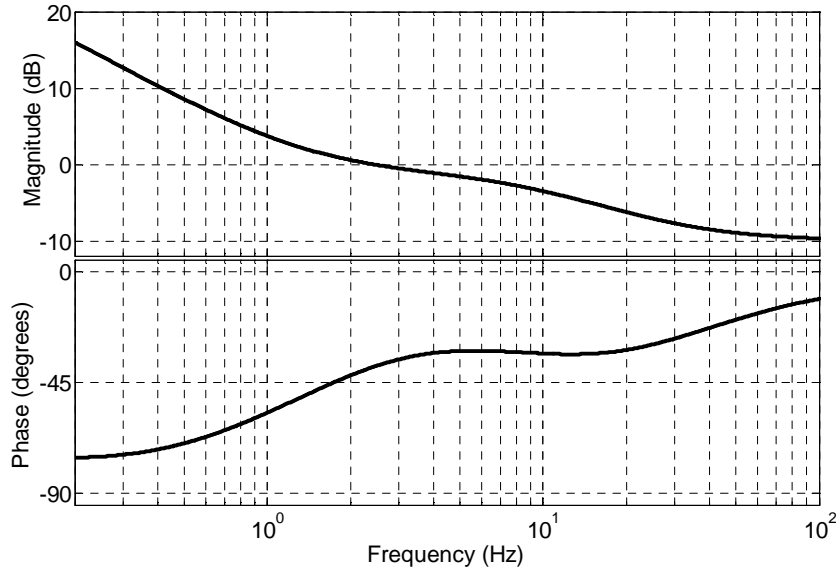


Fig. 8-25: Frequency response of $R_v(j\omega)H_v(j\omega)$.

Once $R_v(s)H_v(s)$, C_{bus} and τ have been characterized, the fitting performance of the overall generator model has been evaluated by comparing the frequency response of the identified output impedance $Z_o(s)$ (8-22) with that of the resulting model (8-1). As shown in Fig. 8-26, the output impedance of the model is very close to that directly identified from the measured load step, so the model has been correctly parameterized.

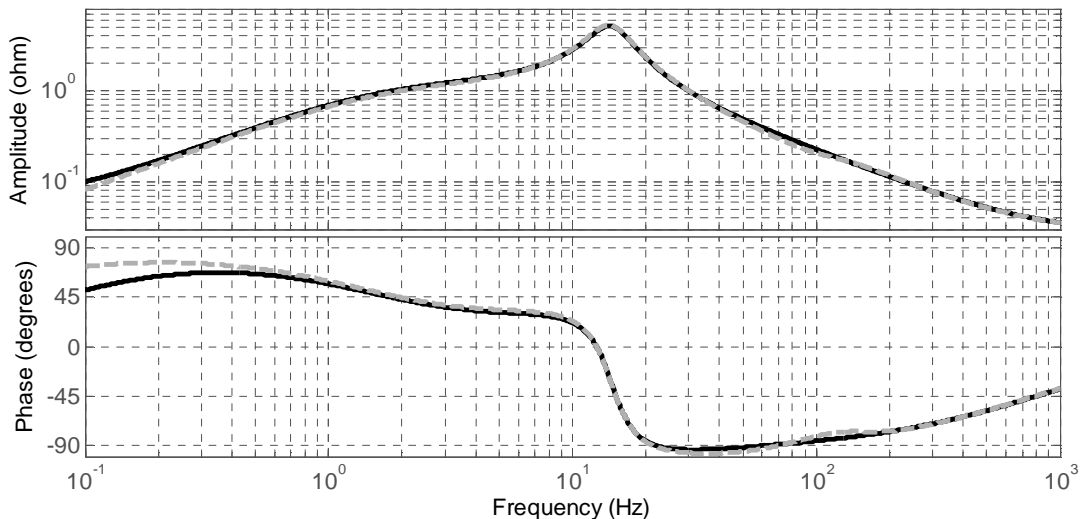


Fig. 8-26: Comparison between the output impedance of the SRSG model (grey dashed line) with the output impedance directly identified from the measured v_{bus} and i_{bus} (dark line).

8.4.2.3 Incorporating clamping functions CF

The SRSG under experimental study is provided with a set of clamping functions which are known in advance. They act as follows on the voltage compensator, which is a PI type.

- The output of the proportional term K_p is clamped to zero while $v_{ref}-v_{bus} < 0$ V.
- The output of the integral term K_i is reset if $v_{ref}-v_{bus} < -18$ V.
- The minimum value of the regulator output, v_{com} , is limited to zero if the commanded signal from the PI is lower than zero.

These clamping functions are activated during a step down in load to limit the maximum output voltage of the generator. Fig. 8-27 illustrates the behavior of the clamping functions under a load step from 20 kW to 15 kW at $n_m = 7,000$ rpm. When the load is stepped, v_{bus} increases because the difference between i_m and i_o charges C_{bus} . Consequently, $v_{ref}-v_{bus} < 0$ V, so the proportional term is disabled. Once $v_{ref}-v_{bus} < -18$ V, the integral term is reset, $v_{com} = 0$ and then v_{bus} decreases suddenly. Finally, when $v_{ref}-v_{bus} \geq 0$ V the regulator is re-enabled to control v_{bus} .

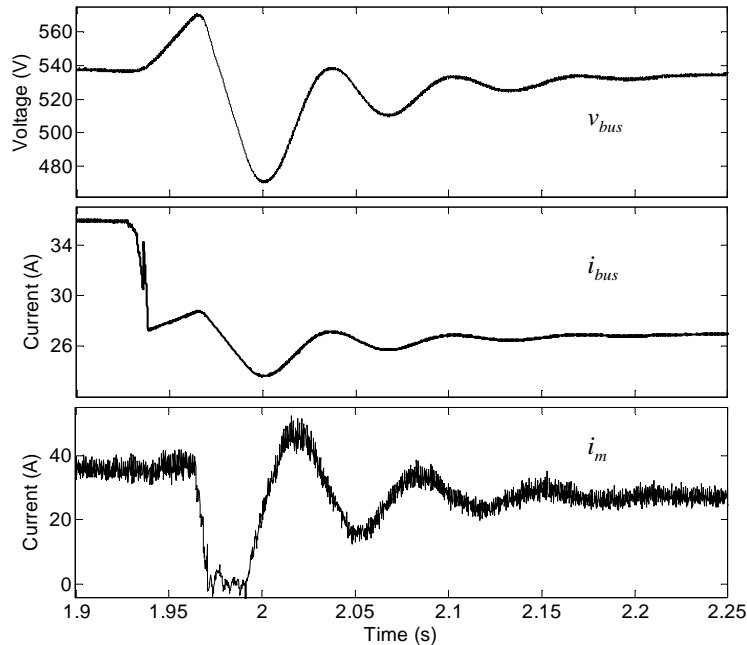


Fig. 8-27: SRSG response under a load step from 15 kW to 20 kW at constant speed $n_m = 7,000$ rpm.

To implement those clamping functions, the identified transfer function $R_v(s)H_v(s)$ has been split in two. By expressing (8-23) in a zero-pole-gain representation, the following expression is obtained:

$$R_v(s)H_v(s) = 0.293 \cdot \frac{(s+9.04)(s+174.2)(s+10000)}{(s+0.158)(s+62.8)(s+9226)} \quad (8-24)$$

The lowest frequency pole-zero pair corresponds to the PI compensator $R_v(s)$. Thus, by moving the lowest frequency pole to $s \rightarrow 0$ and neglecting the high frequency pole-zero pair, expressions for $R_v(s)$ and $H_v(s)$ are obtained as follows.

$$R_v(s) = \frac{s+9.04}{s} \quad H_v(s) = 0.293 \cdot \frac{10000}{9226} \cdot \frac{(s+174.2)}{(s+62.82)} \quad (8-25)$$

From (8-25), the proportional and integral terms of the *PI* compensator are obtained: $K_p = 1$ and $K_i = 9.04$.

Moreover, when $v_{com} = 0$, it has been found that the SRM is rapidly de-energized so that i_m suddenly decreases to zero with a slew rate of 4.2 A/ms. This nonlinear effect cannot be accounted for by the transfer function model $H_v(s)$. In order to reproduce such an effect, $H_v(s)$ has been represented in a state-space form with a resettable integrator followed by a slew-rate limiter. The state space form of a first-order transfer function is given by (8-26), where A, B, C and D are constant coefficients, $y(t)$ is the output signal and $u(t)$ is the input signal.

$$\begin{cases} \dot{x}(t) = A \cdot x(t) + B \cdot u(t) \\ y(t) = C \cdot x(t) + D \cdot u(t) \end{cases} \quad (8-26)$$

The integrator of the state-space model is reset when $v_{com} = 0$ and then the machine de-energizing is properly reproduced. The resulting implementation of the generator network, including the above explained effects, is shown in Fig. 8-28.

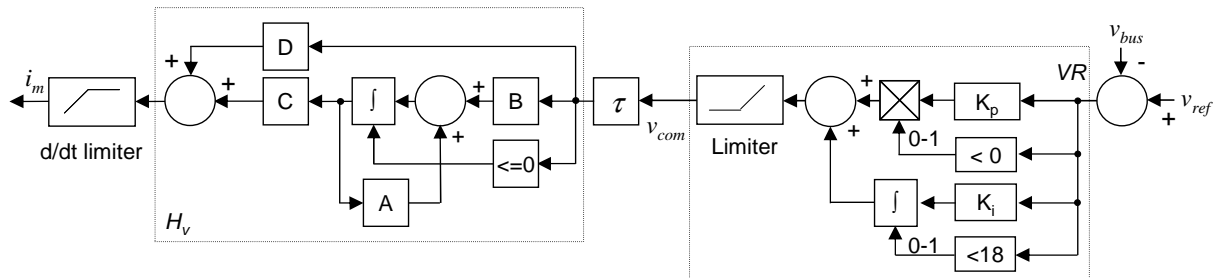


Fig. 8-28: Implementation of the generator network for the experimental SRSG.

The clamping functions are specific to the SRSG under test, but they allow the flexibility of the proposed ‘grey-box’ behavioral model to be demonstrated, as special features such as clamping functions, anti-windup or other features of the actual controller can easily be included in the model.

8.4.2.4 Remarks on dynamics dependence on operating point

At this point, the dynamics of the SRSG when generating has been assumed to be linear. However, actually there is a certain dependence on operating point. In order to analyze such dependences, the output impedance has been identified on different operating points. The results are shown in Fig. 8-29. As can be seen, all the impedances exhibit similar magnitude above the resonance frequency, which may be expected, since it is dominated by the output capacitor C_{bus} . However, below the resonance frequency, slight differences in magnitude are evidenced, which also affects slightly the resonance frequency.

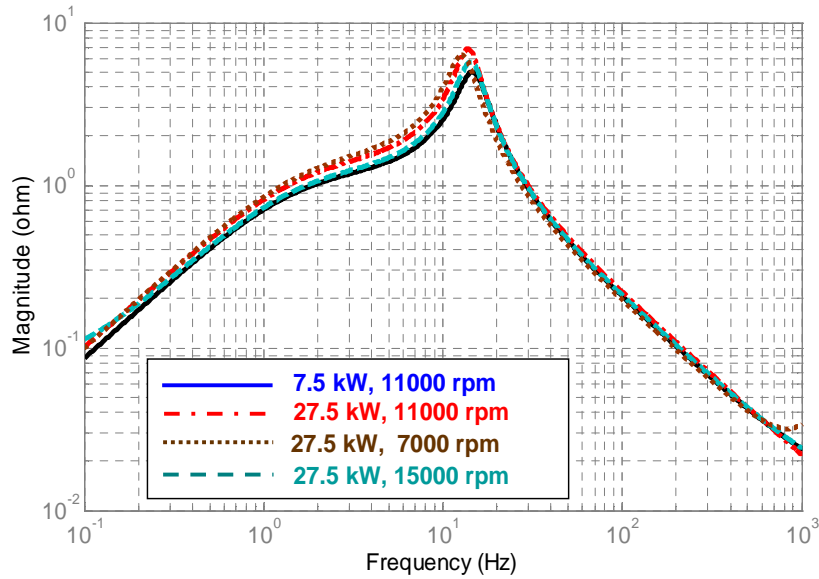


Fig. 8-29: Identified output impedance as a function of the operating point.

The proposed model cannot account for such dynamics dependence, as it exhibits linear behavior when neither the clamping functions nor the limiters are working. However, one may think about replacing the transfer function H_v (which represents the machine and driver dynamics) by a LLMN. The use of LLMNs into the feedback loop of the model for the SRSR has not been studied in depth and requires further research.

8.4.2.5 Model validation under operation as a generator

The ‘grey-box’ model of the SRSR has been implemented in the circuit simulator PSIM for validation purposes. A set of load step tests have been carried out both experimentally and by simulation and the results from both tests have been compared. Both a passive and a constant power load have been used.

8.4.2.5.1 Resistive load steps

Several steps with different magnitudes have been performed at different speeds in order to validate the model behavior over the full operating range. The experimental setup and the simulation schematic are shown in Fig. 8-30.

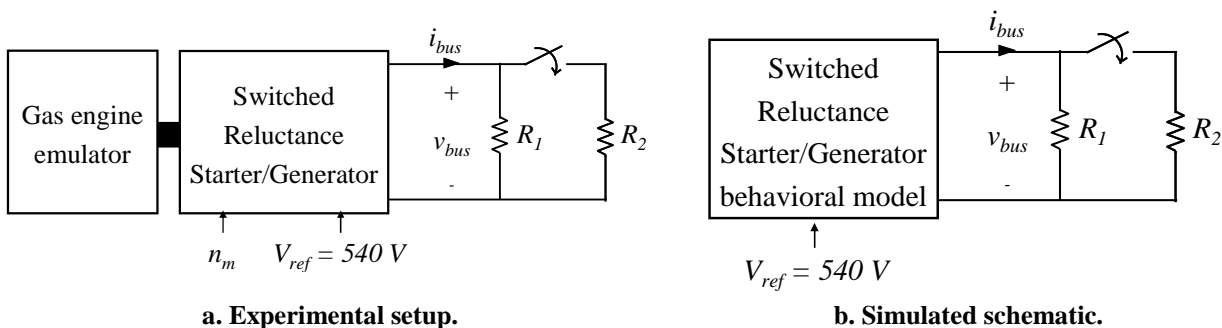


Fig. 8-30: Validation of the model under generating operation with a passive stepped load.

Fig. 8-31 shows a comparison between the measured response and the simulated response for two 5 kW load steps. The first test, shown in Fig. 8-31a, corresponds to that used for model identification

(15 kW to 20 kW at $n_m = 7,000$ rpm^{8.5}). As may be expected, the model response is very close to the measured response. The second test, shown in Fig. 8-31b, is a step from 25 kW to full load (30 kW) at $n_m = 11,000$ rpm. Small differences between the model response and the measured response are observed. Those differences are due to slight nonlinearities of the SRM not reproduced by the model, since the block H_v has been approximated by a LTI model.

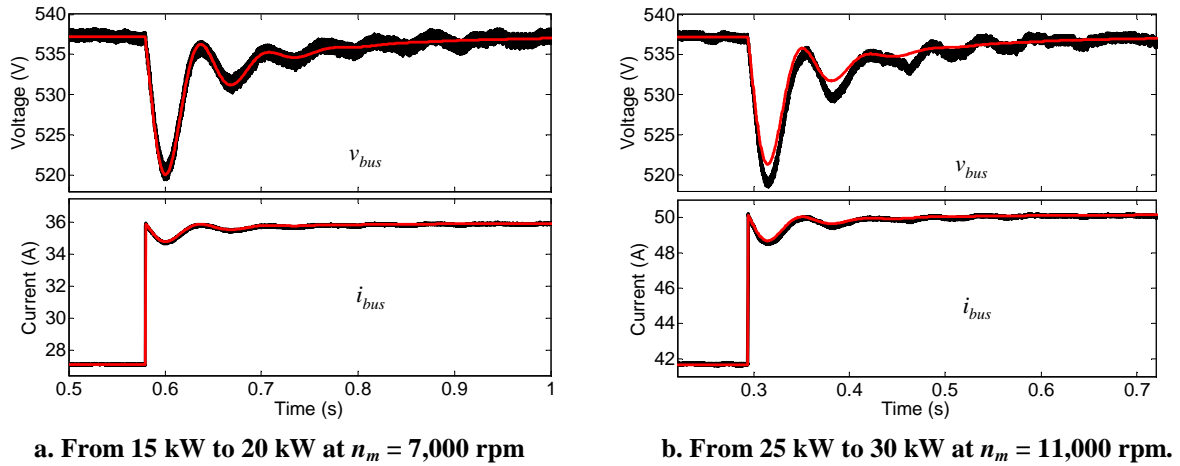


Fig. 8-31 Measured response (dark traces) vs simulated response (red traces) under resistive load steps.

Fig. 8-32 shows validation results for a step increase and decrease in load from 10 kW to 20 kW and back at maximum speed, 15,000 rpm. The non-symmetrical behavior of the actual SRSR is shown under this test, which is due to the activation of the clamping functions during the step decrease in load. As can be seen, the model reproduces properly the response of the SRSR both under the step increase and the step decrease in load. This validates the clamping functions implemented in the model.

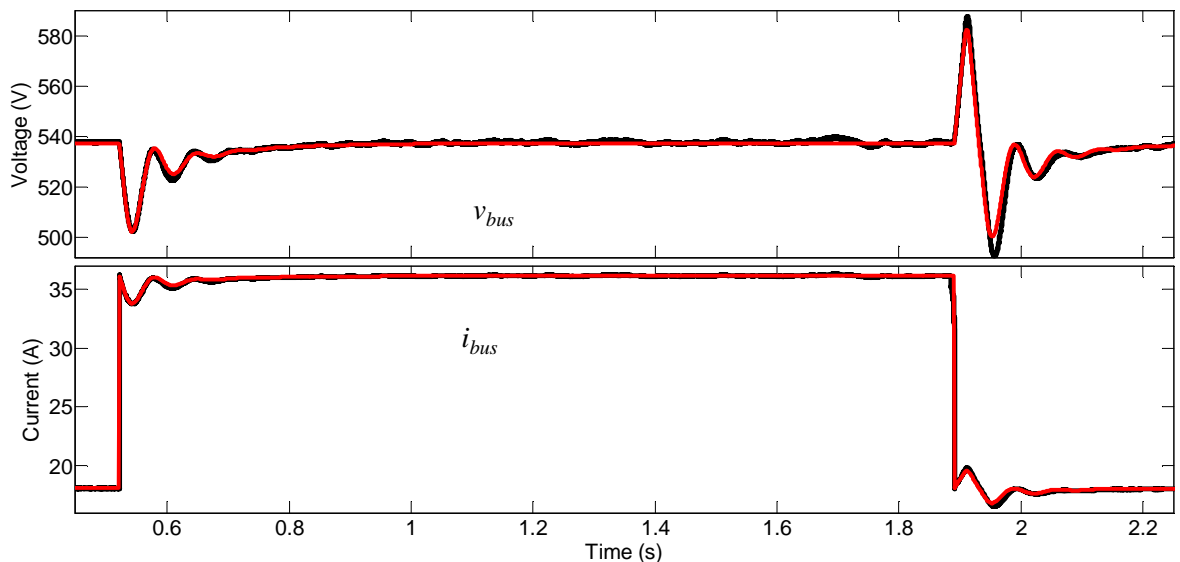


Fig. 8-32: Measured response (black traces) vs simulated response (red traces). Resistive load step up from 10 kW to 20 kW and back at $n_m = 15,000$ rpm.

In order to illustrate the importance of the clamping functions, the simulation test shown above have been repeated but now disabling the CF block. The results are shown in Fig. 8-33. As can be

^{8.5} The reference and measured speed signals are denoted as n_{m-ref} and n_m , as they are expressed in rpm.

seen, the response of the model during a step up in load remains unaffected, but large differences are found out under the step down.

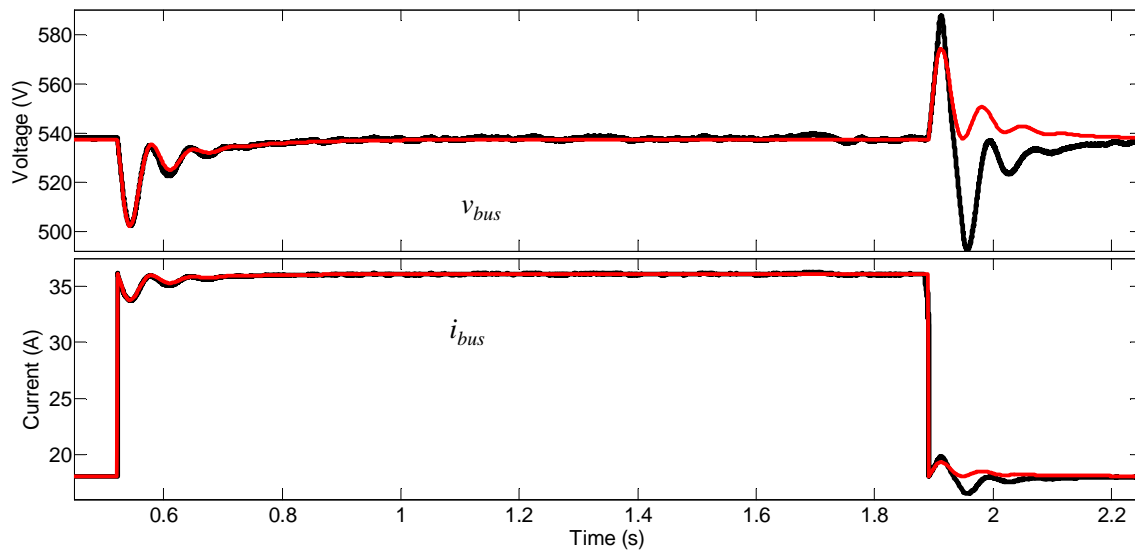


Fig. 8-33: Measured response (black traces) vs simulated response (red traces). Resistive load step up from 10 kW to 20 kW and back at $n_m = 15,000$ rpm without the clamping functions CF.

8.4.2.5.2 Constant power load steps

The bidirectional power converter has been configured as a constant power load in order to carry out several power step tests. The experimental setup is shown in Fig. 8-34a. The load is commanded by a high bandwidth control loop so, for modeling purposes, it can be assumed infinite. Thereby, it has been implemented in PSIM by a controlled current source connected in parallel with the DC link capacitor of the converter, as shown in Fig. 8-34b. The capacitance of the active load DC link capacitor is $110 \mu F$.

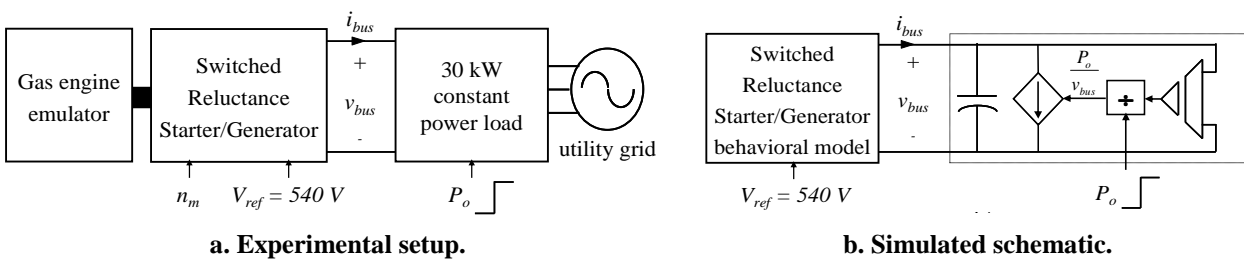
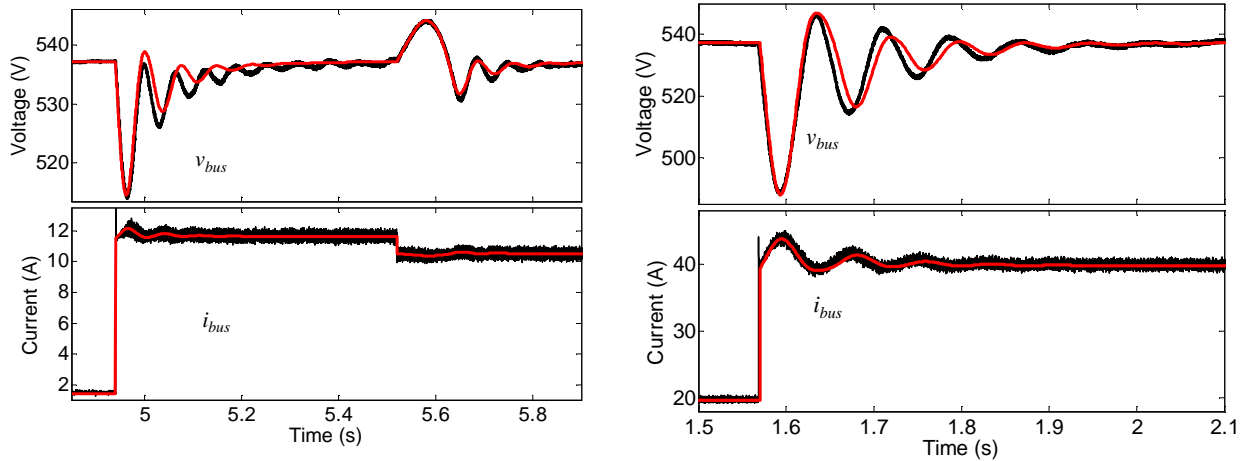


Fig. 8-34: Validation of the model under generating operation with a constant power load.

A comparison between the measured response and the simulated response for step increases and decreases in constant power are shown in Fig. 8-35a and Fig. 8-35b. As can be seen, the simulated response is close to the measured one in all cases. The observed differences are relatively small and, as discussed earlier, they are due to slight nonlinearities of the SRM which are not accounted for by the model. Nevertheless, the key transient response characteristics such as the settling time and the overshoot are predicted by the model with a good degree of accuracy.



a. Step from 850 W to 6.3 kW followed by step down to 5.6 Kw.

b. Step from 11 kW to 22 kW.

Fig. 8-35: Measured response (black traces) vs simulated response (grey traces) under constant power load steps at $n_m = 7,000$ rpm.

8.4.3 Starter operation

Once the generating operation has been modeled and validated, the SRSG under motoring operation has been tackled. The identification procedure described in section 8.3.4 has been followed.

8.4.3.1 Power balance block

The total moment of inertia J has been identified from a constant acceleration test. To maximize Δi_{bus} a high acceleration rate (355 rpm/s) was used up to the maximum motoring speed of 5,000 rpm, and a constant load torque of 15 Nm was imposed on the SRM by the engine emulator dynamometer. Fig. 8-36 shows the bus voltage, the current drawn by the machine and the speed. By applying (8-18), the resulting moment of inertia J is 0.15 kg m^2 .

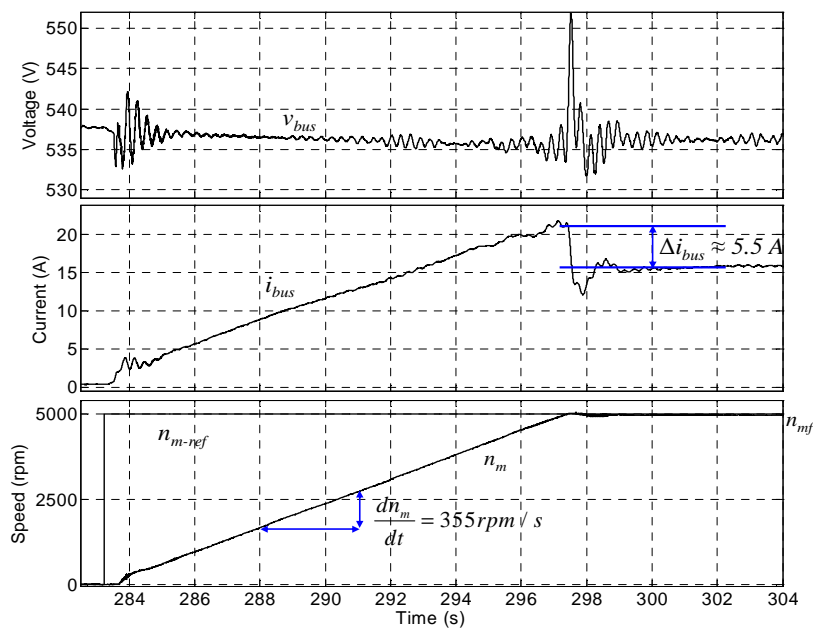


Fig. 8-36: Constant acceleration test from 0 to 5000 rpm at constant $T_{load} = 15$ Nm.

The power losses are obtained from the difference between the input electrical power and the output mechanical power over the operating range of the SRSR. The calculated power losses, $P_{loss-total}$, from measured data are shown in Fig. 8-37. These data are implemented in the model using a look-up table as a function of T_{load} and ω

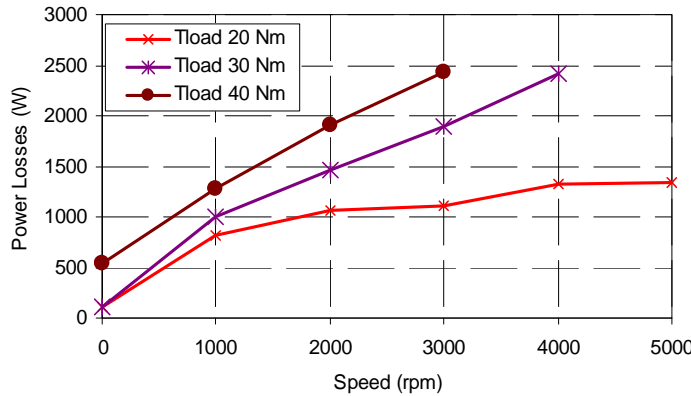


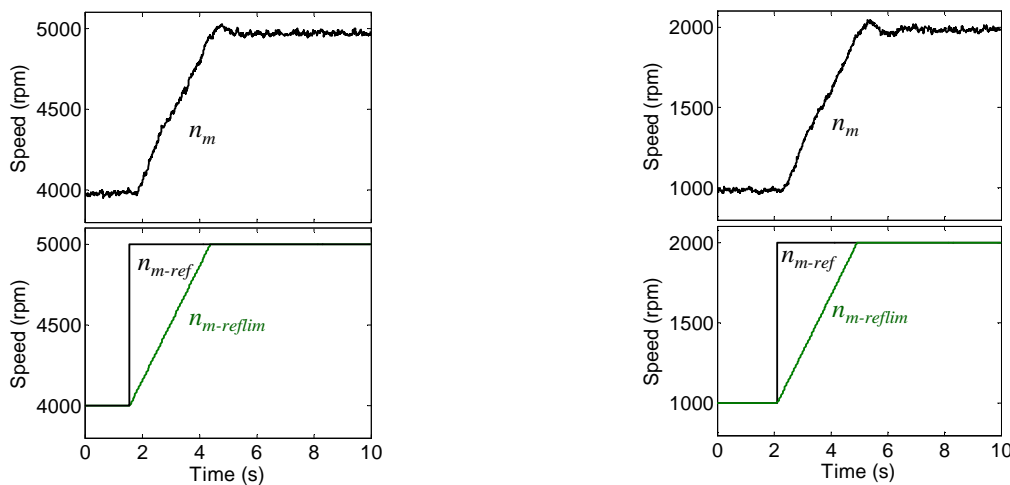
Fig. 8-37: Power losses as a function of load torque T_{load} and speed n_m .

8.4.3.2 Closed loop speed transfer function $G_\omega(s)$

$G_\omega(s)$ has been identified by applying a step to ω_{ref} while T_{load} is kept constant, as shown in Fig. 8-17a. Several step tests have been carried out at a variety of speed and torque operating points to evaluate the transfer function. The magnitude of the steps was relatively small so that approximately linear operation was ensured.

The response of the SRSR to two 1,000 rpm steps is depicted in Fig. 8-38. The first one is applied from 4,000 rpm to 5,000 rpm at low torque, $T_{load} = 5$ Nm. The second one is applied from a lower speed, 1,000 rpm to 2,000 rpm, but at higher torque ($T_{load} = 40$ Nm). Although a step is applied, the actual signal received by the controller has an acceleration limit of 355 rpm/s. This is shown by $n_{m-reflim}$.

As can be seen in Fig. 8-38, the speed response is similar in both cases, meaning that $G_\omega(s)$ can be assumed independent of ω and T_{load} . This is confirmed later on by means of a bode plot.



a. From 4,000 to 5,000 rpm at $T_{load} = 10$ Nm.

b. From 1,000 to 2,000 rpm at $T_{load} = 40$ Nm.

Fig. 8-38: Speed transient responses at constant load torque.

Transfer function models $G_{\omega}(s)$ are identified from both tests using the *oe* function of Matlab. The rate limited speed signal $n_{m-reflim}$ is converted from rpm to rad/s, resulting in $\omega_{ref-lim}$. This is used with ω to identify $G_{\omega}(s)$ ^{8.6}. Second order transfer functions yield good fitting results as depicted in Fig. 8-39, where the fitting results are evaluated using the *compare* function of Matlab.

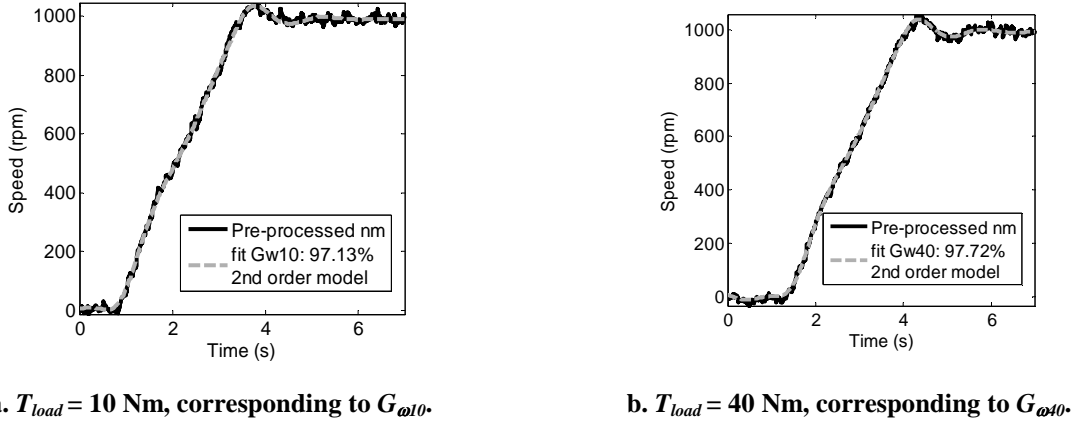


Fig. 8-39: Fitting results of $G_{\omega}(q)$ for $T_{load} = 10$ Nm and $T_{load} = 40$ Nm.

The identified transfer functions, after transformation from discrete to continuous time domain, are given by (8-27). Their frequency responses are compared in Fig. 8-40. Both frequency responses are similar. Only differences are noticed above 1 Hz, but considering the slew rate limitations of ω_{ref} , those differences can be neglected. Therefore, it confirms that $G_{\omega}(s)$ can be assumed independent of operating point.

$$G_{\omega 10}(s) = \frac{4.403 \cdot 10^{-4} s^2 + 0.8901s + 19.12}{s^2 + 2.622s + 19.29}, \quad G_{\omega 40}(s) = \frac{4.956 \cdot 10^{-6} s^2 + 0.01982s + 19.82}{s^2 + 2.408s + 19.99} \quad (8-27)$$

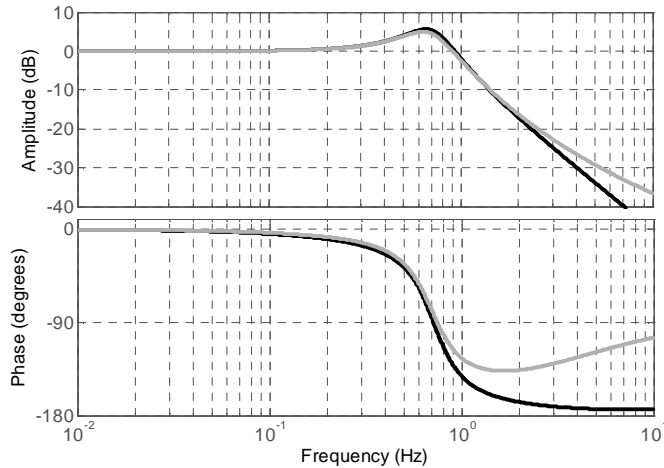


Fig. 8-40: Frequency response of the closed-loop speed transfer function, at two operating points. Dark line: $G_{\omega 10}(j\omega)$. Grey line: $G_{\omega 40}(j\omega)$.

8.4.3.3 Load torque transfer function $G_T(s)$

$G_T(s)$ has been identified by applying a step to T_{load} while ω_{ref} while is kept constant, as shown in Fig. 8-17b. Dynamic dependences on operating point has been also analyzed.

^{8.6} The signal $\omega_{ref-lim}$ is considered instead of ω_{ref} in the cost function (8-20).

The response of the SRSG to two 5 Nm T_{load} steps at different operating points is shown in Fig. 8-41. The speed response is similar in both cases. When T_{load} increases the speed initially reduces, due to the mismatch between electrical input and mechanical output power, the speed then returns to the reference value under the operation of the speed controller. Whilst similar oscillation frequencies are observed, slightly higher damping is evident in the test in Fig. 8-41b, suggesting $G_T(s)$ depends slightly on operating point.

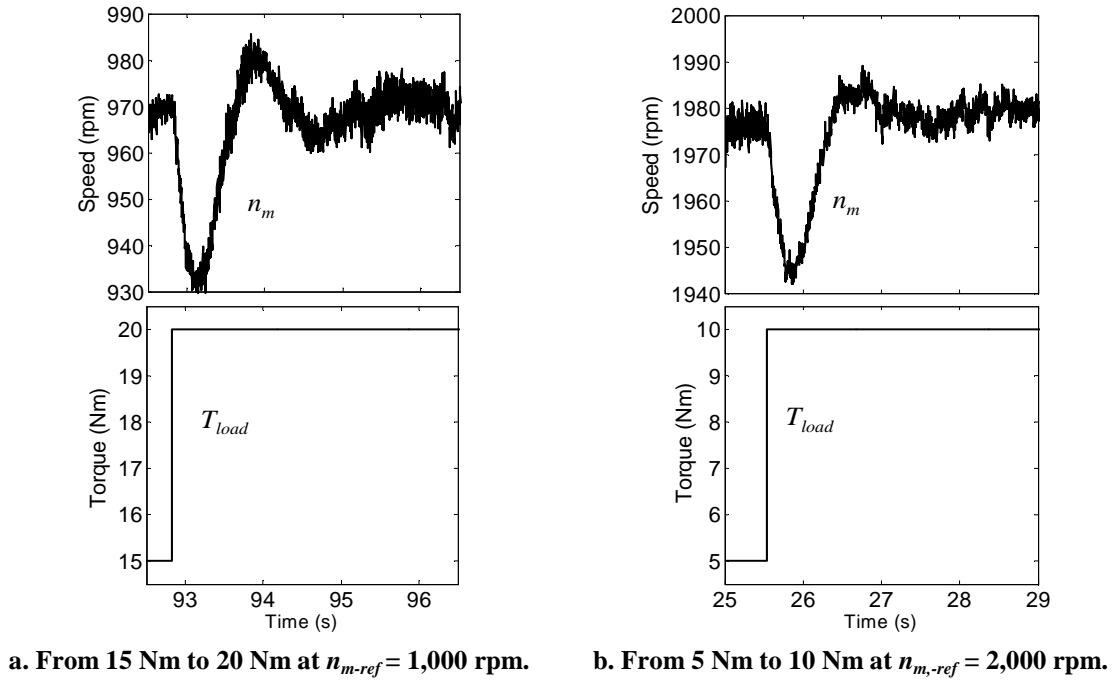


Fig. 8-41: Speed responses for a load torque step at constant reference speed.

Transfer function models for $G_T(s)$ have been identified from both tests. Good identification results are achieved with third order transfer functions, as depicted in Fig. 8-42. G_{T1000} and G_{T2000} correspond to the transfer functions identified at 1,000 rpm and 2,000 rpm, respectively.

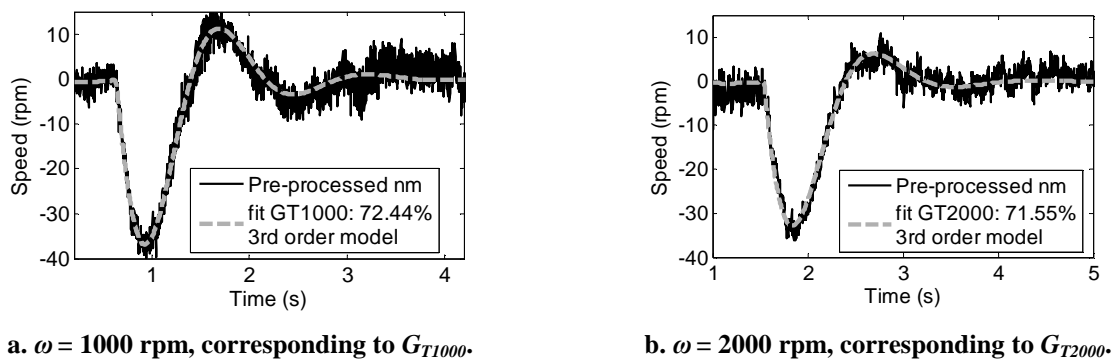


Fig. 8-42: Fitting results of $G_T(q)$ for $\omega = 1000$ rpm and $\omega = 2000$ rpm.

The transfer functions are expressed in (8-28) after transformation to continuous time domain, and their frequency responses are compared in Fig. 8-43, where it is seen that there is a slight difference in damping.

$$\begin{cases} G_{T1000}(s) = \frac{0.0003208s^3 + 0.6416s^2 + 320.8s - 0.6002}{s^3 + 62.39s^2 + 204.3s + 1150} \\ G_{T2000}(s) = \frac{0.00169s^3 + 3.38s^2 + 1690s + 7.036}{s^3 + 339.1s^2 + 1306s + 5730} \end{cases} \quad (8-28)$$

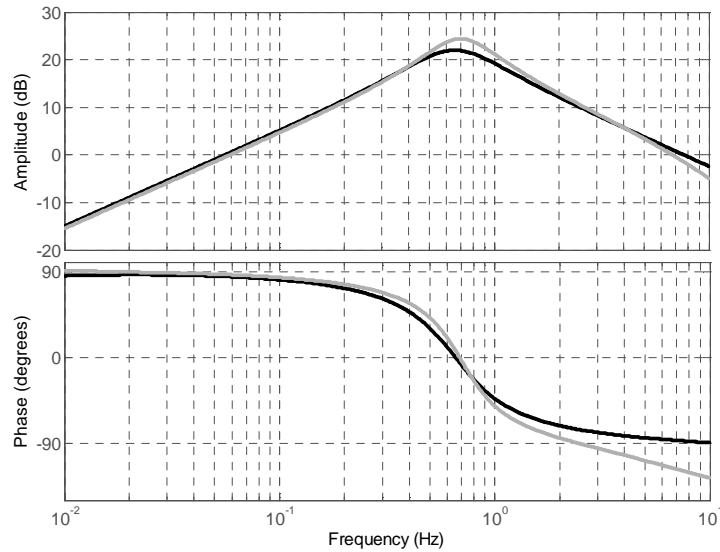


Fig. 8-43: Frequency response of the load torque transfer function, as a function of the operating point given by speed. Dark line: $G_{T2000}(j\omega)$. Grey line: $G_{T1000}(j\omega)$.

It was concluded that $G_T(s)$ depends only slightly on T_{load} , with damping reducing at higher T_{load} . However, the nonlinearity is relatively low so it has been neglected for the sake of a simple model. The resulting implementation of the speed dynamics block is shown in Fig. 8-44, including the slew rate limiter of the speed reference signal. It is worth noticing that, if the behavioral model should account for dynamic dependence on operating point, $G_\omega(s)$ and $G_T(s)$ could be replaced by LLMN, but this would have the cost of increased complexity.

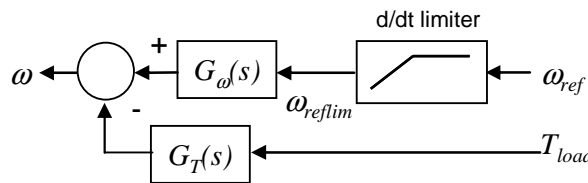


Fig. 8-44: Diagram of speed dynamics block.

8.4.3.4 Model validation under operation as a starter

The model of the SRS in motoring mode has been implemented in the circuit simulator PSIM and a set of starting profiles have been experimentally tested to validate the simulation model. The experimental setup is shown in Fig. 8-45a and the equivalent simulation model is shown in Fig. 8-45b. Load torque T_{load} and speed n_{m-ref} profiles are sent from the FCS to the gas-engine emulator and the SRS, respectively, while the APU regulates the DC-bus to 540 V. To complete the simulation model, a model of the APU is required.

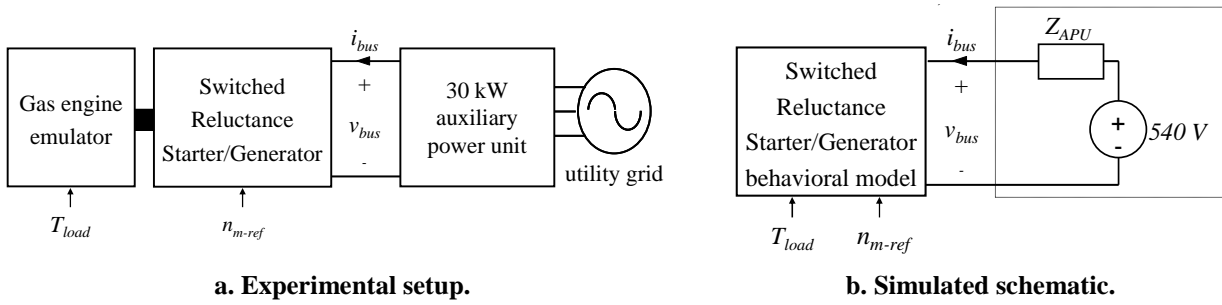


Fig. 8-45: Validation of the model under motoring operation.

8.4.3.4.1 Modeling the Auxiliary Power Unit

The APU has been modeled by using the black-box technique described in chapter 4. The model consists of a Thevenin network comprising a DC source and a transfer function output impedance $Z_{APU}(s)$ (see Fig. 8-45b), that has been identified from a load step. The transient response of the APU under a 5 kW load step up and the fitting results are shown in Fig. 8-46. The large deviation in v_{bus} evidences that Z_{APU} is relatively large.

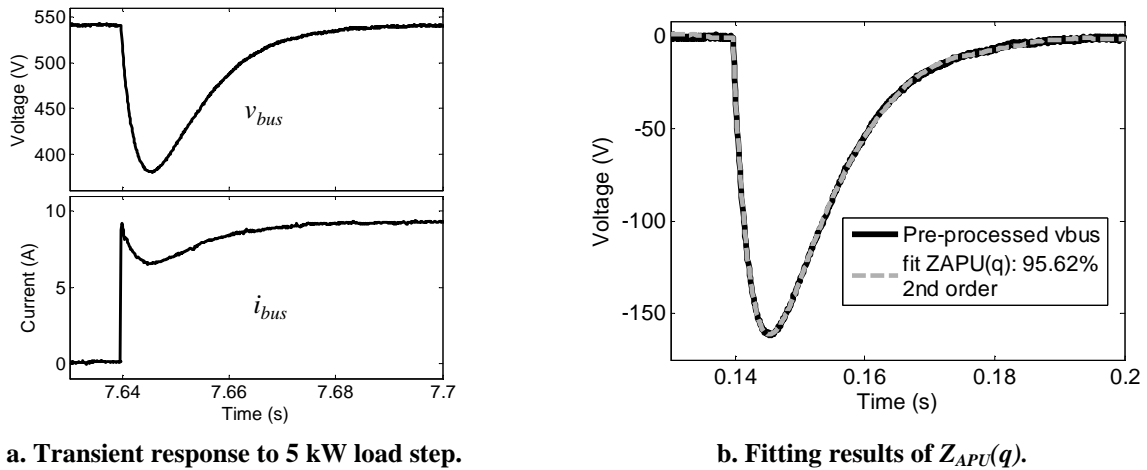


Fig. 8-46: Identifying the output impedance of the APU Z_{APU} .

The transfer function $Z_{APU}(s)$ is given by (8-29) and its bode plot is shown in Fig. 8-47, showing that it has a much higher natural frequency (~ 25 Hz) than the transfer functions associated to the speed dynamics (Fig. 8-40 and Fig. 8-43).

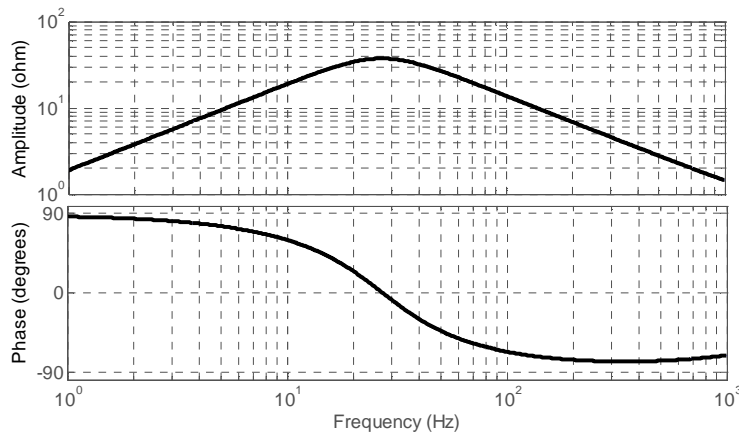


Fig. 8-47: Frequency response of the APU impedance.

$$Z_{APU}(s) = \frac{0.43s^2 + 8762s + 1003}{s^2 + 232.9s + 2.9 \cdot 10^4} \quad (8-29)$$

8.4.3.4.2 Validation test 1: constant acceleration profile at constant load torque

The first validation test consists in applying a constant acceleration profile of 100 rpm/s while the load torque is kept constant at 8 Nm. Fig. 8-48 shows a good correlation between the actual response and the model response for DC-bus voltage, current and speed during both the transient and steady-state periods. Note that the current transient after the maximum speed is reached is well reproduced. However, at the beginning of the transient a higher mismatch is observed, as the machine evidences an extra current consumption just at the beginning of operation which cannot be predicted by the proposed model.

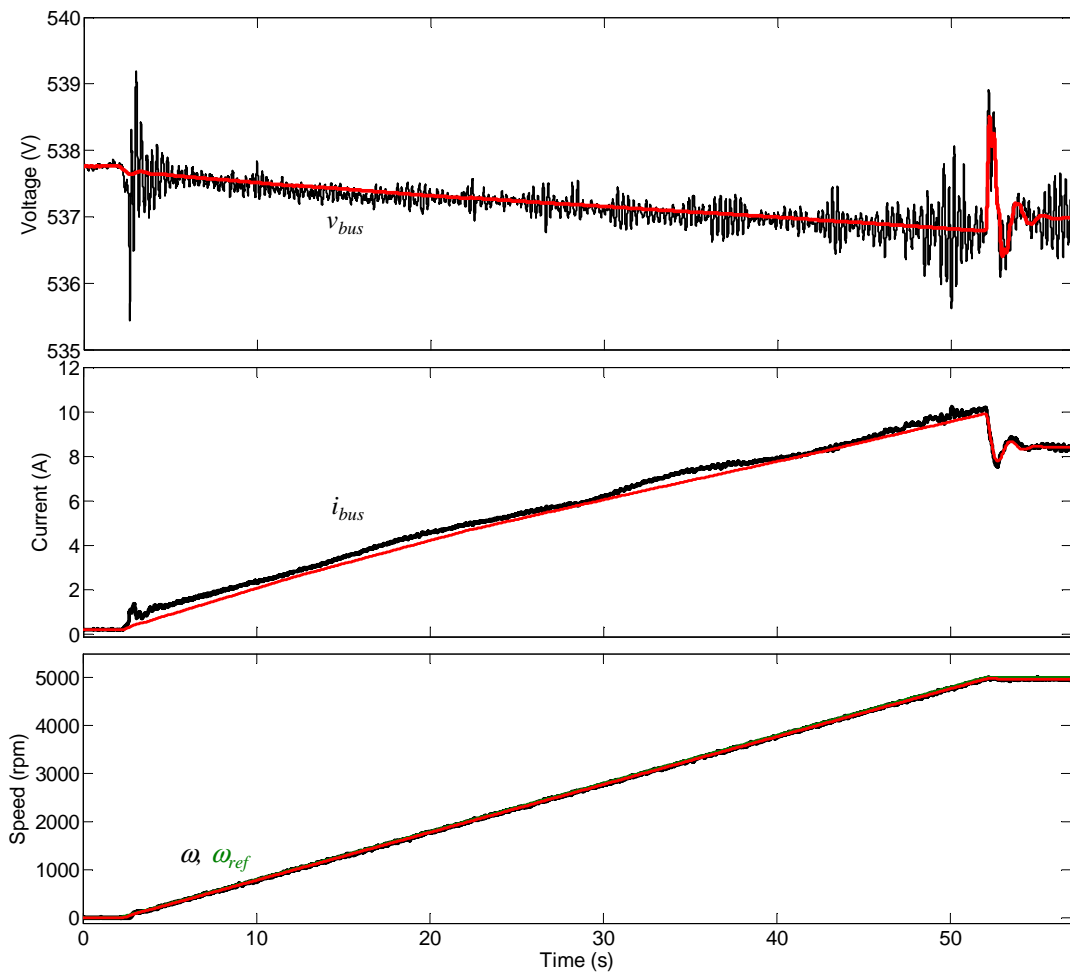


Fig. 8-48: Measured response (black traces) vs simulated response (red traces) under a constant acceleration profile of 100 rpm/s at $T_{load} = 8$ Nm, the green trace corresponds to the reference speed.

8.4.3.4.3 Validation test 2: actual gas turbine starting profile

The second validation test for the SRSR model is the electric start of the gas-engine, previously shown in Fig. 8-4. A 2.5 kW background load has been connected to the DC-bus to represent electrical loads which must be on-line before the gas-engine can be started. The APU controller features a droop voltage profile, so the voltage significantly decreases as the current increases.

The comparison between the experimental measurements and the simulation results is shown in Fig. 8-49. Dynamic interactions are noticeable as the bus voltage oscillates after the maximum power

level is reached. These oscillations are associated to the ‘quasi’ constant-power-load behavior exhibited by the SRSG at the DC port, as the mechanical time constants are much slower than the electrical ones.

As can be seen in Fig. 8-49, the input current consumption i_{bus} is well predicted by the model, as the difference between simulation and experimental waveforms is relatively small. The dynamic interactions are predicted by the model. Nevertheless, a higher oscillation is predicted by the simulation than was measured. The reason why those differences are found may be due to additional damping in the test setup and the inner current loop dynamics which are not explicitly accounted for in the starter model. Note that v_{bus} is assumed instantaneously to change i_m in the model, but in the experimental system there may be some delay, due to the current loop dynamics (as demonstrated under generator operation), which may damp the system oscillation.

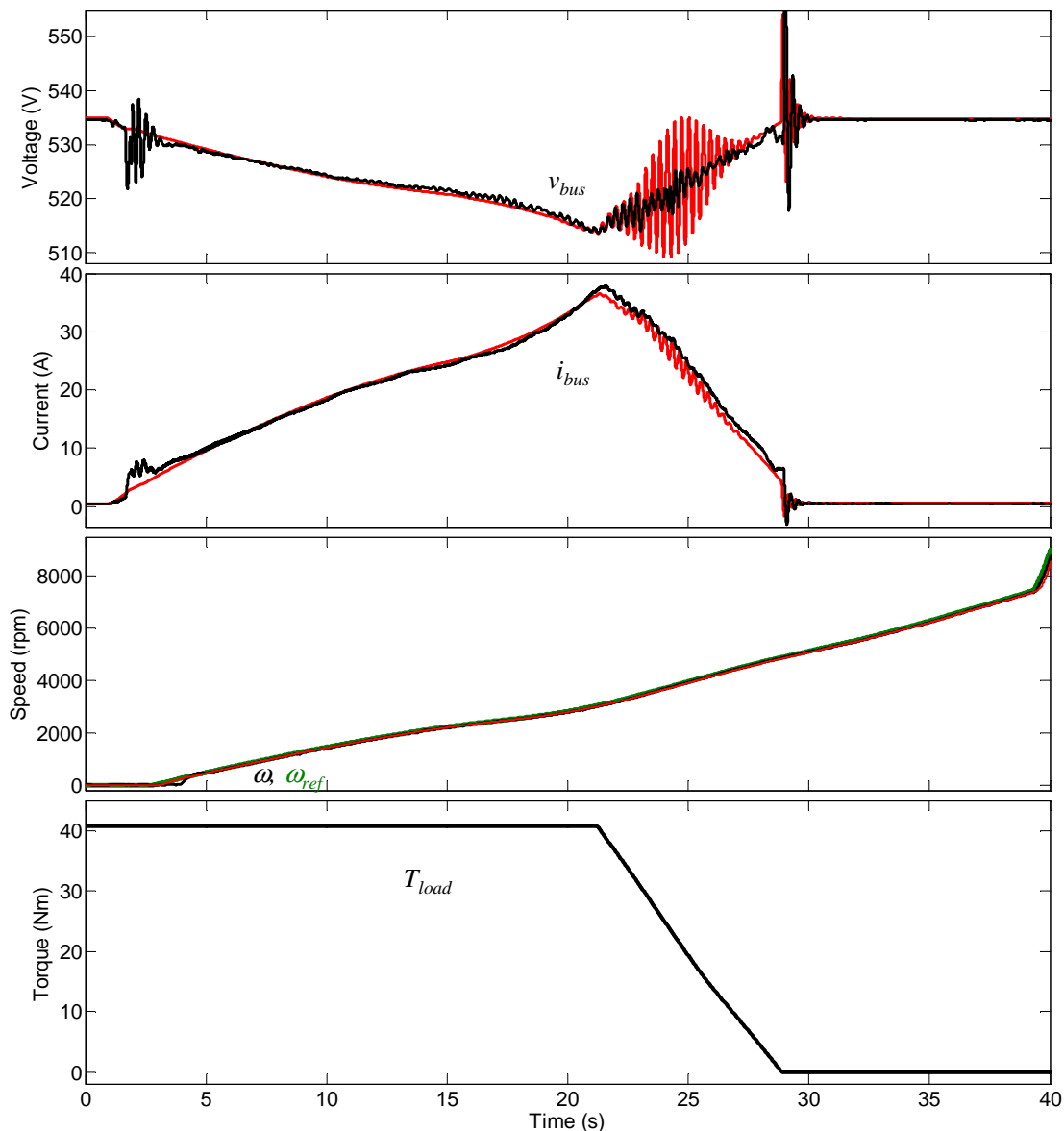


Fig. 8-49: Measured response (black traces) vs simulated response (red traces) under a real starting profile, the green trace corresponds to the reference speed.

8.5 Conclusions

In this chapter, **as an original contribution, a system-level behavioral modeling technique is proposed for a bidirectional subsystem: a switched reluctance starter/generators (SRSG)**. The proposed model structure consists of a DC link capacitor in parallel with a controlled current source. The current source is driven by either a generator network (generator operation) or a starter network (starter operation). This approach reproduces the static and dynamic behavior of the SRSG in terms of its input-output signals and is parameterized by means of simple transient tests on the SRSG hardware. The proposed model is a “grey-box” type, meaning that represents in part the internal structure of the SRSG and prior information about internal data can be readily used to partially parameterize the model. This model can be also complemented with clamping and anti-windup functions.

Moreover, an identification procedure of the model has been originally proposed. This procedure consists of experimental tests and parameterization of the model from measured responses. The identification procedure relies on concept managed in previous chapters, i.e. simple step tests and parametric identification algorithms.

A comprehensive illustration of the proposed methodology has been presented by making use of an actual SRSG located in an aerospace test facility. For validation purposes, the model has been implemented in a virtual test bed and its response has been compared to that of the real system under a variety of tests.

- Under generating operation, passive and active load steps have been tested. In all cases, the model has reproduced with good accuracy the actual system response. The capability of the model to include clamping functions for the voltage regulator has also been illustrated.
- Under motoring operation, the model has been validated by comparing the measured and model responses for two tests, a constant acceleration test and a gas-engine start. The model predicts properly the static and dynamic response of the system in both cases. Dynamic interactions between the SRSG and power sources tied to the DC bus (such as the APU), due to the ‘quasi’ constant-power-load behavior of the SRSG, can be predicted as well.

9 Simple Identification Method based on Sequential Characterization of Low-Order Submodels

9.1	Introduction.....	309
9.2	Proposed reduced order transfer function models	309
9.2.1	Modelling of systems with overdamped response	310
9.2.2	Modelling of systems with underdamped response	312
9.2.3	Summary of reduced order transfer function models.....	313
9.3	Sequential identification of submodels.....	314
9.3.1	Identification of first-order submodel	315
9.3.2	Identification of second-order critically damped submodel.....	315
9.3.3	Identification of second-order under-damped submodel.....	316
9.3.4	Discussion	316
9.4	Experimental validation	316
9.4.1	Output impedance of a DC-DC buck converter	317
9.4.2	Output impedance of a line conmutated rectifier	319
9.5	Conclusions.....	321

9.1 Introduction

Throughout previous chapters, transfer function models have been identified from the transient response of power electronics converters and subsystems under step excitation. The parameters of the transient function models have been fitted using parametric identification methods, based on optimization algorithms.

However, parametric identification techniques typically require optimization algorithms which could be complex from the point of view of power electronics engineers^{9.1}. Hence, dedicated tools may be needed to put them into practice, such as the Matlab System Identification Toolbox used throughout this thesis.

In this chapter, an alternative identification procedure of transfer function models is introduced. The method is based on a **sequential identification of first order and second order submodels from the transient response of the converter (or subsystem) under step tests**.

The main features of the method are summarized below:

- The proposed method is simple. The parameters of the models can be fitted by using analytical expressions or normalized plots, corresponding to basic first and second order transfer function submodels.
- The method requires a few points taken from the step response to identify the model parameters. Therefore, this is a suitable mean to get models from manufacturers' datasheets. Manufacturers' often provide the step response of their converters within the datasheets, so the user may just need to take few points from the graph.
- This procedure can be used to capture only the dominant poles of the system. Hence, this is useful to fit reduced-order models. Reduced-order models are suitable when large power systems are simulated and, thereby, the optimization of computational requirements is a critical point.

However, this method is less general than the conventional approach (based on optimization algorithms) and it is restricted to the scenarios described later on.

The method herein introduced will be illustrated over the output networks of power converters with tightly regulated DC output port (e.g. DC-DC converters modeled in chapter 4). Nevertheless, the method could be extended to address other networks and power converters.

9.2 Proposed reduced order transfer function models

Any causal LTI model can be described by means of the transfer function models given by (9-1), where $m \leq n$.

$$G(s) = \frac{b_m \cdot s^m + b_{m-1} \cdot s^{m-1} + \dots + b_o}{a_n \cdot s^n + a_{n-1} \cdot s^{n-1} + \dots + a_o} \quad (9-1)$$

^{9.1} Mathematical aspects about parametric identification based on optimization algorithms are given in appendix A.4.

Using partial fraction expansion, (9-1) can be rewritten as the sum of sum of N_1 first-order models and N_2 second-order submodels as follows.

$$G(s) = K_0 + \sum_{i=1}^{N_1} \frac{K_{1i}}{s + \omega_{1i}} + \sum_{j=1}^{N_2} \frac{K_{21j} \cdot s + K_{22j}}{s^2 + 2 \cdot \zeta_{2j} \cdot \omega_{2j} \cdot s + \omega_{2j}^2} \quad (9-2)$$

Regarding converters with regulated DC output (DC-DC or AC-DC), the output impedance can be written as follows, where v_{streg} denotes the static load regulation effects and $Z_{o0}(s)$ denotes the output impedance after subtraction of steady-state response (more details are described in chapter 4)^{9.2}.

$$Z_o(s) = Z_{o0}(s) - \frac{\partial v_{streg}(I_o, V_i)}{\partial I_o} \quad (9-3)$$

A zero at the origin appears in the transfer functions of Z_{o0} because it has null response at steady-state. This means $b_0 = 0$ in the general transfer function given by (9-1), resulting in the following partial fraction expansion:

$$Z_{o0}(s) = \sum_{i=1}^{N_1} \frac{K_{1i} \cdot s}{s + \omega_{1i}} + \sum_{j=1}^{N_2} \frac{K_{21j} \cdot s^2 + K_{22j} \cdot s}{s^2 + 2 \cdot \zeta_{2j} \cdot \omega_{2j} \cdot s + \omega_{2j}^2} \quad (9-4)$$

As can be seen, the step response of such a LTI model is equivalent to the impulse response of a LTI model with the same parameters but without the zero at the origin. As a consequence, **the step response can be analyzed as the sum of basic impulse responses of first-order a second-order submodels**. Considering only the dominant first-order and second-order submodels, a reduced order model can be derived. The dominant submodels are determined from the step response.

Two kinds of step responses can generally be found: overdamped and underdamped.

9.2.1 Modelling of systems with overdamped response

A typical overdamped response of a power converter is shown in Fig. 9-1. This response is exhibited by CMC DC-DC converters (inner current loop plus outer voltage loop), with relatively high phase margin, under a load step. The phase margin of the simulated case is 60° and the crossover frequency is 10 kHz.

The inner loop is usually much faster than the outer loop. Therefore, from the point of view of the outer loop, the converter can be seen as a programmable current source in parallel with the output capacitor (a first order model). Hence, a PI regulator (sometimes provided with a high-frequency pole for switching ripple filtering) is often applied as outer compensator (see Fig. 9-1).

Hence, by neglecting high frequency dynamics, the converter can be well approximated as a second order model. In case of an overdamped response, the dynamics can be well approximated by the sum of the responses of two first-order submodels, as expressed below:

$$Z_{o0A}(s) = \frac{K_{11} \cdot s}{s + \omega_{11}} + \frac{K_{12} \cdot s}{s + \omega_{12}} \quad (9-5)$$

^{9.2} This equation is valid for regulated and un-regulated converters. In case of converters with output voltage regulated with integral action, then $Z_o(s) \approx Z_{o0}(s)$.

Fig. 9-2a. shows how this response is approximated by (9-5): the slowest exponential evolution (time $t > 12$ ms) is modeled by the slowest submodel '*fos1*', and the initial transient ($10 \text{ ms} < t < 12$ ms) is modeled by both '*fos1*' and an additional first order submodel, '*fos2*'. The frequency response of the approximated transfer function and the true one are compared in Fig. 9-2b. As can be seen, the reduced-order model (2nd order) is quite close to the true one (6th order). Note that $Z_o(s) = Z_{o0}(s)$ in this case.

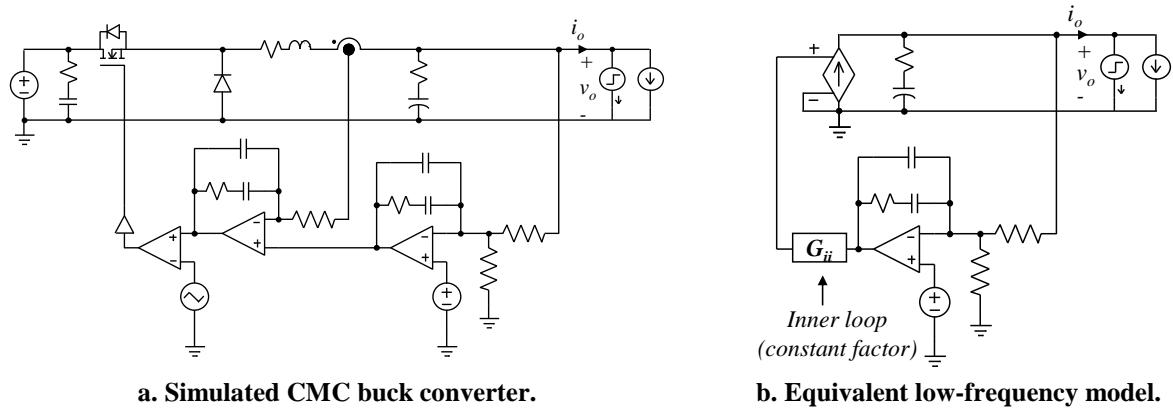


Fig. 9-1: Overdamped transient response of an average CMC buck converter under a load current step.

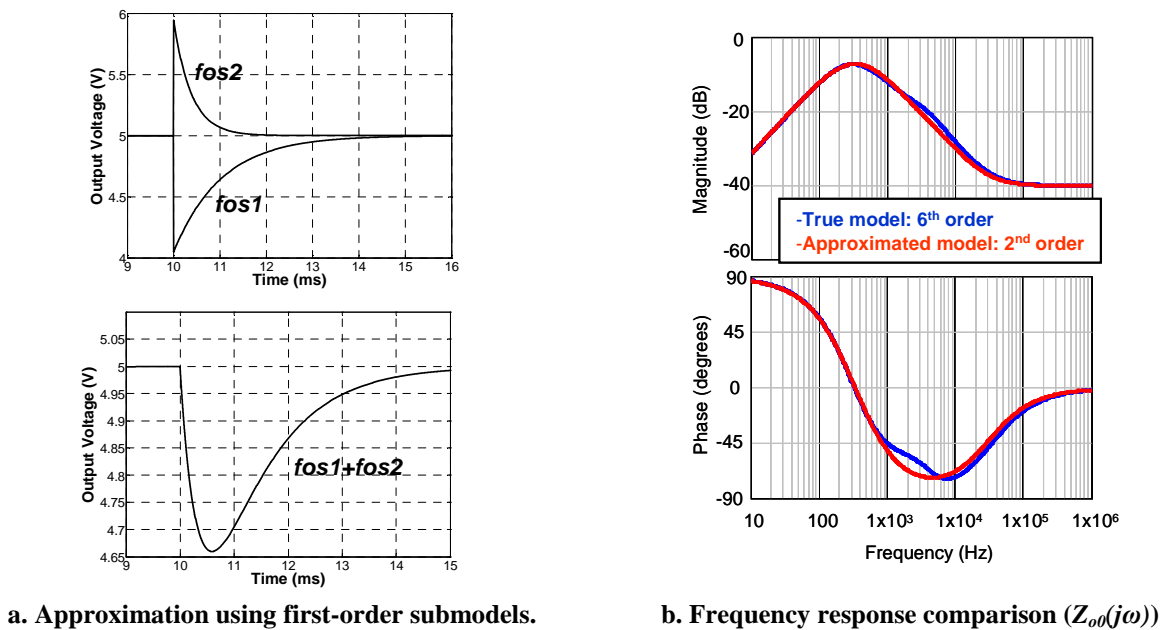


Fig. 9-2: Fitting the overdamped response of a CMC buck using first-order submodels.

If both real poles are very close to each other, the system can be modeled by means of (9-6), which corresponds to a critically-damped second-order LTI model^{9.3}.

$$Z_{o0B}(s) = \frac{K_{13} \cdot s}{(s + \omega_{13})^2} \quad (9-6)$$

9.2.2 Modelling of systems with underdamped response

Second-order overdamped response, such as that above shown, is typically exhibited by CMC converters. However, underdamped response is usually exhibited by power converters with VMC. Such response is associated to the power stage dynamics combined with the voltage compensator dynamics. Fig. 9-3 shows the response of a VMC buck converter under a load current step, where the power stage features 2nd order (due to the output LC filter) and the control stage features 3rd order (PID regulator with high frequency poles). The phase margin is near 45° and the crossover frequency is 30 kHz.

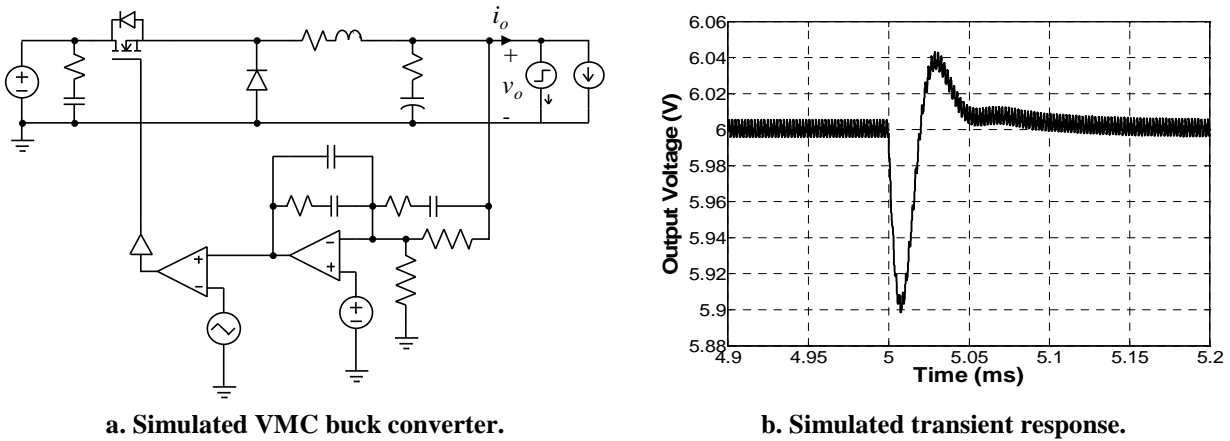


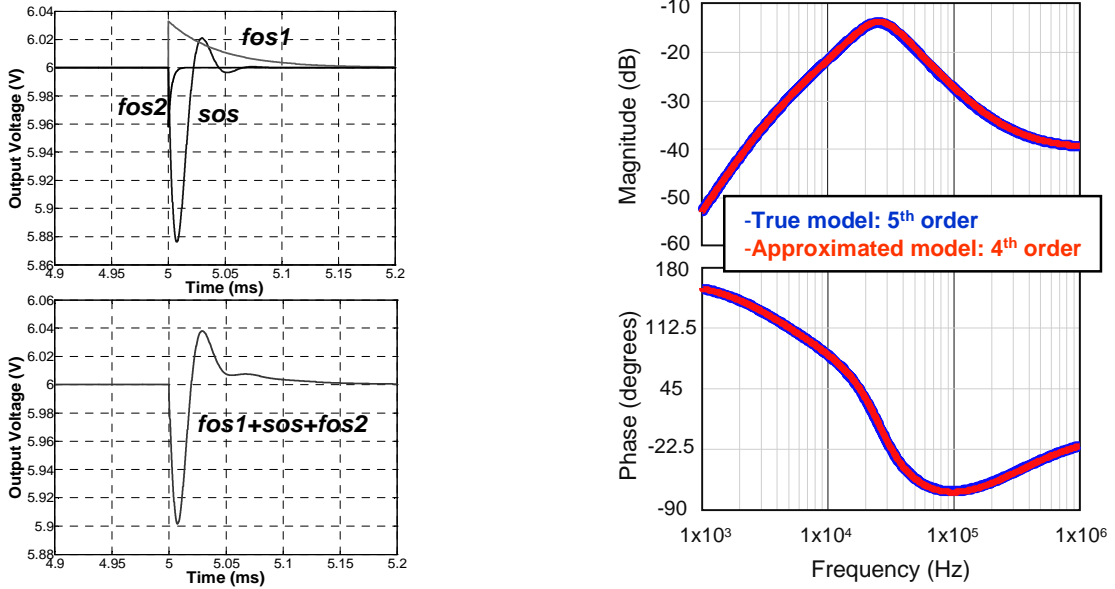
Fig. 9-3: Underdamped transient response of a VMC buck converter under a load current step.

Most underdamped responses can be properly approximated by the sum of the responses of first-order submodel and a second order submodel. In this example, the sum of two first order submodels, namely ‘*fos1*’ and ‘*fos2*’, and a second-order submodel, namely ‘*sos*’, lead to good fitting results, as shown in Fig. 9-4a. The approximated model is given by (9-7). K_{21} term is associated to any phase displacement (initial response different from zero).

$$Z_{o0C}(s) = \frac{K_{11} \cdot s}{s + \omega_{11}} + \frac{K_{12} \cdot s}{s + \omega_{12}} + \frac{K_{21} \cdot s^2 + K_{22} \cdot s}{s^2 + 2 \cdot \zeta_2 \cdot \omega_{21} \cdot s + \omega_{21}^2} \quad (9-7)$$

. The frequency response of the approximated transfer function and the true one are compared in Fig. 9-4b. Both are very close, although the order reduction is less than in the previous example (from 5th order to 4th order). Note that, as in the previous case, $Z_o(s) = Z_{o0}(s)$.

^{9.3} Quadratic term in the denominator is neglected, as it allows using simple analytical expressions to fit its parameters from the step response (this is explained in the next section). Regarding output impedance modeling, this essentially means that ESR effects are neglected.



a. Approximation using first-order and second-order submodels.

b. Frequency response comparison ($Z_{oo}(j\omega)$).

Fig. 9-4: Fitting the underdamped response of a VMC buck using first-order and second-order submodels.

In some cases, a transient response close to a pure second-order system response can be found. This is the case of CMC converters with low phase margin or VMC converters whose complex conjugate poles are dominant. Then, a single second-order model can be utilized, as follows:

$$Z_{ooD}(s) = \frac{K_{21} \cdot s^2 + K_{22} \cdot s}{s^2 + 2 \cdot \zeta_{21} \cdot \omega_{21} \cdot s + \omega_{21}^2} \tag{9-8}$$

9.2.3 Summary of reduced order transfer function models

Table 10.1 summarizes the proposed reduced-order models. They can be applied to model the dynamic networks, into the output network of a regulated DC-DC converter model, in many practical cases. Nevertheless, in some cases, higher order models could be required.

Step response	Model order	Transfer function
Overdamped	2 nd	$\frac{K_{11} \cdot s}{s + \omega_{11}} + \frac{K_{12} \cdot s}{s + \omega_{12}}$
	2 nd	$\frac{K_{13} \cdot s}{(s + \omega_{13})^2}$
Underdamped	2 nd	$\frac{K_{21} \cdot s^2 + K_{22} \cdot s}{s^2 + 2 \cdot \zeta_{21} \cdot \omega_{21} \cdot s + \omega_{21}^2}$
	3 rd	$\frac{K_{11} \cdot s}{s + \omega_{11}} + \frac{K_{21} \cdot s^2 + K_{22} \cdot s}{s^2 + 2 \cdot \zeta_{21} \cdot \omega_{21} \cdot s + \omega_{21}^2}$
	4 th	$\frac{K_{11} \cdot s}{s + \omega_{11}} + \frac{K_{12} \cdot s}{s + \omega_{12}} + \frac{K_{21} \cdot s^2 + K_{22} \cdot s}{s^2 + 2 \cdot \zeta_{21} \cdot \omega_{21} \cdot s + \omega_{21}^2}$

Table 9.1 Reduced-order models for the output port of a DC-DC converter.

9.3 Sequential identification of submodels

In this section, a simple identification method of the reduced-order models described above is presented. The method consists in splitting the step response of the converter as the sum of first and second order responses, which are identified sequentially by using simple analytical equations.

The proposed method is illustrated in Fig. 9-5 by making use of the VMC buck converter previously shown in Fig. 9-3. Three low-order submodels are sequentially identified by following the tasks listed below.

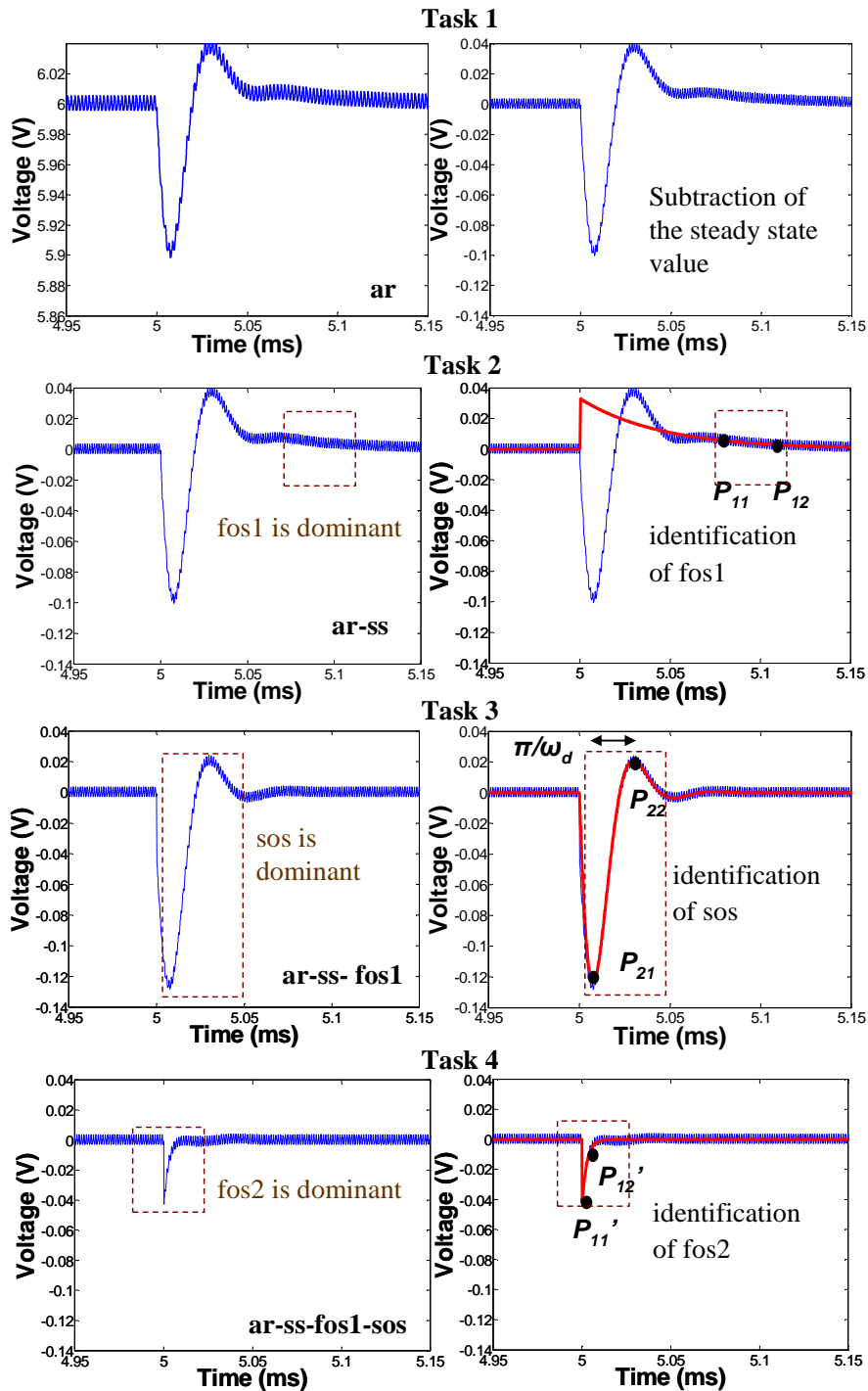


Fig. 9-5: Iterative identification procedure applied on the response of a VMC buck shown in Fig. 9-3.

1. Subtract the steady-state value 'ss' from the measured response 'ar' before and after the step. The difference between the value before and after the step gives the static load regulation (in this simulated case the static load regulation is negligible). Following this, pre-filtering can be optionally applied, in a similar way as explained in chapter 4.
2. Find a time interval at the end of the transient response for which only the response of a single submodel is dominant and identify this subsystem. In this case, an exponential evolution is found, so a first-order subsystem 'fos1' is fitted.
3. Subtract from 'ar-ss' the effect of the identified submodel 'fos1'. Identify a new dominant submodel at the end of the new response. An underdamped response is clearly found in this case, so a second-order submodel 'sos' is fitted.
4. Subtract from 'ar-ss-fos1' the effect of the identified submodel 'sos' and identify the remaining submodels (in this case, another first-order submodel 'fos2').

Once the submodels have been identified, the full transfer function model can be made up by summing the identified submodels. The identification of first-order and second-order submodels can be carried out using either normalized plots or analytical expressions. Some analytical expressions are given below. Of course, other classical expressions or graphs for characterization of first and second order systems may be used.

9.3.1 Identification of first-order submodel

First-order submodels are defined by two parameters: a gain K_I and a time constant $\tau_I=1/\omega_I$. Both parameters can be estimated by selecting two points $P_{I1}(y_{I1}, t_{I1})$ and $P_{I2}(y_{I2}, t_{I2})$ into the transient response of the submodel, and applying (9-9) (Δu is the magnitude of the step). Both task 2 and task 4 (Fig. 9-5) illustrate the identification of first-order submodels.

$$\left\{ \begin{array}{l} y(s) = u(s) \cdot LTI_1(s) = \frac{\Delta u}{s} \cdot \frac{K_{I1} \cdot s}{s + \omega_{I1}} \rightarrow y(t) = \Delta u \cdot K_{I1} \cdot e^{-t \cdot \omega_{I1}} \\ \omega_{I1} = \frac{\ln\left(\frac{y_{I1}}{y_{I2}}\right)}{t_{I2} - t_{I1}}, \quad K_{I1} = \frac{y_{I2}}{\Delta u} \cdot e^{t_{I2} \cdot \omega_{I1}} \quad \text{or} \quad K_{I1} = \frac{y_{I1}}{\Delta u} \cdot e^{t_{I1} \cdot \omega_{I1}} \end{array} \right. \quad (9-9)$$

9.3.2 Identification of second-order critically damped submodel

Critically-damped submodels are defined by a constant (K_{I3}) and an angular frequency (ω_{I3}). This submodel should be identified when an overdamped response, in which both real poles are very close to each other, is found. The identification can be carried out by selecting the minimum point of the transient response, namely $P_p(y_p, t_p)$, and applying (9-10).

$$\left\{ \begin{array}{l} y(s) = u(s) \cdot LTI_1'(s) = \frac{\Delta u}{s} \cdot \frac{K_{I3} \cdot s}{(s + \omega_{I3})^2} \rightarrow y(t) = \Delta u \cdot K_{I3} \cdot t \cdot e^{-t \cdot \omega_{I3}} \\ \omega_{I3} = \frac{1}{t_p}, \quad K_{I3} = \frac{y_p}{\Delta u} \cdot \frac{e^{t_p \cdot \omega_{I3}}}{t_p} \end{array} \right. \quad (9-10)$$

9.3.3 Identification of second-order under-damped submodel

Second-order submodels are parameterized by identifying their gains K_{21} and K_{22} , oscillation frequency ω_2 and damping factor ζ_2 . The identification can be carried out by measuring the damped oscillation frequency ω_d , selecting two maximum and/or minimum points (either local or absolute), into the transient response of the submodel, $P_{21}(y_{21}, t_{21})$, $P_{22}(y_{22}, t_{22})$ and applying (9-11). Factor φ represents phase displacement, so that $\varphi = 0$ means $K_{21} = 0$ and null initial conditions.

Task 3 (see Fig. 9-5) illustrates the identification of second-order under-damped submodels by making use of (9-11).

$$y(s) = u(s) \cdot LTI_2(s) = \frac{\Delta u}{s} \cdot \frac{K_{21} \cdot s^2 + K_{22} \cdot s}{s^2 + 2 \cdot \zeta_2 \cdot \omega_2 \cdot s + \omega_2^2} \rightarrow y(t) = \Delta u \cdot G \cdot e^{-t \cdot \zeta_2 \cdot \omega_2} \cdot \sin\left(\omega_2 \cdot \sqrt{1 - \zeta_2^2} \cdot t + \varphi\right)$$

$$\zeta_2 = \frac{\ln\left(\left|\frac{y_{21}}{y_{22}}\right|\right) \cdot \frac{1}{(t_{22} - t_{21}) \cdot \omega_d}}{\sqrt{1 + \left[\ln\left(\left|\frac{y_{21}}{y_{22}}\right|\right) \cdot \frac{1}{(t_{22} - t_{21}) \cdot \omega_d}\right]^2}}, \quad \varphi = \text{atan}\left(\frac{\sqrt{1 - \zeta_2^2}}{\zeta_2}\right) - \omega_d \cdot t_{21}, \quad \omega_2 = \frac{\omega_d}{\sqrt{1 - \zeta_2^2}} \quad (9-11)$$

$$G = \frac{y_{12}}{\Delta u} \cdot \frac{e^{t_{12} \cdot \zeta_2 \cdot \omega_2}}{\sin(\omega_d \cdot t + \varphi)}, \quad K_{21} = \frac{\tan(\varphi)}{\sqrt{1 + \tan^2(\varphi)}} \cdot G, \quad K_{22} = K_{21} \cdot \zeta_2 \cdot \omega_2 + \frac{G}{\sqrt{1 + \tan^2(\varphi)}} \cdot \omega_d$$

9.3.4 Discussion

Compared to optimization algorithms, this method has the following advantages and limitations.

- **Advantages:**
 - Easy to apply. The user only needs to take a few points from the transient response, as well as simple analytical expressions, to fit the transfer functions. Therefore, it could even be applied directly on waveforms provided in datasheets.
- **Limitations:**
 - If the response of each submodel is separated enough from the response of the others, an accurate fit can be performed using the proposed method. However, if the submodels responses are not separate enough, finding the best fit could be more difficult.
 - The step should be close to an ideal step. If the step is carried out by switching a resistor, the equivalent load impedance, just after the step, should be much higher than the output impedance of the converter.

9.4 Experimental validation

The output impedance of several commercial converters has been identified by means of the proposed technique. The identification results have been compared to those obtained by means of the parametric identification algorithm applied throughout this thesis, i.e. Gauss Newton Search by means of the 'oe' function of Matlab.

9.4.1 Output impedance of a DC-DC buck converter

The output impedance of the buck converter by Texas PTN78020W, modeled in chapter 4, has been identified by using the proposed technique^{9.4}. A resistive load has been switched off, yielding a step in load current from 2.62 A to 1.7 A. Details about the experimental setup can be found in section 4.4. As demonstrated in the appointed section, cross-coupling effects are negligible on $Z_o(s)$, so the identified transfer function is assumed to be un-terminated.

Fig. 9-6 illustrates the resulting transient waveforms and the identification process, which is described below:

- Task 1: the effect of the static regulation has been subtracted from the measured waveform. In this case, the load regulation is not null ($v_{streg} = -0.003 \cdot i_o$), meaning that there is a slight difference in steady-state value before and after the step.
- Task 2: a second-order model underdamped model has been fitted using (9-11). The resulting model already yields acceptable fitting results. Nevertheless, for illustrative purposes, additional first order submodels have been identified to get better fitting results.
- Tasks 3 and 4: the second-order response has been subtracted from the transient response, and first order models have been sequentially fitted by using (9-9). It is worth noticing that the difference between the gains of both first-order submodels allow modelling accurately the initial sudden rise due to the ESR of the output capacitor. The resulting fourth order model yields a good fit also at the beginning of the transient.

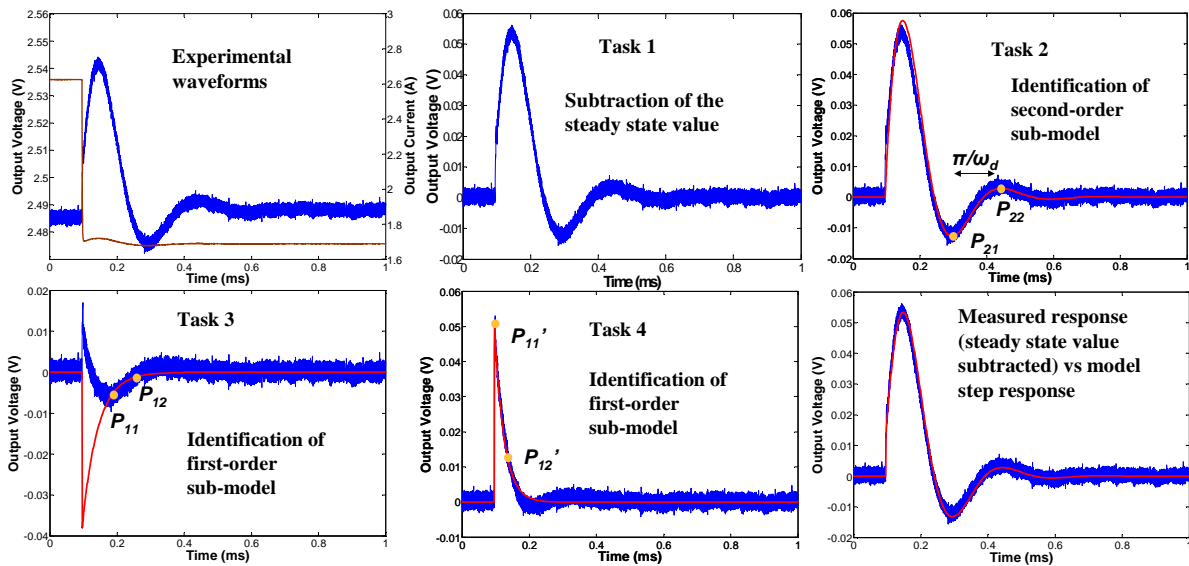


Fig. 9-6: Fitting the output impedance of a buck converter through sequential identification of submodels.

^{9.4} The converter herein modeled (Texas Instruments PTN78020W) is the same model, but a different unit, from that tackled in chapter 4.

The resulting transfer function model for $Z_o(s)$, after summing the effects of v_{streg} and $Z_{o0}(s)$, is given below.

$$Z_o(s)_{sequential} = \underbrace{\frac{0.055 \cdot s}{s + 3.523 \cdot 10^4} - \frac{0.041 \cdot s}{s + 2.167 \cdot 10^4} + \frac{2.489 \cdot 10^3 \cdot s}{s^2 + 2.042 \cdot 10^4 \cdot s + 5.573 \cdot 10^8}}_{Z_{o0}(s)} + \frac{0.003}{\frac{\partial v_{streg}}{\partial i_o}} \quad (9-12)$$

In order to validate the identification results, a transfer function model has been identified through nonlinear optimization using the ‘oe’ function of Matlab (Gauss Newton Search). The fitting result (after offset subtraction and pre-filtering) is shown in Fig. 9-7. As can be seen, the fit is very accurate. More details about such parametric identification through optimization algorithm can be found in section 4.3.2 and appendix A.4.

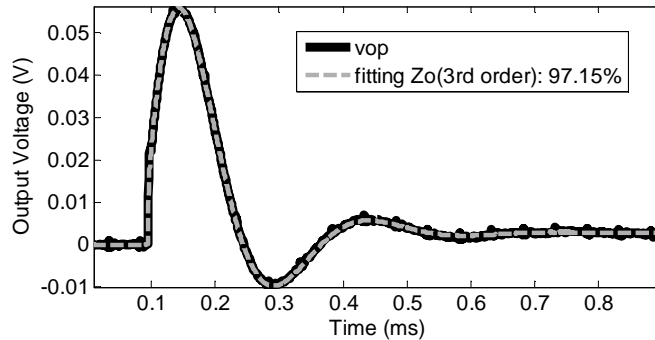


Fig. 9-7: Fitting response of a buck converter through a nonlinear optimization algorithm.

$$Z_o(s)_{oe} = \frac{0.1356 \cdot s^3 + 6.964 \cdot 10^5 \cdot s^2 + 9.2 \cdot 10^{10} \cdot s + 6.61 \cdot 10^{13}}{s^3 + 4.044 \cdot 10^7 \cdot s^2 + 7.361 \cdot 10^{11} \cdot s + 2.209 \cdot 10^{16}} \quad (9-13)$$

The frequency response of the identified models, through a sequential identification of submodels, is compared to the frequency response of the model identified by means of nonlinear optimization. The comparison results are plotted in Fig. 9-8. Both a fourth order model (9-12) and a second order model (only third and fourth addend in (9-12)) are compared.

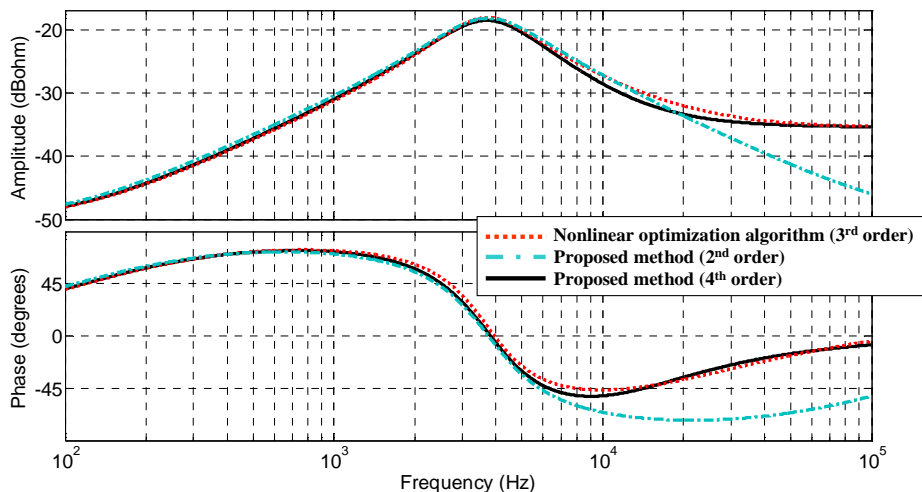


Fig. 9-8: Comparison of the frequency response of identified models using sequential estimation with the response of a model identified using a nonlinear optimization algorithm: buck converter.

As can be seen in Fig. 9-8, both the 2nd order model and the 4th order model yield similar fitting results below 8 kHz. It is worth remarking that the difference in the peak of the magnitude (which is

a critical point in terms of system-level stability analysis and transient response prediction) is approximately 0.5 dBΩ (a relatively low error). Above 8 kHz, the 4th order transfer function is more accurate and the difference with respect to the 3rd order transfer function is always less than 2 dB. The differences are attributed to the assumptions about the current waveform (it is assumed to be an ideal step), as well as error due to the done approximations (i.e. sum of submodels).

As a conclusion, the output impedance of this converter can be properly identified by means of the proposed technique.

9.4.2 Output impedance of a line commutated rectifier

The output impedance of a 40 kW line-commutated rectifier has been identified using the proposed technique. It delivers power from the 3Ø utility grid to a 270 V_{DC} bus of a MEA test bed. This converter has been already introduced in section 5.6. However, as a difference from section 5.6 (where the rectifier was operating in DCM), the converter has been herein operated in CCM (where the impedance is nearly linear).

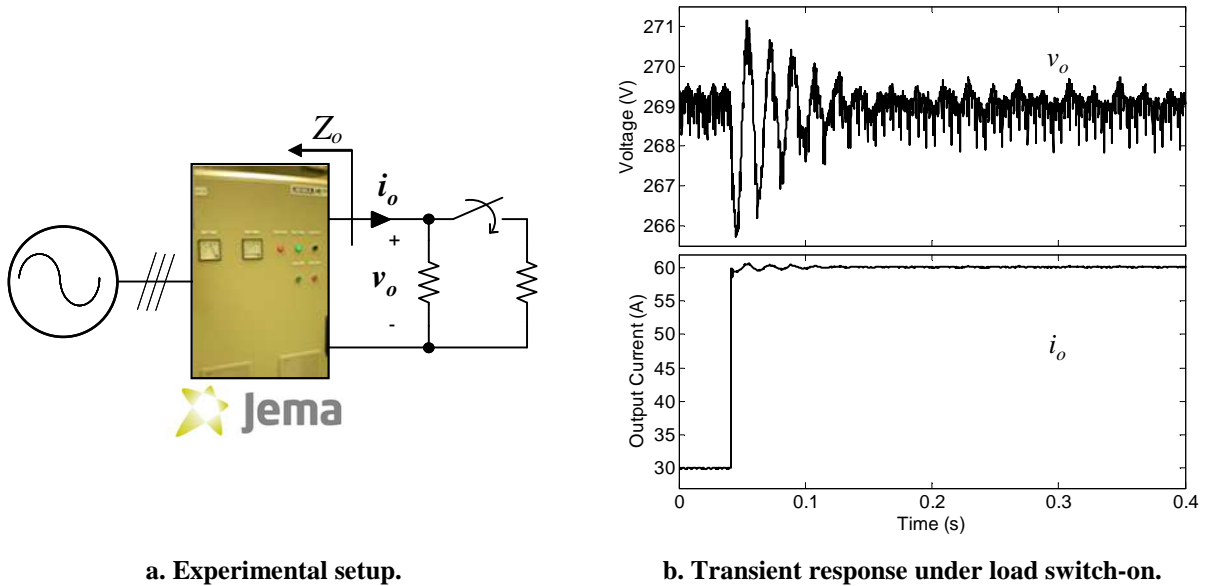
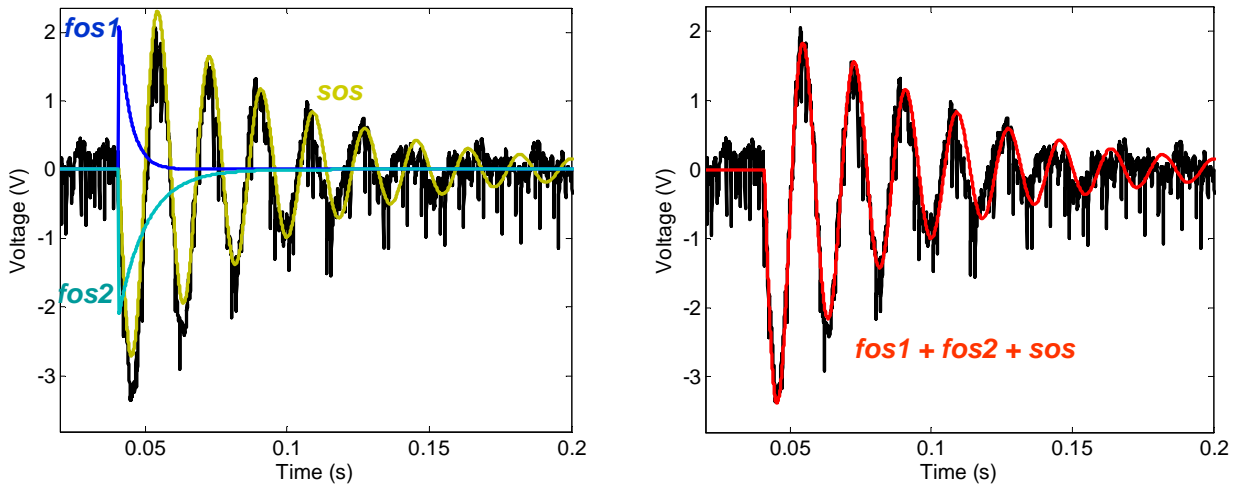


Fig. 9-9: Transient response of a 40 kW line commutated rectifier under a load step.

Note that the output current waveform is close to an ideal step (taking into account the time constants of the converter), so the proposed method can be applied. The waveform exhibits a clear underdamped response with relatively small damping factor. Therefore, a second-order submodel has been estimated, assuming that it is dominant above 80 ms, approximately. Following this, two first-order submodels have been added to obtain a finer fit at the beginning of the transient.

The resulting transfer function model is given by (9-14). The observed static load regulation is very small and has been approximated by a linear function $v_{streg} = -0.0016 \cdot i_o$.

$$Z_o(s)_{sequential} = \underbrace{\frac{0.07 \cdot s}{s+100} - \frac{0.07 \cdot s}{s+250} + \frac{34 \cdot s}{s^2 + 37 \cdot s + 1.19 \cdot 10^5}}_{Z_{o0}(s)} + \underbrace{0.0016}_{\frac{\partial v_{streg}}{\partial i_o}} \quad (9-14)$$



a. Three fitted submodels superimposed to the measured waveform (after offset subtraction).

b. Response of the sum of submodels (assuming ideal step excitation) compared to the response of the real system after offset subtraction.

Fig. 9-10: Fitting the response of a line commutated rectifier through sequential identification of submodels.

After that, a transfer function model has been fitted using nonlinear optimization through the 'oe' function of Matlab. No pre-filtering has been applied on the measured transient. As shown in Fig. 9-11 a fourth order model yields a good estimate.

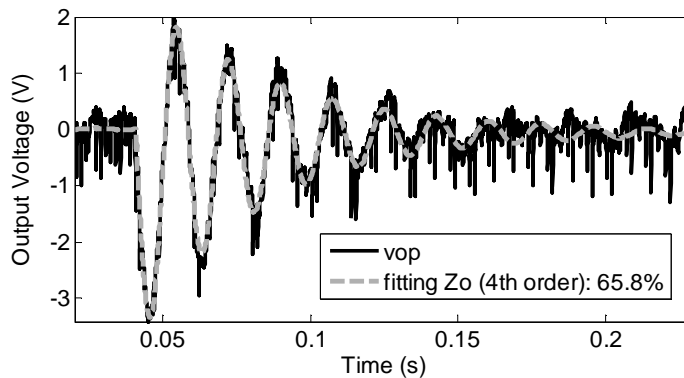


Fig. 9-11: Fitting the response of a line commutated rectifier through a nonlinear optimization algorithm.

The resulting transfer function, after transformation into continuous time domain, is given by (9-15).

$$Z_o(s)_{oe} = \frac{0.08919 \cdot s^4 + 4963 \cdot s^3 + 2.522 \cdot 10^7 \cdot s^2 + 2.768 \cdot 10^9 \cdot s + 4.516 \cdot 10^9}{s^4 + 6.945 \cdot 10^5 \cdot s^3 + 4.793 \cdot 10^7 \cdot s^2 + 8.856 \cdot 10^{10} \cdot s + 2.821 \cdot 10^{12}} \quad (9-15)$$

Finally, the frequency response of the identified models, through a sequential identification of submodels, is compared to the frequency response of the model identified using the algorithm 'oe' (see Fig. 9-12). Again, both a fourth order model (9-14) and a second order model (only third and fourth addend in (9-14)) are considered for the comparison.

It can be noticed that every model yields similar response near the resonance frequency (the deviation is approximately 2 Hz). However, below 20 Hz, the 4th order model, obtained using sequential estimation, is closer to the model obtained using nonlinear optimization (the difference is less than 3 dB within the shown bandwidth). As a conclusion, the output impedance of the rectifier has been also well estimated using the presented technique.

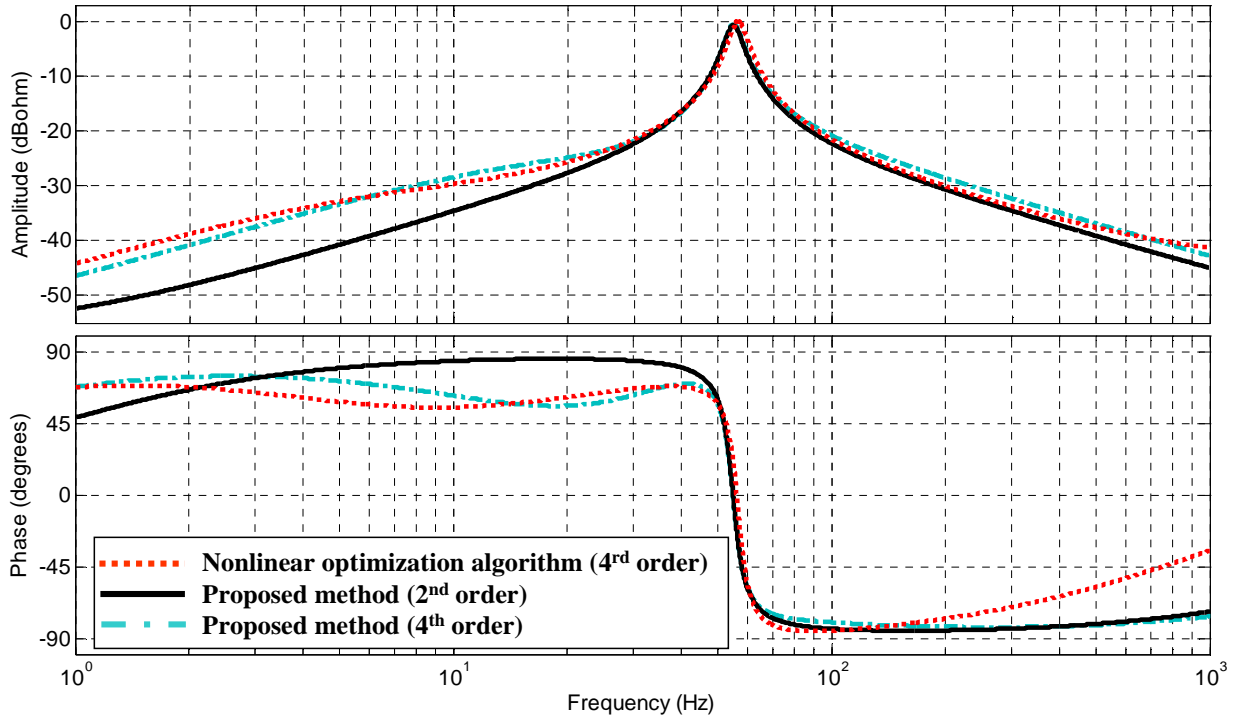


Fig. 9-12: Comparison of the frequency response of identified models using sequential estimation with the response of a model identified using a nonlinear optimization algorithm: line commutated rectifier.

9.5 Conclusions

A simple identification method for black-box models of power converters, based on a sequential identification of first and second order submodels, has been introduced. The method has been illustrated on the identification of the output impedance of converters with regulated DC output voltage.

- First, a set of reduced-order LTI models has been proposed. Reduced-order models are appropriated when large power systems are analyzed, since the simulation time can be optimized. Those models can be selected by simply analyzing the step response of the converter.
- Second, the sequential identification procedure has been exposed. The transient response is split as the sum of first and second order models. Each submodel is identified by means of analytic equations. In order to apply the method, just few points of the transient response have to be measured. Limitations of the method, in comparison with optimization algorithms, have been described as well.
- Finally, the method has been applied to identify a black-box model of the output impedance of both an actual commercial DC-DC converter and an actual line commutated rectifier (the latter is applied in a test bed of an aircraft power system). The good agreement between the response of the real converters and the response of the identified models validate the proposed procedure.

The exposed ideas could be adapted to address modeling of other transfer function models into black-box models, such as back-current-gain, input-admittance, etc.

10 Systematization of the Modeling and Identification Methods

10.1	Introduction.....	325
10.2	Modeling of unidirectional subsystems	325
10.2.1	Systematization of the procedure and review of models.....	325
10.2.2	Deriving models of other subsystems	328
10.3	Identification of unidirectional subsystems	329
10.3.1	Systematization of the procedure and review of proposed methods	329
10.3.2	Deriving identification methods of other subsystems	333
10.4	Modeling and identification of bidirectional subsystems	334
10.4.1	Revision of proposed model.....	334
10.4.2	Conceptual approach for power converters.....	335
10.5	Conclusions.....	335

10.1 Introduction

Behavioral models and identification methods for a variety of power electronics converters and subsystems have been described in this thesis. Each model (and identification process) has own particularities, but all of them have been derived by following a common, systematic procedure.

In this chapter, an overview of the modeling and identification methods proposed in this thesis is presented. Both methods are described in a systematic manner, and models derived in this thesis are briefly reviewed (as well as their identification methods). The aim is to establish the basis to derive models of other converters and subsystems that have not been tackled in this thesis. Hence, systematic derivation of a model and an identification method for an active rectifier is illustrated.

Section 10.2 and section 10.3 address unidirectional and bidirectional converters, respectively.

10.2 Modeling of unidirectional subsystems

10.2.1 Systematization of the procedure and review of models

Every model for unidirectional converters and subsystems has been derived the systematic process shown in Fig. 10-1. It consists in a set of sequential tasks. Systematic derivation of models by following such tasks is illustrated in Fig. 10-2 and Fig. 10-3.

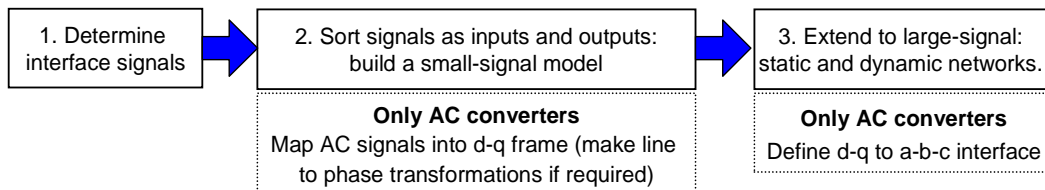


Fig. 10-1: Flowchart of the systematic modeling procedure.

1. Determine interface signals of the modeled converter with the rest of the system.
2. Sort the interface signals into two groups: ‘ m ’ model inputs and ‘ n ’ model outputs. Then, a small-signal model of the converter, consisting of ‘ $m \times n$ ’ transfer functions, is simply obtained by relating all model inputs with all model outputs. If the converter includes any AC interface, the AC signals are mapped into d - q frame.
3. Extend to large-signal: static and dynamic networks are defined as follows.
 - **Dynamic networks:** Every transfer function into the model is replaced with a dynamic network that can be a transfer function model, a gain-scheduled transfer function or a local linear models network (details are given in chapters 3 and 4). Every dynamic network has null response at steady-state.
 - **Static networks:** Each static network determines the static response of one model output as a function of all the model inputs.
 - **a - b - c / d - q interface (three-phase AC converters only):** the d - q networks have to be interfaced with the external AC bus through a a - b - c to d - q transformation for the model inputs, and d - q to a - b - c transformation for the model outputs.

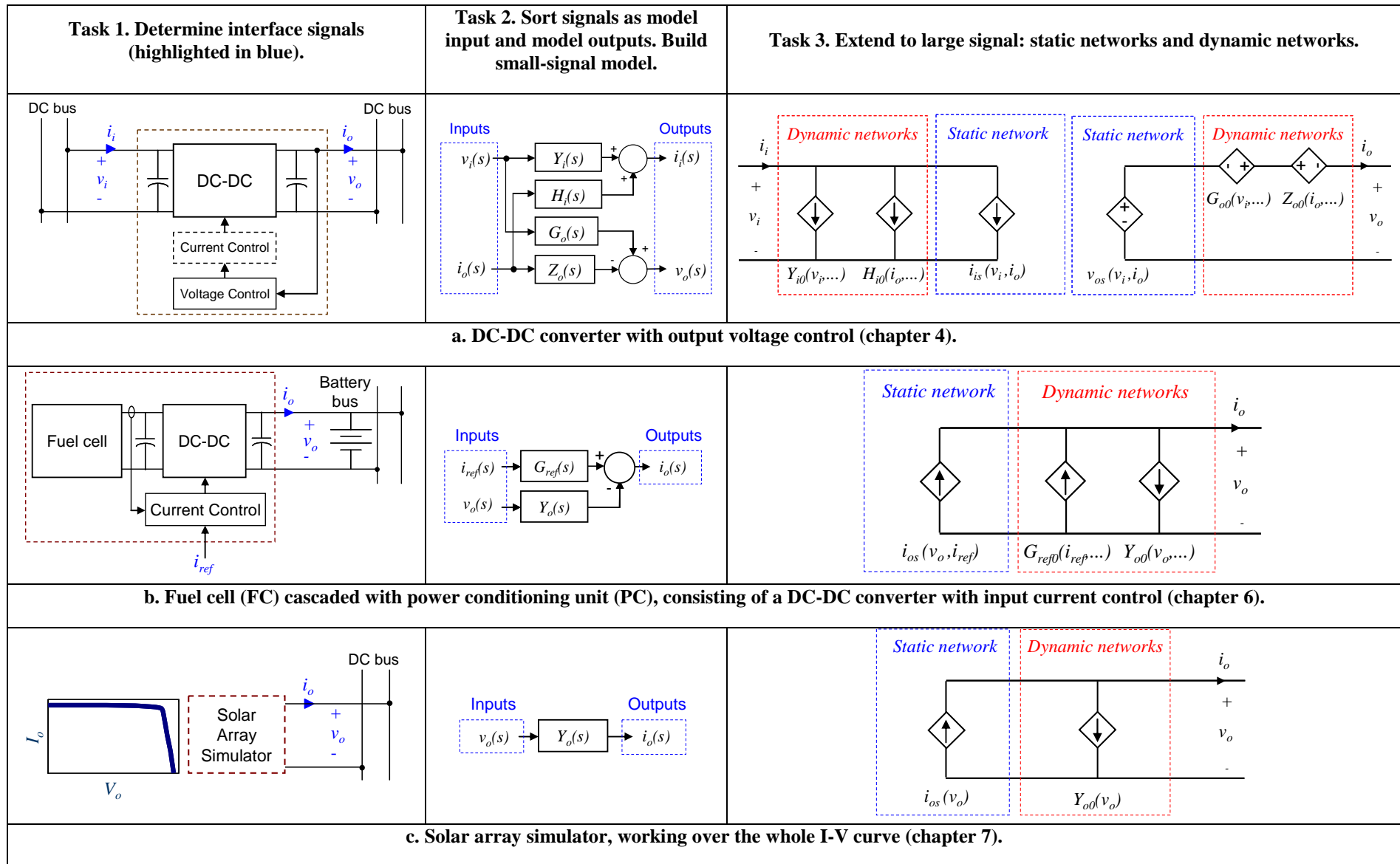


Fig. 10-2: Deriving behavioral models for DC converters and subsystems.

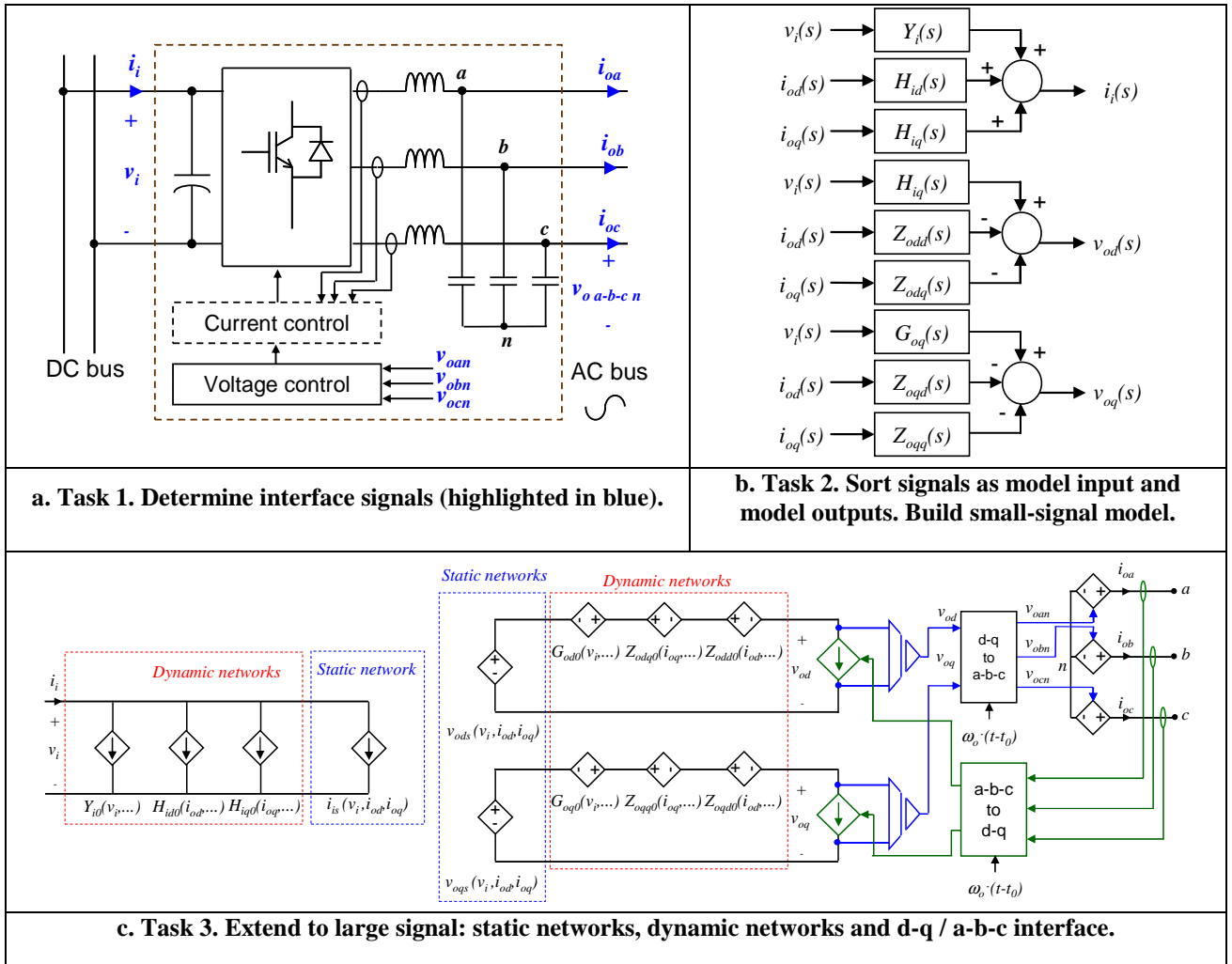


Fig. 10-3: Deriving a behavioral model for three-phase VSI with output voltage control (chapter 5).

A key aspect is to sort properly the interface signals as model inputs and outputs. To do so, the following guidelines can be taken into account.

- **The controlled signal is always a model output.** For instance, if the converter comprises a voltage control loop, the output voltage will be a model output.
- **If the controlled signal is tightly regulated, the corresponding static network can be approximated as a constant factor.** The other static network, which represents the static power balance, can be merged with the back-current-gain (or equivalent dynamic network), yielding a simpler model (refer to chapter 4 and chapter 5).
- **The un-regulated port will be modeled as a Norton network when tied to a bus whose voltage is imposed by other subsystem.** For instance, if the output port of a power converter is tied to a battery bus, the output current will be always a model output (refer to chapter 6) and Fig. 10-2b.

At this point, it is worth reminding the relationship between the small-signal models and the large-signal ones. To illustrate it, consider the large-signal model for the solar array simulator given by (10-1). Under small-signal perturbations, the following relationship between the small-signal model and the large-signal one holds. Similar relationships are derived for the remaining models.

$$\frac{i_o(s)}{v_o(s)} = -Y_o(s) = -Y_{o0}(s) + \frac{\partial i_{os}(V_o)}{\partial v_o} \quad (10-1)$$

10.2.2 Deriving models of other subsystems

This systematic procedure can be applied to model other converters that have not been tackled in this thesis. For example, the active front end (AFE) rectifier is part of three-phase AC systems for all electric ships, more electric aircrafts and microgrids. This converter behaves as a constant-power-load, so it represents a potential source of unstable situations. Hence, modeling and identification of this converter is a matter of interest. By applying the described systematic procedure, a model for such a converter is easily derived (see Fig. 10-4).

The converter is provided with an inner current loop for power factor correction plus an outer voltage loop for output voltage control. Therefore, the DC output current and AC input voltage are model inputs, while the AC input current and DC output voltage are model outputs. In this example, the AC bus comprises three wires, so the phase-to-phase voltage has been considered as model input. Hence, the line current is transformed to phase-phase current (e.g. i_{iab}) before mapping it into d - q frame. Consequently, the d - q to a - b - c interface is implemented by using a delta current sink (see Fig. 10-4).

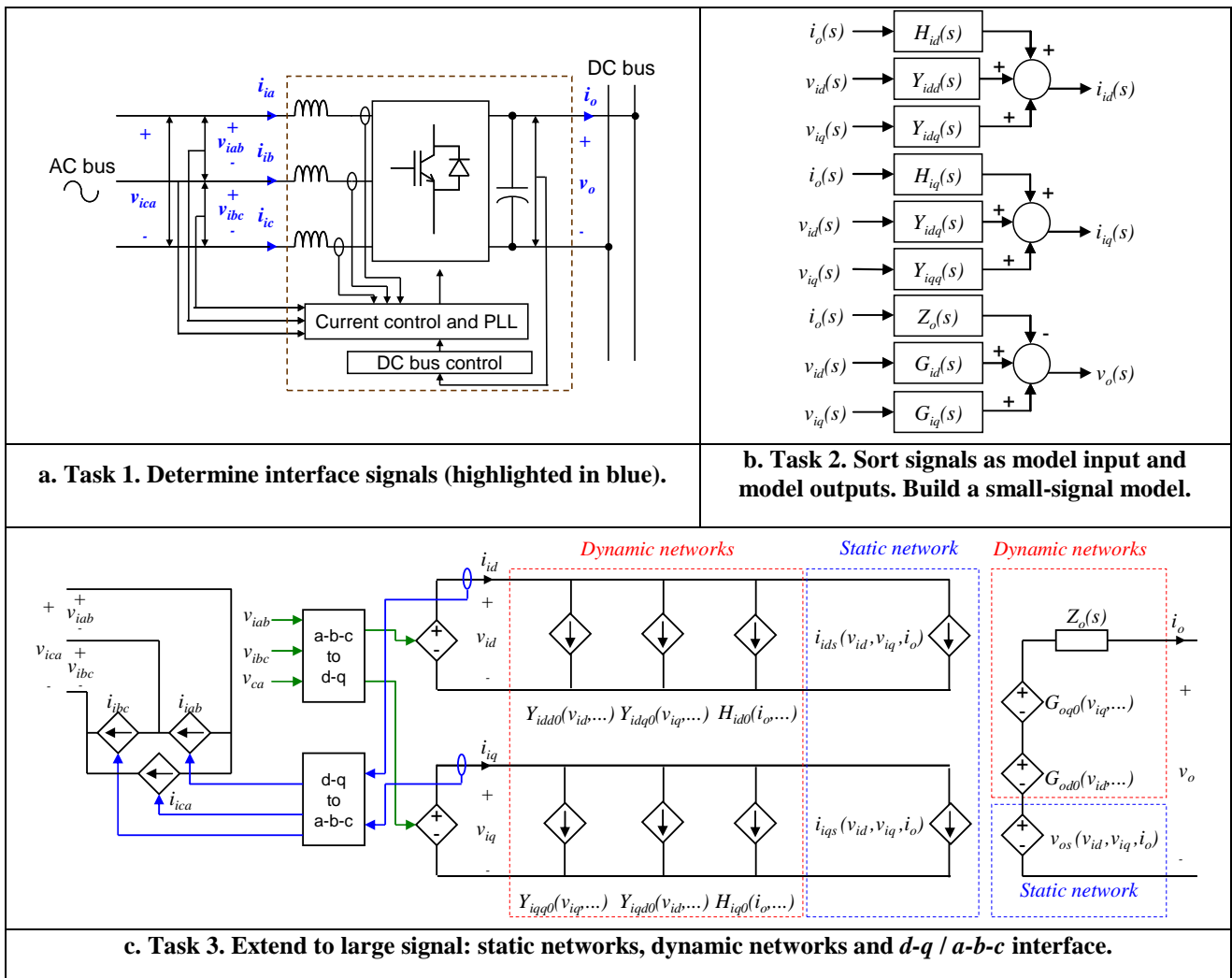


Fig. 10-4: Deriving a behavioral black-box model for a three-phase active front end (AFE) rectifier.

10.3 Identification of unidirectional subsystems

10.3.1 Systematization of the procedure and review of proposed methods

The identification of behavioral models is also carried out in a systematic manner. A flowchart of the procedure is depicted in Fig. 11-5. It is described below, considering a subsystem model with ' n ' inputs and ' m ' outputs.

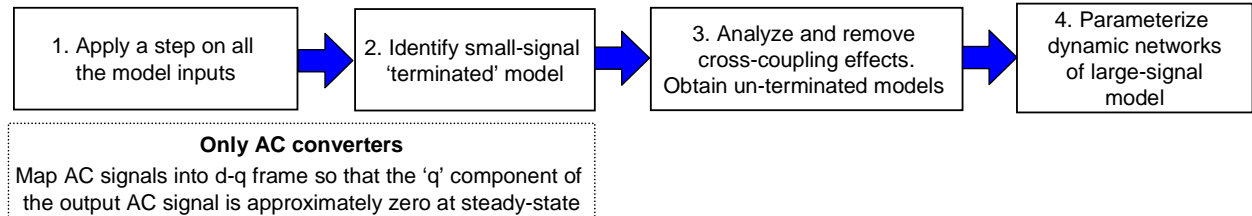


Fig. 11-5: Flowchart of the systematic identification procedure.

1. **Apply step tests.** Under each test, only one input signal is stepped while the other ones are kept constants. Therefore, ' n ' types of test are required. Note that AC transient signals have to be mapped into d-q frame, so that the ' q ' component of the output signal is approximately zero at steady-state.
 - **Current steps. Shunt injection** circuits are used, consisting of a switch connected in series with passive impedance^{10.1}.
 - **DC current:** a resistor is switched off/on.
 - **Three-phase AC current:** ' d ' and ' q ' components are separately stepped as follows.
 - The ' d ' component is stepped by switching on/off a resistor (active power step).
 - The ' q ' component is stepped by switching off a capacitor (reactive power step).
 - **Voltage steps. Series injection** circuits are used, consisting of a switch connected in parallel with a passive impedance or an array of diodes.
 - **DC voltage:** the voltage step is applied by making short-circuits on an array of diodes or a resistor.
 - **Three-phase AC voltage:** the ' d ' and ' q ' components are separately stepped as follows.
 - The ' d ' component is stepped by making a short-circuit on a resistor (active power step).
 - The ' q ' component is stepped by making a short-circuit on and inductor (reactive power step).
2. **Identify small-signal 'terminated models'.** The second task consists in identifying 'terminated' transfer functions (subscript ' m '), corresponding to local small-signal models, using parametric identification techniques.

^{10.1} Current steps can be also carried out using active equipment, such as an electronic load.

3. Analyze and remove cross-coupling effects: obtain un-terminated transfer functions.

From this task, un-terminated transfer function models are obtained. It is carried out as follows.

- For each test, the ‘*n*’ model inputs are convoluted with the identified transfer functions and the ‘*m*’ model outputs are compared to each other. If the output signal related to the stepped input is dominant over the others, then the cross-coupling effects, under such a test, are negligible.
- The significant cross-coupling effects are removed by multiplying by the inverse of a decoupling matrix (refer to chapters 4, 5 and 6 for details).

4. Post-process the un-terminated transfer functions to build dynamic networks. It is carried out as follows.

- Subtraction of the steady-state response (every transfer function).
- Gain-normalization (only if gain-scheduled transfer functions are used).

For illustrative purposes, the identification tests proposed along this thesis (task 1) are summarized below. Tasks 2 to 4 are not particularized for each case because they are always carried out in a similar manner. Particularities of some modeled subsystems are discussed as well.

Fig. 10-6 and Fig. 10-7 show the identification tests corresponding to power electronics converters, where both series injection and shunt injection on DC signals and AC signals are illustrated.

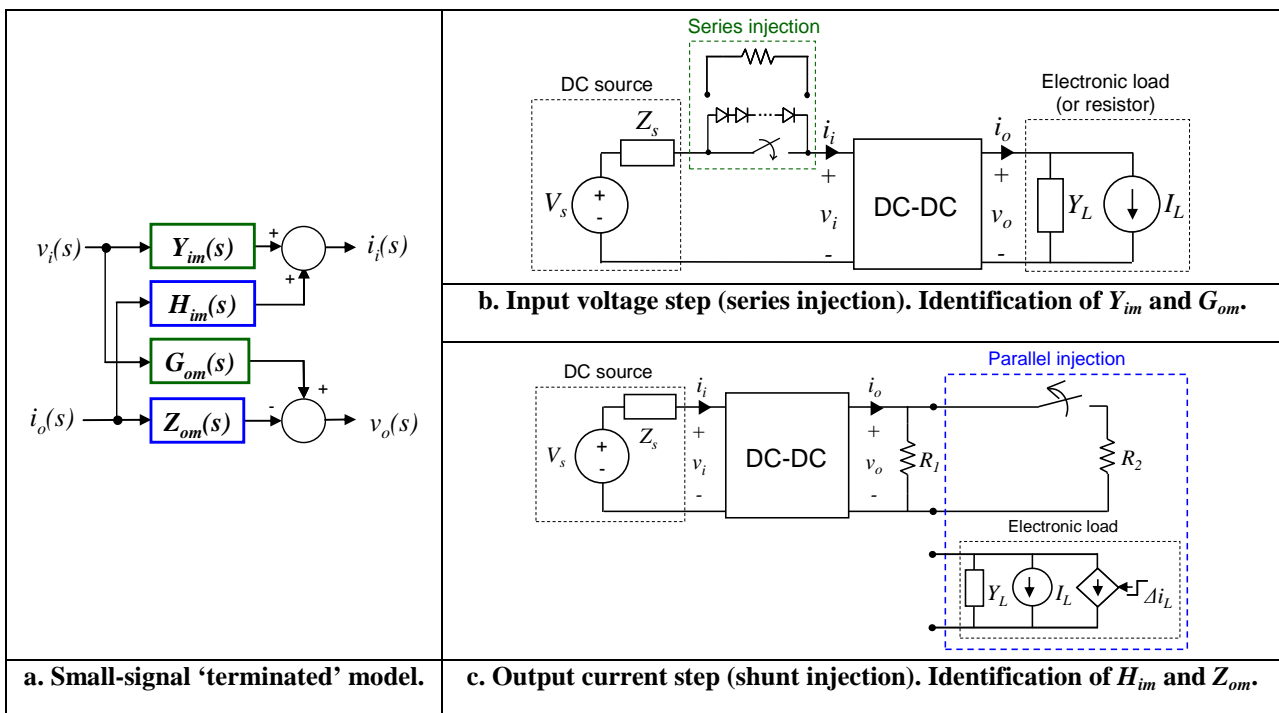


Fig. 10-6: Identification of behavioral model for a DC-DC converter with output voltage control (chapter 4).

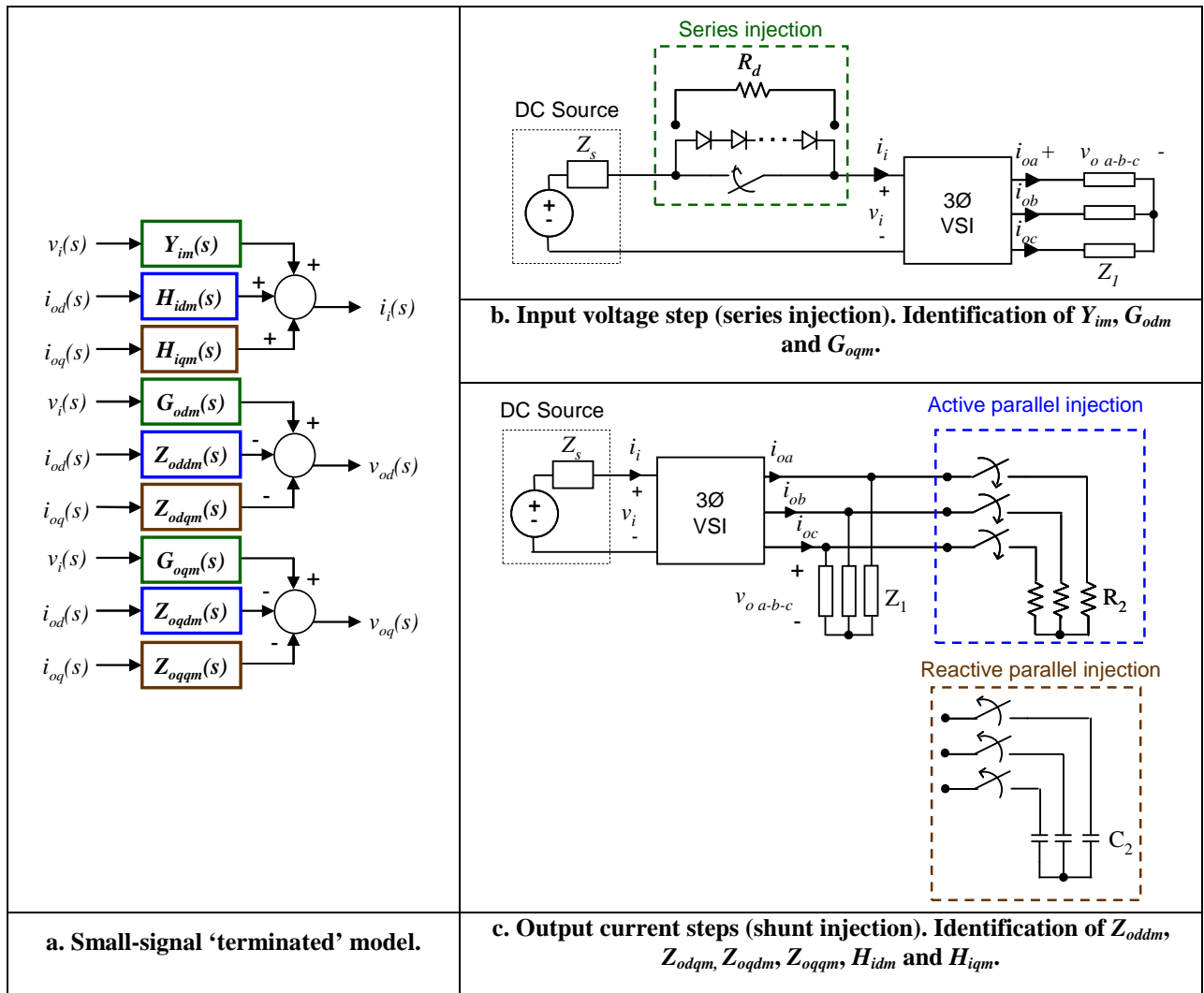


Fig. 10-7: Identification of behavioral model for a three-phase VSI with output voltage control (chapter 5).

Fig. 10-8 depicts the behavioral model of the FC cascaded with PCU. This subsystem features the following particularity: the PCU is provided with input current control, meaning that it behaves at the output port as a constant power source under constant reference signal I_{ref} . Therefore, in order to identify the output admittance, either series (stepping v_o) or shunt injection (stepping i_o) can be applied. However, the output port is made up using a Norton network because the subsystem supplies a battery bus. Consequently, if shunt injection is applied the identified impedance has to be inverted to obtain an admittance model. Note also that, in this particular case, the un-terminated output admittance, Y_o , is directly obtained from the output voltage step because I_{ref} can be kept constant, as this control signal is typically well decoupled from the power signals.

Fig. 10-9 depicts the identification procedure of behavioral models for solar array simulators. Series injection is shown, although shunt injection could be also applied to make the step in this particular case (refer to chapter 7 for more details). As there is a single input, un-terminated small-signal models are directly identified.

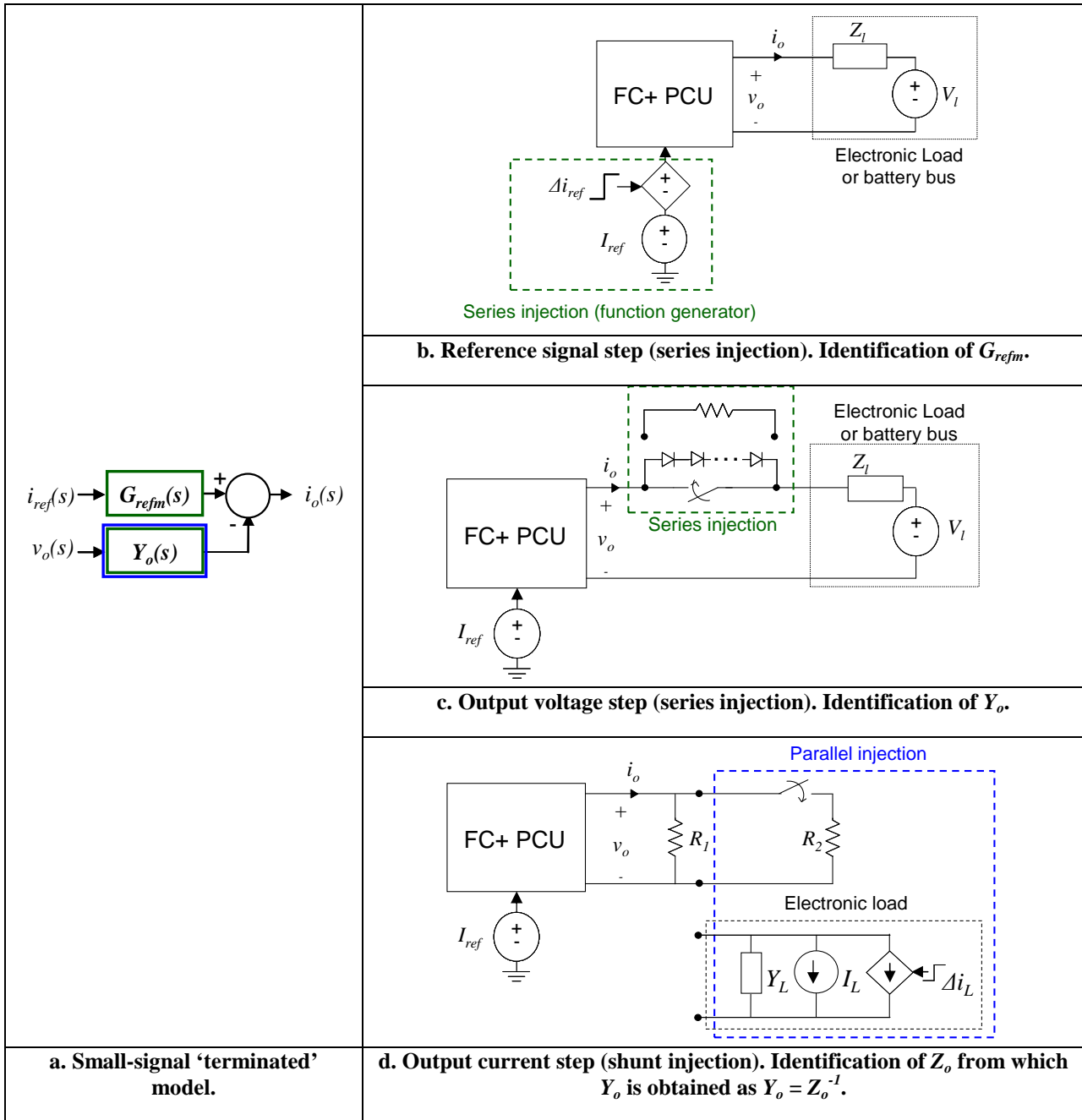


Fig. 10-8: Identification of DC-DC converter with output voltage regulation.

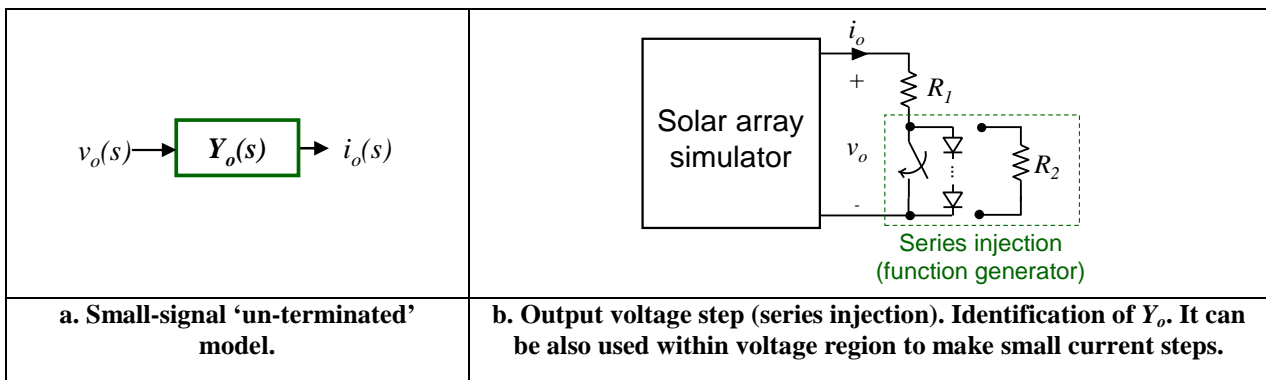


Fig. 10-9: Identification of behavioral model for a solar array simulator within the whole I-V curve.

10.3.2 Deriving identification methods of other subsystems

Finally, Fig. 10-10 illustrates the identification procedure corresponding to the AFE rectifier. The identification of the output port is similar to that of DC-DC converters. However, the converter features an AC input port, which is modeled by using a Norton approach (see Fig. 10-4). Therefore, series injection is applied to step the d-q components of the voltage. By setting the transformation so that $I_{iq} \approx 0$, then the ‘d’ component could be stepped by making a short-circuit on resistors, while the ‘q’ component could be stepped by making a short-circuit on an inductor. Compared to Fig. 10-7, one may note that those tests are dual to those used for current injection (shunt injection is applied by switching off capacitors, while series injection is done by making short-circuit on inductors).

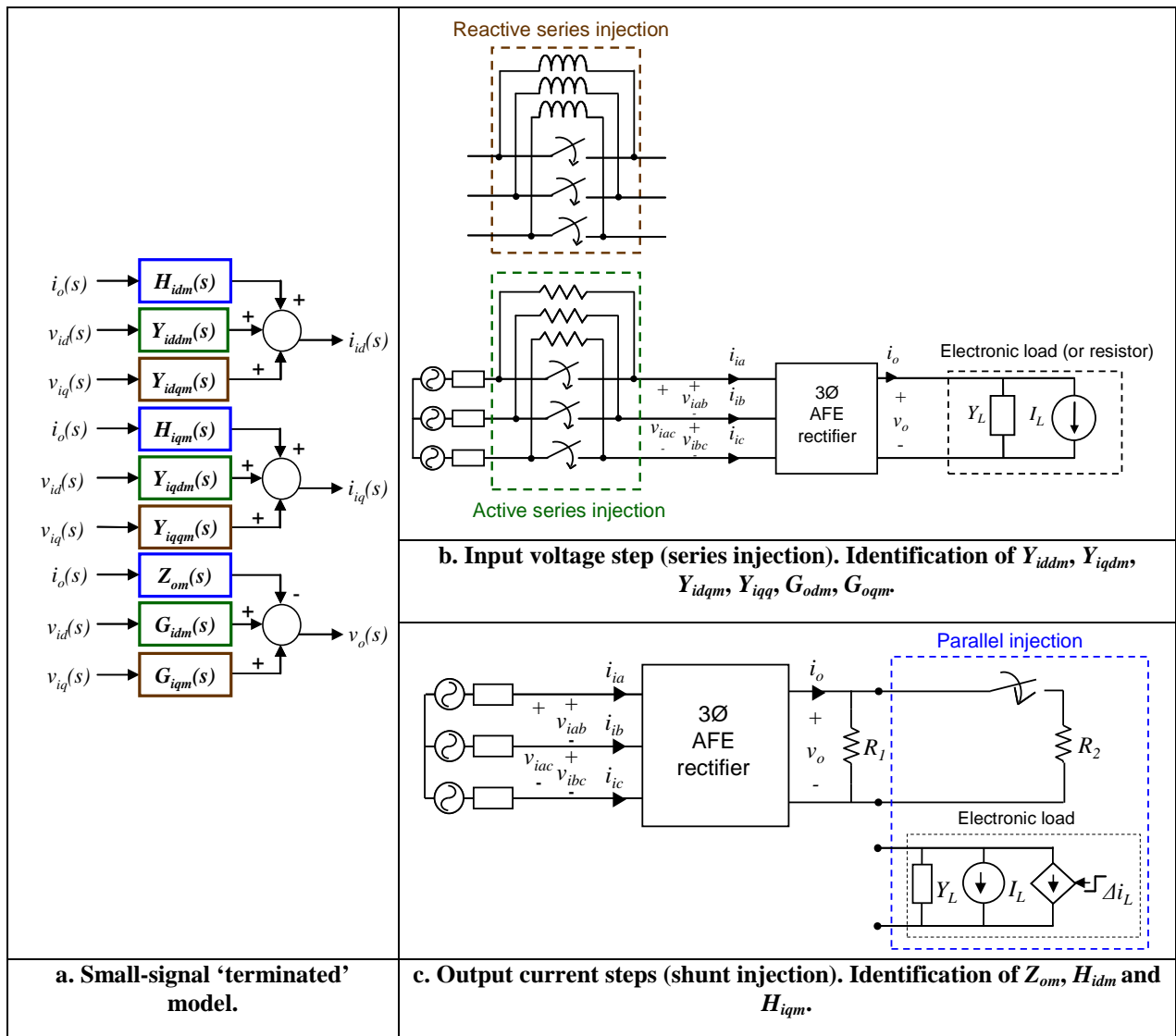


Fig. 10-10: Identification of behavioral model for a three-phase AFE with output voltage control (chapter 5).

10.4 Modeling and identification of bidirectional subsystems

In this thesis a bidirectional subsystem has been modeled and identified (chapter 8). The tackled subsystem is a switched reluctance starter-generator (SRSRG).

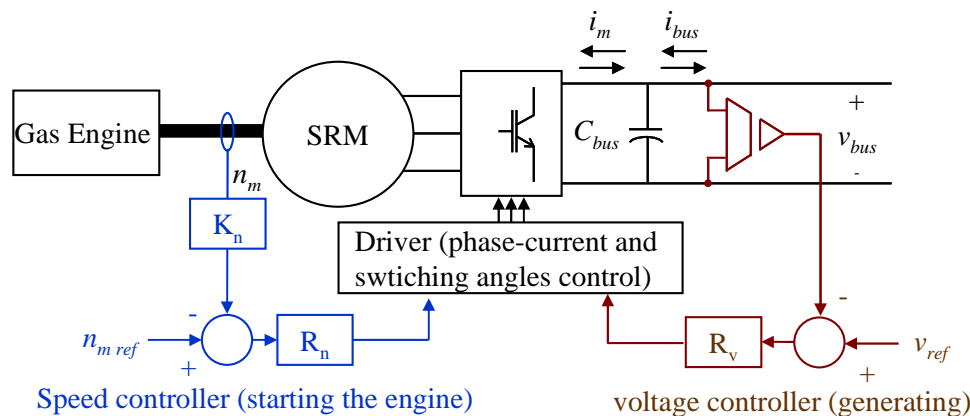
In this section, the key points of the proposed procedure are summarized and the key aspects are pointed out. Hence, a conceptual approach for modeling of other bidirectional subsystems is derived.

10.4.1 Revision of proposed model

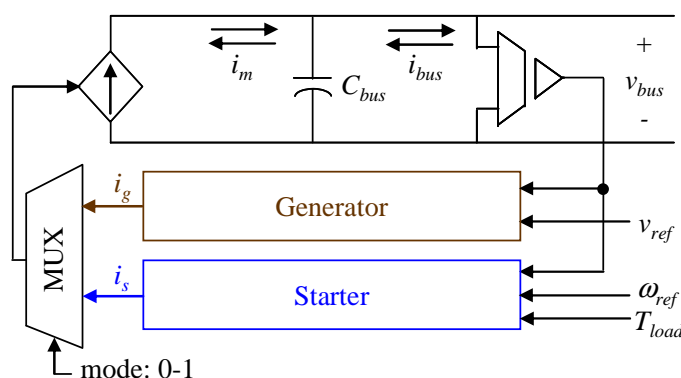
Fig. 10-11 summarizes the modeling of the SRSRG. It comprises a controlled current source in parallel with the DC link capacitor. The controlled current source is driven by two blocks, one for operation as a starter (current drawn from the DC bus) and other for operation as a generator (current delivered to the bus). This way, the same power circuit can be used to represent both operating modes. The operation of both blocks is summarized below (more details are given in chapter 8).

- The generator block includes the dynamics associated to the voltage regulation (including the compensator R_v and additional dynamics between the R_v output and the machine current i_m).
- The block starter comprises an electromechanical power balance and mechanical dynamics.

In both cases, the identification is carried out by applying some steps in current i_{bus} , torque T_{load} and speed reference ω_{ref} , as well as some static tests.



a. Subsystem diagram.



b. Behavioral model (grey-box approach).

Fig. 10-11: Behavioral modeling of a DC starter-generator system.

10.4.2 Conceptual approach for power converters

From the description given above, one may conclude that this modeling and identification approach could be adapted to address DC starter/generators based on other machine technology. Furthermore, such ideas could be also applied to address power electronics converters by modeling both ports in that manner. Fig. 10-12 depicts a conceptual diagram of a behavioral model for a bidirectional converter consisting of two ports, labeled as '1' and '2'. Each port could be modeled using a current source/sink in parallel with a capacitor. Each power source/sink could be driven by two networks 'A' and 'B', one for each power flow.

Network's inputs as well as their internal structure would depend on the considered application, but ideas similar to those exposed above (modeling of controlled signal loop and instantaneous power balance) may be also considered.

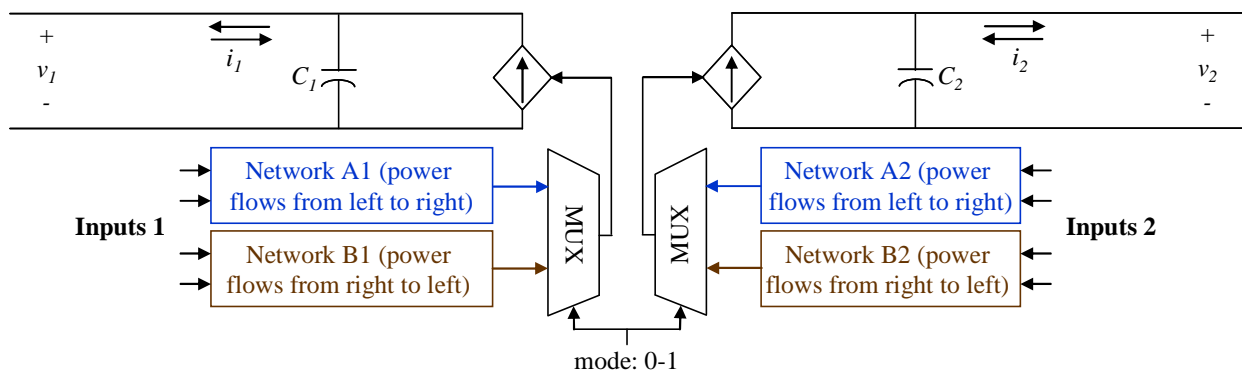


Fig. 10-12: Conceptual diagram of a behavioral model for a bidirectional DC-DC converter.

10.5 Conclusions

In this chapter, a review of the models and identification methods proposed in this thesis has been presented. Both methods have been described in a systematic manner, so that they could be used to address not only the converters (and power electronics based subsystems) tackled in this thesis, but also other ones that can be found in distributed power systems.

- First, the modeling and identification procedure of unidirectional converters (and subsystems) presented in this thesis has been briefly reviewed and described in a systematic manner. From such a systematic description, a model and an identification method for an active front end have been derived.
- Second, the modeling and identification of bidirectional converters have been discussed. First, the switched reluctance starter-generator addressed in chapter 8 has been reviewed, and conceptual ideas to model other starter-generators, as well as power converters, have been pointed out.

11 Conclusions, contributions and future work

11.1	Conclusions and contributions.....	339
11.1.1	Modeling	340
11.1.1.1	Description of contributions	340
11.1.1.2	Capabilities and limitations of the modeling technique	341
11.1.2	Identification	342
11.1.2.1	Description of contributions	342
11.1.2.2	Features and limitations of the identification technique.....	343
11.2	Future work.....	343
11.2.1	Modeling	343
11.2.2	Identification	344

11.1 Conclusions and contributions

The research work reported in this PhD thesis has focused on the development of system-level behavioral modeling and identification techniques for power electronics converters and subsystems.

This work has been developed to address the current lack of system-level models, herein referred to as “behavioral models”, oriented to integration of distributed power systems made up by multiple power electronics converters and subsystems which are provided by a variety of external manufacturers.

Fig. 11-1 shows a summary of main contributions, sorted into two groups: modeling and identification. Details about them are given throughout the next sections.

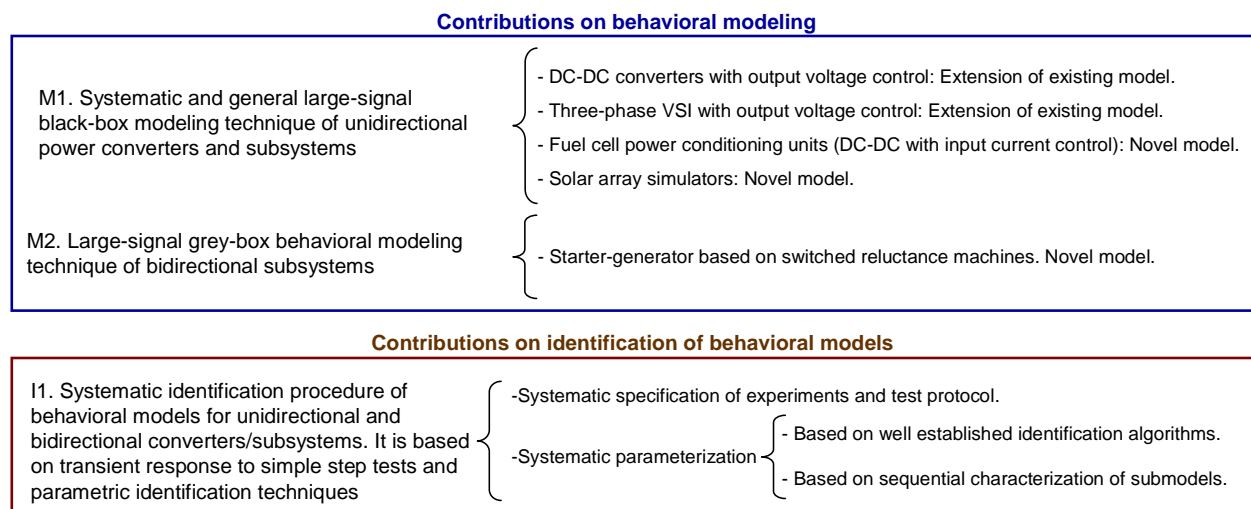


Fig. 11-1: Overview of main contributions of this thesis.

The main characteristics of the behavioral models as well as the identification method are described below:

- **Models characteristics:** The behavioral models reproduce the large-signal averaged behavior of the modeled power converter / subsystem, in terms of their input-output signals. These models are oriented to integration of power distribution systems made up by multiple power electronics converters and subsystems. They can be used to evaluate system-level dynamic and static response, including transient response, stability and energy efficiency among others.
- **Identification characteristics:** The model parameters are obtained from the transient response of the converter/subsystem under a set of simple and practical step tests. Thus, the system designer can obtain a model of the converters or subsystems even if no information is available due to manufacturer’s confidentiality.

In the following sections, a detailed description about the contributions is presented. Main conclusions about modeling and identification techniques are discussed as well, including most significant features and limitations.

11.1.1 Modeling

11.1.1.1 Description of contributions

Contributions on modeling are split into two groups: unidirectional subsystems/converters (M1) and bidirectional ones (M2).

M.1. A systematic and general procedure to develop large-signal black-box behavioral models of unidirectional power converters / subsystems has been presented. Starting from an existing modeling technique for DC-DC converters based on g-parameters models [138], [146], a general and systematic approach has been derived to address any power converter / subsystem. Essentially, the models are comprised of static networks cascaded to dynamic networks.

The technique has been applied to derive large-signal black-box models of the following subsystems:

- **M.1.1. DC-DC converters with output voltage control** (chapter 4). The presented model adds additional features in comparison to the existing one, such as soft-start networks as well as nonlinear modeling of static line and load regulation.
- **M.1.2. Three-phase voltage source inverters with output voltage control** (chapter 5). The existing model, oriented only to small-signal analysis within $d-q$ frame, has been extended to large-signal. Additional contributions are listed below:
 - **M.1.2.1. Orthogonal properties** of the $d-q$ output impedance of VSIs with linear and symmetric control scheme have been described and validated by simulation.
 - **M.1.2.2. Modeling under un-balanced conditions** in three and four wire systems (using delta/triangle transformers) have been addressed and validated by simulation.
- **M.1.3. DC-DC converters with input current control cascaded with fuel cells** (chapter 6). A novel large-signal behavioral model for this type of subsystems has been presented.
- **M.1.4. Solar Array Simulators** (chapter 7). A novel large-signal behavioral model has been described.

A review of guidelines for systematic derivation of models has been described in chapter 10. Thus, the bases to derive large-signal models of other subsystems have been stated.

M.2. A novel large-signal grey-box behavioral modeling approach for bidirectional subsystems has been presented. This technique has been **particularly applied to a switched reluctance starter-generator** (chapter 8). The model consists of the DC bus capacitor connected in parallel with a controlled current source/sink, which is driven by two networks: one for each operating mode (starter and generator). This model is referred to as a ‘grey-box’ because it partially represents the structure of the starter generator. A conceptual approach to extend the technique to other bidirectional subsystems has been introduced in chapter 10.

11.1.1.2 Capabilities and limitations of the modeling technique

All of the developed models have been validated by comparing the experimental response of the real converter/subsystem with the response of the corresponding model under a set of large-signal tests. As demonstrated, the models have the following capabilities and limitations.

Models capabilities:

The models have been proven to address properly the following phenomena.

- **Static behavior and transient behavior under large-signal perturbations**, including load transients, disturbances at the distribution bus, etc. (chapters 4 to 7).
- **Dynamic interactions between converters and subsystems**, including **instability** due to low-frequency constant-power-load behavior of regulated converters (chapter 4 and chapter 7).
- **Soft-start and inrush current under hot-swap** to the distribution bus (chapter 4 and chapter 5).

Models limitations:

However, as every model of a physical system, this modeling technique exhibits some limitations. Specifically, **the models have limited accuracy with converter/subsystems that exhibit dynamic nonlinearities**. The models have limited accuracy under the following situations:

- Modeling response of converters/subsystems with **continuous nonlinear dynamics under large perturbations** (large variations of operating point). In general, the higher the dependence on operating point, the lower the model accuracy. These limitations were evidenced in section 4.5.2, where a power supply with significant dynamics dependence on operating point was modeled.
- Modeling response of converters/subsystems with **discontinuous dynamics under perturbations around the discontinuity**. Such discontinuities can be due to non-smooth variations of the control parameters, jumps from DCM to CCM^{11.1} or jumps from voltage region to current region (solar array simulators), among others. Examples of this were analyzed in sections 4.5.1 and 7.5.

Such limitations are due to the fact that nonlinear modeling is addressed by LLMNs or gain-scheduled transfer functions, which are only an approximation to the true nonlinear dynamics. Nevertheless, it is worth remarking that, even in case of strong dependence on operating point, **LLMNs reproduce properly the subsystem response under relatively small perturbations**, so that the ‘local’ nonlinearities are slight.

Nevertheless, there is an exception for the latter limitations (related to discontinuous dynamics). It corresponds to the **grey-box model for starter-generators** described in chapter 8. This model includes a representation of the actual voltage regulator. Consequently, **it can address discontinuous nonlinearities related to the voltage controller** (anti-windup, clamping, etc).

^{11.1} Jumps from DCM to CCM may not lead to significant variations on the converter dynamics in case of buck-derived converters provided with current-mode-control (inner inductor current loop plus outer voltage loop) as the converter behaves as a current programmed source driven by the outer regulator under both operating modes.

11.1.2 Identification

11.1.2.1 Description of contributions

The contributions on identification described in this thesis are described below.

I.1: A systematic identification method of behavioral models, based on transient response measurements under step tests, has been originally presented in this thesis. Starting from the idea of using steps to identify behavioral “grey-box” models of DC-DC converters (which was firstly described in [135], [159]), a general and systematic procedure to identify behavioral models for any power converter / subsystems has been described. These methods have been applied on a variety of unidirectional subsystems/converters as well as a bidirectional starter-generator. The proposed identification method consists of two differentiated parts: experimental tests and parameterization of models (from measurements).

- **I.1.1. Experimental tests: A systematic definition of experiments and protocols for testing of power converters/subsystems has been presented.** The proposed tests (current and voltage steps) are easy to apply and can be carried out using passive loads and switches (and optionally electronic load^{11.2}). The key idea is to step only one input signal at each time while the others are kept constant. Practical implementations have been described for several unidirectional power converters/subsystems, including DC and three-phase AC interface (mapped into $d-q$ frame), as well as a bidirectional starter-generator.
- **I.1.2. Parameterization of models: A systematic procedure to identify the parameters of the behavioral models** has been described. Transfer functions, included in the dynamic networks of the behavioral models, are identified by applying **parametric identification techniques** on the transient response measurements. The static networks are simply identified from static tests. Two methods have been described to identify the transfer functions.
 - **Well established parametric identification algorithms** based on **minimization** of the sum of **squared prediction error** (i.e. difference between predicted output and measured output under step excitation) **has been originally applied to identify behavioral models.** Throughout this thesis, **Gauss-Newton iterative** search has been applied using the System Identification Toolbox of Matlab (*'oe'* function). The selected transfer function model structure is called **'Output Error'** (chapters 4 to 8). Using these algorithms, the identification can be successfully done even if the excitation signal is not an ideal step.
 - **An alternative method has been presented as an original contribution (chapter 9).** It consists in **splitting** the response as the **sum of responses of first and second order transfer functions**, followed by **sequential identification** of them by using **simple analytical expressions or normalized plots.** Using this method, minimization algorithms, which can be complex to use without dedicated tools, are avoided. However, this technique assumes an ideal step as input signal, meaning that it is effective only when the excitation signal resembles an ideal step. Moreover, the dynamics has to be well described by transfer functions whose dominating poles are well separated from each other.

^{11.2} The proposed tests have been inspired in a previous contribution oriented to identification of a grey-box behavioral model for DC-DC converter different from that considered in this thesis (model by J. Oliver, chapter 2). In the mentioned contribution, load steps are applied to identify a network comprised of passive components.

It is also worth remarking the work presented on cross-coupling of the identified transfer functions with the load/source used to set the operating point. A **simple method to quantify the importance of cross-coupling effects**, into time-domain, **has been originally proposed**. Moreover, **an existing method to remove cross-coupling effects**, based on frequency response measurements and oriented to DC-DC converters [150], has been **adapted to time-domain measurements and extended** to other power electronics converters or subsystems.

11.1.2.2 Features and limitations of the identification technique

Main features of the identification technique:

Compared to AC sweep tests, the most important advantage of step tests is the **practicality and simplicity of the experimental setup**.

Comparisons between experimental AC sweep test results and frequency response of identified models from step tests have demonstrated good performance of the identification technique.

It is worth remarking that **the first full identification method of behavioral models for three-phase VSIs** has been proposed in this thesis (chapter 5). Existing techniques were only oriented to the d-q output impedance and were based on AC sweep tests. The proposed technique, based on step tests, is significantly simpler from a practical point of view.

Limitations of the identification technique:

However, the step signal introduces simultaneous excitation at all frequencies. Its power spectral density decreases as the frequency increases. Therefore, **identification is more accurate at low frequency than at high frequency**. This is not the case when using AC sweep tests, as all the excitation energy is concentrated on only one frequency at each time.

Nevertheless, in the framework of system-level analysis and integration, low-frequency dynamics, which is typically related to the outer loop control and energy storage components (i.e. inductors, capacitors), is usually more important than high frequency dynamics. Moreover, the constant power load behavior of regulated converters, which is one of the most important concerns regarding system-level integration, is typically found within the control bandwidth, where the control stage is capable of keeping constant the regulated signal.

11.2 Future work

Future lines of research on behavioral modeling and identification may focus on the following topics.

11.2.1 Modeling

In terms of modeling, the following work may immediately follow this thesis:

- Development of large-signal behavioral models of other converters and subsystems, including those listed below, could be derived. To do so, guidelines presented in chapter 10 could be applied.
 - Three-phase rectifiers, both controlled (e.g. active front end rectifier) and un-controlled (diode rectifiers).

- Single phase AC converters, including inverters and power factor correctors.
- Bidirectional power electronics converters.
- Synchronous generators.
- Experimental validation of the modeling under un-balanced conditions for three-phase VSIs based on three wires and four wires with delta-triangle transfer function (validated at the moment only by simulation). Extend the modeling of un-balanced conditions to four wire systems based on four leg converters and split DC link capacitor.

From a longer term perspective, the following works could be carried out:

- Improvement of the modeling technique for power converters and subsystems with strong nonlinearities. In replacement of LLMNs with local feedback (used in this thesis), the following approaches could be considered, among others:
 - Nonlinear polynomial models, such as nonlinear output error model (NOE).
 - Local linear model networks with global feedback (introduced in section 4.5.3).
- Development of metrics to validate the models could be established. For instance, a ‘worst case’ validation tests could be defined, together with a threshold fitting percentage, so that the model would not be acceptable if the fitting percentage is below the above mentioned threshold.

11.2.2 Identification

Concerning identification, the following work may immediately follow this thesis:

- Extension of the identification technique to address other power electronics converters, according to the guidelines presented in chapter 10.

From a longer term perspective, the following works could be carried out:

- Instead of using a step signal as excitation signal, study other binary signals. For example, Pseudorandom Binary Signals (PRBS) could be used to modulate the switch used to make the load step. Compared to the step signal (which favors low-frequencies over high-frequencies), the PRBS features a flat spectrum, so no frequencies are favored.
- Exploration of Multiple Input Multiple Output (MIMO) identification algorithms to identify the full model from a single dataset. It may avoid the need of cross-coupling removal, but all the experiment should be carried out in a synchronized manner and captured in a single dataset.
- Development of techniques to better determine confidence on identification results. It would be interesting to determine the bandwidth for which the signal-to-noise ratio of the step is high enough, so that the model can be confidently identified. Quantification of fitting performance, in terms of frequency domain instead of time domain, is also a matter of interest.

12 Difussion of Results and related Projects and Collaborations

12.1 Publications	347
12.1.1 International Journal Papers	347
12.1.2 International Conference Papers	347
12.1.3 National Conference Papers	348
12.1.4 Other publications on behavioral modeling (not included in this thesis).....	348
12.1.4.1 International Journal Papers	348
12.1.4.2 International Conference Papers.....	349
12.1.4.3 National Conference Papers	349
12.2 Related Research and Development Projects.....	349
12.2.1 Private Projects.....	349
12.2.2 Public Projects.....	350
12.3 Collaboration with Research Centres and Universities.....	350

This work has been developed between 2008 and 2012 in the framework of several research and development projects, as well as research visits to other research centres and universities. The results of this thesis have been published in peer reviewed international journals, international conferences and national conferences.

Below, a list of the resulting publications, related R&D projects and research visits is provided.

12.1 Publications

12.1.1 International Journal Papers

- **V. Valdivia**, A. Barrado, A. Lazaro, P. Zumel, C. Raga, C. Fernandez, “Simple Modeling and Identification Procedures for “Black –Box” Behavioral Modeling of Power Converters Based on Transient Response Analysis”, **IEEE Transactions on Power Electronics**, vol. 24, issue 12, Dec. 2009. *Special Issue on Modeling and Advanced Control in Power Electronics*.
- C. Fernandez, P. Zumel, **V. Valdivia**, A. Fernandez-Herrero, A., M. Sanz, A. Lázaro, A. Barrado, “Simple model and experimental identification of a fuel cell based power supply oriented to system-level analysis”, **IEEE Transactions on Power Electronics**, vol 26, issue 7, July 2010.
- **V. Valdivia**, A. Lázaro, A. Barrado, P. Zumel, C. Fernández, M. Sanz, “Impedance Identification Procedure of Three-Phase Balanced Voltage Source Inverters Based on Transient Response Measurements” **IEEE Transactions on Power Electronics**, vol. 26, issue 12. Dec. 2011.
- **V. Valdivia**, A. Lázaro, A. Barrado, P. Zumel, C. Fernández, M. Sanz, “Black-Box Modeling of Three-Phase Inverters for System-Level Analysis” **IEEE Transactions on Industrial Electronics**, vol. 59, no. 9, September 2012. *Special Issue on The More Electric Aircraft: Power Electronics, Machine and Drives*.
- **V. Valdivia**, A. Barrado, A. Lazaro, M. Sanz, D. Lopez del Moral, C. Raga, “Black-Box Behavioral Modeling and Identification of DC-DC Converters with Input Current Control for Fuel Cell Power Conditioning”, **IEEE Transactions on Industrial Electronics**. **Accepted**.
- **V. Valdivia**, A. Barrado, A. Lázaro, R. Todd, A. Forsyth, F. Bryan, “Behavioural Modelling of a Switched Reluctance Generator for Aircraft Power Systems”, **IEEE Transactions on Industrial Electronics**, provisionally accepted (*currently under major revision*).

12.1.2 International Conference Papers

- **V. Valdivia**, A. Barrado, A. Lázaro, M. Sanz, D. López del Moral, C. Raga, “System-Level Black-Box Modeling of DC-DC Converters with Input Current Control for Fuel-Cells Power Conditioning” **IEEE APEC 2012**, Oral Presentation.
- **V. Valdivia**, A. Lázaro, A. Barrado, P. Zumel, C. Fernández, M. Sanz, “System-Level Behavioral Black-Box Modeling of Three-Phase DCAC Converters for the More-Electric-Aircraft”, **SAE Aerotech Conference and Exposition 2011**, Oral Presentation.

- **V. Valdivia**, A. Barrado, A. Lazaro, C. Fernández, P. Zumel, “System-Level Behavioral Black-Box Modeling of DC-DC Converters for the More-Electric-Aircraft Based on Time Domain Measurements” **SAE Aerotech Conference and Exposition 2011**, Oral Presentation.
- **V. Valdivia**, A. Barrado, A. Lázaro, P. Rueda, A. Fernández, F. Tonicello, O. Mourra, “Analysis of Dynamic Interactions Between Solar Array Simulators and Spacecraft Power Conditioning and Distribution Units”, **ESPC 2011**, Oral Presentation.
- **V. Valdivia**, A. Lázaro, A. Barrado, P. Zumel, C. Fernández, Impedance identification method of three-phase balanced voltage source inverters based on load current steps, **IEEE COMPEL 2010**, Oral Presentation.
- **V. Valdivia**, A. Lázaro, A. Barrado, P. Zumel, C. Fernández, M. Sanz, “Black-Box Modeling of Three Phase Voltage Source Inverters Based on Transient Response Analysis”, **IEEE APEC 2010**, Oral Presentation.
- **V. Valdivia**, A. Barrado, A. Lazaro, C. Fernández, P. Zumel, “Black-Box Modeling of DC-DC Converters Based on Transient Response Analysis and Parametric Identification Methods”, **IEEE APEC 2010**, Oral Presentation.
- **V. Valdivia**, A. Barrado, A. Lazaro, P. Zumel, C. Raga, “Easy Identification Procedure for Behavioral “Black Box” Modeling of Power Electronics Converters with Reduced Order Based on Transient Response Analysis” , **IEEE APEC 2009**. Oral presentation.

12.1.3 National Conference Papers

- **V. Valdivia**, A. Barrado, A. Lázaro, P. Zumel, C. Fernández, “Modelado Caja Negra de Convertidores DC-DC Basado en la Respuesta Transitoria y en Algoritmos de Identificación Paramétrica”, **SAAEI 2010**, Oral Presentation.
- **V. Valdivia**, A. Barrado, A. Lazaro, P. Zumel, M. Sanz, “Procedimientos Sencillos de Modelado e Identificación de Modelos Comportamentales “Caja Negra” Basados en el Análisis de la Respuesta Transitoria”, **SAAEI 2009**, Oral Presentation.
- **V. Valdivia**, A. Barrado, A. Lazaro, C. Fernandez, M. Sanz, “Modelado Comportamental “Caja Negra” y Técnica de Identificación de Inversores Trifásicos con Tensión de Salida Controlada”, **SAAEI 2009**, Oral Presentation.

12.1.4 Other publications on behavioral modeling (not included in this thesis)

12.1.4.1 International Journal Papers

- **V. Valdivia**, D. Lopez del Moral, M. Sanz, A. Barrado, A. Lázaro, F. Tonicello, “Simple modelling method of tantalum capacitors”, **IET Electronics Letters**, Vol. 47, issue 1, Jan 2011.

12.1.4.2 International Conference Papers

- **V. Valdivia**, D. López del Moral, M. Sanz, A. Barrado, A. Lázaro, F. Tonicello, “Simple and Systematic Modeling Procedure of Capacitors Based on Frequency Response”, **IEEE APEC 2011** Oral Presentation.
- **V. Valdivia**, A. Barrado, A. Lazaro, P. Zumel, “New Nonlinear Dynamic Behavioral "Black Box" Modeling and Identification Procedure for Voltage Controlled Buck Derived DC-DC Converters”, **IEEE APEC 2009**, Oral presentation.
- **V. Valdivia**, A. Lazaro, A. Barrado, M. Sanz, C. Raga, C. Fernandez, “Behavioral Modeling of Current Controlled Inverters for Large Signal Analysis”, **IEEE IECON 2008**, Poster.

12.1.4.3 National Conference Papers

- **V. Valdivia**, A. Lázaro, A. Barrado, M. Sanz, C. Raga, C. Fernández, “Modelado Comportamental de Inversores Controlados en Corriente para Análisis en Gran Señal”, **SAAEI 2008**, Oral Presentation.
- **V. Valdivia**, A. Barrado, A. Lazaro, P. Zumel, C. Fernandez, “Modelado Comportamental Tipo “Caja Gris” de Convertidores Derivados del Reductor y Controlados en Modo Tensión”, **SAAEI 2009**, Poster.
- C. Fernández, P. Zumel, **V. Valdivia**, A. Fernández-Herrero, M. Sanz, A. Lázaro, A. Barrado, “Identificación y modelo comportamental de un sistema basado en pila de combustible de metanol”, **SAAEI 2010**, Oral Presentation.
- **V. Valdivia**, D. López del Moral, C. M. Sanz, A. Barrado, A. Lázaro, “Procedimiento Simple y Sistemático de Modelado de Condensadores Basado en la Respuesta en Frecuencia” **SAAEI 2011**, Oral Presentation.

12.2 Related Research and Development Projects

Part of this work has been developed in the framework of the following research and development projects. A brief description is also included.

12.2.1 Private Projects

- **High Voltage Direct Current (HVDC). Founded by EADS CASA.** A “More Electric Aircraft” Power Distribution based on 270 V_{DC} bus was studied in this project. As part of it, the behavioral modeling method of three-phase converters (chapter 5) was developed, as well as the first steps into the black-box modeling of DC-DC converters (chapter 4) and the simplified identification method presented in chapter 9.
- **Cátedra Besel (long term collaboration with Besel S.A).** As part of this project, the modeling of power conditioning units based on fuel cells and DC-DC converters with input current control was carried out (chapter 6).

12.2.2 Public Projects

The work presented in this thesis has been developed in the frame work of the following projects founded with public founding:

- **Modelado y Diseño de Sistemas Electrónicos Aeroespaciales. Nivel Subsistema. (Modelling and Design of Aerospace Electronics Systems. Subsystem level).** Founded by the Spanish Ministry of Education and Science.
- **Sistemas de Alimentación para Aplicaciones Embarcadas y Portátiles basadas en Fuentes y Dispositivos de Almacenamiento de Energía Emergentes (Power systems for onboard and portable applications based on emerging energy sources and storage devices).** Founded by the Spanish Ministry of Science and Innovation.

12.3 Collaboration with Research Centres and Universities

Part of the results of this PhD thesis has been obtained during research visits carried out by the author. These are listed and briefly described below.

- **European Space Research and Technology Centre (ESTEC), European Space Agency (ESA). From September to December 2009.** The behavioral modeling and identification technique of solar array simulators was developed, as well as the analysis of dynamic interactions between it and the power conditioning and distribution units (chapter 7). The latter part has had a remarkable impact on the space industry. It was demonstrated that some solar array simulators typically used in space industry can lead to wrong conclusions about stability of power conditioning and distribution units for satellites. This issue was communicated to European companies that were making use of such simulators.
- **Rolls Royce University Technology Centre. Power Conversion Group. University of Manchester. From January to February 2011.** During this research visit, the author developed the behavioral modeling method of starter generators based on switched reluctance machines (chapter 8).
- **Center for Power Electronics Systems (CPES). Virginia Polytechnic Institute and State University. From February to April 2012.** The author developed work related to analysis of confidence on identification results. This work is beyond the scope of this thesis.

A. Appendix

A.1. Mathematical derivation of behavioral models from switching models	353
A.1.1. Buck converter (chapter 3)	353
A.1.1.1. Small-signal terminal modeling of the power stage	354
A.1.1.2. Small-signal terminal modeling of the control stage	356
A.1.1.3. Small-signal terminal modeling of the closed-loop converter	356
A.1.1.4. Numerical data: theoretical transfer functions	357
A.1.1.5. Numerical data: identified transfer functions	358
A.1.2. Three-phase voltage source inverter (chapter 5)	359
A.1.2.1. Small-signal terminal d-q modeling of the power stage	361
A.1.2.2. Small-signal terminal d-q modeling of the control stage	362
A.1.2.3. Small-signal terminal d-q modeling of the closed-loop converter	364
A.1.2.4. Remarks on linear and orthogonal properties of the output impedance	364
A.1.2.5. Numerical data: identified transfer functions and simulated model	365
A.2. Black-box model of buck-boost converter	367
A.2.1. Converter description	367
A.2.2. Analysis of linearity	367
A.2.3. Black-box model parameters	368
A.3. Small-signal stability analysis of power distribution systems	371
A.3.1. Basics	371
A.3.2. Stability of intermediate bus architecture (chapter 4)	371
A.3.3. Stability of spacecraft system involving a solar array simulator (chapter 7)	374
A.4. Some mathematical aspects about parametric identification	377
A.4.1. Model structures	377
A.4.1.1. Equation error family of models	377
A.4.1.2. Output error family of models	378
A.4.2. Optimization problem	379
A.4.2.1. The prediction error method	379
A.4.2.2. ARX model: a linear optimization problem	380
A.4.2.3. OE model: a nonlinear optimization problem	381
A.4.2.4. ARMAX and BJ models	382
A.4.2.5. Pre-filtering as a way of tuning the noise model	383

A.1. Mathematical derivation of behavioral models from switching models

In this appendix, g-parameters behavioral models of a DC-DC converter and a three-phase VSI, presented in chapter 3 and 5 respectively, are derived analytically by following a systematic procedure.

A.1.1. Buck converter (chapter 3)

Fig. A-1 shows the switching model of this converter (it was originally presented in Fig. 3-6). The control stage is comprised of an inner current loop and an outer voltage loop.

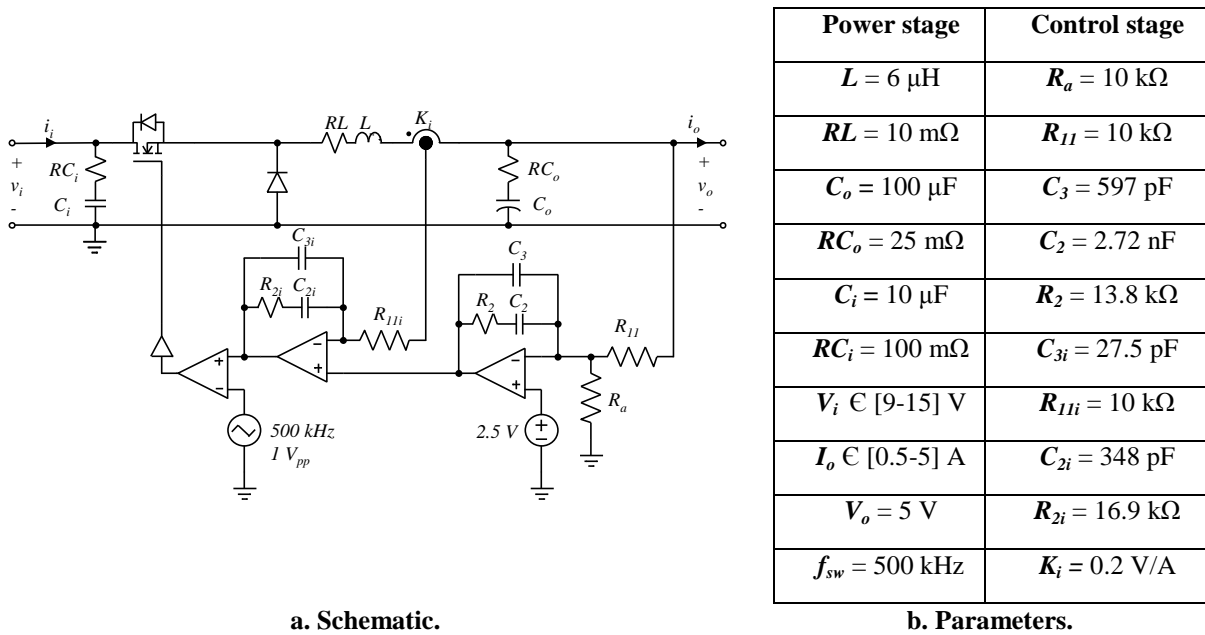


Fig. A-1: Current-Mode-Controlled (CMC) buck converter: switching model.

The small-signal g-parameters model corresponding to this converter is reminded in Fig. A-2. It can be described by the equations shown below.

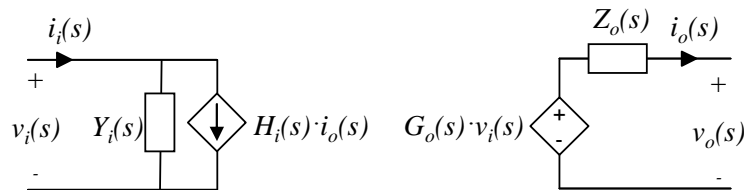


Fig. A-2: Terminal g-parameters black-box model for a DC-DC converter.

$$\begin{pmatrix} i_i(s) \\ v_o(s) \end{pmatrix} = \begin{pmatrix} Y_i(s) & H_i(s) \\ G_o(s) & -Z_o(s) \end{pmatrix} \cdot \begin{pmatrix} v_i(s) \\ i_o(s) \end{pmatrix} \quad (\text{A-1})$$

A g-parameters behavioral model can be obtained from switching model in a systematic way as follows:

- First, obtain a conventional small-signal model by averaging the power stage, followed by linearization on a local operating point.

- Second, small-signal input-output models for the power stage and the control stage are obtained separately.
- Third, both models are blended together to build a model of the overall closed-loop converter.

The small-signal model of the power converter herein analyzed can be explained by means of the block diagram depicted in Fig. A-3. Every transfer function related only to the power stage is denoted by subscript *OL*, which means ‘open loop’.

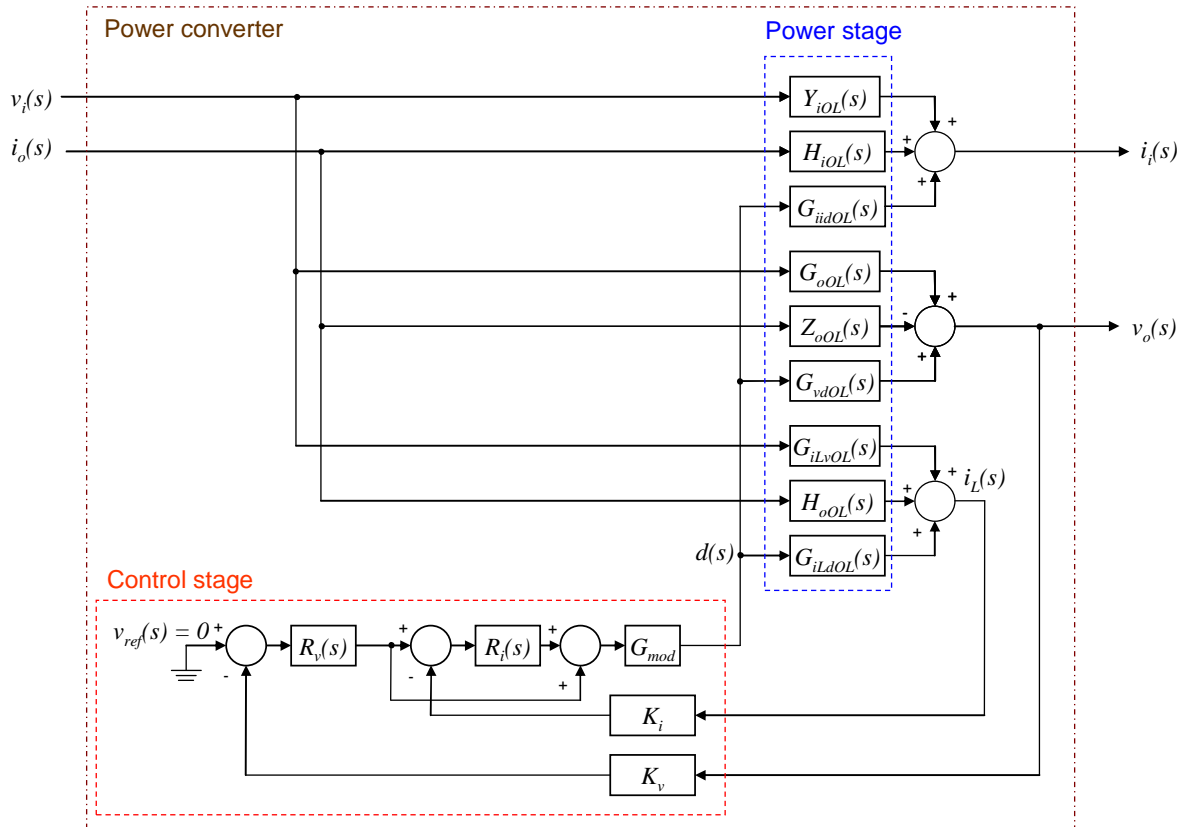


Fig. A-3: Small-signal model of an average current-mode-controlled DC-DC converter.

Below, analytical expressions for the transfer functions into Fig. A-3 are derived.

A.1.1.1. Small-signal terminal modeling of the power stage

The conventional small-signal terminal model for the buck converter under CCM is shown in Fig. A-4.

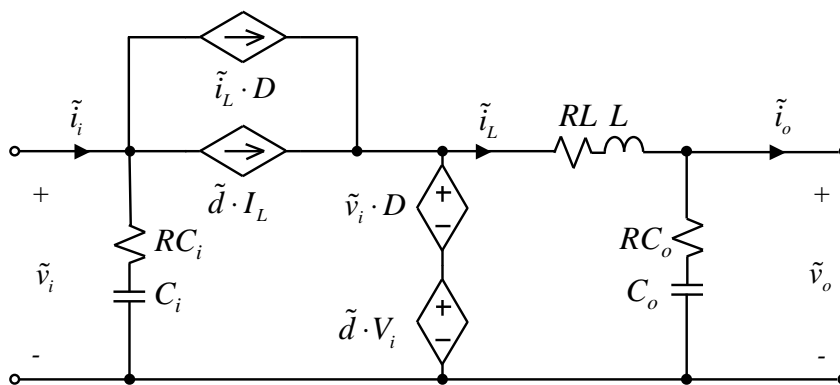


Fig. A-4: Small-signal model for the buck-converter under CCM.

The sough terminal model is characterized by output current, input voltage and duty cycle as model inputs, and output voltage and input current as model outputs. This is described below.

$$\begin{pmatrix} i_i(s) \\ v_o(s) \\ i_L(s) \end{pmatrix} = \begin{pmatrix} G_{iidOL}(s) & Y_{iOL}(s) & H_{iOL}(s) \\ G_{vdOL}(s) & G_{oOL}(s) & -Z_{oOL}(s) \\ G_{iLdOL}(s) & G_{iLvOL}(s) & H_{oOL}(s) \end{pmatrix} \begin{pmatrix} d(s) \\ v_i(s) \\ i_o(s) \end{pmatrix} \quad (\text{A-2})$$

The following definitions are considered for the inductor impedance and capacitors admittance.

$$Z_L(s) = RL + s \cdot L, \quad Y_{Co}(s) = \frac{s \cdot C_o}{s \cdot C_o \cdot RC_o + 1}, \quad Y_{Ci}(s) = \frac{s \cdot C_i}{s \cdot C_i \cdot RC_i + 1} \quad (\text{A-3})$$

By applying perturbations on only one input signal while the others are kept constant, the following expressions are derived:

$$\begin{aligned} i_i \Leftrightarrow & \begin{cases} G_{iidOL}(s) = \left. \frac{i_i(s)}{d(s)} \right|_{v_i(s)=0, i_o(s)=0} = I_L + V_i \cdot D \cdot \frac{Y_{Co}(s)}{Z_L(s) \cdot Y_{Co}(s) + 1} \\ Y_{iOL}(s) = \left. \frac{i_i(s)}{v_i(s)} \right|_{d(s)=0, i_o(s)=0} = Y_{Ci}(s) + D^2 \cdot \frac{Y_{Co}(s)}{Z_L(s) \cdot Y_{Co}(s) + 1} \\ H_{iOL}(s) = \left. \frac{i_i(s)}{i_o(s)} \right|_{d(s)=0, v_i(s)=0} = D \cdot \frac{1}{Z_L(s) \cdot Y_{Co}(s) + 1} \end{cases} \\ v_o \Leftrightarrow & \begin{cases} G_{vdOL}(s) = \left. \frac{v_o(s)}{d(s)} \right|_{v_i(s)=0, i_o(s)=0} = V_i \cdot \frac{1}{Z_L(s) \cdot Y_{Co}(s) + 1} \\ G_{oOL}(s) = \left. \frac{v_o(s)}{v_i(s)} \right|_{d(s)=0, i_o(s)=0} = D \cdot \frac{1}{Z_L(s) \cdot Y_{Co}(s) + 1} \\ Z_{oOL}(s) = \left. -\frac{v_o(s)}{i_o(s)} \right|_{d(s)=0, v_i(s)=0} = \frac{Z_L(s)}{Z_L(s) \cdot Y_{Co}(s) + 1} \end{cases} \quad (\text{A-4}) \\ i_L \Leftrightarrow & \begin{cases} G_{iLdOL}(s) = \left. \frac{i_L(s)}{d(s)} \right|_{v_i(s)=0, i_o(s)=0} = V_i \cdot \frac{Y_{Co}(s)}{Z_L(s) \cdot Y_{Co}(s) + 1} \\ G_{iLvOL}(s) = \left. \frac{i_L(s)}{v_i(s)} \right|_{d(s)=0, i_o(s)=0} = D \cdot \frac{Y_{Co}(s)}{Z_L(s) \cdot Y_{Co}(s) + 1} \\ H_{oOL}(s) = \left. \frac{i_L(s)}{i_o(s)} \right|_{d(s)=0, v_i(s)=0} = \frac{1}{Z_L(s) \cdot Y_{Co}(s) + 1} \end{cases} \end{aligned}$$

Excepting $Z_{oOL}(s)$ and $H_{oOL}(s)$, these transfer functions are dependant of operating point. It can be expressed only as a function of model inputs, V_i , I_o , by means of the following expressions (V_o is fixed due to the integral action of the voltage compensator).

$$I_L = I_o, \quad D = \frac{V_o + Z_L(0) \cdot I_o}{V_i} \quad (\text{A-5})$$

A.1.1.2. Small-signal terminal modeling of the control stage

The control stage, shown in Fig. A-1, can be represented by the small-signal model depicted in Fig. A-5. The modulator has been simply modeled by means of a proportional block.

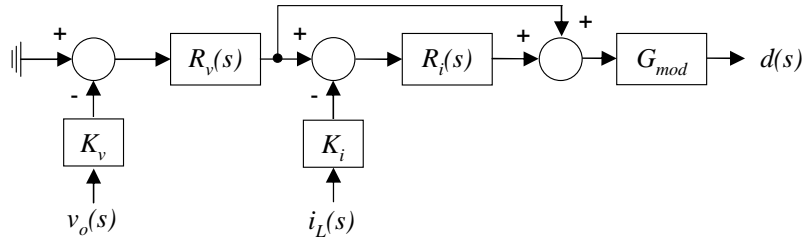


Fig. A-5: Small-signal model for the control stage of a buck-converter with averaged current mode control.

Each component shown in Fig. A-5 is defined as follows (the regulators are PI with high frequency attenuation, so-called ‘type 2’ regulators):

$$\left\{ \begin{array}{l} K_i = 0.2, K_v = 1, G_{\text{mod}} = 1 \\ R_i(s) = \left[\frac{\frac{1}{C_{3i} \cdot s} \cdot \left(R_{2i} + \frac{1}{C_{2i} \cdot s} \right)}{\frac{1}{C_{3i} \cdot s} + R_{2i} + \frac{1}{C_{2i} \cdot s}} \right] \cdot \frac{1}{R_{11i}}, R_v(s) = \left[\frac{\frac{1}{C_3 \cdot s} \cdot \left(R_2 + \frac{1}{C_2 \cdot s} \right)}{\frac{1}{C_3 \cdot s} + R_2 + \frac{1}{C_2 \cdot s}} \right] \cdot \frac{1}{R_{11}} \end{array} \right. \quad (\text{A-6})$$

By analyzing the model shown in Fig. A-5, the duty cycle can be expressed as a function of the feedback signals as follows. Auxiliary transfer functions $F_v(s)$ and $F_i(s)$ are herein defined to simplify the subsequent mathematics.

$$d(s) = \left(\underbrace{-G_{\text{mod}} \cdot R_v(s) \cdot (1 + R_i(s))}_{F_v(s)} \quad \underbrace{-G_{\text{mod}} \cdot K_i \cdot R_i(s)}_{F_i(s)} \right) \cdot \begin{pmatrix} v_o(s) \\ i_L(s) \end{pmatrix} \quad (\text{A-7})$$

A.1.1.3. Small-signal terminal modeling of the closed-loop converter

Finally, the power stage model and the control stage model are blended to build a terminal model of the closed-loop converter. To simplify the subsequent mathematics, the following transfer function for the combined inner-outer loop gain is defined:

$$T_l(s) = F_v(s) \cdot G_{\text{vdOL}}(s) + F_i(s) \cdot G_{\text{iLdOL}}(s) \quad (\text{A-8})$$

By combining (A-2) with (A-7) and considering (A-8), the duty cycle can be exclusively expressed as a function of model inputs as follows:

$$d(s) = \left(\frac{-F_v(s) \cdot G_{\text{oOL}}(s) + F_i(s) \cdot G_{\text{iLvOL}}(s)}{1 + T_l(s)} \quad \frac{-F_v(s) \cdot Z_{\text{oOL}}(s) + F_i(s) \cdot H_{\text{oOL}}(s)}{1 + T_l(s)} \right) \cdot \begin{pmatrix} v_i(s) \\ i_o(s) \end{pmatrix} \quad (\text{A-9})$$

By replacing (A-9) into (A-2), the $v_o(s)$ and $i_i(s)$ dependence on $d(s)$ can be removed, and the following transfer functions are obtained for the closed-loop black-box model:

$$\left\{ \begin{array}{l} G_o(s) = G_{oOL}(s) - G_{vdOL}(s) \cdot \frac{F_v(s) \cdot G_{oOL}(s) + F_i(s) \cdot G_{viLOL}(s)}{1 + T_l(s)} \\ Z_o(s) = Z_{oOL}(s) + G_{vdOL}(s) \cdot \frac{-F_v(s) \cdot Z_{oOL}(s) + F_i(s) \cdot H_{oOL}(s)}{1 + T_l(s)} \\ Y_i(s) = Y_{iOL}(s) - G_{iidOL}(s) \cdot \frac{F_v(s) \cdot G_{oOL}(s) + F_i(s) \cdot G_{viLOL}(s)}{1 + T_l(s)} \\ H_i(s) = H_{iOL}(s) - G_{iidOL}(s) \cdot \frac{-F_v(s) \cdot Z_{oOL}(s) + F_i(s) \cdot H_{oOL}(s)}{1 + T_l(s)} \end{array} \right. \quad (\text{A-10})$$

By expressing (A-10) as a function of power stage parameters and rearranging, the following equations are derived. Note that D is expressed as a function of model inputs in (A-5).

$$\left\{ \begin{array}{l} G_o(s) = \frac{D}{1 + Y_{Co}(s) \cdot Z_L(s) + G_{mod} \cdot V_i \cdot (R_v(s) \cdot (1 + R_i(s)) + R_i(s) \cdot K_i \cdot Y_{Co}(s))} \\ Z_o(s) = \frac{Z_L(s) + G_{mod} \cdot V_i \cdot K_i \cdot R_i(s)}{1 + Y_{Co}(s) \cdot Z_L(s) + G_{mod} \cdot V_i \cdot (R_v(s) \cdot (1 + R_i(s)) + R_i(s) \cdot K_i \cdot Y_{Co}(s))} \\ Y_i(s) = Y_{Ci}(s) - \frac{G_{mod} \cdot I_o \cdot D \cdot (R_v(s) \cdot (1 + R_i(s)) + R_i(s) \cdot K_i \cdot Y_{Co}(s)) - Y_{Co}(s) \cdot D^2}{1 + Y_{Co}(s) \cdot Z_L(s) + G_{mod} \cdot V_i \cdot (R_v(s) \cdot (1 + R_i(s)) + R_i(s) \cdot K_i \cdot Y_{Co}(s))} \\ H_i(s) = \frac{D + G_{mod} \cdot (I_o \cdot (R_v(s) \cdot Z_L(s) + R_i(s) \cdot (-K_i + R_v(s) \cdot Z_L(s))) + V_i \cdot R_v(s) \cdot D \cdot (1 + R_i(s)))}{1 + Y_{Co}(s) \cdot Z_L(s) + G_{mod} \cdot V_i \cdot (R_v(s) \cdot (1 + R_i(s)) + R_i(s) \cdot K_i \cdot Y_{Co}(s))} \end{array} \right. \quad (\text{A-11})$$

A.1.1.4. Numerical data: theoretical transfer functions

The transfer functions corresponding to the simulated black-box model are given below. These transfer functions have been obtained from numerical analysis of the above shown transfer functions, evaluated for the following operating points.

- $Z_o(s)$ has been evaluated for $V_i = 12$ V.
- $H_i(s)$ has been evaluated for $V_i = 12$ V and $I_o = 2.5$ A.
- $Y_i(s)$ has been evaluated for $V_i = 12$ V and $I_o = 2.5$ A.
- $G_o(s)$ has been evaluated for $V_i = 9$ V, $V_i = 15$ V and $I_o = 2.5$ A.

$$\begin{aligned}
Z_o(s) &:= \frac{1.28e34s + 1.93e29s^2 + 1.03e24s^3 + 2.43e18s^4 + 2.5e12s^5 + 872907.0s^6}{9.55e34s + 2.22e30s^2 + 1.82e25s^3 + 6.35e19s^4 + 8.64e13s^5 + 3.49e7s^6 + 1.92e39} \\
H_i(s) &:= \frac{4.0e33s + 4.77e28s^2 + 1.83e23s^3 + 2.36e17s^4 + 4.26e10s^5 + 8.1e37}{9.55e33s + 2.22e29s^2 + 1.82e24s^3 + 6.35e18s^4 + 8.64e12s^5 + 3.49e6s^6 + 1.92e38} \\
Y_i(s) &:= \frac{8.75e38s + 4.56e34s^2 + 1.09e30s^3 + 9.05e24s^4 + 3.17e19s^5 + 4.32e13s^6 + 1.75e7s^7 - 1.68e42}{1.0e39s + 2.46e34s^2 + 2.38e29s^3 + 1.09e24s^4 + 2.45e18s^5 + 2.51e12s^6 + 872907.0s^7 + 1.92e43} \\
G_o9(s) &:= \frac{1.26e27s^2 + 1.22e22s^3 + 2.62e16s^4 + 9.14e9s^5}{6.37e33s + 1.49e29s^2 + 1.22e24s^3 + 4.65e18s^4 + 8.64e12s^5 + 3.49e6s^6 + 1.28e38} \\
G_o15(s) &:= \frac{3.35e26s^2 + 3.24e21s^3 + 6.99e15s^4 + 2.44e9s^5}{5.97e33s + 1.39e29s^2 + 1.14e24s^3 + 3.81e18s^4 + 4.32e12s^5 + 1.75e6s^6 + 1.2e38}
\end{aligned} \tag{A-12}$$

$Y_i(s)$ and $H_i(s)$ require the following post-processing actions, as explained in chapter 4:

$$Y_{i0}(s) = Y_i(s) - Y_i(0), \quad H_{iL}(s) = H_i(s) \cdot \frac{V_{ss}}{H_i(0)} \tag{A-13}$$

This yields the following expressions:

$$\begin{aligned}
Y_{i0}(s) &:= \frac{7.7e40s + 3.82e36s^2 + 8.92e31s^3 + 7.32e26s^4 + 2.56e21s^5 + 3.47e15s^6 + 1.4e9s^7 + 3.85e41}{8.03e40s + 1.97e36s^2 + 1.9e31s^3 + 8.72e25s^4 + 1.96e20s^5 + 2.01e14s^6 + 6.98e7s^7 + 1.54e45} \\
H_{iL}(s) &:= \frac{1.89e35s + 2.26e30s^2 + 8.69e24s^3 + 1.12e19s^4 + 2.02e12s^5 + 3.84e39}{3.82e34s + 8.89e29s^2 + 7.28e24s^3 + 2.54e19s^4 + 3.46e13s^5 + 1.4e7s^6 + 7.7e38}
\end{aligned} \tag{A-14}$$

A.1.1.5. Numerical data: identified transfer functions

The transfer functions identified from step tests in chapter 3 are given below:

$$\begin{aligned}
Z_o(s) &:= \frac{0.02353s^3 + 1.71310^4 \cdot s^2 + 1.78710^9 \cdot s + 6.23210^9}{s^3 + 2.41610^5 \cdot s^2 + 1.18610^{10} \cdot s + 2.69710^{14}} \\
G_o(s) &:= \frac{0.0006489s^4 + 330s^3 + 7.61910^8 \cdot s^2 + -2.77510^{10} \cdot s + 9.31510^{13}}{s^4 + 4.36810^5 \cdot s^3 + 9.11510^{10} \cdot s^2 + 4.45110^{15} \cdot s + 1.00810^{20}} \\
H_i(s) &:= \frac{-0.001387s^4 + 307s^3 + 1.71710^{10} \cdot s^2 + 2.0810^{15} \cdot s + 4.63110^{19}}{s^4 + 4.96910^5 \cdot s^3 + 8.95510^{10} \cdot s^2 + 4.20510^{15} \cdot s + 9.21310^{19}} \\
Y_i(s) &:= \frac{20.04s - 2.471 \cdot 10^4}{s + 4.00510^5}
\end{aligned} \tag{A-15}$$

A.1.2. Three-phase voltage source inverter (chapter 5)

A switching model of the three-phase voltage source inverter (VSI) is shown in Fig. A-6 (it was originally presented in Fig. 5-24). It is provided with inner inductor current loop plus outer voltage loop, both of them implemented into stationary ‘ α - β ’ frame. The fundamental frequency is 50 Hz.

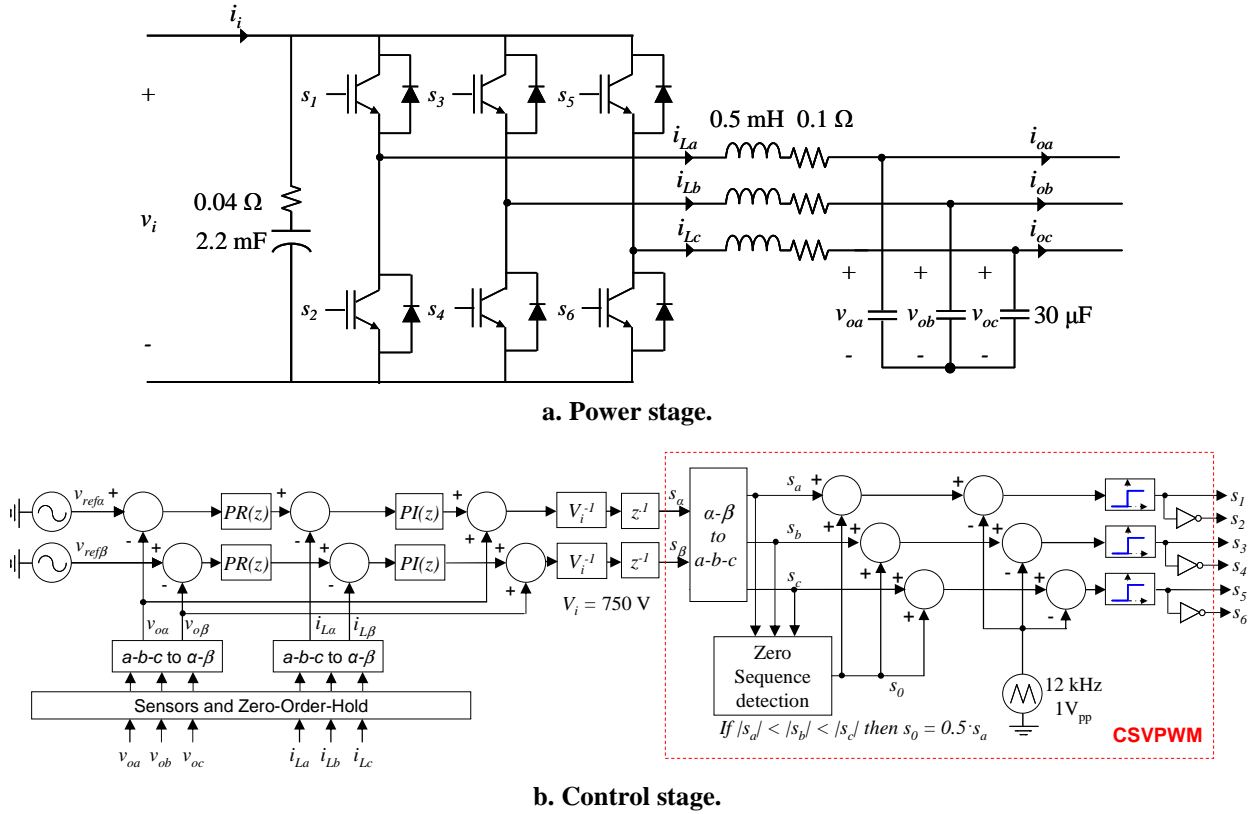
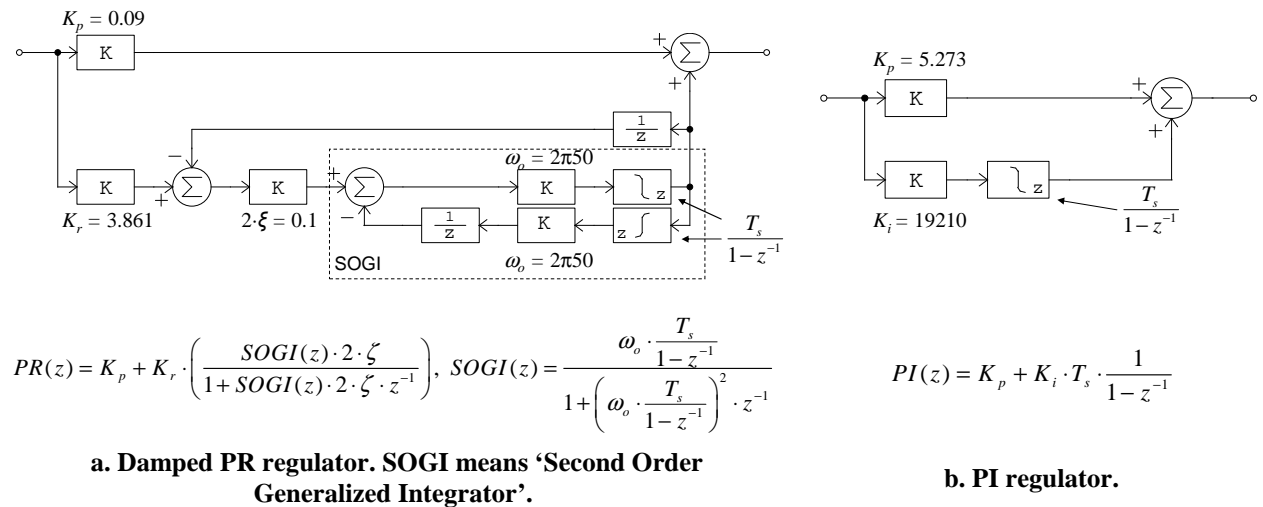


Fig. A-6: Three-phase VSI simulated in PSIM (switching model).

Both regulators have been implemented in PSIM using Backward Euler integrators and unit-delay blocks (see Fig. A-7). The sampling frequency is $f_s = T_s^{-1} = 24$ kHz (double sampling per switching period) and $\omega_o = 2\pi 50$ rad/seg. Both the voltage sensors and the current sensors feature unity gain.



$$PR(z) = K_p + K_r \cdot \left(\frac{SOGI(z) \cdot 2 \cdot \zeta}{1 + SOGI(z) \cdot 2 \cdot \zeta \cdot z^{-1}} \right), \quad SOGI(z) = \frac{\omega_o \cdot \frac{T_s}{1-z^{-1}}}{1 + \left(\omega_o \cdot \frac{T_s}{1-z^{-1}} \right)^2 \cdot z^{-1}}$$

$$PI(z) = K_p + K_i \cdot T_s \cdot \frac{1}{1-z^{-1}}$$

a. Damped PR regulator. SOGI means ‘Second Order Generalized Integrator’.

b. PI regulator.

Fig. A-7: Discrete voltage and current regulators.

The small-signal terminal g-parameters model for this converter is reminded in Fig. A-8.

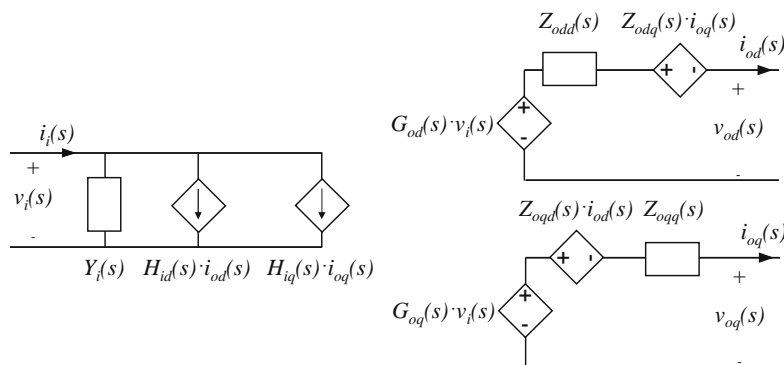


Fig. A-8: Terminal d-q g-parameters black-box model for a three-phase Voltage Source Inverter.

For the convenience of the analysis, vector notation is used to denote d-q signals. The following definitions are considered hereinafter.

$$\begin{cases} \vec{v}_{odq}(s) = \begin{pmatrix} v_{od}(s) \\ v_{oq}(s) \end{pmatrix}, \vec{i}_{odq}(s) = \begin{pmatrix} i_{od}(s) \\ i_{oq}(s) \end{pmatrix}, \vec{d}_{dq}(s) = \begin{pmatrix} d_d(s) \\ d_q(s) \end{pmatrix}, \vec{i}_{Ldq}(s) = \begin{pmatrix} i_{Ld}(s) \\ i_{Lq}(s) \end{pmatrix} \\ [Z_o(s)]_{dq \ 2 \times 2} = \begin{pmatrix} Z_{odd}(s) & Z_{odq}(s) \\ Z_{oqd}(s) & Z_{oqq}(s) \end{pmatrix}, [G_o(s)]_{dq \ 2 \times 1} = \begin{pmatrix} G_{od}(s) \\ G_{oq}(s) \end{pmatrix}, [H_i(s)]_{dq \ 1 \times 2} = \begin{pmatrix} H_{id}(s) & H_{iq}(s) \end{pmatrix} \end{cases} \quad (\text{A-16})$$

Thus, the g-parameters model can be described by the following expression:

$$\begin{pmatrix} \vec{i}_i(s) \\ \vec{v}_{odq}(s) \end{pmatrix} = \begin{pmatrix} Y_i(s) & [H_i(s)]_{dq} \\ [G_o(s)]_{dq} & -[Z_o(s)]_{dq} \end{pmatrix} \cdot \begin{pmatrix} v_i(s) \\ \vec{i}_{odq}(s) \end{pmatrix} \quad (\text{A-17})$$

In order to obtain an analytical expression for (A-17), input-output models for the power stage and the control stage are obtained separately. After that, both models are blended. The block-diagram, including the small-signal model of the power stage and the control stage, is depicted in Fig. A-9.

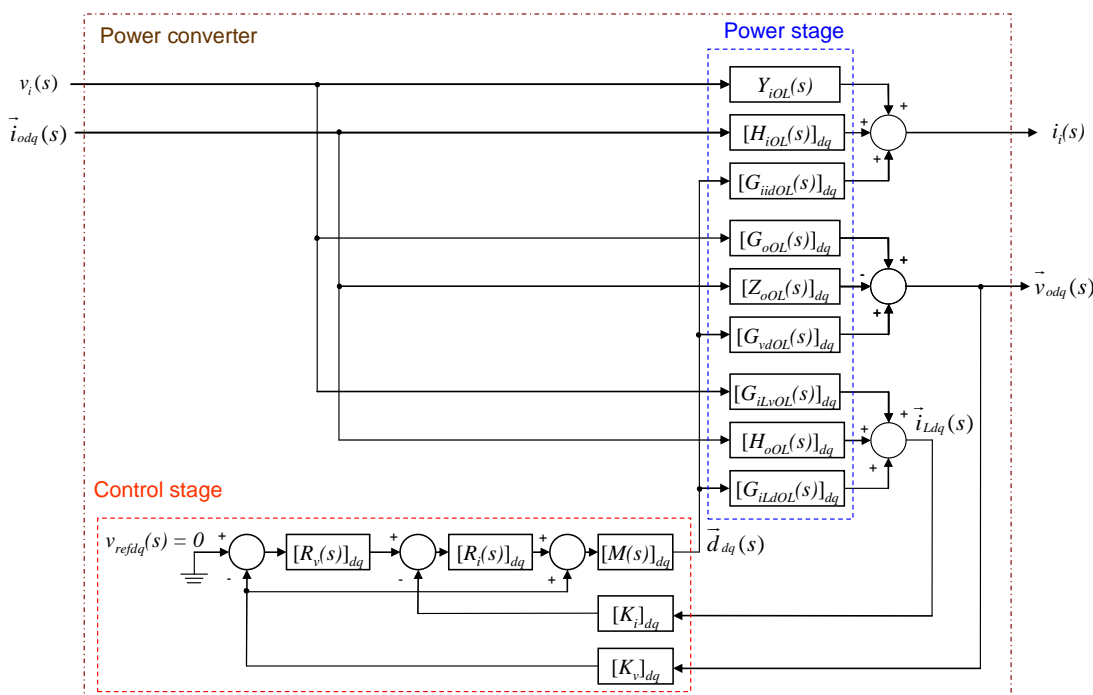


Fig. A-9: d-q frame small-signal model of a three-phase VSI comprised of double loop control scheme.

A.1.2.1. Small-signal terminal d-q modeling of the power stage

The model of the power stage into d - q coordinates is well known [100] and is shown in Fig. A-10. No dead times into the modulation have been considered when deriving this model.

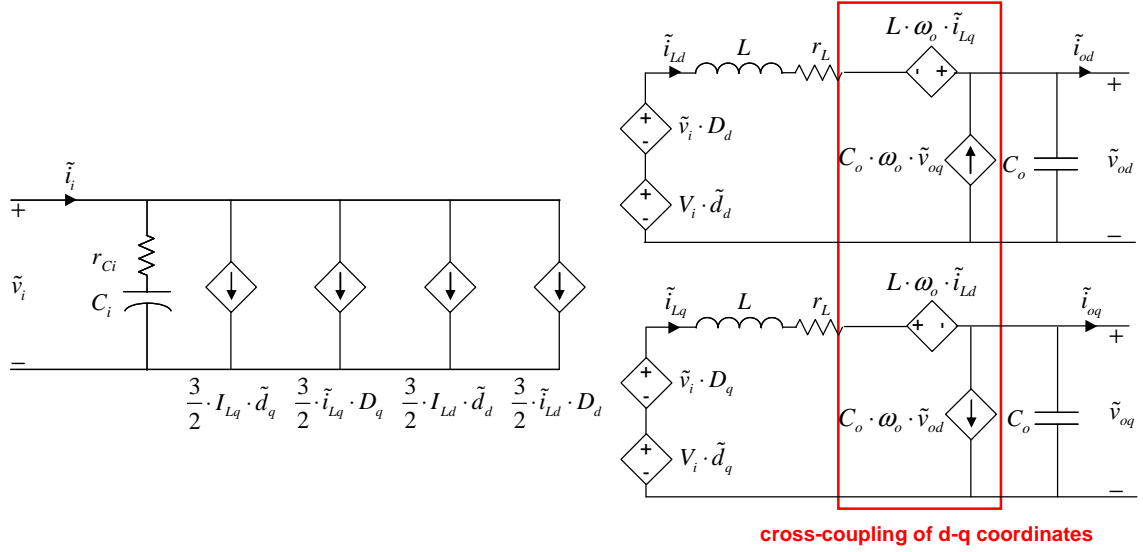


Fig. A-10: Small-signal d - q model of a three-phase Voltage Source Inverter (power stage only).

The sough terminal model is characterized by output current, input voltage and duty cycle as model inputs, and output voltage and input current as model outputs. This is mathematically described below:

$$\begin{pmatrix} i_i(s) \\ \vec{v}_{odq}(s) \\ \vec{i}_{Ldq}(s) \end{pmatrix} = \begin{pmatrix} [G_{iidOL}(s)]_{dq} & Y_{iOL}(s) & [H_{iOL}(s)]_{dq} \\ [G_{vdOL}(s)]_{dq} & [G_{oOL}(s)]_{dq} & -[Z_{oOL}(s)]_{dq} \\ [G_{iLdOL}(s)]_{dq} & [G_{iLvOL}(s)]_{dq} & [H_{oOL}(s)]_{dq} \end{pmatrix} \begin{pmatrix} \vec{d}_{dq}(s) \\ v_i(s) \\ \vec{i}_{odq}(s) \end{pmatrix} \quad (\text{A-18})$$

Expressions into (A-18) are obtained by analyzing the circuit shown in Fig. A-10. The capacitors admittance and inductor impedance can be expressed as follows.

$$[Z_L(s)]_{dq} = \begin{pmatrix} s \cdot L + r_L & -\omega_o L \\ \omega_o L & s \cdot L + r_L \end{pmatrix}, [Y_{Co}(s)]_{dq} = \begin{pmatrix} s \cdot C_o & -\omega_o C_o \\ \omega_o C_o & s \cdot C_o \end{pmatrix}, Y_{Ci}(s) = \frac{s \cdot C_i}{s \cdot C_i \cdot r_{Ci} + 1} \quad (\text{A-19})$$

After some mathematics, expressions given by (A-20) and (A-21) are derived (where $[I]$ denotes the identity matrix).

$$i_i \Leftrightarrow \begin{cases} [G_{iidOL}(s)]_{dq \ 1 \times 2} = \frac{3}{2} \cdot \left(\vec{I}_L^T + V_i \cdot \vec{D}_{dq}^T \cdot \left([Z_L(s)]_{dq} [Y_{Co}(s)]_{dq} + [I] \right)^{-1} \cdot [Y_{Co}(s)]_{dq} \right) \\ Y_{iOL}(s) = Y_{Ci}(s) + \frac{3}{2} \cdot \vec{D}_{dq}^T \cdot \left([Z_L(s)]_{dq} [Y_{Co}(s)]_{dq} + [I] \right)^{-1} \cdot [Y_{Co}(s)]_{dq} \cdot \vec{D}_{dq} \\ [H_{iOL}(s)]_{dq \ 1 \times 2} = \frac{3}{2} \cdot \vec{D}_{dq}^T \cdot \left([Z_L(s)]_{dq} [Y_{Co}(s)]_{dq} + [I] \right)^{-1} \end{cases} \quad (\text{A-20})$$

$$\vec{v}_{odq} \Leftrightarrow \begin{cases} [G_{vdOL}(s)]_{dq \ 2 \times 2} = V_i \cdot \left([Z_L(s)]_{dq} [Y_{Co}(s)]_{dq} + [I] \right)^{-1} \\ [G_{oOL}(s)]_{dq \ 2 \times 1} = \left([Z_L(s)]_{dq} [Y_{Co}(s)]_{dq} + [I] \right)^{-1} \cdot \bar{D}_{dq} \\ [Z_{oOL}(s)]_{dq \ 2 \times 2} = \left([Z_L(s)]_{dq} [Y_{Co}(s)]_{dq} + [I] \right)^{-1} \cdot [Z_L(s)]_{dq} \end{cases} \quad (\text{A-21})$$

$$\vec{i}_{Ldq} \Leftrightarrow \begin{cases} [G_{iLdOL}(s)]_{dq \ 2 \times 2} = V_i \cdot \left([Z_L(s)]_{dq} [Y_{Co}(s)]_{dq} + [I] \right)^{-1} \cdot [Y_{Co}(s)]_{dq} \\ [G_{iLvOL}(s)]_{dq \ 2 \times 1} = \left([Z_L(s)]_{dq} [Y_{Co}(s)]_{dq} + [I] \right)^{-1} \cdot [Y_{Co}(s)]_{dq} \cdot \bar{D}_{dq} \\ [H_{oOL}(s)]_{dq \ 2 \times 2} = \left([Z_L(s)]_{dq} [Y_{Co}(s)]_{dq} + [I] \right)^{-1} \end{cases}$$

Note also that, excepting $[Z_{oOL}]_{dq}$ and $[H_{oOL}]_{dq}$, these matrixes are dependant of operating point. Such operating point can be expressed as a function of model inputs by means of the following expressions:

$$\begin{cases} \vec{I}_{Ldq} = \vec{I}_{odq} + [Y_{Co}(0)]_{dq} \cdot \vec{V}_{odq} \\ \bar{D}_{dq} = V_i^{-1} \cdot \left([I] + [Z_L(0)]_{dq} \cdot [Y_{Co}(0)]_{dq} \right) \cdot \vec{V}_{odq} + V_i^{-1} \cdot [Z_L(0)]_{dq} \cdot \vec{I}_{odq} \end{cases} \quad (\text{A-22})$$

Equations above shown evidence the dynamic similarities between a buck converter and a three-phase VSI. In fact, excepting the vector notation, (A-20) and (A-21) are equivalent to (A-4). This is due to the fact that both converters are dynamically equivalent, as they consist of a switching bridge cascaded with a LC filter.

A.1.2.2. Small-signal terminal d-q modeling of the control stage

Following this, a small-signal model of the control stage, mapped into synchronous d - q frame, is obtained. Such task is not obvious, as the converter is regulated into stationary α - β frame. First, the small-signal equivalent model, into α - β frame, is described taking into account the following points:

- The model is represented into Laplace domain, so the regulators are mapped considering $z = e^{sT_s}$.
- The modulator can be well approximated as a gain G_{mod} cascaded with a half a sampling period delay $e^{-sT_s/2}$ [180], [189].
- One-cycle transport delay e^{-sT_s} is taken into account in front of the modulator, corresponding to synchronous digital schemes. The modulator, the sampling delay and the scaling factor V_i^{-1} are herein grouped into the matrix $M(s)$.

The resulting equivalent circuit is shown in Fig. A-11, where $K_v = 1$, $K_i = 1$ and $G_{mod} = 1$.

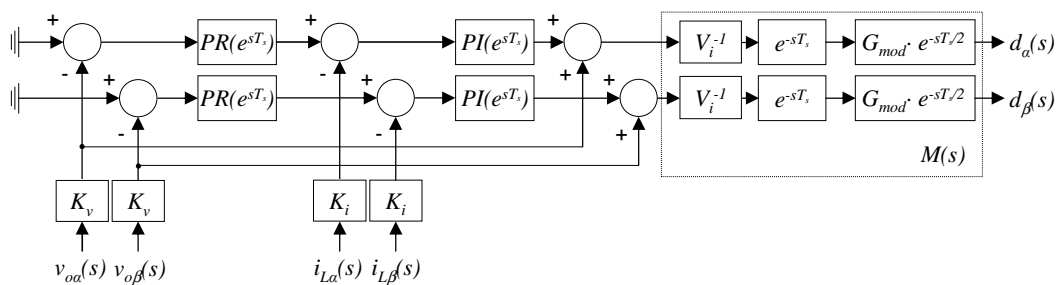


Fig. A-11: Small-signal model of the control stage into α - β coordinates.

To describe the dynamics of the control scheme in matrix form, the following definitions are considered:

$$\begin{aligned} [R_i(s)]_{\alpha\beta} &= \begin{pmatrix} PI(e^{sT_s}) & 0 \\ 0 & PI(e^{sT_s}) \end{pmatrix}, [R_v(s)]_{\alpha\beta} = \begin{pmatrix} PR(e^{sT_s}) & 0 \\ 0 & PR(e^{sT_s}) \end{pmatrix} \\ [K_v]_{\alpha\beta} &= \begin{pmatrix} K_v & 0 \\ 0 & K_v \end{pmatrix}, [K_i]_{\alpha\beta} = \begin{pmatrix} K_i & 0 \\ 0 & K_i \end{pmatrix}, [M(s)]_{\alpha\beta} = \begin{pmatrix} V_i^{-1} \cdot G_{\text{mod}} \cdot e^{-s\frac{3}{2}T_s} & 0 \\ 0 & V_i^{-1} \cdot G_{\text{mod}} \cdot e^{-s\frac{3}{2}T_s} \end{pmatrix} \end{aligned} \quad (\text{A-23})$$

Thus, the duty cycle can be expressed as a function of the feedback signals as follows:

$$\vec{d}_{\alpha\beta}(s) = \begin{pmatrix} -[M(s)]_{\alpha\beta}[K_v]_{\alpha\beta}([R_v(s)]_{\alpha\beta}[R_i(s)]_{\alpha\beta} - [I]) & -[M(s)]_{\alpha\beta}[R_i(s)]_{\alpha\beta}[K_i]_{\alpha\beta} \end{pmatrix} \cdot \begin{pmatrix} \vec{v}_{\alpha\beta}(s) \\ \vec{i}_{L\alpha\beta}(s) \end{pmatrix} \quad (\text{A-24})$$

Following this, (A-24) is mapped into d - q frame. According to [199], any dynamic system described by (A-25) into α - β frame, can be mapped into d - q frame as given by (A-26).

$$\begin{pmatrix} y_\alpha(s) \\ y_\beta(s) \end{pmatrix} = \begin{pmatrix} G(s) & 0 \\ 0 & G(s) \end{pmatrix} \cdot \begin{pmatrix} u_\alpha(s) \\ u_\beta(s) \end{pmatrix} \quad (\text{A-25})$$

$$\begin{pmatrix} y_d \\ y_q \end{pmatrix} = \begin{pmatrix} \frac{G(s+j\omega_o) + G(s-j\omega_o)}{2} & j\frac{G(s+j\omega_o) - G(s-j\omega_o)}{2} \\ -j\frac{G(s+j\omega_o) - G(s-j\omega_o)}{2} & \frac{G(s+j\omega_o) + G(s-j\omega_o)}{2} \end{pmatrix} \cdot \begin{pmatrix} u_d(s) \\ u_q(s) \end{pmatrix} \quad (\text{A-26})$$

By making use of this transformation, every matrix into (A-23) can be rewritten as follows:

$$\begin{aligned} [R_i(s)]_{dq} &= \begin{pmatrix} \frac{PI(e^{(s+j\omega_o)T_s}) + PI(e^{(s-j\omega_o)T_s})}{2} & j\frac{PI(e^{(s+j\omega_o)T_s}) - PI(e^{(s-j\omega_o)T_s})}{2} \\ -j\frac{PI(e^{(s+j\omega_o)T_s}) - PI(e^{(s-j\omega_o)T_s})}{2} & \frac{PI(e^{(s+j\omega_o)T_s}) + PI(e^{(s-j\omega_o)T_s})}{2} \end{pmatrix} \\ [R_v(s)]_{dq} &= \begin{pmatrix} \frac{PR(e^{(s+j\omega_o)T_s}) + PR(e^{(s-j\omega_o)T_s})}{2} & j\frac{PR(e^{(s+j\omega_o)T_s}) - PR(e^{(s-j\omega_o)T_s})}{2} \\ -j\frac{PR(e^{(s+j\omega_o)T_s}) - PR(e^{(s-j\omega_o)T_s})}{2} & \frac{PR(e^{(s+j\omega_o)T_s}) + PR(e^{(s-j\omega_o)T_s})}{2} \end{pmatrix} \\ [M(s)]_{dq} &= \begin{pmatrix} V_i^{-1} \cdot G_{\text{mod}} \cdot \frac{e^{-\frac{3}{2}(s+j\omega_o)T_s} + e^{-\frac{3}{2}(s-j\omega_o)T_s}}{2} & j \cdot V_i^{-1} \cdot G_{\text{mod}} \cdot \frac{e^{-\frac{3}{2}(s+j\omega_o)T_s} - e^{-\frac{3}{2}(s-j\omega_o)T_s}}{2} \\ -j \cdot V_i^{-1} \cdot G_{\text{mod}} \cdot \frac{e^{-\frac{3}{2}(s+j\omega_o)T_s} - e^{-\frac{3}{2}(s-j\omega_o)T_s}}{2} & V_i^{-1} \cdot G_{\text{mod}} \cdot \frac{e^{-\frac{3}{2}(s+j\omega_o)T_s} + e^{-\frac{3}{2}(s-j\omega_o)T_s}}{2} \end{pmatrix} \\ [K_v]_{dq} &= \begin{pmatrix} K_v & 0 \\ 0 & K_v \end{pmatrix}, [K_i]_{dq} = \begin{pmatrix} K_i & 0 \\ 0 & K_i \end{pmatrix} \end{aligned} \quad (\text{A-27})$$

Finally, an input-output expression for the control stage, into d - q frame, is derived. Matrixes $[F_v(s)]_{dq}$ and $[F_i(s)]_{dq}$ are herein defined to simplify the subsequent mathematics.

$$\vec{d}_{dq}(s) = \begin{pmatrix} -\underbrace{[M(s)]_{dq}[K_v]_{dq}([R_v(s)]_{dq}[R_i(s)]_{dq} - [I])}_{[F_v(s)]_{dq}} - \underbrace{[M(s)]_{dq}[R_i(s)]_{dq}[K_i]_{dq}}_{[F_i(s)]_{dq}} \end{pmatrix} \begin{pmatrix} \vec{v}_{odq}(s) \\ \vec{i}_{Ldq}(s) \end{pmatrix} \quad (\text{A-28})$$

A.1.2.3. Small-signal terminal d-q modeling of the closed-loop converter

Once input-output models of the power stage and the control stage have been defined, both of them can be blended to build a small-signal model of the closed-loop converter.

To simplify the subsequent mathematics, the following matrix for the combined inner-outer loop-gain is defined.

$$[T_l(s)]_{dq} = [F_v(s)]_{dq} \cdot [G_{vdOL}(s)]_{dq} + [F_i(s)]_{dq} \cdot [G_{iLdOL}(s)]_{dq} \quad (\text{A-29})$$

Combining (A-28) with (A-18), and using (A-29), the duty cycle can be expressed as a function of model inputs as follows:

$$\begin{aligned} \vec{d}_{dq}(s) = & -\left([I] + [T_l(s)]_{dq}\right)^{-1} \cdot \left([F_v(s)]_{dq} \cdot [G_{oOL}(s)]_{dq} + [F_i(s)]_{dq} \cdot [G_{viLOL}(s)]_{dq}\right) \cdot v_i(s) - \\ & -\left([I] + [T_l(s)]_{dq}\right)^{-1} \cdot \left(-[F_v(s)]_{dq} \cdot [Z_{oOL}(s)]_{dq} + [F_i(s)]_{dq} \cdot [H_{oOL}(s)]_{dq}\right) \cdot \vec{i}_{odq}(s) \end{aligned} \quad (\text{A-30})$$

By replacing (A-30) into (A-18), the model outputs dependence on the duty cycle is removed, and expressions for the closed-loop black-box model are derived.

$$\begin{cases} [G_o(s)]_{dq} = [G_{oOL}(s)]_{dq} - [G_{vdOL}(s)]_{dq} \cdot \left([I] + [T_l(s)]_{dq}\right)^{-1} \cdot \left([F_v(s)]_{dq} \cdot [G_{oOL}(s)]_{dq} + [F_i(s)]_{dq} \cdot [G_{viLOL}(s)]_{dq}\right) \\ [Z_o(s)]_{dq} = [Z_{oOL}(s)]_{dq} + [G_{vdOL}(s)]_{dq} \cdot \left([I] + [T_l(s)]_{dq}\right)^{-1} \cdot \left(-[F_v(s)]_{dq} \cdot [Z_{oOL}(s)]_{dq} + [F_i(s)]_{dq} \cdot [H_{oOL}(s)]_{dq}\right) \\ Y_i(s) = Y_{iOL}(s) - [G_{iidOL}(s)]_{dq} \cdot \left([I] + [T_l(s)]_{dq}\right)^{-1} \cdot \left([F_v(s)]_{dq} \cdot [G_{oOL}(s)]_{dq} + [F_i(s)]_{dq} \cdot [G_{viLOL}(s)]_{dq}\right) \\ [H_i(s)]_{dq} = [H_{iOL}(s)]_{dq} - [G_{iidOL}(s)]_{dq} \cdot \left([I] + [T_l(s)]_{dq}\right)^{-1} \cdot \left(-[F_v(s)]_{dq} \cdot [Z_{oOL}(s)]_{dq} + [F_i(s)]_{dq} \cdot [H_{oOL}(s)]_{dq}\right) \end{cases} \quad (\text{A-31})$$

Expressions into (A-31) are plotted in section 5.5 for analysis of linearity and validation of identification results. The transfer functions into (A-31) cannot be directly implemented into a circuit simulator, as the regulator and the delays are expressed into Laplace domain using an exponential function. If implementation into a simulation were required, polynomial expressions could be obtained by using zero-order-hold or Tustin approximations.

A.1.2.4. Remarks on linear and orthogonal properties of the output impedance

Linear and orthogonal properties for the output impedance of three-phase VSIs were described in section 5.4. Such properties are evidenced on the mathematical analysis presented above.

- **Linearity:** As described in section 5.4, the output impedance of three-phase VSIs with capacitive input filter (such as that herein tackled), is independent of I_{od} , I_{oq} , as long as the control stage dynamics do not depend on the operating point. Such statement has been demonstrated in this appendix, as $[Z_o(s)]_{dq}$ is determined by matrixes which are independent of I_{od} , I_{oq} . In general, such statement will be valid as long as $[F_v(s)]_{dq}$ and $[F_i(s)]_{dq}$ are independent of I_{od} , I_{oq} .
- **Orthogonality:** The orthogonal properties of the impedance are also evidenced. By looking at (A-31), one can notice that $[Z_o(s)]_{dq}$ is determined by multiplication, summation and inversion

of orthogonal matrixes. Hence, it is also orthogonal. Orthogonality of each matrix into the second row in (A-31) is discussed below:

- The matrixes related to the power stage, $[Z_{oOL}(s)]_{dq}$, $[H_{oOL}(s)]_{dq}$, $[G_{vdOL}(s)]_{dq}$ and $[G_{iLdOL}(s)]_{dq}$, (see (A-21)) are orthogonal because they are exclusively determined by the inductor impedance and the capacitor admittance matrixes, $[Z_L(s)]_{dq}$ and $[Y_{Co}(s)]_{dq}$ which are also orthogonal (see (A-19)).
- The matrixes related to the control stage, $[F_v(s)]_{dq}$ and $[F_i(s)]_{dq}$, are orthogonal because both α - β coordinates are controlled in a symmetrical manner, using the same control parameters. Moreover, when mapping the control scheme into d - q , orthogonal properties are maintained (see (A-26)). Essentially, this is because the α - β to d - q transformation is orthogonal. In general, orthogonal properties would be found also in case of d - q frame or a - b - c control schemes, as long as all the coordinates all regulated in a symmetric, linear manner and no dynamics dependence on I_{od} , I_{oq} is introduced.

A.1.2.5. Numerical data: identified transfer functions and simulated model

The identified transfer functions from simulated step tests are given below.

$$\begin{aligned}
Z_{odd}(s) &:= \frac{0.754s^5 + 2.734 \cdot 10^4 \cdot s^4 + 2.238 \cdot 10^8 \cdot s^3 + 4.575 \cdot 10^{10} \cdot s^2 + 4.7 \cdot 10^{13} \cdot s + 7.16 \cdot 10^{14}}{s^5 + 8726s^4 + 2.521 \cdot 10^7 \cdot s^3 + 3.226 \cdot 10^{10} \cdot s^2 + 6.609 \cdot 10^{12} \cdot s + 2.892 \cdot 10^{15}} \\
Z_{oqq}(s) &:= \frac{0.7277s^5 + 2.65 \cdot 10^4 \cdot s^4 + 2.187 \cdot 10^8 \cdot s^3 + 4.581 \cdot 10^{10} \cdot s^2 + 4.628 \cdot 10^{13} \cdot s + 7.003 \cdot 10^{14}}{s^5 + 8549s^4 + 2.458 \cdot 10^7 \cdot s^3 + 3.197 \cdot 10^{10} \cdot s^2 + 6.518 \cdot 10^{12} \cdot s + 2.86 \cdot 10^{15}} \\
Z_{oqd}(s) &:= \frac{-0.009559s^6 - 488.9s^5 + -6.862 \cdot 10^6 \cdot s^4 - 1.31 \cdot 10^{10} \cdot s^3 + 5.063 \cdot 10^{13} \cdot s^2 + -3.621 \cdot 10^{14} \cdot s - 8.431 \cdot 10^{16}}{s^6 + 4779s^5 + 1.836 \cdot 10^7 \cdot s^4 + 3.066 \cdot 10^{10} \cdot s^3 + 2.793 \cdot 10^{13} \cdot s^2 + 6.104 \cdot 10^{15} \cdot s + 2.288 \cdot 10^{18}} \\
Z_{odq}(s) &:= \frac{0.004366s^6 + 305.3s^5 + 6.895 \cdot 10^6 \cdot s^4 + 4.477 \cdot 10^{10} \cdot s^3 - 1.247 \cdot 10^{14} \cdot s^2 - 2.852 \cdot 10^{14} \cdot s - 4.864 \cdot 10^{17}}{s^6 + 8089s^5 + 3.154 \cdot 10^7 \cdot s^4 + 6.152 \cdot 10^{10} \cdot s^3 + 6.168 \cdot 10^{13} \cdot s^2 + 1.325 \cdot 10^{16} \cdot s + 5.227 \cdot 10^{18}} \\
H_{id0}(s) &:= \frac{-0.001056s^6 - 184.7s^5 + 1.845 \cdot 10^6 \cdot s^4 + 1.128 \cdot 10^{12} \cdot s^3 + 9.377 \cdot 10^{15} \cdot s^2 + 8.843 \cdot 10^{19} \cdot s + 1.435 \cdot 10^{23}}{s^6 + 2.612 \cdot 10^4 \cdot s^5 + 7.267 \cdot 10^8 \cdot s^4 + 7.721 \cdot 10^{12} \cdot s^3 + 6.31 \cdot 10^{16} \cdot s^2 + 1.58 \cdot 10^{20} \cdot s + 2.321 \cdot 10^{23}} \\
H_{id1}(s) &:= \frac{-0.09648s^5 + 2776s^4 + 8.48 \cdot 10^6 \cdot s^3 + 7.008 \cdot 10^{10} \cdot s^2 + 1.066 \cdot 10^{13} \cdot s + 7.894 \cdot 10^{15}}{s^5 + 1.777 \cdot 10^4 \cdot s^4 + 5.761 \cdot 10^7 \cdot s^3 + 1.259 \cdot 10^{11} \cdot s^2 + 2.752 \cdot 10^{13} \cdot s + 1.288 \cdot 10^{16}} \\
H_{iq}(s) &:= \frac{-0.003311s^6 + 194.6s^5 + 6.123 \cdot 10^6 \cdot s^4 - 1.098 \cdot 10^{10} \cdot s^3 - 1.1513 \cdot 10^{12} \cdot s^2 - 5.555 \cdot 10^{13} \cdot s - 6.844 \cdot 10^{16}}{s^6 + 2.257 \cdot 10^4 \cdot s^5 + 1.116 \cdot 10^8 \cdot s^4 + 2.627 \cdot 10^{11} \cdot s^3 + 2.859 \cdot 10^{14} \cdot s^2 + 7.498 \cdot 10^{16} \cdot s + 2.434 \cdot 10^{19}} \\
Y_{\check{i}}(s) &:= \frac{25.23s^2 + 3.025 \cdot 10^6 \cdot s + -9.024 \cdot 10^6}{s^2 + 1.326 \cdot 10^5 \cdot s + 1.372 \cdot 10^9} \\
G_{od}(s) &:= \frac{0.0004786s^6 + 229.8s^5 + 4.138 \cdot 10^7 \cdot s^4 + 3.313 \cdot 10^{12} \cdot s^3 + 9.965 \cdot 10^{16} \cdot s^2 + 1.248 \cdot 10^{19} \cdot s + 1.446 \cdot 10^{21}}{s^6 + 1.286 \cdot 10^5 \cdot s^5 + 2.337 \cdot 10^9 \cdot s^4 + 4.886 \cdot 10^{13} \cdot s^3 + 2.462 \cdot 10^{17} \cdot s^2 + 6.2 \cdot 10^{20} \cdot s + 5.548 \cdot 10^{23}} \\
G_{oq}(s) &:= \frac{0.004522s^4 + 508s^3 - 3.998 \cdot 10^6 \cdot s^2 + 1.859 \cdot 10^{10} \cdot s + 7.933 \cdot 10^{11}}{s^4 + 2.677 \cdot 10^4 \cdot s^3 + 7.739 \cdot 10^7 \cdot s^2 + 1.937 \cdot 10^{11} \cdot s + 1.481 \cdot 10^{14}}
\end{aligned} \tag{A-32}$$

In order to build the large-signal black-box model, $Y_i(s)$ and $H_i(s)$ require the following post-processing actions, as explained in chapter 5.

$$\begin{cases} Y_{i0}(s) = Y_i(s) - Y_i(0), H_{iq}(s) = H_{iq0}(s) - H_{iq}(0) \\ H_{idL0}(s) = H_{id0}(s) \cdot \frac{V_{dss}}{H_{id0}(0)}, H_{idL12}(s) = H_{id12}(s) \cdot \frac{V_{dss}}{H_{id12}(0)} \end{cases} \quad (\text{A-33})$$

This yields the following transfer functions:

$$\begin{aligned} \text{HidL0}(s) &:= \frac{1.39e27s + 1.47e23s^2 + 1.77e19s^3 + 2.9e13s^4 - 2.9e9s^5 - 16599.0s^6 + 2.26e30}{4.94e24s + 1.97e21s^2 + 2.41e17s^3 + 2.27e13s^4 + 8.16e8s^5 + 31250.0s^6 + 7.25e27} \\ \text{HidL12}(s) &:= \frac{1.69e20s + 1.11e18s^2 + 1.34e14s^3 + 4.4e10s^4 - 1.53e6s^5 + 1.25e23}{8.6e17s + 3.93e15s^2 + 1.8e12s^3 + 5.55e8s^4 + 31250.0s^5 + 4.02e20} \\ \text{Hiq0}(s) &:= -\frac{1.55e20s + -3.47e17s^2 - 1.02e16s^3 + 6.44e12s^4 + 2.58e8s^5 - 499.0s^6}{7.5e22s + 2.86e20s^2 + 2.63e17s^3 + 1.12e14s^4 + 2.26e10s^5 + 1.0e6s^6 + 2.43e25} \\ \text{Yi0}(s) &:= \frac{3.03e12s + 2.52e7s^2}{1.33e11s + 1.0e6s^2 + 1.37e15} \end{aligned} \quad (\text{A-34})$$

The black-box model has been implemented using all the transfer functions provided by (A-34) and $Z_{odd}(s)$, $Z_{oqd}(s)$, $G_{od}(s)$ and $G_{oq}(s)$ provided by (A-32). It has been assumed that $Z_{oqq}(s) = Z_{odd}(s)$ and $Z_{odq}(s) = -Z_{oqd}(s)$.

A.2. Black-box model of buck-boost converter

A.2.1. Converter description

In this appendix, details of a black-box model of a commercial POL buck-boost converter are provided. This converter is used as part of a distributed power system analyzed in section 4.6. A picture of the converter is shown in Fig. A-12.



Fig. A-12: Commercial DC-DC buck-boost converter by Texas Instruments PTN78020A [256].

In the tested application, the converter is fed from a regulated 12 V bus and the output current ranges from 0.5 A to 4 A. The switching frequency is $f_{sw} = 500$ kHz.

This unit has to be provided with external capacitors. At the input port, ceramic capacitors summing 16.8 μF has been connected in parallel with a 100 μF electrolytic. At the output port, a 100 μF electrolytic capacitor has been connected in parallel with an additional 63 μF ceramic capacitor (low voltage).

A.2.2. Analysis of linearity

Several step tests were carried out on different operating points, given by I_o , within the selected working region. It was found that the dynamic dependence on I_o is slight, so it has been neglected for the sake of simplicity.

Fig. A-13 and Fig. A-14 show the frequency response of the small-signal transfer functions $Y_i(s)$, $G_o(s)$, $Z_o(s)$ and $H_i(s)$ identified for different operating points.

- In case of $Y_i(s)$, only dependence is observed at low frequency, which comes from the CPL behavior of the converter due to the control loop. At higher frequencies, the impedance of the input capacitors is dominant.
- Concerning $G_o(s)$, also slight dependence is observed at low frequency, where the magnitude is very low. Therefore, it can be neglected.
- Regarding $Z_o(s)$, only a slight dependence is observed for frequencies below 10 kHz. Nevertheless, differences in magnitude between the maximum and minimum impedance are less than 4 dB. For frequencies above 10 kHz, the impedance is mostly determined by the output capacitors.
- Concerning $H_i(s)$, dependence on I_o at low-frequency is observed. This is essentially attributed to the efficiency dependence on I_o . Near the switching frequency, some significant dependence is also observed.

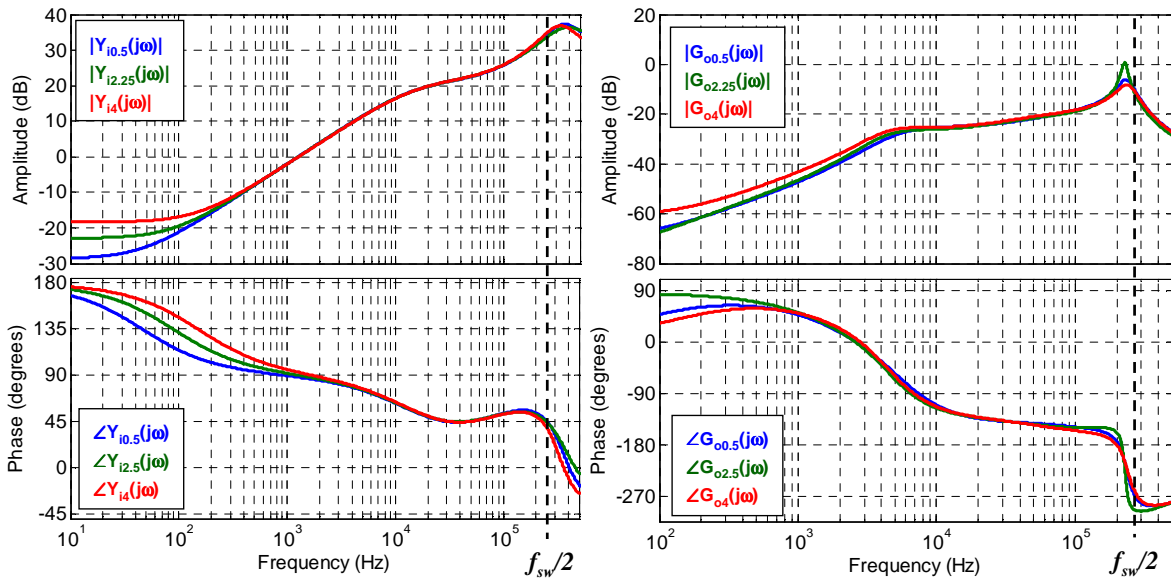


Fig. A-13: Bode plot of $Y_i(j\omega)$ and $G_o(j\omega)$ for $I_o = 0.5$ A, 2.25 A and 4 A.

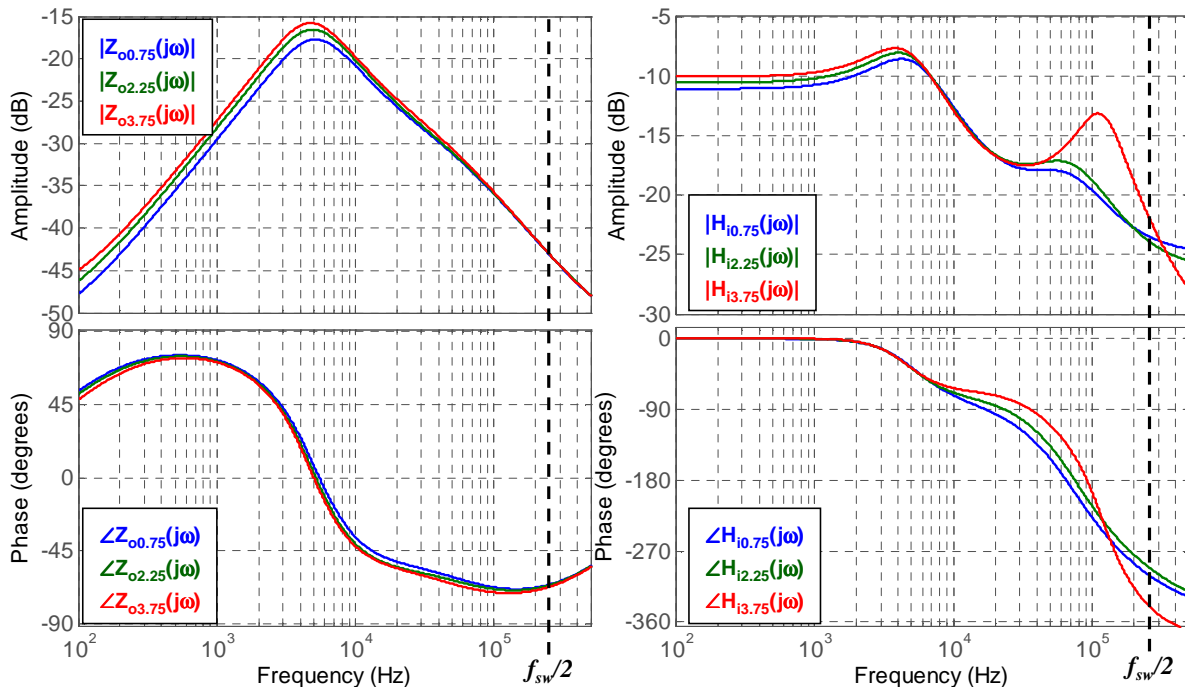


Fig. A-14: Bode plot of $Z_o(j\omega)$ and $H_i(j\omega)$ for $I_o = 0.75$ A, 2.25 A and 3.75 A.

A.2.3. Black-box model parameters

According to the analysis of linearity, every dynamic network has been modeled by a single LTI model excepting the back-current-gain, which has been built using a gain-scheduled transfer function. This way, both the efficiency dependence on operating point and the CPL behavior are incorporated into it.

On the other hand, the line and load regulation is very narrow within the modeled working range, so the simplified approach described in 4.2.4 has been used. The resulting black-box model is that shown in Fig. A-15.

The model parameters are given below, as well as the measured efficiency as a function of I_o .

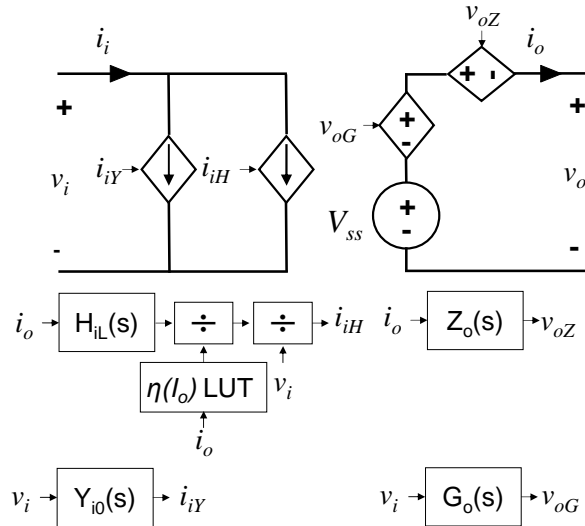


Fig. A-15: Black-box model of the buck-boost converter PTN78020A for $V_i = 12$ V and $I_o \in [0.5-4]$ A.

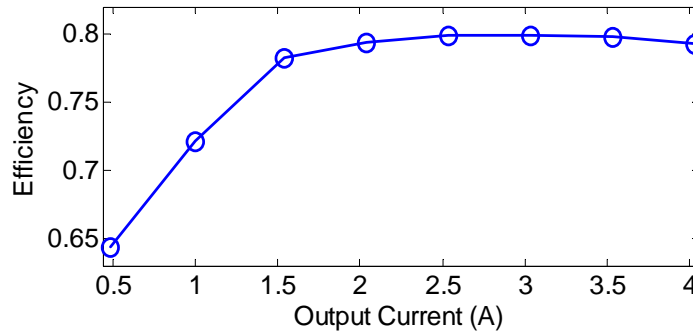


Fig. A-16: Transient response of the commercial POL buck-boost converter as a function of I_o .

$$\begin{aligned}
 Z_o(s) &= \frac{0.002126s^3 + 1.099 \cdot 10^4 s^2 + 1.807 \cdot 10^9 s + 7.005 \cdot 10^{11}}{s^3 + 3.429 \cdot 10^5 s^2 + 1.337 \cdot 10^{10} s + 2.919 \cdot 10^{14}} \\
 H_i(s) &= \frac{0.04867s^4 - 7.199 \cdot 10^4 s^3 + 9.172 \cdot 10^9 s^2 + 2.687 \cdot 10^{15} s + 5.857 \cdot 10^{19}}{s^4 + 6.715 \cdot 10^5 s^3 + 2.356 \cdot 10^{11} s^2 + 8.924 \cdot 10^{15} s + 1.978 \cdot 10^{20}} \\
 Y_i(s) &= \frac{26.81s^3 + 1.473 \cdot 10^8 s^2 + 6.637 \cdot 10^{13} s - 3.763 \cdot 10^{16}}{s^3 + 2.391 \cdot 10^6 s^2 + 5.848 \cdot 10^{12} s + 5.301 \cdot 10^{17}} \\
 G_o(s) &= \frac{-0.01034s^5 - 9.129 \cdot 10^4 s^4 - 2.019 \cdot 10^{11} s^3 - 1.913 \cdot 10^{16} s^2 + 2.912 \cdot 10^{20} s + 1.12 \cdot 10^{22}}{s^5 + 4.273 \cdot 10^5 s^4 + 2.099 \cdot 10^{12} s^3 + 5.945 \cdot 10^{17} s^2 + 1.994 \cdot 10^{22} s + 4.403 \cdot 10^{26}}
 \end{aligned} \tag{A-35}$$

A.3. Small-signal stability analysis of power distribution systems

Dynamic interactions between source subsystems and load subsystems can be analyzed by making use of small-signal impedance based models of them. In this section, the basics of the method are described and put into practice to predict instability. Such instability problems were experimentally found in chapter 4 and chapter 7 on DC power distribution systems.

A.3.1. Basics

Consider a simple power distribution system comprised of a source subsystem feeding a load subsystem. Assuming local linear behavior, the interconnected system may be represented as shown in Fig. A-17. The source is modeled by a Thevenin network, where $v_s(s)$ is the output voltage when un-loaded and $Z_s(s)$ is its output impedance. The load is represented by its input impedance, $Z_l(s) = Y_l(s)^{-1}$.

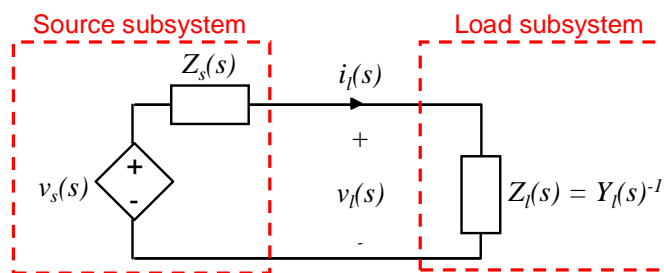


Fig. A-17: Interconnected source subsystem and load subsystem.

Assume the source is stable at no load conditions and the load is stable when supplied from an ideal source (i.e. $Z_s(s)$ and $Y_l(s)$ are stable). The transfer function of the interconnected system is simply given by the following expression:

$$\frac{v_l(s)}{v_s(s)} = \frac{Z_l(s)}{Z_l(s) + Z_s(s)} = \frac{1}{1 + \frac{Z_s(s)}{Z_l(s)}} = \frac{1}{1 + L(s)}, \quad L(s) = \frac{Z_s(s)}{Z_l(s)} \text{ or } Z_s(s) \cdot Y_l(s) \quad (\text{A-36})$$

As can be seen, stability of the system is determined by the zeroes of $(1+L(s))$. In fact, $L(s)$ may be seen as a ‘loop gain’ of the interconnected subsystem (minor loop gain). Therefore, the system is stable if $L(s)$ fulfill the Nyquist criterion [55], [61].

According to the Nyquist criterion, stability can be analyzed by drawing $L(j\omega)$ on a polar plot for $\omega \in (-\infty, +\infty)$. The interconnected system will be stable if the number of counterclockwise encirclements of the point $(-1, 0)$ is equal to the number of right-half-plane poles of $L(j\omega)$. However, $Z_s(s)$ and $Y_l(s)$ are stable, so the general requirement simplifies to the following one: the interconnected subsystem will be stable if $L(j\omega)$ does not encircle the point $(-1, 0)$.

A.3.2. Stability of intermediate bus architecture (chapter 4)

In chapter 4, stability problems were found during the analysis of a power distribution system based on intermediate bus architecture (IBA). Instability was caused by dynamic interactions between a front-end converter and the bus converter, when an inductor was located between them.

Such problem can be studied by making use of the black-box models of the power converters, linearized on a local operating point. The interface between the bus converter (referred to hereinafter

as load subsystem) and the front-end converter in series with the RL cell (referred to hereinafter as source subsystem). The output impedance of the source converter and the input admittance of the load converter are denoted as Z_s and Y_l , respectively. A simplified diagram of the interconnected subsystem is depicted in Fig. A-18.

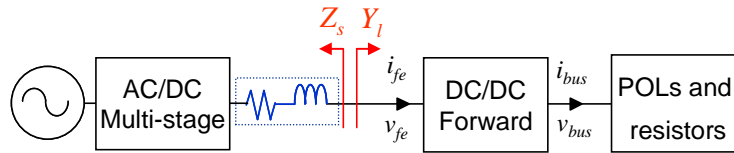


Fig. A-18: Diagram of the interconnected system.

Fig. A-19 shows the response of the system under a bus power step from $I_{bus} = 3.5$ A to $I_{bus} = 9.3$ A and back. As can be seen, the system is originally stable. However, after the step up in load power is carried out, divergent oscillations are found, which clearly evidences the existence of right half plane poles on the interconnected system. Such oscillation is extinguished as soon as the bus power goes back to the original level.

Note that the divergent oscillation is not reflected at the bus voltage, because the audiosusceptibility of the forward converter is very low. However, if the high bus current level, $I_{bus} = 9.3$ A, were maintained, the input voltage v_{fe} could go out of range and the forward converter could be switched off.

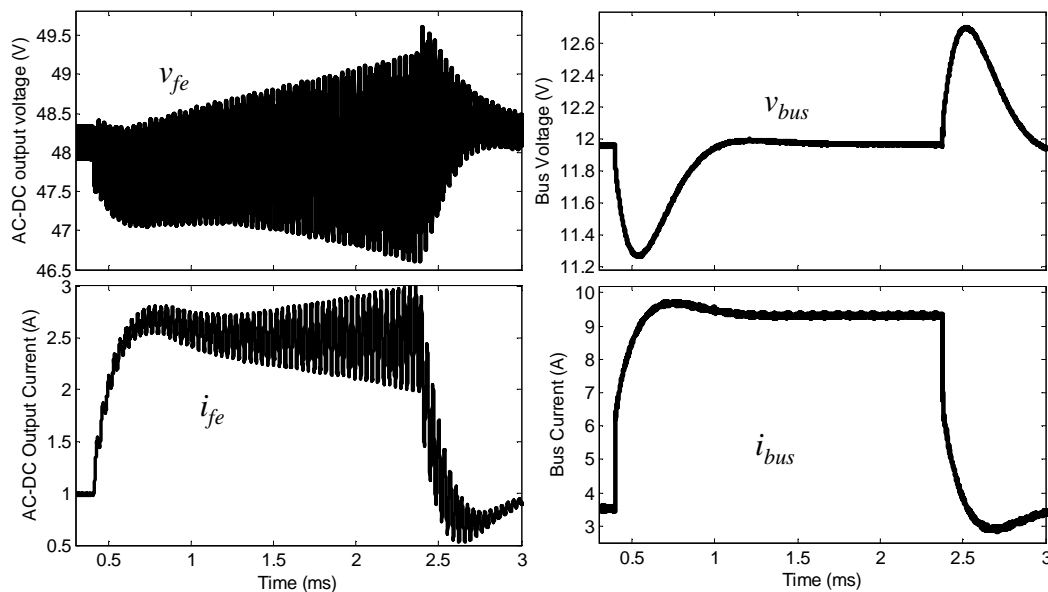


Fig. A-19: Response of the system to an step in load current from $I_{bus} = 3.5$ A to $I_{bus} = 9.3$ A.

These oscillations were predicted by simulation in chapter 4. However, they could be also predicted by making use of the analysis method described above.

In order to derive an analytical expression for the minor loop gain $L(j\omega)$ (A-36), the equivalent system made up by black-box models is analyzed. It is depicted in Fig. A-20, where constant bus current (I_{bus}) is assumed. The dynamics networks for Z_{oo} and Y_{io} are comprised of local linear model networks (LLMN) weighted as a function of the operating point, which is determined by the load current level (I_{fe} and I_{bus} , respectively).

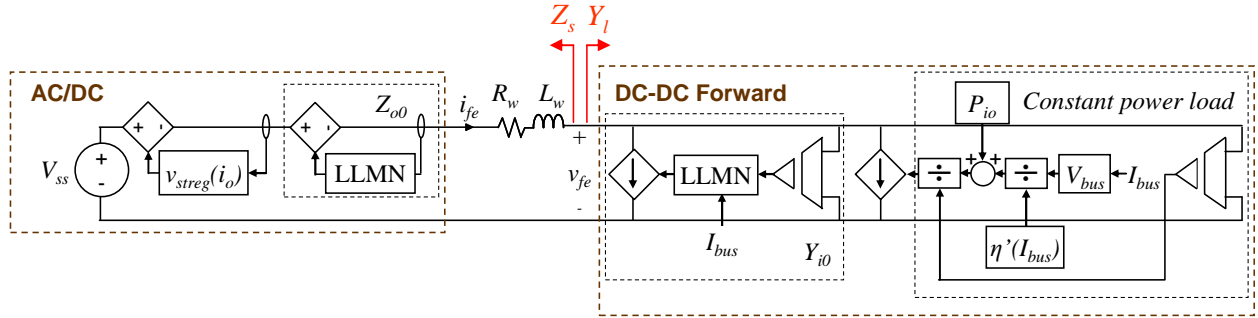


Fig. A-20: Equivalent circuit made up by black-box models, particularized for constant bus current I_{bus} .

Notice that for constant bus current, I_{bus} , the forward converter behaves as a CPL in parallel with Y_{i0} . By applying small-signal perturbations, the following expressions for Z_s and Y_l are obtained. **As can be seen, the CPL behaves as a negative incremental resistor. This is the reason why the minor loop gain $L(j\omega)$ may encircle the point $(-1, 0)$ above a certain power level threshold.**

By applying small-signal perturbations, transfer function models for the source impedance and the load admittance are obtained as follows. Details about the transfer functions into (A-37) are given in section 4.5.

$$\begin{cases} Z_s(s) = -\frac{\partial v_{streg}(I_o)}{I_o} + \sum_{j=1}^N WF_Z(I_{fe}) \cdot Z_{o0j}(s) + R_w + L_w \cdot s \\ Y_l(s) = \sum_{j=1}^N WF_Y(I_{bus}) \cdot Y_{i0j}(s) - \underbrace{\left(\frac{V_{bus} \cdot I_{bus}}{\eta'(I_{bus})} + P_{io} \right)}_{\text{negative resistor}} \cdot \frac{1}{V_{fe}^2} = \sum_{j=1}^N WF_Y(I_{bus}) \cdot Y_{i0j}(s) - \frac{I_{fe}}{V_{fe}} \end{cases} \quad (\text{A-37})$$

The transfer functions in (A-37) have been evaluated for both current levels depicted in Fig. A-19. The corresponding operating points are denoted as ‘a’ $\equiv (I_{bus} = 3.5 \text{ A}, I_{fe} = 0.97 \text{ A})$ and ‘b’ $\equiv (I_{bus} = 9.3 \text{ A}, I_{fe} = 2.5 \text{ A})$. The bode plots of $Z_s(j\omega)$ and $Z_l(j\omega)$, as well as the Nyquist diagram corresponding to $L(j\omega) = Z_s(j\omega) \cdot Y_l(j\omega)$, are drawn in Fig. A-21 and discussed below.

- Bode plot for $Z_s(j\omega)$: The impedance is dominated by the AC-DC converter (and the resistor R_w) below 5 kHz. Above 5 kHz, this impedance is mainly determined by the inductor.
- Bode plot for $Z_l(j\omega) = Y_l(j\omega)^{-1}$: At low-frequency, the load impedance behaves as a negative resistor, resulting from the CPL behavior of the forward converter. As the frequency increases this is dominated by the input filter of the converter. This impedance intersects $Z_s(j\omega)$ around 28.5 kHz. It corresponds to the resonance frequency between the input capacitor of the forward and the inductor L_w and is the oscillation frequency of the voltage v_{fe} .
- Polar plot for $L(j\omega) = Z_s(j\omega) \cdot Z_l(j\omega)^{-1}$: The polar plot allows determining the system stability. The diagram has been plotted for $f \in (-250 \text{ kHz}, 250 \text{ kHz})$. No encirclement of $(-1,0)$ is found for the operating point ‘a’, meaning that the system is stable. However, for the operating point ‘b’, the Nyquist path encircles the $(-1,0)$ point, so the system is unstable. This is in agreement with the experimental measurements shown in Fig. A-19.

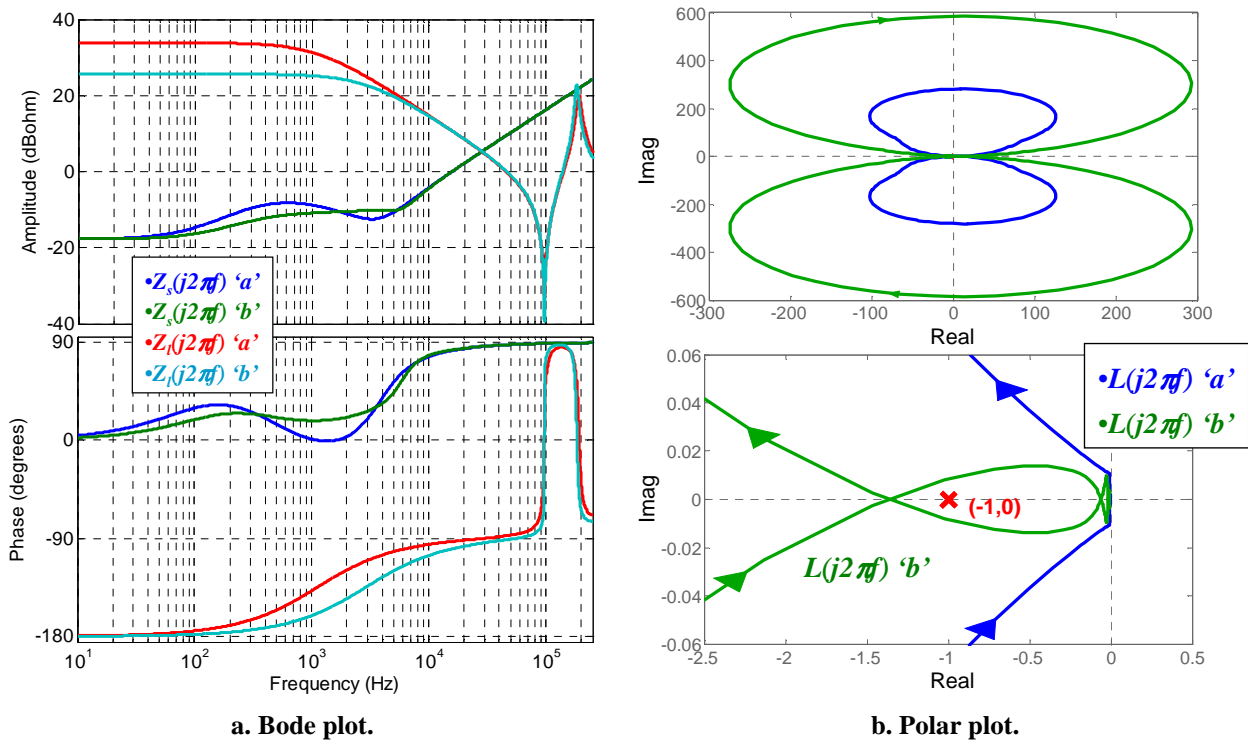


Fig. A-21: Analysis of system-level stability.

Therefore, it has been demonstrated that the black-box models can be used to predict system-level stability, not only by simulation, but also by analytical methods.

A.3.3. Stability of spacecraft system involving a solar array simulator (chapter 7)

In chapter 7, stability problems were observed due to dynamic interactions of a solar array simulator (SAS) with a solar array regulator (SAR) provided with output voltage control.

The experimental setup is reminded in Fig. 7-23. A boost converter provided with average current-mode-control (inner inductor current loop plus outer voltage loop) was applied as a SAR, while two solar array simulators (SASs), named SAS2 and SAS3, were applied at the input port.

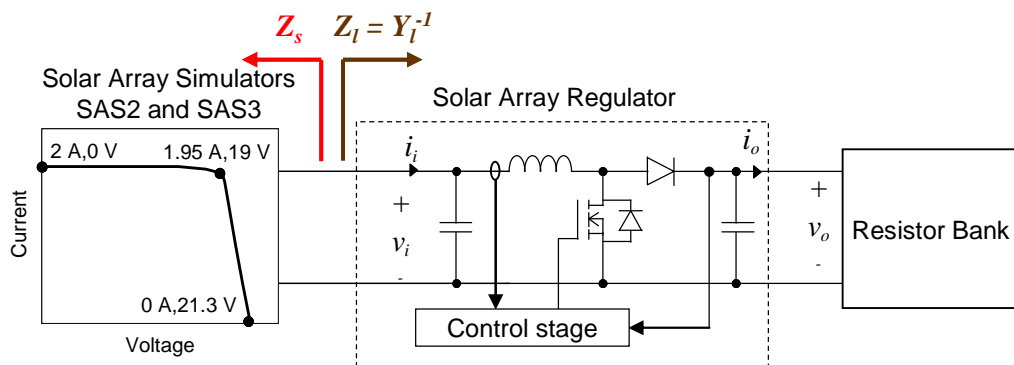


Fig. A-22: System under experimental study.

The obtained response under a load step from $P_o = 4.5$ W to $P_o = 28$ W is depicted in Fig. A-23. As can be seen, the system was found to be stable when using SAS2. However, when using SAS3, the system was stable for $P_o = 4.5$ W but unstable for $P_o = 28$ W.

Such problem can be analytically predicted by making use of small-signals impedance models of the solar array simulators (herein source subsystems) and boost converter (herein load subsystem). As a difference from the system tackled in section A.3.2, the stability has been analyzed directly by means of frequency responses experimentally measured through AC sweeps.

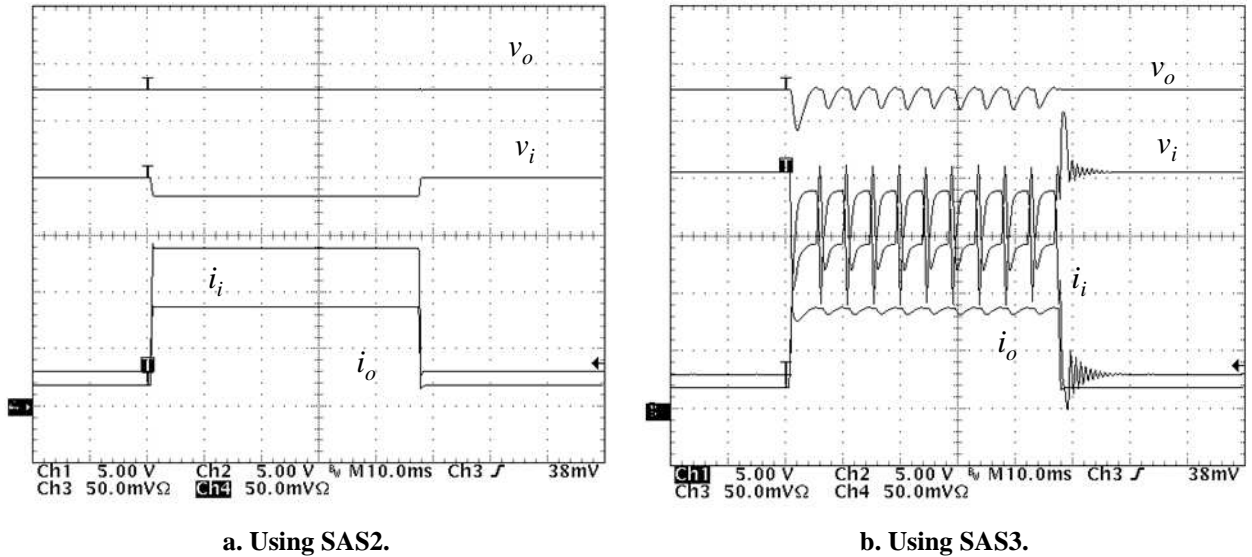


Fig. A-23: Transient response of the SAR under a resistive load step from 4.5 W to 28 W and back.

The impedances have been characterized by drawing sinusoidal current perturbations with a current amplifier, as shown in Fig. A-24a. The impedances has been characterized for both operating points depicted above, herein referred to as ‘a’ ($P_o=4.5$ W) and ‘b’ ($P_o=28$ W). The input impedance of the converter has been characterized by using SAS2 at the input port, as otherwise the system would become unstable for $P_o=28$ W.

The measured frequency responses are drawn in Fig. A-24b and discussed below.

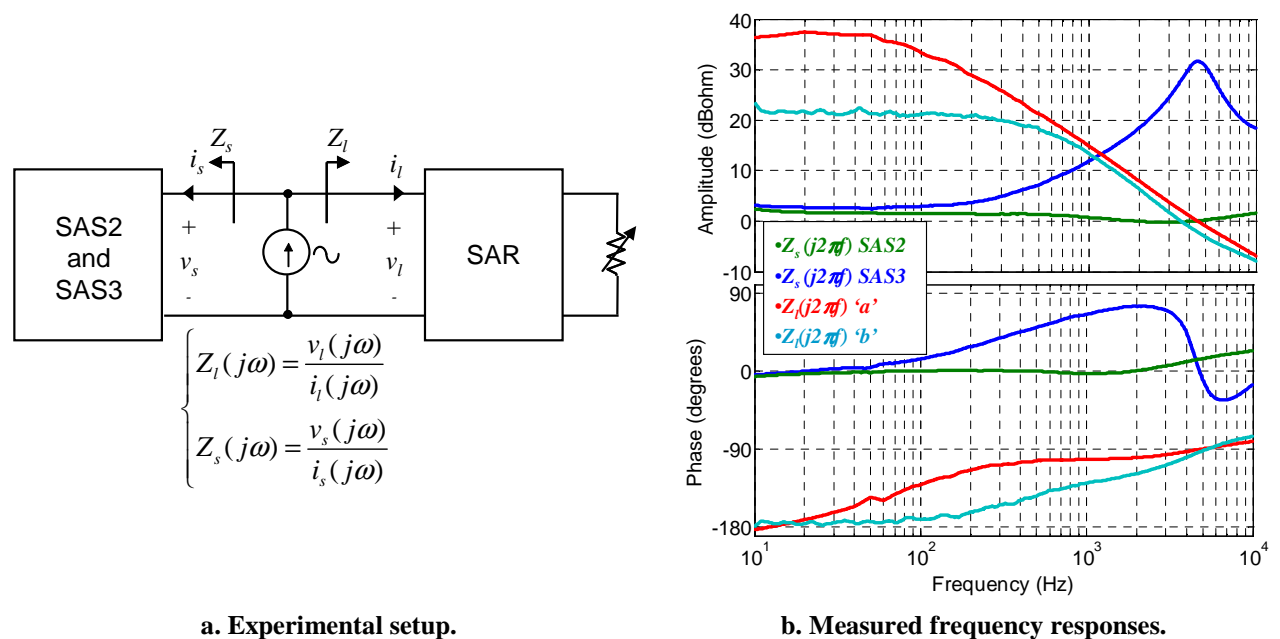
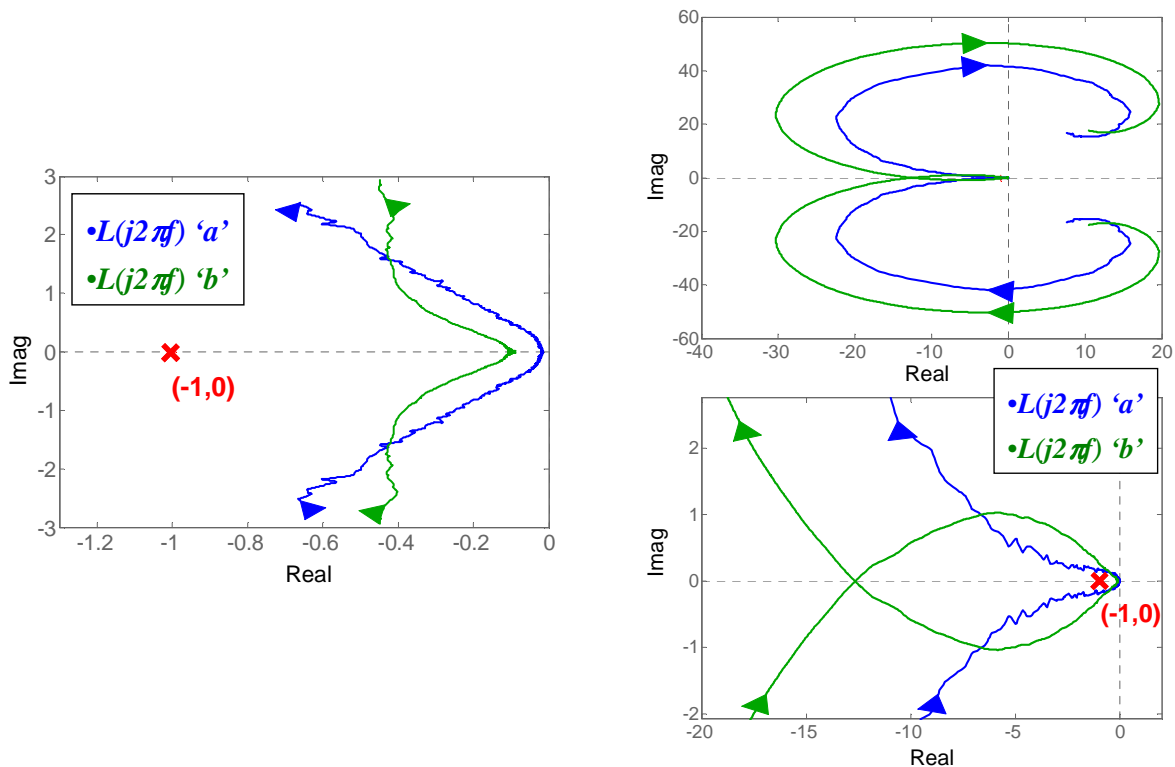


Fig. A-24: Frequency response characterization of the subsystem impedances and obtained results.

- The output impedance of the SASs is approximately linear within the working region, so the same frequency response is considered for both operating points.
- The input impedance of the boost converter behaves, approximately, as a negative resistor (due to its low-frequency CPL behavior) in parallel with its input capacitor.

Fig. A-25 shows the corresponding Nyquist diagrams of the minor loop gain for both solar array simulators. A discussion is given below.



a. Using SAS2.

b. Using SAS3 (detail around the (-1,0) point is shown below).

Fig. A-25: Nyquist diagram $L(j2\pi f)$ from experimental measurements for $f \in (10 \text{ Hz}, 10 \text{ kHz})$.

- If SAS2 is used, no significant dynamic interaction is predicted because the Nyquist path lies far from $(-1, 0)$.
- If SAS3 is applied, the system is stable for $P_o = 4.5 \text{ W}$. However, instability is predicted for $P_o = 28 \text{ W}$ because the Nyquist path circles the $(-1, 0)$ point. Such instability is essentially found out because of the resonance exhibited by this SAS.

Those observations are in agreement with the experimental results. Therefore, the usefulness of this analysis method, to predict instability in systems involving solar array simulators, has been demonstrated.

A.4. Some mathematical aspects about parametric identification

In this section, some mathematical aspects about parametric identification are described. These aspects were omitted in section 4 for the sake of a fluent exposition of the identification method.

The following aspects are herein discussed:

- Types of transfer function models.
- Optimization problem for each transfer function model.
- Impact of measurements pre-filtering on the optimization problem.

From the point of view of the author, the information herein presented may help starters who want to know the possible options in the parametric identification framework, and are interested in the basic mathematical aspects of the fitting process. This description is focused on transfer function models, so identification of state space models is not discussed. Information herein presented has been obtained from [66], [67], [68] and [72].

A.4.1. Model structures

The structure of the general transfer function model, identified through parametric methods, is given by (A-38), where $e(k)$ is white noise, $u(k)$ is the measured system input, $y(k)$ is the measured system output and q is a shift operator meaning $q^{-1}x(k) = x(k-1)$. $G(q)$ and $H(q)$ are the so-called input transfer function and noise transfer function, respectively^{A.1}.

$$y(k) = G(q) \cdot u(k) + H(q) \cdot e(k) \quad (\text{A-38})$$

This way, $H(q) \cdot e(k)$ allows modeling any noise realization, with a frequency spectrum different from that of white noise, and reproduces the stochastic part of the measured $y(k)$. On the other hand, the term $G(q) \cdot u(k)$ represents the deterministic part of $y(k)$.

Depending on the properties of $G(q)$ and $H(q)$, several transfer function models are defined. This is an important point, since the type of optimization algorithm, used for identification, will be strongly determined by those properties, as well as the fitting results. They can be classified within two groups: equation-error kind of models and output-error kind of models.

Below, such classification of models is described. Later on, advantages and disadvantages of them, in terms of optimization problem complexity and identification performance, are discussed.

A.4.1.1. Equation error family of models

These kind of models are characterized by a common denominator $A(q)$ shared by both $G(q)$ and $H(q)$, so they cannot be described separately. Hence, these models are suitable when the dominating disturbance makes influence “early” on the system dynamics. Two common configurations are the autoregressive with exogenous input (ARX) model and the autoregressive moving average with exogenous input (ARMAX) model (see Fig. A-26).

- The ARX model is the simplest model. It consists expressing the error as white noise that enters directly into the differential equation as follows. This results in a noise model $H(q) = 1/A(q)$.

^{A.1} It is hereinafter assumed that any offset in the measurements have been already subtracted.

$$y(k) + a_1 \cdot y(k-1) + \dots + a_{n_a} \cdot y(k-n) = b_1 \cdot u(k-1) + \dots + b_{n_b} \cdot u(k-m) + e(k) \quad (\text{A-39})$$

- The ARMAX model adds flexibility to the description of the noise model by filtering $e(k)$ through the polynomial $C(q)$ as follows. This results in a noise model $H(q) = C(q)/A(q)$.

$$y(k) + a_1 \cdot y(k-1) + \dots + a_{n_a} \cdot y(k-n) = b_1 \cdot u(k-1) + \dots + b_{n_b} \cdot u(k-m) + c(k) \cdot e(k) + c_1(k) \cdot e(k-1) + \dots + c_{n_c}(k) \cdot e(k-1) \quad (\text{A-40})$$

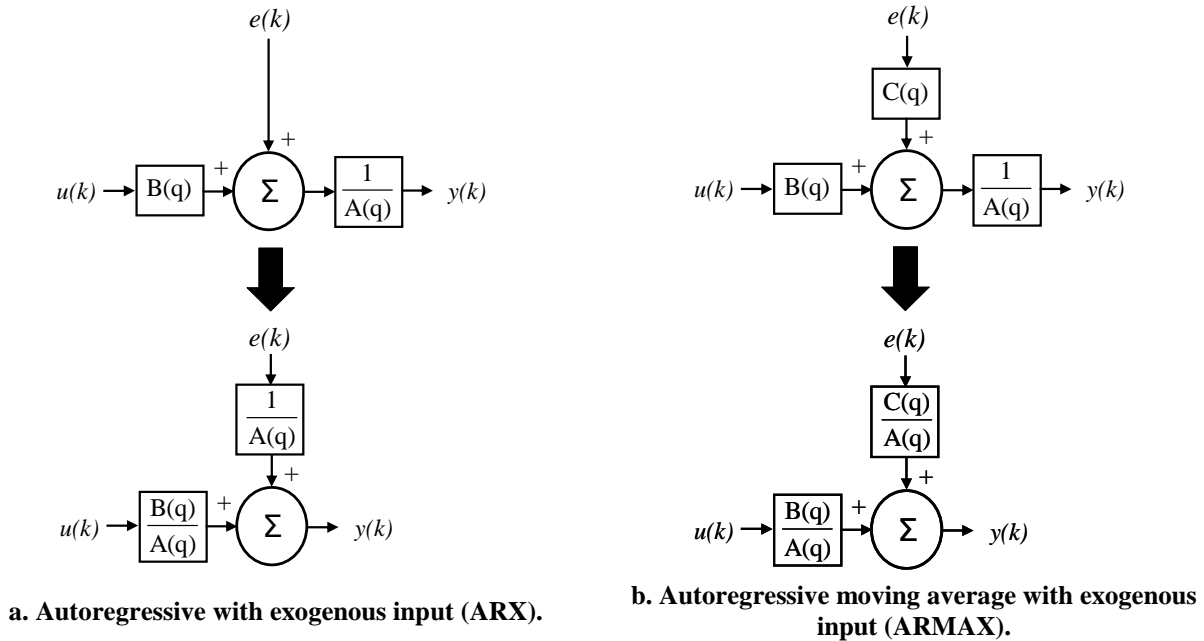


Fig. A-26: Equation error family of models.

A.4.1.2. Output error family of models

These models are characterized by independent descriptions of $G(q)$ and $H(q)$, i.e. no parameters are shared. They assume that the dominating noise is directly added at the output. The most common ones are the so-called Output Error (OE) model and Bob Jenkins (BJ) model (see Fig. A-27).

- The OE model assumes white noise representation that is directly added to the process output, as shown below. It corresponds to unity gain noise model $H(q) = 1$.

$$\begin{cases} w(k) + a_1 \cdot w(k-1) + \dots + a_{n_a} \cdot w(k-n) = b_1 \cdot u(k-1) + \dots + b_{n_b} \cdot u(k-m) \\ y(k) = w(k) + e(k) \end{cases} \quad (\text{A-41})$$

- The BJ model is obtained by adding to OE a noise model independent of the deterministic model, $H(q) = C(q)/D(q)$. It is the most flexible, but also most complex, model structure. The corresponding differential equation is given below.

$$\begin{cases} w(k) + a_1 \cdot w(k-1) + \dots + a_{n_a} \cdot w(k-n) = b_1 \cdot u(k-1) + \dots + b_{n_b} \cdot u(k-m) \\ w(k) + d_1 \cdot w(k-1) + \dots + d_{n_d} \cdot w(k-n) + c(k) \cdot e(k) + c_1(k) \cdot e(k-1) + \dots + \\ + c_{n_c}(k) \cdot e(k-n) = d_1 \cdot y(k-1) + \dots + d_{n_d} \cdot y(k-m) \end{cases} \quad (\text{A-42})$$

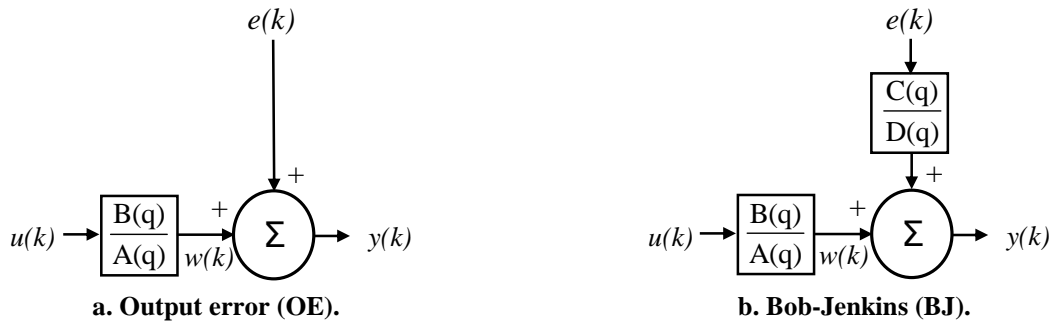


Fig. A-27: Output error family of models.

A.4.2. Optimization problem

Selection of the model structure has a significant impact on the subsequent optimization problem. In this section, some basic aspects about it are discussed.

A.4.2.1. The prediction error method

A common method to fit the parameters of a parametric model, denoted by the vector θ , is the Prediction Error Method (PEM). It consists in minimizing the prediction error $\varepsilon(k)$, defined as the difference between the actual output $y(k)$ and the predicted output $\hat{y}(k)$.

$$\varepsilon(k) = y(k) - \hat{y}(k) \tag{A-43}$$

The model parameters are fitted by minimizing a certain cost function of $\varepsilon(k)$. The sum of squared prediction errors is a typical choice (A-44)^{A.2}, where N is the number of samples ('*argmin*' denotes minimizing argument). This function is optimal (in the maximum likelihood sense) if the noise is Gaussian distributed, among other statistical properties [68].

$$COF = \sum_{k=1}^N \varepsilon^2(k), \quad \theta = \underset{\theta}{\operatorname{argmin}} COF \tag{A-44}$$

In order to minimize (A-44), the predicted output $\hat{y}(k)$ has to be expressed as a function of the model parameters and measurements. The optimal predictor for $\hat{y}(k)$ can be derived in a simple manner as follows [68].

Consider the general parametric model defined by (A-38). If the model is capable of extracting all information out from the input-output signals, the difference between the actual output $y(k)$ and the predicted output $\hat{y}(k)$ should be white noise, $e(k)$, as this is the only unpredictable part in (A-38). Hence, the following equation is obtained.

$$\varepsilon(k) = e(k) = y(k) - \hat{y}(k) \tag{A-45}$$

By combining (A-45) and (A-38), $e(k)$ can be removed, leading to the following definition of the optimal predictor.

$$\hat{y}(k) = \frac{G(q)}{H(q)} \cdot u(k) + \left(1 - \frac{1}{H(q)}\right) \cdot y(k) \tag{A-46}$$

^{A.2} The cost function is typically denoted in System Identification literature as V . However, acronym COF is used in this thesis to avoid confusion with steady-state voltage.

Finally, by replacing (A-46) into (A-43) and rearranging, the following expression for the prediction error is obtained. Further mathematical aspects about it can be found in [66].

$$\varepsilon(k) = \frac{1}{H(q)} \cdot (y(k) - G(q) \cdot u(k)) \quad (\text{A-47})$$

Below, the prediction error is particularized for the model structures discussed above and some optimization methods are discussed.

A.4.2.2. ARX model: a linear optimization problem

The ARX model is featured by $G(q) = B(q)/A(q)$ and $H(q) = 1/A(q)$, so the following expressions for the optimal predictor and the prediction error are obtained.

$$\begin{cases} \hat{y}(k) = B(q) \cdot u(k) - (1 - A(q)) \cdot y(k) \\ \varepsilon(k) = A(q) \cdot y(k) - B(q) \cdot u(k) \end{cases} \quad (\text{A-48})$$

As can be seen, there is a linear relationship between the prediction error and the model parameters. This is a key feature of the ARX model, as the sum of squared prediction errors (A-44) results in a simple linear least-square problem.

The least-squares problem is stated below [66]. Considering an ARX model defined by (A-39), the regression vector φ and the parameters vector θ can be defined as follows:

$$\begin{cases} \varphi(k) = (-y(k-1) \quad \cdots \quad y(k-n_a) \quad u(k-1) \quad \cdots \quad u(k-n_b))^T \\ \theta = (a_1 \quad \cdots \quad a_{n_a} \quad b_1 \quad \cdots \quad b_{n_b})^T \end{cases} \quad (\text{A-49})$$

The predicted output and the prediction error can be expressed in a linear manner as follows:

$$\begin{cases} \hat{y}(k) = \varphi^T(k) \cdot \theta \\ \varepsilon(k) = y(k) - \varphi^T(k) \cdot \theta \end{cases} \quad (\text{A-50})$$

Minimization of the sum of squared errors yields the following expression for the model parameters.

$$\theta = \arg \min \sum_{k=1}^N \varepsilon^2(k) = \left[\sum_{k=1}^N \varphi(k) \varphi^T(k) \right]^{-1} \left[\sum_{k=1}^N \varphi(k) y(k) \right] \quad (\text{A-51})$$

Consequently, the parameters can be directly obtained just by solving numerically (A-51). This is a great advantage of the ARX model over other models. However, due to the required matrix inversion, bad conditioning problems may arise if the datalength and model order are high. To avoid it, mathematical methods, such as *QR* factorization, can be used to solve the least squares problem. For instance, the Matlab function ‘*arx*’ solves the problem in this way.

A major drawback of ARX is that, if the true system does not meet the noise assumptions made by this model (i.e. $H(q) = 1/A(q)$), then consistency and biasing problems arise. Such effects are briefly described below [68]. More details can be found in [66].

- Bias^{A.3} means that the model parameters systematically deviate from their optimal values.

^{A.3} This is a statistical concept, different from bias in the sense of steady-state signals in electronics.

- Non-consistency means that the bias does not approach zero as N tends to infinity.

Real systems rarely meet the condition $H(q) = 1/A(q)$, so bias and consistency problems typically arise when fitting an ARX model, meaning a degradation of the fitting performance. Consequently, higher model order for $A(q)$ and $B(q)$ than necessary may be required to obtain a good fit. Nevertheless, under very low noise content, such problems may be less important [67].

Finally, some additional aspects of interested are pointed out:

- Alternative methods to the direct least-squares solution have been developed, such as the instrumental variable method [72], aiming to avoid non-consistency while retaining the linear properties of the ARX model [68]. This method can be applied using the Matlab function ‘iv’.
- Unstable models can be identified with equation error models (ARX and ARMAX). This is because the denominator of the input model, $A(q)$, only appears in the numerator of the prediction error equation. Hence, the predictor is stable even if $G(q)$ is unstable [68].

A.4.2.3. OE model: a nonlinear optimization problem

Models belonging to the family of output error models feature a noise model $H(q)$ that is independent of the deterministic model $G(q)$. However, all of them are nonlinear in their parameters and are more complex to estimate than equation error models [68]. For example, OE model is characterized by $G(q) = B(q)/A(q)$ and $H(q) = 1$, which results in the following prediction error:

$$\begin{cases} \hat{y}(k) = \frac{B(q)}{A(q)} \cdot u(k) \\ \varepsilon(k) = y(k) - \frac{B(q)}{A(q)} \cdot u(k) \end{cases} \quad (\text{A-52})$$

One key advantage of output error family of models over equation error models is that they are always estimated un-biased and consistently. It holds because $G(q)$ and $H(q)$ are independent. Therefore, good fitting results for $G(q)$ can be obtained using a reasonable number of parameters, even if the noise model is not appropriate. In fact, as demonstrated throughout this thesis, OE models yield good fitting results using a relatively low number of parameters even using noisy signals (whose noise realization is clearly different from white noise).

On the other hand, it is worth point out that output error models yield always stable models. This is because $A(q)$ appears in the denominator of $\hat{y}(k)$, so the predictor is stable only if $G(q)$ is stable.

Along this thesis, this model has been estimated using the ‘oe’ function implemented in the System Identification Toolbox of Matlab. By means of this function, the sum of squared prediction errors, given by (A-44), has been minimized by using Gauss-Newton search [67], [72]. For illustrative purposes, the basis of this method is herein described^{A.4}. The idea behind Newton methods is to search for a minimum of COF by minimizing its derivative with respect to the vector of parameters θ :

^{A.4} The aim is to give some insight about the method, so details about the implementation of the Matlab function may differ from this explanation.

$$\frac{d}{d\theta} COF = 0 \quad (\text{A-53})$$

This equation is numerically solved by iteratively selecting ' θ ' as follows, where ' it ' denotes iteration number, ' μ ' denotes a step length parameter, ' g ' denotes the gradient of the cost function (first derivative) and ' H ' denotes the Hessian (second derivative).

$$\theta_{(it+1)} = \theta_{(it)} - \mu_{(it)} [H_{(it)}]^{-1} g_{(it)} \quad (\text{A-54})$$

In case of a quadratic function, such as (A-44), the gradient and the Hessian are defined as follows, where $\lambda(k)$ represents the derivative of the predicted output. If Gauss-Newton search is used, the second term in H is neglected.

$$\begin{cases} g = \frac{d}{d\theta} CF = -2 \sum_{k=1}^N \underbrace{\left(\frac{d}{d\theta} \hat{y}(k) \right)}_{\lambda(k)} \cdot \varepsilon(k) \\ H = \frac{d^2}{d\theta^2} CF = 2 \sum_{k=1}^N \left(\lambda(k)^T \cdot \lambda(k) + \frac{d\lambda(k)}{d\theta} \cdot \varepsilon(k) \right) \underset{\text{Gauss-Newton}}{\approx} 2 \sum_{k=1}^N \left(\lambda(k)^T \cdot \lambda(k) \right) \end{cases} \quad (\text{A-55})$$

Below, the expressions above shown are particularized for the Output Error model and Gauss-Newton search. In this case the predicted output and the vector of parameters are defined as:

$$\begin{cases} \hat{y}(k) = \frac{B(q)}{A(q)} \cdot u(k) \\ \theta = [a_1 \quad \dots \quad a_{n_a} \quad b_1 \quad \dots \quad b_n] \end{cases} \quad (\text{A-56})$$

The derivate of the predicted output is given by the following expression.

$$\lambda(k) = \left[-\frac{B(q)}{A^2(q)} u(k-1) \quad \dots \quad -\frac{B(q)}{A^2(q)} u(k-n_a) \quad \frac{1}{A(q)} u(k-1) \quad \dots \quad \frac{1}{A(q)} u(k-n_b) \right]^T \quad (\text{A-57})$$

Substituting (A-57) and (A-55) into (A-54), the following equation results for the iterative search of parameters θ . The search finished when the variation of θ is below a certain threshold level.

$$\theta_{(it+1)} = \theta_{(it)} - \mu_{(it)} \left[\sum_{k=1}^N \lambda_{(it)}(k)^T \cdot \lambda_{(it)}(k) \right]^{-1} \sum_{k=1}^N \lambda_{(it)}(k)^T \cdot \varepsilon_{(it)}(k) \quad (\text{A-58})$$

A.4.2.4. ARMAX and BJ models

Finally, some comments are given about the other two typical model structures: ARMAX and BJ.

ARMAX: The ARMAX model is featured by $G(q) = B(q)/A(q)$ and $H(q) = C(q)/A(q)$, so the following prediction error results.

$$\varepsilon(k) = \frac{A(q)}{C(q)} \cdot y(k) - \frac{B(q)}{C(q)} \cdot u(k) \quad (\text{A-59})$$

As a difference from ARX, $\varepsilon(k)$ is nonlinear in its parameters. However, such nonlinearity is found only in terms of the noise model. Hence, it can be expressed in a pseudo-linear form as follows [68]:

$$\varepsilon(k) = A(q) \cdot y(k) - B(q) \cdot u(k) + (1 - C(q)) \cdot \varepsilon(k) \quad (\text{A-60})$$

Then, effective pseudo-linear algorithms, such as the extended least-squares method, can be used to minimize it. It consists in estimating an ARX model and using the resulting prediction errors as regressors to minimize (A-60). This process is iteratively applied until convergence is achieved. Nevertheless, nonlinear iterative methods can be also used. In general, ARMAX is simpler to minimize than BJ and OE [68]. However, $H(q)$ shares denominator with $G(q)$.

BJ: Concerning BJ, this is the most general and flexible structure. However, many parameters have to be estimated and the description of the prediction error is the most complex (A-61). Consequently, in practice, this structure is the less utilized.

$$\varepsilon(k) = \frac{B(q)D(q)}{A(q)C(q)}u(k) + \frac{C(q) - D(q)}{C(q)} \cdot y(k) \quad (\text{A-61})$$

A.4.2.5. Pre-filtering as a way of tuning the noise model

As explained in chapter 4, pre-filtering can be used to minimize noise and switching ripple. Mathematically, pre-filtering has some important implications which are worth to discuss [66], [68].

For the sake of clarity, the general parametric model is recalled below:

$$y(k) = G(q) \cdot u(k) + H(q) \cdot e(k) \quad (\text{A-62})$$

Consider both the input and the output signals are pre-filtered through $L(q)$. This yields the following expression:

$$L(q) \cdot y(k) = G(q) \cdot L(q) \cdot u(k) + H(q) \cdot e(k) \quad (\text{A-63})$$

Rearranging (A-63) yields (A-64), which shows that pre-filtering both $u(k)$ and $y(k)$ through $L(q)$ is equivalent to change the noise model from $H(q)$ to $H'(q) = H(q)/L(q)$.

$$y(k) = G(q) \cdot u(k) + \underbrace{\frac{H(q)}{L(q)}}_{H'(q)} \cdot e(k) \quad (\text{A-64})$$

The general expression for the prediction error (A-47) can be rewritten accordingly. This yields the following minimization function:

$$COF = \sum_{k=1}^N \varepsilon^2(k) = \left[\frac{L(q)}{H(q)} \cdot (y(k) - G(q) \cdot u(k)) \right]^2 \quad (\text{A-65})$$

Therefore, pre-filtering can be seen as a way of fixing desired properties to the noise model. In case of an OE model, pre-filtering means fixing the disturbance model to $H'(q) = 1/L(q)$.

B. References

B.1. Power distribution systems	387
B.1.1. Telecommunications, datacenters and computers	387
B.1.2. The more electric aircraft	387
B.1.3. Electric vehicles	388
B.1.4. All Electric Ships	388
B.1.5. Microgrids and Nanogrids.....	388
B.1.6. Spacecraft.....	389
B.2. Constant Power Loads and system-level stability.....	389
B.3. System Identification	390
B.4. Modeling and identification of Power Electronics Converters.....	391
B.4.1. Converter-level modeling and identification.....	391
B.4.2. System-level modeling and identification.....	394
B.5. Three Phase Voltage Source Converters	396
B.6. Fuel Cells.....	398
B.7. Switched Reluctance Starter Generators.....	398
B.8. Solar array and solar array simulators	400
B.9. Various.....	400
B.10. Technical notes, datasheets and software tools	400

B.1. Power distribution systems

B.1.1. Telecommunications, datacenters and computers

- [1] W. A. Tabisz, M. M. Jovanovic and F. C. Lee "Present and future of distributed power systems", Proc. IEEE Appl. Power Electron. Conf. Expo. (APEC), pp.11 1992.
- [2] B. Mammano, "Distributed Power Systems," Unitrode Power Supply Design Seminar, SEM 900, 1993.
- [3] R. Miftakhutdinov, "Power distribution architecture for tele- and data communication system based on new generation intermediate bus converter," in proc. of International Telecommunications Energy Conference (INTELEC), 2008, pp. 1-8.
- [4] P. Lindman and L. Thorsell "Applying distributed power modules in telecom systems", IEEE Trans. Power Electron., vol. 11, pp.365 1996.
- [5] R. White, "Emerging on-board power architectures", Proc. IEEE APEC conf. 2003, pp.799 2003.
- [6] L. Brush, "Distributed power architecture demand characteristics", Proc. IEEE APEC conf. 2004, pp.342 2004.
- [7] S. Luo, I. Batarseh, "A review of distributed power systems part I: DC distributed power system", IEEE Aerosp. Electron. Syst. Mag., vol. 20, pp.5 2005.
- [8] M. Barry, "Design Issues in regulated and unregulated Intermediate Bus converters", in proc. of 19th IEEE Appl. Power Electron. Conf. (APEC), 2004, pp.1389-1394.

B.1.2. The more electric aircraft

- [9] R. Jayabalan , B. Fahimi , A. Koenig and S. Pekarek "Applications of power electronics-based systems in vehicular technology: State of the art and future trends", Proc. IEEE Power Electron. Spec. Conf. (PESC 2004), pp.1887, 2004.
- [10] Maldonado, M. A., et al. Power management and distribution system for a More electric aircraft (MADMEL)–Program status. In Proceedings of the Intersociety Energy Conversion Engineering Conference (IECEC), Aug. 1997, 274—279.
- [11] J.A. Weimer, Electrical Power Technology for the More Electric Aircraft, Proc. of IEEE 12th Digital Avionics Systems Conf., 1993, pp. 445-450.
- [12] A. Emadi and M. Ehsani "Aircraft power systems: Technology, state of the art and future trends", IEEE Aerosp. Electron. Syst. Mag., vol. 15, pp.28 2000.
- [13] J. A. Rosero , J. A. Ortega , E. Aldabas and L. Romeral "Moving towards a more electric aircraft", IEEE Aerosp. Electron. Syst. Mag., vol. 22, pp.3 2007.
- [14] R. Todd, and A. J. Forsyth, "HIL Emulation of All-Electric UAV Power Systems", in proc. of IEEE Energy Conversion Congress and Exposition (ECCE), 2009 pp. 411 – 416.
- [15] D. Izquierdo, "Estrategias Avanzadas de Control, Modelado, Diseño e Implementación de Controladores de Potencia de Estado Sólido (SSPC) para su Aplicación en Sistemas de Distribución de Potencia Eléctrica Embarcados", PhD. Thesis, Dec. 2010, Carlos III University of Madrid, Leganes, Spain, online available at <http://e-archivo.uc3m.es/> (last visit May'12).
- [16] D. Izquierdo, R. Azcona, F. del Cerro, C. Fernandez, B. Delicado, "Electrical power distribution system (HV270DC), for application in more electric aircraft", in Proc. of IEEE Appl. Power Electron. Conf. (APEC), pp 1300-1305, 21-25 Feb. 2010.
- [17] F. del Cerro, "Aviones más Eléctricos", presented at the 3rd Edition of the Annual Meeting of CEI-UPM, Madrid 27-28 May 2010. online available at <http://www.cei.upm.es> (last visit May'12).

- [18] D. Izquierdo, A. Barrado, C. Raga, M. Sanz, A. Lazaro, "Protection Devices for Aircraft Electrical Power Distribution Systems: State of the Art", IEEE. Trans. on Aerospace and Electronics Systems, Volume: 47 , Issue: 3, pp. 1538 – 1550, 2011.
- [19] J. Sun, "Ac power electronics systems: stability and power quality," in Proc. IEEE COMPEL Workshop 2008, pp. 1 – 10.
- [20] Tim Nelson, "787 Systems and Performance", Boeing Commercial Airplanes, Flight Operations Engineering, 2005, online available at <http://dibley.eu.com> (last visit May'12).

B.1.3. Electric vehicles

- [21] X. Xu, "Automotive power electronics-opportunities and challenges", Proc. Int. Conf. Electric Machines and Drives, pp.260 -262 1999.
- [22] J. M. Miller, A. Emadi, A. V. Rajarathnam, and M. Ehsani, "Current status and future trends in more electric car power systems", Proc. IEEE Veh. Technol. Conf., 1999.
- [23] C. C. Chan, "The state of the art of electric and hybrid vehicles", Proc. IEEE, vol. 90, no. 2, pp. 247–275, Feb. 2002.
- [24] A. Emadi, Sheldon S. Williamson, and Alireza Khaligh, "Power electronics intensive solutions for advanced electric, hybrid electric, and fuel cell vehicular power systems," IEEE Trans. Power Electron., vol. 21, no. 3, pp. 567-577, May 2006.
- [25] A. Emadi, Y. J. Lee; K. Rajashekara, "Power Electronics and Motor Drives in Electric, Hybrid Electric, and Plug-In Hybrid Electric Vehicles", IEEE Trans. Ind. Electron., vol. 55, no. 6, pp. 2237-2245, Jun. 2008.
- [26] P. Thounthong, S. Raël, and B. Davat, "Control algorithm of fuel cell and batteries for distributed generation system," IEEE Trans. Energy Conversion, vol. 23, pp. 148–155, Mar. 2008.
- [27] C. C. Chan "The state of the art of electric, hybrid, and fuel cell vehicles", Proc. IEEE, vol. 95, pp.704 2007.

B.1.4. All Electric Ships

- [28] B. Wagner, "All-Electric Ship Could Begin to Take Shape By 2012", NDIA National Defense Magazine, November 2007, online available at <http://www.nationaldefensemagazine.org> (last visit May'12).
- [29] A. Ouroua , L. Domaschk and J. H. Beno "Electric ship power system integration analyses through modeling and simulation", Proc. IEEE 2005 Electr. Ship Technol. Symp. (ESTS), pp. 70.
- [30] C.G., Hodge, "Modern applications of power electronics to marine propulsion systems", in proc. of the 14th International Symposium on Power Semiconductor Devices and ICs, 2002, pp. 9-16.
- [31] S. D. Sudhoff , S. Pekarek , B. Kuhn , S. Glover , J. Sauer and D. Delisle "Naval combat survivability testbeds for investigation of issues in shipboard power electronics based power and propulsions systems", Proc. IEEE Power Eng. Soc. Summer Meet., vol. 1, pp.347 2002.
- [32] Y. Xie , G. Seenumani , J. Sun , Y. Liu and Z. Li "A PC-cluster based real-time simulator for all electric ship integrated power systems analysis and optimization", Proc. IEEE 2007 Electr. Ship Technol. Symp. (ESTS), pp.396.

B.1.5. Microgrids and Nanogrids

- [33] R. Lasseter "Microgrids", Proc. IEEE Power Eng. Soc. Winter Meet., pp.305 2002.
- [34] N. Hatziargyriou , H. Asano , R. Irvani and C. Marnay, "Microgrids", IEEE Power Energy Mag., vol. 5, pp.78 2007.
- [35] M. Barnes , J. Kondoh , H. Asano , J. Oyarzabal , G. Ventakaramanan , R. Lasseter , N. Hatziargyriou and T. Green "Real-world microgrids- An overview", Proc. IEEE Int. Conf. Syst. Syst. Eng., pp.1 2007.

- [36] Lasseter, R.H.; Eto, J.H.; Schenkman, B.; Stevens, J.; Vollkommer, H.; Klapp, D.; Linton, E.; Hurtado, H.; Roy, J. "CERTS Microgrid Laboratory Test Bed", IEEE Transactions on Power Delivery, vol. 26, no. 1, 2011, pp. 325-332.
- [37] J. M. Guerrero, J. C. Vasquez, J. Matas, L. Garcia de Vicuña, and M. Castilla, "Hierarchical control of droop-controlled AC and DC microgrids—A general approach toward standardization", IEEE Trans. Ind. Electron., vol. 58, no. 1, pp. 158–172, Jan. 2011.
- [38] Arnedo, L.; Dwari, S.; Blasko, V.; Park, S., "80 kW hybrid solar inverter for standalone and grid connected applications", in proc. of the 27th Applied Power Electronics Conference and Exposition (APEC), IEEE, 2012, pp. 270 – 276.
- [39] D. Boroyevich, I. Cvetkovic, Dong Dong, R. Burgos, F. Wang, F. Lee, "Future electronic power distribution systems: a contemplative view" in proc. of 12th International Conference on Optimization of Electrical and Electronic Equipment (OPTIM), 2010.
- [40] P. Mattavelli, "CPES Initiative on Sustainable Buildings and Nanogrids", special presentation at IEEE Appl. Power Electron. Conf. (APEC), 2011, online available at: <http://www.apec-conf.org/2011/> (last visit May'12).
- [41] D. Boroyevich, I. Cvetkovic, D. Dong, "Intergrid: A Future Electronic Energy Network?", in proc. of CPES Annual Power Electronics Conference, 2012.
- [42] D. Boroyevich, "Intergrid: A Future Electronic Energy Network?", plenary presentation at IEEE Appl. Power Electron. Conf. (APEC), 2011, online available at: <http://www.apec-conf.org/2011/> (last visit May'12).

B.1.6. Spacecraft

- [43] Ley, W.; Wittmann, K.; Hallmann, W. Handbook of Space Technology; Wiley Press: New York, 2009
- [44] A. Weinberg, D. O Sullivan, "The sequential Serial Shunt Regulator -S³R", Proceedings of the Third ESTEC Spacecraft Power Conditioning Seminar, Noordwijk, The Netherlands, 21-23 September 1977.
- [45] P. Perol, "Another look at the sequential switching shunt regulator," in record, 5th European Space Power Conf. (ESPC), 1998, ESA SP-416, pp. 79–84.
- [46] A. Fernandez, F. Tonicello, J. Aroca, O. Mourra, "Battery discharge regulator for space applications based on the boost converter" proc. of the 25th IEEE APEC, 2010.
- [47] O. Mourra, A. Fernandez, F. Tonicello, "Buck Boost Regulator (B2R) for spacecraft SA Power Conversion", proc. of the 25th IEEE APEC, 2010.
- [48] H. Jensen, J. Laursen, "Power Conditioning Unit for Rosetta/Mars Express" , proc. of the 6th ESPC, 2002.
- [49] F. Tonicello, H. Jensen, J. Laursen, "Power Conditioning Unit for Rosetta/Mars Express- Lessons learnt", proc. of the 6th ESPC, May 2002.
- [50] O. Garcia, P. Alou, J. Oliver, D. Diaz, D. Meneses, J. Cobos, A. Soto, E. Lapeña, J. Rancaño, "Boost-based MPPT Converter Topology Trade-off for Space Applications" , proc. of the 8th ESPC, 2008.
- [51] H. Jensen, "Power Conditioning Unit for BepiColombo Transfer Module", proc. of the 8th ESPC, 2008.

B.2. Constant Power Loads and system-level stability

- [52] M. Cespedes, L. Xing, J. Sun, "Constant-Power Load System Stabilization by Passive Damping", IEEE Transactions on Power Electronics, Volume: 26 , Issue: 7, 2011 , pp. 1832 – 1836
- [53] R. D. Middlebrook, "Input filter considerations in design and application of switching regulators", IEEE Industry Applicat. Soc. Annu. Meeting, 1976 Record.
- [54] B. H. Cho , J. R. Lee and F. C. Lee "Large-signal stability analysis of spacecraft power processing systems", IEEE Trans. Power Electron., vol. 5, pp.110 1990.

- [55] C. M. Wildrick and F. C. Lee, "A method of defining the load impedance specification for a stable distributed power system", *IEEE Trans. Power Electron.*, vol. 10, pp.280 -285 1995.
- [56] Griffio, A.; Jiabin Wang, "Large Signal Stability Analysis of 'More Electric' Aircraft Power Systems with Constant Power Loads" *IEEE Trans. Aero. Electron. Systems*, vol. 48, no. 1, 2012, pp. 477-489.
- [57] J. R. LeSage, R.G. Longoria, W. Shutt, "Power system stability analysis of synthesized complex impedance loads on an electric ship", in *proc. of IEEE Electric Ship Technologies Symposium (ESTS)*, 2011, pp. 34-37.
- [58] A. Emadi, A. Khaligh, C. H. Rivetta and G. A. Williamson, "Constant power loads and negative impedance instability in automotive systems: Definition, modeling, stability, and control of power electronic converters and motor drives", *IEEE Trans. Veh. Technol.*, vol. 55, pp.1112, 2006.
- [59] M. Belkhat, "Stability criteria for AC power systems with regulated loads", Ph.D. Dissertation, Purdue University, December, 1997.
- [60] R. Burgos , D. Boroyevich , F. Wang , K. Karimi and G. Francis "On the Ac stability of high power factor three-phase rectifiers", *Proc. 2010 IEEE Energy Convers. Congr. Expo. (ECCE)*, pp.2047 -2054.
- [61] J. Sun, "Small-signal methods for AC distributed power systems—A review," *IEEE Trans. Power Electron.*, vol. 24, no. 11, pp. 2545–2554, Nov. 2009.
- [62] B. Wen, D. Boroyevich, P. Mattavelli, Z. Shen, R. Burgos, "Experimental Verification of The Generalized Nyquist Stability Criterion for Balanced Three-phase Ac Systems in the Presence of Constant Power Loads", in *Proc. 2012 IEEE Energy Convers. Congr. Expo. (ECCE)*, pp. 3926-3933.
- [63] Y. V. Panov and F. C. Lee, "Modeling and stability analysis of a dc power system with solid state power controllers". in *proc. Of IEEE Appl. Power Electronc. Conf. (APEC)*, vol. 2, Mar. 3-7, 1996, pp. 685-691.
- [64] H. Bae, J. Lee, S. Park, B. Cho, "Large-signal stability analysis of SA power system", *IEEE Trans. Aero. Electron. Sys.*, vol. 44, n. 2, pp: 538-547, 2008.

B.3. System Identification

- [65] L. Ljung, "Perspectives on system identification", *Annual Reviews in Control*, vol. 34, no. 1, Ap. 2010, pp. 1–12.
- [66] L. Ljung, "System Identification: Theory for the User", 1999, Prentice-Hall.
- [67] L. Ljung, T. Glad, "Modeling of Dynamic Systems", Prentice Hall, 1994.
- [68] O. Nelles, "Nonlinear System Identification", 2001, Springer-Verlag.
- [69] Torsten Bohlin, "Practical Grey-box process identification", 2006, Springer.
- [70] Gabor Horvath, "Neural Networks for Instrumentation, Measurements and Related Industrial applications, chapter 4", 2003, IOS Press, Nato Science Series.
- [71] J. Sedano Franco, J. R. Villar Flecha, "Introducción a la identificación de sistemas", *Técnica Industrial*, no. 256, April 2005, pp. 31-36.
- [72] Y. Zhu, "Multivariable system identification for process control", 2001, Elsevier.
- [73] T. Söderström, P. Stoica, "System Identification", 1989, Prentice Hall.
- [74] G. Gregorčič and G. Lightbody, "Nonlinear system identification: From multiple-model networks to Gaussian processes," *Engineering Applications of Artificial Intelligence*, vol. 21, October 2008, pp. 1035-1055.

B.4. Modeling and identification of Power Electronics Converters

B.4.1. Converter-level modeling and identification

- [75] D. Maksimovic, A. M. Stankovic, V. J. Thsottuvelil and G. C. Verghese, "Modeling and simulation of power electronic converters", Proc. IEEE, vol. 89, pp.898 2001.
- [76] N. O. Sokal, R. Redl, "Computer program for fast simulation and optimization of single-ended inductor-fed zero-voltage switching series-resonant DC/DC converters and DC/AC inverters with any loading topology", in Proc. of IEEE Appl. Power Electron. Conf. (APEC) 1989, pp. 303- 314.
- [77] Jun Wang, Tiefu Zhao, Jun Li, Huang, A.Q., Callanan, R., Husna, F., Agarwal, A., "Characterization, Modeling, and Application of 10-kV SiC MOSFET", IEEE Trans. on Electron Devices, vol. 55, no. 8, 2008, pp. 1798-1806.
- [78] H. A. Peterson, J. P. C. Krause, J. F. Luini, and C. H. Thomas, "An analog computer study of a parallel ac and dc power system," IEEE Trans. Power App. Syst., vol. PAS-85, no. 3, pp. 191–209, Mar. 1966.
- [79] T. A. Lipo, "Analog computer simulation of a three-phase full wave controlled rectifier bridge", Proc. IEEE, pp.2137 1969.
- [80] G. W. Wester, "Low-frequency characterization of switched dc-dc converters", PhD Thesis, 1972, California Institute of Technology, Pasadena.
- [81] W. Wester and R. D. Middlebrook, "Low-Frequency Characterization of Switched DC-to-DC Converters," in proc. of IEEE Power Processing and Electronics Specialists Conference, May 1972, pp. 9 – 20.
- [82] G. W. Wester and R. D. Middlebrook "Low-frequency characterization of switched dc-dc converters", IEEE Trans. Aerosp. Electron. Syst., vol. AES-9, pp.376, 1973.
- [83] R. D Middlebrook, S. Cuk, "A general Unified Approach to Modeling Switching Converter Power Stage", in proceedings of IEEE Power Electronic Specialists Conference PESC, 1976, pp 18-34.
- [84] S. Cuk and R. D. Middlebrook, "A general unified approach to modeling switching DC-to-DC converters in discontinuous conduction mode", in proceedings of IEEE Power Electronic Specialists Conference PESC, 1977, pp.36 -57.
- [85] S. P. Hsu , A. Brown , L. Rensink and R. Middlebrook, "Modelling and analysis of switching dc-to-dc converters in constant-frequency current programmed mode", Proc. IEEE 10th Annu. Power Electron. Spec. Conf., pp.284 -301 1979.
- [86] V. Vorperian y S. Cuk, "Small signal analysis of resonant converters", IEEE Power Electronics Specialists Conference, 1983, págs. 269-282.
- [87] V. Vorperian, "Analysis of Resonant Converters", PhD Thesis, 1984, California Institute of Technology, Pasadena.
- [88] V. Vorperian, "Simplified analysis of PWM converters using model of PWM switch I: Continuous conduction mode", IEEE Trans. Aerosp. Electron. Syst., vol. 26, pp.490 1990.
- [89] V. Vorperian, "Simplified analysis of PWM converters using model of PWM switch. II. Discontinuous conduction mode", IEEE Trans. Aerosp. Electron. Syst., vol. 26, pp.497 1990.
- [90] E. van Dijk, H. J. N. Spruijt, D. M. O'Sullivan, J.B. Klaassens, "PWM-Switch Modeling of DC-DC Converters", IEEE Trans. Power Electron, Vol. 10, No. 6, November 1995, pp. 659-665.
- [91] P. T. Krein, J. Bentsman, R. M. Bass, and B. C. Lesieutre, "On the use of averaging for the analysis of power electronic systems", IEEE Trans. Power Electron., vol. 5, pp.182 -190, 1990.
- [92] S. R. Sanders, J. M. Noworolski, X. Z. Liu, and G. C. Verghese, "Generalized averaging method for power conversion circuits", IEEE Trans. Power Electron., vol. 6, pp.251 -259 1991.

- [93] V. A. Caliskan, G. C. Verghese, and A. M. Stankovic, "Multifrequency averaging of dc/dc converters", *IEEE Trans. Power Electron.*, vol. 14, pp.124 -133 1999.
- [94] R. B. Ridley, "A new, continuous-time model for current-mode control [power convertors]", *IEEE Trans. Power Electron.*, vol. 6, no. 2, 1991, pp. 271-280.
- [95] J. A. Oliver, J. A. Cobos, J. Uceda, M. Rascon and C. Quiones, "Systematic approach for developing large-signal averaged models of multioutput PWM converters", in *Proc. of IEEE PESC 2000*, vol. 2, pp.696.
- [96] J. Sun , D. Mitchell , M. Greuel , P. Krein and R. Bass, "Averaged modeling of PWM converters operating in discontinuous conduction mode", *IEEE Trans. Power Electron.*, vol. 16, no. 4, pp.482 -492 2001.
- [97] Feng Yu, F.C. Lee, P. Mattavelli, "A small signal model for average current mode control based on describing function approach", in *Proc. IEEE Energy Convers. Congr. Expo. (ECCE)*, 2011, pp. 405-412.
- [98] J. Li and F. C. Lee, "New modeling approach and equivalent circuit representation for current-mode control," *IEEE Trans. Power Electron.*, vol. 25, no. 5, May 2010, pp. 1218–1230.
- [99] Y. Yan, F. C. Lee, P. Mattavelli, "Unified Three-Terminal Switch Model for Current Mode Controls", *IEEE Trans. Power Electron.*, vol. 27, no.9, Sept. 2012 , pp. 4060-4070.
- [100] S. Hiti, D. Boroyevich and C. Cuadros, "Small-signal modeling and control of three-phase PWM converters", *Proc. Ind. Appl. Soc. Annu. Meeting*, vol. 2, pp.1143 1994.
- [101] R. Burgos , D. Boroyevich , F. Wang , K. Karimi and G. Francis "On the Ac stability of high power factor three-phase rectifiers", *Proc. 2010 IEEE Energy Convers. Congr. Expo. (ECCE)*, pp.2047-2054.
- [102] S. Ahmed, Z. Shen, P. Mattavelli, D. Boroyevich, M. Jaksic, K. Karimi, J. Fu, "Small-signal model of a voltage source inverter (VSI) considering the dead-time effect and space vector modulation types", *Proc. 26th IEEE Appl. Power Electron. Conf. (APEC 2011)*, pp. 685-690.
- [103] S. D. Sudhoff , "Analysis and average-value modeling of dual line-commutated converter- 6-phase synchronous machine systems", *IEEE Trans. Energy Convers.*, vol. 8, pp.411 1993.
- [104] L. A. Schlabach, "Analysis of discontinuous current in a 12-pulse thyristor DC motor drive", *IEEE Trans. on Industry Applications*, Vol. 27, No. 6, Nov/Dec 1991.
- [105] A. Baghranian and A. J. Forsyth, "Averaged-value models of twelve-pulse rectifiers for aerospace applications", *Proc. 2nd Int. Conf. Power Electronics, Machines and Drives*, vol. 1, pp.220. 2004.
- [106] H. Zhu , R. P. Burgos , F. Lacaux , A. Uan-Zo-li , D. K. Linder , F. Wang and D. Boroyevich "Average modeling of three-phase and nine-phase diode rectifiers with improved ac current and dc voltage dynamics", *Proc. 31st Annu. Conf. IEEE Industrial Electron. Soc.*, pp.1024, 2005.
- [107] R. Burgos, D. Boroyevich, F. Wang, K. Karimi, G. Francis, "Ac stability of high power factor multi-pulse rectifiers", *Proc. 2011 IEEE Energy Convers. Congr. Expo. (ECCE)*, pp. 3758-3765.
- [108] S. Chiniforoosh, H. Atighechi, A. Davoudi, J. Jatskevich, A. Yazdani, S. Filizadeh, M. Saeedifard, J.A. Martinez, V. Sood, K. Strunz, J. Mahseredjian, V. Dinavahi, "Dynamic Average Modeling of Front-End Diode Rectifier Loads Considering Discontinuous Conduction Mode and Unbalanced Operation", *IEEE Trans. Power Delivery*, vol. 27, no. 1, 2012, pp. 421-429.
- [109] R. B. Ridley, "Average small-signal analysis of the boost power factor correction circuit", in *proc. of Virginia Power Electronics Center (VPEC) Seminar*, Blacksburg, September 25-27, 1989, pp. 108-120.
- [110] A. Capel, J. G. Ferrante y R. Prajoux, "Dynamic behaviour and z-transform stability analysis of dc/dc regulators with a non linear PWM control loop", in *proc. of IEEE Power Electron. Specialists Conf. (PESC)*, vol. 1, 1973, pp. 149-157.
- [111] A. Capel, J. G. Ferrante, and R. Prajoux, "State variable stability analysis of multiloop PWM controlled DC/DC regulators in light and heavy mode," in *proc. of IEEE Power Electron. Specialists Conf. (PESC)*, June 1975, pp. 91-103.

- [112] G. C. Verghese, M. E. Elbuluk and J. G. Kassakian, "A general approach to sampled-data modeling for power electronic circuits", *IEEE Trans. Power Electron.*, vol. PE-1, pp.76-86, 1986.
- [113] A. R. Brown and R. D. Middlebrook, "Sampled-data modeling of switching regulators", in *Proc. Power Electronics Specialists Conf.*, June 29-July 3, 1981, pp. 349-369.
- [114] R. D. Middlebrook, "Measurement of loop gain in feedback systems", *International Journal of Electronics*, vol. 38, no. 4, 1975, pp. 485-512.
- [115] P. Maranesi, "Small-signal circuit modeling in the frequency-domain by computer-aided time-domain simulation," *IEEE Trans. Power Electron.*, vol. 7, pp. 83-88, Jan. 1992.
- [116] P. Huynh and B. H. Cho, "Empirical small-signal modeling of switching converters using Pspice", in *proc. of IEEE Power Electronics Specialists Conference (PESC)*, vol. 2, 1995, pp. 809-815.
- [117] J. Y. Choi, B. H. Cho, H. F. VanLandingham, H. Mok and J. H. Song, "System Identification of Power Converters Based on a Black-Box Approach", *IEEE Transactions on Circuit and Systems - I: Fundamental Theory and Applications*, vol. 45, no. 11, 1998.
- [118] R. C. Wong and J. Groves, "An automated small-signal frequency-domain analyzer for general periodic-operating systems as obtained via time-domain simulation", *IEEE Power Electronics Specialists Conf. (PESC)*, pp.801-808, 1995.
- [119] D. Maksimovic, "Automated small-signal analysis of switching converters using a general-purpose time-domain simulator", in *proc. of Thirteenth Annual Applied Power Electronics Conference and Exposition (APEC)*, 1998, vol. 1, pp. 357-362.
- [120] B. Miao, R. Zane and D. Maksimovic, "System identification of power converters with digital control through cross-correlation methods", *IEEE Trans. Power Electron.*, vol. 20, pp.1093-1102, 2005.
- [121] M. Shirazi, J. Morroni, A. Dolgov, R. Zane and D. Maksimovic, "Integration of frequency response measurement capabilities in digital controllers for DC-DC converters", *IEEE Trans. Power Electron.*, vol. 23, pp. 2524-2533, 2008.
- [122] A. Barkley and E. Santi "Improved online identification of a DC/DC converter and its control loop gain using cross-correlation methods", *IEEE Trans. Power Electron.*, vol. 24, pp.2021-2030, 2009.
- [123] T. Roinila, T. Helin, M. Vilkkko, T. Suntio, and H. Koivisto, "Circular correlation based identification of switching power converter with uncertainty analysis using fuzzy density approach," *Simul. Model. Practice Theory*, vol. 17, pp. 1043-1058, 2009.
- [124] T. Roinila, M. Vilkkko, T. Suntio, "Fast Loop Gain Measurement of a Switched-Mode Converter Using a Binary Signal With a Specified Fourier Amplitude Spectrum", *IEEE Trans. Power Electron.*, vol. 24, no. 12, 2009, pp. 2746-2755.
- [125] T. Roinila, M. Vilkkko, T. Suntio, "Frequency-Response Measurement of Switched-Mode Power Supplies in the Presence of Nonlinear Distortions", *IEEE Trans. Power Electron.*, vol. 25, no. 8, 2010, pp. 2179-2187.
- [126] A. Fernandez-Herrero, C. Fernandez, C. Carreras, P. Zumel, A. Lazaro, A. Barrado, "Use of multisine excitations for frequency-response measurement of nonlinear DC-DC switching converters", in *proc. of IEEE 27th Annual Applied Power Electronics Conference and Exposition (APEC)*, 2012, pp. 735-739.
- [127] M. M. Peretz and S. Ben-Yaakov, "Time domain identification of PWM converters for digital controllers design", *Proc. IEEE Power Electron. Spec. Conf.*, pp.809-813, 2007.
- [128] F. Huerta, S. Cóbrecas, F.J. Rodríguez, D. Pizarro, F.J. Meca, "Black-box Identification for an auto-tuned current controller working with Voltage Source Converters connected to the grid through a LCL filter", in *proc. of IEEE International Symposium on Industrial Electronics (ISIE)*, 2010, pp. 96-101.
- [129] B. Johansson and M. Lenells, "Possibilities of obtaining small-signal models of DC-to-DC power converters by means of system identification," in *Proc. Telecommunications Energy Conf.*, 2000, pp. 65-75.

- [130] K. T. Chau y C. C. Chan, "Nonlinear identification of power electronic systems", in proc. of IEEE International Conference on Power Electronics and Drive Systems, vol. 1, 1995, pp 329-334, pp. 329-334.
- [131] R. Leyva, L. Martinez-Salamero, B. Jammes, J.C. Marpinard, F. Guinjoan, "Identification and control of power converters by means of neural networks", IEEE Transactions on Circuits and Systems I: Fundamental Theory and Applications, vol. 44, no. 8, 1997, pp. 735-742.
- [132] F. Alonge, F. D'Ippolito, F. M. Raimondi, S. Tumminaro, "Nonlinear Modeling of DC/DC Converters Using the Hammerstein's Approach" IEEE Transactions on Power Electronics, vol. 22, no. 4, Jul. 2007, pp. 1210 – 1221.
- [133] N. Patcharaprakiti, K. Kirtikara, C. Jivacate, A. Sangswang, K. Tunlasakun, B. Muenpinij, "System identification with cross validation technique for modeling inverter of photovoltaic system", in proc. of 2nd International Conference on Mechanical and Electrical Technology (ICMET), 2010, pp. 594-598.

B.4.2. System-level modeling and identification

- [134] L. Arnedo, "System-Level black-Box Models for Dc-DC Converters", PhD Thesis, 2008, Virginia Polytechnic Institute and State University, Blacksburg.
- [135] J. Oliver, "Modelado Comportamental de Convertidores CC-CC para el análisis y Simulación de Sistemas Distribuidos de Potencia", PhD Thesis, 2007, Universidad Politécnica de Madrid, Madrid.
- [136] J.A. Oliver, R. Prieto, L. Laguna, and J.A. Cobos, "Modeling and simulation requirements for the analysis and design of dc distributed power electronic systems". In proc. of 11th IEEE International Power Electronics Congress (CIEP) 2008, pages 204 -209, 2008.
- [137] B. H. Cho, "Modeling and Analysis of Spacecraft Power Systems", PhD Thesis, 1985, Virginia Polytechnic Institute and State University, Blacksburg.
- [138] B. H. Cho and F. C. Y. Lee "Modeling and analysis of spacecraft power systems", IEEE Trans. Power Electron., vol. 3, pp.44, 1988.
- [139] J.R. Lee, B.H. Cho, S.J. Kim, F.C. Lee, "Modeling and simulation of spacecraft power systems", IEEE. Trans. Aerosp. Electron. Syst., vol. 24, no. 3, 1988, pp. 295-304.
- [140] B. H. Cho, J. R. Lee and F. C. Lee, "Large-signal stability analysis of spacecraft power processing systems", IEEE Trans. Power Electron., vol. 5, pp.110 1990.
- [141] R. D. Middlebrook "Input filter considerations in design and application of switching regulators", Rec.1976 IEEE Ind. Appl. Soc. Annu. Meeting, pp.366 -382.
- [142] T.Suntio, D.Gadoura, "Use of unterminated two-port modeling technique in analysis of input filter interactions in telecom DPS systems" ; in proceedings of The 4th IEEE International Telecommunications and Energy Conference, 29 Sept.-3 Oct. 2002 pp.560 -565.
- [143] S. Vesti, J.A. Oliver, R. Prieto, J.A. Cobos, J. Huusari, T. Suntio, "Practical characterization of input-parallel-connected converters with a common input filter", Proc. 2012 IEEE Appl. Power Electron. Conf. (APEC), pp. 1845-1852.
- [144] L. Arnedo , R. Burgos , F. Wang and D. Boroyevich "Black-box terminal characterization modeling of DC-to-DC converters", Proc. 2007 IEEE Appl. Power Electron. Conf. (APEC), pp.457 -463.
- [145] L. Arnedo, D. Boroyevich, R. Burgos, and F. Wang, "Polytopic black-box modeling of DC–DC converters," in Proc. IEEE Power Electron. Spec. Conf., Jun. 15–19, 2008, pp. 1015–1021.
- [146] L. Arnedo, R. Burgos, D. Boroyevich, F. Wang, "System-Level Black-Box Dc to Dc Converter models", in Proc. of IEEE Appl. Power Electron. Conf. (APEC), Page(s):1476 – 1481, 15-19 Feb. 2009.
- [147] Y. Panov and M. Jovanovic, "Practical issues of input/output impedance measurements in switching power supplies and application of measured data to stability analysis," in Proc. 2005 IEEE Appl. Power Electron. Conf. (APEC), vol. 2, pp. 1339–1345.

- [148] L. Arnedo, D. Boroyevich, R. Burgos, and F. Wang, "Un-terminated frequency response measurements and model order reduction for black-box terminal characterization models," in Proc. IEEE Appl. Power Electron. Conf., Feb. 24–28, 2008, pp. 1054–1060.
- [149] I. Cvetkovic, D. Boroyevich, P. Mattavelli, F. C. Lee, and D. Dong, "Non-linear, Hybrid Terminal Behavioral Modeling of a DC-based Nanogrid System," in proc. of APEC, 2011, pp. 1251-1258.
- [150] I. Cvetkovic, D. Boroyevich, P. Mattavelli, F. C. Lee, and D. Dong, "Un-terminated, low-frequency terminal behavioral model of DC–DC converters," in Proc. IEEE Appl. Power Electron. Conf., Mar. 2011, pp. 1873–1880.
- [151] S. Hiti, V. Vlatokovic, D. Boroyevich, and F. Lee, "A new control algorithm for three-phase PWM buck rectifier with input displacement factor compensation," IEEE Trans. Power Electron., vol. 9, no. 2, pp. 173–180, Mar. 1994.
- [152] M. Belkhat, "Stability criteria for AC power systems with regulated loads," Ph.D. dissertation, Purdue Univ., West Lafayette, IN, 1997.
- [153] D. Boroyevich, R. Burgos, L. Arnedo, and F. Wang, "Synthesis and integration of future electronic power distribution systems," in Proc. of Power Conversion Conf. PCC - Nagoya, Apr. 2–5, 2007, pp. 1–8.
- [154] I. Cvetkovic, M. Jaksic, D. Boroyevich, P. Mattavelli, F.C. Lee, Z. Shen, S. Ahmed, D. Dong, "Un-terminated, low-frequency terminal-behavioral d-q model of three-phase converters", in proc. 2011 IEEE Energy Convers. Congr. Expo. (ECCE), pp. 791 – 798.
- [155] M. Belkhat and M. L. Williams, "Impedance extraction techniques for DC and AC systems," presented at the Naval Symp. Electr. Mach., Philadelphia, PA, 2000.
- [156] Y.A. Familiant, J. Huang, K.A. Corzine, M. Belkhat, "New Techniques for Measuring Impedance Characteristics of Three-Phase AC Power Systems", IEEE Trans. Power Electron., vol. 24, no.7, pp. 1802 – 1810, July. 2009.
- [157] G. Francis, R. Burgos, D. Boroyevich, F. Wang, K. Karimi, "An algorithm and implementation system for measuring impedance in the D-Q domain", proc. 2011 IEEE ECCE, pp. 3221 – 3228.
- [158] J. Huang, K. A. Corzine, and M. Belkhat, "Small-signal impedance measurement of power-electronics-based AC power systems using line-to-line current injection," IEEE Trans. Power Electron., vol. 24, no. 2, pp. 445–455, Feb. 2009.
- [159] J. A. Oliver , R. Prieto , V. Romero and J. A. Cobos "Behavioral modeling of dc-dc converters for large-signal simulation of distributed power systems", Proc. IEEE Appl. Power Electron. Conf. (APEC 2006), pp.1054.
- [160] J. Oliver, R. Prieto, J. Cobos, P. Alou, and O. Garcia, "Hybrid Wiener-Hammerstein Structure for Grey-Box Modeling of DC DC Converters," in Proc. of IEEE Appl. Power Electron. Conf. (APEC), Page(s):280-285, 15-19 Feb. 2009.
- [161] S. Vesti, P. Alou, J.A. Oliver, O. Garcia, R. Prieto and J.A. Cobos, "Modeling and Simulation of a Distributed Power System for Avionic Application", in proc. of ECCE, 2010.
- [162] P. San Roman, J. A. Oliver, P. Alou, O. Garcia, J.A. Cobos, R. Prieto, "Non-linear gain-look-up table based approach for modeling a family of DC to DC converters based on transient response analysis", in proc. of Seminario Anual de Automática, Electrónica Industrial e Instrumentación (SAAEI), Jul. 2011, pp. 107-112.
- [163] J. A. Oliver , R. Prieto , V. Romero and J. A. Cobos "Behavioral modeling of multi-output DC-DC converters for large signal simulation of distributed power systems", Proc. IEEE Power Electron. Spec. Conf. (PESC 2006), pp.1.
- [164] L. Ran, S. Gokani, J. Clare, K. J. Bradley, and C. Christopoulos, "Conducted electromagnetic emissions in induction motor drive systems. II. frequency domain models," IEEE Trans. Power Electron., vol. 13, no. 4, pp. 768–776, Nov. 1998.

- [165] L. Qian, W. Fei, and D. Boroyevich, "Modular-terminal-behavioral (MTB) model for characterizing switching module conducted EMI generation in converter systems," *IEEE Trans. Power Electron.*, vol. 21, no. 6, pp. 1804–1814, Nov. 2006.
- [166] H. Bishnoi, A.C. Baisden, P. Mattavelli, D. Boroyevich, "Analysis of EMI Terminal Modeling of Switched Power Converters", *IEEE Transactions on Power Electronics*, vol. 27, no. 9, 2012, pp. 3924-3933.
- [167] J. Guerrero-Perez, A. Molina-Garcia, J.A. Villarejo, J.A. Fuentes, F. Ruz, "Behavioral modeling and simulation of single-phase grid-connected photovoltaic inverters", in *proc. of Int. Symp. Ind. Electron. (ISIE)*, 2010, pp. 2351-2356.
- [168] K. S. Tam, L. Yang, "Functional models for space power electronic circuits", *IEEE. Trans. Aerosp. Electron. Syst.*, vol. 31, no. 1, 1995, pp. 288-296.
- [169] A. Emadi, "Modeling and analysis of multiconverter DC power electronic systems using the generalized state-space averaging method", *IEEE Trans. Ind. Electron.*, vol. 51, no. 3, 2004, pp. 661-668.
- [170] S. Glover, "Modeling and stability analysis of power electronics based systems", PhD Thesis, 2003, Purdue University, Indiana.
- [171] R. Wang , J. Liu and H. Wang "Universal approach to modeling current mode controlled converters in distributed power systems for large-signal subsystem interactions investigation", *Proc. IEEE Appl. Power Electron. Conf. (APEC)*, 2007, pp.442-448.
- [172] S.V. Bozhko, T. Wu, G.M. Asher, P.W. Wheeler, "Accelerated functional-level modeling of more-electric aircraft electrical power system", in *proc. of Electrical Systems for Aircraft, Railway and Ship Propulsion (ESARS)*, 2010, pp. 1-6.
- [173] P. A. Yeaman, "High Current Low Voltage Solution For Microprocessor applications input", White paper, Vicor Corporation, USA, online available at <http://cdn.vicorpower.com/> (last visit Jun. 2012).
- [174] A. Barrado, D. Izquierdo, C. Raga, M. Sanz, A. Lázaro. "Behavioral Modeling of Solid State Power Controllers (SSPC) for Distributed Power Systems", in *Proc. of IEEE Appl. Power Electron. Conf. (APEC)*, 15-19 Feb. 2009.
- ## B.5. Three Phase Voltage Source Converters
- [175] F. D. Freijedo, J. Doval-Gandoy, O. Lopez, P. Fernandez-Comesana, and C. Martinez-Penalver, "A signal-processing adaptive algorithm for selective current harmonic cancellation in active power filters," *IEEE Trans. Ind. Electron.*, vol. 56, no. 8, pp. 2829–2840, Aug. 2009.
- [176] A. Yazdani and R. Iravani, "Voltage-Sourced Converters in Power Systems", 2010, IEEE/Wiley
- [177] R. Zhang, F. C. Lee, D. Boroyevich and H. Mao, "New high power, high performance power converter systems", *IEEE Trans. Power Electron.*, vol. 15, no. 3, pp.456 - 463 , 2000.
- [178] R. Zhang, "High performance power converter systems for nonlinear and unbalanced load/source", PhD Dissertation, Virginia Polytechnic Institute and State University, Blacksburg, 1998.
- [179] R. H. Park, "Two-reaction theory of synchronous machines generalized method of analysis-part I," *Transactions of the AIEE*, vol. 48, pp. 716- 727, Jul. 1929.
- [180] S. Buso and P. Mattavelli, "Digital Control in Power Electronics" (Synthesis Lectures on Power Electronics), San Rafael, CA: Morgan & Claypool Publisher, 2006.
- [181] P. C. Loh, M. J. Newman, D. N. Zmood, and D. G. Holmes, "A comparative analysis of multi-loop voltage regulation strategies for single and three phase UPS systems," *IEEE Trans. Power Electron.*, vol. 18, no. 5, pp. 1176-1185, Sep. 2003.
- [182] J. Choi and B. Kim, "Improved digital control scheme of three phase UPS inverter using double control strategy," in *Proc. IEEE APEC*, 1997, pp. 820–824.

- [183] M. J. Ryan, R. W. De Doncker and R. D. Lorenz, "Decoupled control of a four-leg inverter via a new 4x4 transformation matrix", *IEEE Trans. Power Electron.*, vol. 16, p.694 , 2001.
- [184] U. B. Jensen, F. Blaabjerg, and K. Pedersen, "A new control method for 400-Hz ground power units for airplanes", *IEEE Trans. Ind. Applicat.*, vol. 36, pp.180 - 187 , 2000.
- [185] U. Borup , P. N. Enjeti and F. Blaabjerg "A new space-vector-based control method for UPS systems powering non-linear and unbalanced loads", *IEEE Trans. Ind. Applicat.*, vol. 37, no. 6, pp.1864 - 1870 , 2001.
- [186] A. Kusko, D. Galler, N. Medora, "Output impedance of PWM UPS inverter-feedback vs. filters", in records of the IEEE Industry Applications Society Annual Meeting, 1990., vol. 2, pp. 1044-1048.
- [187] M. P. Kazmierkowski and L. Malesani, "Current control techniques for three phase voltage-source PWM converters: A survey," *IEEE Trans. Ind. Applicat.*, vol. 45, pp. 691-703, Sept./Oct. 1998.
- [188] P. Mattavelli, "Synchronous-frame harmonic control for high performance AC power supplies," *IEEE Trans. Ind. Applicat.*, vol. 37, pp. 864–872, May/June 2001.
- [189] D. G. Holmes , T. A. Lipo , B. P. McGrath and W. Y. Kong, "Optimized design of stationary frame three phase AC current regulators", *IEEE Trans. Power Electron.*, vol. 24, p.2417 , 2009.
- [190] R.J. Kerkman, T. M. Rowan, "Voltage controlled current regulated PWM inverters", *IEEE Trans. Ind. Applicat.*, vol. 26, no. 2, pp. 244 – 251, 1990.
- [191] P. Varela, D. Meneses, O. García, J. A. Oliver, P. Alou, J. A. Cobos, "Current mode with RMS voltage and offset control loops for a single-phase aircraft inverter suitable for parallel and 3-phase operation modes", in proc. of third IEEE Energy Conversion Congress and Exposition (ECCE), 2011, pp. 2562 – 2567.
- [192] Botteron, F., Pinheiro. H., "Discrete-time internal model controller for three phase PWM inverters with insulator transformer," *Electric Power Applications*, IEE Proceedings, vol. 53, Jan., 2006, pp. 57-67.
- [193] I. Quesada, A. Lazaro, C. Martinez, A. Barrado, M. Sanz, C. Fernandez, R. Vazquez, I. Gonzalez, "Modulation Technique for Low Frequency Harmonic Cancellation in Auxiliary Railway Power Supplies", *IEEE Trans. Ind. Electron.*, vol. 58, no. 9, pp. 3976-3987, 2011.
- [194] Z. Shen, M. Jaksic, S. Ahmed, P. Mattavelli, D. Boroyevich, "Parametric study of dead time effect on three phase AC output impedance of Voltage Source Inverter (VSI)", in proc. of 14th European Conference on Power Electronics and Applications (EPE 2011), 2011, pp. 1 – 8.
- [195] A. M. Hava , R. J. Kerkman and T. A. Lipo, "Simple analytical and graphical methods for carrier-based PWM-VSI drives", *IEEE Trans. Power Electron.*, vol. 14, no. 1, pp. 49 - 61 , 1999.
- [196] C.L. Fortescue, "Method of Symmetrical Coordinates Applied to Solution of Poly-Phase Networks," *Transactions of the AIEE*, Vol.37, pp.1027-1140, 1918.
- [197] Z. Li, Y. Li, P. Wang, H. Zhu, F. Gao, "Three-Phase PWM Inverters with Three-Phase Output Transformer and Three-Phase Filter Inductor", in proc. of International Conference on Electrical Machines and Systems, 2008, ICEMS, pp. 1116-1121.
- [198] D. N. Zmood, "A systematic development of improved linear regulators for sinusoidal power converters", PhD dissertation, Monash University, Victoria, 2002.
- [199] D. N. Zmood, D. G. Holmes, and G. Bode, "Frequency domain analysis of three phase linear current regulators," *IEEE Trans. Ind. Applicat.*, vol.37, pp. 601-610, Mar./Apr. 2001.
- [200] Yifan Zhao, T. A. Lipo, "Space vector PWM control of dual three-phase induction machine using vector space decomposition", *IEEE Trans. Ind. App.*, vol. 31, no. 5, 1995, pp. 1100-1109.

B.6. Fuel Cells

- [201] J.A. Oliver, P. Zumel, M. Sanz, C. Raga, D. Izquierdo, O. Garcia, A. Barrado, R. Prieto, R. Azcona, B. Delicado, J. A. Cobos, "High level decision methodology for the selection of a fuel cell based power distribution architecture for an aircraft application", in proc. of IEEE Energy Conversion Congress and Exposition, ECCE 2009.
- [202] Rajashekara, K.; Grieve, J.; Daggett, D.; "Hybrid fuel cell power in aircraft" IEEE Industry Applications Magazine, vol. 14, n° 4, pp. 54 – 60, Aug. 2008.
- [203] P. Thounthong, B. Davat, S. Rael, P. Sethakul, "Fuel cell high-power applications" IEEE Ind. Electron. Magazine, vol. 3, no. 1, pp. 32-46, Mar. 2009.
- [204] S. Bontour, J. M. Kauffmann, D. Hissel, H. Gualous, and F. Hare, "Design of a Parallel Fuel Cell-Supercapacitor Auxiliary Power Unit (APU)," in proc. of the Eighth International Conference on Electrical Machines and Systems, ICEMS 2005.
- [205] M.R. Nikzad, A. Radan, "Accurate Loss Modelling of Fuel Cell Boost Converter and Traction Inverter for Efficiency Calculation in Fuel Cell-Battery Hybrid Vehicles", in proc. of Power Electronic & Drive Systems & Technologies Conference (PEDSTC), pp. 218-223, 2010.
- [206] F. Segura, J. M. Andújar and E. Durán, "Analog Current Control Techniques for Power Control in PEM Fuel-Cell Hybrid Systems: A Critical Review and a Practical Application", IEEE Trans. Ind. Electron., vol. 58, n° 4 pp. 1171–1184, Apr. 2011.
- [207] J.M. Lee, B.H. Cho, "A Dynamic Model of a PEM Fuel Cell System", in Proc. of IEEE Appl. Power Electron. Conf. (APEC), Page(s): 720 - 724, 15-19 Feb. 2009.
- [208] M. Ordonez, M. O. Sonnaillon, J. E. Quaiçoe, M. T. Iqbal, "An Embedded Frequency Response Analyzer for Fuel Cell Monitoring and Characterization", IEEE Trans. Ind. Electron., vol. 57, no. 6, pp. 1925–1934, Jun. 2010.
- [209] P. Thounthong, B. Davat, S. Ral and P. Sethakul "Fuel starvation: Analysis of a PEM fuel cell system", IEEE Ind. Appl. Mag., vol. 15, p.52, 2009.
- [210] H.J. Avelar, E.A.A. Coelho, J.R. Camacho, J.B.V. Junior, L.C. Freitas, M. Wu, "PEM Fuel Cell Dynamic Model for Electronic Circuit Simulator", in proc. of IEEE Electrical Power & Energy Conference (EPEC), 2009.

B.7. Switched Reluctance Starter Generators

- [211] S. R. MacMinn and W. D. Jones, "A very high speed switched reluctance starter-generator for aircraft engine applications," in Proc. NAECON'89, May 1989, pp. 1758–1764.
- [212] E. Richter, and C. Ferreira, "Performance Evaluation of a 250 kW Switched Reluctance Starter Generator", Rec. of the 1995 IEEE Industry Applications Conference, Vol.1, pp. 434-440.
- [213] C. A. Ferreira, S. R. Jones, W. S. Heglund, and W. D. Jones, "Detailed design of a 30-kW switched reluctance starter/generator system for a gas turbine engine application", IEEE Trans. Ind. Applicat., vol. 31, pp.553 - 561, 1995.
- [214] A. V. Radun, C. A. Ferreira, and E. Richter, "Two channel switched reluctance starter/generator results," IEEE Trans. Ind. Appl., vol. 34, no. 5, pp. 1026–1034, Sep./Dec. 1998.
- [215] S. Shoujun, L. Weiguo, D. Peitsch, U. Schaeferb, "Detailed Design of a High Speed Switched Reluctance Starter/Generator for More/All Electric Aircraft", Chinese Journal of Aeronautics Vol. 23 no. 2, Ap. 2010 pp 216-226
- [216] M. E. Elbuluk and M. D. Kankam, "Potential starter/generator technology for future aerospace application", IEEE Aerosp. Electron. Syst. Mag., vol. 11, pp.17 1996

- [217] L. Han, J. Wang, D. Howe, "Stability Assessment of Distributed DC Power Systems for 'MoreElectric' Aircraft", in proc. of the 4th IET International Conference on Power Electronics, Machines and Drives, 2008, pp. 162 – 166.
- [218] T.L. Skvarenina, S. Pekarek, O. Wasynczuk, P.C. Krause, R.J. Thibodeaux, J. Weimer "Simulation of a switched reluctance, more electric aircraft power system using a graphical user interface", proc. of the 32nd Intersociety Energy Conversion Engineering Conference (IECEC'97), Vol. 1, July 27–August 1 (1997) pp. 580–584
- [219] B. Fahimi , A. Emadi and R. B. Sepe "A switched reluctance machine-based starter/alternator for more electric cars", IEEE Trans. Energy Convers., vol. 19, pp.116 2004
- [220] N. Schofield and S. Long "Generator operation of a switched reluctance starter/generator at extended speeds", IEEE Trans. Veh. Technol., vol. 58, pp.48 2009
- [221] H. Chen and Z. Shao "Turn-on angle control for switched reluctance wind power generator system", Proc. 30th Annu. Conf. IEEE Ind. Electron. Soc., pp.2367 2004
- [222] O. Ichinokura, T. Kikuchi, K. Nakamura, T. Watanabe and H. Guol, "Dynamic simulation model of switched reluctance generator," IEEE Trans. Mag., vol. 39, no.5, Part 2, pp. 3253 - 3255, Sept. 2003.
- [223] F. Soares and P. J. Costa, "Simulation of a 6/4 switched reluctance motor based on Matlab/Simulink environment", IEEE Trans. Aero Electron., vol. 37, no. 3, pp.989 -609, 2001
- [224] Chang Yan Tai; Eric, C.K.W., "A simulation model for a 4 phase switched reluctance motor for PSIM", in proc. of 4th International Conference on Power Electronics Systems and Applications (PESA), 2011
- [225] C. Roux and M. M. Morcos "On the use of a simplified model for switched reluctance motors", IEEE Trans. Energy Convers., vol. 17, 2002.
- [226] C. Zhuping, L. Deliang, "Simulation of Switched Reluctance Starter/Generator System Based on Simpler", in proc. of the 8th Int. Conf. on Electrical Machines and Systems, 2005. ICEMS 2005, vol. 1, pp. 564-567.
- [227] W. Ding, D. Liang, "A Fast Analytical Model for an Integrated Switched Reluctance Starter/Generator", IEEE. Trans. Energy Conv. vol. 25, no. 4, pp. 948-956, Dec. 2010.
- [228] W. Ding and D. L. Liang "Modeling of a 6/4 switched reluctance motor using adaptive neural fuzzy inference system", IEEE Trans. Mag., vol. 44, no. 7, pp.1796 -1804 2008
- [229] X. D. Xue , K. W. E. Cheng and S. L. Ho "Simulation of switched reluctance motor drives using two dimensional bicubic spline", IEEE Trans. Energy Convers., vol. 17, no. 4, pp.471 -477 2002
- [230] C.L. Xia, M. Xue, T.N. Shi, "A new rapid nonlinear simulation method for switched reluctance motors", IEEE. Trans. Energy Convers., 2009.
- [231] D. B. Wicklund and D. S. Zinger, "Voltage feedback signal conditioning in switched reluctance generation systems", Proc. IEEE Appl. Power Electron. Conf. Expo, pp.376 2000.
- [232] T.J.E. Miller, "Switched Reluctance Motors and Their Control", Oxford, UK: Magma Physics Publishing and Clarendon Press-Oxford, 1993
- [233] T.J.E. Miller, "Optimal design of switched reluctance motors", IEEE Trans. Ind. Electron., volume: 49 Issue: 1, pp. 15 - 27, Feb 2002
- [234] D. A. Torrey, "Switched reluctance generators and their control", IEEE Trans. Ind. Electron., vol. 49 no. 1, Feb. 2002, pp. 3-14.
- [235] F. Blaabjerg , P. C. Kjaer , P. O. Rasmussen and C. Cossar, "Improved digital current control methods in switched reluctance motor drives", IEEE Trans. Power Electron., vol. 14, p.563 , 1999.
- [236] Y. Chang and C. Liaw, "On the design of power circuit and control scheme for switched reluctance generator", IEEE Trans. Power Electron., vol. 23, p.445 , 2008.

- [237] H. Hannoun, M. Hilaiet, C. Marchand, “Design of an SRM Speed Control Strategy for a Wide Range of Operating Speeds”, IEEE Trans. on Ind. Electron., vol .57 no.9, Sept. 2010, pp. 2911 – 2921
- [238] Lukic, Srdjan M. Emadi, Ali, ”State-Switching Control Technique for Switched Reluctance Motor Drives: Theory and Implementation”, IEEE Transactions on Ind. Electron., Vol.57, Iss.9, pp.2932, Sept. 2010.

B.8. Solar arrays and solar array simulators

- [239] W. Koestler, M. Meusel, T. Kubera, & T. Torunski, “Triple Junction Solar Cells With 30.0% Efficiency and next generation cell concepts”, in proc. of 9th European Space Power Conference (ESPC), Jun. 2011.
- [240] P. Rueda, E. Fernandez. “Multi-junction Ga/As Solar Cell Capacitance and its Impact upon SA Regulators”, in proc. of the 6th European Space Power Conference (ESPC), May 2002.
- [241] Neugnot, N., Barde, H., Baur, C., de Luca, A., Chouffot, R., Gueunier-Farret, M., Kleider, J.P., “Dynamic Modelling of Multi Junction GaAs SAs”, proc. of the 8th ESPC, Sept 2008.
- [242] A. Garrigos, J.M. Blanes, J.A. Carrasco, J.B. Ejea, “Influence of the Parasitic Solar Array Capacitance in the Sequential Switching Shunt Series Regulator”, in proc. of IEEE Mediterranean Electrotechnical Conference, MELECON, pp:1198-1201, 16-19 May 2006.
- [243] A. Tambini, F. Antonini, A. Corbelli, F. Rossi & Tortora, “Solar Array Simulator for Microsatellites Power System Testing”, in proc. of 9th European Space Power Conference (ESPC), Jun. 2011.
- [244] N. Schmitz, G. Carroll & R. Clegg, “A Practical Guide to Solar Array Simulation and PCDU test”, in proc. of 9th European Space Power Conference (ESPC), Jun. 2011.
- [245] M.G. Villalva, J.R. Gazoli, E.R. Filho, “Comprehensive Approach to Modelling and Simulation of Photovoltaic Arrays” IEEE Trans. Power Electron., vol. 24, no. 5, pp. 1198-1208, May. 2009
- [246] Azurspace Solar Power GmbH website: “<http://www.azurspace.com/index.php?page=12>” (last visit April 2012).

B.9. Various

- [247] Oppenheim, A.V., R.W. Schafer, “Discrete-Time Signal Processing,, 2nd”, Prentice-Hall, 1999.
- [248] S.J. Orfanidis, “Introduction to Signal Processing”, Prentice-Hall, Englewood Cliffs, NJ, 1996.
- [249] A. S. Sedra, K. C. Smith, “Microelectronic circuits 4th ed.”, 1997, Oxford University Press
- [250] H. D. Venable, “ The K Factor: A New Mathematical Tool for Stability Analysis and Synthesis”, in proc. of Powercon 10, March 1983.
- [251] B. Moore, "Principal component analysis in linear systems: Controllability, observability, and model reduction," IEEE Transactions on Automatic Control, vol.26, no.1, pp. 17-32.
- [252] P. Kokotovic; P Sannuti, “Singular perturbation method for reducing the model order in optimal control design” IEEE Transactions on Automatic Control, Volume 13, Issue 4, Aug 1968 pp.377 – 384.
- [253] G. Strang, “Linear Algebra and its Applications” Academic Press, 1980.

B.10. Technical notes, datasheets and software tools

- [254] MATLAB R2008b <http://www.mathworks.com/>
- [255] PSIM 9.0, Powersim Inc., <http://www.powersimtech.com/>
- [256] PTN78020A wide-input adjustable positive-to-negative voltage regulator module. Datasheet, available at (2011): <http://www.ti.com/lit/ds/slts244a/slts244a.pdf>
- [257] UCH-12/12.5-D48NB-C isolated half-brick power converter. Datasheet, available at (2011): http://www.murata-ps.com/data/power/uch_series.pdf

- [258] UC3843A high performance current mode PWM controller datasheet, available at (2011): <http://www.datasheetcatalog.org/datasheet/SGSThompsonMicroelectronics/mXstrqs.pdf>
- [259] LPS-208-M Power Supply. Technical reference note available at (2011): https://www.powerconversion.com/assets/trn_ac-dc_lps200-m_series_rele1308697907_techref.pdf
- [260] L. Ljung, “System Identification Toolbox”, User’s Guide v.R2011b, The Mathworks Inc, available at http://www.mathworks.com/help/pdf_doc/ident/ident.pdf (last visit, Nov. 2011).
- [261] “Control System Toolbox”, User’s Guide v.R2012b, The Mathworks Inc, available at http://www.mathworks.co.jp/help/pdf_doc/control/get_start.pdf (last visit, Feb. 2013).
- [262] Texas Instruments application notes, ““Hot Plug-in” In-rush Current Limiting Circuits for Power Trends’ DC-DC Converter”, Aug. 2000, available at (2011) <http://www.ti.com/lit/an/slta021a/slta021a.pdf>
- [263] MIL-STD-704F, Military Standard, Aircraft Electrical Power Characteristics.
- [264] PTN78020W wide-input adjustable step-down switching regulator. Datasheet online available at <http://focus.ti.com/lit/ds/symlink/ptn78020w.pdf> (last visit, Nov. 2011).
- [265] Tektronix technical documents. TDS5000B, TDS6000B, TDS/CSA7000B Series Acquisition Modes. Online available at: <http://www2.tek.com/cmswpt/tidetails.lotr?ct=TI&cs=apn&ci=2305&lc=EN> (last visit, May 2012).
- [266] OKX T/10 & T/16-D12 Series DC-DC converters. Datasheet online available at <http://www.murata-ps.com/data/power/okx-t10-t16-d12.pdf> (last visit, May. 2012).
- [267] Space Engineering Electrical and Electronic Standard - ECSS EST 20C–European Coordination on Space Standardization, 31 July 2008.
- [268] Azur-Space 3G-28% 3JGaAs solar cell datasheet. Available online at: <http://azurspace.de/index.php?mm=89> (last access, April 2012).
- [269] <http://www.nedstack.com/products/nedstack-p5-hp> (available October 2011).